Models for the H Cluster of the [FeFe]-Hydrogenase: Synthesis, Protonation and Electrochemical Investigations

DISSERTATION

zur Erlangung des akademischen Grades
doctor rerum naturalium (Dr. rer. nat.)

vorgelegt dem Rat der Chemisch-Geowissenschaftlichen Fakultät der
Friedrich-Schiller-Universität Jena

seit 1558

von M.Sc. Laith Almazahreh
geboren am 10.12.1981 in Amman/Jordanien

1. Professor Dr. Wolfgang Weigand, Friedrich-Schiller-Universität Jena

2. Professor Dr. Mohammad El-khateeb, Jordan University of Science and Technology

3. Professor Dr. Philippe Schollhammer, Universite de Bretagne Occidentale

Tag der öffentlichen Verteidigung: 24.06.2015

"Water as a fuel for the future is no pipe dream"

Contents

Abbreviations and Symbols

Anal. calcd	analytical calculated (elemental analysis)
ap	apical
a.u.	atomic unit
ax	axial
ba	basal
bdt	benzenedithiolate
br	broad (IR spectroscopy)
Bu	butyl
C.E.	catalytic efficiency
CpI	*Clostridium pasteurianum* [FeFe]-hydrogenase I
CV	cyclic voltammetry
Cys	cysteine
d	doublet (NMR spectroscopy)
d	diameter
DdH	*Desulfovibrio desulfuricans* [FeFe]-hydrogenase
DEI	direct electron impact
DFT	Density functional theory
DMD	dimethyldioxirane
DMSO	dimethylsulfoxide
dppe	1,2-bis(diphenylphosphanyl)ethane
$dppnO_2$	1,8-bis(diphenylphospineoxide)naphtalen
dppv	*cis*-1,2-bis(diphenylphosphino)ethylene
$E°$	standard potential
$E_{1/2}$	half-wave potential
E_{app}	applied potential
E_{cat}	potential of catalysis
$E°_{ov}$	overall standard potential ($= ½ \{E°_1 + E°_2\}$),
E_{ox}	oxidation potential
E_{pa}	anodic peak potential
E_{pc}	cathodic peak potential
$E°_{HA}$	standard reduction potential of acid HA

EC process	electrochemical-chemical process
EPR	electron paramagnetic resonance
eq	equatorial
equiv.	equivalent(s)
ESI	electrospray ionization
Et	ethyl
Et_2O	diethyl ether
F	Faraday constant
FAB	fast atom bombardment
Fe_d	distal Fe atom
Fe_p	proximal Fe atom
fac-	facial (stereochemistry)
h	hour
H cluster	Hydrogen activating cluster
H_{ox}	H cluster in the oxidized state
H_{red}	H cluster in the reduced state
HOTf	triflic acid
HOTs	*p*-toluenesulfonic acid
I	current
I_{cat}	catalytic current
I_d	current in the absence of acid
I_{pa} or I_p^a	anodic peak current
I_{pc} or I_p^c	cathodic peak current
IR	infrared
iR	uncompensated resistance (*iR* drop)
J	coupling constant
K	equilibrium constant
K_{disp}	equilibrium constant of disproportionation
k	rate constant
L	not clearly defined ligand
m	multiplet
M	metal (M-M bond refers to metal-metal bond)
Me	Methyl
min	minute(s)

m.p.	melting point
m/z	mass-to-charge ratio
MS	mass spectrometry
n	number of electrons
NHE	normal hydrogen electrode
NMR	nuclear magnetic resonance
Ph	phenyl
pK_a	-logK_a, where K_a is the acid dissociation constant
ppm	parts per million
Pr	propyl
PTA	1,3,5-triaza-7-phosphaadamantane
R	organic substituent such as Et, Me, Ph, etc
R	gas constant
RS1 / RS2	reduction step 1 / reduction step 2
r.t.	room temperature
s	singlet (NMR spectroscopy) or second(s) (unit of time)
T	temperature
t	triplet
t-	descriptor for terminal
THF	tetrahydrofuran
TLC	thin layer chromatography
TOF	turnover frequency (TOF)
X	halogen, particularly Cl, Br and I or it could other atoms
v	scan rate
μ	micro
μ-	descriptor for bridging
υ(CO)	carbonyl wavenumber (IR spectroscopy)
δ	chemical shift (NMR spectroscopy)
τ	torsion angle
Θ	twist angle
α	flap angle
κ	shows hapticity in σ-bonding ligands
η	shows hapticity in π-bonding ligands
η	overpotential

Chapter 1
Introduction
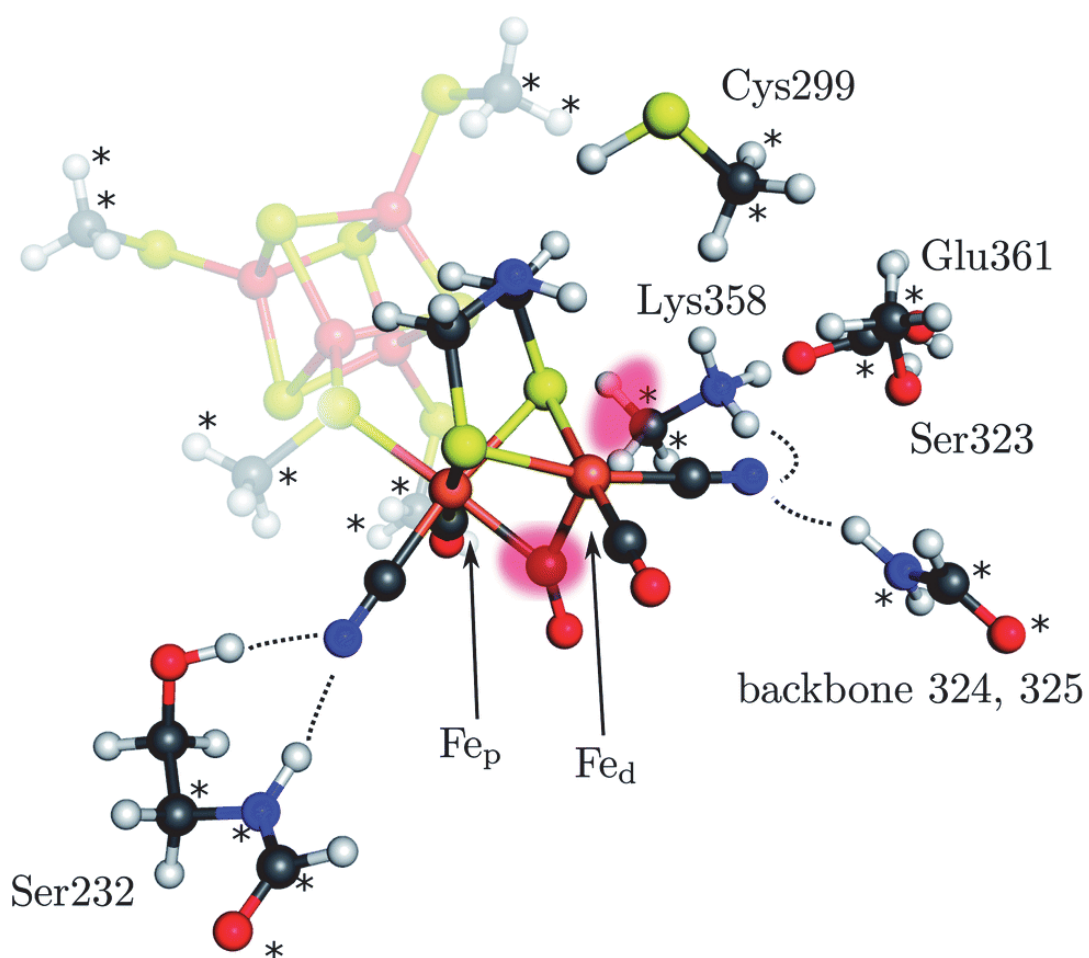
Finkelmann, A. R.; Stiebritza, M. T.; Reiher; M. *Chem. Sci.*, **2014**, *5*, 215

1   Introduction

1.1   The Hydrogen Economy

In step with population growth and industrial advance, global demand for energy has risen inexorably and the major sources of energy are fossil fuels (coal, oil, and natural gas). These fuels are non-renewable and will, one day, be exhausted. Moreover, hydrocarbon fuels produce massive emission of greenhouse gases that are considered to be the main reason of the climate change.[1] In comparison, hydrogen is a promising fuel for the future by virtue of its high energy density[2] and its clean cold combustion product in fuel cells[3]. However, hydrogen is not a primary energy source, but it is instead an energy carrier and it must be manufactured from feedstocks that contain hydrogen compounds. The main methods of producing hydrogen are: Electrolysis[4], natural gas reforming[5] and gasification of coal[6] and biomass[7]. An overview of the various feedstocks and process technologies for hydrogen production is presented in Figure 1-1.
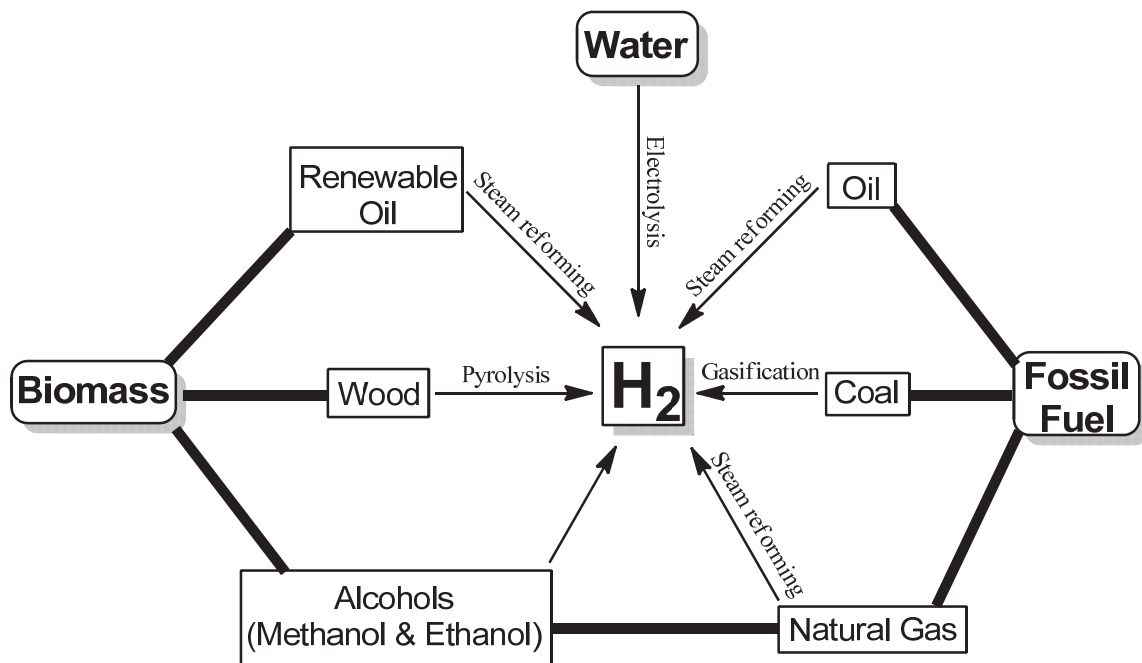
Figure 1-1. Feedstocks and technologies for H_2 production in industry.[4-7]

The cleanest way to produce hydrogen is by electrolysis of water, which is renewable, as it produces only oxygen besides the hydrogen.[3,4] For these reasons, electrolysis is often suggested for the hydrogen economy[8] in the future. A simplified overview of the hydrogen economy is presented in Figure 1-2. To replace the current hydrocarbon economy[5-7] by hydrogen economy, several fundamental problems must be solved vis-à-vis hydrogen generation, storage, transportation and utilization. For the hydrogen economy, a catalyst is necessary for electrolysis and fuel cells. The best known catalyst is Pt,[9] which is very expensive and hence limits the widespread adoption of hydrogen economy. Accordingly, the challenge is to develop a cheap, efficient (low overpotential and high catalytic activity) and robust catalyst as an alternative for Pt.
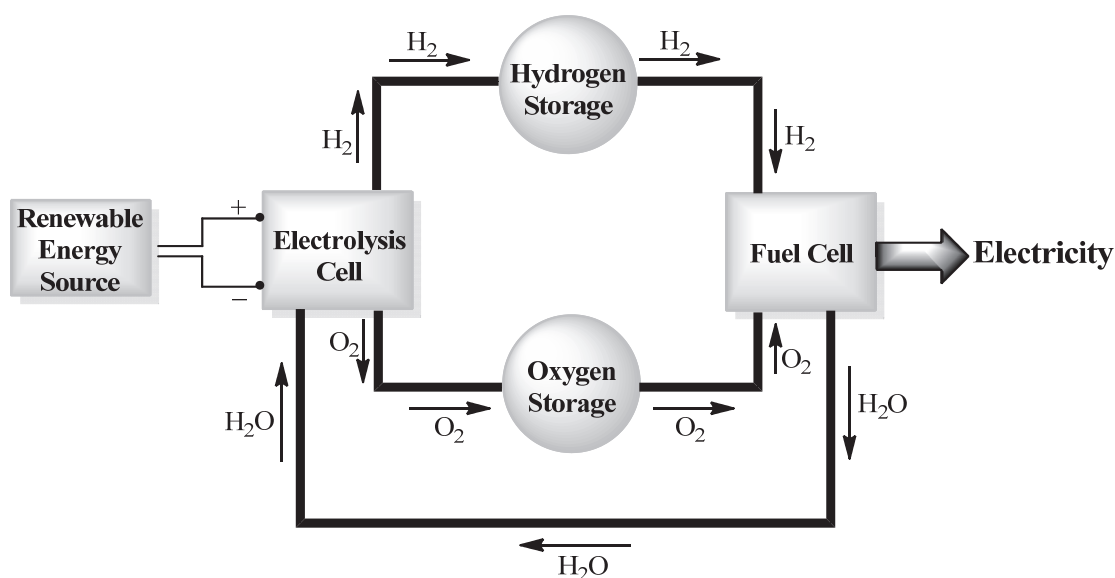
Figure 1-2. Simplified overview for hydrogen economy.[5,8,9]

Indeed, the production and the oxidation of hydrogen are catalyzed in nature with high efficiency and low energy features through enzymes called *hydrogenases*.[10,11] These enzymes are classified into three types based on the metal content of their active site: (*i*) [Fe]-hydrogenases, (*ii*) [FeFe]-hydrogenases and (*iii*) [NiFe]-hydrogenases.[10,11] This thesis focuses on the synthesis of model catalysts mimicking the structure and function of an organometallic cluster, so called H cluster, in the active site of the [FeFe]-hydrogenases.

1.2   [FeFe]-Hydrogenases

[FeFe]-hydrogenases[11] have high ability to catalyze the reversible reduction of protons to generate dihydrogen molecules H_2 (6000-9000 $H_2 \cdot s^{-1}$ per site).[11b,11m]

$$2H^+ \;+\; 2e^- \; \underset{\longleftarrow}{\overset{\text{[FeFe]-hydrogenase}}{\longrightarrow}} \; H_2$$
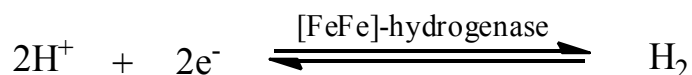
This process occurs in microorganisms at neutral pH and potential of -0.42 V (vs NHE).[11n,11o] These H_2 molecules are used as energy source and transporter in the biological systems.[12] The site of catalysis of [FeFe]-hydrogenases (the active site) contains an organometallic cluster termed as "H cluster" (Figure 1-3), from "hydrogen-activating cluster".[11] A small protein containing iron and sulfur atoms organized as iron-sulfur clusters, in *Clostridium pasteurianum* [FeFe]-hydrogenase I (CpI), called *ferredoxin*, acts as electron transfer agent to provide electrons for production of H_2 molecules.
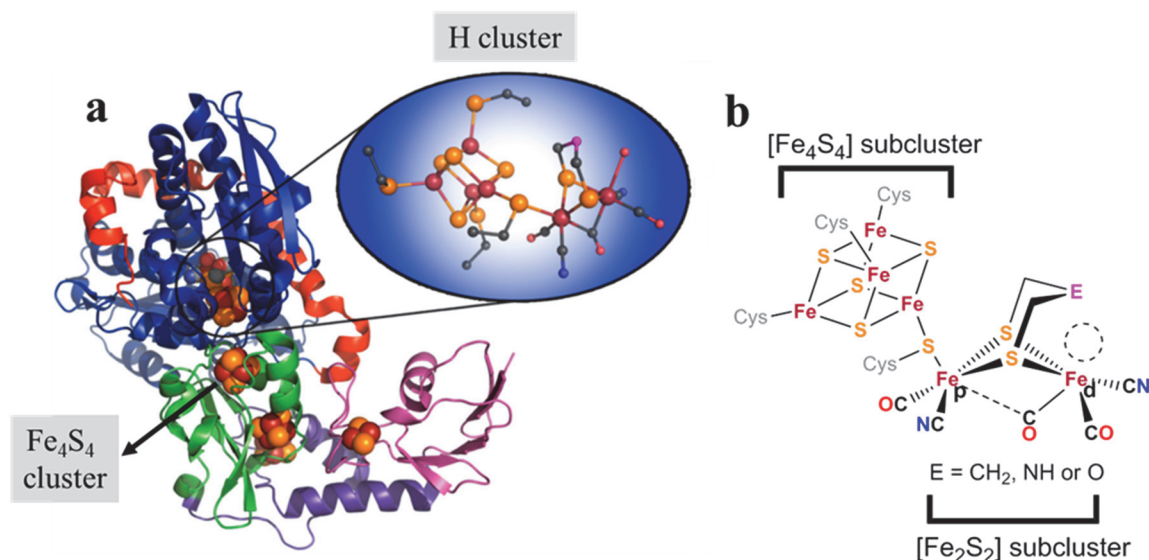
Figure 1-3.[13] (a) Overall fold of Clostridium pasteurianum (CpI) [FeFe]-hydrogenase in domains, which are represented with different colors: C terminus (red), catalytic domain (blue) and ferredoxin-like domains (green, purple, and magenta). The [Fe4S4] clusters and the H cluster are shown as space filling models and zoom of the H cluster as ball and stick representation: rust (Fe), orange (S), black (C), red (O), blue (N), and magenta (unknown E). (b) Schematic representation of the H cluster: Fe$_d$ and Fe$_p$ are distal and proximal Fe atoms, respectively, with respect to the [Fe4S4] subcluster. The dashed circle represents a vacant site.

Crystallographic and spectroscopic studies have shown that the H cluster consists of two Fe atoms making Fe-Fe bond, dithiolato bridge between these Fe atoms forming butterfly structure of the [Fe$_2$S$_2$] core, two unusual types of ligands (CO, CN$^-$) in the coordination sphere of each Fe atom and a [Fe$_4$S$_4$] subcluster bonded to one Fe atom through cysteine thiolate. The [Fe$_4$S$_4$] subcluster is anchored to the protein by three cysteines from the backbone of the protein. The nature of group E in the dithiolato ligand was unknown for long time as to whether it is CH$_2$, NH or O. Earlier structural, theoretical and spectroscopic work suggest that the azadithiolato ligand is most likely.[14-20] Very recently, Lubitz and others provided an experimental evidence that the native dithiolato ligand is the azadithiolate.[21,22] The CN$^-$ ligands of the H cluster interact through hydrogen bonding with the surrounding amino acids (Figure 1-4).[11g,11p] The lysine (Lys237) is closely positioned (440 pm) to the distal iron atom (Fe$_d$) and can act as a possible proton distributor during the dihydrogen production.[11g]
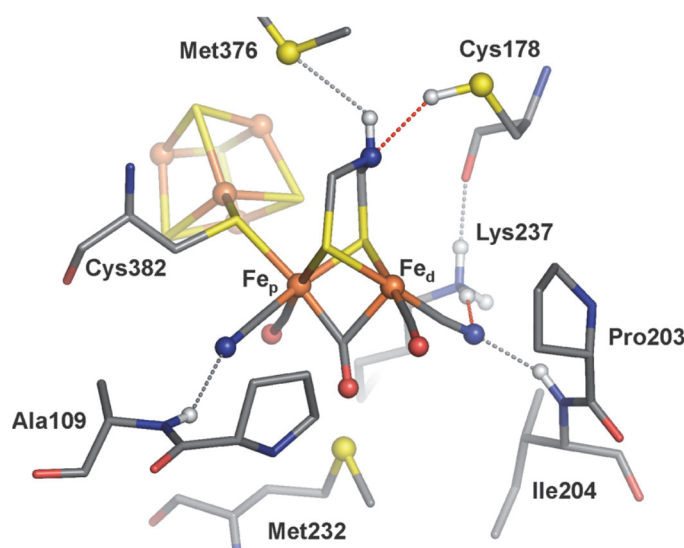
Figure 1-4. Hydrogen bonding between the CN$^-$ ligands of the H cluster (E = NH) and the surrounding amino acids.[11g,11p]

The catalytic mechanism for H$_2$ evolution by the H cluster is not known definitively, nevertheless several feasible mechanisms have been proposed based on theoretical studies.[15-17,23,24] The protonation of the [Fe$_2$S$_2$] core to form terminal or bridging hydrides is a central mechanistic step. Scheme 1-1 shows one of the proposed mechanisms for proton reduction cycle catalyzed by the H cluster with azadithiolato ligand that offers a protonation site at the NH group.[15-17,23,24] As shown in Scheme 1-1, the one-electron

reduction of H_{ox} state[25] moves its semi-bridging CO ligand to a terminal position in H_{red} state[25]. Protonation of the NH group of H_{red} is followed by relay proton to the vacant site via agostic interaction affording a terminal-hydride species. A second protonation step occurs again at the NH group to afford an intermediate with hydride and proton in close proximity. The one-electron reduction of this intermediate releases H_2 molecule via proton relay to close the cycle. The enzymatic catalytic H_2 release and uptake is reversible being dependent upon the concentration of H_2 at the active site. The activity of the enzyme in catalyzing the reaction $H^+ + e^- \leftrightarrow \frac{1}{2} H_2$ is attributed to a structural feature, termed *rotated structure*, which offers a vacant site at Fe_d atom in H_{red} and H_{ox} states. The catalytic formation of H_2 requires interaction of H^+ at the vacant site of H_{red} and the oxidation of H_2 occurs catalytically through binding at the vacant site of H_{ox}.

Scheme 1-1. Possible Catalytic Cycle for H_2 Evolution by [FeFe]-Hydrogenases.[a,15-17,23,24]
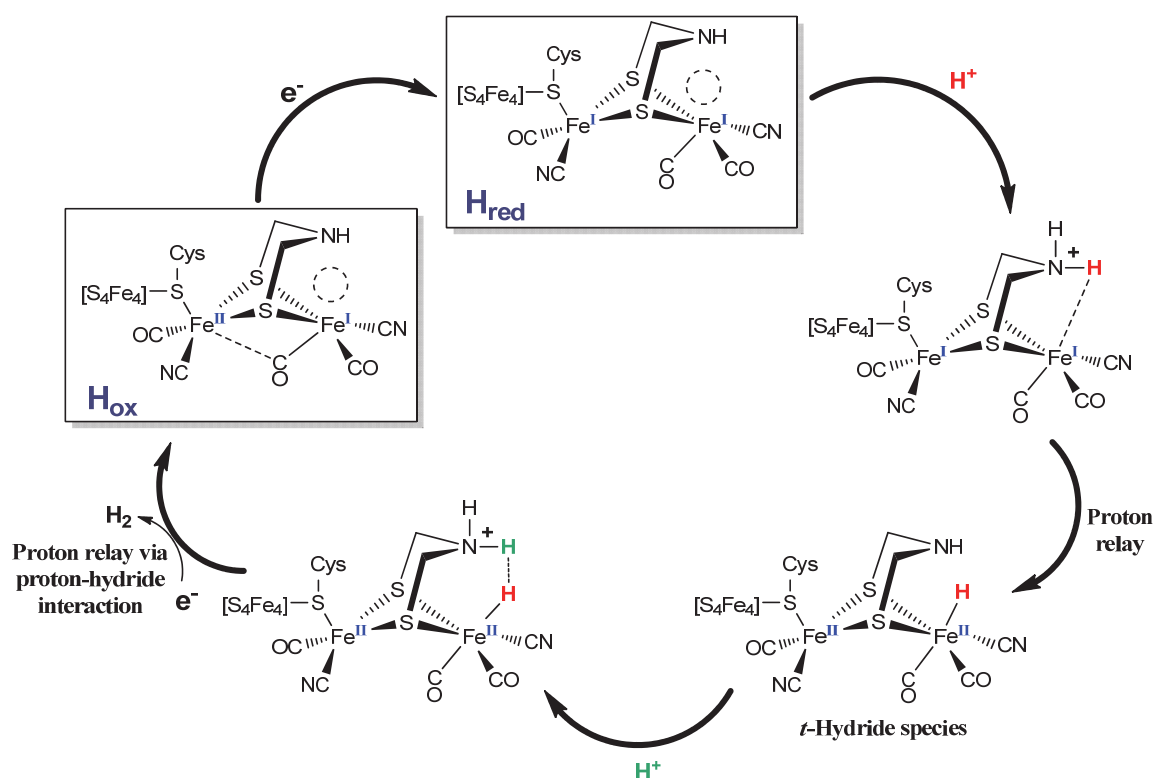
[a] Two states of the H cluster have been demonstrated to be involved in the catalytic cycle are the oxidized H_{ox} and the reduced H_{red} states. Two main differences between H_{ox} and H_{red} states can be seen: (*i*) the oxidation state (indicated in blue) of the Fe_p atom is +2 in H_{ox} and +1 in H_{red}, while it is +1 for Fe_d in both states and (*ii*) one CO ligand is in semi-bridging fashion in H_{ox}, while it is terminal in H_{red}. Based on IR and EPR measurements, five different electronic states (redox states) of the H cluster could be demonstrated.[25]

1.3　　　Synthetic Models for the H Cluster

1.3.1　　　Overview

The high catalytic efficiency and low energy features were the impetus to chemists and engineers for paving the way to macroscale hydrogen production, based on designing of *inexpensive* electrocatalyst model that mimics the structure and function of the H cluster. The synthetic chemistry of compounds structurally related to the H cluster dates back to 1929, when Reihlen et al. described the reaction between $Fe(CO)_5$ and EtSH to afford $[Fe_2(CO)_6\{\mu\text{-}(SEt)_2\}]$ (**1**) (Figure 1-5), but in low yield.[26] In 1937 Hieber et al. introduced a new synthetic approach of these systems using $Fe_3(CO)_{12}$ instead of $Fe(CO)_5$, which resulted in higher yields of $[Fe_2(CO)_6\{\mu\text{-}(SR)_2\}]$.[27] King showed in 1962 that dithiols could be used as well and synthesized $[Fe_2(CO)_6\{\mu\text{-}(SCH_2)_2\}]$ (**2**), Figure 1-5.[28] The molecular structure of complex **1** was reported in 1963 by Dahl and Wei showing butterfly structure of the $[Fe_2S_2]$ core.[29] In 1982, Huttner et al. synthesized the complex $[Fe_2(CO)_6\{\mu\text{-}(SCH_2)_2CH_2\}]$ (**3**), Figure 1-5.[30] In 1999, the molecular structure of the H cluster has been unraveled by two independent groups from two different organisms (DdH and CpI).[31,32] The striking structural resemblance between these complexes (**1**, **2** and **3**) and the H cluster was then recognized (Figure 1-5), which inspired the chemists to synthesize numerous model complexes in order to mimic and to provide a better understanding of the structure and function of the H cluster.

An important development in the synthetic chemistry of this type of molecules was the demonstration in 1999 that two CO ligands of complex **3** could be replaced by cyanide, to give water-soluble dianion **4** (Scheme 1-2).[33-35]
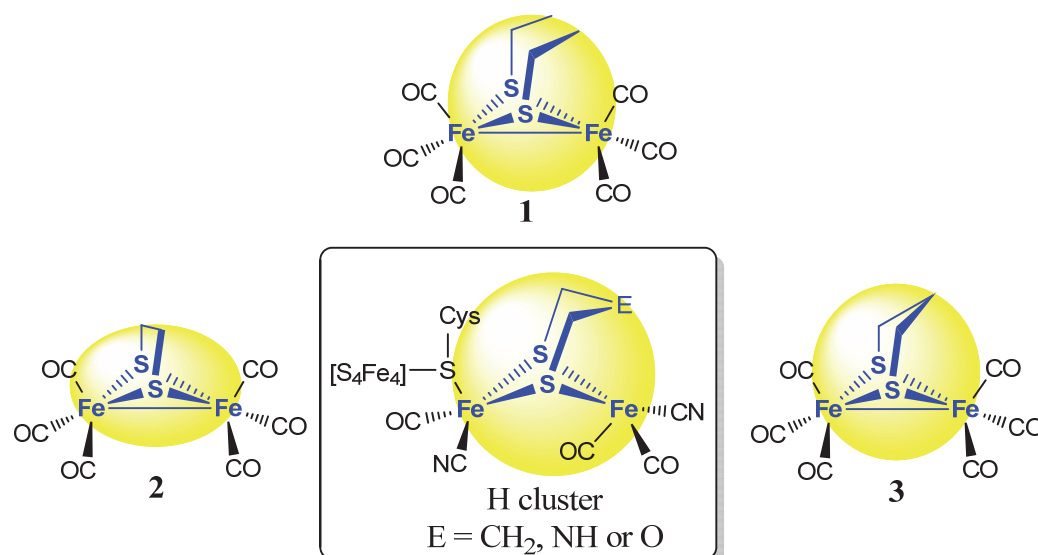
Figure 1-5. Structural resemblance between the H cluster and complexes **1**, **2** and **3**.

Scheme 1-2. Substitution of two CO ligands in complex **3** by two CN⁻ ligands to afford complex **4**.
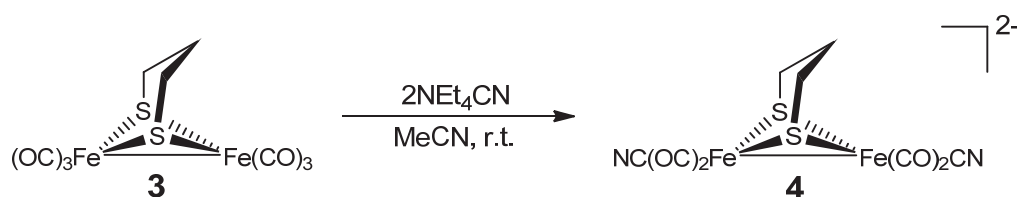
In 2001, Rauchfuss et al. reported the synthesis of complex **5** with azadithiolato ligand (Figure 1-6) by treatment of the in situ generated $[Fe_2(CO)_6\{\mu\text{-}(S^-Li^+)_2\}]$ with bis(chloromethyl)amines, $(ClCH_2)_2NMe$.[36] Furthermore, cyanide-disubstituted complex **6** (Figure 1-6) was prepared.[36] The method described for the synthesis of complex **5** was not successful in affording a complex with the actual dithiolate $-S\text{-}CH_2\text{-}NH\text{-}CH_2\text{-}S\text{-}$. Consequently, Rauchfuss et al. developed a new approach to the NH-bridgehead complex **7** (Figure 1-6) via the condensation of metal sulfides, formaldehyde and primary amine.[37] Complex **8** (Figure 1-6) containing oxygen atom in the bridgehead of the dithiolato ligand was also synthesized by Rauchfuss in 2002 followed by Song and coworkers.[37] Although each iron atom has Fe^I state, these model complexes are diamagnetic due to the Fe-Fe bonding.
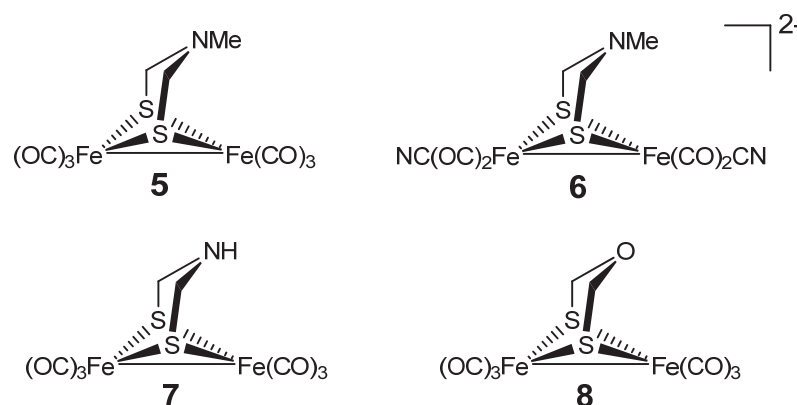
Figure 1-6. Early model complexes of the H cluster.[36,37]

Following these earlier model complexes, the synthetic chemistry has led to numerous [Fe^{I}Fe^I]-hydrogenase model complexes based on:

(i)   altering the bridge in [Fe$_2$(CO)$_6${μ-dithiolate}] (examples in Figure 1-7),

(ii) replacing the S atoms with Se and Te as well as P or N atoms (Figure 1-8) and

(iii) substituting CO ligands by cyanide, phosphanes, phosphites or carbenes (Figures 1-9 to 1-11).
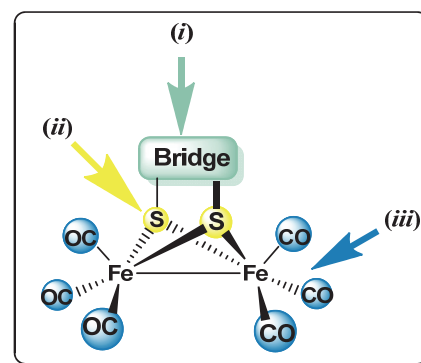
1.3.2   Hexacarbonyl Model Complexes

The complexes shown in Figure 1-7 are termed in the literature as "hexacarbonyl complexes" because their Fe centers contain six CO ligands. Weigand et al. reported series of dithiolate hexacarbonyl complexes in which the typical bridgehead E in the linker -S-CH$_2$-E-CH$_2$-S- (E = CR$_2$, NH or O) is replaced by Se, S as well as SiR$_2$, complexes **23-25**.[47-49] Glass et al. described the synthesis of complex **26** with SnMe$_2$ group in the bridgehead of the dithiolato linker.[50] Moreover, complexes with various R groups bound to the bridgehead, **9-22**,[38-46] or with μ-arenedithiolate, **27-30**,[51-56] have been also reported. Whereas the typical linker between the two Fe atoms is a dithiolate, synthetic hexacarbonyl complexes (Figure 1-8) with diselenate (**32**, **33**, **35-43** and **47**),[58,59,61-64] ditellurate (**34**, **44** and **48**)[60,64,66] and even mixed linkers (**45** and **46**)[65] have

been also reported, notably by Weigand et al. as well as Song et al. Even complexes with μ-N or μ-P atoms are reported, **49-51**.[68-70]

9: R^1 = OH,[38] **10**: R^1 = Me, R^2 = CH_2OH,[39] **11**: R^1 = Me, R^2 = CH_2NH_2,[39] **12**: R^1 = R^2 = Me,[40] **13**: R^1 = R^2 = Et,[40] **14**: R^1 = *n*-Bu, R^2 = Et,[40] **15**: R^1 = COOMe, R^2 = NHBoc (Boc = tert-butoxycarbonyl),[41] **16**: R^1 = COOH,[42] **17**: R^1 = C(O)NHPh[42]

R = *i*-Pr (**18**),[43] CH_2Ph-2-Br (**19**),[44] CH_2CH_2OMe (**20**),[43]

$(H_2C)_2OC$ (**21**),[45] H_2C (**22**)[46]

X = S (**23**),[47] Se (**24**),[48] $SiMe_2$ (**25**),[49] $SnMe_2$ (**26**)[50]

27: R = H,[51-55] **28**: R = Cl,[53] **29**: R = OH,[55,56] **30**: R = OMe[56]

R = H (**31a**),[57] NHCOMe (**31b**),[57] $NHCOCF_3$ (**31c**),[57] NHCOPh (**31d**),[57] NHCO(4-FC_6H_4) (**31e**)[57]
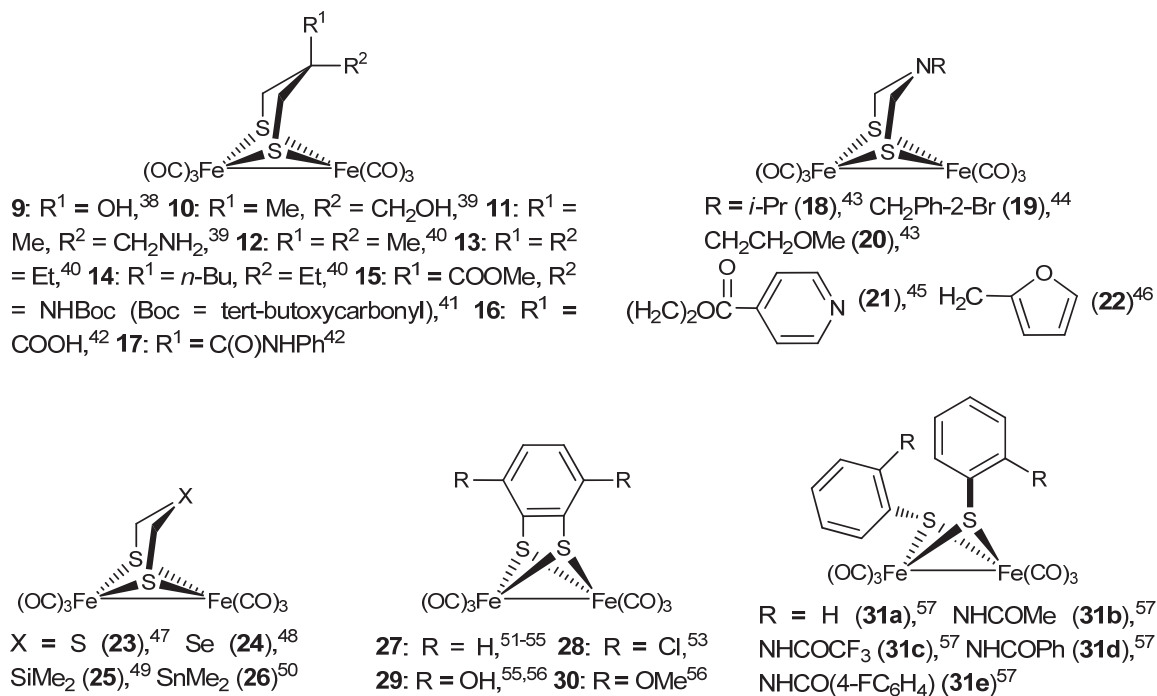
Figure 1-7. Model complexes with various bridges. R = H atom if not specified.

32: R = H, X = Se[58,59]
33: R = Me, X = Se[58]
34: R = H, X = Te[60]

X = S (**35**),[61] Se (**36**),[61] NPh (**37**),[62]
NH (**38**),[63] N(CH$_2$)$_2$OH (**39**),[63]
NCOPh (**40**),[63] NCOMe (**41**),[63]
NCO$_2$CH$_2$Ph (**42**)[63]

X = Se (**43**),[64] Te (**44**)[64]

X = Se (**45**),[65] Te (**46**)[65]

X = Se (**47**),[66] Te (**48**)[66]

49[67]

X = CH$_2$ (**50a**),[68]
N(CH$_2$)$_2$OMe (**50b**)[69]

51[70]
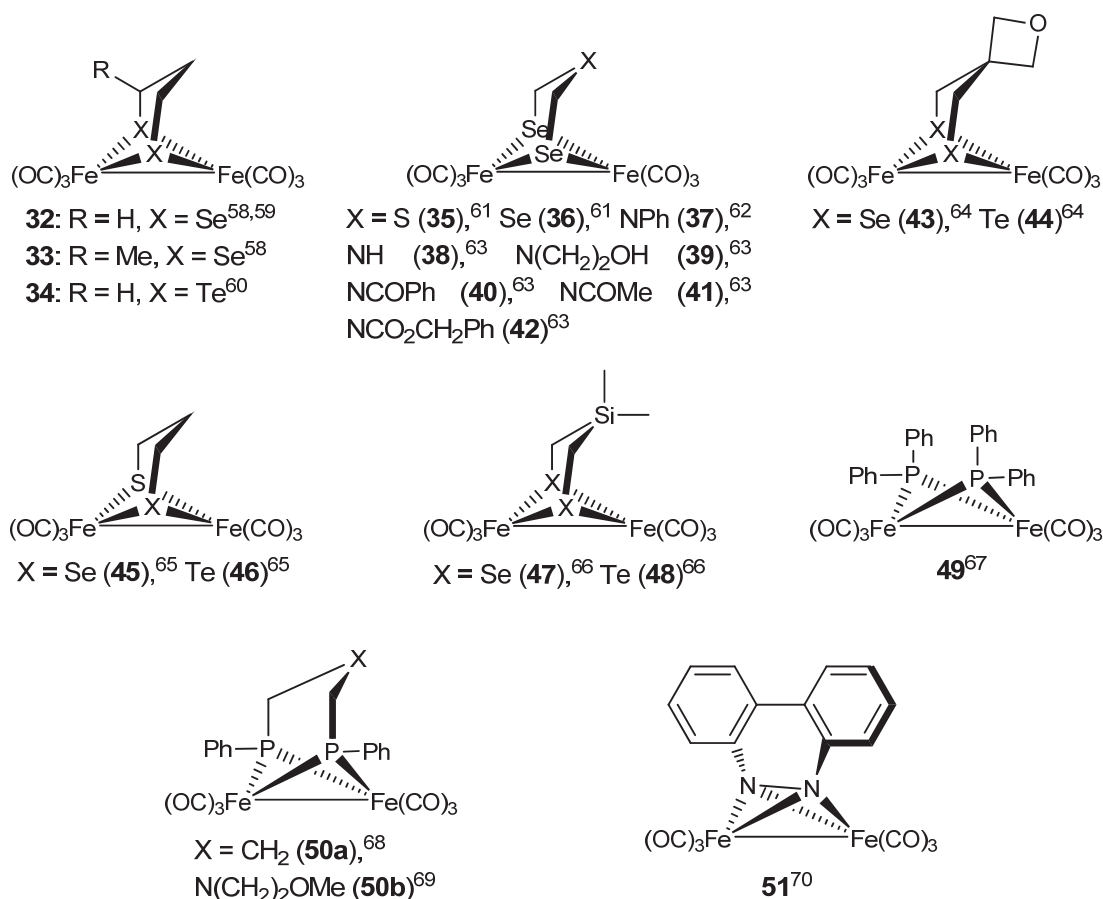
Figure 1-8. Model complexes with various bridging atoms: μ-Se, μ-Te, μ-P and μ-N.

1.3.3   Ligand-Substituted Complexes

Substitution of CO in hexacarbonyl complexes by stronger donor ligands, such as cyanide, phosphines, phosphites or N-heterocyclic carbenes, was performed to mimic the electronic environment of the [FeFe] core of the H cluster (Figures 1-9 to 1-11). Mono-, di- and tetrasubstituted complexes have been described.

• **Monosubstituted Complexes.** Substituting one CO ligand in the hexacarbonyl complexes of the type [Fe$_2$(CO)$_6$$\{\mu$-X$_2$(Bridge)$\}$] (X = S, Se or Te) could occur at the apical or the basal position of the iron atom:
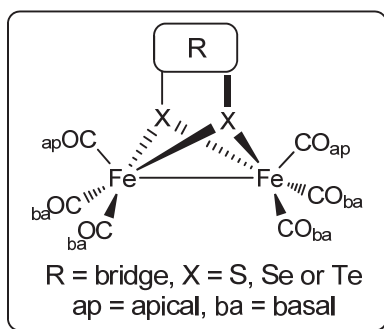
Figure 1-9 shows examples of complexes substituted at the apical (**52-61**, **68-72** and **75**) and basal (**62-67**, **73**, **74** and **76**) sites.
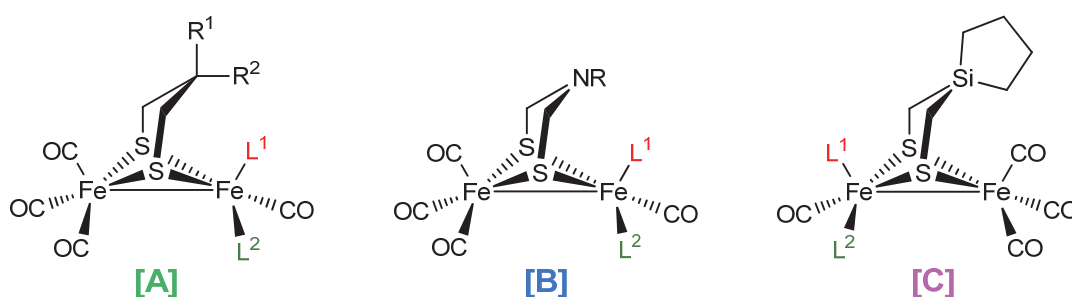
[A] L^1 = PPh$_3$ (**52**),[71] PPh$_3$ (R^1 = R^2 = Me) (**53**),[40] PMe$_3$ (**54**),[71] P(OEt)$_3$ (**55**),[71] PPh$_2$(NHCH$_2$CH$_2$NMe$_2$) (**56**),[72] CN$^-$ (**57**),[33,73] IMes$_2$ (**58**),[74] IMesMe (**59**),[74b] IMe$_2$ (**60**),[74b] IMe$_2$ (R^1 = R^2 = Et) (**61**),[40] L^2 = P(CH$_2$CH$_2$COOH)$_3$ (**62**),[42] PTA (**63**),[75] P(pyd)$_3$ (**64**),[76] n-PrNH$_2$ (**65**),[77] IMes$_2$ (R^1 = R^2 = Me) (**66**),[40] CH$_3$CN (**67**)[77] [B] L^1 = PPh$_3$ (**68**),[78] PPh$_3$ (R = 4-CF$_3$C$_6$F$_4$) (**69**),[79] PPh$_3$ (R = 4-CF$_3$C$_6$H$_4$) (**70**),[79] PMe$_3$ (**71**),[78] P(pyrr)$_3$ (R = PhCH$_2$) (**72**),[80] L^2 = PTA (R = n-Pr) (**73**),[81] DAPTA (R = n-Pr) (**74**)[81] [C] L^1 = PPh$_3$ (**75**),[82] L^2 = CN$^-$ (**76**)[82]

Figure 1-9. Monosubstituted [FeFe]-hydrogenase models at the apical (L^1) or the basal (L^2) position. R = H and L = CO if not specified. The bridgehead C atom of **53** and **61** are oriented towards the Fe(CO)$_3$ unit.

• **Disubstituted Complexes.** There are six possible conformations resulting from substituting two CO groups by other ligands:
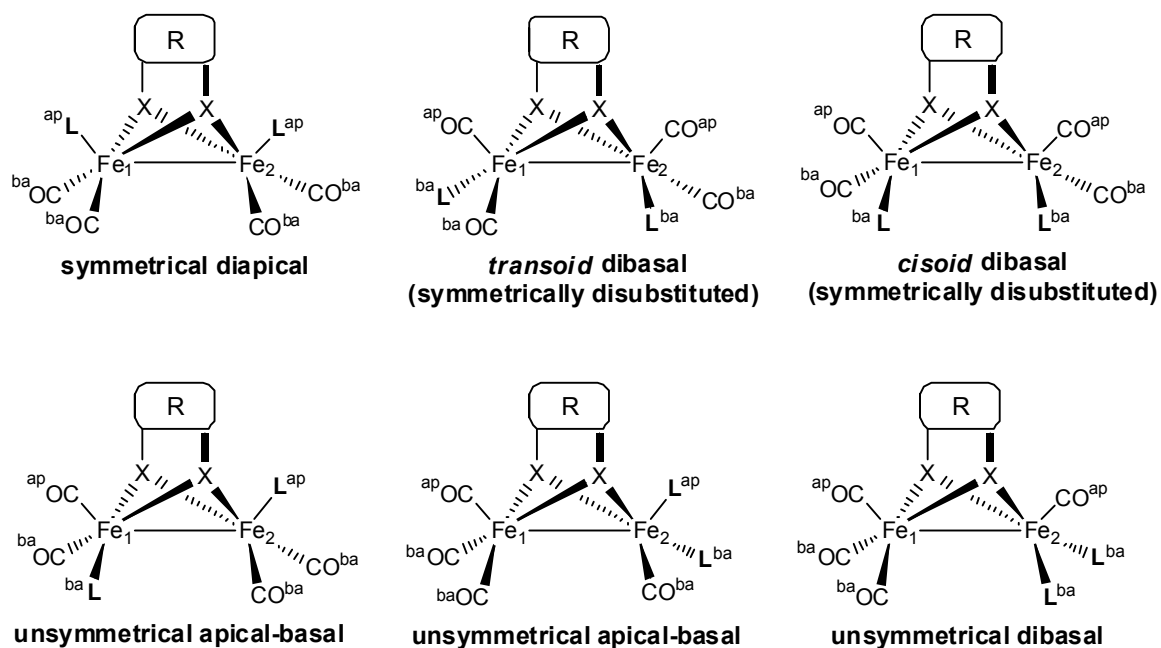
Herein, symmetrical disubstituted complexes are those where the two L ligands are at two different iron atoms whereas the unsymmetrical complexes are those where the two L ligands coordinate at the same iron atom even though the two L ligands may be not similar. For monodentate ligands, the substitution occurs always at two different iron atoms leading to most commonly diapical, *transoid* dibasal and apical-basal conformations in the solid state. Figure 1-10 shows examples of *symmetrically* disubstituted complexes with diapical (**77-80**, **100** and **101**), *transoid* dibasal (**81-84**, **106** and **107**) and apical-basal (**85-88** and **97-99**) conformations.
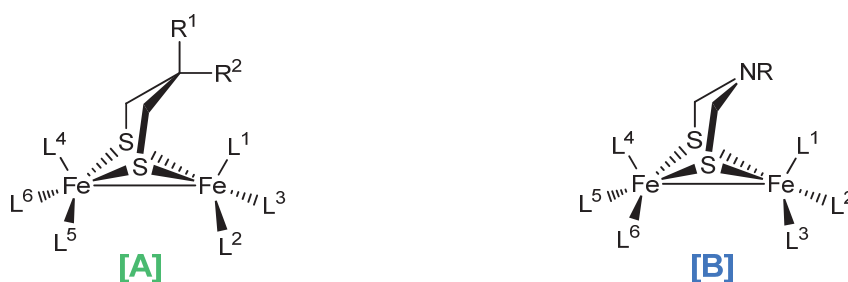
[A] 77: $L^1 = L^4 = P(OMe)_3$;[83] **78**: $L^1 = PPh_3$, $L^4 = P(OEt)_3$;[84] **79**: $L^1 = L^4 = PMe_2Ph$;[71] **80**: $L^1 = L^4 = P(OEt)_3$;[71] **81**: $L^2 = L^6 = PMe_3$ ($R^1 = COOH$);[42] **82**: $L^2 = L^6 = PMe_3$ ($R^1 = R^2 = Me$);[85] **83**: $L^2 = L^6 = PMe_3$;[86] **84**: $L^2 = L^6 = PTA$[75] **85**: $L^1 = PPh_3$, $L^6 = PMe_3$;[84] **86**: $L^1 = P(OEt)_3$, $L^6 = PMe_3$;[84] **87**: $L^1 = L^6 = IMe_2$;[87] **88**: $L^1 = IMes_2$, $L^6 = PMe_3$;[74, 88] **89**: L^4, $L^6 = cis\text{-}Ph_2PCH=CHPPh_2$;[89] **90**: L^1, $L^2 = Ph_2PCH_2CH_2PPh_2$;[90] **91**: L^1, $L^2 = Ph_2PCH_2NMeCH_2PPh_2$;[91] **92**: L^5, $L^6 = Ph_2PCH_2PPh_2$;[92] **93**: L^2, $L^3 = IMeCH_2IMe$;[93] **94**: L^2, $L^5 = Ph_2PCH_2PPh_2$;[94,95] **95**: L^2, $L^5 = Ph_2PCH_2CH_2PPh_2$;[90] **96**: L^2, $L^5 = Ph_2PN(n\text{-}Pr)PPh_2$[96]. **[B] 97**: $L^1 = L^6 = PMe_3$ ($R = c\text{-}C_5H_9$);[97] **98**: $L^1 = L^5 = PMe_3$ ($R = CH_2Ph$);[98,99] **99**: $L^1 = L^5 = PTA$ ($R = n\text{-}Pr$);[100] **100**: $L^1 = L^4 = P(pyrr)_3$ ($R = CH_2Ph$);[101] **101**: $L^1 = L^4 = PMe_3$ ($R = 2\text{-}BrC_6H_4CH_2$);[44] **102**: $L^3 = L^6 = 4\text{-}IC_6H_4NC$ ($R = 4\text{-}CH_3C_6H_4$);[102] **103**: L^5, $L^6 = 1,10\text{-}$ phenanthroline ($R = i\text{-}Pr$);[103] **104**: L^1, $L^2 = Ph_2PCH_2CH_2PPh_2$ ($R = CH_3OCH_2CH_2$);[90] **105**: L^1, $L^2 = Ph_2PCH_2CH_2PPh_2$ ($R = i\text{-}Pr$);[90] **106**: $L^2 = L^6 = PMe_3$ ($R = c\text{-}C_6H_{11}$);[104] **107**: $L^2 = L^6 = PMe_3$ ($R = c\text{-}C_7H_{13}$);[104] **108**: L^3, $L^6 = Ph_2PCH_2PPh_2$ ($R = n\text{-}Pr$);[94] **109**: L^3, $L^6 = Ph_2PCH_2CH_2PPh_2$ ($R = i\text{-}Pr$);[90] **110**: L^1, $L^2 = Ph_2PCH_2CH_2PPh_2$ ($R = CH_3OCH_2CH_2$)[90]

Figure 1-10. Disubstituted [FeFe]-hydrogenase Models. R = H and L = CO if not specified.

Monodentate ligands do not substitute in *cisoid* dibasal fashion, which leads to sterically unfavourable conformation compared to the *transoid* dibasal one. Nevertheless, there is one example of a substituted complex with two monodentate ligands adopting *cisoid* dibasal structure in the solid state, complex **102**. The stability of the *cisoid* dibasal structure of **105** is argued to the π-π stacking interactions of the 4-iodophenylisocyanide ligands in the packing structure of the crystal. In opposite to the monodentate ligands, bidentate ligands can substitute two CO groups forming symmetrical complexes with *cisoid* dibasal conformation (**94-96**, **108** and **109**), while the diapical or *transoid* dibasal chelating manners are inaccessible. Moreover, bidentate ligands can substitute the CO groups bonded to the same iron atom affording unsymmetrical complexes with apical-basal (**89-91**, **104**, **105** and **110**) or dibasal (**92**, **93** and **103**) conformation.

- **Tri- and Tetrasubstituted Complexes.** Examples of this class are depicted in Figure 1-11.
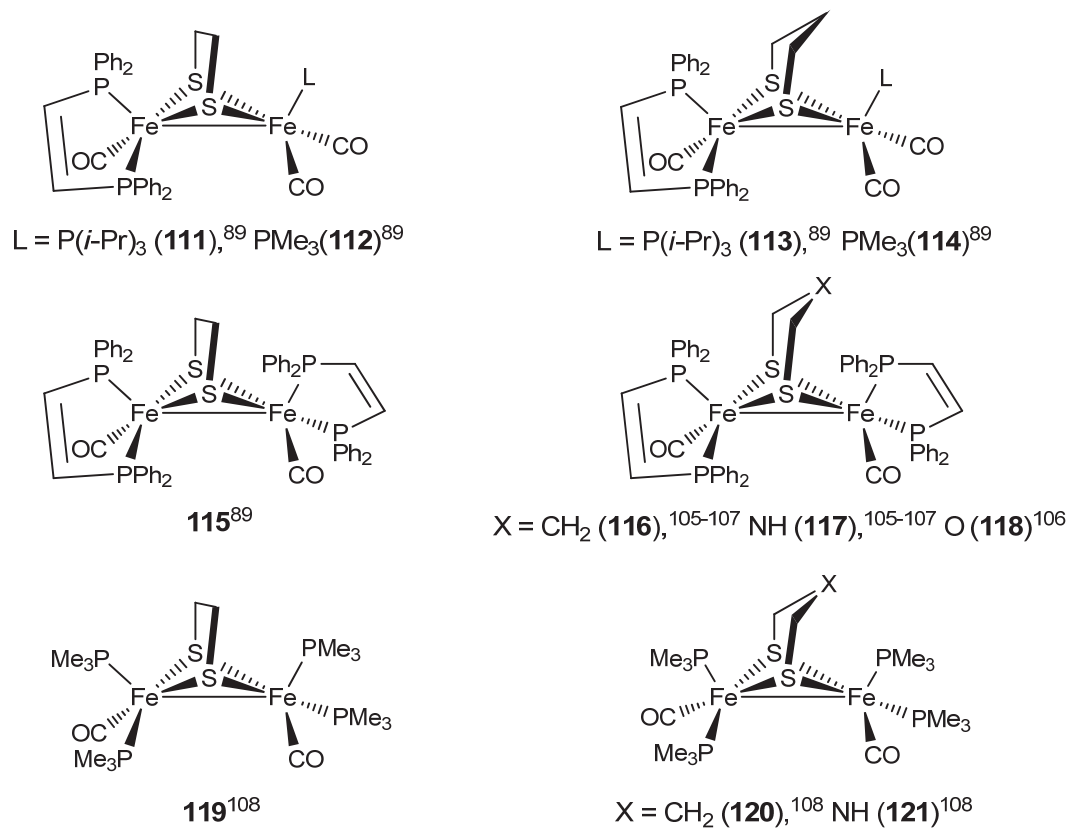
Figure 1-11. Tri- and tetrasubstituted [FeFe]-hydrogenase models.

1.3.4 Fluxional Properties

An intrinsic feature of the $[Fe_2L_6\{\mu\text{-}(SCH_2)_2X\}]$ complexes is the fluxionality of the -S-CH$_2$-X-CH$_2$-S- linker (flipping) as well as the ligand site-exchange at each Fe center resulting from rotation of the FeL$_3$ units:[40,108,109,110]
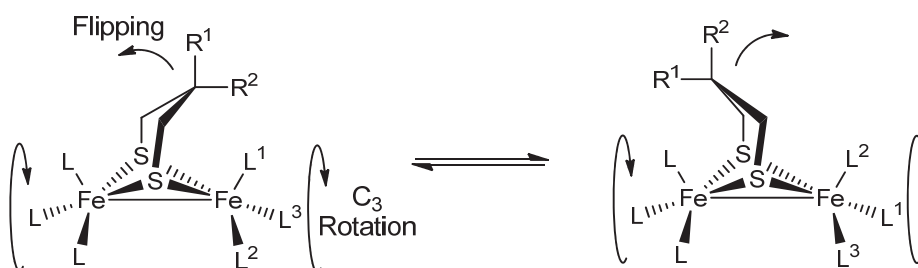
Figure 1-12 shows how the dynamics of the μ-dithiolate in $[Fe_2(CO)_6\{\mu\text{-}(SCH_2)_2NR\}]$ complexes resulting in two conformers, **R$_{ax}$** and **R$_{eq}$**. In **R$_{ax}$**, the R group is on axial the

position of the Fe1S$_2$C$_2$N six-membered ring while it is on the equatorial position of the Fe2S$_2$C$_2$N ring in **R$_{eq}$**.
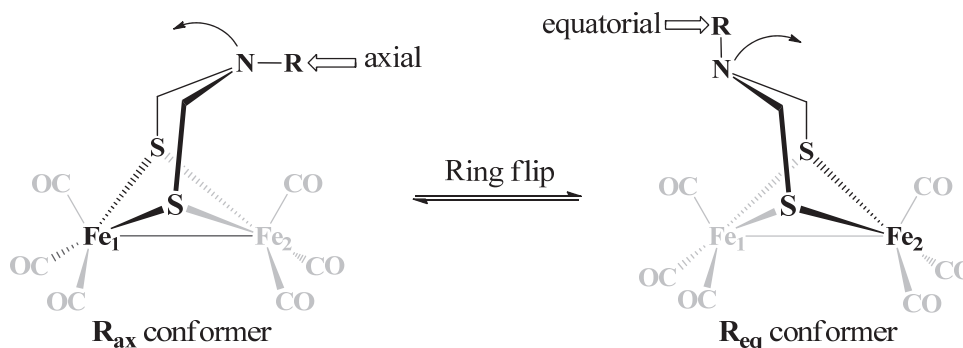
Figure 1-12. Equilibration of the **R$_{ax}$** and **R$_{eq}$** conformers of [Fe$_2$(CO)$_6${μ-(SCH$_2$)$_2$NR}] complexes by ring flip (solution process).

^{1}H NMR spectroscopy provides evidence for this dynamic equilibrium as the protons of each NCH$_2$S moiety appears equivalent at room temperature while these protons become diastereotopic at low temperatures consistent with the slowed ring flip. The first X-ray structural determination of models containing azadithiolato ligand was for complex **5** (R = Me), which reveals the two conformers, **Me$_{ax}$** (60 %) and **Me$_{eq}$** (40 %).[36] Normally, we would expect that the **Me$_{eq}$** conformer is favored because it is unlike **Me$_{ax}$**, which suffers from steric strain between the Me group and the apical CO ligand. The X-ray structural determination of complex **7**, which relieves much of the steric strain in complex **5**, reveals a structure in which the N-H bond is only in axial orientation.[37] The reason for the stabilization of the **R$_{ax}$** conformer of complexes **5** and **7** was explained by DFT calculations in terms of hyperconjugative interaction between the lone pair at the N atom and the two σ*(C-S) orbitals of the **R$_{ax}$** conformer (Figure 1-13), which leads to elongation of the C-S bonds (1.86(8) in complex **5** (average of the two conformers) vs. 1.821(5) in complex **2**).[36]
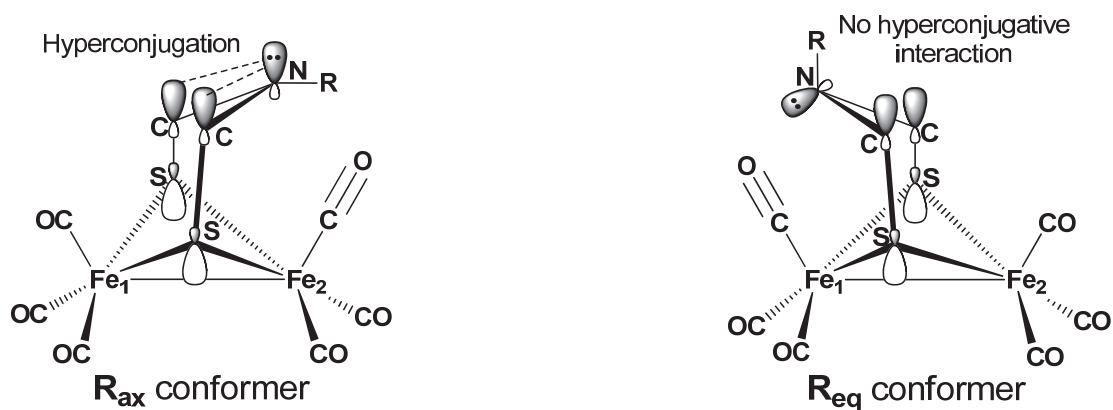
Figure 1-13. Hyperconjugation in the $\mathbf{R_{ax}}$ conformer of $[Fe_2(CO)_6\{\mu\text{-}(SCH_2)_2NR\}]$ complexes.[36]

In contrast to complexes **5** and **7**, the crystals of complexes **18**[43] and **20**[43] are built only from the $\mathbf{R_{eq}}$ conformer, which could be due to the bulkiness of their *i*-Pr and the CH_2CH_2OMe groups, respectively. Replacement of the CH_2CH_2OMe group in complex **20** by CH_2CH_2OH results in stabilizing the $\mathbf{R_{ax}}$ conformer.[45] In the packing structure, the axial CH_2CH_2OH groups form intermolecular hydrogen bonding not only between each other, but also with the oxygen atom of the CO ligand.[45] The axial position of the CH_2CH_2OH group may be necessary for a packing structure involving the described hydrogen bonding.[45]

In the following sections, we will review mechanisms proposed for proton reduction catalyzed by various model complexes. Cyclic voltammetry has been always used for investigating the electrocatalytic properties. Because any proposed catalytic cycle should involve (*i*) electron transfer reactions (i.e. redox processes) and (*ii*) interaction or reaction between the model complexes (the catalyst) and the acid either prior electron transfer or after (i.e. protonation of the neutral complex or its reduced species), understanding the electrochemistry of the model complexes in the absence of acid and their protonation properties before application of potential are essential and necessary to suggest a mechanism for the voltammetric behavior of the complex in the presence of acid.

1.4	**Protonation Properties**

Protonation of $[Fe_2L_6\{\mu\text{-}(SCH_2)_2X\}]$ complexes could take place at one site or more depending on the number of available basic atoms, the strength of the acid as well as the amount of the acid added. The nature of the solvent is found to affect the protonability of

the complex or the regiochemistry of the protonation, a topic will be discussed later. Figure 1-14 shows the possible sites for protonation in the model complexes.
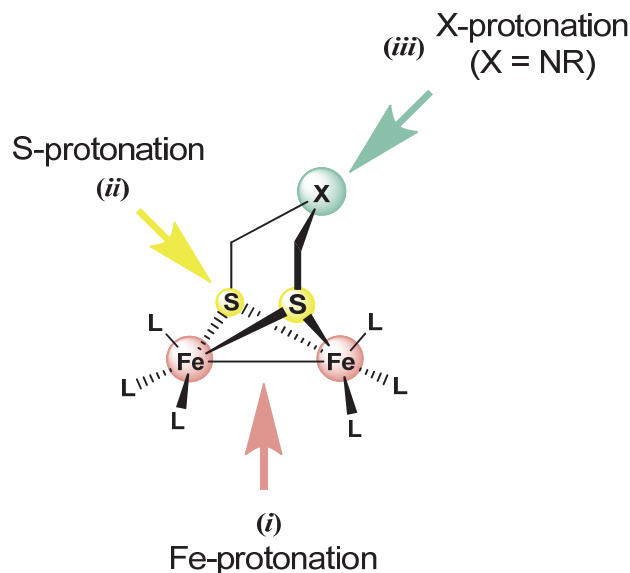
Figure 1-14. Possible sites for protonation in $[Fe_2L_6\{\mu\text{-}(SCH_2)_2X\}]$ complexes.

Protonation at the M-M bond to form hydride species in bridging M-H-M or terminal H-M-M fashion is known in organometallic chemistry. The bonding in M-H-M can be described as 2e3c bond[111], which is similar to the situation in B-H-B bonding.[112] The hydride species are easily detected by ^{1}H NMR spectroscopy in the upfield region. Fe-protonation in $[Fe_2(CO)_{6\text{-}n}L\{\mu\text{-}(SCH_2)_2X\}]$ complexes can also be studied by IR spectroscopy because of the high sensitivity of the carbonyl vibrations to the changes in electron density at the Fe centers. The Fe-protonation of $[Fe_2(CO)_{6\text{-}n}L\{\mu\text{-}(SCH_2)_2X\}]$ to afford μ-hydride or t-hydride species results in changing the formal oxidation state of the iron atoms from $[Fe^IFe^I]$ to $[Fe^{II}Fe^{II}]$.

1.4.1   Protonation of Hexacarbonyl Complexes

- **Fe-Protonation.** Protonation experiments of hexacarbonyl complexes reveal that no protonation is possible at the [FeFe] core even using excess amounts of strong acids such as $HBF_4\cdot Et_2O$ (pK_a (MeCN) $= 0.1$[113]). Only one exception is known, utilizing a special method developed by Heinekey and Matthews to protonate complex **3** based on the high Lewis acidity of $[SiEt_3][B(C_6F_5)_4]/HCl$.[114] The protonated complex **3** was

determined by X-ray crystallography showing μ-hydride complex [Fe$_2$(CO)$_6$(μ-H){μ-(SCH$_2$)$_2$CH$_2$}]$^+$.[114] In the ^{1}H NMR spectrum of complex **3**, sharp singlet at -15.9 ppm is assigned for μ-hydride. The IR spectrum of the protonated complex **3** shows new carbonyl bands shifted from those of the unprotonated complex by 76 cm^{-1} to higher wavenumbers.[114]

• **S-protonation.** The S atoms in [Fe$_2$L$_6${μ-(SCH$_2$)$_2$X}] are known to be susceptible to oxidation[115-118] and alkylation[119,120]. For example, complex **23** reacts with 1 equiv. dimethyldioxirane (DMD) to give the S-oxygenated complex **23a** in quantitative yield (98 %) showing that the μ-S atoms are less reactive toward oxidization than the divalent bridgehead sulfur atom (Scheme 1-3).[115] Oxidation of complex **23** using 2 equiv. of DMD affords complexes **23a**, **23b** and **23c** in 43, 20 and 6 % yield, respectively, reflecting again the same trend of reactivity toward S-oxidation.[115] In the presence of 3 and 4 equiv. DMD, only complexes **23b**, **23c** and **23d** are produced in 75 %, 5 % and 10 % yield, respectively for 3 equiv. DMD, and 54 %, 2 % and 38 % yield, respectively, for 4 equiv. DMD. We may conclude that in addition to the known lability of divalent sulfur atom toward oxidation, the μ-S atoms of hexacarbonyl complexes are also reactive toward formation of sulfones.[115]

Scheme 1-3. S-oxidation of complex **23** in the presence of various equivalents of DMD.[115]
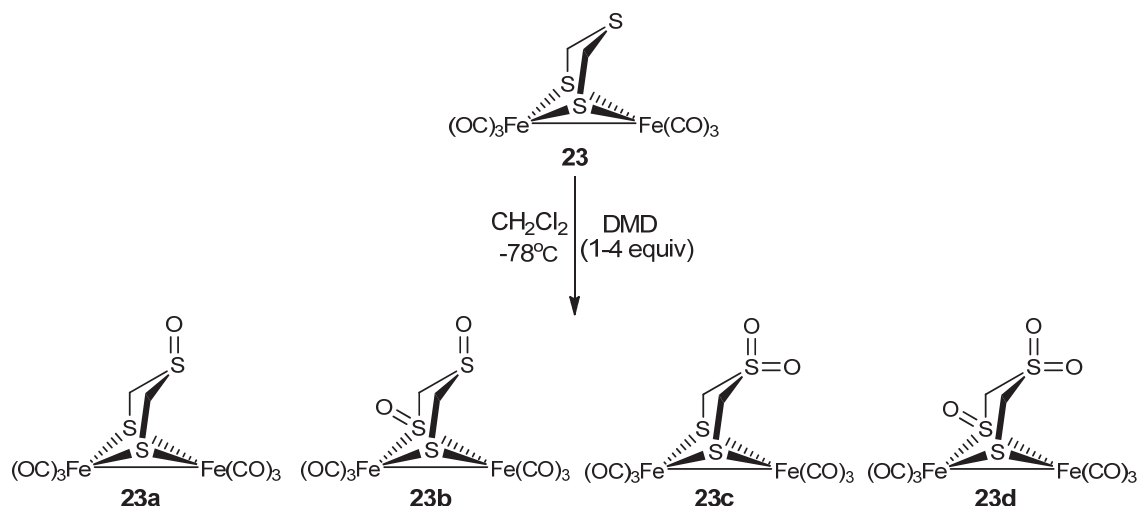
In the packing structure of complex **21**, the μ-S atoms show intermolecular nonbonding contacts with the oxygen atom of the electro-attracting Py-C=O moiety

reflecting the nucleophilicity of the μ-S atoms in the [Fe$_2$S$_2$] models.[45] The OH groups in **29** and the NH groups in **31b-31e** tend to make hydrogen bonding with the μ-S atoms of these complexes.[55-57] Glass et al. showed that the lone pair of the μ-S atoms in complex **26** is destabilized compared to those of other [Fe$_2$(CO)$_6$\{μ-dithiolate\}] complexes owing to an interaction between the σ(Sn-C) orbital with the 3p(μ-S) lone pair.[50] Experimental evidence was given by observing the lowering in the ionization energy of the μ-S atoms upon stannylation of the dithiolate.[50] Regardless of the proclivity of the μ-S atoms toward oxidation, alkylation and hydrogen bonding as well as S···O interaction (described above), the protonation of hexacarbonyl complexes at the μ-S atom is very difficult and only the hexacrbonyl parent of complexes **75** and **76**, i.e. [Fe$_2$(CO)$_6$\{μ-(SCH$_2$)$_2$SiC$_4$H$_8$\}], is reported by Weigand and coworkers to undergo S-protonation.[49] The S-protonation of complex **25** is suggested based on monitoring the changes in the υ(CO) bands in the IR spectrum after addition of excess amounts of HBF$_4$·Et$_2$O. Moreover, electrochemical investigations using pivalic acid proposes that the reduction of **25** is affected by a prior-equilibrium between complex **25** and its adduct with pivalic acid. This adduct is suggested being composed of undissociated pivalic acid coordinated to complex **25** through hydrogen bonding with the μ-S atoms.[49]

- **N-protonation on (μ-SCH$_2$)$_2$NR Ligands.** Protonation at the bridgehead atom X in [Fe$_2$L$_6$\{μ-(SCH$_2$)$_2$X\}] complexes has been reported only for X = NR, but not for X = O, S or Se. The basicity of the nitrogen atom in [Fe$_2$L$_6$\{μ-(SCH$_2$)$_2$NR\}] complexes (pK_a (MeCN) = 8.14 ± 0.2 for **5** and 8.14 ± 0.37 for **7**)[121] is considerably lower than expected for a tertiary amine (pK_a = 18)[121-124]. In organic solvents (e.g. MeCN, CHCl$_3$), the hexacarbonyl complexes could be protonated at the nitrogen atom using only strong acids such as HClO$_4$ and HOTf. N-protonation can be monitored by ^{1}H NMR spectroscopy due to the possibility of detecting a resonance signal in the region of 5.9 ppm for the NH proton.[125] Even if the NH proton is not detected by ^{1}H NMR spectroscopy, a shift of 15-20 cm^{-1} of the υ(CO) bands in the IR spectrum to higher values is used to diagnose N-protonation.[125] The reason for this surprising low basicity of the nitrogen atom in [Fe$_2$L$_6$\{μ-(SCH$_2$)$_2$NR\}] complexes compared to the amines is attributed to the stereoelectronic effect, described in Figure 1-13.[36]

Among the various in situ protonated [Fe$_2$(CO)$_6$\{μ-(SCH$_2$)$_2$NR\}] complexes, only N-protonated complex **19** (using 10 equiv. HClO$_4$) could be isolated and determined by X-ray crystallography owing to the stabilization via intramolecular N-H···Br interaction (3.334(7) Å).[44] While the nitrogen atom in complex **19** is axially substituted with

CH2Ph-2-Br group, the N-protonated complex shows an equatorial position for this group and hence the proton is oriented toward the iron site (Figure 1-15a). The molecular structure of the N-protonated hexacarbonyl complex **50b** is also reported, which shows an axial orientation of the N-H bond (Figure 1-15b).[69]

(a)   (b)
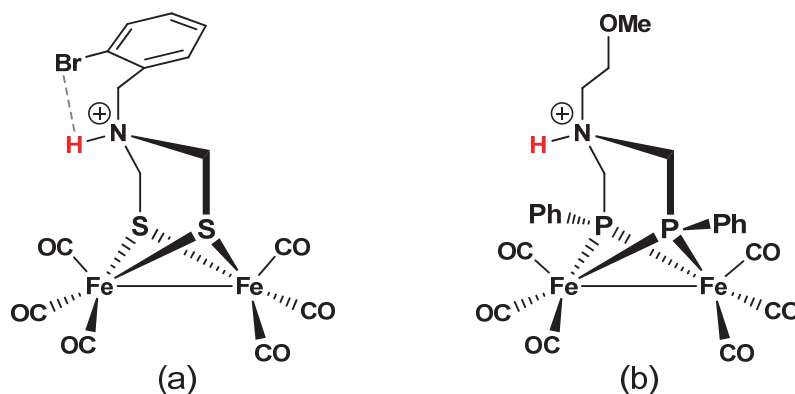
Figure 1-15. The only two N-protonated hexacarbonyl complexes characterized by X-ray crystallography.[44,69]

Protonation of the NR group prevents the ring flip of these systems on the NMR time scale so that the two $Fe(CO)_3$ units become non-equivalent, which is probably due to presence of hydrogen bonding between the NH proton of the N-protonated complex and the oxygen atom of the apical CO ligand, which stabilizes the N-H bond in an axial orientation in the FeS_2C_2N ring.[125,126]

1.4.2   Protonation of Substituted Complexes

In contrast to the hexacarbonyl and the monosubstituted complexes, Fe-protonation is observed for the di-, tri- and tetrasubstituted ones that have higher electron density at the iron atoms.[125] Substitution of CO ligands with stronger σ-donor ligands increases not only the electron density at the Fe atoms, but also at the other protonation sites of complex.[108, 121,125] For example, 4 equiv. of triflic acid are required to fully protonate the amine group in the hexacarbonyl complex $[Fe_2(CO)_6\{\mu\text{-}(SCHMe)_2NH\}]$, while only 1 equiv. is enough in case of the disubstituted complex $[Fe_2(CO)_4(PMe_3)_2\{\mu\text{-}(SCHMe)_2NH\}]$.[121] The pK_a (MeCN) values are found to be 7.98 ± 0.2 and 10.15 ± 0.14 for $[Fe_2(CO)_6\{\mu\text{-}(SCHMe)_2NH_2\}]^+$ and $[Fe_2(CO)_4(PMe_3)_2\{\mu\text{-}(SCHMe)_2NH_2\}]^+$,

respectively.[121] Substituting two CO ligands in **28** with Ph$_2$P-(CH$_2$)$_3$-PPh$_2$ affords an unsymmetrically disubstituted complex, which shows S-protonation as evident by spectroscopy.[127] Protonation of [Fe$_2$(CO)$_4$(PMe$_3$)$_2${μ-(SCH$_2$)$_2$N(C$_6$H$_4$-p-NO$_2$)}] with 4 equiv. HOTf affords two products, S-protonated as well as μ-hydride complexes.[128] As reported, the N atom is not basic enough to be protonated because of the highly electron-withdrawing nature of the -C$_6$H$_4$-p-NO$_2$ group. The above two S-protonated complexes are shown below.
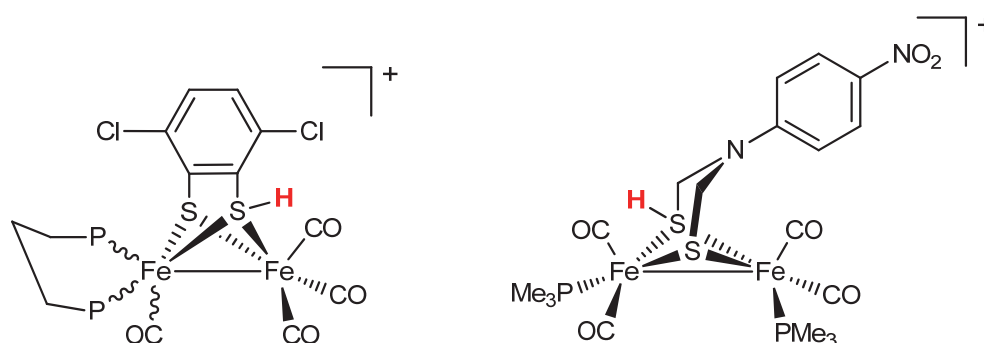
The arrangement of the ligands is found to influence the regiochemistry of Fe-Fe bond protonation.[129] One major difference between the symmetrically and the unsymmetrically disubstituted complexes lies in their protonation.[129] While the former afford exclusively the μ-hydride species upon treatment with an acid, t-hydride species could be detected as an intermediates from the protonation of the unsymmetrical complexes at low temperatures.[129] This difference is explained to arise from the tendency of the unsymmetrically disubstituted complexes to stabilize the rotated structure (Scheme 1-4).[130,131] These t-hydride species undergo isomerization to the thermodynamically more stable μ-hydride form as we will see later. For the same reason, the unsymmetrical coordination environment enhances the reactivity of the complexes toward CO-substitution as well, allowing a third ligand to be installed at the apical site of the Fe(CO)$_3$ unit easier than the parent hexacarbonyl.[130-132]

Scheme 1-4. Protonation of unsymmetrically disubstituted complexes at low temperatures.

Transition state with rotated structure
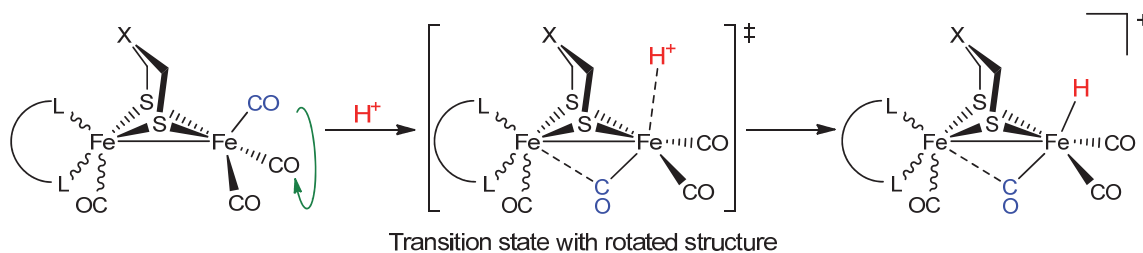
The difference in the regiochemistry of protonation between the symmetrically and the unsymmetrically disubstituted complexes is first described by Schollhammer and coworkers in 2007:[90,133] Protonation of complex **90** by HBF₄·Et₂O in CH₂Cl₂ at -75 °C (Scheme 1-5) results in a *very slow* formation of a *t*-hydride species arising from protonation at the distal Fe atom, **90(*t*-H)d⁺**. Protonation at -50 °C results in another *t*-hydride species **90(*t*-H)p⁺** due to oxidative addition of H⁺ at the proximal Fe atom. These species, **90(*t*-H)d⁺** and **90(*t*-H)p⁺**, isomerize to **90(*μ*-H)⁺** (apical-basal + dibasal) at -30 °C. Complete conversion of the apical-basal isomer into the dibasal one occurs near 25 °C. In contrast, the symmetrically substituted complexes **77** and **83** produce only *μ*-hydride species under the same experimental conditions used for protonation of **90**.[83,86,108,134]

Scheme 1-5. Kinetic and thermodynamic products of protonation of **90**.[133]
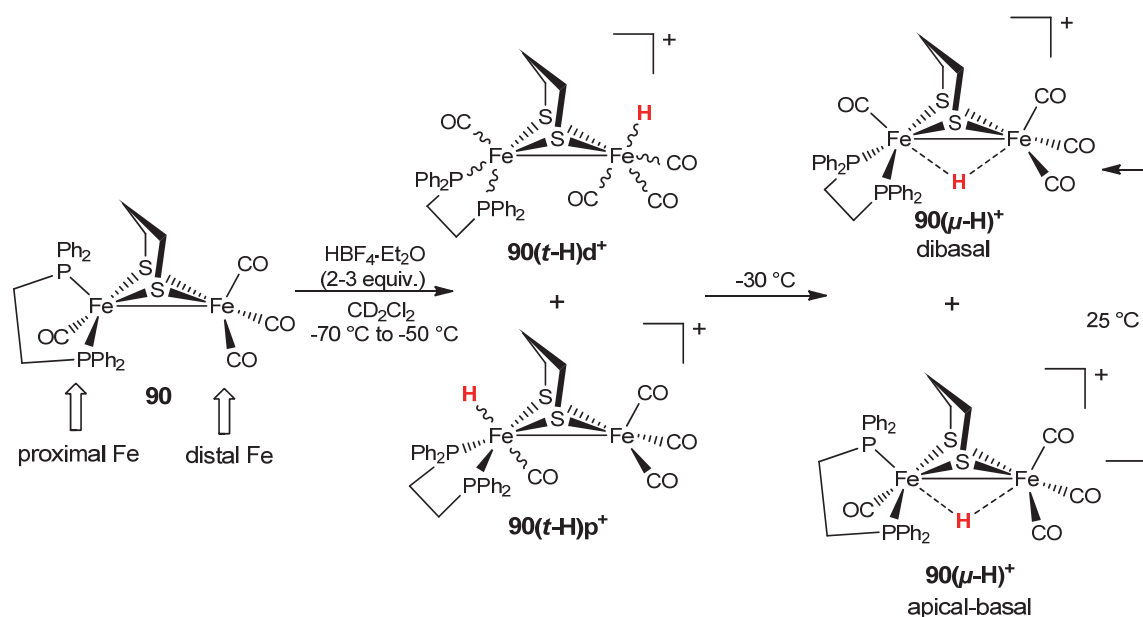
Contrary to **90**, complexes **103** and **105** are protonated exclusively at the N atom by HBF$_4$·Et$_2$O under any condition of temperature and no proton relay from the protonated N atom to the Fe core occurs (Scheme 1-6).[90,103] This behavior is surprising because **103** and **105** have similar ligand set to that of **90**, which undergoes Fe-protonation.

Scheme 1-6. Protonation reactions of complexes **103** and **105**.[90,103]
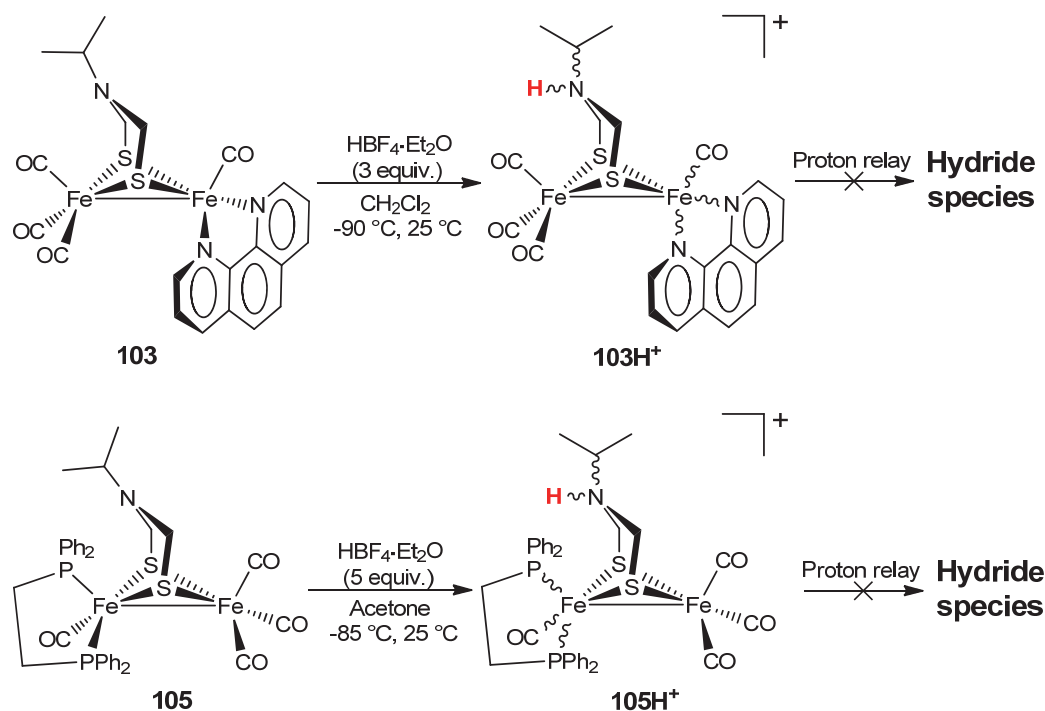
It has been found, experimentally and by DFT studies, that the protonation of complex **98** occurs initially at the N atom rather than the Fe-Fe bond.[99,126] Moreover, N-protonation of **98** elongates the Fe-Fe bond and lowers its basicity. Similarly, the protonation of the Fe-Fe bond to yield the μ-hydride **98(μ-H)$^+$** makes the amine functionality less basic than that in the unprotonated complex **98**.[99,126] Diprotonated complex **98** at both the N atom and the Fe-Fe bond (**98H$_2$$^{2+}$**) is also described using various acids. Scheme 1-7 displays various protonation pathways of **98**. As previously reported,[98,99,125] chloride was found to catalyze tautomerization of the N-protonated complex to the hydride product. In the case of the symmetrically disubstituted complexes (e.g. **83** and **98**) where *t*-hydrides have not been detected at low temperatures, questions have lingered about their presence as *metastable* intermediates.[136-138] Experimental and theoretical studies on the regiochemistry of the electrophilic attack show that the electrophile MeS$^+$ attacks the Fe-Fe bond of **83** at a single metal (terminal attack) to give

83(*t*-SMe)⁺ that isomerizes into the corresponding **83(*μ*-SMe)⁺** derivative.[139] Other studies have shown that the electrophiles may also attack the *μ*-S atoms of the dithiolato linker reflecting the nucleophilicity of the *μ*-S atoms.[119,140]

Scheme 1-7. Protonation pathways of complex **98** in MeCN.[99,126]

Treatment of $[Fe_2(CO)_4(PMe_3)_2\{\mu\text{-}(SCHMe)_2NH\}]$ in MeCN with 1 equiv. anhydrous *p*-toluenesulfonic acid (HOTs, pK_a = 8.7 in MeCN)[113] also shows that the N-protonation is kinetically favored and it is followed by slow tautomerization into the thermodynamic product $[Fe_2(\mu\text{-}H)(CO)_4(PMe_3)_2\{\mu\text{-}(SCHMe)_2NH\}]^+$.[121] The use of NH₄Cl in the protonation experiment accelerates this tautomerization. It is therefore understandable that complexes **103** and **105** are protonated first at the N atoms as a result of kinetic effect, but that no tautomerization is observed could be attributed to the decrease of basicity of the Fe-Fe bond upon N-protonation making the Fe-protonation thermodynamically impossible under the conditions of the study. Puzzling, however, is why the symmetrically disubstituted **98H⁺** and $[Fe_2(CO)_4(PMe_3)_2\{\mu\text{-}(SCHMe)_2NH_2\}]^+$

relay the proton from the N atom to the Fe-Fe bond whereas the unsymmetrically disubstituted **103** and **105** do not.

Rauchfuss and coworkers showed that the *symmetrically* tetrasubstituted complexes **116-118** undergo protonation to form *t*-hydride species at low temperatures that isomerize to μ-hydride products upon warming (Scheme 1-8).[105-107] These results confirm that the *unsymmetrical* arrangement of ligands is not the only key to the formation of *t*-hydride species, but also the electron-richness of the Fe-Fe bond.[105-107] The inset of Scheme 1-8 shows the only molecular structure featuring a *t*-hydride in a close proximity to an ammonium proton [d(FeH···HN) = 1.88(7) Å].[105]

When the strong acid [H(Et$_2$O)$_2$]BAr$^F_4$ {BAr$^F_4{}^-$ = B(3,5-C$_6$H$_3$(CF$_3$)$_2$)$_4{}^-$} is used, fast Fe-protonation occurs for complexes **116-118** at -90 °C, but in the case of the *billion fold* weaker acid [HPMe$_2$Ph]BF$_4$ (pK_a = 5.7 in CD$_2$Cl$_2$) only **117** can be protonated at -90 °C.[105-107] Complex **117** reacts with CF$_3$CO$_2$H (equiv. > 2, pK_a = 12.7 in MeCN)[113] at -40 °C to afford a diprotonated product **117H$_2{}^{2+}$**, but **116** is unaffected by weak acids.[105] The inductive effects of the linker -S-CH$_2$-X-CH$_2$-S- toward the electron density of the [Fe$_2$S$_2$] clusters of **116-118** are comparable; i.e. the Fe-Fe bonds have very similar basicity. Consequently, the Fe-protonation should be controlled by the protophilicity of the heteroatom X such that its protonation facilitates the hydride formation via XH$^+ \to$ Fe proton relay, which only occurs for X = NH. The *t*-hydride species **116(*t*-H)$^+$**, **117(*t*-H)$^+$** and **118(*t*-H)$^+$** are relatively stable at 25 °C against tautomerization into their μ-hydride form ($t_{1/2} \sim$ minutes), which is unlike **90(*t*-H)d$^+$** and **90(*t*-H)p$^+$** (Scheme 1-5) that isomerize to the thermodynamically more stable μ-hydride form at low temperatures. The ability of the Fe atom to receive proton form the N atom in **117H$^+$**, but not in **103H$^+$** and **105H$^+$**, to form *t*-hydride species reflects the higher protophilicity of the iron atoms in **117H$^+$** compared to those of **103H$^+$** and **105H$^+$**.

Scheme 1-8. Protonation of **116-118** and the molecular structure of **117H$_2$$^{2+}$**.[105-107]
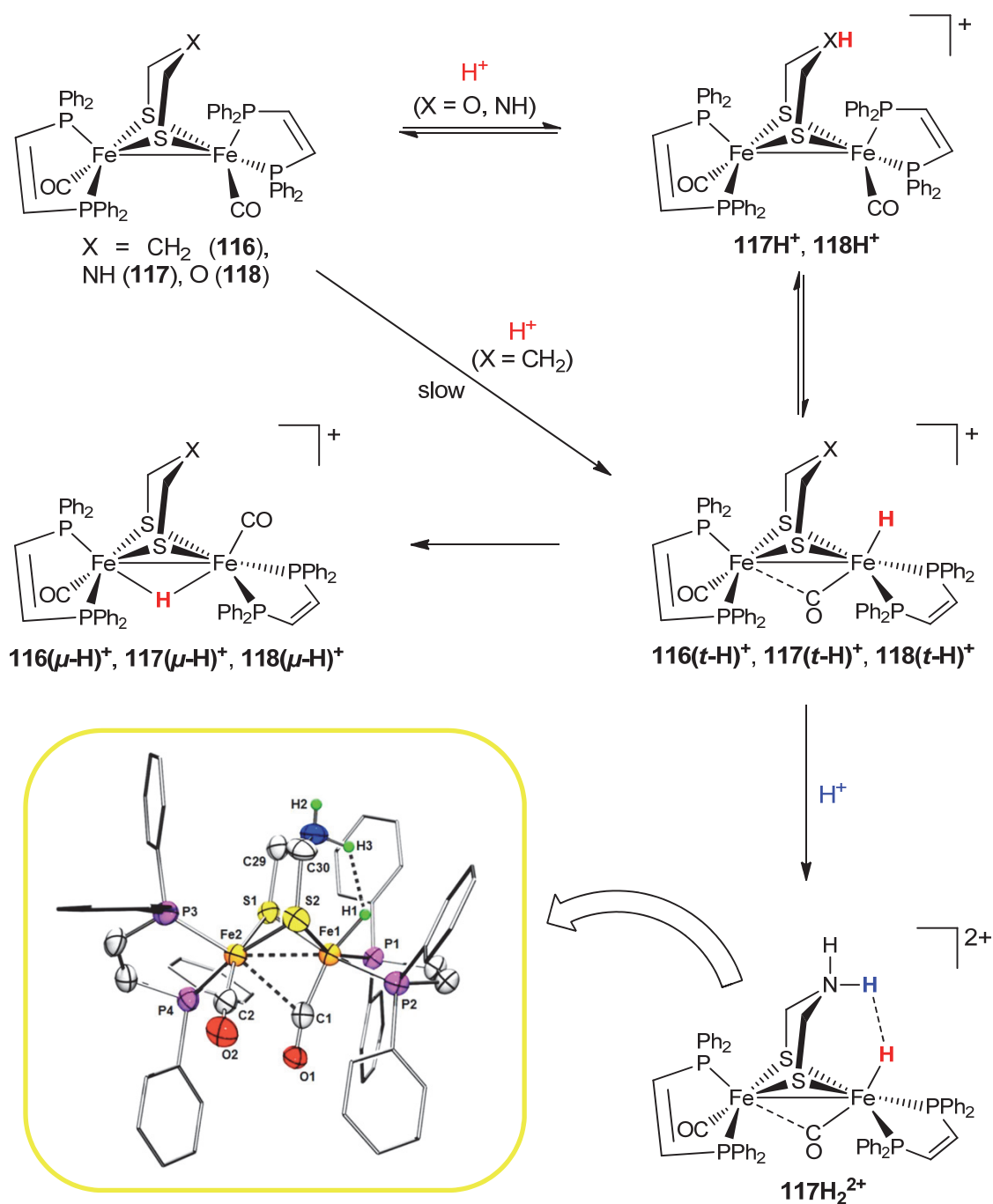
Steric Effect on Rate of Tautomerization. The *t*-hydride species **115(*t*-H)$^+$** tautomerizes very quickly at -20 ºC to **115(*μ*-H)$^+$** (Scheme 1-9a).[105] Relative to **115(*t*-H)$^+$**, **116(*t*-H)$^+$** is kinetically inert toward tautomerization ($t_{1/2} \sim 10$ min, $k_{taut} = 10^{-3}$ s^{-1} at 25 ºC) because the rotation of the FeH(CO)(dppv) site[132] {dppv = *cis*-1,2-bis(diphenylphosphino)ethylene} is inhibited by the steric interaction between the bridgehead methylene group of the -S-CH$_2$-*CH$_2$*-CH$_2$-S- linker and the dppv ligand (Scheme 1-9b).

Scheme 1-9. Relative rates of tautomerization: (a) **115(t-H)$^+$** → **115(μ-H)$^+$** vs. (b) **116(t-H)$^+$** → **116(μ-H)$^+$**.
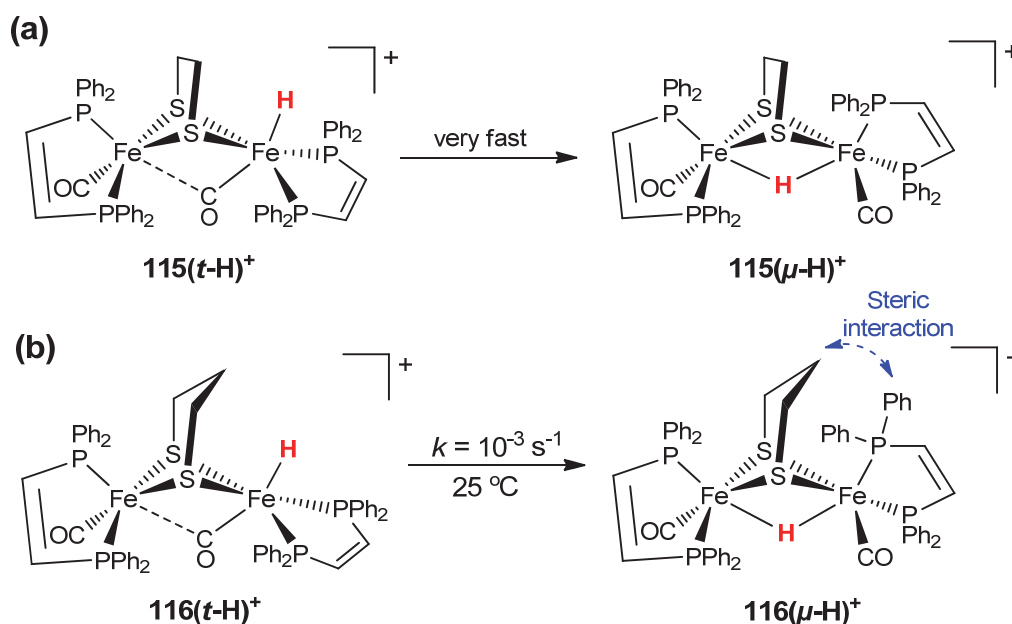
The t-hydride intermediates **116(t-H)$^+$-118(t-H)$^+$** are kinetically more stable than **90(t-H)$^+$** as mentioned above, which is perhaps due to the presence of two chelating dppv ligands in **116(t-H)$^+$-118(t-H)$^+$** making the rotational barrier of either FeH(CO)(dppv) sites higher than that of either FeH(CO)$_3$ or FeH(CO)dppe:
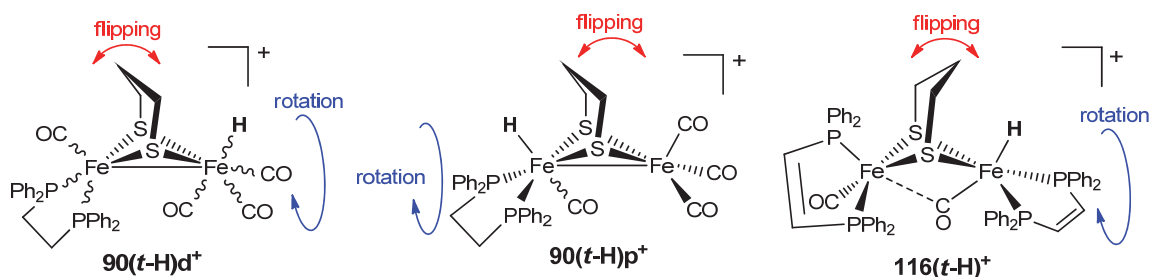
The steric interaction between the FeH(CO)$_3$ unit in **90(t-H)d$^+$** with -S-CH$_2$-CH_2-CH$_2$-S- (while rotation) is less than that in the case of FeH(CO)(dppv) unit of **116(t-H)$^+$**, which has bulkier ligands than the FeH(CO)$_3$ unit. Also, there is less steric clash occurring with the dithiolato ligand during the rotation of the FeH(CO)(dppe) unit in **90(t-H)p$^+$** compared to FeH(CO)(dppv) since the dithiolate of **90(t-H)p$^+$** can flip and position over the less sterically crowded Fe(CO)$_3$ site.

S-Protonated Intermediates. Recently, Rauchfuss and Zampella et al. studied the protonation of **119-121** by [H(Et$_2$O)$_2$]BAr$^F_4$ applying kinetic measurements.[108] A surprising result is the regiochemistry of protonation, which varies with temperature in a manner opposite to what is discussed for **90** and **115-118**. Already at -90 °C the protonation product of **119** is verified to be 100% the *μ*-hydride species **119(*μ*-H)$^+$** whereas the room temperature protonation produces a mixture of **119(*t*-H)$^+$** and **119(*μ*-H)$^+$** in ~ 2:1 ratio. The *t*-hydride **119(*t*-H)$^+$** isomerizes slowly into **119(*μ*-H)$^+$**. *That the low temperature protonation product is the μ-hydride species establishes that* **119(*t*-H)$^+$** *is not an intermediate in the formation of* **119(*μ*-H)$^+$**. Protonation of **120** at -90 °C using 1 equiv. [H(Et$_2$O)$_2$]BAr$^F_4$ affords three products: **120(*μ*-H)$^+$** and **120(*t*-H)$^+$** in 2:1 ratio as well as the S-protonated species **120(S-H)$^+$** as evident by spectroscopy. It has been also proved by spectroscopy that upon rising the temperature to -70 °C, **120(S-H)$^+$** disappears increasing the amount of both **120(*μ*-H)$^+$** and **120(*t*-H)$^+$**. Thus, **120(S-H)$^+$** should be an intermediate in the formation of **120(*μ*-H)$^+$** as well as **120(*t*-H)$^+$**. The fact that **120(*t*-H)$^+$** tautomerizes very slowly into **120(*μ*-H)$^+$** even at 20 °C ($k_{taut} = 10^{-5}$ s^{-1}, $t_{1/2}$ = 2.5 h) is a proof that the formation of **120(*μ*-H)$^+$** does not involve the intermediacy of **120(*t*-H)$^+$** at low temperatures. Because of the remarkable kinetic inertness of the hydride species (i.e. slow tautomerization), kinetic studies of the protonation reaction **120** + [H(Et$_2$O)$_2$]BAr$^F_4$ → **120(*μ*-H)$^+$** + **120(*t*-H)$^+$** is possible. The kinetic investigations agree with pathways to **120(*t*-H)$^+$** and **120(*μ*-H)$^+$** that are first- and second-order in the concentration of **120**, respectively,[108] proposing the mechanisms in Scheme 1-10.

Scheme 1-10. Mechanisms proposed for the two independent pathways for the formation of **120(*t*-H)$^+$** and **120(*μ*-H)$^+$** from protonation of **120**.
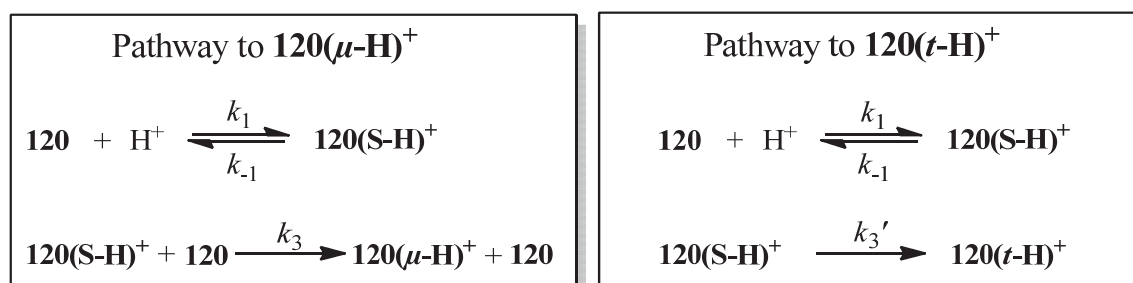
For both mechanisms, **120(S-H)$^+$** is initially formed in a very fast step followed by rate determining step governed by k_3 and $k_3{}'$ for the intermolecular proton transfer from

120(S-H)⁺ to **120** and the intramolecular proton relay from the S atom of **120(S-H)⁺** to one of the Fe atoms, respectively. The rate of **120(μ-H)⁺** formation is thus given by

$$-d[\textbf{120}] \,/\, dt = k_3[\textbf{120(S-H)}^+][\textbf{120}] \tag{1}$$

Applying the pre-equilibrium approximation, we can find the expression for the concentration of the intermediate species

$$[\textbf{120(S-H)}^+] = K[\text{H}^+][\textbf{120}] \tag{2}$$

Where $K = k_1 / k_{-1}$ (equilibrium constant). Thus, the rate law will be

$$-d[\textbf{120}] / dt = (k_1 k_3 / k_{-1})[\text{H}^+][\textbf{120}]^2 = k_\mu[\text{H}^+][\textbf{120}]^2 \tag{3}$$

Where k_μ is the second-order rate constant for the formation of **120(μ-H)⁺**. Similarly, we can find the rate expression for the formation of **120(t-H)⁺**, which will be after applying the pre-equilibrium approximation

$$-d[\textbf{120}] / dt = (k_1 k_3' / k_{-1})[\text{H}^+][\textbf{120}] = k_t[\text{H}^+][\textbf{120}] \tag{4}$$

Where k_t is the first-order rate constant for the formation of **120(t-H)⁺**.

It has been found that the tautomerization of **120(t-H)⁺** into **120(μ-H)⁺** is accelerated by increasing the acid concentration. The mechanism of the acid-catalyzed tautomerization is shown in Scheme 1-11. The S-protonation weakens the Fe-S bonding and hence assisting the rotation of the FeH(CO)(PMe₃)₂ unit.[108] Scheme 1-12 summarizes the protonation mechanisms described above.

Scheme 1-11. Acid-catalyzed tautomerization.[108]
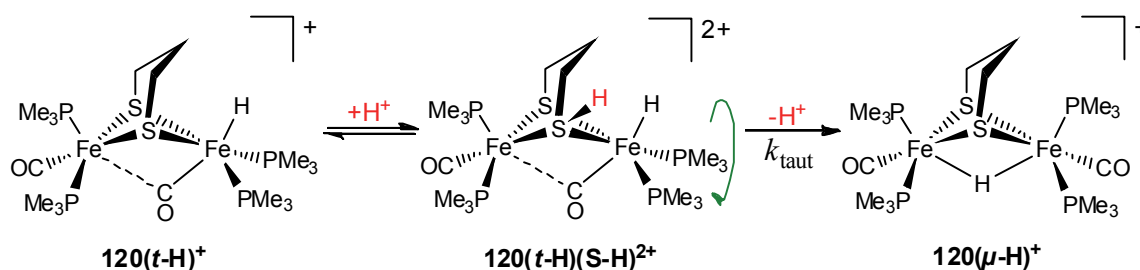
Scheme 1-12. Mechanisms for the independent pathways for the formation of the *t*- and *μ*-hydride species. DFT-optimized structure of the transition state for proton transfer from S to Fe in the S-protonated species is shown.[108]
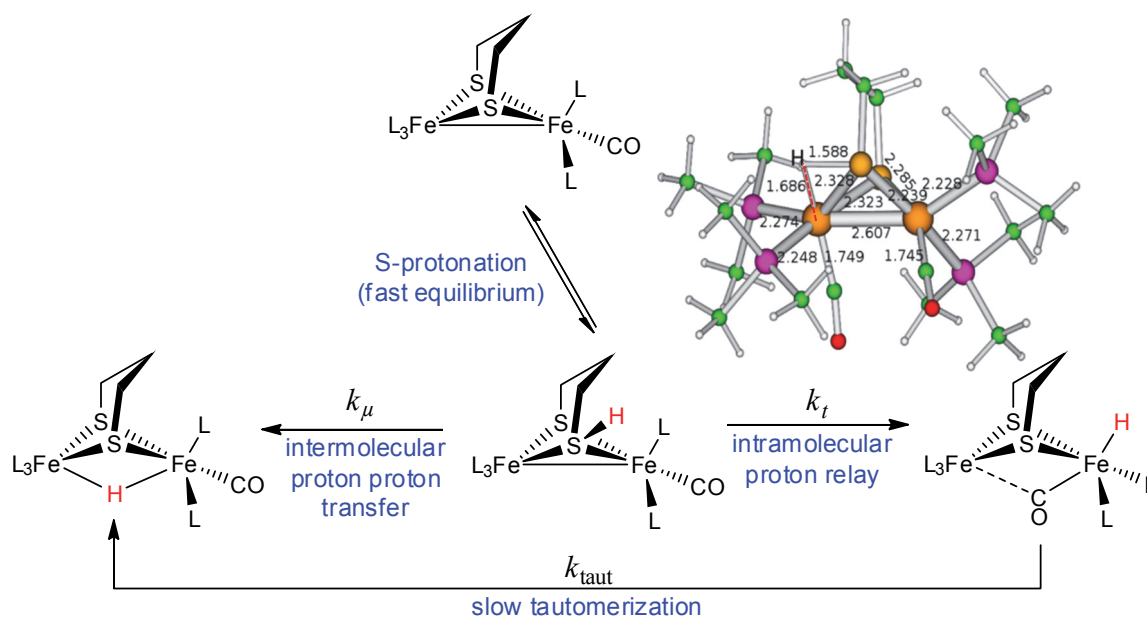
Protonation of **121** with [H(Et$_2$O)$_2$]BAr$^F_4$ affords exclusively *t*-hydride species regardless of the temperature.[108] Unlike **119** and **120**, **121** can be also protonated by weak acids such as NH$_4^+$PF$_6^-$ to give *t*-hydride. The regioselectivity of protonation is attributed to the presence of proton relay NH group, which is also the reason for the reversibility of the protonation reaction as well as the existence of two tautomers of **121(*t*-H)$^+$** {symmetrical- (*sym*-) and unsymmetrical- (*unsym*-) tautomers} that are identified by spectroscopy as well as X-ray crystallography (Scheme 1-13).[108]

Scheme 1-13. Two isomers of **121(*t*-H)$^+$** equilibrating via transient ammonium isomer.[108]
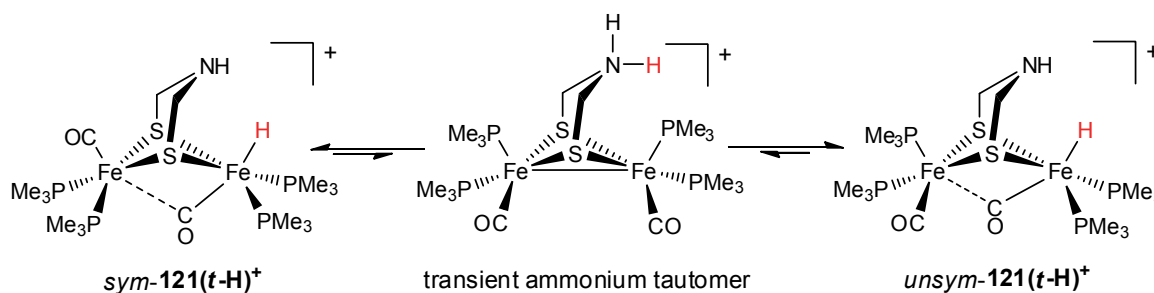
N-protonation occurs upon addition of strong acids to the solution of these hydride species in Scheme 1-13, but without H_2 release. The rate of tautomerization to form the μ-hydride is faster in case of *unsym*-**121(*t*-H)**$^+$ (first-order with $t_{1/2}$ = 4.5 h at 20 ºC) compared to the case of *sym*-**121(*t*-H)**$^+$. The latter tautomerizes via *unsym*-**121(*t*-H)**$^+$.[108]

<div style="background:linear-gradient">

1.4.3   Other Ligand Protonation

</div>

The introduction of a basic group to the bridgehead atom X of the linker -S-CH$_2$-X-CH$_2$-S- or to the ligand L in [Fe$_2$(CO)$_{6-n}$L$_n$\{μ-dithiolate\}] complexes has been also reported in the literature. For example, [Fe$_2$(CO)$_6$\{μ-(SCH$_2$)$_2$C(Me)(CH$_2$NH$_2$)\}] (**11**) can be protonated by 1 equiv. HBF$_4$·Et$_2$O in CH$_2$Cl$_2$ at the N atom of the pendant ligand CH$_2$NH$_2$.[39] [Fe$_2$(CO)$_5$(PPh$_2$NH(CH$_2$)$_2$NMe$_2$)\{μ-(SCH$_2$)$_2$CH$_2$\}] (**56**) is also protonable at the amine functions of the PR$_3$ ligand.[72] The PTA ligands of [Fe$_2$(CO)$_4$(PTA)$_2$\{μ-(SCH$_2$)$_2$CH$_2$)\}] (**84**) are reported to undergo N-protonation, PTA = 1,3,5-triaza-7-phosphaadamantane.[75] Protonation of **91** could occur at the Fe-Fe bond or at the N atom of the ligand -Ph$_2$P-CH$_2$-NMe-CH$_2$-PPh$_2$-.[91] Interestingly, it is found that the protonation depends on the solvent in which the reaction takes place.[91] In CH$_2$Cl$_2$, N-protonation takes place followed by proton relay to the Fe-Fe bond to yield a μ-hydride species **91(μ-H)**$^+$ whereas in acetone the only product that is detected and crystallized is the N-protonated complex **91H**$^+$ (Scheme 1-14). The FeL$_3$ units of **91H**$^+$ are involved in fluxional process exchanging the apical-basal positions of the P atoms of the bis-phosphane ligand, which may assist the proton relay from the N atom to the Fe-Fe bond.

Scheme 1-14. Protonation of **91** in CH_2Cl_2 or acetone with $HBF_4 \cdot Et_2O$.[91]
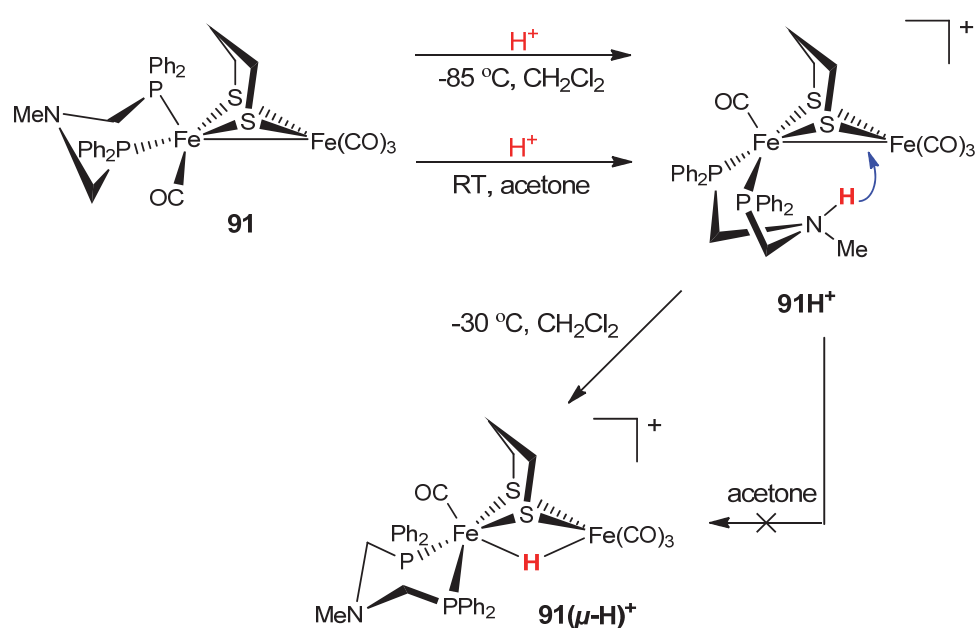
1.5 Reduction of [Fe^{I}Fe^I] Models in the Absence of Acid

1.5.1 Basic Concepts[141-149]

Cyclic voltammetric investigations show that the [Fe^{I}Fe^I] models undergo two successive electron reduction steps; *RS1* and *RS2* at standard potentials of $E°_1$ and $E°_2$, respectively:

$$Fe^IFe^I \ + \ e^- \ \underset{}{\overset{E°_1}{\rightleftharpoons}} \ Fe^IFe^0 \qquad\qquad (RS1)$$

$$Fe^IFe^0 \ + \ e^- \ \underset{}{\overset{E°_2}{\rightleftharpoons}} \ Fe^0Fe^0 \qquad\qquad (RS2)$$

The standard potential of a redox couple is a thermodynamic property, which is related to the difference in free energy between the redox couple species ($\Delta G° = -nFE°$, F is Faraday constant). $\Delta G°$ is a state function, which means that it depends on the initial and the final states of the system. Thus, $E°$ is determined by the relative energies of the redox couple. Herein the following cases are possible concerning the relative values of $E°_1$ and $E°_2$:

(i) $E°_2$ is more negative than $E°_1$: This case is the normal ordering of potentials and *RS2* is thermodynamically less favorable than *RS1* as expected due to electrostatic effect: the second electron is inserted into an anion whereas the first electron into a neutral species. In this case, *RS1* and *RS2* are two distinct elementary steps that proceed in a stepwise fashion. When $E°_1$ and $E°_2$ are well separated, the cyclic voltammogram will show two reduction events corresponding to *RS1* and *RS2*. For example, the cyclic voltammogram of the complex shown in the inset of Figure 1-16 features two electrochemically reversible events at $E°_1 = -0.88$ V and $E°_2 = -1.13$ V.[148b]
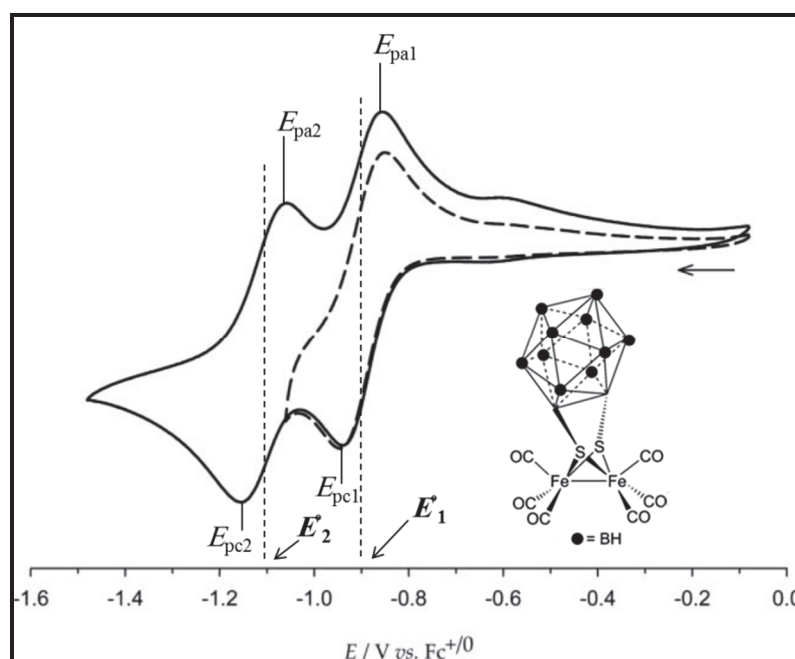
Figure 1-16. Cyclic voltammograms of 3 mM complex (inset) in (MeCN/0.1 M NBu4PF6) solution at scan rate of 100 mV·s⁻¹. E_{pa1} and E_{pa2} are the anodic peak potentials corresponding to the first and the second events, respectively. E_{pc1} and E_{pc2} are the cathodic peak potentials corresponding to the first and the second events, respectively. The dashed curve is obtained when the potential scan is switched before the second reduction takes place.[148b]

The standard potential $E°$ is measured as the half-wave potential, $E_{1/2} = \frac{1}{2}(E_{pc} + E_{pa})$, for reactions that are both chemically and electrochemically reversible. $E°_1$ and $E°_2$ in Figure 1-16 are determined in this way. This approximation is valid because for the reversible reaction $O + n\text{e}^- \leftrightarrow R$, Nernst equation should be satisfied:

$$E = E° - \frac{RT}{nF}\left(\frac{[\text{R}]}{[\text{O}]}\right)_{t,x=0} \tag{5}$$

In eq 5, t refers to the time-dependency of [R] / [O] ratio during the voltammetry and $x = 0$ means that the concentrations are in the diffusion layer rather than in the bulk. When the current is half its maximum value, which is at $E = E_{1/2}$, the surface concentration of O will have dropped to half its original concentration (i.e. concentration in the bulk) and the surface concentration of R will have risen to half the bulk concentration of O:

$$E_{1/2} = E^\circ - \frac{RT}{nF}\left(\frac{[O]_0/2}{[O]_0/2}\right)_{t,x=0} = E^\circ - \frac{RT}{nF}\ln(1) \tag{6}$$

Hence

$$E_{1/2} = E^\circ \tag{7}$$

When the process is irreversible, the value of the peak potential E_{pc} is usually reported.

(ii) E°_2 is less negative than E°_1: This case refers to a condition that has been called *potential inversion* such that in voltammetry *RS1* and *RS2* proceed simultaneously resulting in a single voltammetric peak.[141-149] In other words, potential inversion refers to a case when the insertion of the second electron (*RS2*) is thermodynamically easier than the insertion of the first electron (*RS1*), which practically leads to the formation of Fe^0Fe^0 at the same potentials required for the formation of Fe^IFe^0. At first glance, this phenomenon seems to contradict the electrostatic argument offered in case *i*. Nonetheless, another factor, structural change associated with one or both of the electron transfers, is at work leading to potential inversion. A common situation is that the product of *RS1* (Fe^IFe^0) is unstable with respect to disproportionation; $2\times Fe^IFe^0 \leftrightarrow Fe^IFe^I + Fe^0Fe^0$. When the structural change results in highly stabilized dianion Fe^0Fe^0 relative to the monoanionic intermediate Fe^IFe^0, then this monoanion is reduced before it is able to escape from the electrode surface accounting for the potential inversion. When the extent of potential inversion is so high, the energy of the intermediate Fe^IFe^0 is so large that its concentration is negligible and hence the reduction proceeds via concerted two-electron process from a thermodynamic point of view. Concerted two-electron transfer means that no intermediate exists, not that the two electrons tunnel through the barrier simultaneously.[150]

(***iii***) **Potential compression:** An overall two-electron voltammetric peak could be observed not only as a result of potential inversion, but also when $E°_1$ and $E°_2$ are closely spaced, i.e. $|E°_1 - E°_2| \approx 0$.

In all cases (*i, ii* and *iii*), the disproportionation of the monoanion can take place in the diffusion layer, but whether it is favored or not would depend on the relative values of $E°_1$ and $E°_2$. The equilibrium constant of disproportionation, K_{disp}, can be calculated from the values of the individual standard reduction potentials ($E°_1$ and $E°_2$). Assuming that the reduction of A occurs by following mechanism:

$$A + e^- \rightleftharpoons A^- \qquad E°_1$$

$$A^- + e^- \rightleftharpoons A^{2-} \qquad E°_2$$

$$2A^- \rightleftharpoons A + A^{2-} \qquad K_{disp}$$
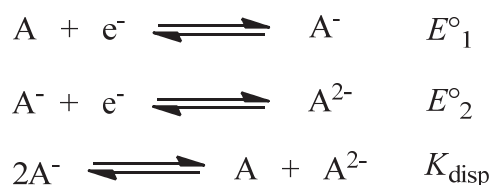
The equilibrium constant, K_{disp}, is related to the free energy change, $\Delta G°_{disp}$ and the difference between $E°_1$ and $E°_2$ is given by

$$\Delta G°_{disp} = - RT \ln K_{disp} = -F(E°_2 - E°_1) \tag{8}$$

here

$$K_{disp} = \frac{[A][A^{2-}]}{[A^-]^2} \tag{9}$$

so

$$\ln K_{disp} = -\frac{F}{RT}(E°_1 - E°_2) \tag{10}$$

and

$$K_{disp} = e^{-\left[\frac{F}{RT}(E°_1 - E°_2)\right]} \tag{11}$$

Eq 11 implies the following:

• In case of normal ordering of potentials ($E°_1 - E°_2 > 0$), disproportionation is not favored ($K_{disp} < 1$) and the intermediate A^- is able to survive in the diffusion layer until the applied potential $E_{app} \geq E°_2$.

- In case of potential inversion ($E°_1 - E°_2 < 0$), disproportionation is thermodynamically favored ($K_{disp} > 1$). Once A⁻ is formed at $E°_1$ necessary to reduce A, it undergoes spontaneous disproportionation and accepts another electron from the electrode at the same potential $E°_1$. The intermediate A⁻ can often be detected by spectroscopy, such as electron paramagnetic[151] and infrared measurements of CO bands[152], only if the potential inversion is mild ($0 < E°_1 - E°_2 \leq -0.3$ V). When the inversion is very strong, the two electron reduction proceeds in concerted process and the intermediate cannot be detected.[141]

- In case of potential compression ($E°_1 - E°_2 \approx 0$), $K_{disp} \approx 1$.

| 1.5.2 | **Structural Changes Associated with Reduction** |

According to various DFT calculations,[43,52,149,153] the first electron reduction affords a monoanion with elongated Fe-Fe bond compared to that of the neutral complex (Scheme 1-16). As shown in Scheme 1-16, there are two types of structural arrangements for the dianionic state obtained after two-electron transfer:

(i) **Symmetrical structure.** The [Fe$_2$S$_2$] core remains a symmetrical building block with two bridging thiolate functions. The Fe-Fe distance in this case is nonbonding.

(ii) **Inverted / Rotated Structure.** In this arrangement there is a dramatic change in the structure due to a *chemical process* including cleavage of one of the Fe-S bonds and rotation of one Fe(CO)$_3$ unit to allow orientation of one of its CO ligands into bridging or semi-bridging position to delocalize the negative charge. Thus, the dianion in the inverted (rotated) state is more stable than in the symmetrical one. The structural change can either be concerned with one of the electron transfers or appears as the intervening step of an ECE process. When the structural change accompanies the electron transfers, then potential inversion will be observed, $E°_1 - E°_2 < 0$.

The occurrence of potential inversion requires low barrier $\Delta G^{\ddagger}$ for the chemical process to take place within the time scale of the experiment.[154] In this case an overall two-electron reduction with inverted potentials will be observed at $E°_{ov}$:[154]

$$E°_{ov} = \frac{1}{2} (E°_1 + E°_2) \tag{12}$$

Whether the monoanion is an intermediate or not is determined by the relative values of the two individual one-electron standard potentials or K_{disp} of the process $2 \times$ monoanion $\leftrightarrow$ neutral complex + dianion as discussed before.

Scheme 1-16. Structural changes calculated for the reduced species of the [FeFe]-hydrogenase models.
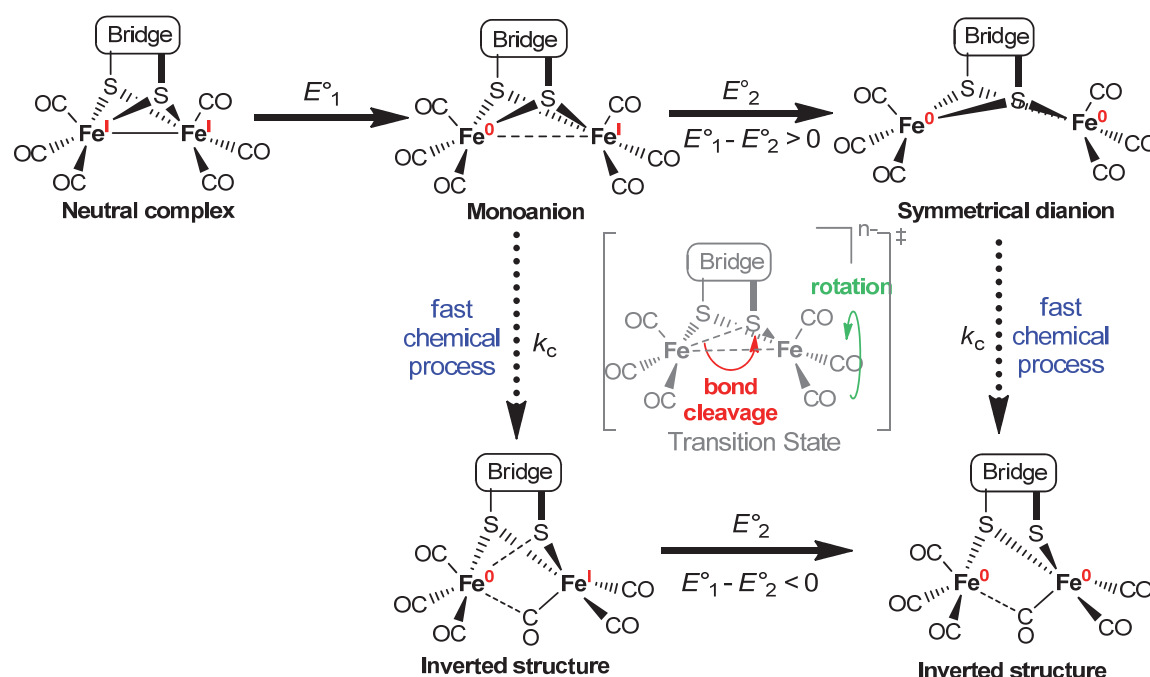
1.5.3　Structure-Redox Properties Relationship

1.5.3.1　One-Electron or Two-Electron Reduction?

A fundamental question for understanding the catalytic mechanism of proton reduction by the model complexes is related to their electron transfer chemistry in acid-free media. Whether or not the reduction step is a reversible one-electron or two-electrons is one of the most important questions. Cyclic voltammetric studies established that the electron transfer chemistry of [Fe$_2$(CO)$_6${μ-dithiolate}] systems are dependent on the nature of the dithiolato bridge.[129,149,154] For example, replacement of the N-H group in complex **7** by N-*i*Pr (in complex **18**) or N-CH$_2$CH$_2$OMe (in complex **20**) alters the voltammetric process from two sequential one-electron reduction steps for **7** to a two-electron reduction in a single step for **18** and **20**.[43,78] The complexes containing benzenedithiolate (**27-30**) undergo also reversible two-electron reduction in a single

step.[51-56] Complex **8**, which contains -S-CH$_2$-O-CH$_2$-S- linker, is reduced in two sequential one-electron steps[37b] whereas complexes **23**, **35** and **36** with S or Se bridgehead atom undergo two-electron reduction with inversion of potentials[47,61]. The computations on complexes **23**, **35** and **36** indicates that their HOMO is primarily the lone pair of the bridgehead S or Se atom with some delocalization to the [FeFe] core.[47,61] This direct through-space interaction may favor the inverted/rotated structures for the dianions **23**$^{2-}$, **35**$^{2-}$ and **36**$^{2-}$. The complexes of the type [Fe$_2$(CO)$_6${μ-(SCH$_2$)$_2$SiR$_2$}] also also exhibit potential inversion of the two-electron reduction steps. An experimental proof for the formation of μ-CO in the dianion of [Fe$_2$(CO)$_6${μ-(SCH$_2$)$_2$SiC$_4$H$_8$}] is provided by measuring the IR spectrum (υ(CO) region) of the two-electron reduced complex obtained from the reaction of Na/Hg with [Fe$_2$(CO)$_6${μ-(SCH$_2$)$_2$SiC$_4$H$_8$}].[49] The IR spectrum after the two-electron reduction of [Fe$_2$(CO)$_6${μ-(SCH$_2$)$_2$SiC$_4$H$_8$}] reveals a band at 1726 cm^{-1} due to the formation of μ-CO, which is an indication of the rotated structure of the dianion.[49] The diphosphido- and bis(phosphide)-bridged hexacarbonyl diiron complexes (**49**, **50a** and **50b**) also undergo two-electron reduction in a single step.[67-69] The number of electrons involved in the reduction of complex **51** can be dependent on the solvent being used in the experiment as will be discussed in Section 1.5.3.9.[70]

The voltammetric reduction of complex **3** was studies in great detail, in particular by IR spectroelectrochemistry and X-ray crystallography.[11a,155-158] These studies confirm that complex **3** is reduced in a single one-electron step producing an unstable anion that undergoes fast chemical reactions leading to products **P1-P4** (Scheme 1-17). **P1** is obtained after further reduction of **3**$^-$. The attack of **P1** on **3** affords **P2** as confirmed by EXAFS in an electrochemical flow cell experiment. Independently, Heinekey et al. identified the structure of **P2** by synthesis and X-ray determination.[156-158] Another pathway for the decomposition starts with ligand-loss from **3**$^-$ to give **P3** that dimerizes into tetranuclear **P4** product. The support for the second decomposition pathway came from the isolation of a tetranuclear analogue of **P4**.[155-158]

Scheme 1-17. Pathways of decomposition of the monoanion **3**⁻ during the voltammetric experiment.[11a,155-158]
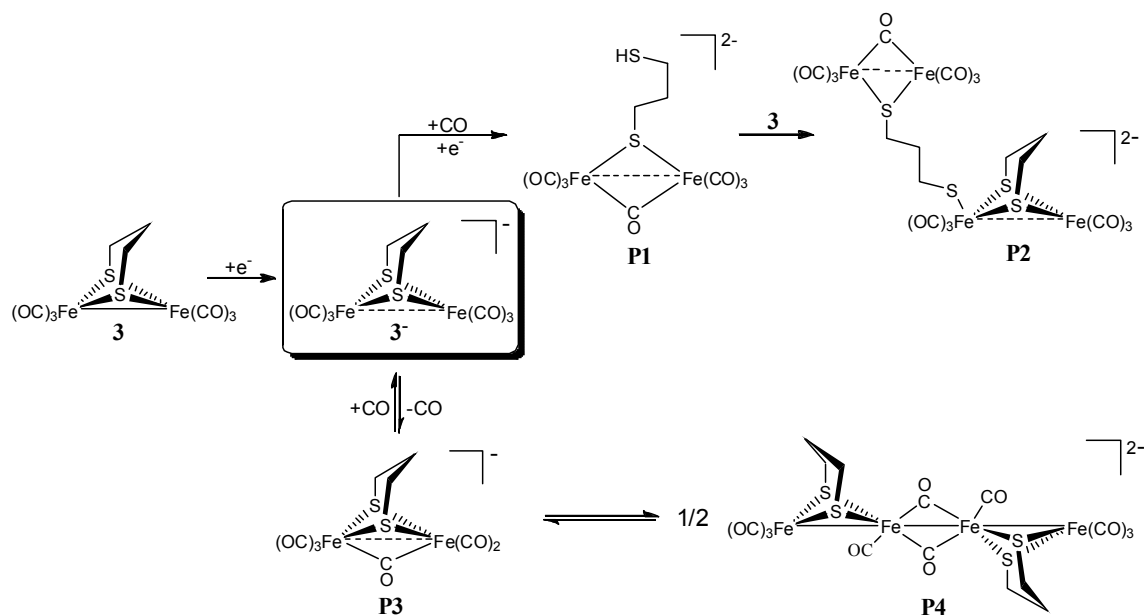
1.5.3.2   Effect of the Bridgehead E of the -S-CH₂-E-CH₂-S- Linker on the Reduction Potential

Table 1-1 summarizes the reduction potentials of hexacarbonyl complexes with various bridgehead atoms/groups in their -S-CH₂-E-CH₂-S- Linker. From Table 1-1 we can notice the following trend for the ease of reduction: **23** > **8** ~ **7** > **3**. The electron-withdrawing nature of N and O atoms in complexes **7** and **8** might be the reason for their ease of reduction compared to complex **3**. That complex **23** has the least negative reduction potential in this series could be attributed to the phenomenon of potential inversion. Unfortunately, the electrochemistry of **24** is not reported. For this reason, comparing the reduction potentials of **35** and **36**, which have the same μ-Se atoms with different bridgehead atoms, may show us the effect of replacing the S by Se in the bridgehead. The Se atom makes the reduction potential less negative by 35 mV. In total picture, the effect of the bridgehead E toward the redox properties of the [Fe₂S₂] core is very small, of the order of 100 mV.

Table 1-1. Reduction potentials of hexacarbonyl complexes having different bridgehead atoms/groups. Potentials are in V (vs. ferrocenium/ferrocene couple) measured in MeCN.

Complex	No.	E_{pc}	Reference
$[Fe_2(CO)_6\{\mu\text{-}(SCH_2)_2CH_2\}]^a$	**3**	-1.66 ± 0.06 V	33, 43, 71, 73, 96, 158-160
$[Fe_2(CO)_6\{\mu\text{-}(SCH_2)_2NH\}]^a$	**7**	-1.58	78
$[Fe_2(CO)_6\{\mu\text{-}(SCH_2)_2O\}]^a$	**8**	-1.59	37b
$[Fe_2(CO)_6\{\mu\text{-}(SCH_2)_2S\}]^b$	**23**	-1.48, -1.45	47, 61
$[Fe_2(CO)_6\{\mu\text{-}(SCH_2)_2Se\}]$	**24**	–	48[c]
$[Fe_2(CO)_6\{\mu\text{-}(SeCH_2)_2S\}]^b$	**35**	-1.45	61
$[Fe_2(CO)_6\{\mu\text{-}(SeCH_2)_2Se\}]^b$	**36**	-1.42	61

[a]These complexes are reduced with the normal ordering of potentials. [b]These complexes undergo two-electron reduction in a single step due to potential inversion. For complex **23**, the individual standard reduction potentials are estimated by digital simulations to be $E°_1$ = -1.505 V and $E°_2$ = -1.390 V vs. ferrocenium/ferrocene couple. [c]unpublished.

1.5.3.3 Effect of the R Groups of the -S-CH₂-X-CH₂-S- (X = CR₂ or NR) Linker on the Reduction Potential

Table 1-2 shows the influence of R group in $[Fe_2(CO)_6\{\mu\text{-}(SCH_2)_2X\}]$ (X = CR₂ or NR) toward the reduction potential of the [Fe₂S₂] cluster. The reduction potentials of complexes **12**, **13**, **16** and **17** are falling in the range of -1.61 to -1.67 V. The reduction potential of complex **3** (-1.66 ± 0.06 V) is quite close to these complexes. The reduction potential of complex **7** is -1.58 V, which is within the narrow range of -1.55 to -1.62 V of complexes **18**, **19** and **22** showing again that R does not affect the reduction potential significantly. However, slight differences can be seen related to the electron-withdrawing or donating effect of the R group resulting in the following order of ease of reduction: **22** ~ **19** > **7** > **18**.

Table 1-2. Reduction potentials of $[Fe_2(CO)_6\{\mu\text{-}(SCH_2)_2X\}]$ (X = CR_2 or NR) complexes. Potentials are in V (vs. ferrocenium/ferrocene couple) measured in MeCN.

Complex	No.	E_{pc}	Reference
$[Fe_2(CO)_6\{\mu\text{-}(SCH_2)_2CH_2\}]$	**3**	-1.66 ± 0.06 V	See Table 1-1
$[Fe_2(CO)_6\{\mu\text{-}(SCH_2)_2CMe_2\}]$[a]	**12**	-1.61	40
$[Fe_2(CO)_6\{\mu\text{-}(SCH_2)_2CEt_2\}]$[a]	**13**	-1.67	40
$[Fe_2(CO)_6\{\mu\text{-}(SCH_2)_2C(H)(CO_2H)\}]$	**16**	-1.64	42
$[Fe_2(CO)_6\{\mu\text{-}(SCH_2)_2C(H)(CONHPh)\}]$	**17**	-1.67	42
$[Fe_2(CO)_6\{\mu\text{-}(SCH_2)_2NH\}]$	**7**	-1.58	78
$[Fe_2(CO)_6\{\mu\text{-}(SCH_2)_2N(i\text{-}Pr)\}]$[b]	**18**	-1.62	43
$[Fe_2(CO)_6\{\mu\text{-}(SCH_2)_2N(CH_2Ph\text{-}2\text{-}Br)\}]$	**19**	-1.56	44
$[Fe_2(CO)_6\{\mu\text{-}(SCH_2)_2N(2\text{-}furylmethyl)\}]$	**22**	-1.55	46

[a]Our recent cyclic voltammetric investigations (*unpublished*) reveal that these models complexes undergo two-electron reduction in a single step due to potential inversion in MeCN or CH_2Cl_2 solutions, which is contrary to the literature. [b]This complex undergoes two-electron reduction in single step and the value in the table is for the first one-electron reduction, i.e. $E°_1$.

1.5.3.4   Effect of the Bridging Atoms μ-X of the -X-CH$_2$-E-CH$_2$-X- Linker on the Reduction Potential

Table 1-3 shows several hexacarbonyl complexes having μ-dithiolato, μ-diselenato and μ-ditellurato linkers. Replacing the μ-S atoms in **3** by μ-Se and μ-Te in **32** and **34**, respectively, results in a small anodic shift. We can also see the following trend for the ease of reduction: **44** > **43** > $[Fe_2(CO)_6\{\mu\text{-}(SCH_2)_2C(CH_2)_2O\}]$ showing again the same effect. The trend of less negative reduction potentials from μ-S to μ-Te is counter to the expectation based on the trend in electron richness in the [FeFe] core indicated by carbonyl stretching frequencies of the complexes [υ(CO): μ-S > μ-Se > μ-Te]. By comparing the complexes **25**, **47** and **45**, we find that the reduction potentials are identical within experimental. Indeed, the relation between the μ-chalcogen atom in these complexes and the reduction potential of the complexes is not clear, but in general the effect is small.

Table 1-3. Reduction potentials of dithiolate, diselenate and ditellurate complexes. Potentials are in V (vs. ferrocenium/ferrocene couple) measured in MeCN solution at 0.1 V·s^{-1}.

Complex	No.	E_{pc}	Reference
$[Fe_2(CO)_6\{\mu\text{-}(SCH_2)_2CH_2\}]^a$	**3**	-1.67	See Table 1-1
$[Fe_2(CO)_6\{\mu\text{-}(SeCH_2)_2CH_2\}]^a$	**32**	-1.61	58, 59
$[Fe_2(CO)_6\{\mu\text{-}(TeCH_2)_2CH_2\}]^a$	**34**	-1.58	60
$[Fe_2(CO)_6\{\mu\text{-}(SCH_2)_2C(CH_2)_2O\}]^a$	–	-1.60	64
$[Fe_2(CO)_6\{\mu\text{-}(SeCH_2)_2C(CH_2)_2O\}]^a$	**43**	-1.55	64
$[Fe_2(CO)_6\{\mu\text{-}(TeCH_2)_2C(CH_2)_2O\}]^a$	**44**	-1.53	64
$[Fe_2(CO)_6\{\mu\text{-}(SCH_2)_2SiMe_2\}]^b$	**25**	-1.52	66
$[Fe_2(CO)_6\{\mu\text{-}(SeCH_2)_2SiMe_2\}]^b$	**47**	-1.51	66
$[Fe_2(CO)_6\{\mu\text{-}(TeCH_2)_2SiMe_2\}]^b$	**48**	-1.51	66

[a]The tabulated E_{pc} values for these complexes are for the first one-electron reduction wave. [b]These complexes undergo two-electron reduction in a single step due to potential inversion.

1.5.3.5 Effect of CO Substitution by PR$_3$ on the Reduction Potential

Replacement of the CO ligands on the [FeFe] core by phosphanes or phosphites results in a significant effects on the reduction potential of the complex. Comparison between the reduction potential of the hexacarbonyl **3** with some of its PR$_3$-substituted complexes is shown in Table 1-4. Replacement of one CO ligand in **3** by PR$_3$ in **52**, **54** and **55** causes a substantial cathodic shift of reduction potentials reflecting the higher electron-donating ability of these ligands compared to CO. The greatest shift is caused by PMe$_3$, which is stronger σ-donor ligand than PPh$_3$ or P(OEt)$_3$.[161-163] Substituting a second CO ligand by PR$_3$ results in an additional cathodic shift on going from **54** to **83**.

Table 1-4. Reduction potentials of the parent hexacarbonyl **3** and some of its PR$_3$-substituted complexes. Potentials are in V (vs. ferrocenium/ferrocene couple) measured in MeCN.

Complex	No.	E_{pc}	Reference
[Fe$_2$(CO)$_6${μ-(SCH$_2$)$_2$CH$_2$}]	**3**	-1.66 ± 0.06 V	See Table 1-1
[Fe$_2$(CO)$_5$(*PMe$_3$*){μ-(SCH$_2$)$_2$CH$_2$}]	**54**	-1.94	71
[Fe$_2$(CO)$_5$(*PPh$_3$*){μ-(SCH$_2$)$_2$CH$_2$}]	**52**	-1.84	71
[Fe$_2$(CO)$_5$(*P(OEt)$_3$*){μ-(SCH$_2$)$_2$CH$_2$}]	**55**	-1.81	71
[Fe$_2$(CO)$_4$(*PMe$_3$*)$_2${μ-(SCH$_2$)$_2$CH$_2$}]	**83**	-2.31	86

1.5.3.6 Effect of Internal Hydrogen Bonding on the Reduction Potential

Complex **27** undergoes reduction at $E°_{ov}$ = -1.30 ± 0.04 V,[51-55] which is significantly less negative than the reduction potentials of the hexacarbonyl complexes with -S-CH$_2$-E-CH$_2$-S- bridges (Tables 1-1 to 1-3). The reason could be due to the more electronegative sp^2 carbon atoms directly bonded to the sulfur atoms in complex **27** compared to the sp^3 carbon atoms in -S-CH$_2$-E-CH$_2$-S- bridges. Substitution on the benzene ring of complex **27** shifts slightly the reduction potential to more or less negative values, which is in consistent with the electron-donating or withdrawing effect of the substituent R.
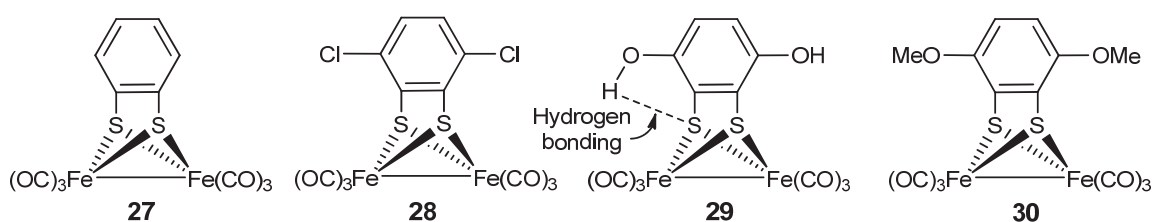
Complex **30** is reduced at slightly more negative potential ($E°_{ov}$ = -1.34 V vs. ferrocenium/ferrocene couple in MeCN)[56] compared to complex **27** whereas complex **28** is reduced at less negative potential ($E°_{ov}$ = -1.20 V vs. ferrocenium/ferrocene couple in MeCN)[53]. Even though the OH substituents in complex **29** are electron donating to the benzene ring, the reduction potential of complex **29** ($E°_{ov}$ = -1.28 V vs. ferrocenium/ferrocene couple in MeCN)[55,56] is less negative than that of complex **27**,

which is attributed (using DFT calculations) to the presence of *hydrogen bonding* between the OH groups and the S atoms in the neutral and the reduced forms of complex **29**.[55,56]

Complexes **31b-31e** (Figure 1-7) show internal N-H···S hydrogen bonding in the solid state (see Figure 1-17 for complex **31d**) and in the solution as evident by X-ray crystallography and ^{1}H NMR spectroscopy, respectively.[57]
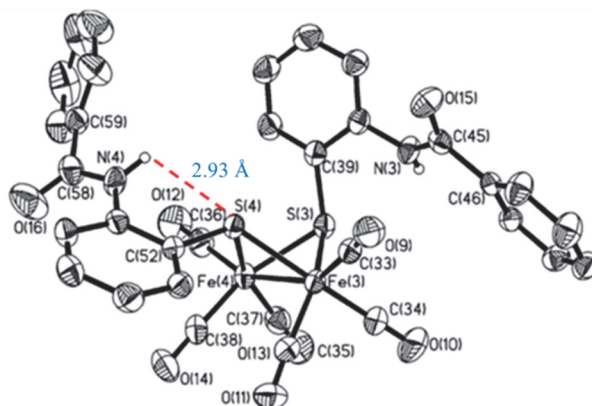
Figure 1-17. Molecular structure of complex **31d** showing an intramolecular N-H···S hydrogen bonding (red dashed line) of 2.93 Å.[57]

The reduction peaks at E_{pc1} (vs. ferrocenium/ferrocene couple in MeCN) = -1.29, -1.22, -1.24 (or -1.57 V in CH$_2$Cl$_2$) and -1.19 V (or -1.43 V CH$_2$Cl$_2$) of complexes **31b**, **31c**, **31d** and **31e**, respectively, show large anodic shifts from those of complexes **31a** (-1.51 V in MeCN or -1.88 V in CH$_2$Cl$_2$) and **3** (E_{pc} = -1.66 V in MeCN). The proclivity to hydrogen bonding should be enhanced after reduction because of the greater negative charge at the [Fe$_2$S$_2$] core, although a computational study for the presence of hydrogen bonding in the reduced species of complexes **31b-31e** is not performed. The presence of hydrogen bonding besides the electron withdrawing nature of the NHCOR substituents in complexes **31b-31e** explain their ease of reduction relative to **31a** and **3**. *In conclusion, the internal hydrogen bonding to μ-S lowers its electron donating capability and stabilizes the reduced species resulting in less negative potential required for the electron transfer processes.* These studies may drop a hint that the hydrogen bonding between the NH of the amido group in the protein and the μ-S in the H cluster may stabilize the H cluster and have a contribution to the low reduction potential.

1.5.3.7   Effect of Protonation on the Reduction Potential

Table 1-5 shows the reduction potentials of complexes **18-22** in the neutral and N-protonated forms. The N-protonated complex undergoes reduction at ~ 400 mV less negative potential than its neutral form. It is also evident by IR spectroscopy that N-protonation shifts the values of $\upsilon(CO)$ to higher wavenumbers by 15-20 cm^{-1} (in average) reflecting the decreased electron density of the Fe atoms upon N-protonation, which explains the ease of reducing the N-protonated complex (a *cation*) compared to its unprotonated form.[11a,125,129,149,164]

Table 1-5. Reduction potentials of [Fe$_2$(CO)$_6${μ-(SCH$_2$)$_2$NR}] and [Fe$_2$(CO)$_6${μ-(SCH$_2$)$_2$NHR}]$^+$ complexes in MeCN. Potentials are in V vs. ferrocenium/ferrocene couple.

R	Complex	$E_{1/2}$ (neutral form)	E_{pc} (N-protonated form)	Reference
i-Pr	**18**	-1.58	-1.17	43
CH$_2$Ph-2-Br	**19**	-1.48	-1.01	44
CH$_2$CH$_2$OMe	**20**	-1.56	-1.19	43
2-furylmethyl	**22**	-1.55	-1.13	46

The effect will become much greater if the protonation occurs at the Fe-Fe bond to afford a μ-hydride species (Table 1-6). This is because of the great change in the electron density of the Fe atoms upon oxidative addition of H$^+$: Fe^I-Fe^I $\rightarrow$ Fe^{II}-H-Fe^{II}. Upon Fe-protonation an anodic shift of ~ 0.7-1.0 V is observed.[164]

It is found that the *regiochemistry of Fe-protonation* is important in determining the magnitude of the anodic shift in reduction potentials. If the protonation takes place at a single Fe atom to give a *t*-hydride, the anodic shift will be higher by ~ 100-200 mV than in the case of μ-hydride formation (Table 1-7). Simply stated, the *t*-hydride complex undergoes reduction more easily than the corresponding μ-hydride complex. The pK_a (MeCN) of **116(*t*-H)$^+$** is estimated to be 16 and that of **116(μ-H)$^+$** is greater than 18.6, which means that the former is a stronger acid than **116(μ-H)$^+$** and hence it undergoes reduction more easily.[105]

Table 1-6. Effect of Fe-protonation on the reduction potentials. Potentials are in V (MeCN solution) vs. ferrocenium/ferrocene couple.

Complex	No.	E_{pc} (neutral)	E_{pc} (FeHFe)[a]	Reference
$[Fe_2(CO)_4(\kappa^2\text{-PNP})\{\mu\text{-}(SCH_2)_2CH_2\}]^b$	**91**	-2.3	-1.26	91
$[Fe_2(CO)_4(PMe_3)_2\{\mu\text{-}(SCH_2)_2N(CH_2Ph)\}]$	**98**	-2.18	-1.10	99, 135
$[Fe_2(CO)_4(\kappa^2\text{-L})\{\mu\text{-}(SCH_2)_2CH_2\}]^c$	**93**	-2.42	-1.48	93
$[Fe_2(CO)_4(PMe_3)_2\{\mu\text{-}(SCH_2)_2CH_2\}]$	**83**	-2.31	-1.39	86

[a]Reduction potentials of the Fe-protonated forms that are μ-hydride species. [b]PNP = $(Ph_2PCH_2)_2NMe$. Reduction potentials measured in CH_2Cl_2 solution. [c]L = $CH_2(IMe)_2$ = $I_{Me}\text{-}CH_2\text{-}I_{Me}$, where I_{Me} = 1-methylimidazol-2-ylidene.

Table 1-7. Dependence of reduction potential on the regiochemistry of Fe-protonation. Potentials are vs. ferrocenium/ferrocene couple.[105]

Complex[a]	No.	$E_{1/2}$ / V $(CH_2Cl_2)^b$
$[Fe_2(CO)_2(\kappa^2\text{-dppv})_2\{\mu\text{-}(SCH_2)_2CH_2\}]$	**116**	–[c]
$[Fe_2(CO)_2(\kappa^2\text{-dppv})_2\{\mu\text{-}(SCH_2)_2NH\}]$	**117**	–[c]
$[Fe_2(CO)_2(\mu\text{-}H)(\kappa^2\text{-dppv})_2\{\mu\text{-}(SCH_2)_2CH_2\}]^+$	**116(μ-H)$^+$**	-1.8
$[Fe_2(CO)_2(t\text{-}H)(\kappa^2\text{-dppv})_2\{\mu\text{-}(SCH_2)_2CH_2\}]^+$	**116(t-H)$^+$**	-1.67
$[Fe_2(CO)_2(t\text{-}H)(\kappa^2\text{-dppv})_2\{\mu\text{-}(SCH_2)_2NH\}]^+$	**117(t-H)$^+$**	-1.64[d]
$[Fe_2(CO)_2(t\text{-}H)(\kappa^2\text{-dppv})_2\{\mu\text{-}(SCH_2)_2NH_2\}]^{2+}$	**117H$_2^{2+}$**	-1.3[d]
$[Fe_2(CO)_2(\mu\text{-}H)(\kappa^2\text{-dppv})_2\{\mu\text{-}(SCH_2)_2NH\}]^+$	**117(μ-H)$^+$**	-1.86

[a]dppv = $Ph_2P\text{-}CH=CH\text{-}PPh_2$. [b]The reduction of these complexes is one-electron process. [c]Not reported. [d]irreversible.

1.5.3.8   Peak-Splitting of the Two-Electron Reduction Waves

Consider the case of a single two-electron wave for which the rate constant of the second electron transfer is higher than that for the first electron transfer ($k°_2 \ll k°_1$). In this case, increasing the scan rate increases the peak-to-peak separation (ΔE_p) corresponding to the second electron transfer ($\Delta E_p = E_{pc2} - E_{pa2}$) more than that of the first electron transfer ($\Delta E_p = E_{pc1} - E_{pa1}$). At high scan rates, wave-splitting could be observed. Another important factor for wave-splitting is the separation of the formal one-electron transfer potentials ($\Delta E°$). The favorable condition for wave-splitting is the small

separation in formal potentials coupled with a low ratio of $k^{\circ}_2 / k^{\circ}_1$.[43,54,165,166] The CV curves of complex **20** obtained at 0.04 V·s^{-1} ≤ v ≤ 40 V·s^{-1} demonstrate that the two separate one-electron reduction steps can be observed at fast scan rates (Figure 1-18, where the peaks 1 and 2 are for the reduction of **20** and **20**$^-$, respectively, and the peaks 1′ and 2′ peaks are for the oxidation of **20**$^-$ and **20**$^{2-}$, respectively).[43] Wave-splitting is not observed for the two-electron reduction of complex **23** or **27** for which the second heterogeneous rate constant is, respectively larger than, or similar to, first.[47b,54]
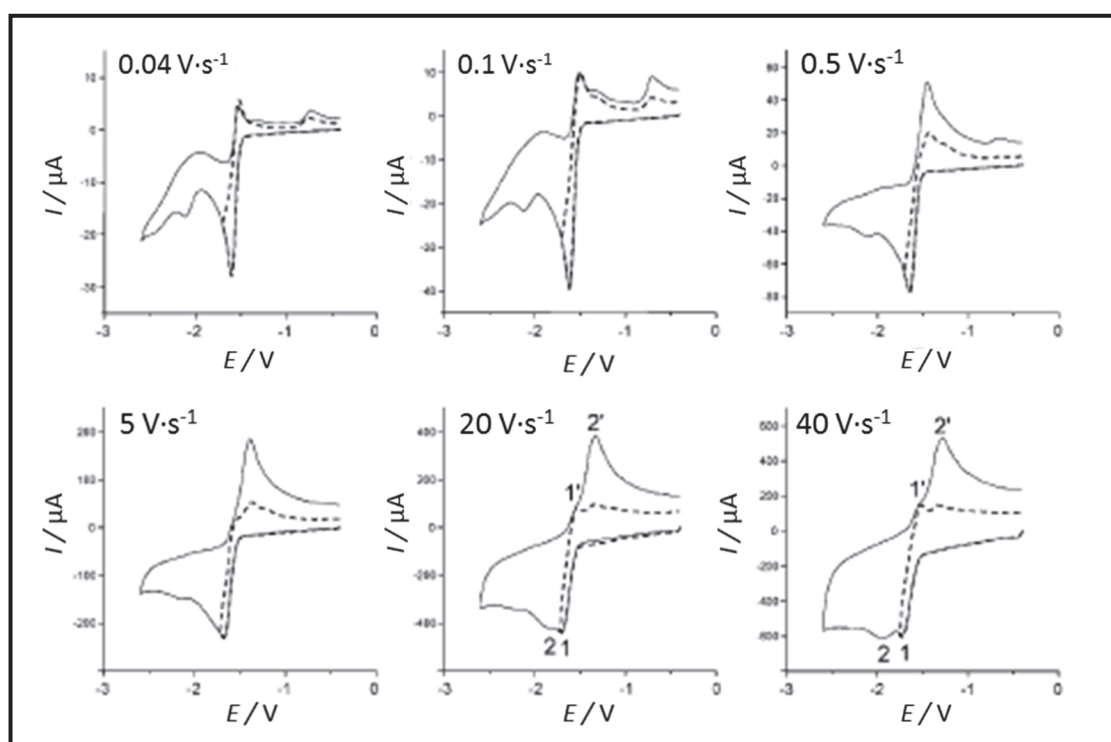
Figure 1-18. Cyclic voltammetry of complex **20** in MeCN/[NBu$_4$][PF$_6$] under Ar at different scan rates (vitreous carbon electrode; potentials are in V vs. ferrocenium/ferrocene couple).[43]

1.5.3.9   Solvent Effect on the Reduction Potential

The thermodynamics of the electron transfer, determined by ΔG° and E°, depend not only on the chemical structure of reactants and the products, but also on the medium (solvent, electrolyte) in which the redox reactions take place.[141] For the case of the normal ordering of potentials ($E^{\circ}_1 - E^{\circ}_2 > 0$), MO calculations predicted that $E^{\circ}_1 - E^{\circ}_2$ in the gas phase is +4-5 V owing to the electron-repulsion energy[167].[141] In cases where the reversible standard potentials have been measured, it is found that E°_2 is ~ +0.5-0.8 V

more negative than $E°_1$.[141] In solution there is an interaction between the solute species and the solvent molecules. The solvation stabilizes the species by an amount of energy termed solvation energy. *The solvation energy of the ions depends approximately on the square of the charge number.*[141] Thus, the solvation energy of the dianion is four times that of the monoanion and the solvation energy of the neutral species is quite small and can be neglected. Therefore, this solvation effect compresses the large gas-phase potential differences to smaller ones in solution. Also, different solvents have different solvation energies. The same complex may undergo two-electron uptake with potential inversion in one solvent, but in another solvent not. For example, in MeCN complex **27** undergoes an overall two-electron reduction with calculated $E°_1$ = -1.52 V and $E°_2$ = -1.06 V while in THF it shows no potential inversion ($E°_1$ = -1.485 V and $E°_2$ = -1.500 V; found by experiment).[52] Figure 1-19 shows the cyclic voltammograms of Complex **51** in MeCN, THF and CH_2Cl_2/Bu_4NPF_6 solutions. The separation between the two half-wave potentials ($\Delta E_{1/2}$) of complex **51** is small and depends on the solvent: $\Delta E_{1/2}$ = 0.12 V (MeCN) or 0.19 V (THF). In CH_2Cl_2 the two one-electron transfer processes occur in single wave with $E°_{ov}$ = -1.55 V.[70]
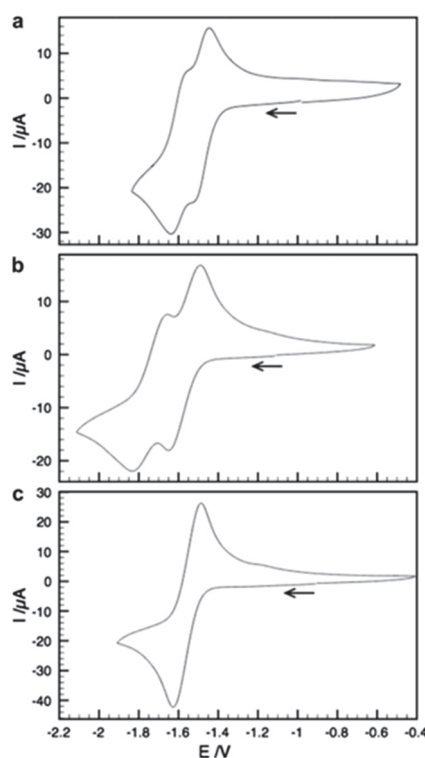
Figure 1-19. Voltammograms of 1 mM complex **51** in (a) MeCN, (b) THF and (c) CH_2Cl_2/Bu_4NPF_6 at 0.1 V·s^{-1} (glassy carbon electrode; *E* is vs. ferrocenium/ferrocene.[70]

1.6   Reduction of [Fe^{I}Fe^I] Models in the Presence of Acid

1.6.1   Proton Reduction Catalyzed by Hexacarbonyl Complexes

[Fe$_2$(CO)$_6${μ-(SCH$_2$)$_2$CH$_2$}] (3). When weak acids, such as CH$_3$CO$_2$H (pK_a = 22.3 in MeCN)[113], are used in the cyclic voltammetry of complex **3**, the electrocatalytic proton reduction is achieved when the potential is stepped sufficiently negative after the first electron reduction (**3** + e$^-$ → **3$^-$**) takes place. The monoanion **3$^-$** is not protonable by CH$_3$CO$_2$H[168] and hence the catalytic process should be supported by the decay product(s) of **3$^-$** (Scheme 1-18). Paradoxically, the use of acids sufficiently strong to protonate **3$^-$** engages pathways for H$_2$ formation and hence avoiding us from the complicated chemistry in the case of weak acids, which is not related to that of the H cluster. The mechanistic investigations as well as DFT studies of the electrocatalytic proton reduction catalyzed by **3** in the presence of *p*-toluenesulfonic acid (HOTs, pK_a = 8.3 in MeCN)[113] in THF show that once **3** is reduced at -1.7 V (vs. ferrocenium/ferrocene couple), the monoanion **3$^-$** undergoes fast protonation to afford **3H**, which is reduced at potential similar to, or more positive than, that of **3**.[156,169,170] The resulting **3H$^-$** is in turn protonated to **3H$_2$** that slowly releases H$_2$ (k ~ 4 s^{-1}) regenerating **3**. Another catalytic process is observed at potential more negative than that of the first process (~ -1.95 V vs. ferrocenium/ferrocene couple), which is attributed to reduction of **3H$_2$** to **3H$_2^-$** that releases H$_2$ much faster than **3H$_2$** (k ~ 10^4 s^{-1}).[156,169,170] Scheme 1-18 shows the H$_2$ releasing pathways catalyzed by **3** along with the DFT calculated intermediates. The protonation of **3$^-$** gives μ-hydride intermediate **3H** and the protonation of its reduced form **3H$^-$** results in two isomers of the diprotonated species **3H$_2$**, one with two protons on the metal centers and the other with μ-hydride and protonated S atom.[170]

Scheme 1-18. Proposed mechanism, showing DFT calculated intermediates, for the pathways of H_2 production catalyzed by **3**.[156,169,170]
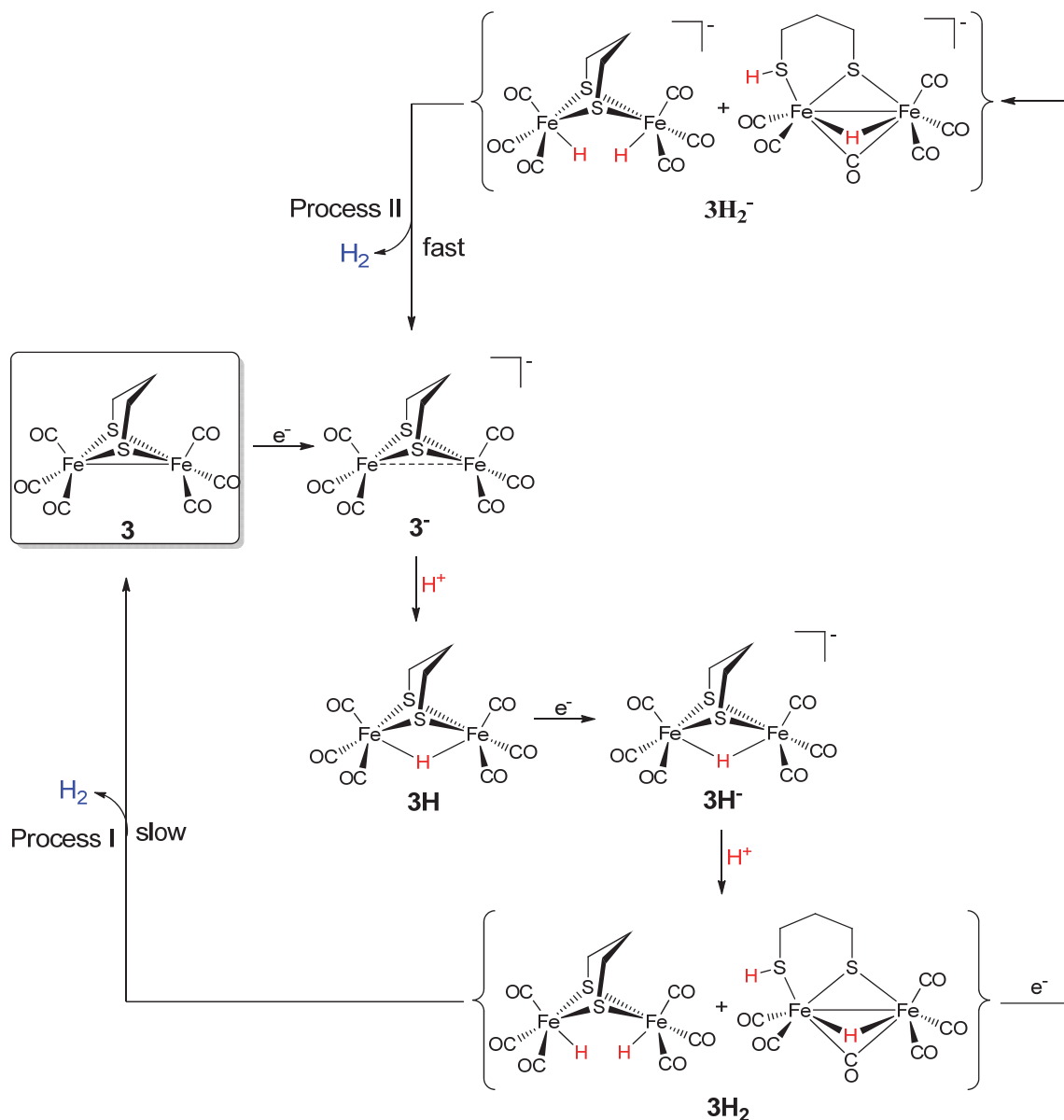
[Fe₂(CO)₆{μ-S₂C₆H₄}] (27). In contrary to complex **3**, the voltammetric reduction of complex **27** is a reversible two-electron transfer in a single step.[51-55] In the presence of CH_3CO_2H, the dianion **27²⁻** undergoes the first protonation step to give μ-hydride intermediate **27H⁻** as was revealed by electrochemical and DFT studies.[52] Further reduction and protonation lead to H_2 elimination and regeneration of the monoanion **27⁻**.[52] Scheme 1-19 shows the mechanism proposed for the catalytic proton reduction by **27** as well as the calculated structures of the intermediates.

Scheme 1-19. Electrocatalytic reduction of CH_3CO_2H in the presence of model complex **27**.[52]
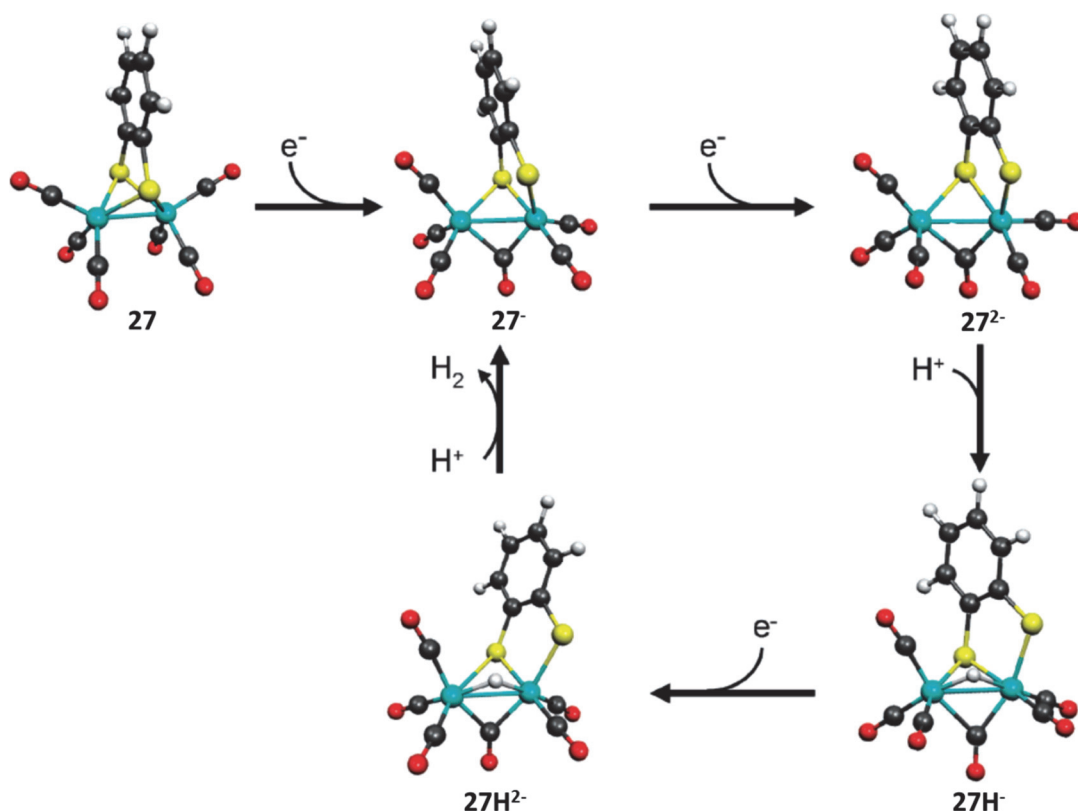
Whereas the catalytic process of the reduction of CH_3CO_2H in the presence of complex **27** occurs at ~ -2 V (vs. ferrocenium/ferrocene couple) in MeCN, the catalytic reduction of HOTs by **27** occurs at ~ -1.3 V (vs. ferrocenium/ferrocene couple) in MeCN. This difference is due to the fact that HOTs can protonate the intermediate **27H⁻** to give **27H₂**, which releases H_2. The intermediate **27H⁻** must be first reduced (at ~ -2 V vs. ferrocenium/ferrocene couple in MeCN) to **27H²⁻** to be basic enough to abstract proton from CH_3CO_2H.[51-55]

[Fe₂(CO)₆{μ-(PPhCH₂)₂CH₂}] (50a). The voltammetric reduction of complex **50a** in the presence of various concentrations of HOTs in THF shows two catalytic processes at ~ -2 V and -2.4 V (vs. ferrocenium/ferrocene couple).[68] The current response of **50a** to the HOTs concentration is similar to that of **3**, in which the H_2 formation follows two-electron reduction of the complex with faster H_2 production following further reduction. Nevertheless, the mechanism is different because the reduction of **50a** in the absence of acid follows a single step two-electron transfer process, where the reduction potential of **50a** (the neutral form) is 67 mV more negative than that of **50a⁻** (the monoanion).[68] Thus,

the first protonation step occurs after the two-electron reduction of **50a** at ~ -2 V (vs. ferrocenium/ferrocene couple) affording **50aH⁻**. H₂ evolution occurs slowly after the second protonation step of **50aH⁻**. The reduction of **50aH₂** at ~ -2.4 V (vs. ferrocenium/ferrocene couple) results in a very fast H₂ release from **50aH₂⁻**. The proposed mechanism for the two catalytic reduction pathways of HOTs in the presence of **50a** is shown in Scheme 1-20. The inset of Scheme 1-20 shows the calculated structure of **50aH₂**, but with Me groups at the μ-P atoms rather than the Ph groups.

Scheme 1-20. Proposed mechanism for HOTs reduction in the presence of complex **50a**. The inset shows the calculated structure (in grey) of the intermediate [H₂Fe₂(CO)₆{μ-(PMeCH₂)₂CH₂}] (**50aH₂**).[68]
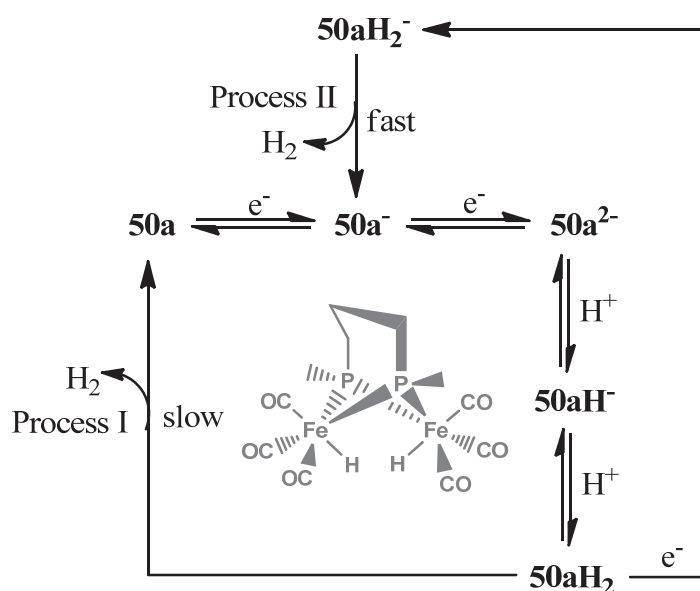
Electrochemical simulation shows that the first-order rate constant of the H₂ release from **3H₂** is larger by a factor of 2 than that that from **50aH₂**. The DFT calculations show that this relative reactivity is related to the H···H distance, which is shorter in **3H₂** than in **50aH₂**.[68] That processes I and II in case of complex **3** (Scheme 1-18) occur at less negative potential than those in case of complex **50a** (Scheme 1-20) can be attributed to the better electron donating ability of the linker -PPh-(CH₂)₃-PPh- in **50a** compared to the dithiolate -S-(CH₂)₃-S- in **3**.

[Fe₂(CO)₆{μ-(SCH₂)₂NR}]. The electrocatalytic reduction of protons by model complexes containing azadithiolato linkers -S-CH₂-NR-CH₂-S- may start with protonation step prior reduction if the source of H⁺ is an acid sufficiently strong to protonate the N atom of the neutral complex, such as HOTs (pK_a = 8.3 in MeCN)[113] or

HBF$_4$·Et$_2$O (pK_a = 0.1 in MeCN)[113]. The first reduction step therefore occurs at the reduction potential of the N-protonated complex. It has been found that CF$_3$CO$_2$H (pK_a = 12.65 in MeCN)[113] does not protonate complex **20** in MeCN solution and hence the catalytic reduction of CF$_3$CO$_2$H in the presence of **20** starts with reduction step rather than protonation.[171] Scheme 1-21 shows the proposed mechanism for proton reduction catalyzed by complex **20** (the same for **18**) in MeCN when HOTs or HBF$_4$·Et$_2$O are used as a source of protons.[43,129,171,172] Digital simulation based on Scheme 1-21 is performed.[171] The reduction of the protonated complex **20H$^+$** into **20H** (-1.2 V vs. ferrocenium/ferrocene couple) is followed by second protonation step to give **20H$_2$$^+$**. The latter undergoes reduction at potential similar or less negative than that of **20H$^+$** to afford **20H$_2$**. The intermediate **20H$_2$** releases H$_2$ slowly (k = 3 s^{-1}) regenerating complex **20** (process I). In case of HBF$_4$·Et$_2$O, H$_2$ evolution occurs at -1.4 V (process II) as a result of reduction of the protonated **20H$_2$** (i.e. **20H$_3$$^+$**). **20H$_2$** is not protonable by HOTs and it has to be reduced first at -1.6 V, then protonation occurs by HOTs to give **20H$_3$$^+$**.[171] The release of H$_2$ from **20H$_2$** could occur via two pathways: (*i*) Bimolecular reaction between two **20H$_2$** entities (Scheme 1-22).[171] If we assume that **20H$_2$** retains the structure of **20H$_2$$^+$**, then a rearrangement that allows the μ-hydride in **20H$_2$** to become in close proximity to the N-H proton is necessary for H$_2$ release via path (*ii*). The evolution of H$_2$ via path (*i*) requires coupling of the N-H proton of one **20H$_2$** species and with the μ-hydride of another **20H$_2$** species to give **20H$^+$** and **20(μ-H)$^-$**. A second bimolecular reaction between **20H$^+$** and **20(μ-H)$^-$** would then produce H$_2$ and **20**. This path clearly leads to slow H$_2$ evolution. It has been found that the rate of H$_2$ release from [Fe$_2$(μ-H)(CO)$_6${μ-(SCH$_2$)$_2$NR}] via intramolecular N-H···H-Fe proton-hydride coupling can be accelerated if the structure in the ground state resembles that of the H cluster; i.e. rotated structure in which the Fe(CO)$_3$ units are in staggered conformation. If the ground state structure of **20H$_2$** was the transition state (rotated state) shown in Scheme 1-22, then **20H$_2$** would release H$_2$ via N-H···H-Fe coupling without the need of structural rearrangement.

Scheme 1-21. Proposed mechanism for proton reduction catalyzed by complex **20** in MeCN in the presence of HOTs or HBF$_4$·Et$_2$O. The structures of the intermediates **20H$_2$**, **20H$_3^+$** and **20H$_3$** are proposed to be similar to the calculated structures of **20^{2-}** since the iron core of these intermediates accumulates two electrons. The potentials are vs. ferrocenium/ferrocene couple.[129,171]
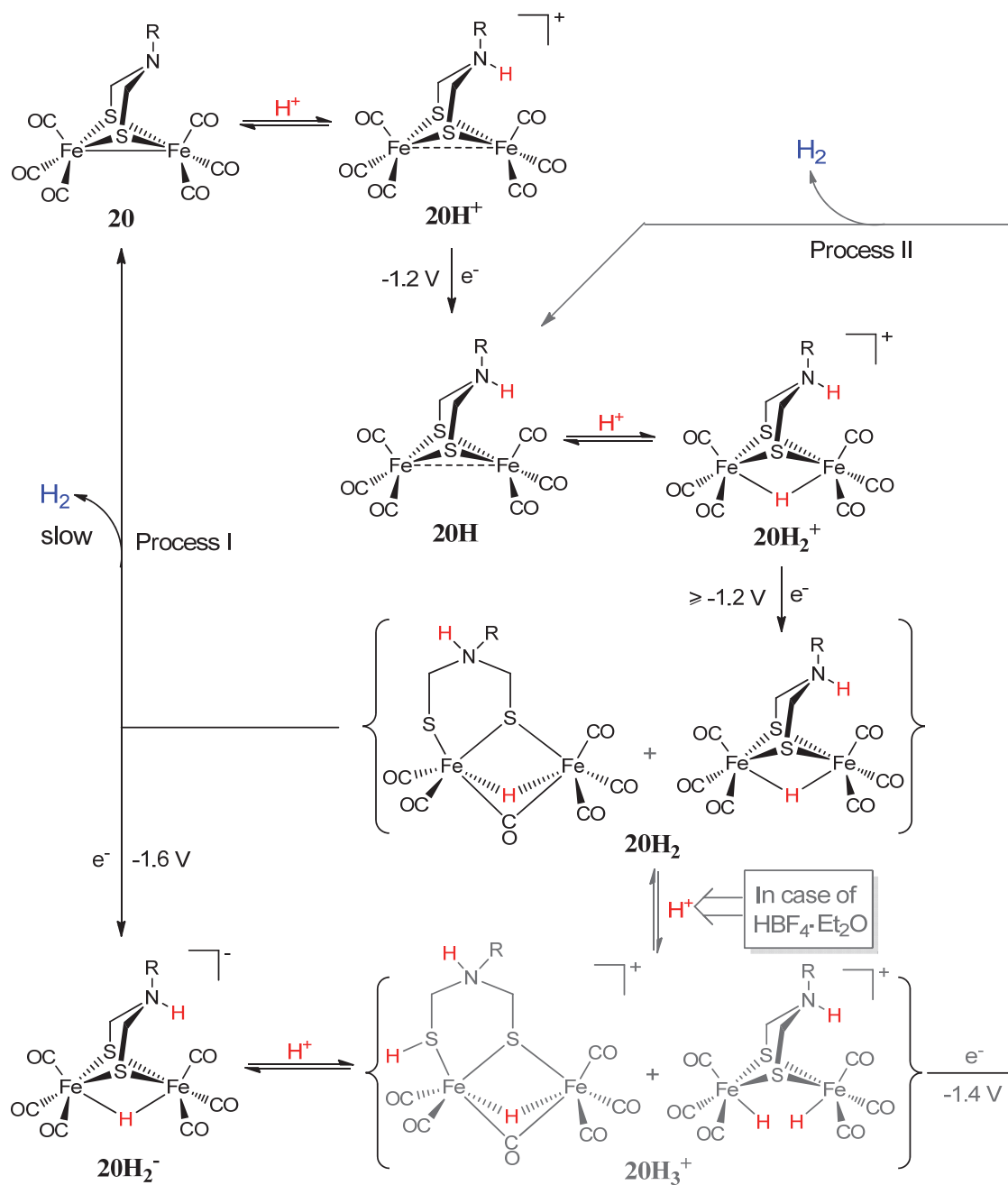
Scheme 1-22. Proposed mechanism for H₂ release from the **20H₂** intermediate.[129,171]
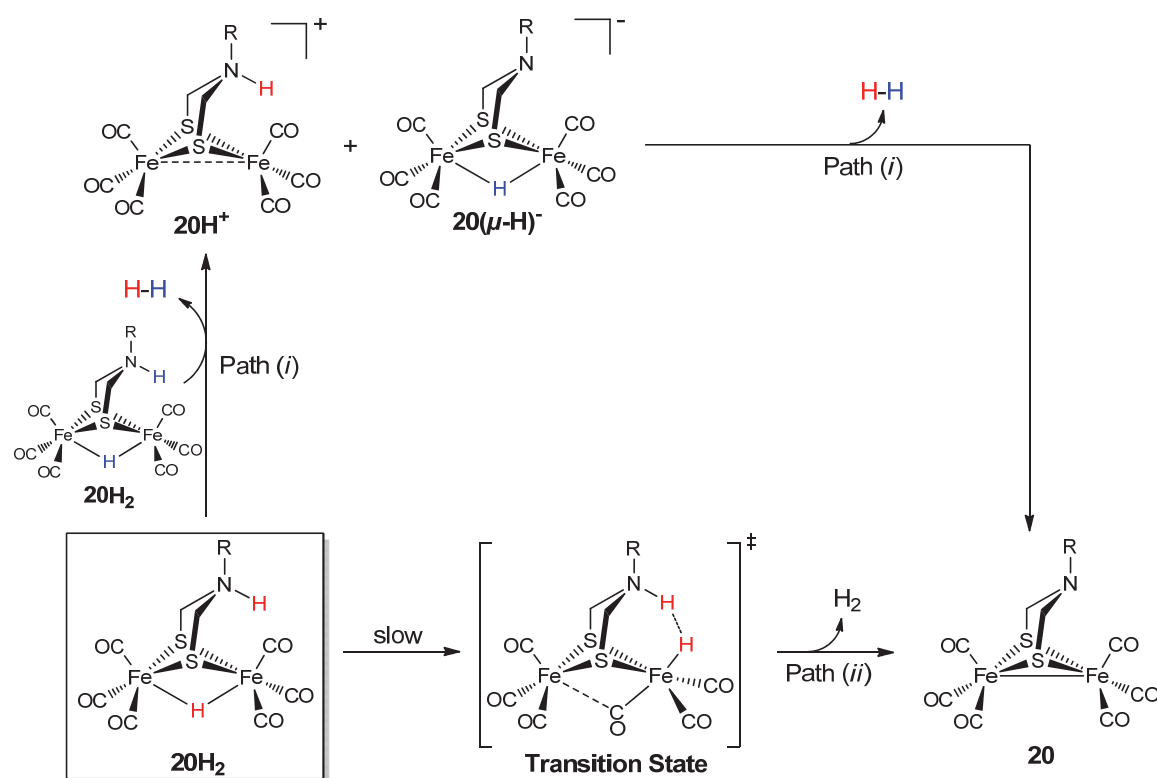
[Fe₂(CO)₆{μ-(SCH₂)₂SiC₄H₈}]. The electrochemical studies on [Fe₂(CO)₆{μ-(SCH₂)₂SiC₄H₈}] in the presence of the weak pivalic acid HP (CMe₃CO₂H)[173] reflects the reactivity of the μ-S atoms in model complexes containing Si heteroatom in the bridgehead of the dithiolato linker.[49] It has been shown by experiments and simulations that the catalytic reduction of HP by [Fe₂(CO)₆{μ-(SCH₂)₂SiC₄H₈}] in MeCN is influenced by a thermodynamic process prior reduction in which the neutral complex and an adduct, formed from coordination of the undissociated HP molecule to the μ-S atoms of the complex via hydrogen bonding, are in a state of equilibrium:
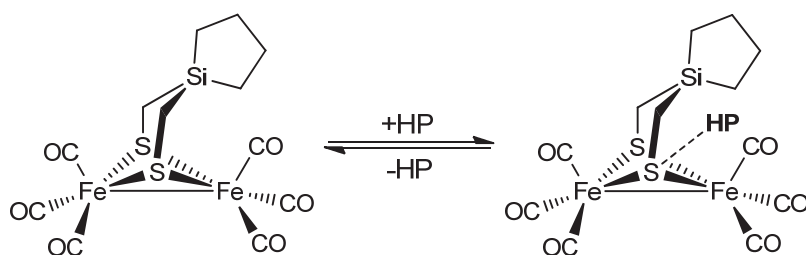
The reduction process leads to the dissociation of HP and protonation. Further reduction and protonation steps lead to H_2 production at three different potentials with high activity.[49]

1.6.2   Proton Reduction Catalyzed by Substituted Complexes

$[Fe_2(CO)_4(PMe_3)_2\{\mu-(SCH_2)_2E\}]$ (E = CH$_2$, NR). The mechanism for electrocatalytic proton reduction by disubstituted complexes can start with Fe-protonation before reduction if an appropriate acid is used, which is in contrast to their hexacarbonyl parents.[44,75,86,97,99,129,174] For example, in the presence of strong acids, complex **83** (X = CH$_2$) is protonated to afford μ-hydride **83(μ-H)$^+$** then the first electron transfer step occurs at the reduction potential of **83(μ-H)$^+$**.[75,86,174-176] If CH_3CO_2H (pK_a = 22.3 in MeCN)[113] is used for the voltammetric experiment, the first step in the catalytic cycle is the reduction of the neutral complex **83** followed by protonation of the reduction products.[75] Complexes **98** (E = NCH$_2$Ph)[98,99] and **101** (E = NCH$_2$C$_6$H$_4$-2-Br)[44] catalyze the reduction of CH_3CO_2H in a similar manner to **83** as this acid does not protonate neither the amine function in **98** and **101** nor the Fe-Fe bond. Complex **98** catalyzes the reduction of $HClO_4$ (pK_a = 2.0 in MeCN)[113] at ~ -1.5 V (vs. ferrocenium/ferrocene couple), the reduction potential for the N-protonated complex **98H$^+$**. On the experimental time-scale, neither **98(μ-H)$^+$** nor the doubly protonated complex **98H$_2$$^{2+}$** (Scheme 1-7) exhibits catalytic behavior. As reported, **101(μ-H)$^+$** catalyzes the reduction of HOTf.

$[Fe_2(CO)_2(\kappa^2-dppv)\{\mu-(SCH_2)_2E\}]$. The *t*-hydrides of complexes **116** (E = CH$_2$)[105-107], **117** (E = NH)[105-107] and **118** (E = O)[106] are stable and sufficiently long-lived at mild temperatures (0 ºC) allowing cyclic voltammetric investigations. The catalytic activity of **116(t-H)$^+$-118(t-H)$^+$** is dependent on the strength of the acid used as well as the nature of E. For example, only **117(t-H)$^+$** is catalytically active toward reduction of [HPMe$_2$Ph]BF$_4$ (pK_a = 5.7, CD$_2$Cl$_2$)[177], CF_3CO_2H (pK_a = 12.7 in MeCN)[113] or $ClCH_2CO_2H$ (pK_a = 15.3 in MeCN)[177] whereas **118(t-H)$^+$** and **116(t-H)$^+$** are not and require very strong acid such as HBF$_4$·Et$_2$O (pK_a = -3 in MeCN)[178].[105-107] Using very strong acids, the catalytic activity of **118(t-H)$^+$** is much higher than that of **116(t-H)$^+$** reflecting the role of even the very weakly basic ether group in **118(t-H)$^+$** in proton relay. Scheme 1-23 displays the proposed mechanism for H_2 production catalyzed by **116** in the presence of HBF$_4$·Et$_2$O in CH_2Cl_2 solution at 0 ºC.

Scheme 1-23. Proposed mechanism for reduction of HBF$_4$·Et$_2$O catalyzed by **116** in CH$_2$Cl$_2$ at 0 ºC.[105-107,179-181]

In the presence of HBF$_4$·Et$_2$O, **116** is protonated at 0 ºC to afford **116(*t*-H)$^+$** that undergoes reversible one-electron reduction at -1.67 V (vs. ferrocenium/ferrocene couple). The protonation of **116(*t*-H)** results in H$_2$ release and formation of the 33e$^-$ rotated cation **116$^+$** that is then reduced at ~ -0.8 V (vs. ferrocenium/ferrocene couple) completing the cycle. The final reduction step **116$^+$** + e$^-$ → **116** is investigated independently.[89,179-181] Scheme 1-24 shows the mechanism for the catalytic reduction of weak and strong acids catalyzed by **117** in CH$_2$Cl$_2$ at 0 ºC, which is proposed based on protonation studies (Scheme 1-8) as well as DFT calculations.[182] Acids that can protonate **117** at both the N and Fe atoms to give **117H$_2$$^{2+}$**, such as HBF$_4$·Et$_2$O (p$K_a$ = -3 in MeCN)[178] and CF$_3$CO$_2$H (pK_a = 12.7 in MeCN)[113], are called herein strong acids while those acids that lead only to the *t*-hydride **117(*t*-H)$^+$** are said to be weak, such as ClCH$_2$CO$_2$H (pK_a = 15.3 in MeCN)[177]. The pK_a of **117(*t*-H)$^+$** is estimated at 16 in MeCN. [HNMe$_3$]BAr$^F_4$ (pK_a = 17.6 in MeCN)[113] does not convert **117** into detectable levels of **117(*t*-H)$^+$** at low temperatures, but quantitatively produces **117(μ-H)$^+$** at room temperature.
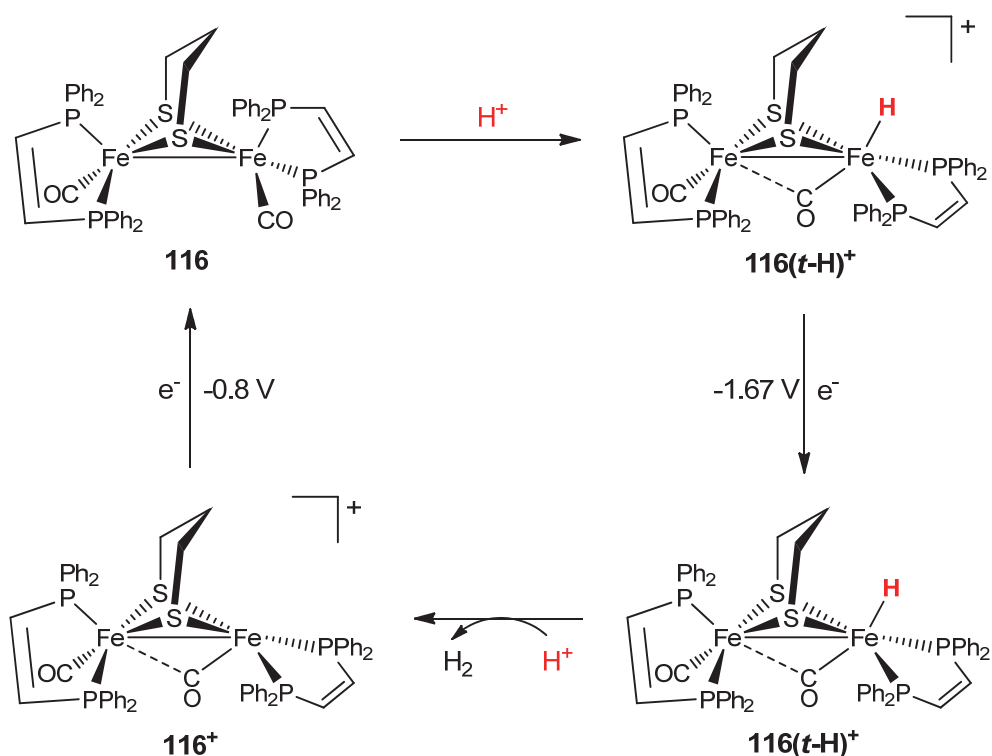
Scheme 1-24. Proposed mechanism for H2 production from strong and weak acids catalyzed by **117**.[182]
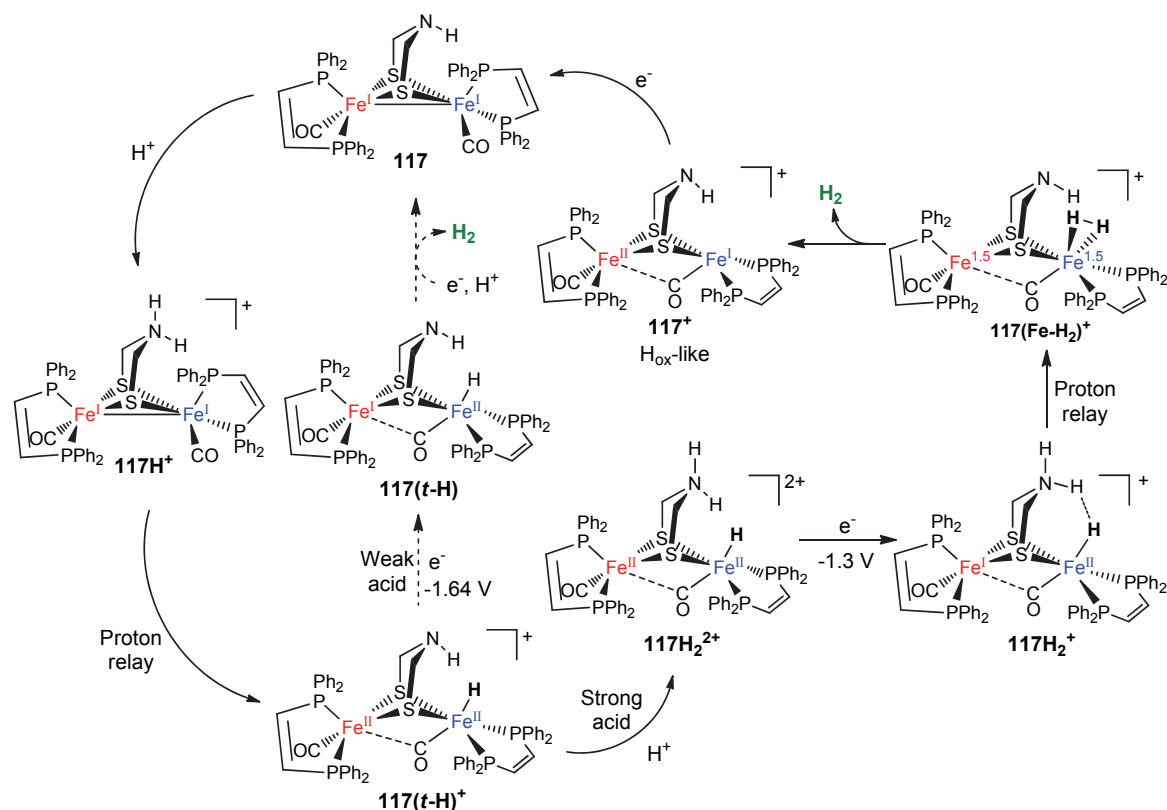
A comparison between complexes **116** and **117** with respect to the electrocatalytical properties using various acids is summarized in Table 1-8 whereby we can notice the following:[105]

- The best catalyst is $117H_2^{2+}$, where it has the highest turnover frequency (TOF) and the lowest overpotential (η). The high catalytic activity of $117H_2^{2+}$ may arise from the fact that the ammonium proton and the *t*-hydride are in close proximity facilitating the intramolecular proton transfer $117H^+ \rightarrow 117(Fe-H_2)^+$ (Scheme 1-24).

- $117(t-H)^+$ is better catalyst than $116(t-H)^+$ in terms of kinetics and thermodynamics even if they are almost isostructural. While $116(t-H)^+$ is not responsive to weak acids (as discussed before), $117(t-H)^+$ does owing to the relay activity of the basic amine functionality. Remember that at low temperatures the neutral complex **116** forms *t*-hydrides only from strong acids such as $HBF_4 \cdot Et_2O$ while the weaker acids such as $ClCH_2CO_2H$ and CF_3CO_2H protonate **117** in CH_2Cl_2 leading to $117(t-H)^+$ and $117H_2^{2+}$, respectively.

- *t*-Hydride species are much more catalytically active toward H_2 production than the μ-hydride species. Moreover, the *t*-hydride species **117(*t*-H)$^+$** catalyzes the reduction of $ClCH_2CO_2H$ at less negative potentials than their μ-hydride counterparts.

Table 1-8. Electrocatalytical properties of **116** and **117** in the presence of acids.[a, 105]

Acid	Catalyst	$E_{1/2}$ / V $(CH_2Cl_2)^b$	E_{cat} / V $(CH_2Cl_2)^c$	TOF^d / s^{-1}	η^e / V
$ClCH_2CO_2H$	**117(*t*-H)$^+$**	-1.64 (irreversible)	-1.49	5000	0.71
CF_3CO_2H	**117H$_2^{2+}$**	-1.3 (irreversible)	-1.11	58000	0.51
$ClCH_2CO_2H$	**117(μ-H)$^+$**	-1.86	-1.72	20	0.90
$HBF_4 \cdot Et_2O$	**116(*t*-H)$^+$**	-1.67	-1.49	5	1.32
$ClCH_2CO_2H$	**116(μ-H)$^+$**	-1.8	-1.78	3	0.95

[a]*t*-hydride species are generated in situ at a temperature where they are stable (0 °C) whereas the corresponding μ-hydrides are isolated as BF_4^- salts prior experiments. Potentials are vs. ferrocenium/ferrocene couple. [b]Half-wave potential. All cations undergo one-electron reduction process. [c]The catalytic potentials are calculated by the method reported by Fourmond et al.[183] [d]Turnover frequency. [e]Overpotential $(\eta) = E°_{HA/H2} - E_{cat}$, where $E°_{HA/H2}$ is the standard reduction potential of the acid HA.[183]

1.7   [Fe$_2$S$_3$] Model Complexes

The model complexes in Figures (1-7 to 1-11) can be considered as [Fe$_2$S$_2$] systems while the H cluster has [Fe$_2$S$_3$] core (Figure 1-3). The synthetic chemistry has also led to [Fe$_2$S$_3$] models shown in Figure 1-20. Formation of these [Fe$_2$S$_3$] complexes requires thioether as pendant ligand (**123-124** and **126**) or the use of nonpendant SR$_2$ ligands in **125** and **127-131**. The mechanism of cyanation of complexes **122** and **123** to give mono- and dicyanide-substituted products has been proposed as shown in Scheme 1-25.[159] The first step is a concerted process involving fast regioselective attack by cyanide and decoordination of the thioether ligand to afford **M1** as intermediate. **M1** undergoes then slower re-binding of the thioether with concerted dissociation of CO ligand to afford complex **132**, which was characterized by X-ray crystallography. This mechanism was revealed by stopped-flow FTIR mechanistic study. The use of two or more equivalents of CN^- proceeds via **M1** to afford **M2** as a moderately stable intermediate, which rearranges slowly at r.t. affording the thermally stable product **P** in which all CO ligands are terminal. Indeed, **M2** remains up till now the first and only example of subsite structure, which has both two CN^- ligands and μ-CO ligand.
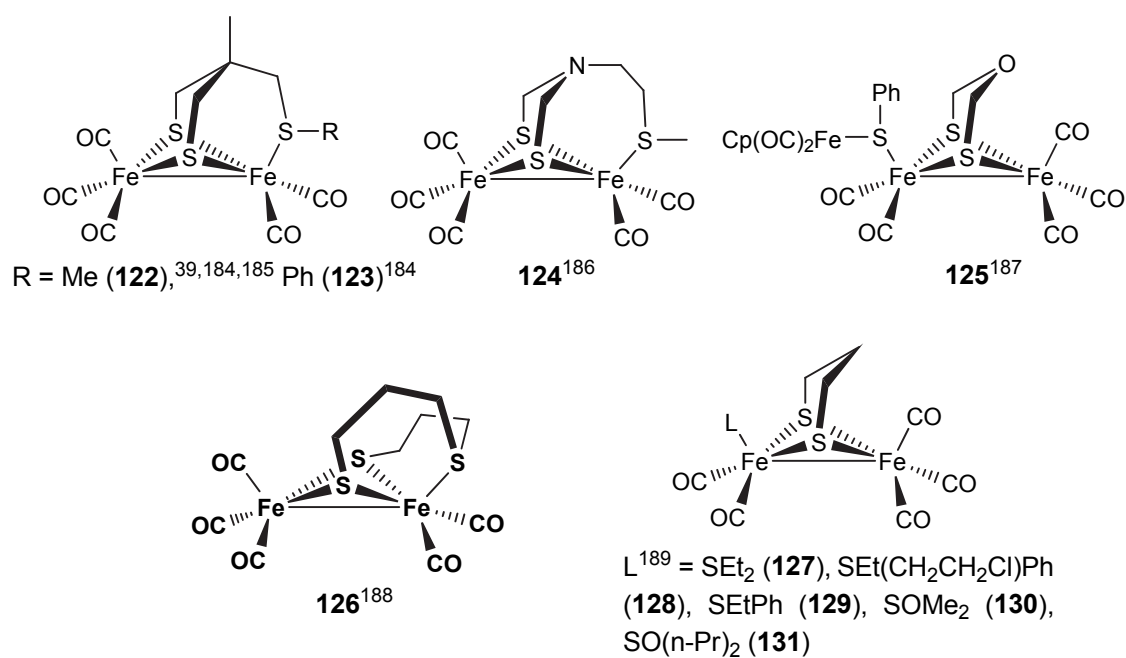
Figure 1-20. [FeFe]-hydrogenase models featuring a [Fe$_2$S$_3$] core.

Scheme 1-25. Proposed mechanism of Cyanation of complexes **122** and **123**.[159]
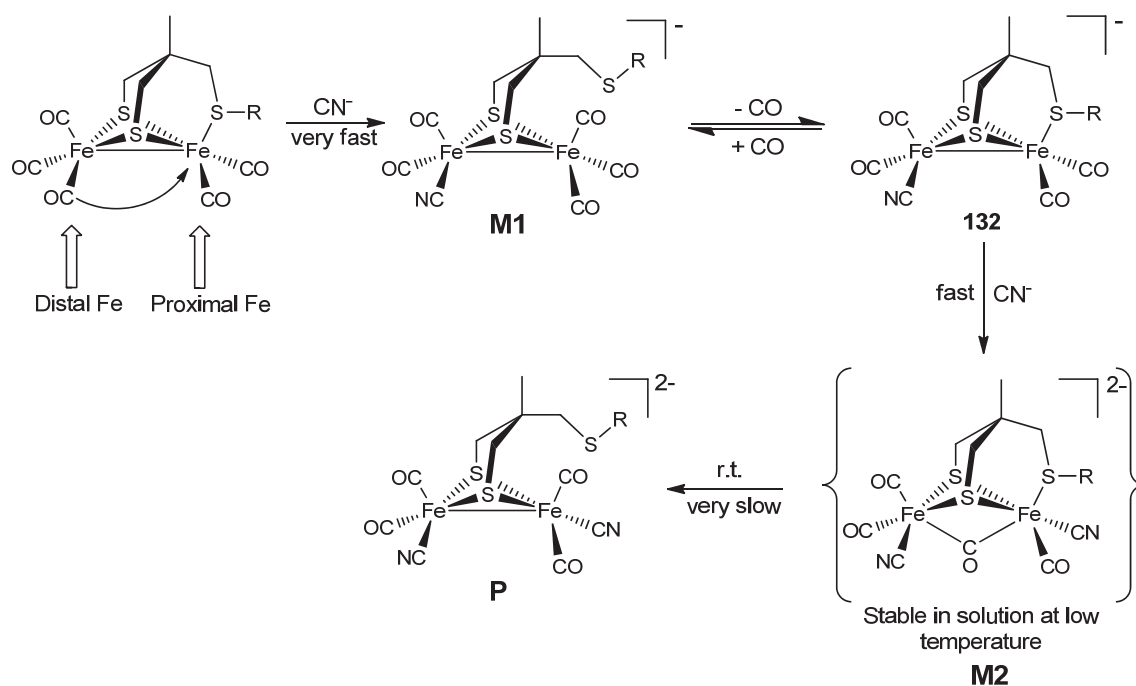
Weigand and coworkers studied the substitution reactions on **126** using P(OMe)$_3$ and provided further proof for the suggested mechanism of cyanation (Scheme 1-25) by isolating and characterizing an intermediate analogous to **M1**. This study is summarized in Scheme 1-26.

Scheme 1-26. Substitution Pathway in complex **126** by P(OMe)₃.[188]
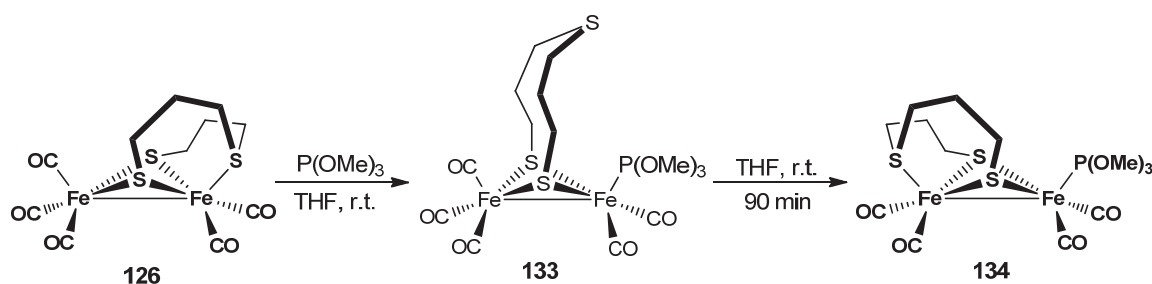
Complex **126** reacts with 1 equiv. P(OMe)₃ at r.t. to afford first the kinetically controlled product **133**, which upon standing at r.t. for 90 min undergoes intramolecular substitution of CO by the pendant thioether to afford the thermodynamic product **134**. In contrast, performing the reaction under reflux conditions produces exclusively complex **134**. The kinetic product **133** was isolated and characterized by spectroscopic techniques and X-ray crystallography. Complex **133** can be viewed as an analogous to **M1** and hence this study by Weigand et al. contributed to better understanding of the "on-off" coordination mode of the pendant thioether group.

1.8   Motivation

The preceding sections summarize some of the most important developments in the synthetic chemistry of models for the H cluster of the [FeFe]-hydrogenase. The investigations of the ability of the models toward the electrocatalytic reduction of protons showed that the presence of protonation sites on the model complex is important to lower the overpotential and to enhance the catalytic activity.

Figure 1-21 provides an overview for different derivatization strategies of various [FeFe]-hydrogenase models that are described in this thesis.
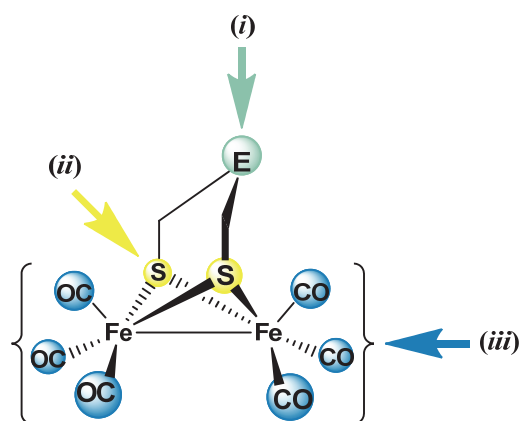
Figure 1-21. Possible derivatization of [FeFe]-hydrogenase models.

These strategies of this thesis involve:

(i) Introduction of a phosphine oxide functionality (Chapters 2 and 4) as well as unusual heteroatoms, Ge and Sn, to the bridgehead E of the μ-dithiolato linker (Chapters 6 and 7).

(ii) Studying the influence of the presence of μ-Se instead of the μ-S atoms toward the redox properties of the [Fe$_2$S$_2$] cluster (Chapter 5).

(iii) Substitution of one CO ligand by stronger donor PPh$_3$ and P(OEt)$_3$ ligands (Chapters 3 and 5).

Chapter 2 describes the synthesis and characterization of a novel [FeFe]-hydrogenase model complex containing phosphine oxide in the dithiolato ligand, namely [Fe$_2$(CO)$_6$\{μ-(SCH$_2$)$_2$(Ph)P=O\}] (**137**). Complex **137** was prepared via reaction of equimolar quantities of (μ-LiS)$_2$Fe$_2$(CO)$_6$ with O=P(Ph)(CH$_2$Cl)$_2$. The protonation properties of complex **137** have been investigated by monitoring the changes in IR (in the υ(CO) region) and ^{31}P\{^{1}H\} NMR spectra upon addition of pyridinium tetrafluoroborate [HPy][BF$_4$] and HBF$_4$·Et$_2$O, suggesting protonation of the P=O functionality. In addition, high-level DFT calculations on the protonation sites of complex **137** in CH$_2$Cl$_2$ have been performed and support our experimental observations that the P=O unit is protonated by HBF$_4$·Et$_2$O. Cyclic voltammetric experiments of complex **137** showed anodic shift of the oxidation peak upon addition of HBF$_4$·Et$_2$O proposing CE process. The influence of replacing the Ph group in complex **137** by an Et group in [Fe$_2$(CO)$_6$\{μ-(SCH$_2$)$_2$(Et)P=O\}] (**144**) toward the protonation properties as well as the electrocatalytic behavior is discussed in great details in Chapter 4. While complex **137** requires an excess amount of strong acids (100 equiv.) to be fully protonated at the P=O functionality in CH$_2$Cl$_2$

solution, only few equivalents of moderately strong acids (such as HBF$_4$·Et$_2$O) are enough for full P=O-protonation of complex **144** as evident by IR spectroscopy and cyclic voltammetry. To the best of my knowledge, complex **144** represents the first example of a protonable hexacarbonyl complex using moderately strong acids (CF$_3$CO$_2$H).

Chapters 3 describes the influence of substituting one CO ligand in [Fe$_2$(CO)$_6${μ-(SCH$_2$)$_2$(Ph)P=O}] (**137**) by better σ-donor L ligands affording [Fe$_2$(CO)$_5$(L){μ-(SCH$_2$)$_2$(Ph)P=O}] {L = PPh$_3$ (**138**) and P(OEt)$_3$ (**139**)} in relation to the steric interactions and the voltammetric behavior. Cyclic voltammetric investigations under N$_2$ and CO showed remarkable differences in the electrochemical behaviour of complexes **138** and **139**: (*i*) Complex **138** tends to expel PPh$_3$ upon reduction whereas complex **139** exhibits chemical reversibility and (*ii*) Under CO, complex **139** reacts with CO affording a new compound **P**, which shows reversible wave at $E_{1/2}$ ~ -0.9 V (vs ferrocenium/ferrocene couple) while the presence of CO assists the formation of**137** during the voltammetric experiment of **138**. Using DFT calculations we provide an explanation for the difference in stabilities between the Fe-PPh$_3$ and Fe-P(OEt)$_3$ bonds.

Chapter 5 shows that the presence of OH groups in complexes [Fe$_2$(CO)$_6${μ-(SCH$_2$)$_2$C(CH$_2$OH)$_2$}] (**147**) and [Fe$_2$(CO)$_6${μ-(SeCH$_2$)$_2$C(CH$_2$OH)$_2$}] (**148**) is found to influence the cathodic processes and their potentials. Complex **147** catalyzes the reduction of protons from CH$_3$CO$_2$H with less overpotential than that in the case of complex **148**. The reduction of complex [Fe$_2$(CO)$_5$PPh$_3${μ-(SCH$_2$)$_2$C(CH$_2$OH)$_2$}] (**149**) shows behavior similar to that of complex **138** such that the Fe-PPh$_3$ bond undergoes dissociation after reduction.

Chapters 6 and 7 introduce the syntheses of novel [FeFe]-hydrogenase models, [Fe$_2$(CO)$_6${μ-(SCH$_2$)$_2$E}] (E = GeMe$_2$ (**150**), SnMe$_2$ (**151**), SnPh$_2$ (**153**)). The syntheses of these complexes were performed via reaction of equimolar quantities of (μ-LiS)$_2$Fe$_2$(CO)$_6$ with E(CH$_2$X)$_2$, which led to the formation of dimeric complexes in case of E = SnMe$_2$ and SnPh$_2$, [Fe$_2$(CO)$_6${μ-(SCH$_2$)$_2$E}]$_2$ (SnMe$_2$ (**152**), SnPh$_2$ (**154**)). Complexes **150** and **151** are unique in featuring planar structures (almost C$_{2v}$ symmetry) such that the FeC$_2$S$_2$E six-membered rings adopt a half-chair conformation, which is the transition state described for the equilibration between the chair/boat conformations of all other reported models. IR spectroscopy suggests protonation of the μ-S atoms of complex **150** in CH$_2$Cl$_2$ using strong acids such as HBF$_4$·Et$_2$O or CF$_3$SO$_3$H, but not in the cases of [Fe$_2$(CO)$_6${μ-(SCH$_2$)$_2$E}] (E = C (**12**), Si (**25**)) reflecting the effect of the Ge

atom toward the electron density of the μ-S atoms. Cyclic voltammetric investigations on complex **150** in CH_2Cl_2/NBu_4PF_6 solution show that the cathodic process follows an ECE mechanism. The reduction of CF_3SO_3H and $HBF_4 \cdot Et_2O$ in the presence of complex **150** in CH_2Cl_2/NBu_4PF_6 solution is described (0.5-2 equiv. acid).

A side project of my work (Chapter 8) describes the synthesis and characterization of various Ni^{II}, Pd^{II} and Pt^{II} complexes with carbamodithioate or carbamoselenothioate chelating ligands, complexes **155-163**.

Chapter 2

A Novel [FeFe]-Hydrogenase Model with (SCH$_2$)$_2$P=O Moiety

(Publication Number 1)
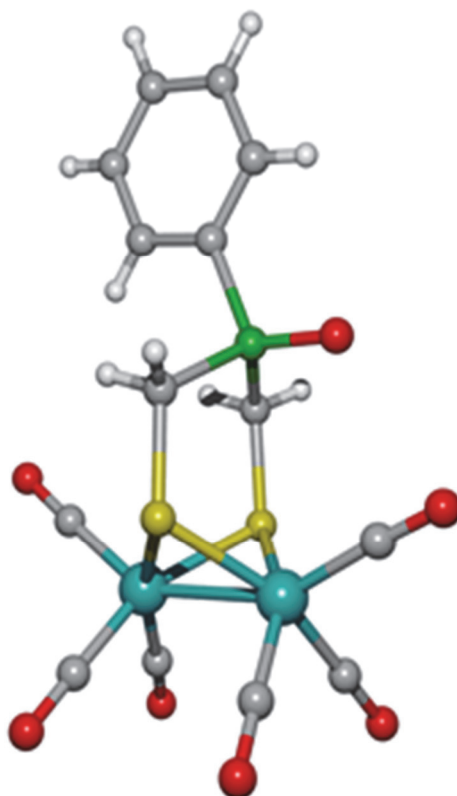
2 A Novel [FeFe]-Hydrogenase Model with $(SCH_2)_2P=O$ Moiety

In step with population growth and industrial advance, global demand for energy has risen inexorably and the major sources of energy are fossil fuels (coal, oil, and natural gas). These fuels are non-renewable and will, one day, be exhausted. Moreover, hydrocarbon fuels produce massive emission of greenhouse gases that are considered to be the main reason of the climate change.[1] In comparison, hydrogen is a promising energy source for the future by virtue of its high energy density and its clean cold combustion product in fuel cells. Nature produces hydrogen to provide energy through enzymes. An example of such kind of enzymes are the [FeFe] hydrogenases that catalyze the reversible process of dihydrogen formation from protons ($2H^+ + 2e^- \leftrightarrow H_2$).[11] Since the active sites of the [FeFe]-hydrogenase in *Desulfovibrio desulfuricans*[11g] and *Clostridium pasteurianum*[11h] were reported, numerous [FeFe]-hydrogenase models have been prepared in order to mimic and to provide a better understanding of the structure and function of the active site of the enzyme (Figure 1-3)[11]. Protonation of the iron centers to form terminal or bridging hydrides, as well as the nitrogen atom of the $(SCH_2)_2NH$ linker is considered as a fundamental step in the function of the active site to catalyze the production of hydrogen molecule.[15-17,23,24] In the biological system, the azadithiolato cofactor, $(SCH_2)_2NH$, is proposed to shuttle protons to and from the diiron core via an agostic or hydrido-proton interaction (Figure 2-1 and Scheme 1-1).[15-17,23,24]
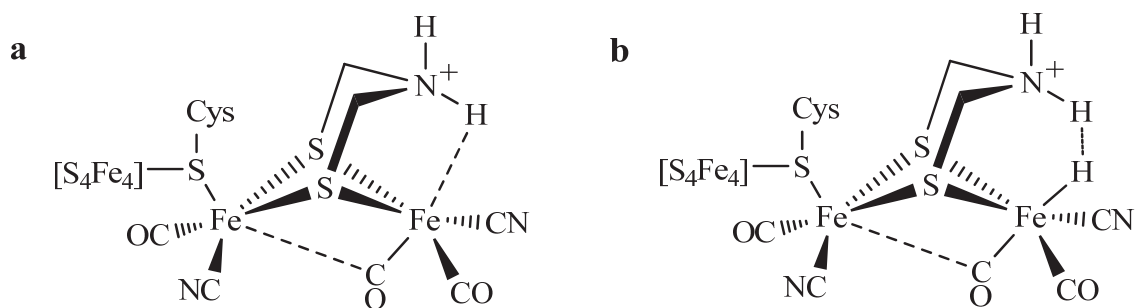
Figure 2-1. Possible intermediates leading to proton relay via (a) agostic interaction and (b) hydrido-proton interaction.

Focusing on the proposed biological role of the -S-CH2-E-CH2-S- linker in the catalytic reduction of protons to hydrogen molecule, Weigand et al. reported various model complexes in which the typical bridgehead atoms (E = C, N, O) are replaced by sulfur,[47,115,190] selenium,[48,58,61] or silicon[49,66,82,191,192] atoms. The protonation properties (Fe-, N- and S-protonation) of various model complexes are described.[125] Recently, Song et al. described the reaction of $(\mu\text{-}HS)_2Fe_2(CO)_6$ with $RP(CH_2OH)_2$ (R = Ph; η^5-$C_5H_4CH_2FeCp$) affording $Fe_2S_2(CO)_5PR_3$ instead of $[Fe_2(CO)_6\{\mu\text{-}(SCH_2)_2PR\}]$ (Scheme 2-1).[193] This reaction pattern can be attributed to the high nucleophilicity of phosphines leading to substitution of the CO ligand in $(\mu\text{-}RS)_2Fe_2(CO)_6$ rather than the formation of $[Fe_2(CO)_6\{\mu\text{-}(SCH_2)_2PR\}]$.[194-196]

Scheme 2-1. Reaction of $(\mu\text{-}HS)_2Fe_2(CO)_6$ and $RP(CH_2OH)_2$ (R = Ph; η^5-$C_5H_4CH_2FeCp$) to afford $Fe_2S_2(CO)_5PR(CH_2OH)_2$ as reported by Song et al..[193]
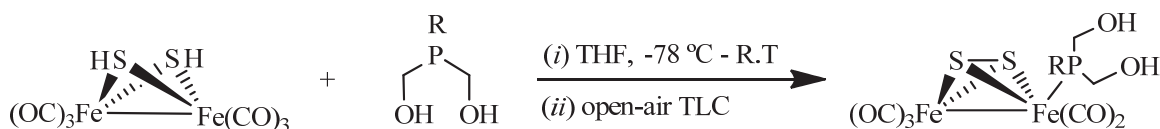
Herein we introduce the synthesis of [FeFe]-hydrogenase model complex, $[Fe_2(CO)_6\{\mu\text{-}(SCH_2)_2(Ph)P{=}O\}]$ (**137**), with a phosphine oxide in the dithiolato linker by utilizing a phosphine oxide containing ligand, thus eliminating the free electron pair on phosphorous and preventing coordination to the iron center. Moreover, the P=O functionality could provide a potential site for protonation as it is shown for 1,8-bis(diphenylphospineoxide)naphtalen (dppnO2).[197] Beside the low pK_a values reported for tertiary phosphine oxides (p$K_a \approx 4$)[198], Schmutzler et al. provided experimental proof of a protonated dppnO2 species in the presence of CF_3SO_3H.[197]

The main focus of this chapter is to investigate the influence of the dithiolato linker $(SCH_2)_2P{=}O$ toward the protonation properties of complex **137**. Therefore, we examined the protophilic features by IR and $^{31}P\{^1H\}$NMR spectroscopic monitoring of the protonation reaction of complex **137** in the presence of the moderately strong pyridinum acid (HPy$^+$, pK_a (MeCN) = 12.3)[113] and HBF4·Et2O (pK_a (MeCN) = 0.1)[113]. These experiments suggest a direct protonation of the P=O functionality in the case of HBF4·Et2O. In addition, we performed high level DFT calculations on the P=O- and the S-protonation states using HPy$^+$ and HBF4 as the source of protons. To further confirm

the protonation and to probe its impact on the redox properties of the [Fe₂S₂] core, cyclic voltammetric oxidation of complex **137** in the absence and presence of HBF₄·Et₂O has been investigated.

We herein report the first model in which protonation occurs at the oxygen atom of the bridgehead P=O group. This P=O function is in an axial position in complex **137**, as determined by X-ray diffraction. Hence the protonated species could relay protons to the iron centers during the catalytic turnover of complex **137** or related models.

2.1 Results and Discussion

2.1.1 Synthesis and Characterization

The reaction of *in situ* generated $(\mu\text{-LiS})_2\text{Fe}_2(\text{CO})_6$[199-201] with 1 equiv. of $\text{O=P(Ph)(CH}_2\text{Cl})_2$[202,203] afforded $[\text{Fe}_2(\text{CO})_6\{\mu\text{-(SCH}_2)_2(\text{Ph})\text{P=O}\}]$ (**137**) in 21 % yield as an air-stable red solid (Scheme 2-2). Subsequently, complex **137** was characterized by ^1H, $^{13}\text{C}\{^1\text{H}\}$ and $^{31}\text{P}\{^1\text{H}\}$ NMR as well as IR and UV-vis spectroscopic techniques, mass spectrometry, elemental analysis and X-ray crystallography.

Scheme 2-2. Reaction of in situ generated $\text{Li}_2[\text{Fe}_2\text{S}_2(\text{CO})_6]$ and $\text{O=P(Ph)(CH}_2\text{Cl})_2$ to afford complex **137**.
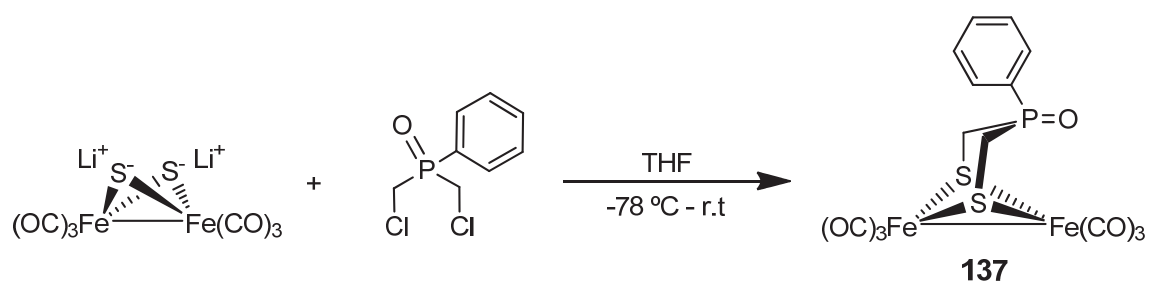
Spectroscopic Studies. *Full details for the synthesis and spectroscopic characterization of the ligand $O=P(Ph)(CH_2Cl)_2$ are provided in the Experimental Part.* The mass spectrum of complex **137** showed the parent ion peak at *m/z* 440 [M - 2CO]⁺ and the consecutive loss of four CO ligands. The IR spectrum of complex **137** (KBr pellet) exhibited three absorption bands at 1990, 2003, 2041, 2079 cm⁻¹ for the terminal CO ligands. The $^{31}\text{P}\{^1\text{H}\}$ NMR showed one peak at 30.6 ppm. The $^{13}\text{C}\{^1\text{H}\}$ NMR spectrum of complex **137** showed a doublet centered at 20.4 ppm for the methylene

carbons due to the coupling with the phosphorous atom. Further signals in the region of 129.0-132.9 ppm for the phenyl carbons and two signals at 206.0 and 207.0 ppm for the terminal carbonyl carbon atoms were observed. The ^1H NMR spectrum of complex **137** recorded at room temperature showed a multiplet in the region of 7.4-7.6 ppm for the aromatic protons of the phenyl ring as well as a doublet at 2.06 ppm and a triplet at 2.75 ppm for the diastereotopic methylene protons. To understand the splitting pattern of the axial and equatorial methylene protons in the ^1H NMR spectrum, $^1H\{^{31}P\}$ NMR experiment was performed. This experiment showed that when ^1H and ^{31}P nuclei were decoupled, the doublet at 2.06 ppm was not altered. In contrast, the triplet at 2.75 ppm became a doublet. Consequently, $^2J_{HH}$ and $^2J_{HP}$ can be determined as 14.9, 15.6 Hz, respectively (Figure 2-2).
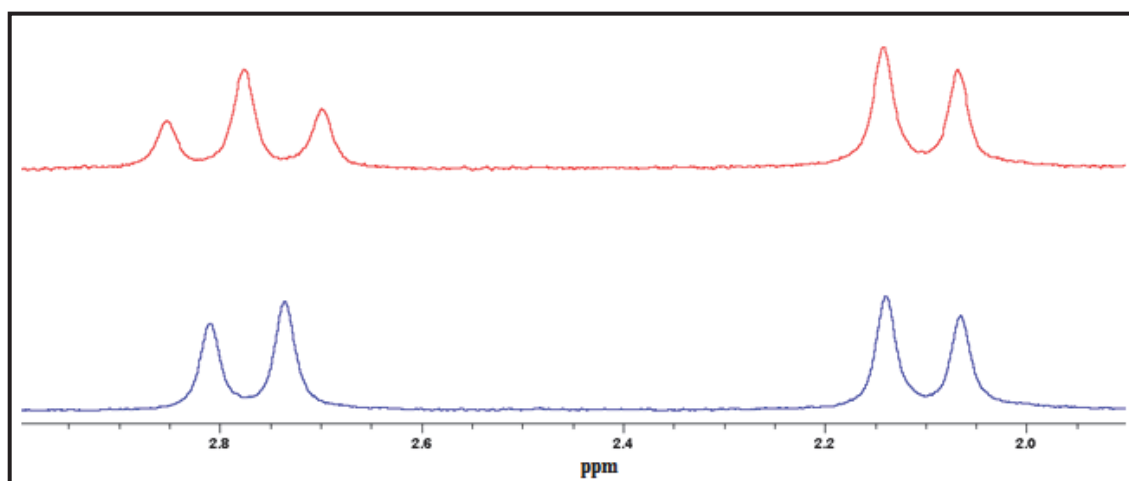
Figure 2-2. ^1H NMR (red) and $^1H\{^{31}P\}$ NMR (blue) spectra of the diastereotopic methylene protons in complex **137**.

The UV-Vis spectrum of complex **137** in MeCN (4.6×10^{-5} M) showed two bands for the [Fe$_2$S$_2$] cluster (Figure 2-3):

(i) absorption at 334 nm ($\varepsilon = 12000$ cm^{-1}·M^{-1}) assigned to the $\sigma \rightarrow \sigma^*$ transition associated with the [FeFe] core[204] and

(ii) a weak broad absorption at 471 nm ($\varepsilon = 960$ cm^{-1}·M^{-1}) arises from d(Fe)-d(Fe*) transition within each iron center.
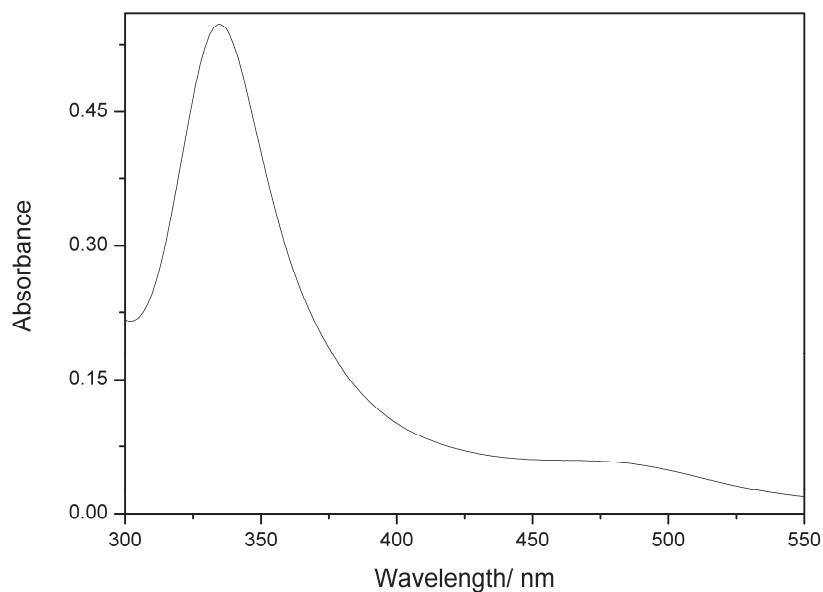
Figure 2-3. The UV-Vis spectrum of complex **137** in MeCN (4.6×10^{-5} M).

Molecular Structures. Single crystals suitable for molecular structure determinations were obtained by diffusion of pentane into a CH_2Cl_2 solution of complex **137** at 4 °C. The molecular structure of complex **137** is shown in Figures 2-4. *Crystal of the ligand O=P(Ph)(CH₂Cl)₂ were obtained in the same way for complex 137 (Supporting Information, Figure S2-1).* The geometry around each iron center in complex **137** can be best described as distorted octahedral, with three carbonyl ligands in facial fashion, two bridging sulfur atoms and one iron atom. The bicyclic [Fe₂S₂] structure in complex **137** reveals butterfly conformation. The phosphorous atom of the linker $(SCH_2)_2P=O$ has a distorted tetrahedral geometry. The average P-C-S bond angle, 118.2°, is comparable to the previously described models with $(SCH_2)_2E$ linker (E = CR_2,[200] O,[187] NR,[78] S[47,115,190] and Se[48,58,61]).
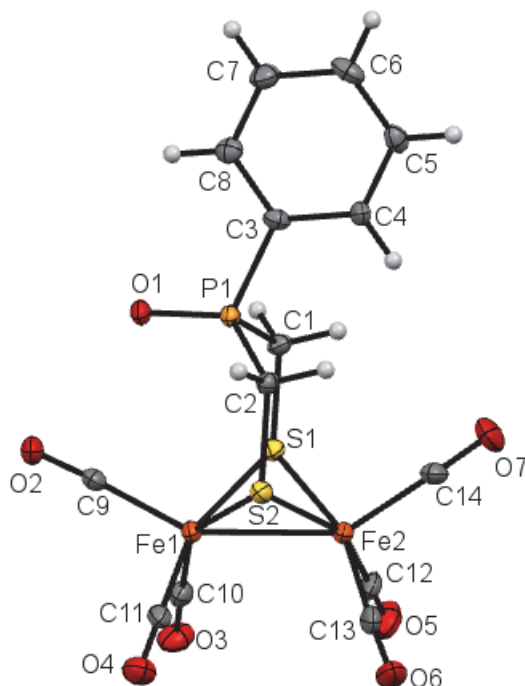
Figure 2-4. Molecular structure (50 % probability) of [Fe$_2$(CO)$_6${μ-(SCH$_2$)$_2$(Ph)P=O}] (**137**).

The Fe-Fe bond length in complex **137**, 2.5148(9) Å, is similar to that in [Fe$_2$(CO)$_6${μ-(SCH$_2$)$_2$S=O}], 2.5127(6) Å[115], but slightly shorter than those of the H-cluster, 2.55-2.62 Å[18,31,32]. The average Fe-CO bond length in complex **137** is 1.803 Å and is comparable to that in [Fe$_2$(CO)$_6${μ-(SCH$_2$)$_2$S=O}] (**23a**), 1.807 Å[115]. While the oxygen atom of the S=O functionality in the FeS$_2$C$_2$S chair conformational six-membered ring in **23a** is equatorial, the oxygen atom of the P=O functionality in complex **137** occupies an axial position in the Fe(2)S$_2$C$_2$P ring (Figure 2-5) and is therefore parallel to the Fe-Fe bond, which could be important for proton relay.
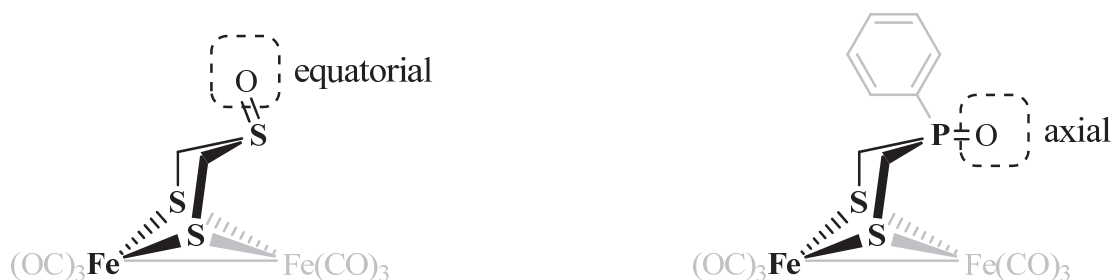
Figure 2-5. Comparison between the stereochemistry of the S=O and the P=O functionalities in **23a** (left)[115] and complex **137** (right), respectively.

2.1.2   Protonation Studies

In order to gain insight into the protonation processes involving complex **137**, the moderately strong acid, pyridinium tetrafluoroborate [HPy][BF$_4$], and the very strong acid HBF$_4$·Et$_2$O were reacted with **137**. The reactions were monitored by IR spectroscopy, which is a highly sensitive technique to probe the protonation state of the complex due to the high sensitivity of the carbonyl vibrations to the changes in electron density at the iron centers.[99,205]

Two protonation states can be considered for complex **137**:

(i)   **137H$^+$(S)**, as a result of protonation at the dithiolato sulfur atom and

(ii)   **137H$^+$(O),** owing to protonation at oxygen atom of the P=O functionality as shown in Scheme 2-3.

Protonation at Fe-Fe bond is unlikely in our case, since no hydride species have been observed for hexacarbonyl complexes upon reaction with the herein used acids. Only one exception is known, utilizing a special method to protonate [Fe$_2$(CO)$_6${μ-(SCH$_2$)$_2$CH$_2$}] based on the high Lewis acidity of [SiEt$_3$][B(C$_6$F$_5$)$_4$]/HCl.[114] In addition, protonation at the iron centers is known in complexes containing strongly electron donating substituents at the [Fe$_2$S$_2$] core.[108,125] Protonation of the sulfur atom or the iron centers would result in a significant shift of the carbonyl bands in the IR spectrum. In case of the reported S-protonation states, the shifts were in the range of 30-130 cm^{-1} and it is 70-110 cm^{-1} in case of Fe-protonation states.[108,125] Formation of **137H$^+$(O)** state is expected to shift the carbonyl wavenumbers similar to the reported values of protonated complexes at a pendant pyridine or amine functionality that is either attached to the dithiolato linker or to mono- and bidentate phosphine ligands (8-12 cm^{-1}).[125]

Scheme 2-3. Possible protonation states of complex **137**.
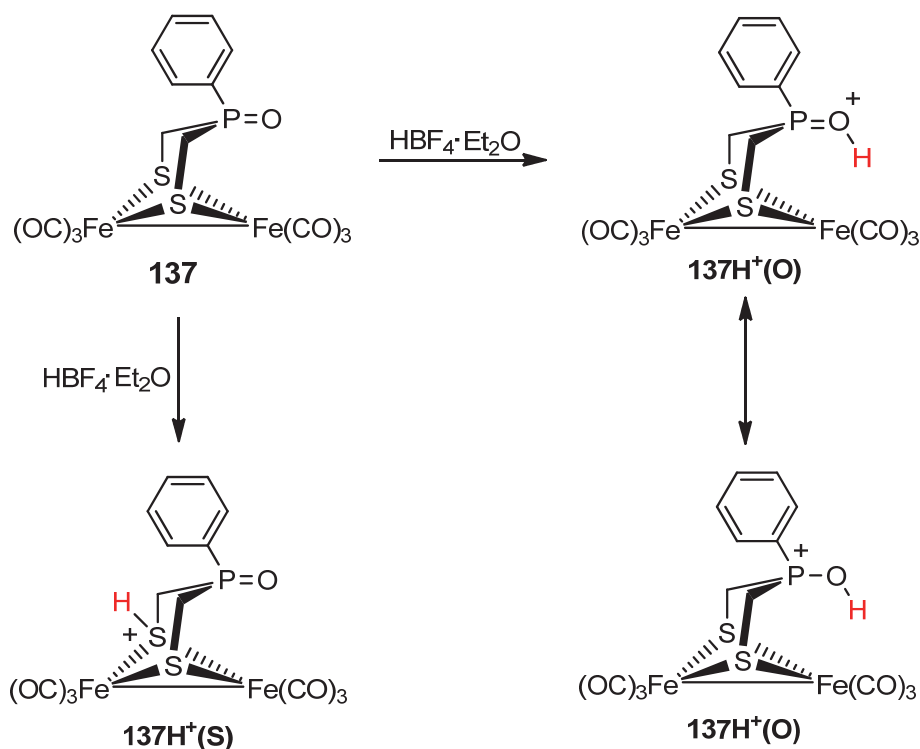
Treating the MeCN solution of complex **137** with excess HPy^{+*} under N$_2$ resulted neither in a change of position nor intensity of the carbonyl bands in the IR spectrum. This result means that HPy$^+$ does not protonate complex **137** in MeCN. On the other hand, upon addition of excess HBF$_4$·Et$_2$O (100 equiv.) to the CH$_2$Cl$_2$ solution of complex **137** under N$_2$, a shift of the carbonyl bands by ~ 10 cm^{-1} to higher wavenumbers was observed, which suggests protonation of the P=O function and formation of **137H$^+$(O)** state (Figure 2-6a). Subsequent addition of Et$_3$N (100 equiv.) quantitatively restores complex **137** reflecting the reversibility of the process as observed in the IR spectra (Figure 2-6a). In addition, ^{31}P{^{1}H} NMR spectroscopy can provide another evidence for the formation of **137H$^+$(O)** state, as the reported protonation of related phosphine oxides resulted in a downfield shift of the ^{31}P{^{1}H} NMR signal in the range of 27-38 ppm.[197,206] The ^{31}P{^{1}H} NMR signal of complex **137** in the presence of excess HBF$_4$·Et$_2$O became less shielded by 36.6 ppm (Figure 2-6b), which is in consistent with protonation of the P=O functionality.

---

* The synthetic procedure of this acid is provided in the experimental part.
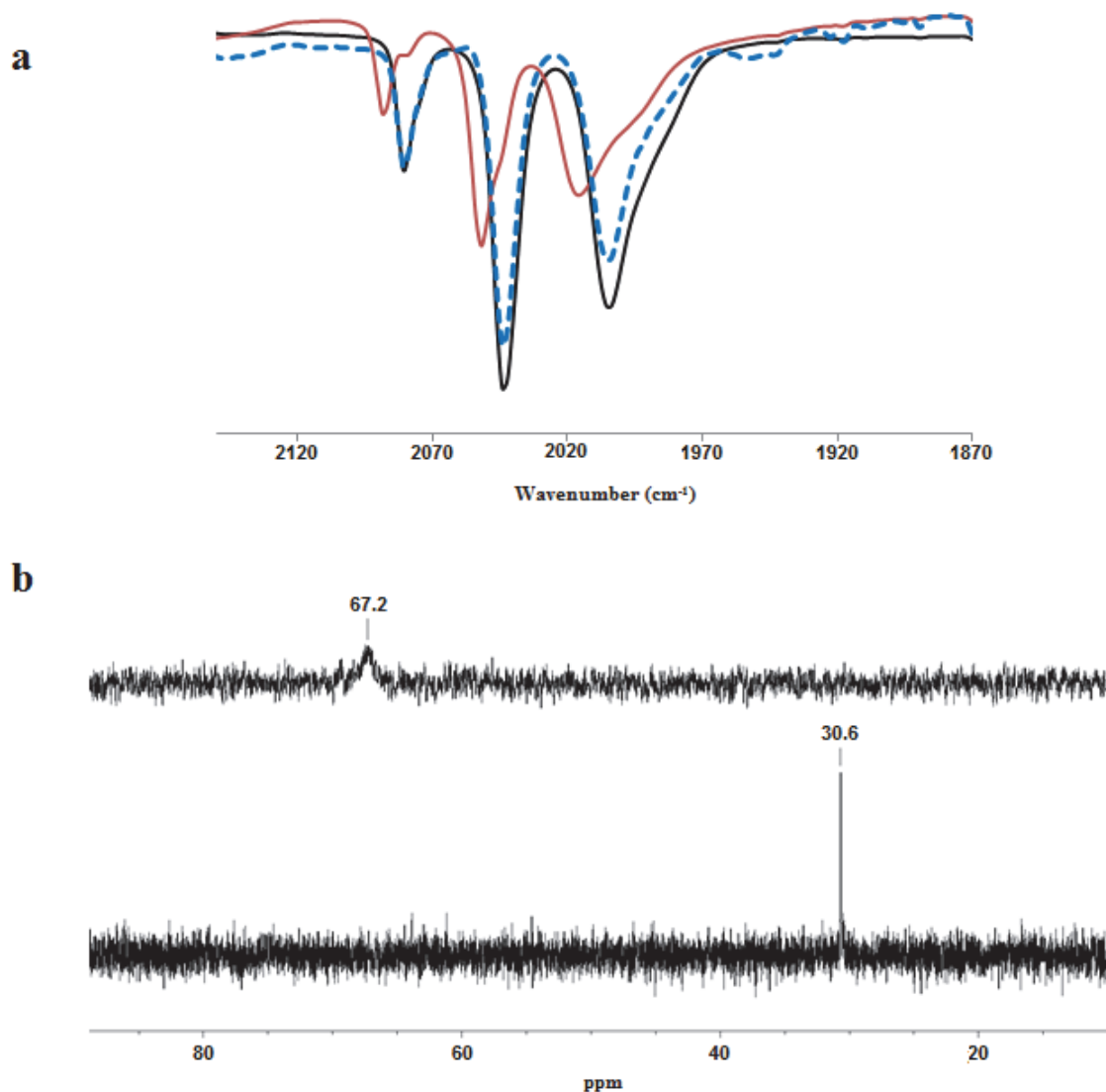
Figure 2-6. (a) IR spectra of complex **137** (CH_2Cl_2 solution) in the absence of acid (black line), in the presence of $HBF_4·Et_2O$ (red line) and after addition of Et_3N (dashed blue line). (b) $^{31}P\{^1H\}$ NMR spectra of complex **137** (CH_2Cl_2 solution) in the absence (bottom) and presence (top) of $HBF_4·Et_2O$.

2.1.3   DFT Investigation of the Protonation

To investigate the mechanistic details of the protonation of complex **137**, high level DFT calculations related to the potential protonation pathways depicted in Scheme 2-3 were performed. B3LYP-6-311++G(d,p) functional and basis set as implemented in *Gaussian09*.[207-210] As the formation of hydrogen bonded adducts represents bimolecular reactions, thermal and entropic corrections were considered. The resulting values E_{corr} and in addition, the relative Gibbs free energies ΔG for the elementary steps of the protonation reactions allow a more realistic estimate of the intrinsic relative energy

relationships than those resulting from relative E values. In addition, all compounds have been further calculated using a continuum solvent model for CH_2Cl_2.[211] All energy values E_{corr} and E_{CPCM} as well as the results of frequency calculations of the gas phase calculations are summarized in Table S2-1 (Supporting Information).

First of all, the molecular structure of complex **137** was calculated in order to prove the applicability of the applied level of theory. It can be seen from Table 2-1 containing the relevant bond lengths that the calculations nicely correspond to the experimentally derived values from the crystal structure analysis. We assumed that a protonation reaction should take place by a series of elementary steps first producing an adduct of the corresponding acid and complex **137** with a hydrogen bond established between acidic hydrogen atoms and the corresponding basic site in complex **137** at which protonation will occur. Calculations have been performed with two potential basic sites in complex **137**: the P=O functionality of the bridgehead and the sulfur atoms that act as bridging ligands for the iron tricarbonyl moieties. According to the experiments described above, HBF_4 has been introduced to the calculations as protonating agent. Corresponding results with HPy^+ as the proton source are shown in the Supporting Information (Table S2-2).

Table 2-1. Calculated bond lengths compared to X-ray data of **137** (acid: HBF_4) [Å].

Bond[a]	137_{exp}	137_{calc}	$137H^+(O)$	$137H^+(S)$	$137HBF_4(O)$	$137HBF_4(S)$
Fe1-Fe2	2.515	2.512	2.520	2.561	2.517	2.518
Fe1-S1	2.259	2.327	2.321	2.299	2.310	2.309
Fe1-S2	2.256	2.327	2.321	2.336	2.332	2.320
Fe2-S1	2.258	2.319	2.310	2.277	2.313	2.319
Fe2-S2	2.260	2.319	2.310	2.329	2.316	2.332
S1-C1	1.824	1.843	1.848	1.839	1.838	1.845
S2-C2	1.831	1.843	1.848	1.854	1.847	1.845
C1-P1	1.796	1.832	1.812	1.864	1.811	1.832
C2-P1	1.799	1.832	1.812	1.838	1.810	1.833
P1-O1	1.484	1.497	1.596	1.493	1.563	1.497
H-O		-	0.968	-	1.037	-
H-O		-	2.114		-	-
H-S		-	-	1.354	-	2.068
H-F		-	-	-	1.394	0.954

[a]Atom numbering corresponds to Figure 2-4, atoms without numbering correspond to protonation of O or S, respectively.

In summary two acid-base adducts with HBF_4 being attached to the P=O or S atoms of complex **137** (**137HBF_4(O)** and **137HBF_4(S)**) and both protonated species **137H^+(O)** and **137H^+(S)** have been calculated. The calculated energies that are presented in Table S2-1 show that protonation at the P=O functionality of the ligand is always energetically preferred over the reaction at the bridging thiolate. In the gas phase **137H^+(O)** is 86.6 kJ·mol^{-1} lower in energy than **137H^+(S)** whereas this energy gap slightly decreases to 70.8 kJ·mol^{-1} if solvation effects caused by CH_2Cl_2 are taken into account. If the hydrogen bonded adducts **137HBF_4(O)** and the isomeric **137HBF_4(S)** are compared the former is 58.0 kJ·mol^{-1} lower in energy in the gas phase but 93.4 kJ·mol^{-1} lower in energy in the solvent model. The molecular structures of all calculated compounds are depicted in Figure 2-7, the most important bond lengths are presented in Table 2-1 (Figure S2-2 and Table S2-2 for the use of HPy^+ as the acid).
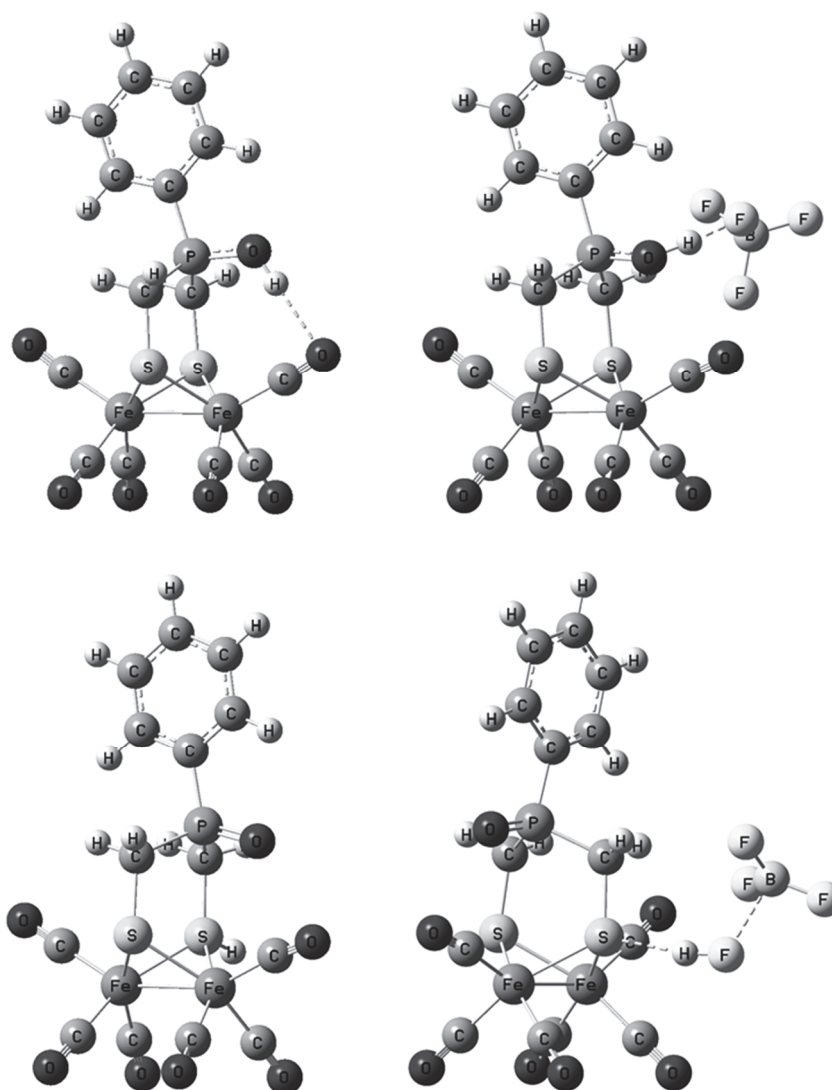
Figure 2-7. Calculated structures of **137H⁺(O)** (top left), **137HBF₄(O)** (top right), **137H⁺(S)** (down left) and **137HBF₄(S)** (down right).

In addition, we have calculated the carbonyl stretching frequencies, $\upsilon(CO)$, for the species **137**, **137H⁺(O)**, **137H⁺(S)**, **137HBF₄(O)**, **137HBF₄(S)**, **137HPy⁺(O)** and **137HPy⁺(S)** (see the Supporting Information, Table S2-3). The *ion-paring effect* of the counter anion on the $\upsilon(CO)$ wavenumbers is discussed under Table S2-3.

| 2.1.4 | **Electrochemical Properties** |

The cyclic voltammetric reduction of complex **137** in $MeCN/NBu_4PF_6$ using a hanging mercury drop electrode is shown in Figure 2-8 (solid lines).
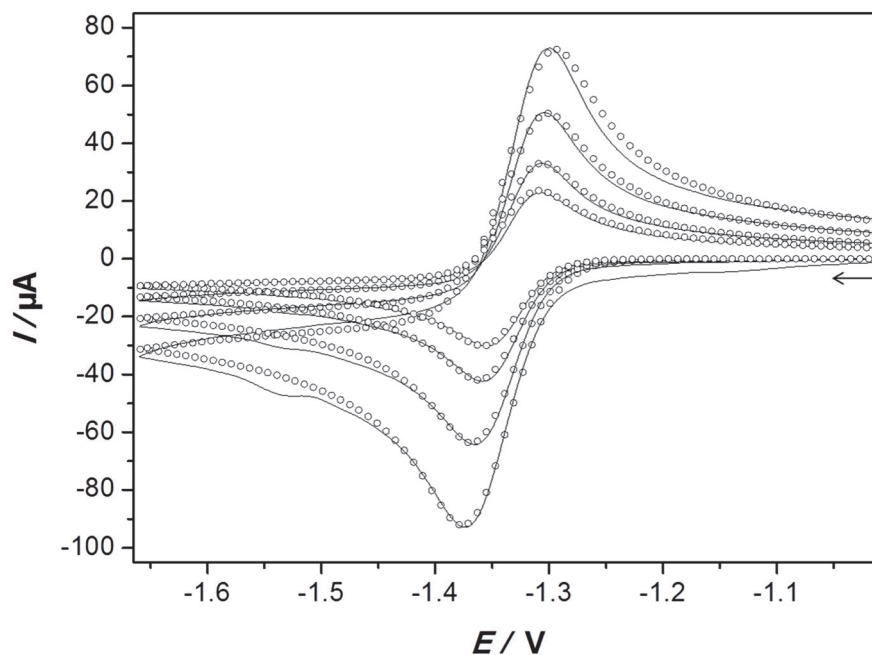
Figure 2-8. Cyclic voltammetric reduction of 0.9 mM complex **137** $(MeCN/NBu_4PF_6$ solution) on a mercury drop electrode using scan rates of 1, 2, 5 and 10 $V·s^{-1}$ (solid lines) and simulated CVs (open circles). The simulations were executed for the mechanism given by eq. (*M1 - M3*). Referenced against the ferrocenium/ferrocene couple. The arrow indicates the scan direction.

The reduction process appears to be quasi-reversible, but an adsorption process producing a prewave that grows linearly with the scan rate affects it (Figure S2-3). For this reason only CVs measured with scan rates ≤ 10 $V·s^{-1}$ were used for evaluating our experiments by digital simulation[212] (Figure 2-8). The latter was done assuming equal charge transfer coefficients, $\alpha = 0.5$, for all charge transfer steps and the same diffusion coefficient, D, for all diiron species. The simplest mechanism able to reproduce the experimental CVs sufficiently well consists in two successive one-electron steps with the second standard potential more positive than the first one. The potential inversion (see Section 1.5.1) observed in the reduction of complex **137** is indicative of structural change accompanying mechanism (*M1*) to (*M3*), shown below, and may arise from the cleavage

of the Fe-Fe bond and one of the Fe-S bonds as already observed for various hexacarbonyl diiron dithiolate complexes (see Section 1.5.2).

Fe-Fe + e$^-$ ↔ Fe ⋯Fe$^-$	$(E°_1, k°_1 \geq 0.2$ cm·s$^{-1})$	(M1)
Fe ⋯Fe$^-$ ↔ Fe Fe$^-$	(K, k_f)	(M2)
Fe Fe$^-$ + e$^-$ ↔ $^-$Fe Fe$^-$	$(E°_2, k°_2 \geq 1$ cm·s$^{-1})$	(M3)

A comparison between the experimental CVs and those simulated on the basis of mechanism (M1) to (M3) is shown in Figure 2-8. The diffusion coefficient for complex **137** determined in this way was $D \approx 9 \times 10^{-6}$ cm²·s^{-1}. Due to the scan rate restrictions mentioned above it was only possible to estimate limiting values for the kinetic constants $k°_1$, $k°_2$ and k_f. Even the standard (or half-wave) potentials cannot be exactly determined for such a mechanism due to a parameter coupling between the thermodynamic and kinetic constants. That means, the potential shift effected for the CVs by variation of $E°_1$ can be compensated by changing K, the difference $E°_1 - E°_2$ and the rate constants correspondingly. The most sensible parameters are obtained when K varies from 0.1 to 5 resulting in -1.36 V $\geq E°_1 \geq$ -1.39 V, 10^5 s$^{-1} \leq k_f \leq 10^9$ s^{-1} and -90 mV $\geq E°_1 - E°_2 \geq$ -130 mV.

Electrochemical Oxidation of Complex 137 in the Presence of HBF$_4$·Et$_2$O. The present studies focus on the oxidation of complex **137** in the presence of acids which are strong enough to achieve the protonation of the neutral complex **137**. In our current research we describe how the protonation of the neutral complex **137** to generate **137H$^+$(O)**, which was identified by spectroscopic methods and DFT calculations, affects its oxidation wave. The cyclic voltammetric experiments were performed under conditions similar to the spectroscopic measurements, CH_2Cl_2 as solvent and HBF$_4$·Et$_2$O as protonating acid. In a clear case, if the neutral complex is protonated, then loss of its oxidation wave and appearance of new oxidation event at more positive potential for the protonated product will take place.[171] The difference in oxidation potential (ΔE_{ox}) between the neutral and the protonated complex is dependent on which site of the neutral complex is protonated. If the protonation occurs at the Fe-Fe bond, a positive shift of 0.9-1.5 V can be observed.[86,99] On the other hand, ΔE_{ox} due to protonation at other sites of the complex was found to be in the range of 90-270 mV.[78,99,213] In our case, addition of HBF$_4$·Et$_2$O to a solution of complex **137** in CH_2Cl_2/NBu$_4$PF$_6$ affected the irreversible oxidation wave $(E_{ox} = +0.71$ V) as shown in Figure 2-9. The positive shift of the oxidation peak as a function of the amount of acid added (Figure 2-9) can be explained in

terms of CE process (Scheme 2-4), where the shift of the protonation pre-equilibrium due to the oxidation of the neutral complex at the electrode surface becomes more and more difficult as the concentration of the HBF$_4$·Et$_2$O increases.[34,37]
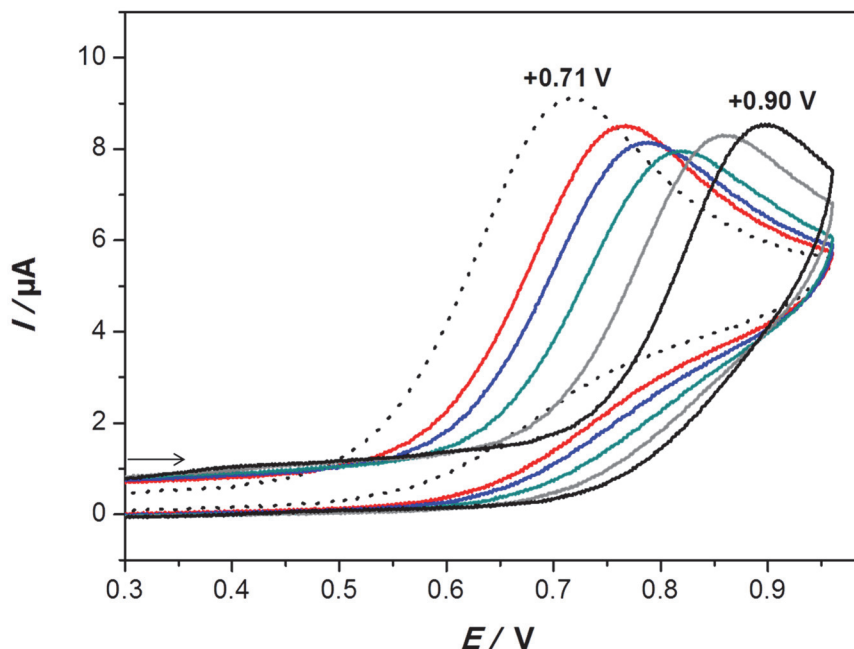
Figure 2-9. Cyclic voltammetric oxidation of 0.907 mM complex **137** (CH$_2$Cl$_2$/NBu$_4$PF$_6$ solution) in the absence and presence of varying HBF$_4$·Et$_2$O concentrations using a scan rate of 0.2 V·s^{-1}. [HBF$_4$·Et$_2$O]/mM = 0 (dotted line), 4 (red), 20 (blue), 37 (green), 60 (gray) and 111 (black). Referenced against the ferrocenium/ferrocene couple. The arrow indicates the scan direction.

Scheme 2-4. Acid-base equilibrium involving complex **137** and its protonated form **137H$^+$(O)**, (CE process).

$$\textbf{137} \quad + \quad \text{HBF}_4\text{·Et}_2\text{O} \quad \rightleftharpoons \quad \textbf{137H}^+\textbf{(O)} \quad + \quad \text{BF}_4^-$$

$E_{ox} = +0.71$ V

Oxidized complex
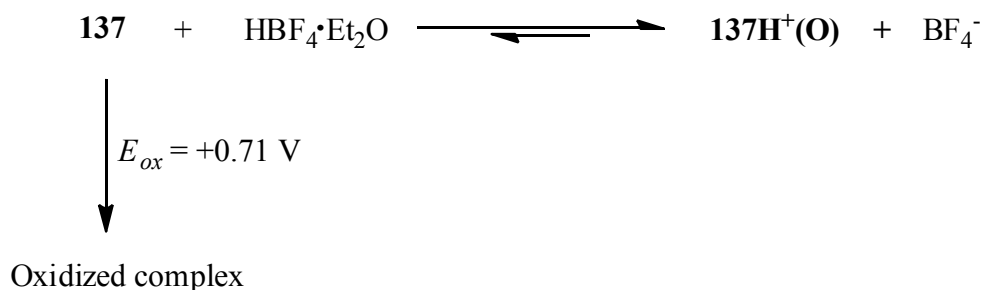
2.2 Conclusions

Model complex $[Fe_2(CO)_6\{\mu\text{-}(SCH_2)_2(Ph)P=O\}]$ (**137**) was synthesized and characterized by ^1H, ^{13}C and $^{31}P\{^1H\}$ NMR as well as IR and UV-Vis spectroscopic techniques, mass spectrometry, elemental analysis and X-ray crystallography. While the IR study suggested that complex **137** does not undergo direct protonation in the presence of excess HPy^+, the protonation state of complex **137** upon addition of $HBF_4 \cdot Et_2O$ was identified as **137H⁺(O)** applying IR and $^{31}P\{^1H\}$ NMR spectroscopic techniques. The experimental results were supported by high-level DFT calculations of the protonation reaction at the oxygen atom of the P=O functionality and the dithiolato sulfur atom. The calculated energies that are presented in Table S2-1 showed that protonation of the P=O functionality is energetically preferred. The calculated shift of the $\upsilon(CO)$ due to the formation of **137HBF₄(O)** is less than the case of **137H⁺(O)** (Table S2-3), suggesting the *ion-pairing effect*. The electrochemical behavior of complex **137** was studied by cyclic voltammetry in the absence and in the presence of $HBF_4 \cdot Et_2O$. Complex **137** undergoes an overall two-electron reduction due to potential inversion of the two individual one-electron processes. The addition of $HBF_4 \cdot Et_2O$ to the electrolyte solution of complex **137** resulted in a positive shift of its oxidation peak as a function of acid concentration suggesting CE process.

Chapter 3

Ligand Effects on the Electrochemical Behavior of $[Fe_2(CO)_5(L)\{\mu\text{-}(SCH_2)_2(Ph)P{=}O\}]$ $(L = PPh_3, P(OEt)_3)$ Complexes

(Publication Number 2)

3 Ligand Effects on the Electrochemical Behavior of [Fe$_2$(CO)$_5$(L){μ-(SCH$_2$)$_2$(Ph)P=O}] (L = PPh$_3$, P(OEt)$_3$) Hydrogenase Model Complexes

[FeFe]-hydrogenases are enzymes that have high efficiency (ca. 10^4 turnover·s^{-1})[11b,11m] to catalyze reduction of protons to form dihydrogen.[11] This process occurs in microorganisms at neutral pH and a potential of -0.42 V (vs NHE).[11n,11o] The high resolution X-ray crystallographic and IR spectroscopic studies revealed that the active site of [FeFe]-hydrogenases (so-called H cluster),[11] isolated from *Clostridium pasteurianum*[11h] and *Desulfovibrio desulfuricans*[11g], consists of a [Fe$_4$S$_4$] cluster attached through a cysteinyl residue to a butterfly [Fe$_2$S$_2$] subcluster (Figure 3-1). The coordination sphere of the iron centers of the [Fe$_2$S$_2$] subcluster contains biologically unusual CO and CN$^-$ ligands. These iron centers are bridged most likely by the azadithiolato ligand -SCH$_2$NHCH$_2$S-.[11p,14,19-25,214] On the functional side of the active site, the protonation of the [Fe$_2$S$_2$] subcluster is a central step during the turnover (Scheme 1-1).[15-17,23,24] In addition, the NH group of the azadithiolate is alleged to relay protons to and from the diiron core via agostic or hydrido-proton interaction (Scheme 1-1). The steric bulk at the proximal Fe atom assists the N-H bond (in green, Figure 3-1) to be in close proximity to the vacant site.[12] Numerous model complexes have been synthesized based on replacing the propane dithiolato bridge in [Fe$_2$(CO)$_6${μ-(SCH$_2$)$_2$CH$_2$}] (**3**) by linkers containing heteroatoms in the bridgehead such as N, O, S, Se and Si (Figure 1-7) to study their influence toward the protonation properties as well as the electrochemical behavior of the model complex in the absence and presence of acids. In addition, the synthetic chemistry involves substitution of the CO ligands in [Fe$_2$(CO)$_6${μ-(SCH$_2$)$_2$X}] (X = CH$_2$, NR, O, SiR$_2$) by cyanide[33,73,159], phosphanes, phosphites, carbenes[40,60,74b,88,102,215], nitrosyl[179,216,217] or sulfides (Figure 1-20). Mono-, di-, tri- and tetrasubstituted model complexes have been described (Figures 1-9 to 1-11).
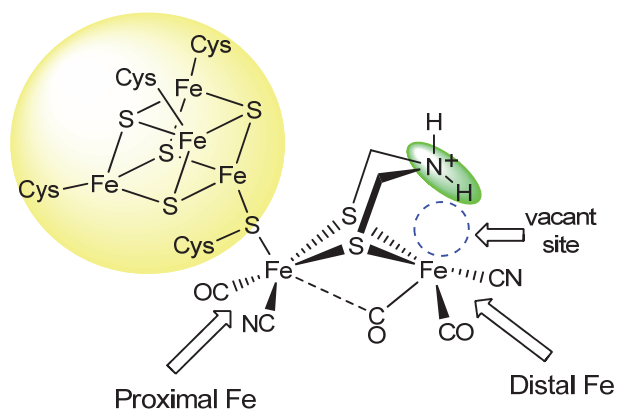
Figure 3-1. The structure of the H cluster.[11]

A basic aim of these substitution reactions is to increase the electron richness at the [Fe$_2$S$_2$] core of the model complex in order to mimic the electronic characteristics of the [Fe$_2$S$_2$] core of the H cluster, which contains strong electron donating CN$^-$ ligands. The enhanced basicity of the [Fe$_2$S$_2$] core of the substituted models results in formation of hydride species prior reduction, but only in the case of the di-, tri-, or tetra-substituted complexes with strongly electron donating substituents such as PMe$_3$ (Section 1.5.2). Substitution of CO ligands with stronger σ-donor ligands increases not only the electron density at the iron sites, but also at the other protonation sites of the model complex (Section 1.4.2). For example, 4 equiv. of triflic acid is required to fully protonate the amine group in the hexacarbonyl complex [Fe$_2$(CO)$_6${μ-(SCHMe)$_2$NH}], while only 1 equiv. is enough in case of the substituted complex [Fe$_2$(CO)$_4$(PMe$_3$)$_2${μ-(SCHMe)$_2$NH}]. Moreover, Rauchfuss and Zampella et al. have recently described the synthesis and protonation kinetics of highly basic PMe$_3$-tetrasubstituted complexes [Fe$_2$(CO)$_2$(PMe$_3$)$_4${μ-(SCH$_2$)$_2$X}] (X = CH$_2$ (**120**) and NH (**121**)) and [Fe$_2$(CO)$_2$(PMe$_3$)$_4${μ-(SCH$_2$)$_2$}] (**119**), which show S-protonation at low temperatures (Scheme 1-12). Mimicking the rotated structure of the H cluster has been always a fundamental aim in the synthetic chemistry of the model complexes.

This Chapter describes the influence of substituting one CO in complex **137** by stronger electron donating and more sterically demanding ligands, PPh$_3$ and P(OEt)$_3$, toward the voltammetric reduction mechanism of the resulting substituted models. Moreover, a remarkable difference in voltammetric behavior between the PR$_3$-substituted complexes is discussed. In addition, DFT calculations are performed to gain insights into

the structural changes accompanying the reduction processes of the hexacarbonyl and the substituted complexes.

3.1   Results and Discussion

3.1.1   Synthesis and Characterization

Treatment of an acetonitrile solution of complex **137** with 1 equiv. trimethylamine N-oxide (Me$_3$NO·2H$_2$O) at room temperature for 30 min resulted in oxidative abstraction of CO (decarbonylation) to yield the in situ acetonitrile complex (Scheme 3-1).[218] Subsequent addition of L (PPh$_3$ or P(OEt)$_3$) afforded the monosubstituted complexes **138** (L = PPh$_3$) and **139** (L = P(OEt)$_3$) in very high yields (98 %) after stirring for 18 h at room temperature (Scheme 3-1). No purification was required after removal of the reaction solvent, only filtration.

Scheme 3-1. Reaction pathway toward monosubstituted complexes **138** and **139**.
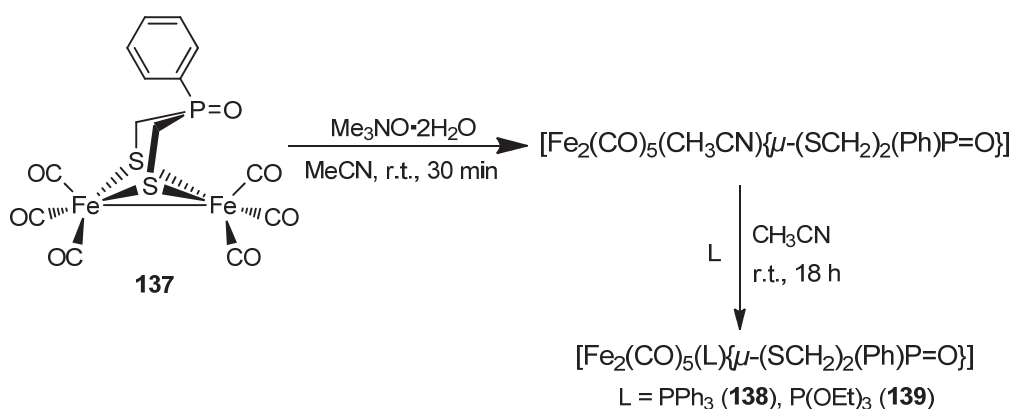
Complexes **138** and **139** were characterized by ^{1}H, ^{13}C and ^{31}P NMR as well as IR spectroscopic techniques, mass spectrometry, elemental analysis and X-ray crystallography. The micro-electrospray ionization mass spectrometry (micro-ESI-MS) of complex **138** showed the parent ion peak at *m/z* 752.7 [M + Na]$^+$ with the isotopic pattern at *m/z* 750.7, 751.7, 753.7, 754.7, 755.7 and 756.7. In the desorption electron impact (DEI) mass spectrum, the observed fragments were at *m/z* 674 [M - 2CO]$^+$, 618 [M - 4CO]$^+$, 590 [M - 5CO]$^+$, 440 [M - CO - PPh$_3$]$^+$, 412 [M - 2CO - PPh$_3$]$^+$, 384 [M - 3CO - PPh$_3$]$^+$, 356 [M - 4CO - PPh$_3$]$^+$ and 328 [M - 5CO - PPh$_3$]$^+$. The micro-ESI-MS of

complex **139** showed the parent ion peak at *m/z* 637. The IR spectrum of complex **138** (KBr pellet) exhibited four absorption bands at 1926, 1965, 1989 and 2049 cm^{-1} in the carbonyl region. In CH$_2$Cl$_2$, the CO ligands stretch at 1941, 1983, 2002 and 2056 cm^{-1}. The IR spectrum of complex **139** in CH$_2$Cl$_2$ exhibited four absorption bands in the carbonyl region (1946, 1983, 2003 and 2058 cm^{-1}). The carbonyl wavenumbers of complexes **138** and **139** are markedly shifted toward lower values relative to those of the hexacarbonyl complex **137** by 36 and 34 cm^{-1}; respectively, in average. The shift in υ(CO) vibration due to replacement of one CO by PPh$_3$ is slightly higher than that by P(OEt)$_3$ suggesting that the electron density available for donation to the iron core by PPh$_3$ is slightly higher than that by P(OEt)$_3$. The ^{31}P{^{1}H} NMR spectrum of complex **138** in CD$_2$Cl$_2$ solution exhibits two sharp signals at 34.7 and 65.8 ppm for the P=O and PPh$_3$, respectively. The ^{31}P{^{1}H} NMR spectrum of complex **139** in CD$_2$Cl$_2$ solution shows one sharp peak at 30.7 ppm for the P=O and a broad one at 170.0 ppm due to the P(OEt)$_3$ substituent. The ^{13}C{^{1}H} NMR spectrum of complex **138** shows a doublet centered at 18.5 ppm due to the methylene carbon atoms ($^1J_{CP}$ = 67.6 Hz), signals in the region of 128-136 ppm for the phenyl carbon atoms and two signals at 208.7 and 213.5 ppm for the terminal carbonyl groups. The ^{13}C{^{1}H} NMR of **139** displays three doublets centered at 16.4 ppm ($^3J_{CP}$ = 6.41 Hz), 19.6 ppm ($^1J_{CP}$ = 62.09 Hz) and 61.95 ppm ($^2J_{CP}$ = 4.58 Hz) assigned to the CH$_3$ groups of the P(OEt)$_3$ substituent, the methylene carbon atoms of the dithiolato bridge, and the methylene carbon atoms of P(OEt)$_3$, respectively. The signals observed in the region of 128-135 ppm are due to the aromatic carbon atoms. The singlet at 208.8 ppm and the doublet centered at 212.3 ppm are attributed to CO groups in the Fe(CO)$_3$ and Fe(CO)$_2$ moieties, respectively. The ^{1}H NMR spectrum of complex **138** shows a splitting pattern of the methylene protons similar to the case of complex **137**, where the axial and the equatorial protons are diastereotopic. While both proton types are coupled by each other, the H-P geminal coupling is observed only for one proton type. The methylene protons of complex **138** are observed as a doublet at 1.18 ppm ($^2J_{HH}$ = 15.2 Hz) and a triplet at 2.32 ppm ($^2J_{HH}$ = $^2J_{HP}$ = 15.2 Hz). Further signals for the protons of the phenyl groups are detected in the range of 6.8-7.8 ppm. The same splitting pattern is also observed for the dithiolato methylene protons of complex **139**. One proton type resonates at 2.20 ppm as a doublet ($^2J_{HH}$ = 14.7 Hz) and the other one at 2.57 ppm as a triplet ($^2J_{HH}$ = 14.7 Hz, $^2J_{HP}$ = 15.5 Hz). The CH$_3$ and CH$_2$ protons of the P(OEt)$_3$ substituent resonate at 1.38 and 4.21 ppm as a triplet and a quintet, respectively. While the splitting pattern of the CH$_3$ group is a result of coupling with vicinal methylene

protons ($^3J_{HH}$ = 7.03 Hz), the splitting of the CH$_2$ arises from H-H and H-P vicinal couplings in equal magnitudes ($^3J_{HH}$ = $^3J_{HP}$ = 7.03 Hz) leading to the observed quintet. Additional signals in the range of 7.4-7.6 ppm are due to the Ph group of complex **139**.

Regioselectivity of Substitution. Indeed, the ^{31}P{^{1}H} and ^{13}C{^{1}H} NMR spectroscopic data describe the regioselectivity of the substitution reactions on complex **137** to afford complexes **138** and **139**. The ^{13}C{^{1}H} NMR spectrum of complex **137** at room temperature, which exhibits two resonance signals at 205.99 and 207.04 ppm (Chapter 2), is consistent with nonequivalent Fe(CO)$_3$ units as a consequence of a desymmetrizing effect of the dithiolato linker, μ-(SCH$_2$)$_2$PhP=O. In principle, there are two possible regioisomers resulting from the substitution of one CO in **137** by a PR$_3$ ligand: a regioisomer with PR$_3$ located under the P=O functionality and another one having PR$_3$ under the Ph group, respectively. The Fe(CO)$_3$ and Fe(CO)$_2$PPh$_3$ moieties of these two possible regioisomers should be nonequivalent. Nevertheless, the ^{31}P{^{1}H} NMR spectrum of **138** or **139** is consistent with the presence of only a single regioisomer (65.82 or 170.0 ppm for the PPh$_3$ or P(OEt)$_3$, respectively). Moreover, ^{13}C{^{1}H} NMR spectra confirm the presence of only one type of Fe(CO)$_3$ and Fe(CO)$_2$PR$_3$ moieties in **138** and **139**, consistent with only one regioisomer for each monosubstituted complex. The regiochemistry of substitution of one CO ligand in [Fe$_2$(CO)$_6${μ-(SCHMe)$_2$NH}] by PMe$_3$ or PPh$_3$ was described by Rauchfuss and co-workers.[121]

Single crystals suitable for molecular structure determinations were obtained by diffusion of pentane into a CH$_2$Cl$_2$ solution of complex **138** at 4 ºC and by evaporation of CH$_2$Cl$_2$ solution of complex **139** at 4 ºC overnight. The molecular structures and the numbering schemes of the complexes are shown in Figure 3-2. The crystal of complex **138** contains three independent molecules, only one of which is shown in Figure 3-2.
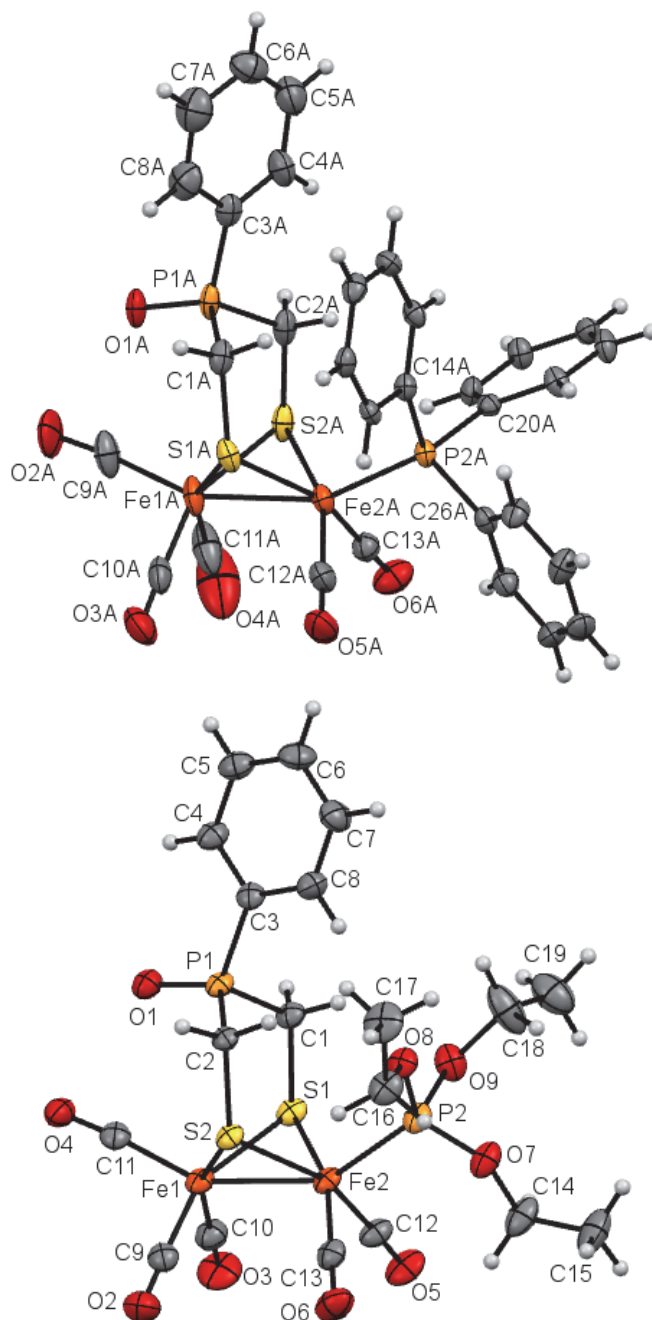
Figure 3-2. Molecular structures (40 % probability level) of complexes **138** (top) and **139** (bottom). Selected bond lengths [Å] and angles [°] of **138** (average): Fe1-Fe2 2.5006(14), Fe2-P2 2.233(2), C9-Fe1-Fe2 156.4(3), P2-Fe2-Fe1 155.4(8). For complex **139**: Fe1-Fe2 2.5152(8), Fe2-P2 2.1687(12), C11-Fe1-Fe2 151.57(13), P2-Fe2-Fe1 147.93(4).

As it can be seen from Figure 3-2, each iron core in complexes **138** and **139** adopts a distorted octahedral structure. In both complexes the two iron atoms are bridged by the dithiolato linker (SCH₂)₂(Ph)P=O, the CO ligands at the Fe1 sites are facial and the PR₃ ligands coordinate to the Fe2 sites on apical position. The bicyclic [Fe₂S₂] structure in

these complexes reveals butterfly conformation. The phosphorus atom of the dithiolato bridge is surrounded in a distorted tetrahedral fashion. The molecular structures of complexes **138** and **139** describe the regiochemistry of the substitution where PR_3 substitutes the apical CO ligands away from the oxygen atom of the P=O functionality. This regioselectivity can be attributed to the lower steric hindrance in the transition state of the substitution at Fe2 than if it was at Fe1 in both complexes. In both complexes, the P=O is oriented toward the Fe1 atom making them potential proton relay models.

The Fe-Fe bond lengths in complexes **138** and **139** (2.5006 Å (average) and 2.5152(8) Å, respectively) are comparable to each other and to that in complex **137** (2.5148(9) Å), but slightly shorter than those of the H cluster (2.55-2.62 Å)[11]. The average Fe2-P2 bond length in complex **138** is 2.2326 Å, which is longer than Fe2-P2 bond length in complex **139** (2.1687(12) Å). These values are consistent with the average Fe-PPh$_3$ and Fe-P(OEt)$_3$ bond lengths (2.247 Å and 2.1808 Å, respectively) in various [FeFe]-hydrogenase complexes.[60,71,82,219] The difference of 0.06 Å between the Fe-PPh$_3$ and Fe-P(OEt)$_3$ bond lengths can be attributed mainly to the higher π-acidity of P(OEt)$_3$ compared to that of PPh$_3$.[161,162]

3.1.2   Ligand Steric Effects

Figure 3-3 shows the effect of the bulkiness of the Ph-P=O moiety as well as the PR_3 ligand in complexes **138** and **139** on the angles OC^{ap}-Fe1-Fe2 (the superscript ap for apical) and R_3P-Fe2-Fe1. We compare the angles with those in complex **137** as well as the previously reported complex **3**[34]. We can notice that the angle OC^{ap}-Fe1-Fe2 is smallest in complex **3** (148.32°) compared to the other complexes that have bulkier μ-$(SCH_2)_2PhP=O$ moieties than μ-$(SCH_2)_2CH_2$ in complex **4**. The angle OC^{ap}-Fe2-Fe1, 146.12(16)°, in complex **137** is smaller than that of OC^{ap}-Fe1-Fe2, 152.17(14)°, owing to the steric interaction between the P=O functionality and the apical CO coordinated to Fe1. The angles OC^{ap}-Fe2-Fe1 in complex **137**, 146.12(16)°, and OC^{ap}-Fe1-Fe2, 148.32°, in complex **3** are comparable, which implies that the spatial region between the Ph ring at the bridgehead of complex **137** and the apical CO at Fe2 has minimum steric interaction. Even when one CO in complex **137** is substituted by P(OEt)$_3$, there is still no significant steric interaction between the apical ligand at Fe2 and the Ph group as indicated by the comparable OC^{ap}-Fe2-Fe1 (146.12(16)°) and (EtO)$_3$P-Fe2-Fe1 (147.93(4)°) angles in

complexes **137** and **139**, respectively. However, the distortion in angles becomes clearer in the case of complex **138** compared to the others. The $Ph_3P\text{-}Fe2\text{-}Fe1$ angle (155.4° in average) is larger than the $(EtO)_3P\text{-}Fe2\text{-}Fe1$ angle because the cone angle of PPh_3 (145°)[220] is significantly larger than that of $P(OEt)_3$ (109°)[220]. This steric interaction between the bulky PPh_3 and the Ph group results in an increased $OC^{ap}\text{-}Fe1\text{-}Fe2$ angle (156.4° in average) compared to those in complexes **137** and **139** (152.17(14)° and 151.57(13)°, respectively).
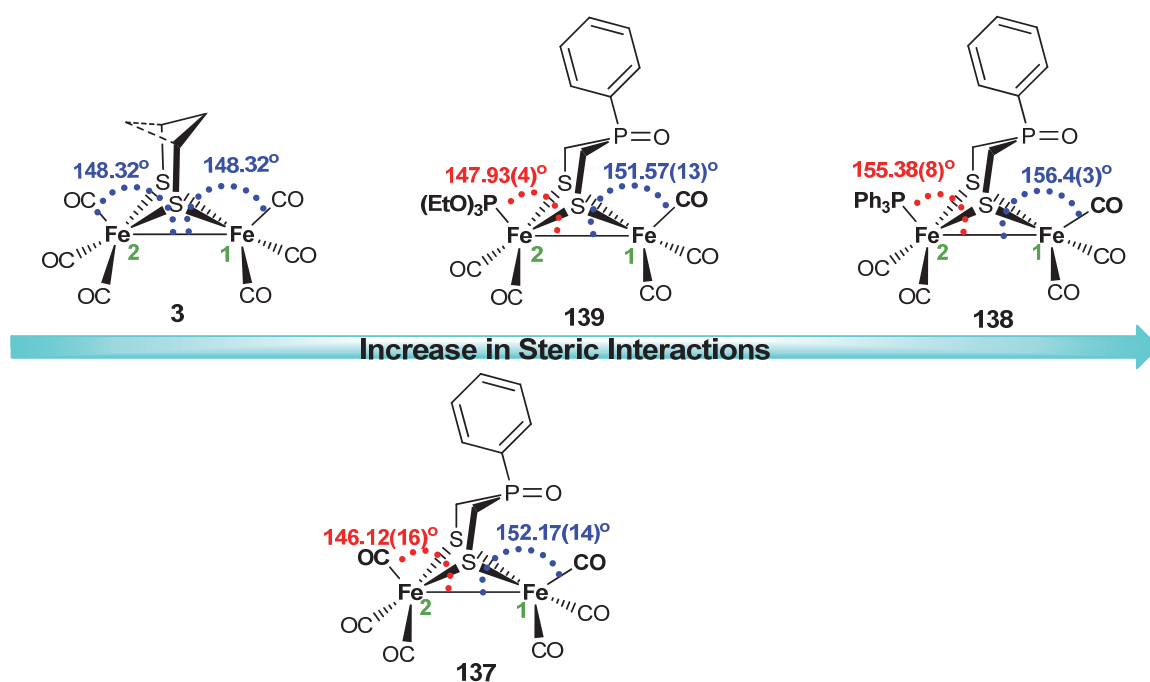
Figure 3-3. Comparison of selected bond angles [°] in complexes **137-139** and **3**[34].

<div style="background:gray">**3.1.3**</div>   **Electrochemistry**

Complex **137** undergoes a quasi-reversible two-electron reduction in $MeCN/NBu_4PF_6$ solution at $E_{1/2} = -1.34$ V ($E_{pc} = -1.39$ V and $E_{pa} = -1.30$ V at 0.2 V·s^{-1}) using mercury drop electrode (Chapter 2). In CH_2Cl_2/NBu_4PF_6 solution, complex **137** also exhibits a quasi-reversible two-electron redox couple but at $E_{1/2} = -1.48$ V ($E_{pc} = -1.52$ V and $E_{pa} = -1.43$ V at 0.2 V·s^{-1}) using a glassy carbon electrode. The electrochemical behavior of complex **137** in CH_2Cl_2/NBu_4PF_6 solution at different scan rates is shown in Figure S3-1. The Plots of the cathodic current (I_p^c) versus the square root of scan rate ($v^{1/2}$) are linear

(Figures S3-2). Indeed, performing the cyclic voltammetry of $O=P(Ph)(CH_2Cl)_2$ in CH_2Cl_2/NBu_4PF_6 solution showed that the phosphine oxide functionality is not reduced and hence it does not lead to interferences in the measurements of the reduction of this class of [FeFe]-hydrogenase models. To investigate the influence of substituting one CO ligand in complex **137** by PPh_3 and $P(OEt)_3$ toward the redox properties of the iron complexes, cyclic voltammetric studies on complexes **138** and **139** have been performed in CH_2Cl_2 using a glassy carbon working electrode.

The cathodic process of complexes **138** and **139** is closer to an overall two-electron reduction process, which occurs at potentials of E_{pc} = -1.78 V and -1.75 V, respectively. The two-electron assignment is based on comparing the normalized cathodic peak current (I_p^c/c; c = concentration of complex) of complexes **138** and **139** with that of complex **137** as well as with the first reduction wave in the cyclic voltammogram of $[Fe_2(CO)_6\{\mu\text{-}Cl_4bpdt\}]$[221] (bpdt = biphenyl-2,2′-dithiolate) under similar conditions. The complex $[Fe_2(CO)_6\{\mu\text{-}Cl_4bpdt\}]$ is already known to exhibit two well-resolved reversible one-electron reduction waves. It has been reported the influence of the steric bulk of the dithiolato ligand on the rotational barrier of the $Fe(CO)_3$ unit for various complexes at the Fe^IFe^I redox state.[110] In contrast to $[Fe(CO)_6\{\mu\text{-}(SCH_2)_2E\}]$ (E = CH_2 (**3**), NH (**7**), NMe (**5**)),[110] complexes **137-139** exhibit torsion angles τ defined by the apical CO across the Fe-Fe bond (OC_{ap}-Fe-Fe-CO_{ap}) due to the presence of sterically demanding Ph-P=O at the bridgehead group. Figure 3-4 shows the view of complex **137** across the Fe-Fe bond and the torsion angle τ. The torsion angle in complexes **138** and **139** are 7.26° and 4.24°, respectively.
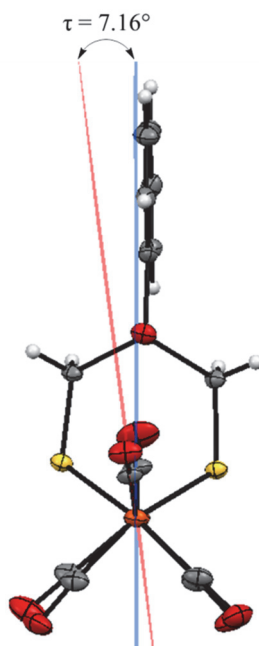
Figure 3-4. A view of complex **137** across the Fe-Fe bond showing the torsion angle (OC$_{ap}$-Fe-Fe-CO$_{ap}$).

The steric interaction between the bridgehead and the apical CO should be increased upon reduction as the DFT calculations (see later) show that the Fe-Fe distance increases and the [Fe$_2$S$_2$] core gets flattened. The reduction therefore facilitates the Fe(CO)$_3$ rotation and the structural changes leading to potential inversion. The higher steric clash between the Ph-P=O group and the apical CO compared to that in the case of CH$_2$, NMe and NH bridgehead groups of **3**, **5** and **7**, respectively, may explain why **137** undergo two-electron reduction with potential inversion (as determined by simulation, Chapter 2) whereas **3**, **5** and **7** do not.

The reduction potential of complex **138** is slightly more negative than that of complex **139** (see above) suggesting that PPh$_3$ is a slightly better donor than P(OEt)$_3$, which is in agreement with the ligand electrochemical parameters (E_L) determined by Lever[163] for P(OMe)$_3$ (E_L = 0.42 V) and PPh$_3$ (E_L = 0.39 V). Unexpectedly, the reduction of complex **139** is much more reversible chemically than that of complex **138**. Thus, while complex **139** undergoes a quasi-reversible reduction at slow to moderate scan rates (0.1-2 V·s^{-1}; Figure 3-5a), the reversibility of the reduction of complex **138** appears to be much more scan rate dependent (Figure 3-5b). The reduction of complex **138** is totally irreversible at 0.05 V·s^{-1} and only a very small re-oxidation peak can be detected at ~ -1.65 V on the return scan upon increasing the scan rate. An additional oxidation feature can be seen in Figure 3-5b at E_{pa} = -1.42 V when the scan rate is 0.2 V·s^{-1}, a

potential that was reported for the oxidation of the hexacarbonyl complex **137** at the Fe^0Fe^0 redox state. This may suggest at this stage of the discussion that the reduction of complex **138** induces the formation of **137²⁻** through the displacement of the PPh₃ ligand in **138⁻** and/or **138²⁻** by a CO ligand coming from another carbonylated species, **S(CO)**, during the reductive process. The enhancement of the chemical reversibility of the two-electron reduction of complex **138** becomes clearer at higher scan rates (Figure S3-3). We may explain the enhanced reversibility of the redox couple (Fe^IFe^I/Fe^0Fe^0) of complex **138** at the higher scan rates in terms of the shorter reaction time scale for the conversion of **138⁻** and **138²⁻** into **137⁻** and **137²⁻**, respectively.
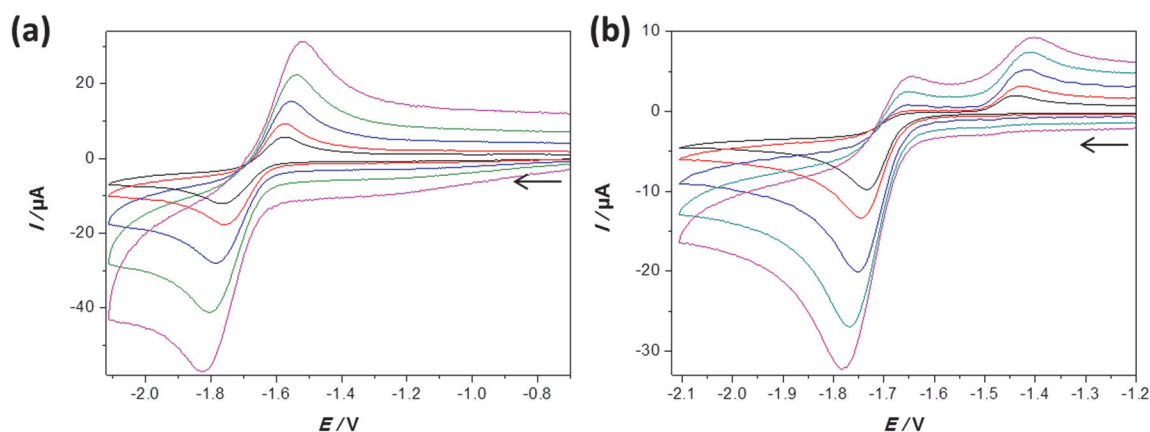
Figure 3-5. Cyclic voltammetry (CH_2Cl_2/NBu_4PF_6 solution) of (a) 0.51 mM $[Fe_2(CO)_5(P(OEt)_3)\{\mu\text{-}(SCH_2)_2(Ph)P=O\}]$ (**139**) at scan rates ($V \cdot s^{-1}$) = 0.1 (black), 0.2 (red), 0.5 (blue), 1 (green) and 2 (purple) and (b) 0.408 mM $[Fe_2(CO)_5(PPh_3)\{\mu\text{-}(SCH_2)_2(Ph)P=O\}]$ (**138**) at scan rate ($V \cdot s^{-1}$) = 0.05 (black), 0.1 (red), 0.2 (blue), 0.4 (green) and 0.6 (purple). Glassy carbon disk (d = 3 mm). E is in V against the ferrocenium/ferrocene couple. The arrows indicate the scan direction.

The oxidation wave at -1.42 V (Figure 3-5b) is found to be reversible on the second cycle as a new reduction event at E_{pc} = -1.52 V is observed and assigned to the process **137** + 2e⁻ → **137²⁻** (Figure 3-6, the black curve). The current of the anodic and the cathodic peaks of the **137/137²⁻** couple are increased when the electrochemical measurements are performed using CO-saturated CH_2Cl_2/NBu_4PF_6 solutions (Figure 3-6, the red curve). These results show that the presence of CO assists the conversion of **138⁻** or **138²⁻** into **137⁻** or **137²⁻** at the electrode surface. Our DFT calculations (see later) provided us hints that the loss of PPh₃ is more likely after the first electron reduction of

complex **138**. Nonetheless, the possible loss of PPh$_3$ from **138^{2-}** cannot be ruled out. The mechanism that describes the cathodic processes of complex **138** in the absence and presence of CO is shown in Scheme 3-2.
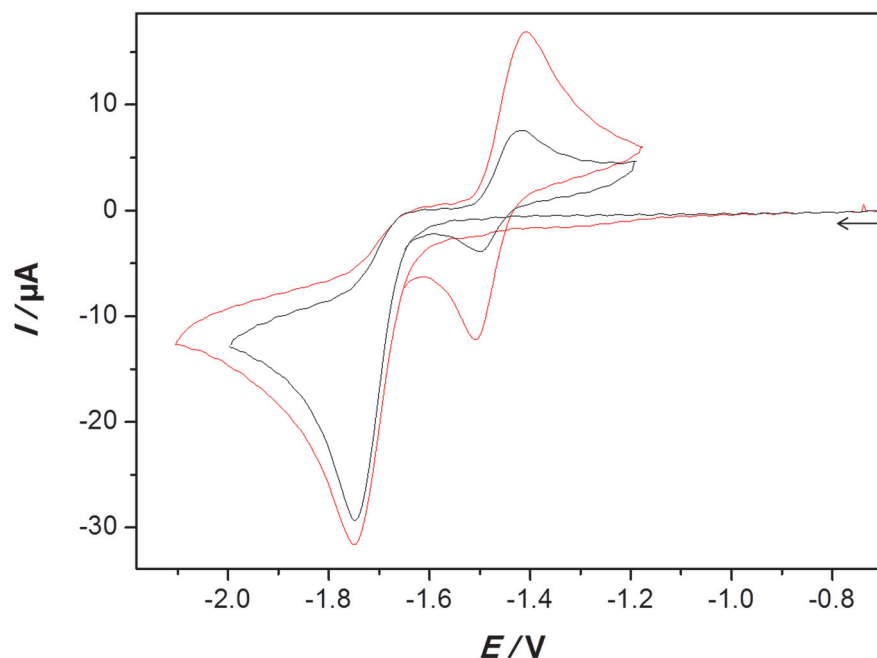
Figure 3-6. Cyclic voltammograms (CH$_2$Cl$_2$/NBu$_4$PF$_6$ solution) of 0.558 mM [Fe$_2$(CO)$_5$(PPh$_3$){μ-(SCH$_2$)$_2$(Ph)P=O}] (**138**) at 0.2 V·s^{-1} under N$_2$ (black) and under CO (red). Glassy carbon disk (d = 3 mm). E is in V against the ferrocenium/ferrocene couple. The arrow indicates the initial scan direction.

Scheme 3-2. Proposed reaction scheme for the cathodic processes of complex **138** in the absence or presence of CO (in red). **S(CO)** refers to any species that act as a source of CO when the experiment is done under N$_2$ atmosphere.
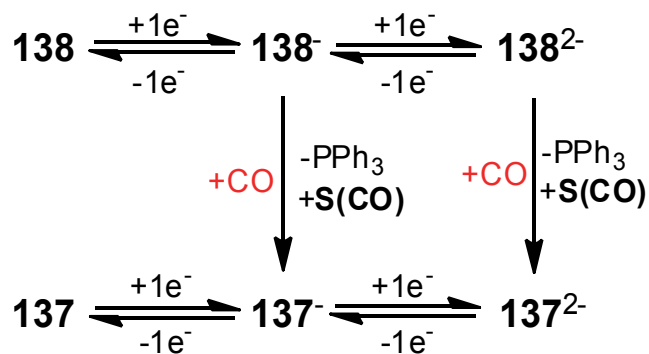
In addition, we have investigated the electrochemical behaviour of complex **139** in CO-saturated CH$_2$Cl$_2$/NBu$_4$PF$_6$ solution (Figure 3-7). The current intensity due to the process **139^{2-}** $\rightarrow$ **139** + 2e$^-$ is visibly lowered after saturating the solution with CO and a new oxidation event due to a product **P** is detected at $E_{1/2}$ ~ -0.9 V (E_{pa} = -0.843 V, E_{pc} = -0.952 V), which shows reversibility in the reverse scan. Scheme 3-3 summarizes the reductive processes in the absence and presence of CO. We suggest that **P** might be obtained from the reaction of CO with **139^{2-}**, an EEC path (E = electron transfer; C = chemical reaction). The fact that P undergoes reversible oxidation indicates that the reaction of **139$^-$** with CO to afford an intermediate **{I}** followed by reduction to give **P** is also a possibility; i.e. an ECE path to **P**. Undoubtedly, a mechanism involving displacement of P(OEt)$_3$ by CO at the redox levels Fe^{0}Fe^I or Fe^{0}Fe^0 of complex **3** is not operative because the reversible redox couple (Fe^{I}Fe^I/Fe^{0}Fe^0) of complex **137** was not detected in contrast to the case of complex **138**. Attempts to gain insight into the structure of P have been made by using DFT calculations, which suggest that **P** may retain a bimetallic structure featuring two [Fe(CO)$_4$] and {Fe(CO)$_2$(P(OEt)$_3$)[(SCH$_2$)$_2$(Ph)P=O]} moieties that could be linked through one sulfur atom or a weak iron-iron interaction (Supporting Information).
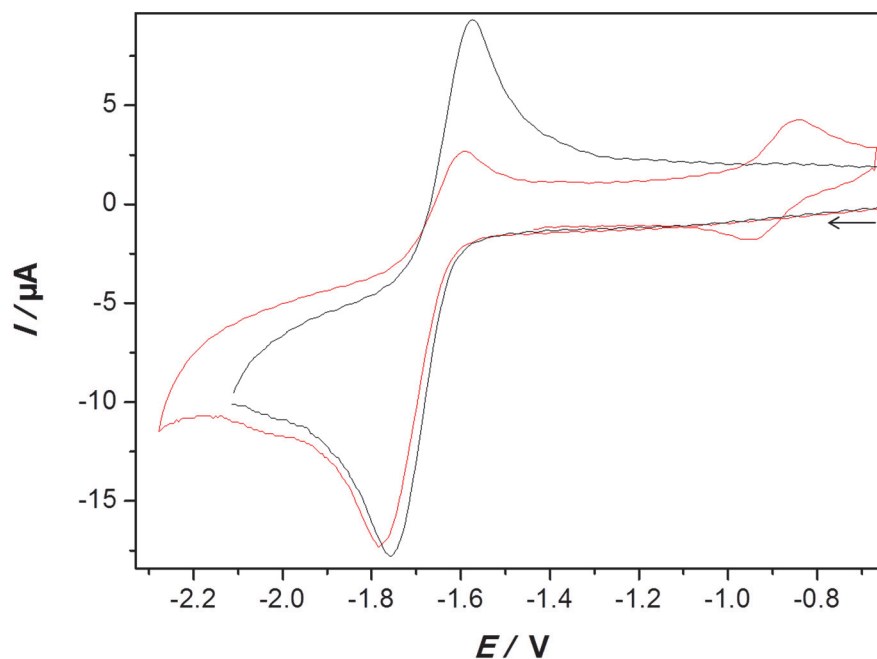
Figure 3-7. Cyclic voltammetry (CH$_2$Cl$_2$/NBu$_4$PF$_6$ solution) of 0.51 mM [Fe$_2$(CO)$_5$(P(OEt)$_3$){μ-(SCH$_2$)$_2$(Ph)P=O}] (**139**) at 0.2 V·s^{-1} under N$_2$ (black) and CO (red). Glassy carbon disk (d = 3 mm). E is in V against the ferrocenium/ferrocene couple. The arrow indicates the initial scan direction.

Scheme 3-3. Reaction scheme for the cathodic processes of complex **139** under N$_2$ (black arrows) and CO (red arrows).
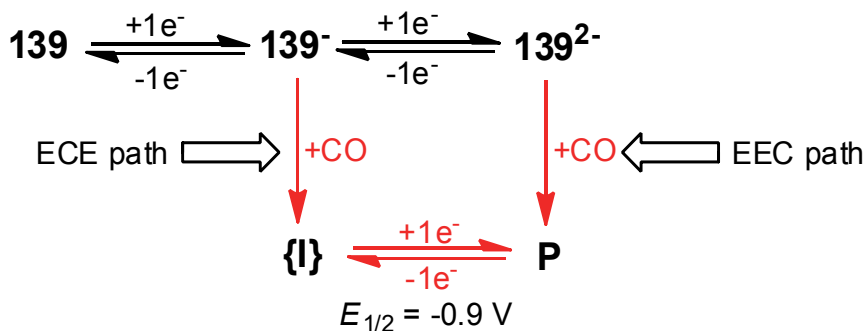
Figure 3-8 shows that increasing the scan rate results in an increase of the reversibility of the reduction of complex **139** under a CO atmosphere, due to a lower conversion of the reduced species into **P**. The reason for this is, again, that the reaction time becomes too short for the chemical process to take place extensively at faster scan rates.
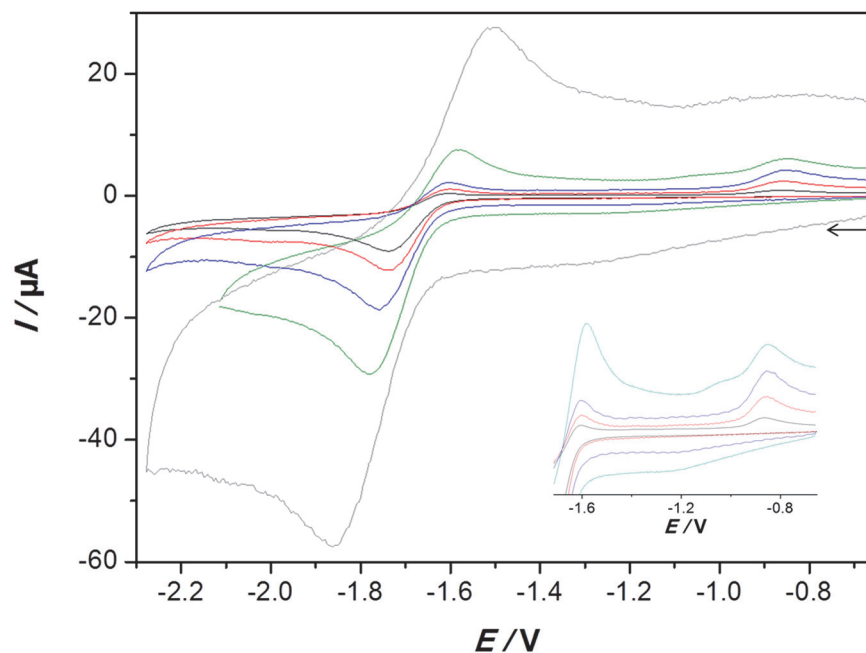
Figure 3-8. Cyclic voltammetry of 0.51 mM [Fe$_2$(CO)$_5$(P(OEt)$_3$){μ-(SCH$_2$)$_2$(Ph)P=O}] (**139**) in CO-saturated CH$_2$Cl$_2$/NBu$_4$PF$_6$ solution at scan rates (V·s^{-1}) = 0.05 (black), 0.1 (red), 0.2 (blue), 0.5 (green) and 2 (grey). The inset shows only the range where the two oxidation peaks occur at the scan rates indicated except the gray curve. Glassy carbon disk (d = 3 mm). E is in V is against the ferrocenium/ferrocene couple. The arrow indicates the scan direction.

The stability of Fe-PR$_3$ against dissociation should be related to the factors affecting the strength of the Fe-P bond during the reduction steps. We have discussed before (Molecular structures) that the Fe-P bond length in the *neutral* complex **139** is shorter than that in complex **2** because the π-back donation n{Fe} → σ*{P-O} is in higher extent than n{Fe} → σ*{P-C}, where n refers to the non-bonding electrons of the Fe atoms. This electronic effect may play a role toward the stability against dissociation of the Fe-PR$_3$ bond. Additionally, it is well known that the rate of dissociation of metal-ligand bond is accelerated for bulky ligands.[220a,222] We have shown before how PPh$_3$ has a more pronounced effect on the bond angles of complex **138** than P(OEt)$_3$ does in complex **139** because of the larger cone angle of PPh$_3$ (145°)[220] compared to P(OEt)$_3$ (109°)[220]. The stepwise electron transfer processes result in structural changes (bond distances, bond angles and stereochemistry) within the [Fe$_2$S$_2$] core as it was described for various [FeFe] models (Scheme 1-16). To gain insights on these structural changes, we have performed DFT calculations for the neutral, monoanion and dianion of complexes **137**, **138** and **139**, which might provide hints on the factors governing the stability of the Fe-P bond after each electron transfer step.

3.1.4   DFT Calculations

The structures of the dinuclear iron compounds **137**, **138** and **139** have been calculated using the program package GAUSSIAN09.[207,208] For iron atoms a relativistic ECP of the Stuttgart-Dresden group (SDD) has been applied.[210] Moreover, analogous compounds with L = PMe₃ (**140**) and P(OMe)₃ (**141**) have been calculated. The corresponding results may be found as supporting information (Table S3-1 and Figure S3-4 as well as Figure S3-5). In recent years many theoretical calculations concerning [FeFe]-hydrogenase models and various aspects of their reactivity and chemical properties as e.g. oxygen affinity, isomerizsation triggered by protonation, electrochemistry or photochemistry have been published.[74b,132,146,147,153,223-231] These studies clearly show that DFT calculations may be considered a tool to understand the experimentally observed behaviors of such model compounds.

The iron carbonyl compounds **137-141** have been considered in the neutral state as well as the products of a formal one- and two-electron reduction. In the case of two electron reduction (i.e. formation of a dianion), it turned out that a rearranged geometry in which only one sulfur atom is acting as a bridging ligand is energetically preferred compared to geometries with two bridging sulfur atoms. Scheme 3-4 summarizes the structural formulae of the species **137-139** in the neutral and reduced forms. Figures 3-9 to 3-11 show the calculated molecular structures of all compounds mentioned in Scheme 3-4 together with the DFT total energies (E_T) relative to the neutral species with the same set of ligands, the number of imaginary frequencies for all stationary points calculated and the most important calculated bond lengths.

Scheme 3-4. Calculated structures of **137-139** in the neutral, monoanionic and dianionic state.

L = CO	**137**	**137⁻**	**137²⁻**	**137a²⁻**	
L = PPh₃	**138**	**138⁻**	**138²⁻**	**138a²⁻**	
L = P(OEt)₃	**139**	**139⁻**	**139²⁻**	**139a²⁻**	**139b²⁻**
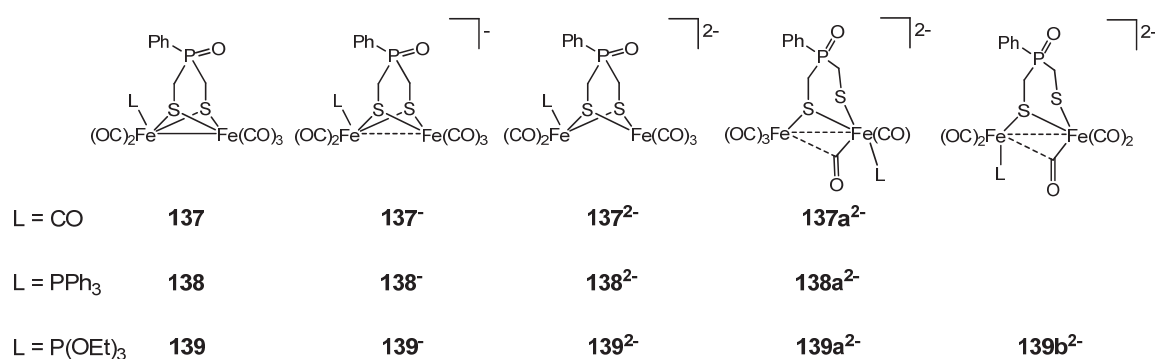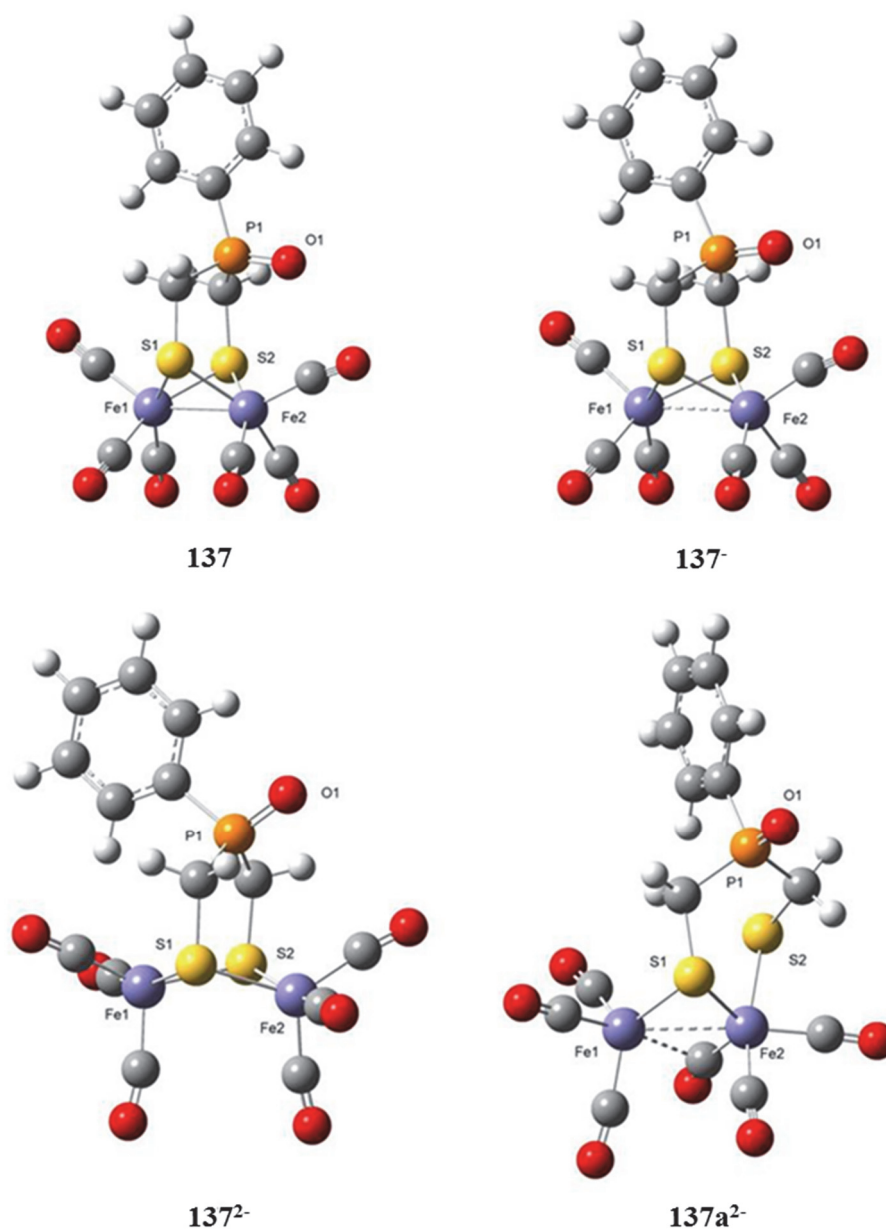
Figure 3-9. Calculated molecular structures and selected bond lengths [pm] of **137**: HF = -2451.489710 a.u., *NImag* = 0, Fe1-Fe2 251.2, Fe1-S1 231.9, Fe1-S2 231.9, Fe2-S1 232.7, Fe2-S2 232.7, P1-O1 149.7; **137⁻**: HF = -2451.571974 a.u. (-216.0 kJ·mol⁻¹ relative to **137**), *NImag* = 0, Fe1-Fe2 281.0, Fe1-S1 237.3, Fe1-S2 237.3, Fe2-S1 236.9, Fe2-S2 236.9, P1-O1 150.1; **137²⁻**: HF = -2451.521008 a.u. (-82.2 kJ·mol⁻¹ relative to **137**), *NImag* = 0, Fe1-Fe2 352.7, Fe1-S1 239.3, Fe1-S2 240.8, Fe2-S1 241.3, Fe2-S2 239.5, P1-O1 151.2; **137a²⁻**: HF = -2451.528961 a.u. (-13.1 kJ·mol⁻¹ relative to **137**), *NImag* = 0, Fe1-Fe2 273.0, Fe1-S1 234.8, Fe2-S1 235.9, Fe2-S2 244.2, P1-O1 151.5.
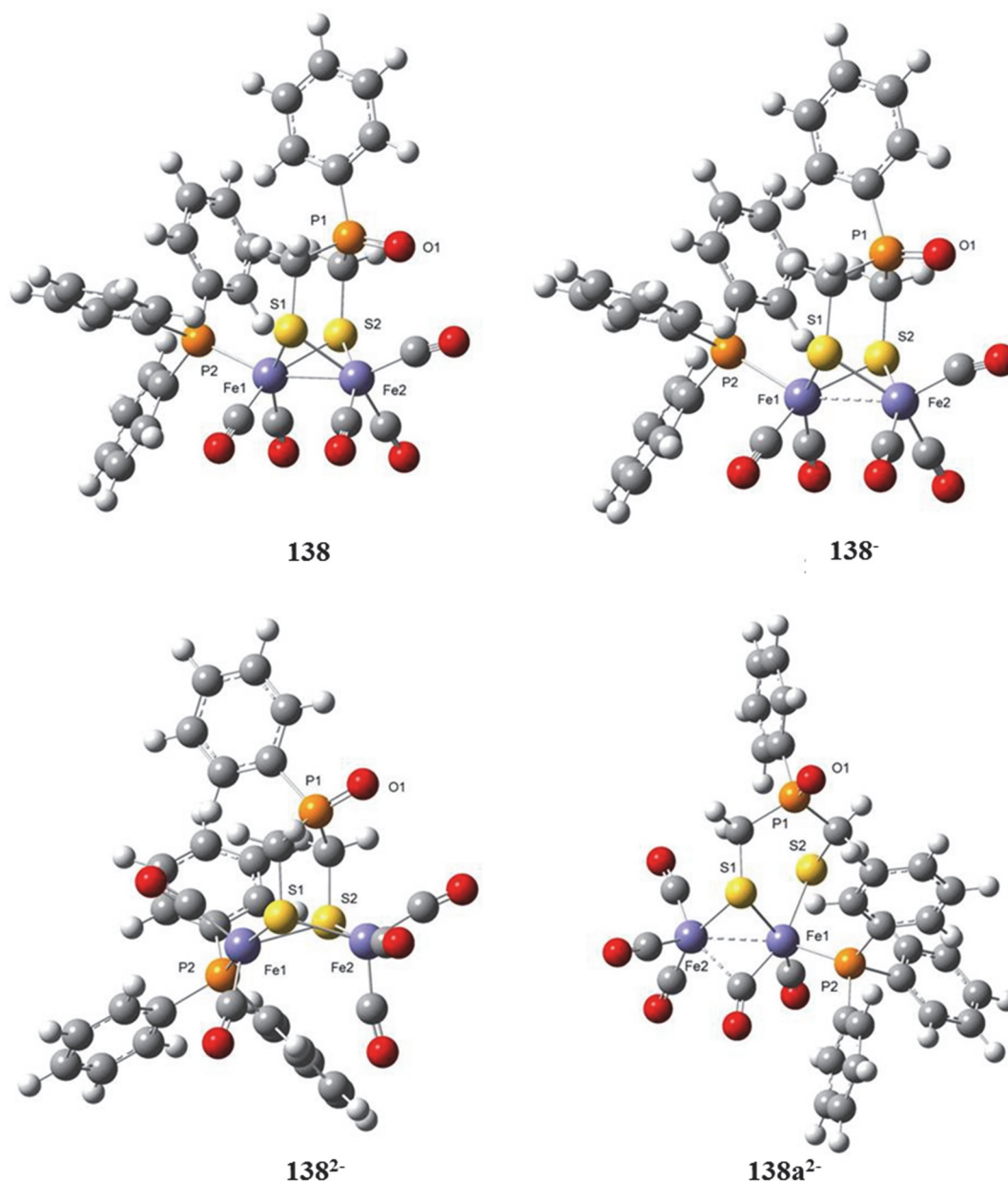
Figure 3-10. Calculated molecular structures and selected bond lengths [pm] of **138**: HF = -3374.353390 a.u., *NImag* = 0, Fe1-Fe2 251.6, Fe1-S1 234.7, Fe1-S2 235.0, Fe2-S1 233.9, Fe2-S2 233.4, Fe1-P2 231.4, P1-O1 150.0; **138$^-$**: HF = -3374.415431 a.u. (-162.9 kJ·mol^{-1} relative to **138**), *NImag* = 0, Fe1-Fe2 274.8, Fe1-S1 238.0, Fe1-S2 238.0, Fe2-S1 240.2, Fe2-S2 238.6, Fe1-P2 241.3, P1-O1 150.2; **138^{2-}**: HF = -3374.356295 a.u. (-7.6 kJ·mol^{-1} relative to **138**), *NImag* = 0, Fe1-Fe2 350.4, Fe1-S1 237.1, Fe1-S2 245.3, Fe2-S1 242.2, Fe2-S2 240.0, Fe1-P2 222.2, P1-O1 151.2; **138a^{2-}**: HF = -3374.367309 a.u. (-36.5 kJ·mol^{-1} relative to **138**), *NImag* = 0, Fe1-Fe2 261.0, Fe1-S1 237.4, Fe1-S2 250.4, Fe2-S1 236.3, Fe1-P2 224.0, P1-O1 151.6.
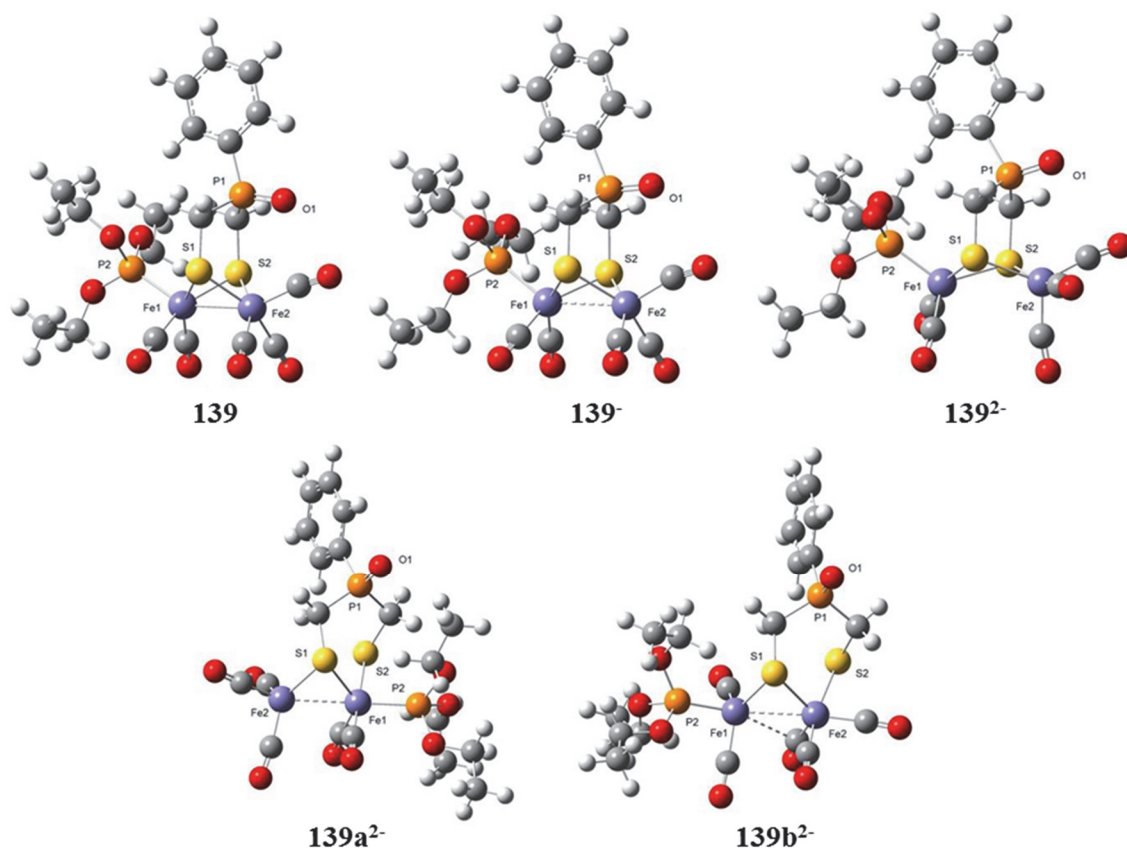
Figure 3-11. Calculated molecular structures and selected bond lengths [pm] of **139**: HF = -3142.854678 a.u., *NImag* = 0, Fe1-Fe2 251.7, Fe1-S1 232.6, Fe1-S2 232.9, Fe2-S1 233.0, Fe2-S2 232.9, Fe1-P2 220.8, P1-O1 150.0; **139⁻**: HF = -3142.922307 a.u. (-177.6 kJ·mol⁻¹ relative to **139**), *NImag* = 0, Fe1-Fe2 278.5, Fe1-S1 236.3, Fe1-S2 237.1, Fe2-S1 237.9, Fe2-S2 237.6, Fe1-P2 221.9, P1-O1 150.3; **139²⁻**: HF = -3142.860589 a.u. (-15.5 kJ·mol⁻¹ relative to **139**), *NImag* = 0, Fe1-Fe2 344.8, Fe1-S1 240.9, Fe1-S2 241.1, Fe2-S1 244.5, Fe2-S2 239.7, Fe1-P2 210.8, P1-O1 151.0; **139a²⁻**: HF = -3142.872079 a.u. (-45.7 kJ·mol⁻¹ relative to **139**), *NImag* = 0, Fe1-Fe2 272.6, Fe1-S1 236.7, Fe1-S2 245.8, Fe2-S1 232.6, Fe1-P2 215.3, P1-O1 151.7; **139b²⁻**: HF = -3142.867376 a.u. (-33.3 kJ·mol⁻¹ relative to **139**), *NImag* = 0, Fe1-Fe2 274.3, Fe1-S1 235.1, Fe2-S1 236.4, Fe2-S2 244.7, Fe1-P2 211.7, P1-O1 151.5.

The results depicted in Figures 3-9 to 3-11 show some interesting trends concerning the relative energies of the compounds although it has to be kept in mind that these calculations are gas phase calculations. So differences in the energies of compounds in different oxidation states do not allow an estimate of real redox potentials or whether a one-electron reduction is preferred over a two-electron process. According to our calculations the product of the one-electron reduction (**137⁻**, **138⁻**, **139⁻**) is always the thermodynamically most stable compound as it is expected due to the typically observed negative electron affinity for the first reduction step whereas the second reduction normally is hampered for electrostatic reasons. In the dianionic state, there are two

possible structural arrangements. Either the $[Fe_2S_2]$ core remains a symmetrical building block with two bridging thiolate functions (**137^{2-}**, **138^{2-}**, **139^{2-}** in Scheme 3-4) or there is a rearrangement leading to an unsymmetrical coordination mode with one bridging thiolate and one thiolate that binds only to one of the iron atoms. In the latter case there are of course two isomers if L ≠ CO with the ligand being bonded to the iron atom exhibiting two Fe-S bonds (**138a^{2-}**, **139a^{2-}**) or the ligand is coordinated to the iron atom with only one additional iron sulfur bond (**139b^{2-}**). For all ligands L = CO, PPh$_3$ and P(OEt)$_3$ the rearranged cluster compounds are thermodynamically favored with respect to the isomers showing a symmetrical $[Fe_2S_2]$ cluster core. In addition, the compounds with L ≠ CO show an enhanced stability for the dianionic isomers with the ligand being bonded to the iron showing two iron-sulfur contacts. The same trends are observed for derivatives with L = PMe$_3$ and P(OMe)$_3$ (*cf.* Supporting Information).

The calculated bond lengths (Figures 3-9 to 3-11) show that upon subsequent reduction of **137**, **138** or **139**, the Fe-Fe distance significantly increases. Correspondingly, the butterfly structure of the $[Fe_2S_2]$ core in the neutral species gets flattened upon reduction ending up to be a bended four-membered ring system in **137^{2-}**, **138^{2-}** and **139^{2-}**. In the dianionic compounds with a rearranged coordination sphere around the iron atoms (**137a^{2-}**, **138a^{2-}**, **139a^{2-}** and **139b^{2-}**), one Fe-S bond is cleaved with respect to the symmetric isomers **137^{2-}**, **138^{2-}** and **139^{2-}**. The Fe-S bond cleavage leads to quite short iron-iron interaction to compensate the electron deficient situation of the iron atom that shows only one Fe-S coordination. This is also the reason for the observation of one semi-bridging CO ligand in **137a^{2-}**, **138a^{2-}** and **139b^{2-}**. Interestingly, this interaction is not observed for **139a^{2-}** (and **141a^{2-}**, *cf.* Supporting Information).

It has been shown by CV measurements that upon reduction of **138**, a significant amount of the hexacarbonyl cluster **137** is formed owing to the loss of PPh$_3$ and subsequent CO addition. Nevertheless, it is not clear whether the elimination of PPh$_3$ takes place after the first or after the second reduction step. Bond length data demonstrate that the first reduction step induces an elongation of the iron phosphorous bond in **138$^-$** compared to **138**, whereas the corresponding bond is quite short in both isomeric compounds **138^{2-}** and **138a^{2-}** after the second reduction step. We therefore estimated the structural implications of the loss of PPh$_3$ from both **138$^-$** and **138a^{2-}** and subsequent addition of CO to the calculated intermediates.

If PPh$_3$ is eliminated from **138$^-$** the resulting anion **142** (Figure 3-12) shows almost identical structural features of the remaining molecule compared to **138$^-$**. The $[Fe_2S_2]$

core is still highly symmetrical although Fe-S and Fe-Fe bond lengths are shortened with respect to **138⁻** in order to compensate the loss of two electrons. A monoanionic isomer with a rearranged cluster core as in the doubly reduced species **138a²⁻** is no minimum on the hyper surface of the monoanion even after PPh₃ is eliminated. If, on the other hand, PPh₃ is split off from the dianion **138a²⁻** the unsymmetrical coordination mode is retained to produce the dianionic intermediate **143**. In contrast to the starting compound (**138a²⁻**), all CO ligands in **143** are now coordinated in a terminal fashion and the Fe-S and Fe-Fe bonds are also shortened as it has been observed in **142**. Interestingly, an isomeric starting compound with three CO ligands coordinated to the iron atom with two iron sulfur contacts and only two CO ligands at the other metal upon geometry optimization ends up in the geometry of **143** since during the calculations one CO is shifted from one iron to the other. From this data it cannot be judged whether the substitution of PPh₃ against CO proceeds from the monoanionic and the dianionic state although the highly elongated iron phosphorous bond length in **138⁻** may give a hint that elimination of PPh₃ from this substrate might be the more likely reaction pathway.

142   **143**
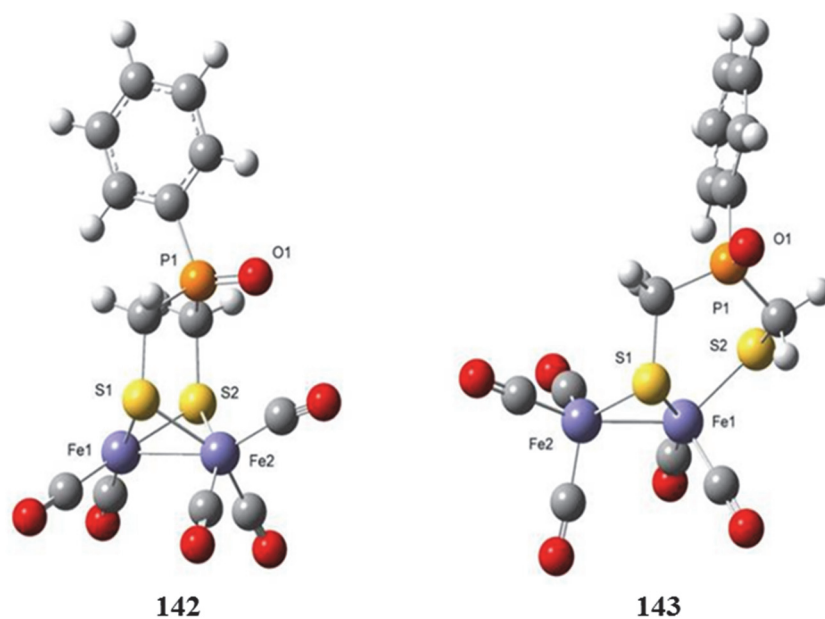
Figure 3-12. Calculated molecular structures and selected bond lengths [pm] of **142**: HF = -2338.194025 a.u., *NImag* = 1 (the very weak imaginary frequency corresponds to the rotation of the iron carbonyl groups relative to each other), Fe1-Fe2 260.8, Fe1-S1 233.6, Fe1-S2 233.6, Fe2-S1 239.4, Fe2-S2 239.4, P1-O1 150.1; **143**: HF = -2338.153575 a.u., *NImag* = 0, Fe1-Fe2 243.7, Fe1-S1 229.5, Fe1-S2 232.7, Fe2-S1 232.3, P1-O1 151.7.

3.2   Conclusions

The monosubstitution of CO ligand in complex **137** by PPh_3 or $P(OEt)_3$ gave complexes **138** and **139**, respectively, in high yields (98 %). The $^{31}P\{^1H\}$ and $^{13}C\{^1H\}$ spectra of complexes **138** and **139** suggest a regioselective substitution of CO by PR_3, which occurs at Fe2 rather than at Fe1 as evident by the molecular structures (Figure 3-2). X-ray crystallography shows that in both **138** and **139** the PR_3 ligand coordinates at the apical position of the iron atom Fe2 (Figure 3-2). The $Fe(CO)_3$ units in complexes **137**, **138** and **139** are more encumbered than the $Fe(CO)_3$ in complex **3**, as evident by comparing their CO^{ap}-Fe1-Fe2 angles, reflecting the steric bulk of the Ph-P=O bridgehead (Figure 3-3). The angles L^{ap}-Fe2-Fe1 (L = CO, PPh_3, $P(OEt)_3$) are comparable for complexes **137** and **139**, but the largest for complex **138** due to the steric effect of the PPh_3 ligand. Our study finds that the higher steric effect of PPh_3 compared to $P(OEt)_3$ results in remarkable differences in the electrochemical behavior between complexes **138** and **139**. The PPh_3 ligand in complex **138** tends to be released after reduction whereas $P(OEt)_3$ in complex **139** does not. Owing to the lower π-acidity and the larger cone angle of PPh_3 compared to $P(OEt)_3$ and based on the results of the DFT calculations, we suggest that the PPh_3 loss occurs most probably upon the first electron reduction step. The presence of CO in the solution assists the formation of **137** in the cyclic voltammetry of **138** by compensating the loss of PPh_3 from the reduced species of **138**. Cyclic voltammetry of complex **139** shows that the Fe-$P(OEt)_3$ bond is stable against dissociation during the cathodic process at all scan rates and even when the solution is saturated with CO. The presence of CO does not lead to substitute the $P(OEt)_3$ to give the hexacarbonyl, but instead it reacts with the reduced species forming a spectroscopically uncharacterized product **P** (Supporting Information). This work shows how the steric and electronic factors affect the kinetic stability of M-L bonds (M = metal; L = ligand).

Chapter 4

Mechanisms of Proton Reduction Catalyzed by [Fe$_2$(CO)$_6${μ-(SCH$_2$)$_2$(R)P=O}] (R = Ph, Et) Models

(Manuscript 1)
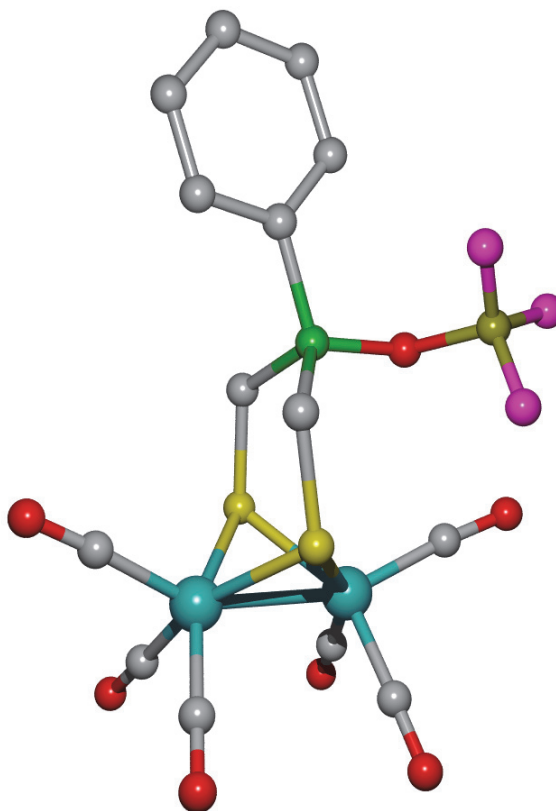
4 Mechanisms of Proton Reduction Catalyzed by [Fe$_2$(CO)$_6${μ-(SCH$_2$)$_2$(R)P=O}] (R = Ph, Et) Models

[FeFe]-hydrogenases have high ability to catalyze the reduction of protons into hydrogen molecules (eq 1), which are used as energy source and transporter in the biological systems.[11]

$$2H^+ \quad + \quad 2e^- \quad \underset{\longleftarrow}{\overset{\text{[FeFe]-hydrogenase}}{\longrightarrow}} \quad H_2 \qquad (1)$$

Crystallographic and spectroscopic studies have shown that the active site of these enzymes (the H cluster, Figure 1-3) consists of two Fe atoms making Fe-Fe bond, dithiolato bridge between these Fe atoms forming butterfly structure of the [Fe$_2$S$_2$] core, two unusual types of ligands (CO, CN$^-$) in the coordination sphere of each Fe atom, and a [Fe$_4$S$_4$] subcluster bonded to one Fe atom. The bridgehead of the dithiolato linker is most likely a NH group. The activity of the enzyme in catalyzing the reaction in eq (1) is attributed to a structural feature, so called *rotated structure*, which offers a vacant site at the distal Fe atom.[11] A proton relay from the NH group to the vacant site (Scheme 4-1, structure **A**) is thought to be a key mechanistic step that results in the formation of a terminal hydride species. Another proton relay mechanism is also possible via hydrido-proton interaction (Scheme 4-1, structure **B**) that lead to H$_2$ formation.[15-17,23,24]

Scheme 4-1. Suggested intermediates involved in proton relay. Proton relay processes are indicated by red arrows in structures **A** and **B**.
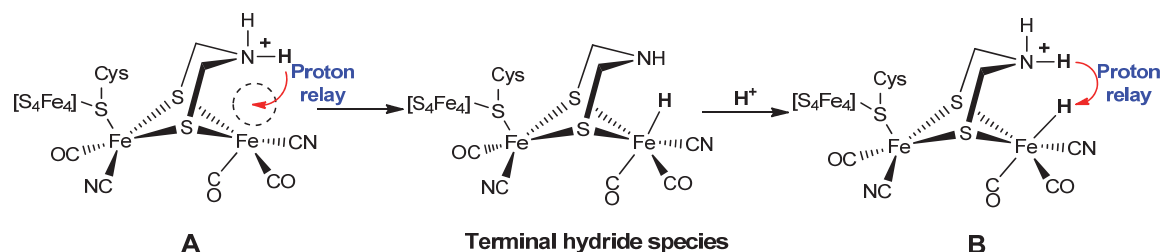
Protonation of model systems of the active site at NR bridgehead groups as well as at N-containing pendant ligands (pyridine or amine functionality) that are either attached to the dithiolato linker or to mono- and bidentate phosphine ligands has been well

investigated in several reports. However, protonation of the amine functionality by moderately strong acids (e.g. CF$_3$CO$_2$H) is only reported for tetrasubstituted model complexes such as complex **117**.[105-107] The protonation of the amine group of the hexacarbonyl complexes [Fe$_2$(CO)$_6${μ-(SCH$_2$)$_2$NR}] requires very strong acids such as HBF$_4$·Et$_2$O. Consequently, the catalytic reduction of moderately strong acids by [Fe$_2$(CO)$_6${μ-(SCH$_2$)$_2$NR}] should start with reduction of the complex for the protonation to be accessible (Section 1.5.1). Chapter 2 describes the synthesis and protonation of a novel type of the [FeFe]-hydrogenase model complexes with phosphine oxide in the dithiolato linker, namely [Fe$_2$(CO)$_6${μ-(SCH$_2$)$_2$(Ph)P=O}] (**137**). The P=O functionality of complex **137** in CH$_2$Cl$_2$ solution can be protonated in the presence of HBF$_4$·Et$_2$O.

In this chapter we show that substituting the Ph group in complex **137** by ethyl group in [Fe$_2$(CO)$_6${(μ-SCH$_2$)$_2$(Et)P=O}] (**144**) results in a pronounced increase in the protophilicity of the P=O functionality. Herein, a mechanism for the formation of P=O-BF$_3$ adduct from the reaction of complex **137** and HBF$_4$·Et$_2$O is described. Moreover, we investigate the mechanism of the catalytic proton reduction by complexes **137** and **144** in the presence of weak and moderately strong acids: CH$_3$CO$_2$H (pK_a = 22.3 in MeCN)[113] and CF$_3$CO$_2$H (pK_a = 12.65 in MeCN)[113]. We show that the mechanism is highly dependent on the solvent being used for the experiment.

4.1   Results and Discussion

4.1.1   Synthesis and Characterization

The reaction of in situ generated (μ-LiS)$_2$Fe$_2$(CO)$_6$[199-201] with 1 equiv. O=P(R)(CH$_2$Cl)$_2$[202,203] afforded [Fe$_2$(CO)$_6${μ-(SCH$_2$)$_2$(R)P=O}] {R = Ph (**137**, see Chapter 2) and Et (**144**)} in 20 % yield (for **144**) as an air-stable red solid (Scheme 4-2). Subsequently, the new complex **144** was characterized by ^{1}H, ^{13}C and ^{31}P{^{1}H} NMR as well as IR spectroscopic techniques, mass spectrometry, elemental analysis and X-ray crystallography.

Scheme 4-2. Reaction of in situ generated Li$_2$[Fe$_2$S$_2$(CO)$_6$] and O=P(R)(CH$_2$Cl)$_2$ to afford complexes **137** and **144**.

R = Ph (**137**), Et (**144**)
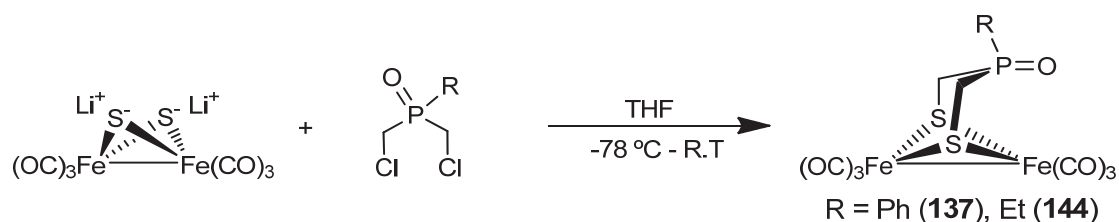
Spectroscopic Characterization. *Full details for the synthesis and spectroscopic data for the ligand O=P(Et)(CH$_2$Cl)$_2$ can be found in the experimental part.* The DEI-MS spectrum of complex **144** afforded the [M - 6CO]$^+$ peak at *m/z* 279. The micro-ESI-MS spectrum of **144** showed the [M + Na]$^+$ peak at *m/z* 470.7. The IR spectrum (KBr pellet) of complex **144** exhibited four absorption bands in the carbonyl region (1951, 1970, 2034, 2076 cm^{-1}). The lower CO frequencies of complex **144** compared to complex **137** (1990, 2003, 2041, 2079) can be attributed to the inductive effect of the R group in the linker (SCH$_2$)RP=O, where the Et group is electron donating and the Ph group is electron withdrawing. The ^{31}P{^{1}H} NMR spectrum of complex **144** showed one peak at 44.7 ppm. The ^{13}C{^{1}H} NMR spectrum of complex **144** showed three doublets centered at 5.31, 18.9, and 25.7 ppm for the *C*H$_3$CH$_2$, CH$_3$*C*H$_2$ and *C*H$_2$S carbon atoms, respectively. Additional signals for the carbonyl carbon atoms were observed at 206.8 and 207.6 ppm. The ^{1}H NMR spectrum of complex **144** showed a splitting pattern for the axial and equatorial methylene protons similar to that of complex **137** (Chapter 2). These protons resonate at 1.69 and 2.71 ppm as doublet and triplet, respectively. The coupling constants were determined as $^2J_{HH}$ = 14.8 and $^2J_{HP}$ = 14.8 Hz. This spectrum showed also one multiplet at 1.6 ppm and another multiplet at 1.06 ppm for the CH$_2$ and CH$_3$ protons of the Et group, respectively.

Molecular Structure of Complex 144. Single crystals suitable for X-ray diffraction studies were obtained by diffusion of pentane into a CH$_2$Cl$_2$ solution of complex **144** at 4 °C. The crystal of complex **144** contains two independent molecules shown in Figure 4-1.
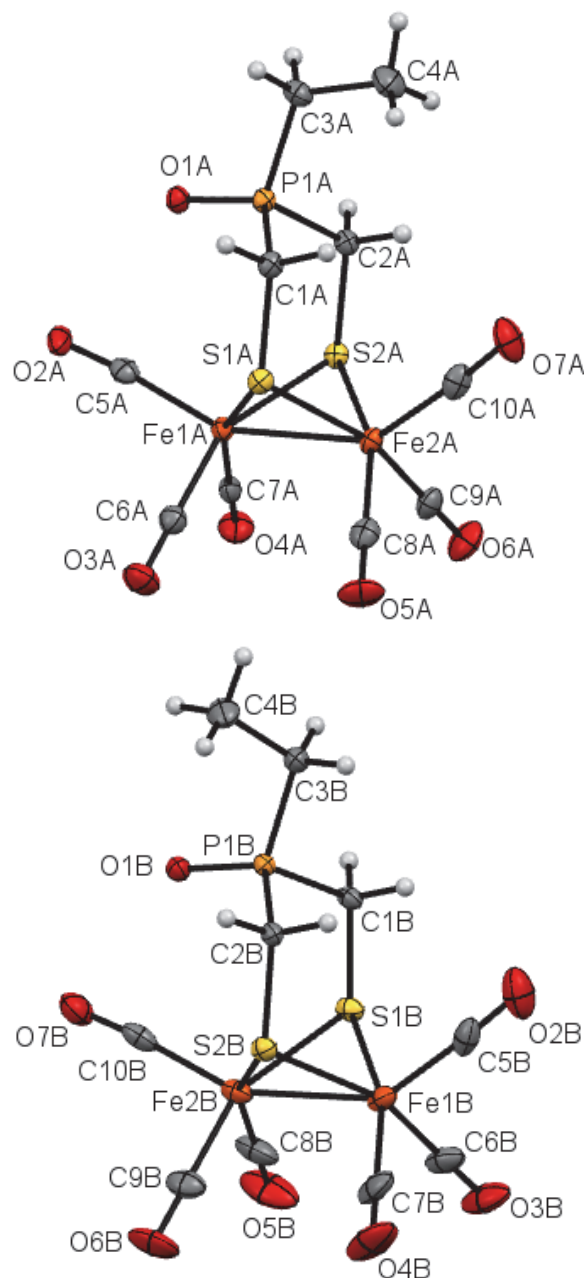
Figure 4-1. Molecular structures (50 % probability level) of the two independent structures of complex **144** (A on the top and B on the bottom).

The geometry of coordination around each iron center in both structures of complex **144** (A and B) can be best described as strongly distorted octahedral, with three carbonyl ligands in facial fashion, two bridging sulfur atoms and one iron atom. The bicyclic [Fe$_2$S$_2$] structures in both complexes have butterfly conformation. The phosphorous atom of the linker (SCH$_2$)$_2$EtP=O is surrounded in a distorted tetrahedral geometry. The stereochemistry of the P=O functionality in complex **144** (structures A and B) is similar to that in complexes **137-139**, where the P=O is always parallel to the Fe-Fe bond. The

two structures show a difference in the torsion angle C5-Fe1-Fe2-C10 (Figure 4-2). The torsion angle is defined by the apical CO groups across the Fe-Fe bond vector. The slightly larger torsion angle in **144**(B) (6.77º) compared to that in **144**(A) is related to the orientation of the Et group. The torsion angle in **137** (7.16º, Figure 3-4) is slightly larger than that in **144** (A and B), which may reflect the higher steric influence of the Ph-P=O group compared to that of the Et-P=O group. The Fe-Fe bond lengths in complexes **137** (2.5148(9) Å) and **144** (2.5108(6) Å [Fe1A-Fe2A], 2.5153(7) Å [Fe1B-Fe2B]) are close to each other. Figure 4-3 displays a comparison between the intramolecular distances P=O---C^{ap} and P---Fe in **137** and **144** (A and B). The longest P=O---C^{ap} and P---Fe distances in **137** compared to **144** (A and B) are consequences of the higher steric bulk of PhP=O compared to EtP=O. The orientation of the Et group triggers a higher steric clash between the bridgehead and the Fe(CO)$_3$ unit in **144**(B) compared to the case of **144**(A), which gives rise to the longer P=O---C^{ap} and P---Fe distances in **144**(B) than those in **144**(A).
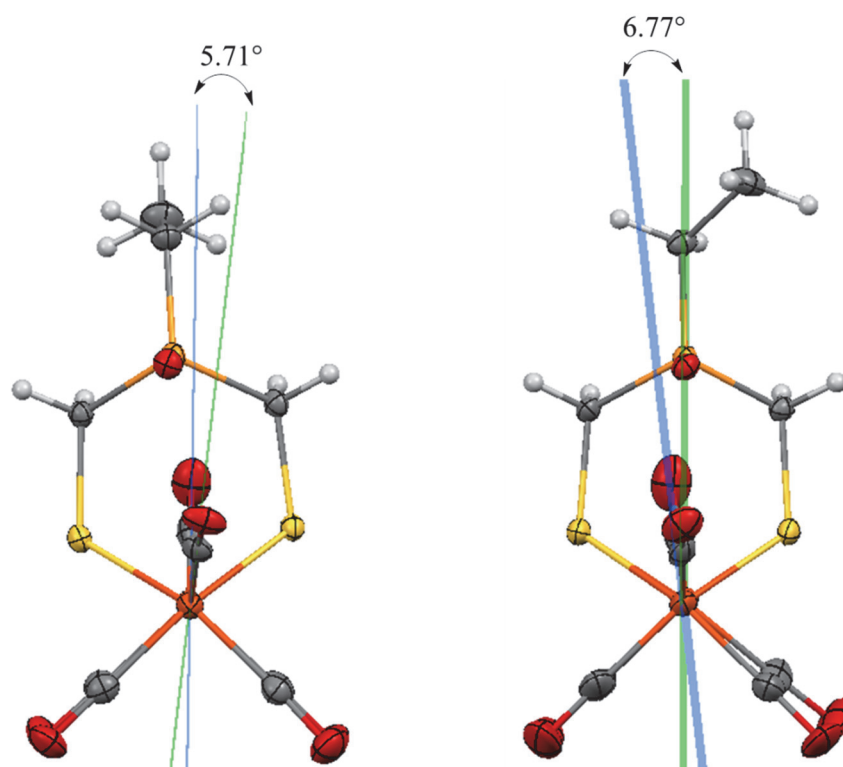
Figure 4-2. Torsion angles in **144**(A) [left] and **144**(B) [right].
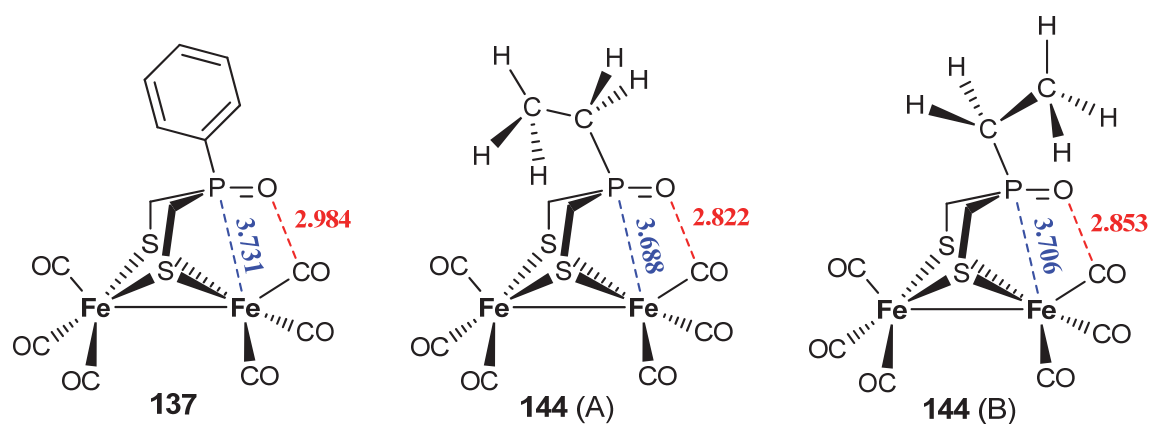
Figure 4-3. Selected intramolecular distances [Å] in **137** and **144** (structures A and B).

4.1.2   Protonation Studies

We have shown in Chapter 2 that only strong acids such as HBF$_4$·Et$_2$O (~ 100 equiv.) can protonate the P=O functionality of complex **137** in CH$_2$Cl$_2$. The P=O group in complex **137** is not basic enough to be protonated by moderately strong acids such as HPy$^+$ in MeCN. Replacement of the Ph group in complex **137** by the Et group in complex **144** is expected to increase the basicity of the P=O functionality. It was possible throughout this structural modification to protonate the P=O functionality of complex **144** in CH$_2$Cl$_2$ solution by equiv. HBF$_4$·Et$_2$O $\geq$ 6.0. We have demonstrated that by following the changes in the carbonyl region of the IR spectrum of complex **144** upon successive additions of HBF$_4$·Et$_2$O (Figure 4-4).
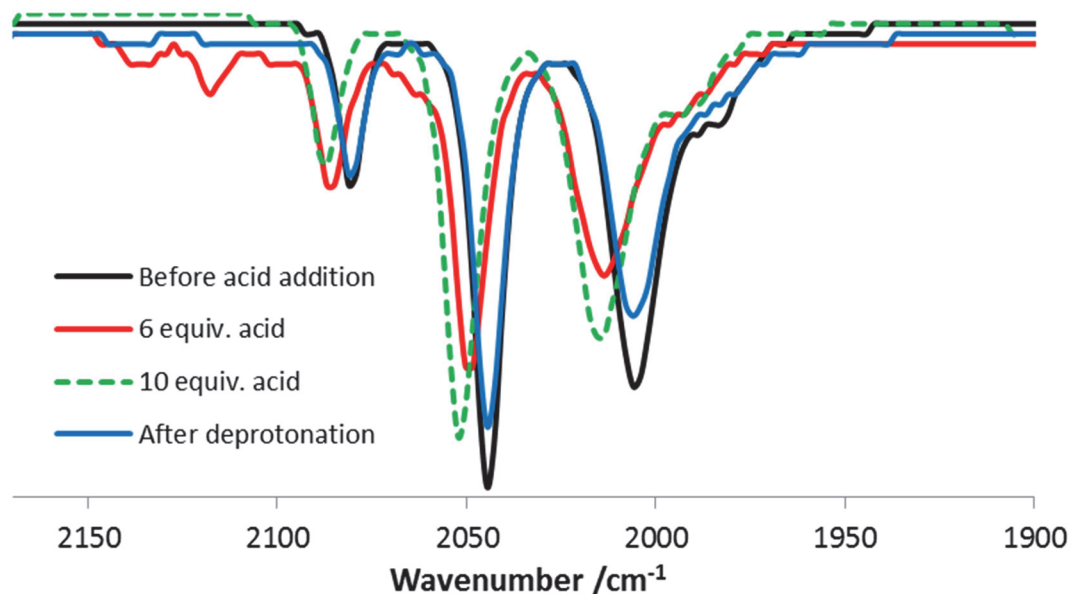
Figure 4-4. The υ(CO) region of the IR spectra of complex **144** + x equiv. HBF$_4$·Et$_2$O in CH$_2$Cl$_2$ solution: x = 0 (black), 6 (red), 10 equiv. (dashed green) and after addition of Et$_3$N (blue).

The presence of 1-3 equiv. HBF$_4$·Et$_2$O in the CH$_2$Cl$_2$ solution of complex **144** did not affect its υ(CO) bands, which means that no reaction took place. The presence of 6.0-10 equiv. HBF$_4$·Et$_2$O resulted in an average shift of the carbonyl bands, $\Delta\upsilon$(CO), by ~ 8 cm^{-1} to higher wavenumbers, which is comparable to that observed in case of complex **137** (~ 10 cm^{-1}) and suggests protonation at the P=O functionality (Figure 2-7a). Stirring the mixture for 2 h showed no change, which reflects the stability of the P=O-protonated **144**. In Figure 4-4, we can notice the presence of three bands at 2099, 2117, 2136 cm^{-1} in the presence of 6.0 equiv. HBF$_4$·Et$_2$O. These small bands, which are due to formation of a transient species, disappeared quickly upon further addition of acid. Addition of Et$_3$N restored the IR signature of the nonprotonated complex **144** without significant decomposition showing that the protonation/deprotonation is a reversible process as in the case of complex **137** (Figure 2-7a).

Figure 4-5 shows the protonation study on **144** in CH$_2$Cl$_2$ (under N$_2$) monitored by IR spectroscopy using the moderately strong acid CF$_3$CO$_2$H (pK_a = 12.65 in MeCN)[113]. An average shift of υ(CO) by only ~ 5 cm^{-1} to higher wavenumbers was observed upon addition of 10-100 equiv. CF$_3$CO$_2$H to the CH$_2$Cl$_2$ solution of complex **144**.[86] On the other hand, the use of MeCN instead of CH$_2$Cl$_2$ as a solvent for the protonation experiment with CF$_3$CO$_2$H showed only a decrease in the intensity of the carbonyl bands,

which suggests decomposition rather than protonation. To the best of our knowledge, no hexacarbonyl model complex containing μ-(SCH$_2$)$_2$NR linker is described to undergo N-protonation by moderately strong acids such as CF$_3$CO$_2$H, but only strong acids (e.g. HBF$_4$·Et$_2$O) is able to protonate the N atom. The N-protonation is described in details in Sections 1.4.1 and 1.4.2.
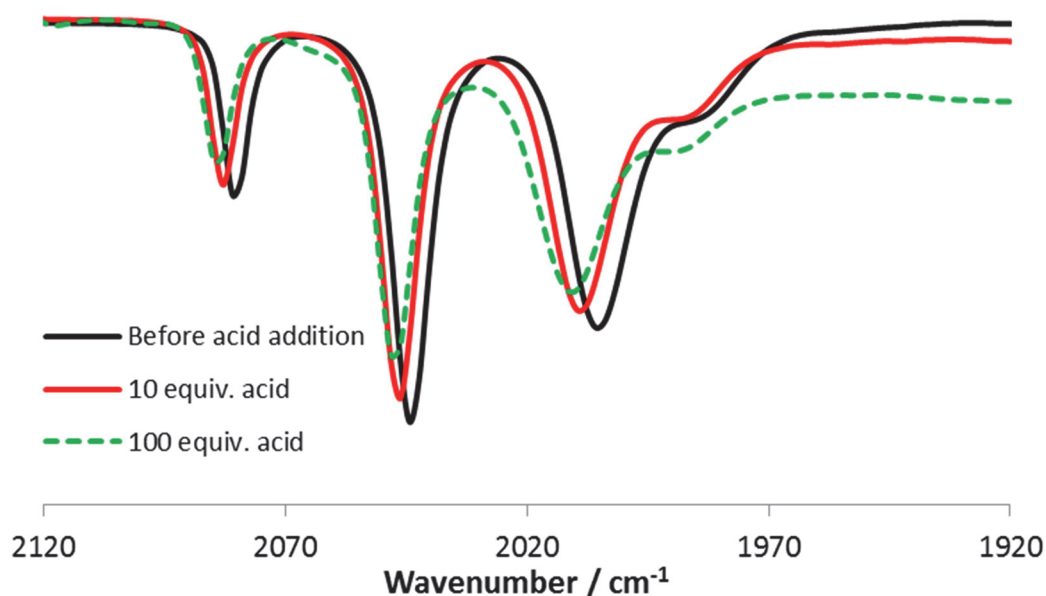
Figure 4-5. The υ(CO) region of the IR spectra of complex **144** + x equiv. CF$_3$CO$_2$H in CH$_2$Cl$_2$ solution: $x = 0$ (black), 10 (red), 100 equiv. (dashed green).

The average shift of the υ(CO) bands upon protonation of the P=O functionality by CF$_3$CO$_2$H ($\sim$ 5 cm^{-1}) is less than that observed upon protonation of complex **137** ($\sim$ 10 cm^{-1}) or **144** ($\sim$ 8 cm^{-1}) by HBF$_4$·Et$_2$O. The DFT calculations on the protonation reaction of complex **137** by HBF$_4$ reflected the effect of ion-pairing on the magnitude of $\Delta\upsilon$(CO), where the calculated shifts in the absence and presence of BF$_4^-$ are 20 cm^{-1} and 7 cm^{-1}, respectively (Table S2-3 and the related text). We therefore assume that the ion-pairing effect of CF$_3$CO$_2^-$ should be more important than that of BF$_4^-$. Complex **144** represents the first example of protonable [FeFe]-hydrogenase hexacarbonyl model by a moderately strong acid, herein CF$_3$CO$_2$H.

Formation of P=O···BF₃ Adduct. Our attempt to crystallize the protonated complex **137** by diffusion of dry pentane into dry CH$_2$Cl$_2$ solution of complex **137** in the presence of excess HBF$_4$·Et$_2$O under N$_2$ overnight led to an unexpected result. Very tiny orange

crystals were obtained in a negligible yield and were identified to be P=O···BF$_3$ adduct (complex **145**, Figure 4-6) instead of the protonated complex.
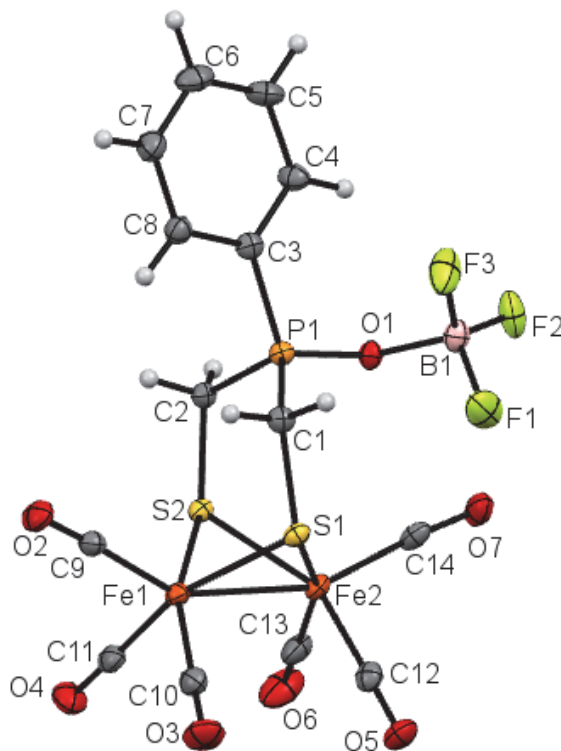
Figure 4-6. Molecular structure (50 % probability level) of complex **145**.

Indeed, such a behavior has been described by Beck et al. for the reaction between HBF$_4$·Et$_2$O and the complexes CpML$_2$CN (M = Fe and L = dppe or M = Ru and L = PPh$_3$) in CH$_2$Cl$_2$ solution (Scheme 4-3).[232] Initially, the protonated complexes at the CN$^-$ ligand are produced, then formation of the CN···BF$_3$ adducts occurs by loss of HF after 18–25 h stirring and precipitation of the product with Et$_2$O.

Scheme 4-3. Reaction of CpML$_2$CN (M = Fe and L = dppe or M = Ru and L = PPh$_3$) with HBF$_4$·Et$_2$O in CH$_2$Cl$_2$ solution.[232]
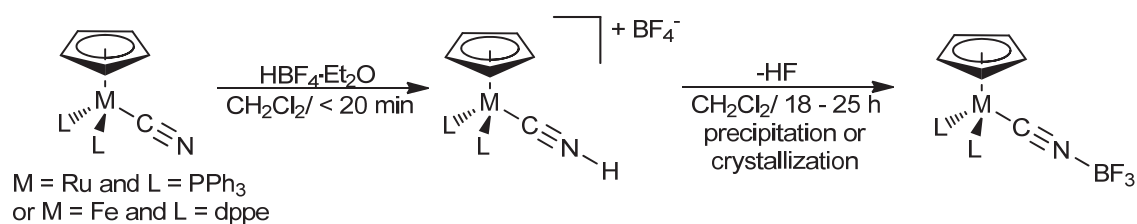
DFT calculations on the **137HBF₄(O)** species (Chapter 2) showed that this ion-pair involves strong hydrogen bonding between the proton at the P=O functionality and one of the fluorine atoms in the BF_4^- anion. This counter anion has a tetrahedral structure with three identical B-F bonds in length (1.389Å on average) and one elongated B-F bond (1.500 Å), which its fluorine atom is involved in the hydrogen bonding. In light of the reported studies in Scheme 4-3 and our DFT calculations on **137HBF₄(O)**, we reasonably suggest that the formation of complex **145** should occur initially via protonation of the P=O functionality in complex **137** to produce **137HBF₄(O)** followed by slow loss of HF molecules during the crystal formation process (Scheme 4-4).

Scheme 4-4. Formation of complex **145** via loss of HF molecules during overnight crystallization in CH₂Cl₂ solution.
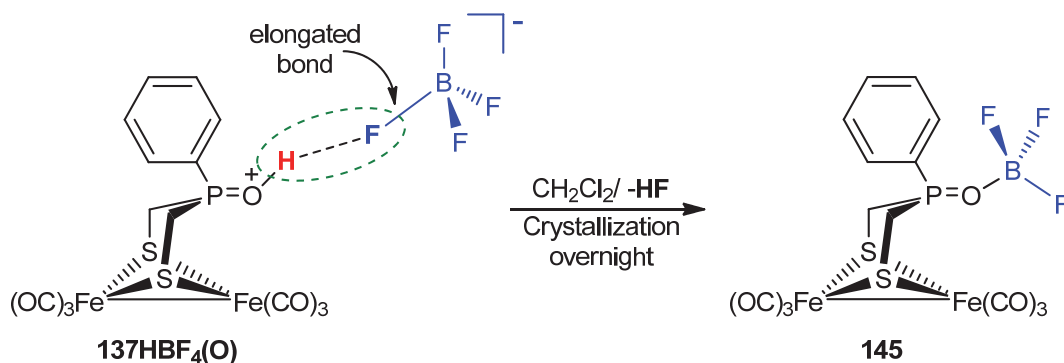
An experimental proof for the mechanism in Scheme 4-4 can be obtained from monitoring the reaction of BF₃·Et₂O with complex **137** in CD₂Cl₂ solution by $^{31}P\{^1H\}$ NMR and IR spectroscopy. The results can be then compared with those found for the reaction of HBF₄·Et₂O with complex **137** in CD₂Cl₂ solution (Figure 2-7). It has been reported that the downfield shift of the $^{31}P\{^1H\}$ NMR signal upon formation of the Et₃P=O···BF₃ and Et₃P=O···HOTf (HOTf = triflic acid) is 23 ppm and 32 ppm, respectively.[206] The lower shift due to Et₃P=O···BF₃ formation compared to that due to protonation of Et₃P=O was explained in terms of the stronger Lewis acidity of H^+ than BF₃.[206] The $^{31}P\{^1H\}$ NMR spectrum of complex **137** in the presence of 2 equiv. BF₃·Et₂O in CD₂Cl₂ solution showed a signal at 54.1 ppm, which is less shielded than that in the absence of BF₃·Et₂O by 23 ppm due to the complexation of BF₃ at the P=O functionality to afford complex **145**. This shift is consistent with that reported for the formation of Et₃P=O···BF₃ and it is smaller than that observed for the reaction between complex **137**

and HBF$_4$·Et$_2$O in CD$_2$Cl$_2$ solution (36.6 ppm, Figure 2-7b). Thus, this experiment confirms that the shift of 36.6 ppm is not owing to the formation of complex **145** (in solution) from the reaction of HBF$_4$·Et$_2$O and complex **137**, but **137HBF$_4$(O)** is formed instead. Moreover, the average shift of the CO bands in the IR spectrum upon addition of 2 equiv. BF$_3$·Et$_2$O to CH$_2$Cl$_2$ solution of complex **137** is ~ 6 cm^{-1} to higher wavenumbers, which is smaller than that reported for the protonation of complex **137** by HBF$_4$·Et$_2$O (~ 10 cm^{-1}, Figure 2-7a). The reaction of complex **144** with 2 equiv. BF$_3$·Et$_2$O in CD$_2$Cl$_2$ solution has been also monitored by ^{31}P{^{1}H} spectroscopy. The ^{31}P{^{1}H} NMR signal of complex **144** in the presence of BF$_3$·Et$_2$O became less shielded by 22.5 ppm, which is consistent with formation of P=O···BF$_3$ adduct **146**. The effect of P=O-protonation and the P=O···BF$_3$ adduct formation on the υ(CO) wavenumbers and the ^{31}P{^{1}H} chemical shift is summarized in Table 4-1.

Table 4-1. Summary of spectroscopic shifts observed upon protonation of P=O and formation of P=O···BF$_3$ adducts (CH$_2$Cl$_2$ solutions of the P=O-species).

Species	^{31}P{^{1}H} NMR downfield shift (ppm)	Shift of υ(CO) bands to higher wavenumbers (cm^{-1})	Reference
137HBF$_4$(O)	36.6	~ 10	Figure 2-7
144HBF$_4$(O)	–	~ 9	Figure 4-4
145	23	~ 6	
146	22.5	–	
Et$_3$P=O·HOTf	32	–	206
Et$_3$P=O·BF$_3$	23	–	206

Furthermore, the ^{19}F NMR spectrum after addition of 2 equiv. BF$_3$·Et$_2$O to the CD$_2$Cl$_2$ solution of complex **137** shows two signals at -142.5 and -153.7 ppm for the F atoms of the coordinated and the free BF$_3$, respectively. In the ^{19}F NMR spectrum of **146**, two signals resonate at -144.2 and -153.8 ppm owing to the F atoms of the coordinated and the non-coordinated BF$_3$.

Figure 4-7 shows that the bond angles C^{ap}-Fe1-Fe2 and C^{ap}-Fe2-Fe1 are larger in **145** than those in **137**. Moreover, the P=O---C and P---Fe1 distances (Figure 4-7) are longer in **145** than those in **137**. Clearly, the formation of **145** from the reaction of **137** and BF$_3$·Et$_2$O increases the steric clash between the bridgehead and the diiron core.
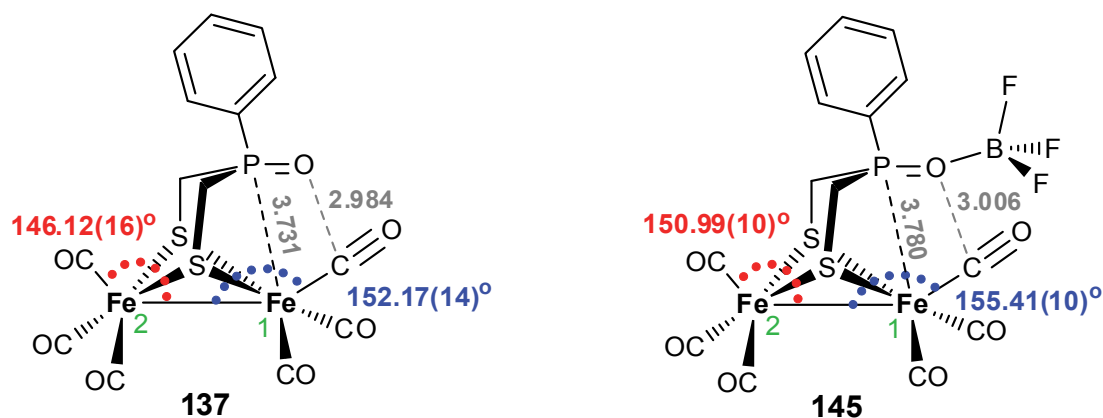
Figure 4-7. Selected bond distances [Å] and angles [°] in **137** and **145**.

<table>
<tr><td>4.1.3</td><td>**Electrochemical Investigations in the Absence of Acids**</td></tr>
</table>

The cyclic voltammetric reduction of complex **144** in CH$_2$Cl$_2$/NBu$_4$PF$_6$ at various scan rates (using glassy carbon electrode) is shown in Figure 4-8.
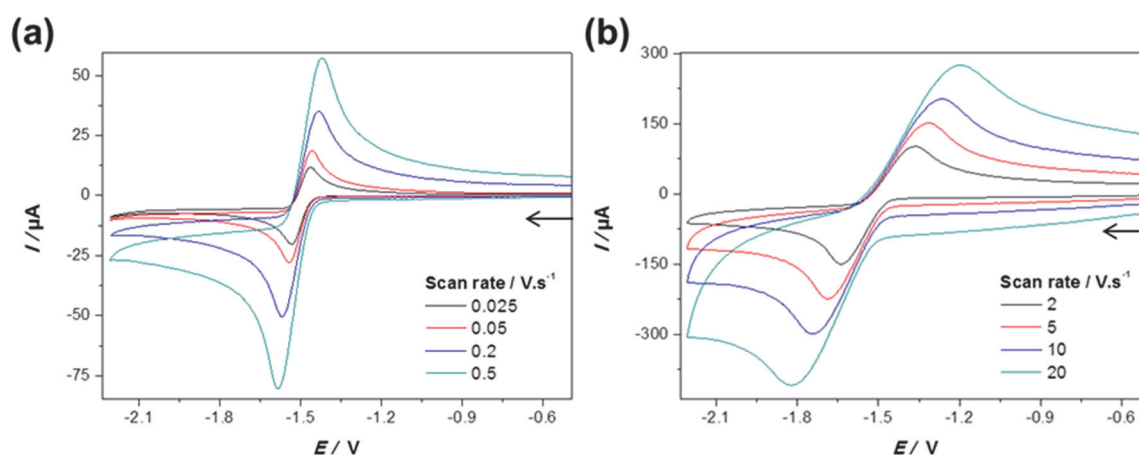
Figure 4-8. Cyclic voltammetric reduction of 1.2 mM complex **144** (CH$_2$Cl$_2$/NBu$_4$PF$_6$ solution) using various scan rates: (a) 0.025-0.5 V·s^{-1} and (b) 2-20 V·s^{-1}. Referenced against the ferrocenium/ferrocene couple. Glassy carbon disk (d = 3 mm). The arrows indicate the scan direction.

Complex **144** exhibits a quasi-reversible reduction at scan rates of 0.025-20 V·s^{-1}. The plot of the cathodic current (I_{pc}) vs. the square root of the scan rate ($v^{1/2}$) is linear showing that reduction is diffusion controlled. The reduction of complex **144** occurs via two-electron transfer in a single step, which was determined by comparing the normalized

current function (I_{pc}/c, c = concentration of complex) of **144** with that of the complex **137** that is confirmed to undergo two-electron reduction with potential inversion (Chapters 2 and 3). In MeCN/NBu$_4$PF$_6$ solution, complex **144** undergoes also an overall two-electron reduction in a single step (Figure 4-9).
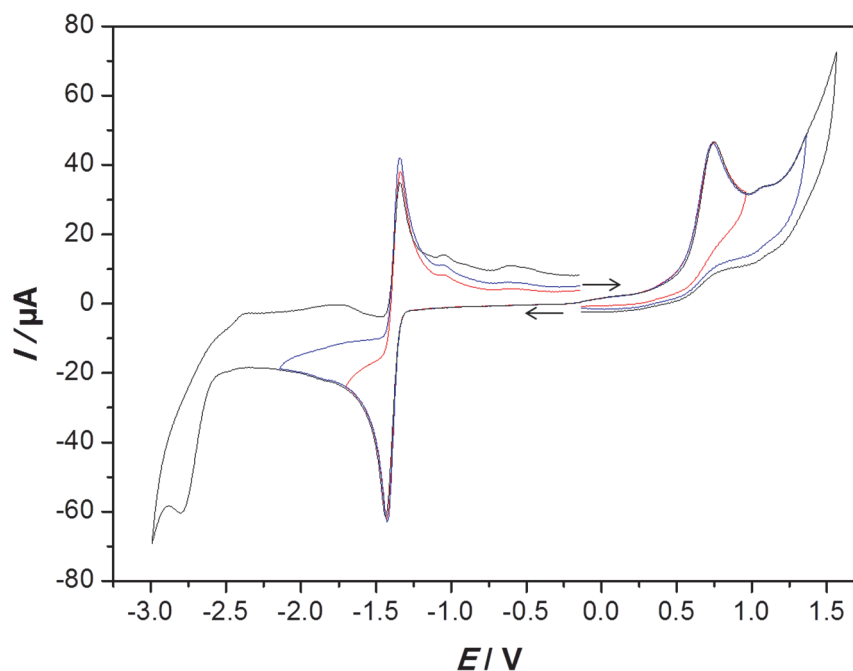
Figure 4-9. Cyclic voltammetric reduction of 1.16 mM complex **144** (MeCN/NBu$_4$PF$_6$ solution) at 0.2 V·s^{-1}. Referenced against the ferrocenium/ferrocene couple. Glassy carbon disk (d = 3 mm). The arrows indicate the scan direction.

Table 4-2 summarizes the redox properties of **137** and **144** in different solvents. In CH$_2$Cl$_2$/NBu$_4$PF$_6$ solution, the half-wave potential of complex **144** ($E_{1/2}$ = -1.51 V) is slightly more negative than that of complex **137** ($E_{1/2}$ = -1.48 V), which reflects the stronger electron donating ability of the Et group in complex **144** compared to the Ph group in complex **137**. Similar trend is found in MeCN/NBu$_4$PF$_6$ solution. Whereas the oxidation potentials of complexes **137** and **144** in CH$_2$Cl$_2$/NBu$_4$PF$_6$ solution are similar (E_{ox} = +0.71 V), complex **144** undergoes oxidation more easily than complex **137** in MeCN/NBu$_4$PF$_6$ solution as **144** has less positive oxidation potential (E_{ox} = +0.74) than that of **137** (E_{ox} = +0.78). This trend reflects again the influence of R in μ-(SCH$_2$)RP=O toward the redox properties of the [Fe$_2$S$_2$] cluster. The influence of these two groups toward the electron density at the iron centers was also revealed by IR spectroscopy (see above).

Table 4-2. Summary of redox properties of **137** and **144** in MeCN and CH$_2$Cl$_2$/NBu$_4$PF$_6$. Potentials (in V vs. ferrocenium/ferrocene couple) are at 0.2 V·s^{-1}.

Complex	$E_{pc}{}^a$	$E_{pa}{}^a$	$E_{1/2}{}^a$	$E_{ox}{}^a$	$E_{pc}{}^b$	$E_{pa}{}^b$	$E_{1/2}{}^b$	$E_{ox}{}^b$
137	-1.42	-1.23	-1.32	+0.78	-1.52	-1.43	-1.48	+0.71
144	-1.43	-1.34	-1.39	+0.74	-1.57	-1.44	-1.51	+0.71

^{a}MeCN/NBu$_4$PF$_6$ solution. ^{b}CH$_2$Cl$_2$/NBu$_4$PF$_6$ solution.

In comparison, the cathodic peak potential (E_{pc}) of the P=O-systems in MeCN solution are less negative than those of various [Fe$_2$(CO)$_6$\{μ-(SCH$_2$)$_2$NR\}] models with -1.49 $\leq E_{pc} \leq$ -1.69 V.[164] The oxidation potentials (MeCN solution) of the P=O-models are generally more positive than those of the [Fe$_2$(CO)$_6$\{μ-(SCH$_2$)$_2$NR\}] complexes (+0.46 $\leq E_{ox} \leq$ +0.73 V).[164] In other words, the reduction of the P=O-complexes is generally easier than in the reduction of [Fe$_2$(CO)$_6$\{μ-(SCH$_2$)$_2$NR\}] whereas the oxidation is harder. This difference is related to the higher electron withdrawing nature of the μ-(SCH$_2$)$_2$(R)P=O compared to μ-(SCH$_2$)$_2$NR.

4.1.4   Electrocatalytic Proton Reduction

In this chapter the mechanism of proton reduction catalyzed by complexes **137** and **144** in the presence of weak and moderately strong acids (CH$_3$CO$_2$H and CF$_3$CO$_2$H, respectively) is discussed.

In The Presence of CH$_3$CO$_2$H. Cyclic voltammetry of complex **137** in the presence of CH$_3$CO$_2$H at different concentrations (Figure 4-10) shows no increase in the current of the two-electron cathodic wave and suppression of the anodic wave for the oxidation of the dianion **137**$^{2-}$. The catalytic reduction of CH$_3$CO$_2$H occurs near ~ -2.1 V as shown in Figure 4-10.
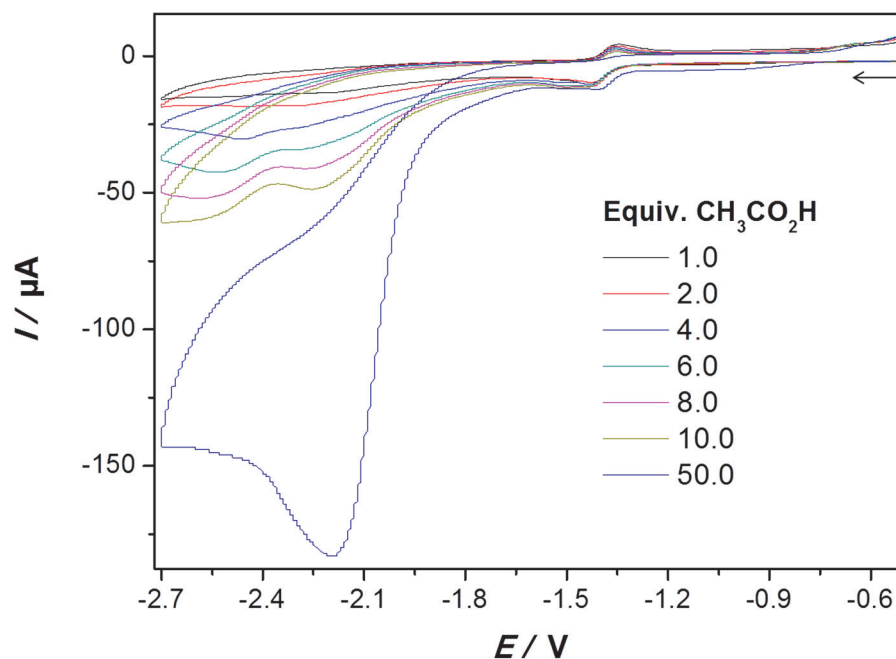
Figure 4-10. Cyclic voltammetry of 1.0 mM complex **137** (MeCN/NBu$_4$PF$_6$ solution) in the presence of varying CH$_3$CO$_2$H concentrations using a scan rate of 0.2 V·s^{-1}. E is in V against the ferrocenium/ferrocene couple. The arrow indicates the scan direction.

This catalytic behavior in the presence of CH$_3$CO$_2$H is similar to what has been observed for other hexacarbonyl complexes that show an overall two-electron reduction in the absence of acid. A detailed analysis of such catalytic behavior for [Fe$_2$(CO)$_6${μ-bdt}] (bdt = benzenedithiolate) complex (**27**) shows that it occurs through an ECEC mechanism (Scheme 1-19).[52] Therefore, we propose that the catalytic reduction of CH$_3$CO$_2$H by complexes **137** also occurs through ECEC mechanism in which the catalyst is the monoanion **137**$^-$ (Scheme 4-5).

Scheme 4-5. Proposed mechanism for electrocatalytic proton reduction by complex **137** in the presence of CH$_3$CO$_2$H.
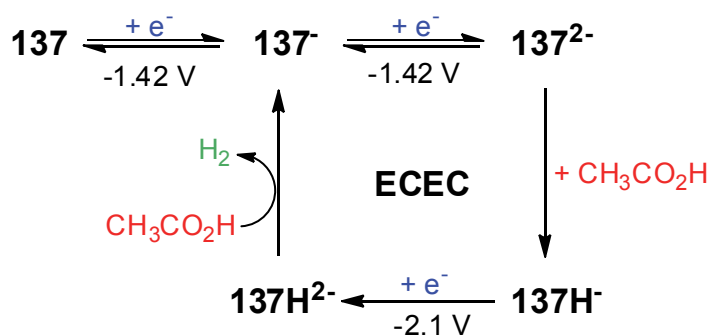
In The Presence of CF$_3$CO$_2$H. We have found by spectroscopy (Figure 4-5) that the neutral complex **144** is protonable at the P=O site in CH$_2$Cl$_2$ solution using CF$_3$CO$_2$H (equiv. $\geq$ 6), while in MeCN is not. In comparison, only strong acids can protonate complex **137** at the P=O group (Figure 2-7). For this reason, we investigate the cyclic voltammetric behavior of complexes **137** and **144** in the presence of CF$_3$CO$_2$H in CH$_2$Cl$_2$ as well as in MeCN solution. The cyclic voltammetry of complex **144** (MeCN/NBu$_4$PF$_6$ solution) in the presence of 0.6-200 equiv. CF$_3$CO$_2$H is shown in Figure 4-11.
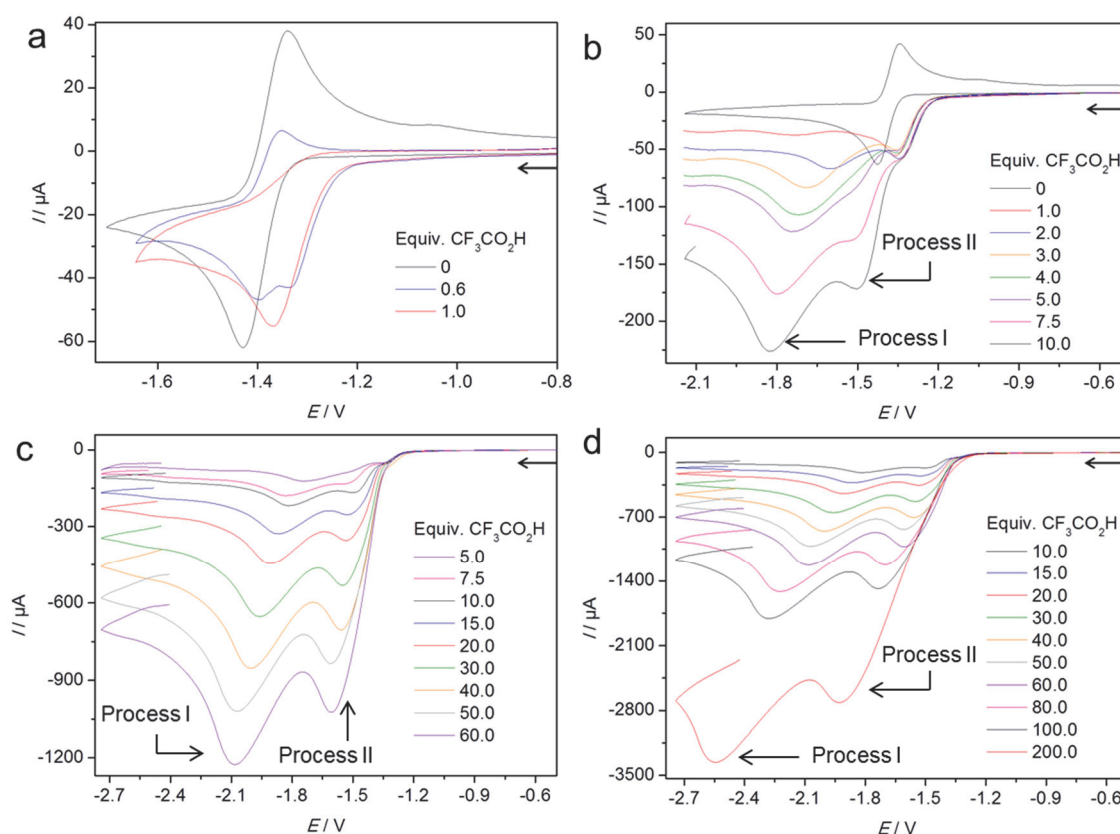
Figure 4-11. Cyclic voltammetry (scan rate 0.2 V·s^{-1}) of 1.16 mM complex **144** (MeCN/NBu$_4$PF$_6$ solution) at various equivalents of CF$_3$CO$_2$H. E is referenced against the ferrocenium/ferrocene couple. Glassy carbon disk (d = 3 mm). The scan direction is indicated by arrows.

Figure 4-11a shows that the addition of 1 equiv. CF$_3$CO$_2$H to the MeCN/NBu$_4$PF$_6$ solution of complex **144** shifts the peak of the two-electron cathodic wave from -1.43 V to -1.37 V (i.e. 60 mV anodic shift) without affecting its current significantly. This small shift is typical when the monoanion **144$^-$** and/or the dianion **144^{2-}** undergo(es) fast protonation to give **144H** and/or **144H$^-$**:[156]

$$144 \underset{-e^-}{\overset{+e^-}{\rightleftharpoons}} 144^- \underset{-e^-}{\overset{+e^-}{\rightleftharpoons}} 144^{2-} \overset{+H^+}{\longrightarrow} 144H^- \quad E_{pc} = \text{-1.37 V (MeCN)}$$
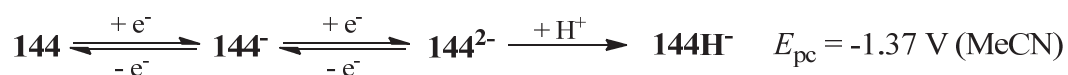
The splitting of the two-electron cathodic wave in the presence of 0.6 equiv. CF$_3$CO$_2$H means that not all reduced species of **144** are protonated. While the current of the peak at -1.37 V remains unchanged with successive additions of CF$_3$CO$_2$H (Figures 4-11b and 4-11c), two catalytic processes (I and II) for H$_2$ release appear at more negative potentials. The fact that there is no increase in the current of the peak at E_{pc} = -1.37 V as the concentration of CF$_3$CO$_2$H increases suggests that **144H$^-$** is not a catalytic species. That the catalysis occurs at potentials more negative than -1.37 V means that further reduction is necessary for release of H$_2$. Process I starts when the solution is less acidic and at more negative potential (2.0 equiv. CF$_3$CO$_2$H, E_{pc} = -1.60 V) than these for process II (equiv. CF$_3$CO$_2$H > 5.0, E_{pc} ~ -1.50 V). This behavior can be explained if process I takes place via reduction of **144H$^-$** into **144H^{2-}** followed by reaction with CF$_3$CO$_2$H to release H$_2$ while process II starts with protonation of **144H$^-$** to **144H$_2$** (when equiv. CF$_3$CO$_2$H ≥ 5.0) that is followed by reduction step and H$_2$ release from **144H$_2$$^-$**. The release of H$_2$ via processes I and II regenerates the monoanion **144$^-$**:

$$144H^- \overset{+e^-}{\longrightarrow} 144H^{2-} \underset{-H_2}{\overset{+H^+}{\longrightarrow}} 144^- \qquad E = \text{-1.6 V (Process I)}$$

$$144H^- \overset{+H^+}{\longrightarrow} 144H_2 \underset{-H_2}{\overset{+e^-}{\longrightarrow}} 144^- \qquad E = \text{-1.5 V (Process II)}$$

It is unambiguous that the reduction potential of **144H$_2$** is less negative than that of **144H$^-$**. The cyclic voltammetry of complex **137** in the presence of CF$_3$CO$_2$H (Figure 4-12) reveals similar behavior to complex **144** in the same medium (MeCN/NBu$_4$PF$_6$).

Figure 4-12. Cyclic voltammetry (scan rate 0.2 V·s^{-1}) of 1.0 mM complex **137** (MeCN/NBu$_4$PF$_6$ solution) at various equivalents of CF$_3$CO$_2$H. Referenced against the ferrocenium/ferrocene couple. Glassy carbon disk (d = 1.6 mm). The scan direction is indicated by arrows.

The addition of 1.0 equiv. CF$_3$CO$_2$H to the MeCN/NBu$_4$PF$_6$ solution of complex **137** shifts the peak of the two-electron cathodic wave from -1.43 V to -1.30 V (i.e. 130 mV to less negative potential) due to the formation of **137H$^-$** instead of **137^{2-}** formed in the absence of acid. Further additions of CF$_3$CO$_2$H show that the catalytic H$_2$ formation occurs via two processes (Figures 4-12b and 4-12c). Process I takes place in the presence of 2.0 equiv. CF$_3$CO$_2$H at -1.54 V whereas process II needs the solution to become more acidic (6.0 equiv. CF$_3$CO$_2$H) to start at a potential less negative than that of process I (-1.38 V). Scheme 4-6 summarizes our proposed mechanism for the reduction of CF$_3$CO$_2$H catalyzed by complexes **137** and **144** in MeCN/NBu$_4$PF$_6$ solution. We can notice from Scheme 4-6 that the H$_2$ release via process I or II occurs at less negative potential in case of complex **137** compared to that of complex **144**. In other words, it is easier to reduce **137H$^-$** than **144H$^-$** in process I. It is also easier to reduce **137H$_2$** than **144H$_2$** in process II. The inductive effect of the R group on the linker (SCH$_2$)RP=O of

these intermediates explains this difference, where the electron donating Et group increases the electron density at the iron sites more than the Ph group.

Scheme 4-6. Proposed catalytic reduction of CF$_3$CO$_2$H by complexes **137** and **144** in MeCN/NBu$_4$PF$_6$ solution.

The protonability of the P=O function of complex **144** in CH$_2$Cl$_2$ solution by CF$_3$CO$_2$H stimulated us to study the effect of protonation on the voltammetric behavior. In contrast to all of the above voltammetric studies in MeCN/NBu$_4$PF$_6$ solution, where only the reduced species of complexes **137** and **144** undergo protonation by CF$_3$CO$_2$H, the addition of CF$_3$CO$_2$H to the CH$_2$Cl$_2$/NBu$_4$PF$_6$ solution of complex **144** resulted in a protonation equilibrium prior to reduction. Figure 4-13 shows the cyclic voltammetry of the CH$_2$Cl$_2$/NBu$_4$PF$_6$ solution of complex **144** in the presence of 0.5-25 equiv. CF$_3$CO$_2$H.

Figure 4-13. Cyclic voltammetry (scan rate 0.2 V·s^{-1}) of 1.2 mM complex **144** (CH$_2$Cl$_2$/NBu$_4$PF$_6$ solution) at various equivalents of CF$_3$CO$_2$H. Referenced against the ferrocenium/ferrocene couple. Glassy carbon disk (d = 3 mm). The scan direction is indicated by arrows.
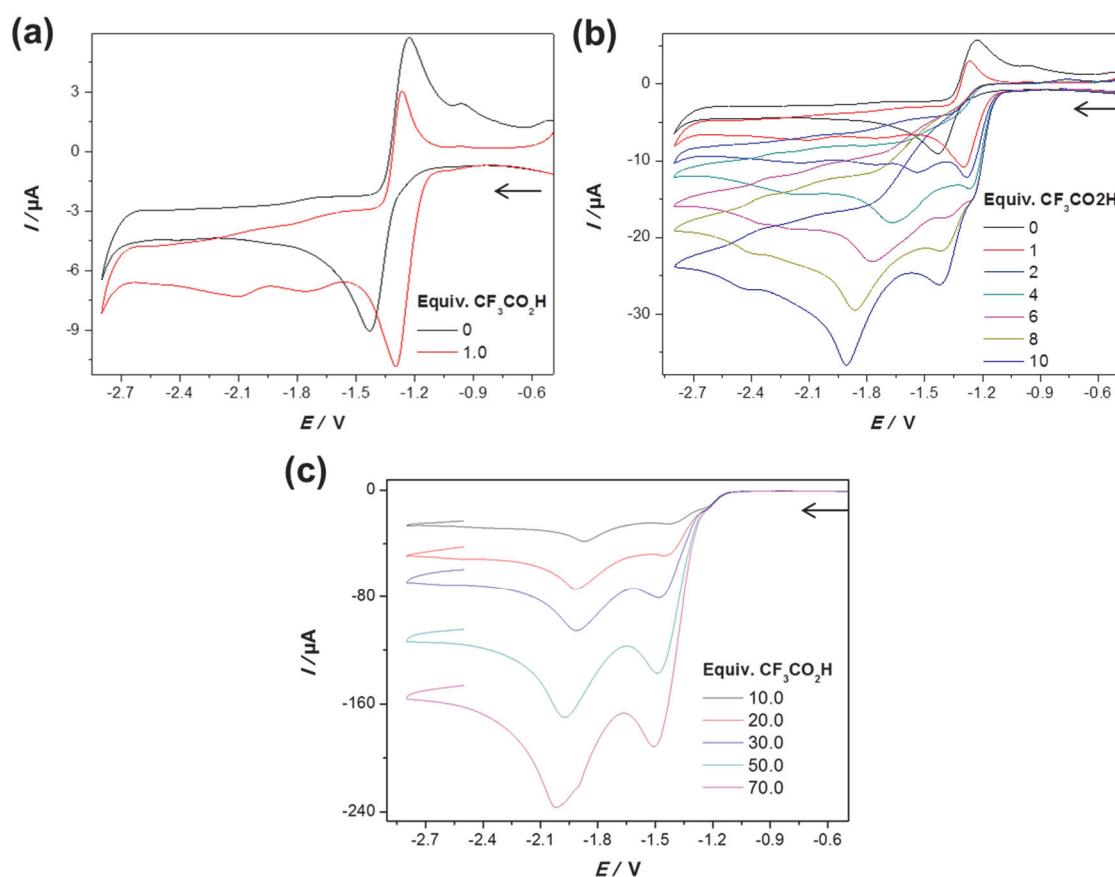
As shown in Figure 4-13a, peak I (E_{pc} = -1.49 V) refers to the reduction of the neutral complex **144** in the presence of CF$_3$CO$_2$H, which occurs at 80 mV less negative potential than that in the absence of acid due to the thermodynamic effect of protonation of the reduced species of **144** affording **144H$^-$**:

$$144 \underset{-\,e^-}{\overset{+\,e^-}{\rightleftharpoons}} 144^- \underset{-\,e^-}{\overset{+\,e^-}{\rightleftharpoons}} 144^{2-} \overset{+\,H^+}{\longrightarrow} 144H^- \quad E_{pc} = \text{-1.49 V (CH}_2\text{Cl}_2)$$

It is clear from Figure 4-13 that the current of peak I remains unaffected by increasing the acid concentration. Peak II (E_{pc} = -1.95 V, Figure 4-13a) arises from reduction of **144H$^-$** to **144H^{2-}** and its current increases slightly with acid concentration and levels off for equiv. CF$_3$CO$_2$H > 3. Peak III (E_{pc} = -1.70 V, Figure 4-13a), which appears when equiv. CF$_3$CO$_2$H = 1.5, could arise from reduction of the protonated form of **144H^{2-}** (i.e. **144H$_2$** + e$^-$ → **144H$_2^-$**), but it seems (probably) that it is related to the growth of the

shoulder IV as [CF$_3$CO$_2$H] increases. This shoulder (at $E \sim$ -1.35 V for 1.0 equiv. CF$_3$CO$_2$H) becomes peak shaped for equiv. CF$_3$CO$_2$H $\geq$ 3.0, peak IV (Figure 4-13b).

Now, we may summarize the reduction potentials of complexes **137** and **144** in the absence and presence of 1 equiv. CF$_3$CO$_2$H in MeCN or CH$_2$Cl$_2$:

$$137 \underset{-\,e^-}{\overset{+\,e^-}{\rightleftharpoons}} 137^- \underset{-\,e^-}{\overset{+\,e^-}{\rightleftharpoons}} 137^{2-} \qquad\qquad E_{pc} = \text{-1.43 V (MeCN), -1.52 V (CH}_2\text{Cl}_2)$$

$$137 \underset{-\,e^-}{\overset{+\,e^-}{\rightleftharpoons}} 137^- \underset{-\,e^-}{\overset{+\,e^-}{\rightleftharpoons}} 137^{2-} \xrightarrow{+\,H^+} 137H^- \quad E_{pc} = \text{-1.30V (MeCN), -1.43 V (CH}_2\text{Cl}_2)$$

$$144 \underset{-\,e^-}{\overset{+\,e^-}{\rightleftharpoons}} 144^- \underset{-\,e^-}{\overset{+\,e^-}{\rightleftharpoons}} 144^{2-} \qquad\qquad E_{pc} = \text{-1.43 V (MeCN), -1.57 V (CH}_2\text{Cl}_2)$$

$$144 \underset{-\,e^-}{\overset{+\,e^-}{\rightleftharpoons}} 144^- \underset{-\,e^-}{\overset{+\,e^-}{\rightleftharpoons}} 144^{2-} \xrightarrow{+\,H^+} 144H^- \quad E_{pc} = \text{-1.37 V (MeCN), -1.49 V (CH}_2\text{Cl}_2)$$

In these equations we can see that the reduction of complex **137** in CH$_2$Cl$_2$ occurs at $\sim$ -1.43 V in the presence of acid, which is not mentioned in the text above. This effect of acid on the reduction of **137** in CH$_2$Cl$_2$ will be discussed later using HBF$_4$·Et$_2$O. From these equations we can notice that the anodic shifts in the reduction potential of **137** and **144** due to the presence of acid are: 130 mV (**137** in MeCN), 90 mV (**137** in CH$_2$Cl$_2$), 60 mV (**144** in MeCN) and 80 mV (**144** in CH$_2$Cl$_2$). In comparison, the shoulder IV at peak I (Figure 4-13), when it starts to appear at 1.0 equiv. CF$_3$CO$_2$H, is shifted by $\sim$ 200 mV from the cathodic peak potential of **144** in the absence of acid. This shift is clearly larger than those mentioned before. In light of this observation, which is only for complex **144** in CH$_2$Cl$_2$/NBu$_4$PF$_6$ solution, and based on the protonability of complex **144** by CF$_3$CO$_2$H in CH$_2$Cl$_2$ solution (Figure 4-5), we ascribe the appearance of the shoulder IV (Figure 4-13) to an equilibrium prior to reduction of **144** involving the neutral complex **144** and its P=O-protonated form, **144H$^+$(O)**:

$$144 \underset{}{\overset{+\,H^+}{\rightleftharpoons}} 144H^+(O) \xrightarrow{+\,e^-} 144H(O) \quad E_{pc} = \text{ca. -1.35 V (CH}_2\text{Cl}_2)$$

As the acid concentration increases (equiv. CF$_3$CO$_2$H $\geq$ 4), only **144H$^+$(O)** is present that is responsible for peak IV and the cathodic event near -1.8 V. The current of peak IV and the peak at -1.8 V increases catalytically showing shift to more negative potentials perhaps due to the high resistance of the CH$_2$Cl$_2$ solvent compared to MeCN[233]. A mechanism for electrocatalytic H$_2$ release from a protonated form of a neutral model

complex **20** was proposed by Talarmin and coworkers applying digital simulations (Scheme 1-21).[171] Herein a similar reaction scheme is proposed to account for the electrocatalysis by **144H$^+$(O)**, Scheme 4-7. Scheme 4-7 displays the suggested mechanisms for the electrocatalytic H$_2$ production by complex **144** in CH$_2$Cl$_2$/NBu$_4$PF$_6$ solution in the presence of CF$_3$CO$_2$H.

Scheme 4-7. Proposed catalytic reduction of CF$_3$CO$_2$H by complex **144** in CH$_2$Cl$_2$/NBu$_4$PF$_6$ solution. The grey path could be important only at acid equiv. < 4.

The behavior of complex **137** in CH$_2$Cl$_2$/NBu$_4$PF$_6$ solution has also been investigated to compare it with that of **144** in the same medium. We used even the quite strong Brønsted acid HBF$_4$·Et$_2$O. The results are shown in Figure 4-14 for the range 0.6-3.3 equiv. HBF$_4$·Et$_2$O. Peak I occurs at 100 mV less negative potential than that of the reduction peak when no acid is present. This difference is again due to the protonation of the reduced species of complex **137** giving **137H$^-$**. Peaks II (at -1.95 V) and III (at -1.69 V) are due to the reduction of **137H$^-$** and **137H$_2$**, respectively. Thus, a protonation equilibrium prior to reduction is not observed in this case (in the presence of 0.6-3.3 equiv. HBF$_4$·Et$_2$O) compared to that depicted in Figure 4-13a.

Figure 4-14. Cyclic voltammetry (scan rate 0.2 V·s^{-1}) of 0.65 mM complex **137** in CH$_2$Cl$_2$/NBu$_4$PF$_6$ solution at various equivalents of HBF$_4$·Et$_2$O. *E* in V is referenced against the ferrocenium/ferrocene couple. Glassy carbon disk (d = 3 mm). The scan direction is indicated by an arrow.
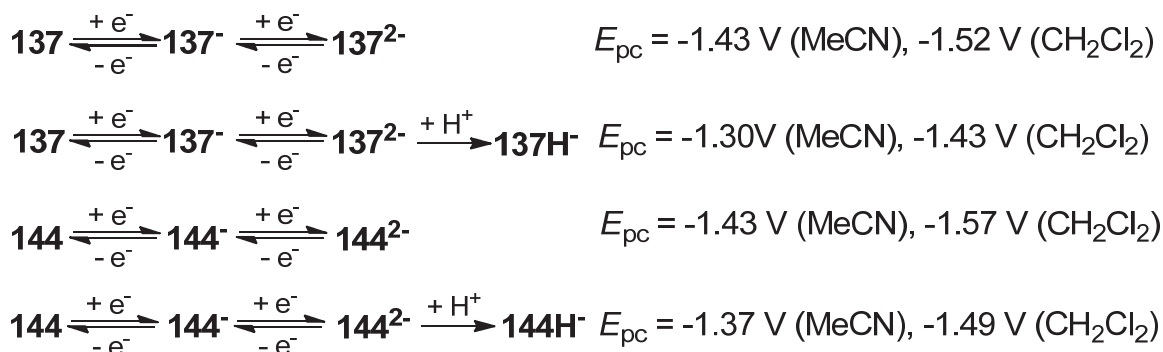
4.1.5   Electrocatalytic Features of the [Fe$_2$(CO)$_6${μ-(SCH$_2$)$_2$RP=O}] Complexes

Two attributes of a good electrocatalyst for the reduction of an acid are:

(i)   The ability to accomplish the catalytsis with low overpotential (η). The overpotential can be estimated by the difference between the standard potential for the reduction of the acid HA ($E°_{HA}$) and the potential where the catalytic reduction takes place (E_{cat}). The potential at half the catalytic peak height is used. A better model complex is able to electrocatalyze the reduction of protons with low overpotential.

(ii)   The high catalytic efficiency (*C.E.*) that reflects the rate of the catalytic process. The catalytic efficiency can be estimated by:[164]

$$C.E. = \frac{I_{cat}\,/\,I_{d}}{Equiv.\ HA}$$

Where I_{cat} and I_d are the catalytic current and the current for the reduction of the catalyst in the absence of acid, respectively. According to the report published by Evans and

others, the catalytic efficiency is classified using the descriptors: W (for weak), M (for medium) and S (for strong). W is assigned for $0 < C.E. < 0.25$, M for $0.25 < C.E. < 0.75$ and S for $C.E. > 0.75$.[164] Table 4-3 summarizes selected electrocatalytical properties of the model complexes **137** and **144**. The reduction of CF$_3$CO$_2$H catalyzed by complex **137** in MeCN occurs with the least overpotential compared to the other cases in Table 4-3. Moreover, complex **137** is catalytically more active toward reduction of CF$_3$CO$_2$H in MeCN via processes I and II than complex **144** does. Direct reduction of CF$_3$CO$_2$H may contribute to the catalytic current of process I in Scheme 4-13. Interestingly, *C.E.* for the reduction of CH$_3$CO$_2$H catalyzed by **137** in MeCN is high compared to previously reported complexes that catalyze the reduction of CH$_3$CO$_2$H with $0.03 < C.E. < 0.65$.[164] The hexacarbonyl complex [Fe$_2$(CO)$_6${μ-(SCH$_2$CH$_2$)$_2$O}] exhibits very strong catalytic activity (*C.E.* ~ 0.91) toward reduction of CH$_3$CO$_2$H in MeCN, but with larger overpotential (η = 700 mV) than that in the case of **137**.

Table 4-3. Electrocatalytic properties of **137**, **144** and **144H$^+$(O)**. Potentials are referenced against ferrocenium/ferrocene couple.

Catalyst	Solvent	Acid	E°_{HA} / V[a]	E_{cat} / V[b]	η / mV[c]	*C.E.*[d]
137	MeCN	CH$_3$CO$_2$H	-1.46	-2.05	590	0.72 (M)
137	MeCN	CF$_3$CO$_2$H	-0.89	-1.36[e]	470[e]	0.81 (S)[e], 0.66 (M)[f]
137	CH$_2$Cl$_2$	HBF$_4$·Et$_2$O	-0.28	-1.37	1090	–[g]
144	MeCN	CF$_3$CO$_2$H	-0.89	-1.5[e]	610[e]	0.602 (M)[e], 0.492 (M)[f]
144H$^+$(O)	CH$_2$Cl$_2$	CF$_3$CO$_2$H	–	-1.48	–	0.486 (M)

[a]Standard potential for reduction of acid HA. This value is not determined in case of CH$_2$Cl$_2$ and hence the overpotentials are not tabulated. [b]Potential of catalysis: Potential at half the catalytic peak height. [c]Overpotential (η) = |E°_{HA} - E_{cat}|. [d]Catalytic efficiency (*C.E.*) is the ratio of (I_{cat}/I_d) divided by [HA]/[catalyst] (i.e. equiv. HA), where I_{cat} and I_d are the catalytic current and the current for the reduction of the catalyst in the absence of HA, respectively. *For complexes that are known to undergo two-electron reduction in a single step, I_d is divided by 2.*[164] [e]For process II (Scheme 4-6). [f]For process I (Scheme 4-6). *Direct reduction of acid probably contributes to to the catalytic current of process I (Scheme 4-6).* [g]Increasing the concentration of HBF$_4$·Et$_2$O shows that the current of peak I (Figure 4-14) increases catalytically. However, a contribution from direct reduction of HBF$_4$·Et$_2$O is probably large at -1.4 V and hence the *C.E.* is not tabulated.

4.1.6	**DFT Calculations on Protonation of Complex 144**

DFT geometry optimizations have been carried out at the BP86/TZVP level and solvent effect has been treated according to the COSMO approach, considering a continuum dielectric with $\varepsilon = 8.93$ (CH$_2$Cl$_2$ solvent).

The experimental and computational studies supported that protonation of complex **137** occurs at the oxygen atom of the P=O functionality. The regiochemistry of protonation of **137** and **144** is supported by the fact that the P=O oxygen shows the most negative atomic charge in both complexes suggesting that it is the preferential site for protonation (Figure 4-15). In addition, the protonation of the P=O functionality leads to the formation of hydrogen bonding between the proton and the apical CO ligand positioned under the bridgehead. This interaction (absent in the other cases) stabilizes the P=OH$^+$ product in both models (Figure 4-16).

Figure 4-15. NBO charges of complexes **137** and **144**.

Figure 4-16. Optimized structures of the most stable protonated form, **137H$^+$(O)** (to the left) and **144H$^+$(O)** (to the right). Distances are in [Å].

Complex **137** can be protonated only by strong acids. On the contrary, protonation of **144** can occur in CH$_2$Cl$_2$ also in the presence of moderately strong acids like CF$_3$CO$_2$H. This difference can be explained in terms of the linker nature. In fact, the replacement of the Ph substituent in complex **137** by an Et functionality in **144** should cause an increase in the basicity of the P=O moiety. The increased proton affinity of complex **144** is confirmed by NBO charges and HOMO atomic population analysis of the P=O functionality (Figure 4-17). Even if the differences are very small, we can notice that the negative charge is slightly more localized on the P=O group of complex **144** in comparison to complex **137** and the HOMO population is higher for the P=O group in **144** than in **137**.

Figure 4-17. Mulliken HOMO population analysis (black values) and NBO charges (red values) of the P=O functionality of model **137** and **144**.

In order to quantify this difference, we computed a relative pK_a (referred to the P=O functionality) between the two complexes. For each model we obtained the K_a values from the relation $\Delta G = -RT \ln K_a$, where T = 298.15 K, R = 1.987 cal·mol^{-1}·K^{-1} and ΔG (kcal·mol^{-1}) is the computed free energy difference between the P=O-protonated species and the neutral one, without considering the free energy of the proton. In fact, what we are interested in is a variation of basicity (ΔpK_a = pK_a(**144**) - pK_a(**137**)) caused by the substitution of the Ph group with an ethyl one. In this way, we do not need to include the solvated $G°$(H$^+$) value in our computations. Our results reveal a ΔpK_a value of 1.44 units (in CH$_2$Cl$_2$), supporting again the improved basicity of **144**. In order to study in a more detail the protonation of **144**, we included explicitly the acid (CF$_3$CO$_2$H) in our computation. In particular, we studied the protonated **144** in the presence of the conjugate base in proximity to the P=OH$^+$ functionality to evaluate the ion-paring effect CF$_3$CO$_2$$^-$ compared to BF$_4$$^-$. Interestingly, we could not find the protonation product with a single molecule of CF$_3$CO$_2$H in CH$_2$Cl$_2$, but only a strong hydrogen bond between the acid and the P=O functionality (Figure 4-18). Therefore, we simulated the presence of more acid equivalents. The results suggest that the minimum number of acid equivalents necessary to obtain the P=OH$^+$ product is 3. In this way each oxygen atom of the carboxylate functionality in CF$_3$CO$_2$$^-$ is involved in a hydrogen bond with the proximate acid molecule. Differently, only 1 equiv. of the stronger HBF$_4$ is needed to obtain the **144H$^+$(O)** product (Figure 4-19). Figure 4-18 shows the different **144**-TFA structures obtained by optimization in implicit solvent. In all of them, a strong hydrogen bond between the P=O functionality and the carboxylic group of CF$_3$CO$_2$$^-$ are present and this interaction is strengthened by the addition of acid molecules (hydrogen bond distance [Å]: 1.47, 1.41 and 1.37 with 1, 2 and 3 CF$_3$CO$_2$H equiv., respectively). The optimized structures of the **144H$^+$(O)** adducts with HBF$_4$ or CF$_3$CO$_2$H as proton source are reported in Figure 4-19. The hydrogen bond distances between the conjugate base and **144H$^+$(O)** underline the more important ion-paring effect of CF$_3$CO$_2$$^-$ compared to BF$_4$$^-$. This behavior is reflected in the average shifts of IR bands observed in the presence of the two different acids. The computed ΔE of **144** protonation by CF$_3$CO$_2$H in CH$_2$Cl$_2$, considering 3 equiv. of acid, is -0.97 kcal·mol^{-1}.

Figure 4-18. Optimized structures (ε = 8.93) of the **144**-CF$_3$CO$_2$H adducts with different number of CF$_3$CO$_2$H equivalents. Distances are in [Å].

Figure 4-19. Optimized structures (ε = 8.93) of the **144H$^+$(O)** adducts with BF$_4^-$ (to the left) or CF$_3$CO$_2^-$ (to the right) as conjugate bases.

4.2   Conclusions

Replacing the Ph group in [Fe$_2$(CO)$_6${μ-(SCH$_2$)$_2$(Ph)P=O}] (**137**) by stronger electron donating Et group in [Fe$_2$(CO)$_6${μ-(SCH$_2$)$_2$(Et)P=O}] (**144**) resulted in great enhancement of the protophilicity of the P=O functionality. Complex **144** is protonable by the moderately strong acid, CF$_3$CO$_2$H, in CH$_2$Cl$_2$ solution whereas complex **137** is not. The protonability of the P=O is dependent on the reaction medium where no protonation takes place in MeCN solution. An indirect evidence for the protonation of the

P=O by HBF$_4$·Et$_2$O is provided by X-ray determination of the product obtained from the reaction of **137** and HBF$_4$·Et$_2$O in CH$_2$Cl$_2$ solution. This product was identified as P=O···BF$_3$ adduct, complex **145**. Using spectroscopic and crystallographic techniques, the mechanism for the formation of complex **145** is proposed to start with loss of HF from the protonated complex **137H$^+$(O)** followed by P=O···BF$_3$ adduct formation. The reaction between complexes **137** and **144** with BF$_3$·Et$_2$O in CH$_2$Cl$_2$ solution generates the P=O···BF$_3$ adducts **145** and **146**, respectively, in solution.

The cyclic voltammetry of complexes **137** and **144** in MeCN or CH$_2$Cl$_2$ solution show that the former undergoes reduction more easily than the latter. In addition, the voltammetric oxidation of complex **137** is harder than that of **144**. These differences reveal the influence of the R groups in μ-(SCH$_2$)$_2$(R)P=O toward the electron density of the iron atoms. Complexes **137** and **144** catalyze the reduction of CH$_3$CO$_2$H by similar mechanism. Also when the stronger acid CF$_3$CO$_2$H is used, there is no difference in the electrocatalytic proton reduction by **137** and **144** in MeCN solution. When the electrocatalytic reduction of CF$_3$CO$_2$H is performed using CH$_2$Cl$_2$ solution, a protonation prior reduction affects the voltammetric behavior even at equiv. CF$_3$CO$_2$H < 2, such that the first electron transfer step is the reduction of **144H$^+$(O)**. In contrary, the voltammetry of **137** in CH$_2$Cl$_2$ in the presence of the quite strong acid HBF$_4$·Et$_2$O (0.6-5.5 equiv.) does not suggest a protonation equilibrium prior reduction. Scheme 4-8 summarizes the proposed pathways for the electrocatalytic proton reduction by **137** and **144**.

Scheme 4-8. Proposed mechanism for proton reduction catalyzed by **137** and **144**.

The catalytic activity of these complexes toward reduction of weak and strong acids in MeCN solution is M to S according to the activity scale proposed by Evans. The electrocatalytic activity for reduction of CF$_3$CO$_2$H in MeCN solution is greater with lower overpotential for the catalyst **137** compared to the case of catalyst **144**.

Chapter 5

Effect of the CH$_2$OH Bridgehead Groups and the Bulky PPh$_3$ Ligand in [Fe$_2$(CO)$_5$L{μ-(ECH$_2$)$_2$C(CH$_2$OH)$_2$}] (E = S or Se and L = CO or PPh$_3$) Complexes Toward the Cathodic Process

(Publication 3 and Manuscript 2)

5   Effect of the CH$_2$OH Bridgehead groups and the Bulky PPh$_3$ Ligand in [Fe$_2$(CO)$_5$L{μ-(ECH$_2$)$_2$C(CH$_2$OH)$_2$}] (E = S or Se and L = CO or PPh$_3$) Complexes toward the Cathodic Process

In nature, the H cluster at the active site of the [FeFe]-hydrogenases catalyzes the reversible H$_2$ reduction of protons (H$^+$ + e$^-$ $\leftrightarrow$ ½ H$_2$).[11] The catalytic activity of the H cluster is attributed to a structural feature, so called *rotated structure*, which offers a vacant site at the distal Fe$_d^I$ in the reduced **H$_{red}$** and the oxidized **H$_{ox}$** states.[11] The catalytic formation of H$_2$ requires interaction of H$^+$ at the vacant site of **H$_{red}$** and the oxidation of H$_2$ occurs catalytically through binding at the vacant site of **H$_{ox}$**. Thus, any successful synthetic model catalyst must possess a vacant coordination site or must be able to generate it during the catalytic cycle.

Numerous model complexes of the type [Fe$_2$(CO)$_{6-n}${μ-dithiolate}] have been synthesized to provide better understanding of the structural features of the **H$_{red}$** state (Figures 1-7 to 1-11). Even models with μ-diselenate and μ-ditellurate linkers are reported notably by Weigand and coworkers (Figure 1-8). The use of heteroatoms that are not found in the structure of the H cluster may afford valuable information and answers for a question such as why does nature use dithiolato linker, but not diselenates? This chapter shows how the voltammetric reduction of [Fe$_2$(CO)$_6${μ-(SCH$_2$)$_2$CR$_2$}] is affected by:

(i)   Replacing the CR$_2$ in complexes **3** (R = H) and **12** (R = Me) by C(CH$_2$OH)$_2$ in [Fe$_2$(CO)$_6${μ-(SCH$_2$)$_2$C(CH$_2$OH)$_2$}] (**147**) (Figure 5-1),

(ii)   Replacing the μ-dithiolate in **147** by μ-diselenate in [Fe$_2$(CO)$_6${μ-(SeCH$_2$)$_2$C(CH$_2$OH)$_2$}] (**148**) (Figure 5-1) and

(iii)   Substituting one CO ligand in **147** by PPh$_3$ in [Fe$_2$(CO)$_5$(PPh$_3$){μ-(SCH$_2$)$_2$C(CH$_2$OH)$_2$}] (**149**) (Figure 5-1).

Figure 5-1. Complexes 147-149 discussed in chapter 5.

The presence of CH$_2$OH groups attached to the bridgehead carbon atom is expected to lower the reduction potential of the [Fe$_2$S$_2$] core due to the effect of hydrogen bonding, which has been described for complex 29[55,56]. Moreover, this chapter discusses the electrocatalytic reduction of CH$_3$CO$_2$H by complexes 147 and 148 in terms of overpotential and catalytic activity.

5.1   Results and Discussion$^\$$
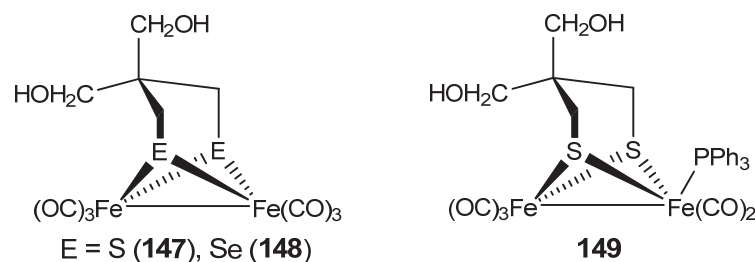
5.1.1   Molecular Structure of 149 and PPh$_3$ Steric Effects

Crystals of 149 were obtained by diffusion of pentane into a CH$_2$Cl$_2$ solution of 149 at 4 °C overnight. Molecular structure and numbering scheme of complex 49 is shown in Figure 5-2.

Each iron core of 139 adopts a distorted octahedral structure and the two iron sites are bridged by the linker (XCH$_2$)$_2$C(CH$_2$OH)$_2$ (E = S or Se). The bicyclic [Fe$_2$S$_2$] structure reveals a butterfly conformation in all complexes. The CO ligands of the Fe(CO)$_3$ unit in 149 are facial and the PPh$_3$ ligand coordinates to the other iron site on an apical position. The bridgehead carbon atom is surrounded in a distorted tetrahedral environment. The

C(CH$_2$OH)$_2$ bridgehead group of **149** points away from the apical PPh$_3$ group to minimize the steric clash.
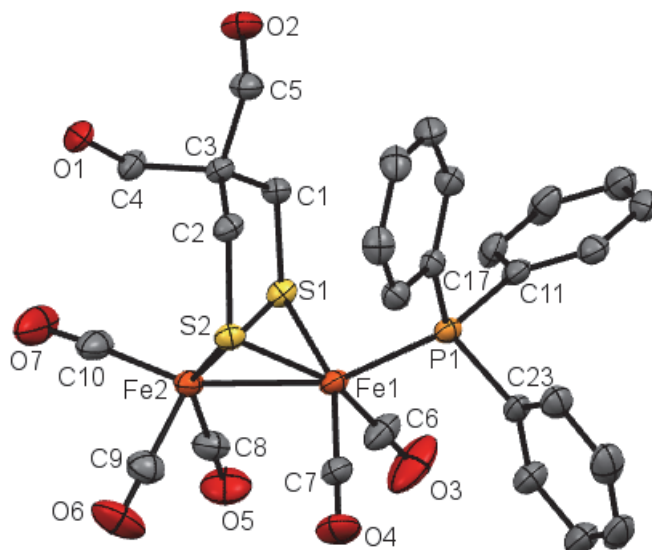
Figure 5-2. Molecular structure (50 % probability) of complex **139**. Hydrogen atoms have been omitted for clarity.

The Fe-Fe bond length in complex **149** is 2.503 Å and its Fe1-P1 distance (2.241 Å) is consistent with the average Fe-PPh$_3$ bond length (2.247 Å) in various [FeFe]-hydrogenase complexes. The angles Fe-Fe-CO$_{ap}$ and Fe-Fe-P in **149** are 158.168(3)° and 156.643(3)°, respectively. The angle Fe-Fe-CO$_{ap}$ in **149** is slightly less than Fe2-Fe1-CO$_{ap}$ (the apical CO under the bridgehead) in **147**, 158.490(0)°, which is related to the torsion angles discussed below.

Torsion angles (τ) in 147-149. In contrast to [Fe$_2$(CO)$_6${μ-(SCH$_2$)$_2$CH$_2$}] (**3**), complexes **147** and **148** exhibit torsion angles defined by the apical CO across the Fe-Fe bond (OC$_{ap}$-Fe-Fe-CO$_{ap}$) due to the presence of sterically demanding CH$_2$OH substituents at the bridgehead atoms. The torsion angle in complex **148** (τ = 11.2°) is larger than that in complex **147** (τ = 8.2°) whereas the basal CO groups in both complexes are almost eclipsed. The influence of the steric demand of the bridgehead toward the solid state structure of the Fe$_2$S$_2$(CO)$_6$ moiety has been also described in [Fe$_2$(CO)$_6${μ-(SCH$_2$)$_2$CR$_2$}] (R = Me (**12**), Et(**13**)), where τ = 6° in **12** and 15.8° in **13**.[40] The smaller torsion angle in complexes **147** and **148** compared to that in **13** is due to the less steric bulk of the CH$_2$OH compared to the Et substituents. The torsion angle

P-Fe2-Fe1-C$_{ap}$ in **149** (τ = 32.8º, Figure 5-3) is remarkably larger than the torsion angle C$_{ap}$-Fe2-Fe1-C$_{ap}$ in its parent hexacarbonyl complex **147** (τ = 8.2º). The larger torsion angle in **149** compared to that of complex **147** explains the difference in their Fe2-Fe1-CO$_{ap}$ angles.
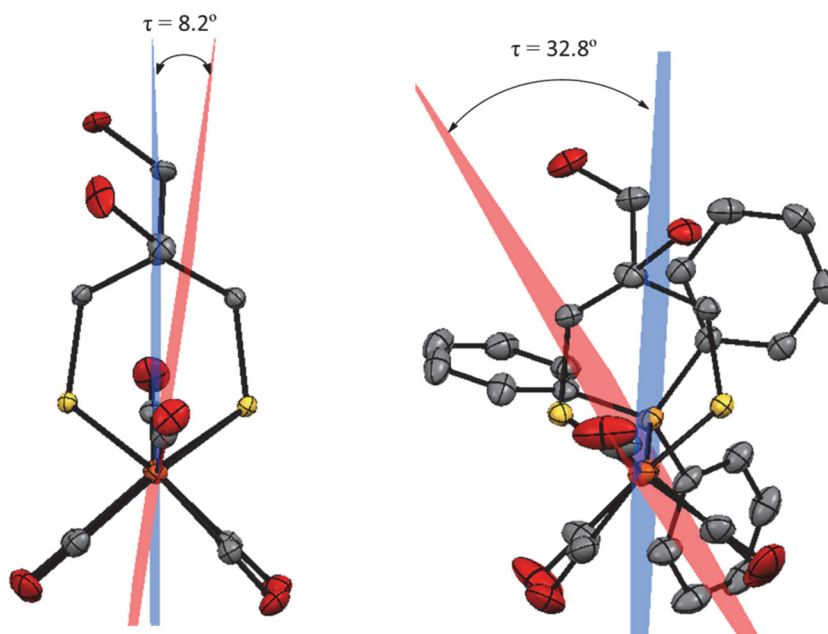
Figure 5-3. Torsion angles (τ) in complexes **147** (left) and **149** (right). Hydrogen atoms have been omitted for clarity.

5.1.2   Electrochemistry of Complexes 147 and 148

Cyclic voltammograms of complexes **147** and **148** are shown in Figure 5-4. Complexes **147** and **148** exhibit reversible cathodic peaks at $E_{1/2}$ = -1.52 V (E_{pc} = -1.55 V, E_{pa} = -1.49 V) and -1.49 V (E_{pc} = -1.52 V, E_{pa} = -1.46 V) vs. ferrocenium/ferrocene, respectively. An additional reduction event (**147**: -1.97, **148**: -1.93 V) can be seen at a potential more negative than that for the primary reduction of the complexes. The oxidative parts of the Cyclic voltammograms show irreversible oxidation events at +0.67 V and +0.58 V for complexes **147** and **148**, respectively.
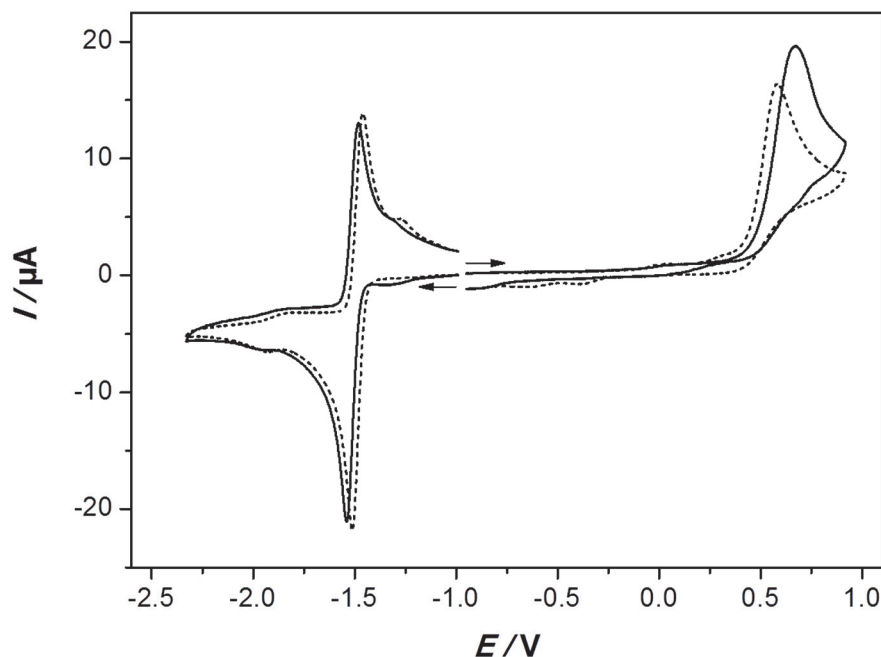
Figure 5-4. CVs of complexes 1.0 mM **147** (solid line) and 1.0 mM **148** (dashed line) in MeCN/[NBu$_4$][BF$_4$] measured at 0.2 V·s^{-1}. E is in V against ferrocenium/ferrocene couple. Glassy carbon disk (d = 1.6 mm). The arrows indicate the scan direction of the reductive and the oxidative parts of the curves.

At a scan rate of 0.2 V·s^{-1} the primary cathodic waves of **147** and **148** are assigned to two successive reduction steps, *RS1* and *RS2*, with closely spaced individual standard reduction potentials, $E°_1$ and $E°_2$, respectively.

$$Fe^IFe^I \ + \ e^- \ \leftrightarrow \ Fe^IFe^0 \qquad (E°_1, k_s^1) \qquad (RS1)$$

$$Fe^IFe^0 \ + \ e^- \ \leftrightarrow \ Fe^0Fe^0 \qquad (E°_2, k_s^2) \qquad (RS2)$$
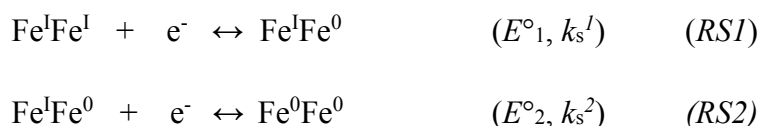
The kinetic parameters k_s^1 and k_s^2 are the heterogeneous electron transfer rate constants for *RS1* and *RS2*, respectively. Thus, the reduction events at -1.97 V and -1.93 V for complex **147** and **148**, respectively, should be due to daughter products of follow-up reactions. It is likely that these chemical reactions involve CO loss either from the anion or the dianion as it was found for various diiron carbonyl complexes.[34,43,156,215,236-241] The conclusion that the primary cathodic waves of complexes **147** and **148** correspond to both *RS1* and *RS2* is based on comparison of the peak height with that of [Fe$_2$(CO)$_6${μ-(SCH$_2$)$_2$CH$_2$}] (**3**), which is closer to a one electron process at 0.2 V·s^{-1} scan rate[88,237]: The peak heights of the cathodic waves of complexes **147** and **148** are almost twice the peak height of **3** under the same conditions (Figures S5-1 and S5-2). In addition, the

intensity of these reduction waves increases at faster scan rates up to 100 V·s⁻¹ while the events at more negative potentials become less visible (Figure 5-5). By increasing the scan rate wave-splitting is not observed for the primary reduction of complexes **147** and **148** even at 100 V·s⁻¹, which implies that the second heterogeneous rate constant k_s^2 is larger than, or similar to k_s^1 (see Section 1.5.3.8).[43,47b,54]
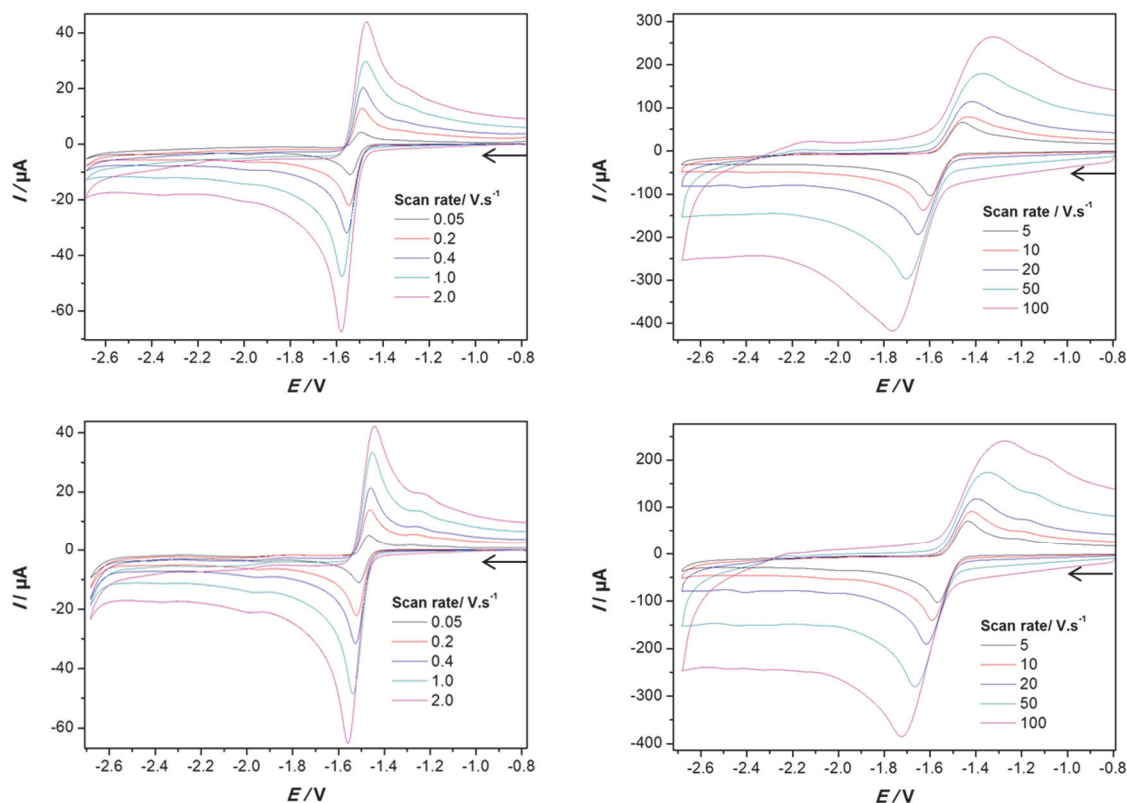
Figure 5-5. Cyclic voltammetry at various scan rates of 1.0 mM complexes **147** (top left and top right) and **148** (bottom left and bottom right) in MeCN/[NBu$_4$][BF$_4$] solution. E is in V against ferrocenium/ferrocene couple. Glassy carbon disk (d = 1.6 mm). The arrows indicate the scan direction.

Effect of Replacing CR$_2$ (R = H, Me, Et) by C(CH$_2$OH)$_2$. First of all, our recent re-investigations of the electrochemistry of [Fe$_2$(CO)$_6${μ-(SCH$_2$)$_2$CMe$_2$}] (**12**) proves that these complexes undergo two-electron reduction in a single step due to potential inversion, which is in contrast to the initial report in 2008.[40] The cyclic voltammetry of complexes [Fe$_2$(CO)$_6${μ-(SCH$_2$)$_2$CH$_2$}] (**3**) and **12** in CH$_2$Cl$_2$/[NBu$_4$][BF$_4$] solutions can be found as Supporting Information. These electrochemical investigations clearly confirm that the reduction wave at -1.66 V in the cyclic voltammogram of complex **3** (Figures S5-3 and S5-4) are due to transfer of one electron whereas the reduction of **12**

occurs via two-electron transfer in a single step (Figures S5-5 to S5-7).$^{££}$ As a conclusion, the replacement of the methylene group *CH$_2$* of the -E-CH$_2$-*CH$_2$*-CH$_2$-E- linker (E = S, Se) by CR$_2$ (R = Me, CH$_2$OH) alters the reduction process from one- into two-electron transfer in a single step. Clearly, these findings reveal the influence of the steric bulk of the CR$_2$ (R = Me, CH$_2$OH) of the -E-CH$_2$-CR$_2$-CH$_2$-E- (E = S, Se) linker toward the reduction mechanism. *The presence of steric bulk on the bridgehead lowers the barrier for structural change accompanying the electron transfer processes that lead to a rotated structure stabilized by formation of semi-bridging CO and cleavage of one of the Fe-S bonds.* The steric bulk effect on the barrier of Fe(CO)$_3$ rotation and its relation to the torsion angle has been already described by Darensbourg and coworker, but only for the ground state of the complexes, i.e. Fe^{I}Fe^I state.[110]

Complexes **147** and **148** in MeCN/[NBu$_4$][BF$_4$] are reduced at ~ 60 mV and ~ 90 mV, respectively, less negative potential compared to [Fe$_2$(CO)$_6${μ-(SCH$_2$)$_2$CMe$_2$}] (**12**). In comparison to [Fe$_2$(CO)$_6${μ-(SCH$_2$)$_2$CEt$_2$}] (**13**), complexes **147** and **148** undergo reduction at 120 mV and 150 mV, respectively, less negative potential (MeCN/[NBu$_4$][BF$_4$] solutions). In other words, replacement of the alkyl bridgehead substituents (Me and Et) in **12** and **13** by CH$_2$OH in complexes **147** and **148** results in a thermodynamic stabilization of the reduced species. We suggest that the CH$_2$OH groups are involved in *hydrogen bonding* to the inverted iron or to the chalcogen atom as shown in Figure 5-6. Clearly, these findings reveal the thermodynamic influence of hydrogen bonding toward the reduction mechanism.

$^{££}$ The electrochemistry of compounds **12** and **13** was first reported by Darensbourg et al. and it was described that these complexes undergo two-electron reduction such that the second reduction step occurs at potential more negative than the first reduction step and hence the first reduction wave in the cyclic voltammograms of **12** or **13** is due to a transfer of one electron.[110] Based on this report and the electrochemical results that suggest a potential inversion for the two-electron reduction of **147** and **148**, we have published a paper titled: "**The Influence of OH Groups in [Fe(CO)$_3$]$_2$[(μ-ECH$_2$)$_2$C(CH$_2$OH)$_2$] (E = S, Se) Complexes toward the Cathodic Process**".[234] In this published paper, we concluded that the replacement of the Me groups in **12** or the Et groups in **13** by CH$_2$OH groups in **147** and **148** alters the reduction mechanism from simple two-electron transfer in two separate steps for **12** and **13** into two-electron reduction in a single step. Therefore, we attributed the potential inversion observed for **147** and **148** to a stabilization effect of the reduced species via hydrogen bonding between the CH$_2$OH groups and one of the μ-E atoms (E = S, Se) or one of the Fe atoms. In this chapter, our published work[234] is corrected and for this reason it was necessary to add the re-investigation of the electrochemistry of **12** to the Supporting Information. The electrochemistry of **3** was also discussed to prove the reinvestigation of **12**. Ralf Trautwein has performed the electrochemistry mesurements of **3** and **12** and provided me with the data to discuss them in the Supporting Information of this thesis.

E = S, Se
n = 1 or 2
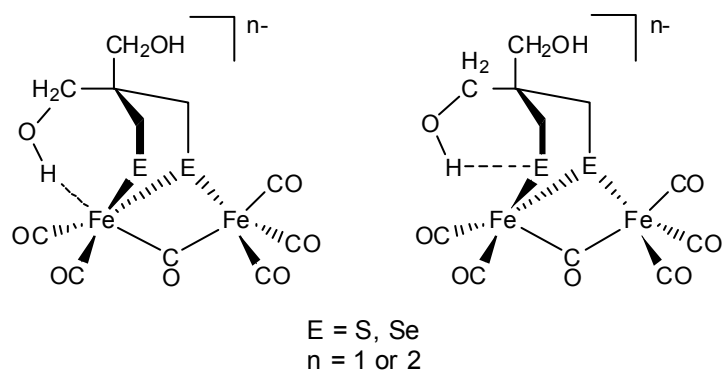
Figure 5-6. Proposed hydrogen bonding in the reduced complexes **147** and **148**.

Electrocatalytic Proton Reduction. Cyclic voltammetry of complexes **147** and **148** in the presence of CH$_3$CO$_2$H at different concentrations show no increase in the current of the two-electron cathodic waves, but suppression of the anodic waves for the oxidation of the dianions. However, the catalytic proton reduction waves are observed near -1.8 V or -1.9 V for complexes **147** and **148**, respectively (Figure 5-7).
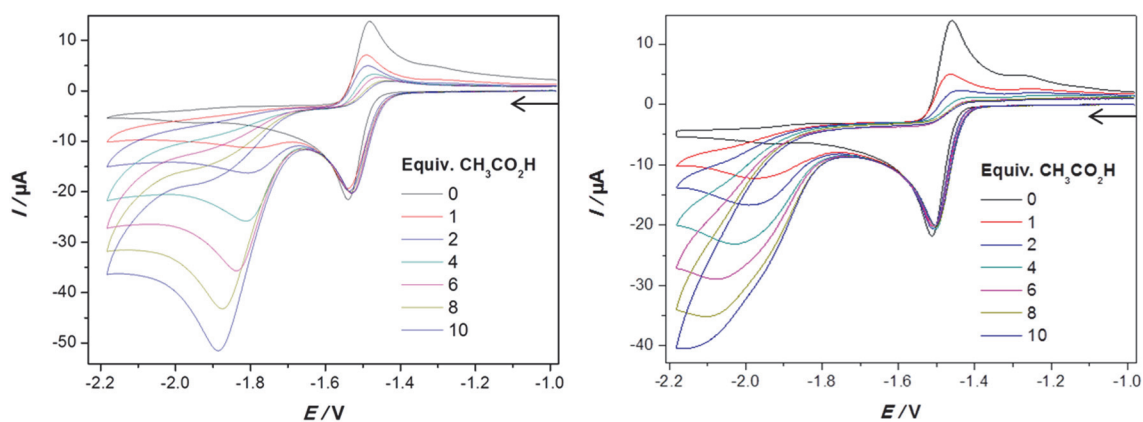
Figure 5-7. Cyclic voltammetry of complexes **147** (1.0 mM) (left) and **148** (1.0 mM) (right) at various concentrations of CH$_3$CO$_2$H (MeCN/[NBu$_4$][BF$_4$] solutions). *E* is in V against ferrocenium/ferrocene couple. Glassy carbon disk (d = 1.6 mm). The arrows indicate the scan direction.

The electrochemical response toward the catalytic reduction of CH$_3$CO$_2$H by complexes **147** and **148** is similar to that described for **137** (Scheme 4-5) as well as [Fe$_2$(CO)$_6${μ-bdt}] (bdt = benzenedithiolate) (**27**)[52]. Scheme 5-1 shows the proposed electrocatalytic mechanism for the reduction of CH$_3$CO$_2$H by complexes **147** or **148** (ECEC mechanism). The overpotential for the reduction of CH$_3$CO$_2$H in

MeCN/[NBu$_4$][BF$_4$] solution in the presence of the catalyst **147** is estimated to be 313 mV while that in the presence of **148** is ca. 440 mV. The lower overpotential in case of **147** compared to **148** may give hints for the use of dithiolato linker instead of diselenate in nature.

Scheme 5-1. Proposed ECEC mechanism for electrocatalytic reduction of CH$_3$CO$_2$H by complex **147** or **148**.
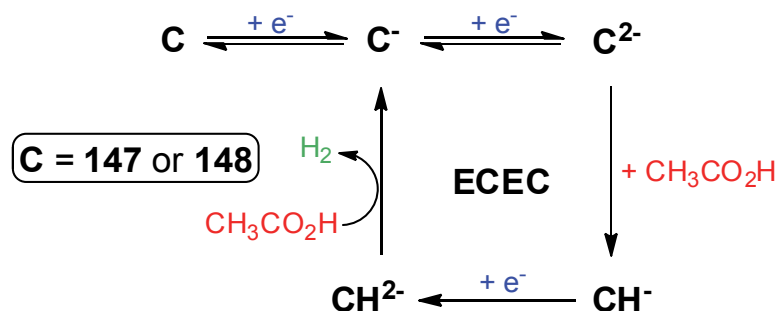
5.1.3   Electrochemistry of the PPh$_3$-Substituted Complex 149 (unpublished)

Figure 5-8 shows the cyclic voltammetry of complex **149** in CH$_2$Cl$_2$/NBu$_4$PF$_6$ solution at various scan rates.
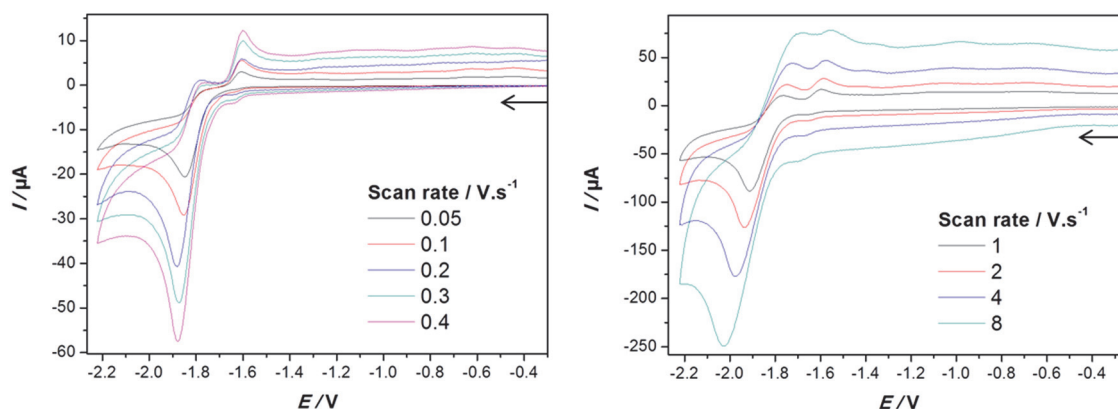
Figure 5-8. Cyclic voltammetry of 1.102 mM **149** (CH$_2$Cl$_2$/NBu$_4$PF$_6$) under N$_2$ atmosphere at various scan rates, 0.05-0.4 V·s^{-1} (to the left) and 1-8 V·s^{-1} (to the right). The potential E in V is against ferrocenium/ferrocene couple. Glassy carbon disk (d = 3 mm). The arrows indicate the scan direction.

In Figure 5-8, we can see that the cathodic wave at E_{pc} = -1.88 V is irreversible at slow scan rates and there are two anodic events in the return sweep: a small peak at ~ -1.78 V, which is related to the cathodic wave, and an oxidation event at ~ -1.6 V. An enhancement of chemical reversibility is observed by increasing the scan rate as the current of the first anodic peak on the return scan increases to become comparable to that of the second anodic peak. The anodic wave at ~ -1.6 V shows reversibility in the reverse scan (Figure 5-9). This redox couple is assigned for the hexacarbonyl complex **147**. The cyclic voltammogram of complex **147** in CH_2Cl_2/NBu_4PF_6 measured at 0.2 $V \cdot s^{-1}$ is shown in Figure 5-10a, $E_{1/2}$ = 1.61 V (E_{pc} = -1.67 V, E_{pa} = -1.54 V). The anodic wave observed at ~ -0.73 V in the return scan of the cyclic voltammetry of complex **147** (Figure 5-10a) is due to oxidation of a product obtained after the reduction of **147** in the forward scan. This oxidation wave is not observed at higher scan rates (Figure 5-10b).
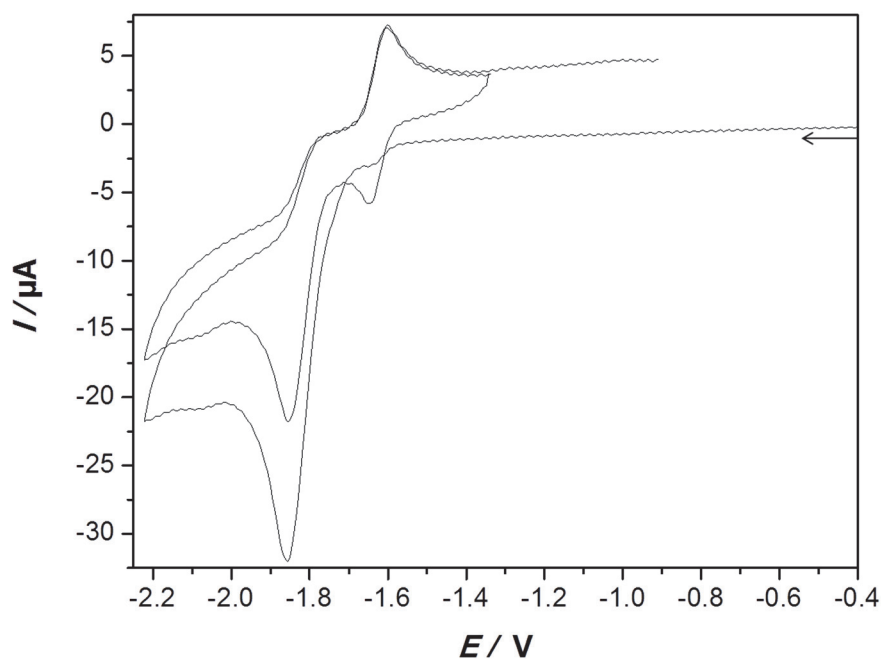
Figure 5-9. Cyclic voltammetry (0.2 $V \cdot s^{-1}$) of 1.102 mM **149** in CH_2Cl_2/NBu_4PF_6 solution under N_2 atmosphere. The potential E in V is against ferrocenium/ferrocene couple. Glassy carbon disk (d = 3 mm). The arrows indicate the scan direction.
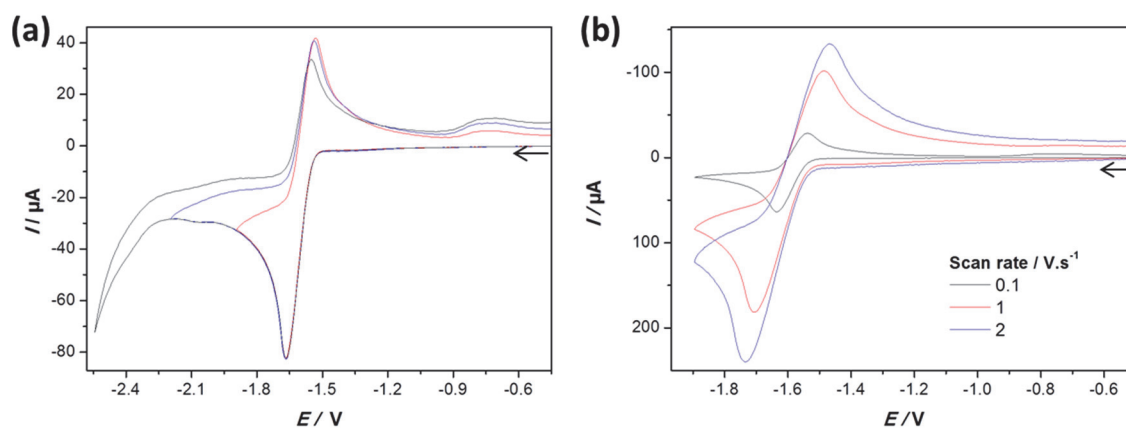
Figure 5-10. Cyclic voltammetry 1.55 mM **147** in CH$_2$Cl$_2$/NBu$_4$PF$_6$ solution under N$_2$ atmosphere at (a) 0.2 V·s^{-1} and (b) various scan rates. The potential E in V is against ferrocenium/ferrocene couple. Glassy carbon disk (d = 3 mm). The arrows indicate the scan direction.

That the hexacarbonyl complex **147** is formed during the cathodic process of complex **149** suggests the loss of the ligand PPh$_3$ after the reduction of **149** that is followed by addition of CO from a carbonylated species, **S(CO)**. Comparing the normalized current function (I_{pc}/c·$v^{1/2}$, c = concentration) for the reduction of complex **147**, that is known to undergo a single step two-electron reduction, and that of complex **149** at 0.05 V·s^{-1} ≥ v ≥ 2 V·s^{-1} (assuming similar diffusion coefficients) suggests a transfer of ~ 1.5 electrons for the reduction of **149**. For example, the normalized current function for the reduction of complexes **147** and **149** at 0.2 V·s^{-1} are 116.5 and 77.7 µA·mM^{-1}·V^{-1}·s$^{1/2}$, respectively (calculated using the experimental conditions in Figures 5-9 and 5-10). Two mechanisms for the formation of the reduced species of **147** from the reduction of **149** may be at work. The first mechanism involves loss of PPh$_3$ after the one-electron reduction of **149** that is followed by formation of **147**$^-$ (Scheme 5-2). Further reduction of the monoaniaon **147**$^-$ should contribute to the observed current for the reduction of **149**, which explains the estimated 1.5 transferred electrons. Fast decomposition after the loss of PPh$_3$ is a likely process as several anodic events are observed in the return scan at potentials less negative than -1.5 V. A second probable mechanism could be that the dianion **149**$^{2-}$ is formed from the reduction of the neutral complex **149**, but a decomposition accompanying the fast loss of PPh$_3$ from **149**$^-$ would limit the formation of **149**$^{2-}$. At scan rate of 20 V·s^{-1}, the reduction of complex **147** is closer to a one-electron transfer process (a typical behaviour for complexes that follow ECE process) with normalized current function of ~ 64.5 µA·mM^{-1}·V^{-1}·s$^{1/2}$ that is comparable to that for the reduction of **149**

(52.2 μA·mM^{-1}·V^{-1}·s$^{1/2}$) at the same scan rate. The loss of PPh$_3$, that leads to formation of **147** accompanied with decomposition, as well as the intervening reaction of the ECE process become less significant at higher scan rates.

Scheme 5-2. Cyclic voltammetric reduction of complex **149** involving the formation of the hexacarbonyl **147**.
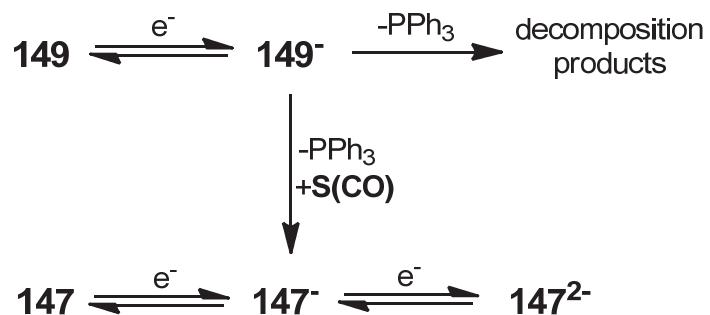
Performing the cyclic voltammetry of **149** under CO atmosphere is anticipated to assist the formation of complex **147**. Cyclic voltammetry of **149** in CO-saturated CH$_2$Cl$_2$/NBu$_4$PF$_6$ solution at various scan rates is shown in Figure 5-11.
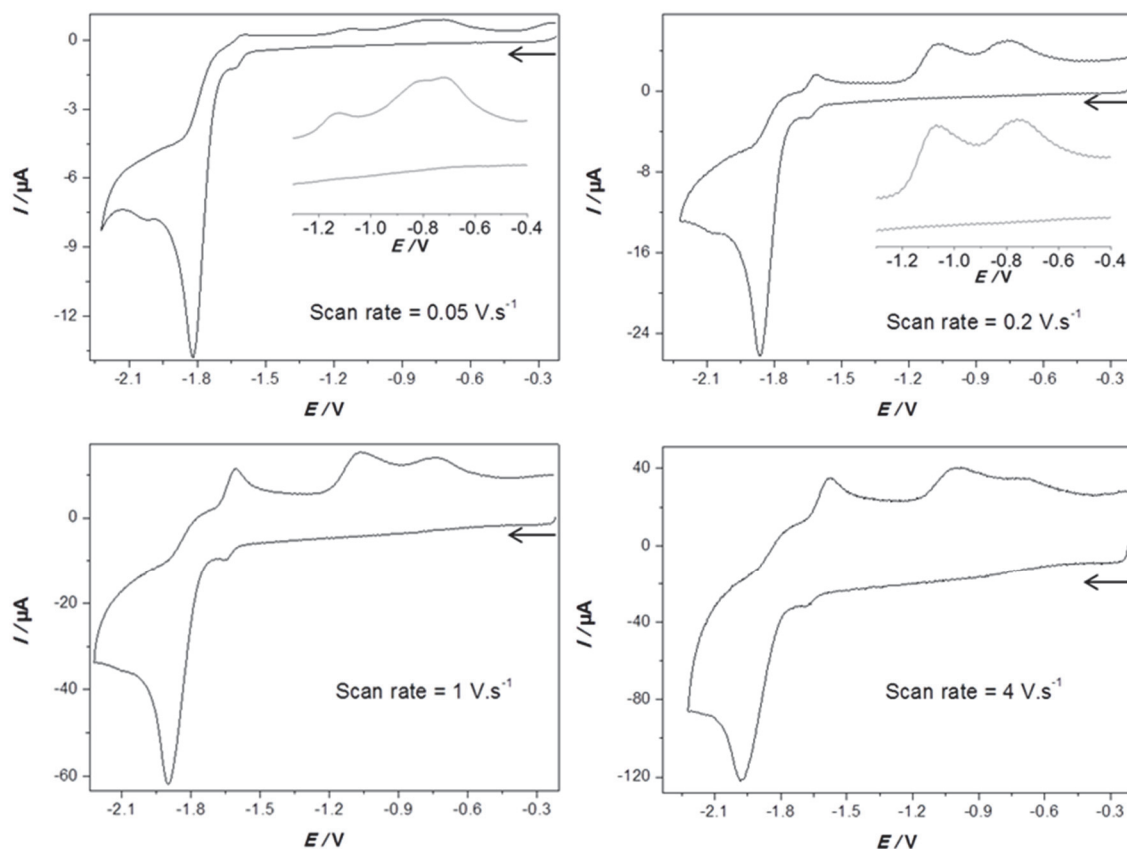
Figure 5-11. Cyclic voltammetry of 1.102 mM **149** in CO-saturated CH$_2$Cl$_2$/NBu$_4$PF$_6$ solution at 0.05 V·s^{-1} $\geq v \geq$ 4 V·s^{-1}. The potential E in V is against ferrocenium/ferrocene couple. Glassy carbon disk (d = 3 mm). The arrows indicate the scan direction.

From Figure 5-11 we can notice the following:

- At all scan rates up to 4 V·s^{-1}, no return peak related to the oxidation of the reduced species of complex **149** is observed that is in contrast to the study under N$_2$ atmosphere where some chemical reversibility could be seen at low scan rates (Figure 5-8).

- The intensity of the wave arising from **147^{2-}** → **147** + 2e$^-$ process that is detected in the cyclic voltammetry of **149** under N$_2$ atmosphere (Figure 5-8) decreases when the experiments are performed under CO atmosphere (at all scan rates in Figure 5-11).

- Two new oxidation events (OE) are observed at ~ -1.07 V (OE-I) and -0.76 V (OE-II) at 0.2 V·s^{-1}, but are not detected under N$_2$ (Figure 5-8). We also can notice that OE-II is indeed a result of two overlapping oxidation processes since OE-II has two peaks at ~ -0.82 V and ~ -0.72 V at 0.05 V·s^{-1}. Increasing the scan rate decreases the peak current ratio I_{pa}(OE-II) / I_{pa}(OE-I). We have found that OE-I and OE-II are irreversible at all scan rates (Figure 5-12, v = 0.2 V·s^{-1}).
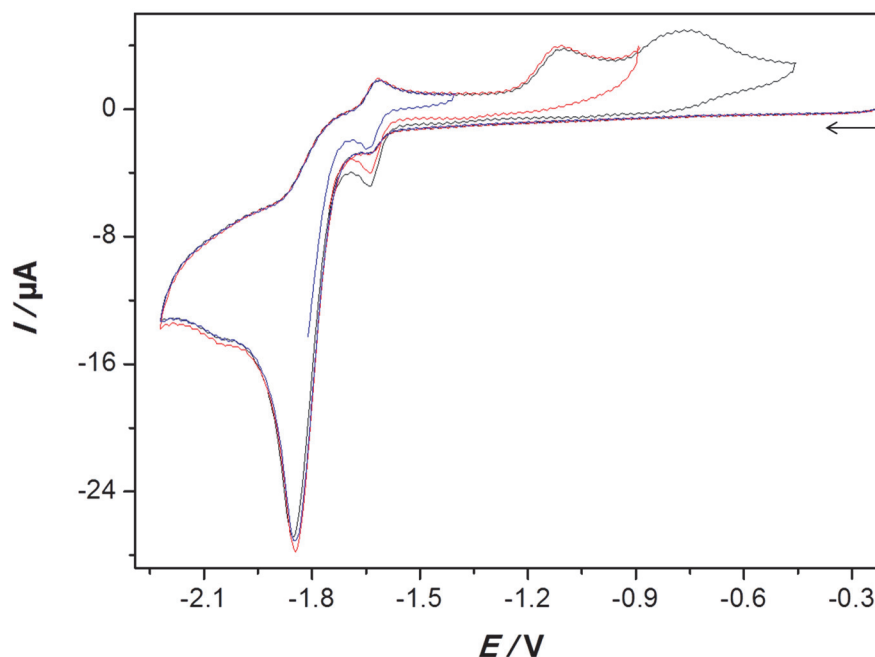
Figure 5-12. Cyclic voltammetry of 1.102 mM **149** in CO-saturated CH$_2$Cl$_2$/NBu$_4$PF$_6$ solution at 0.2 V·s^{-1}. The potential E in V is against ferrocenium/ferrocene couple. Glassy carbon disk (d = 3 mm). The arrows indicate the scan direction.

We explain the above observations by a mechanism involving reaction between the reduced species of **147** and **149** with CO to afford products that are responsible for the oxidation events OE-II and OE-I. Figure 5-13 shows the cyclic voltammetry of complex **147** under CO atmosphere. We can clearly infer from Figure 5-13 that the reduction of **147** is chemically irreversible at slow scan rates, which is due to the reaction between CO and the reduced species of **147**. Increasing the scan rate enhances the chemical reversibility because of the less time scale available for the chemical reaction to take place. The overall current for the reduction of complex **147** is not affected by the presence of CO at all scan rates. The scan rate dependence of the current function (0.05 V·s^{-1} $\geq v \geq$ 40 V·s^{-1}) for the reduction of **147** under N$_2$ is very similar to that under CO. Thus, the reduction under CO atmosphere involves either the reaction between **147**$^{-}$ and CO to give **147CO**$^{-}$ that is reduced at the same reduction potential of **147** or the reaction between **147**$^{2-}$ and CO affording **147CO**$^{2-}$. It is obvious the presence of two overlapping oxidation events in the range 0.05 V·s^{-1} $\geq v \geq$ 0.5 V·s^{-1}. The peak potentials of these oxidation events are: -0.79 V and -0.66 V (at 0.05 V·s^{-1}), -0.78 V and -0.67 V (at 0.1 V·s^{-1}), -0.76 V and -0.69 V (at 0.2 V·s^{-1}) and -0.72 V and -0.67 V (at 0.5 V·s^{-1}). These results confirm that the oxidation event OE-II observed near -0.7 V (Figures 5-11 and

5-12) are due to the formation of **147CO$^{1-/2-}$** during the reduction of **149** under CO atmosphere. Thus, the oxidation event OE-I (-1.07 V, Figures 5-11 and 5-12) should be related to the product obtained from the reaction between the reduced species of complex **149** and CO. We also can notice from Figure 5-13 that the oxidation of **147CO^{2-}** is irreversible at all scan rates up to 10 V·s^{-1}, which could be due to a very fast decomposition process. Scheme 5-3 provides a summary for the possible mechanism for the reduction of complex **149** in a CO-saturated solution.
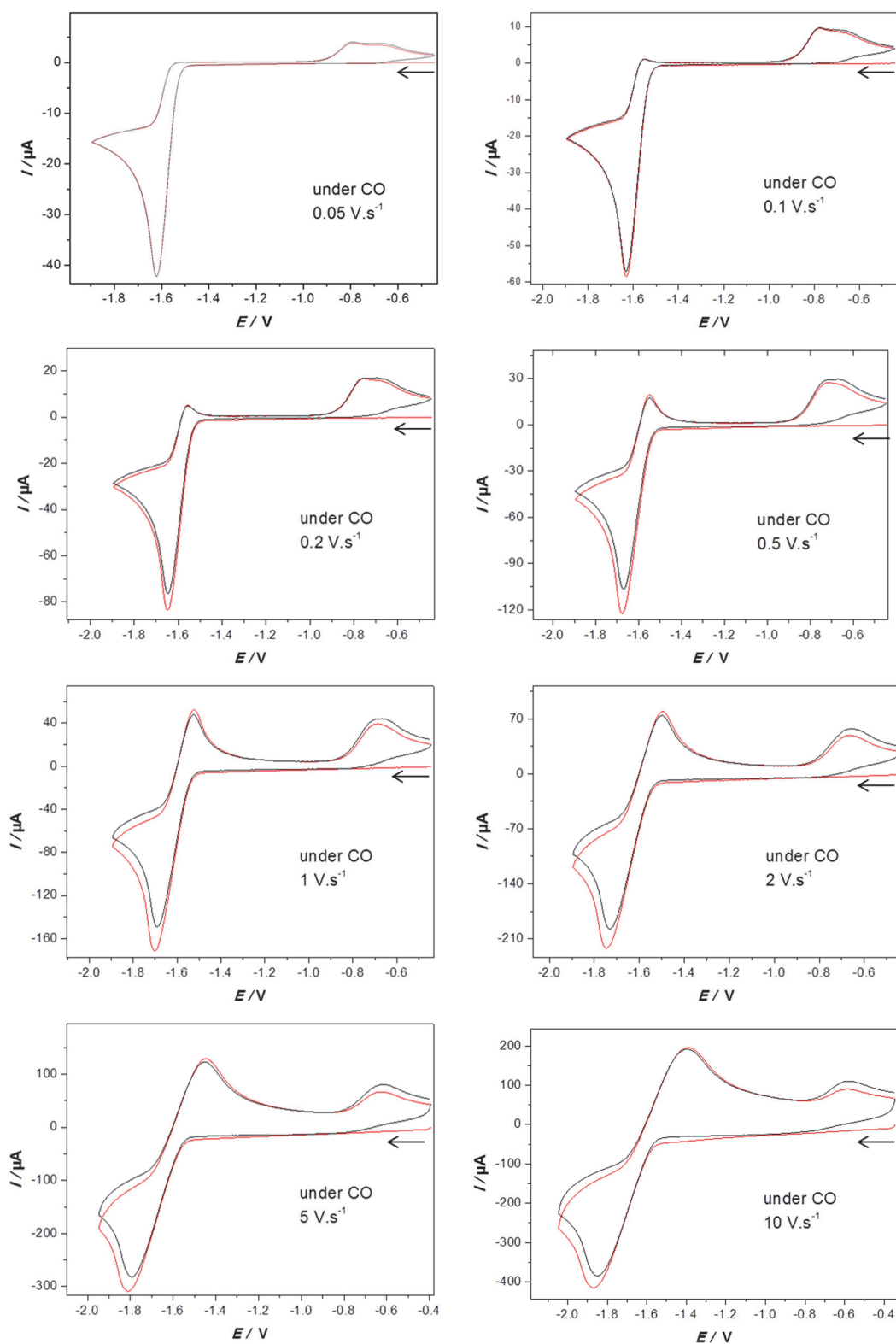
Figure 5-13. Cyclic voltammetry of 1.46 mM **147** in CO-saturated CH$_2$Cl$_2$/NBu$_4$PF$_6$ solution at 0.05 V·s^{-1} $\geq v \geq$ 10 V·s^{-1}. The red and the black curves are for the first and second cycles, respectively. The potential E in V is against ferrocenium/ferrocene couple. Glassy carbon disk (d = 3 mm). The arrows indicate the scan direction.

Scheme 5-3. Cyclic voltammetric processes of complex **149** under CO-atmosphere involving the formation of **147**.
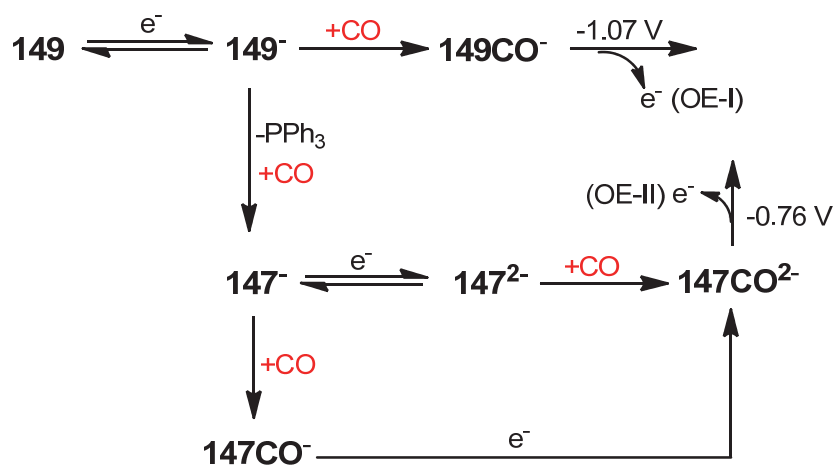
Electrochemistry of [Fe$_2$(CO)$_5$(PPh$_3$){μ-(SCH$_2$)$_2$C(CH$_2$OH)$_2$}] (149) in the Presence of PPh$_3$. If the cyclic voltammetry of complex **149** is performed in the presence of free PPh$_3$ in the solution, the reversibility of the reduction of **149** could be enhanced because any loss of PPh$_3$ from the reduced species of **149** will be compensated by the PPh$_3$, the free ligand. Thus, the formation of **147** could be prevented. Figure 5-14 shows the effect of the presence of various equivalents of PPh$_3$ in the CH$_2$Cl$_2$/NBu$_4$PF$_6$ solution of **149** at 0.2 V·s^{-1}. The presence of 1 equiv. PPh$_3$ (Figure 5-14b) does not clearly influence the cathodic process of **149**, but the chemical reversibility is enhanced and the redox couple at ~ -1.67 V (Figure 5-14a) is absent in the presence of excess PPh$_3$ up to 84 equiv. (Figure 5-14d).
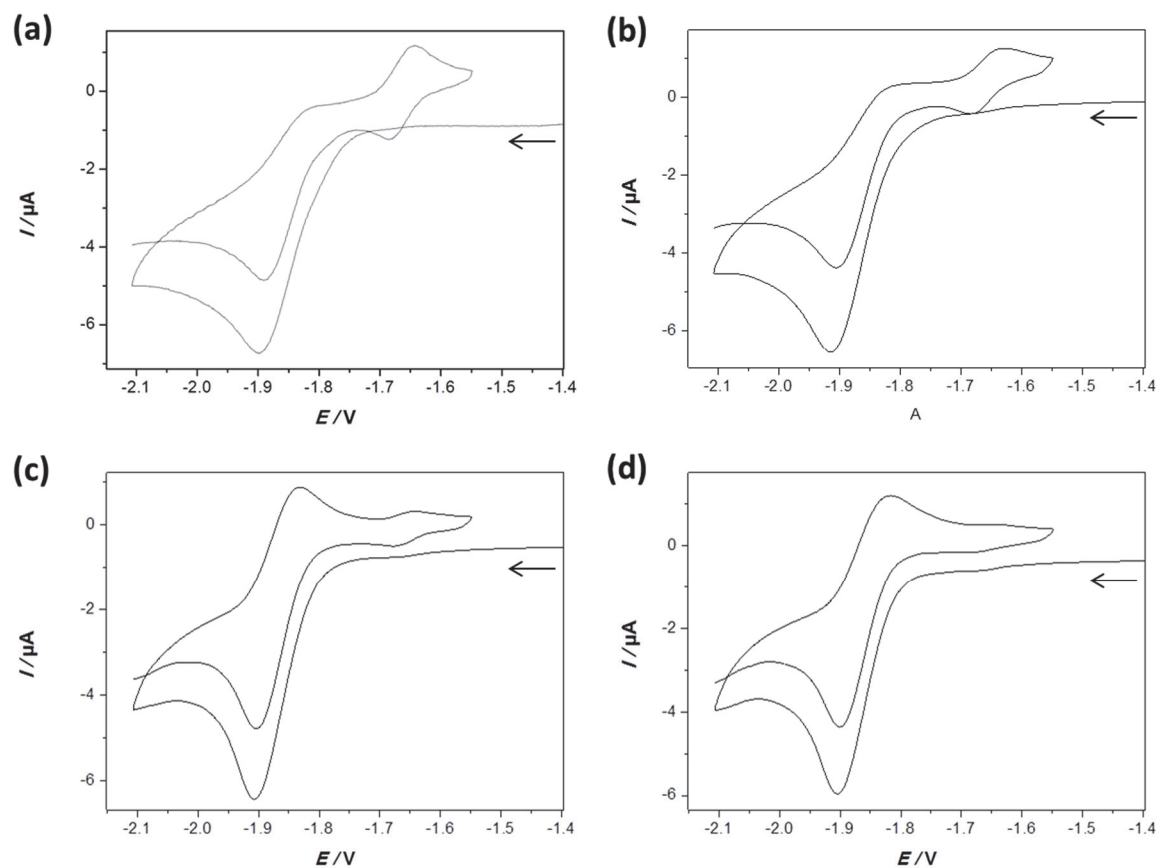
Figure 5-14. Cyclic voltammetry of 0.676 mM **149** in CH$_2$Cl$_2$/NBu$_4$PF$_6$ solution at 0.2 V·s^{-1} in the presence of x equiv. PPh$_3$: (a) x = 0, (b) x = 1, (c) x = 32 and (d) x = 84. The potential E in V is against ferrocenium/ferrocene couple. Glassy carbon disk (d = 1.6 mm). The arrows indicate the scan direction.

5.2   Conclusions

The presence of sterically demanding groups [R = Me (**12**), Et (**13**), CH$_2$OH (**147** or **148**)] at the bridgehead of the [Fe$_2$(CO)$_6${μ-(ECH$_2$)$_2$CR$_2$}] (E = S, Se) complexes results in a torsion angle such that the two Fe(CO)$_3$ units are distorted from the eclipsed conformation exhibited by complex **3** (R = H, E = S). The larger the torsion angle, the lower the barrier of Fe(CO)$_3$ rotation in the ground state Fe^{I}Fe^I of the complex as was reported by Darensbourg et al..[110] The results in this study confirm that the replacement of the R = H in **3** by bulky R substituents in [Fe$_2$(CO)$_6${μ-(ECH$_2$)$_2$CR$_2$}] [R = Me (**12**), Et (**13**), CH$_2$OH (**147** or **148**), E = S, Se] alters the cathodic process from one- into two-electron transfer in a single step. This suggests that the same steric effect described by Darensbourg et al. is also at work during the electron transfer processes such that the steric bulk of the R groups facilitates the structural changes including Fe(CO)$_3$ rotation,

which lead to inverted potentials of the two electron reduction steps. The presence of CH$_2$OH in **147** and **148** makes their reduction potentials less negative than those of **12** and **13** as a result of internal hydrogen bonding. The substitution of S in **147** by Se in **148** results in a longer Fe-Fe bond, smaller CO wavenumbers, a higher overpotential and less activity concerning the catalytic reduction of CH$_3$CO$_2$H.

The dissociation of the Fe-PPh$_3$ bond in **149** is accelerated by reduction and the hexacarbonyl species **147**, **147$^-$** and **147^{2-}** are formed. Performing the cyclic voltammetry of **147** and **149** in CO-saturated solutions shows that the reduced species of both complexes react with CO forming spectroscopically uncharacterized products. The presence of excess amounts of free PPh$_3$ in the solution of **149** compensates the loss of PPh$_3$ upon reduction and hence renders the formation of the hexacarbonyl species **147^{n-}** (n = 0, 1, 2). Reasons for the reactivity of the Fe-PPh$_3$ bond toward dissociation upon reduction are described in Chapter 3 in terms of large cone angle of the PPh$_3$ ligand and its low π-acidity.

Chapter 6

A Novel [FeFe]-Hydrogenase Model with a μ-(SCH$_2$)$_2$GeMe$_2$ Moiety

(Manuscript 3)
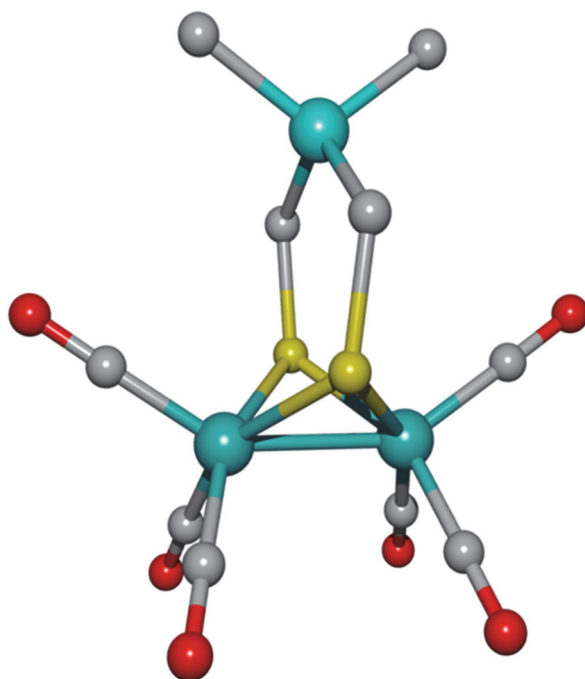
6   A Novel [FeFe]-Hydrogenase Model with a μ-(SCH₂)₂GeMe₂ Moiety

Since the structure of the H cluster of the [FeFe]-hydrogenases was revealed,[11] a plethora of research has been done by many research groups to synthesize models that mimic the structural and functional features of the H cluster. Until now, the nature of E in the dithiolato linker -S-CH₂-E-CH₂-S- of the H cluster has not been definitely identified unambiguously and it was proposed as being CH₂, NH or O. Recent results reported by Lubitz and coworkers strongly suggest that the bridgehead group is an amine.[11p,19,21,22] Such an amine-functionalized dithiolato bridge provides the most chemical relevant understanding for the high catalytic activity of the H cluster toward production of dihydrogen in reason of the possible proton relay role of the amine functionality.

The synthetic models related to the structure of the H cluster may be divided into two categories: (*i*) Bioinspired models containing the linkers -S-CH₂-E-CH₂-S- (E = CR₂, NR, O) and (*ii*) artificial models with abiological dithiolates containing bridgehead heteroatoms such as S[47], Se[48], Si[49] and Sn[50]. This second class of models have been extended to diselenates and ditellurates diiron complexes.[58-64,66] The use of these abiological linkers, notably by Weigand and coworkers, may provide valuable information and answers to basic questions concerning the role of the dithiolato bridge as well as the effect of the unusual heteroatoms E in the bridgehead on the structural and functional properties of such artificial H cluster mimics.

Glass and coworkers showed that the electron density at the μ-S atoms in [Fe₂(CO)₆{μ-(SCH₂)₂SnMe₂}] is higher than that in the case of its carbon analogues due to a σ(Sn-C)↔3p(μ-S) filled-filled interaction.[50] The same effect has been also suggested for Si-containing model complexes to explain the μ-S-protonation reported for [Fe₂(CO)₆{μ-(SCH₂)₂SiC₄H₈}].[49] The replacement of the O atom in [Fe₂(CO)₆{μ-(SCH₂)₂O}][37b] by S or Se atoms[47,48,61] alters the reduction mechanism from one- to two-electrons in a single step.

In continuation of our research on the influence of heteroatoms toward the structural as well as the electrochemical properties of models complexes [Fe₂(CO)₆{μ-(SCH₂)₂ER₂}], we describe in this chapter the synthesis of a novel Ge-containing model complex, [Fe₂(CO)₆{μ-(SCH₂)₂GeMe₂}] (**150**). We show that the molecular structure of

this complex reveals a unique feature compared to all of the previously reported [FeFe]-hydrogenase model complexes. Moreover, we investigate the electrochemical response of **150** in the absence and presence of CF$_3$SO$_3$H (pK_a = 0.7 in MeCN)[113].

6.1　Results and Discussion

6.1.1　Synthesis and Characterization

The reaction of *in situ* generated (μ-LiS)$_2$Fe$_2$(CO)$_6$[201] with 1 equiv. Me$_2$Ge(CH$_2$Cl)$_2$[242] afforded [Fe$_2$(CO)$_6${μ-(SCH$_2$)$_2$GeMe$_2$}] (**150**) in 15 % yield as an air-stable red solids (Scheme 6-1). This complex was characterized by ^{1}H and ^{13}C{^{1}H} NMR as well as IR spectroscopic techniques, MS spectrometry, elemental analysis and X-ray crystallography. The synthesis of the ligand Me$_2$Ge(CH$_2$Cl)$_2$ was performed according to Scheme 6-2.

Scheme 6-1. Synthesis of [Fe$_2$(CO)$_6${μ-(SCH$_2$)$_2$GeMe$_2$}] (**150**).
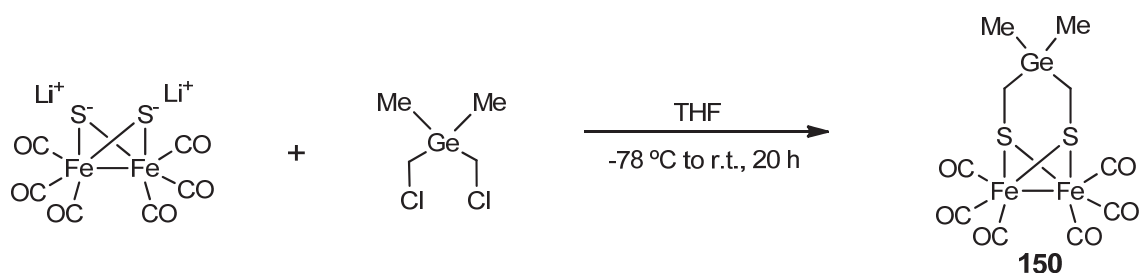
Scheme 6-2. Synthesis of Me$_2$Ge(CH$_2$Cl)$_2$.[242]
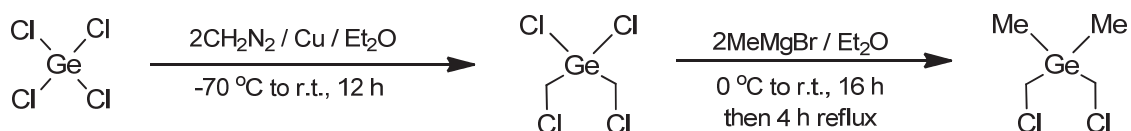
Spectroscopic Characterization. The ESI-MS spectrum of complex **150** shows the parent ion peak at *m/z* 476 [M]$^+$ as well as the consecutive loss of the CO ligands at *m/z* 448 [M - CO]$^+$, 420 [M - 2CO]$^+$, 392 [M - 3CO]$^+$, 364 [M - 4CO]$^+$, 334 [M - 5CO]$^+$ and 308 [M - 6CO]$^+$. The IR spectrum (CH$_2$Cl$_2$ solution) of **150** displays four absorption

bands at 1989, 1996, 2031, 2070 cm^{-1} for terminal CO ligands. The $^{13}C\{^1H\}$ NMR spectrum of complex **150** exhibits a singlets at 0.13, 6.5 and 207.95 ppm for the CH_3, CH_2 and CO carbon atoms, respectively. In the ^1H NMR spectrum, two singlets resonate at 0.26 and 1.66 ppm due to the CH_3 and CH_2 protons, respectively.

Crystal Structure. Single crystals of complex **150** suitable for X-ray structural determination were obtained by slow evaporation of pentane solution at 5 °C. Figure 6-1 shows the molecular structure of **150**.
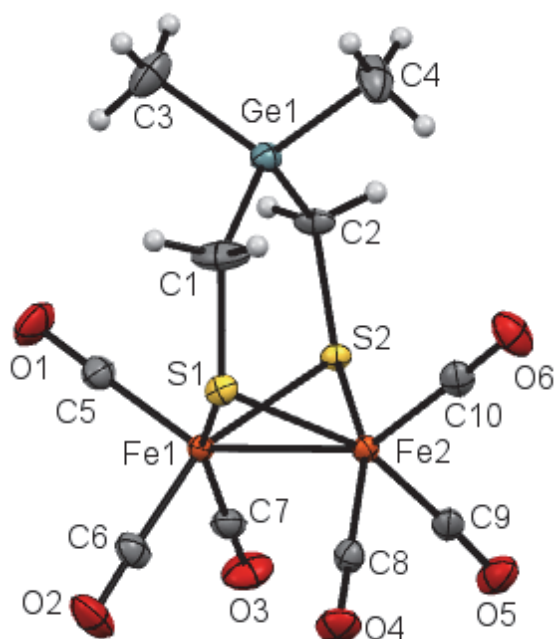
Figure 6-1. Molecular structure of complex **150** (50 % probability). Selected bond lengths [Å] and angles [°]: Fe1-Fe2 2.5128(4), Fe1-S1 2.2577(6), Fe1-S2 2.2506(6), Fe2-S1 2.2435(6), Fe2-S2 2.2623(6), Ge1-C1 1.952(3), Ge1-C2 1.956(2), Ge1-C3 1.941(3), Ge1-C4 1.936(3), Ge1-C1-S1 122.94(14), Ge1-C2-S2 121.90(12), C1-Ge1-C2 111.60(10), C4-Ge1-C2 108.74(12), C4-Ge1-C1 108.64(16), C3-Ge1-C2 108.14(12), C3-Ge1-C1 107.39(15), C4-Ge1-C3 112.36(15).

As shown in Figure 6-1, each iron core of complex **150** represents a distorted octahedron in which the central Fe atom is surrounded by three terminal CO ligands in a facial fashion as well as two S atoms that bridge both iron cores. The bicyclic [Fe$_2$S$_2$] core adopts a typical butterfly conformation. The Fe-Fe bond length in **150**, 2.5128(4) Å, is comparable to that of [Fe$_2$(CO)$_6${μ-(SCH$_2$)$_2$CMe$_2$}] (**12**), 2.494(6) Å[40], and [Fe$_2$(CO)$_6${μ-(SCH$_2$)$_2$SiMe$_2$}] (**25**), 2.5216(6) Å[49], but is shorter than those reported for the H-cluster, 2.55-2.62 Å[11]. The average Ge-C-S bond angles in complex **150** (122.42°)

is larger than the E-C-S angles in the previously reported models containing a μ-(SCH$_2$)$_2$E linker (E = CR$_2$[40], O[37], NR[36], S[47] and Se[48]), but it is comparable to the Si-C-S angle (121.52°)[49] in the analogous silane complex **25**. The bridgehead Ge atom is surrounded in a slightly distorted tetrahedral fashion; the C1-Ge-C2 (111.60(10)°) and C4-Ge1-C3 (112.36(15)°) angles are larger than the other C-Ge-C (108.23° in average) angles in **150**. In comparison, all C-Si-C angles in complex **25** (108.7° in average)[49] are smaller than C1-Ge1-C2 or C4-Ge1-C3 because the Ge atom is larger than the Si atom.

6.1.2   Flap Angle α

All of the previously reported models for the H cluster adopt chair/boat conformation of the two fused six-membered FeS$_2$C$_2$E rings in the solid state while in solution many complexes undergo FeS$_2$C$_2$E ring-flip such that the half-chair conformation is the transition state between the chair and boat conformations (Figure 6-2).[34,110,243]
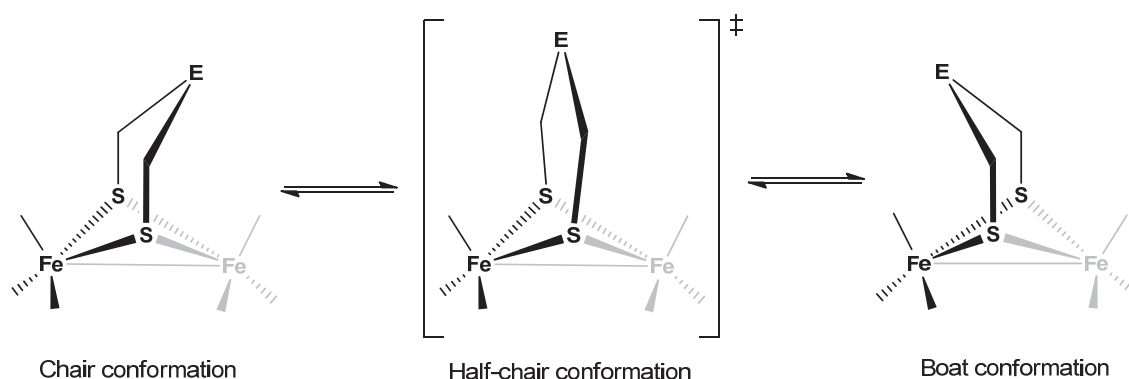
Figure 6-2. Chair/boat conformations of the [FeFe]-hydrogenase model complexes.

The flap angle (α) formed from the intersection between the C$_2$E and S$_2$C$_2$ planes, as shown in Figure 6-3, may be considered as a measure of the distortion of the dithiolate from the planarity. In the half-chair conformation the dithiolato moiety is planar and α = 180°. In comparison to other [Fe$_2$(CO)$_6${μ-(SCH$_2$)$_2$E}] complexes reported in the literature (selected examples are listed in Table 6-1), a unique structural feature of complex **150** is the planarity (almost C$_{2v}$, α = 175.19°). This planarity may allow (by symmetry) a filled-filled interaction between the σ(Ge-C) orbital with the lone pair of the 3p(μ-S) orbital resulting in a higher electron density at the μ-S atoms compared to the

unsymmetrical complexes. More details about the effect of the bridgehead atom on the flap angle of the dithiolato linker can be found in Chapter 7. Further theoretical studies are underway to gain insights into the factors stabilizing the half-chair conformation of the FeS$_2$C$_2$Ge six-membered ring of **150** in comparison to other models featuring distorted dithiolato ligands.
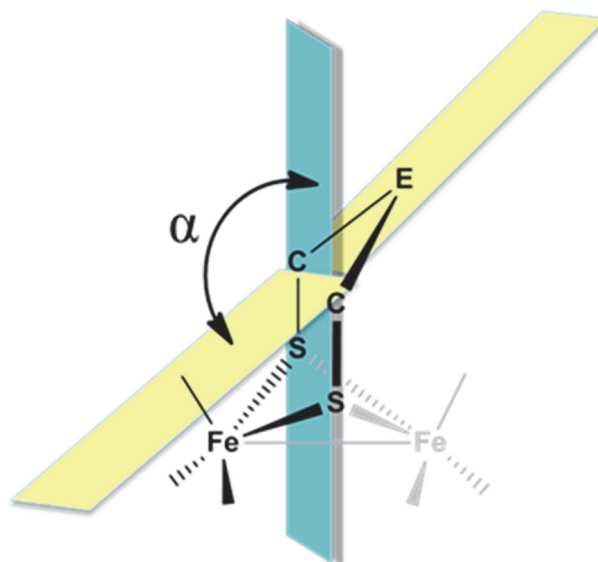
Figure 6-3. Definition of the flap angle α.

Table 6-1. Flap angles α [°] in various model complexes.

Complex	No.	α [°]	Reference
[Fe$_2$(CO)$_6${μ-(SCH$_2$)$_2$CH$_2$}]	**3**	137.09	40, 110
[Fe$_2$(CO)$_6${μ-(SCH$_2$)$_2$CMe$_2$}]	**12**	135.74	40, 110
[Fe$_2$(CO)$_6${μ-(SCH$_2$)$_2$CEt$_2$}]	**13**	136.7	40
[Fe$_2$(CO)$_6${μ-(SCH$_2$)$_2$C(n-Bu)(Et)}]	–	137.7	40
[Fe$_2$(CO)$_6${μ-(SCH$_2$)$_2$SiMe$_2$}]	**25**	150.02	49
[Fe$_2$(CO)$_6${μ-(SCH$_2$)$_2$NH}]	**7**	131.95	110
[Fe$_2$(CO)$_6${μ-(SCH$_2$)$_2$NMe$_{ax}$}]	**5(Me$_{ax}$)**	128.57	110
[Fe$_2$(CO)$_6${μ-(SCH$_2$)$_2$NMe$_{eq}$}]	**5(Me$_{eq}$)**	120.48	110
[Fe$_2$(CO)$_6${μ-(SCH$_2$)$_2$Nt-Bu}]	–	118.46	110
[Fe$_2$(CO)$_6${μ-(SCH$_2$)$_2$GeMe$_2$}]	**150**	175.19	–

6.1.3   **Effect of Presence of Strong Acids on the υ(CO) Bands of Complex 150**

The previous electrochemical and IR spectroscopic studies on the complex [Fe$_2$(CO)$_6${μ-(SCH$_2$)$_2$SiC$_4$H$_8$}] suggested the reactivity of its μ-S atoms toward acids.[49] A IR monitoring of the reaction of **150** with strong acids revealed that the addition of 1-10 equiv. HBF$_4$·Et$_2$O or CF$_3$SO$_3$H to the CH$_2$Cl$_2$ solution of **150** does not affect the υ(CO) bands, but in the presence of 100 equiv. strong acids, the intensity of the bands decreased concomitantly with the appearance of new weak bands, which are shifted at higher wavenumbers (2083, 2107 and 2129 cm^{-1}) by an average of $\Delta\upsilon$(CO) $\sim$ 67 cm^{-1}, compared to that of **150**. This shift is consistent with either Fe- or μ-S-protonation that is observed in the presence of 100 equiv. strong acids (Figure 6-4). However, the Fe-protonation of diiron complexes requires a strong electron donor set of ligands such as PMe$_3$.[125] Thus, we herein suggest a μ-S-protonation of complex **150**. The persistence of the υ(CO) bands of the starting compound after the addition of 100 equiv. acid suggests a partial protonation of **150**.
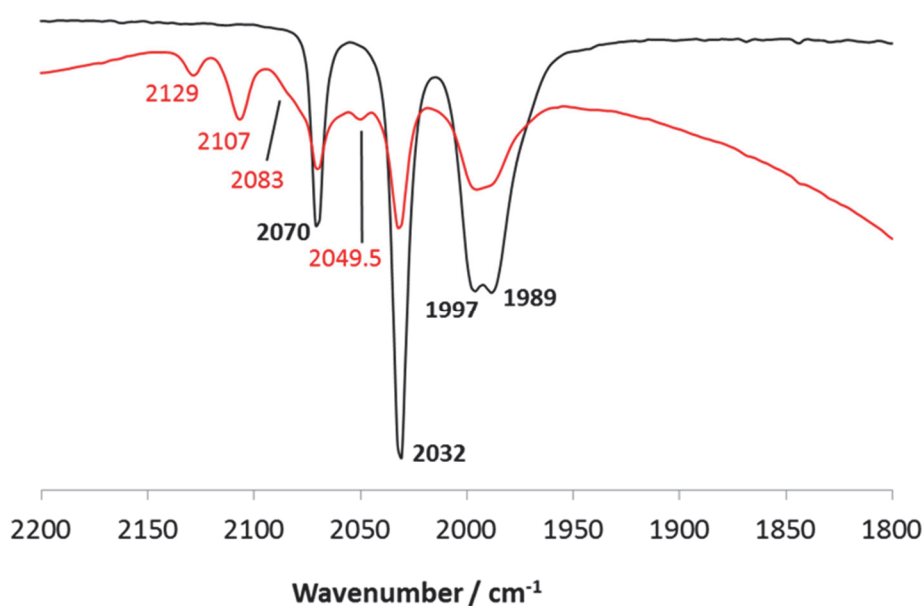
Figure 6-4. IR spectrum of complex **150** in CH$_2$Cl$_2$ solution in the absence (black) and presence of 100 equiv. HBF$_4$·Et$_2$O or CF$_3$SO$_3$H (red).

Performing the IR protonation experiment of complex **150** in MeCN solution showed only decomposition of the complex as all υ(CO) bands disappeared and no new bands

were detected. It is worth noting that the addition of acids to complexes $[Fe_2(CO)_6\{\mu\text{-}(SCH_2)_2EMe_2\}]$ (E = C (**12**) and Si (**25**)) under the same conditions used **150** does not give rise to any protonation process, but instead these complexes underwent decomposition.

6.1.4   **Electrochemistry of Complex 150 in the Absence of Acids**

The cyclic voltammetric reduction of complex **150** in CH_2Cl_2/NBu_4PF_6 at scan rates of $0.05\ V\cdot s^{-1} \leq v \leq 10\ V\cdot s^{-1}$ and $10\ V\cdot s^{-1} \leq v \leq 40\ V\cdot s^{-1}$ are shown in Figure 6-5.
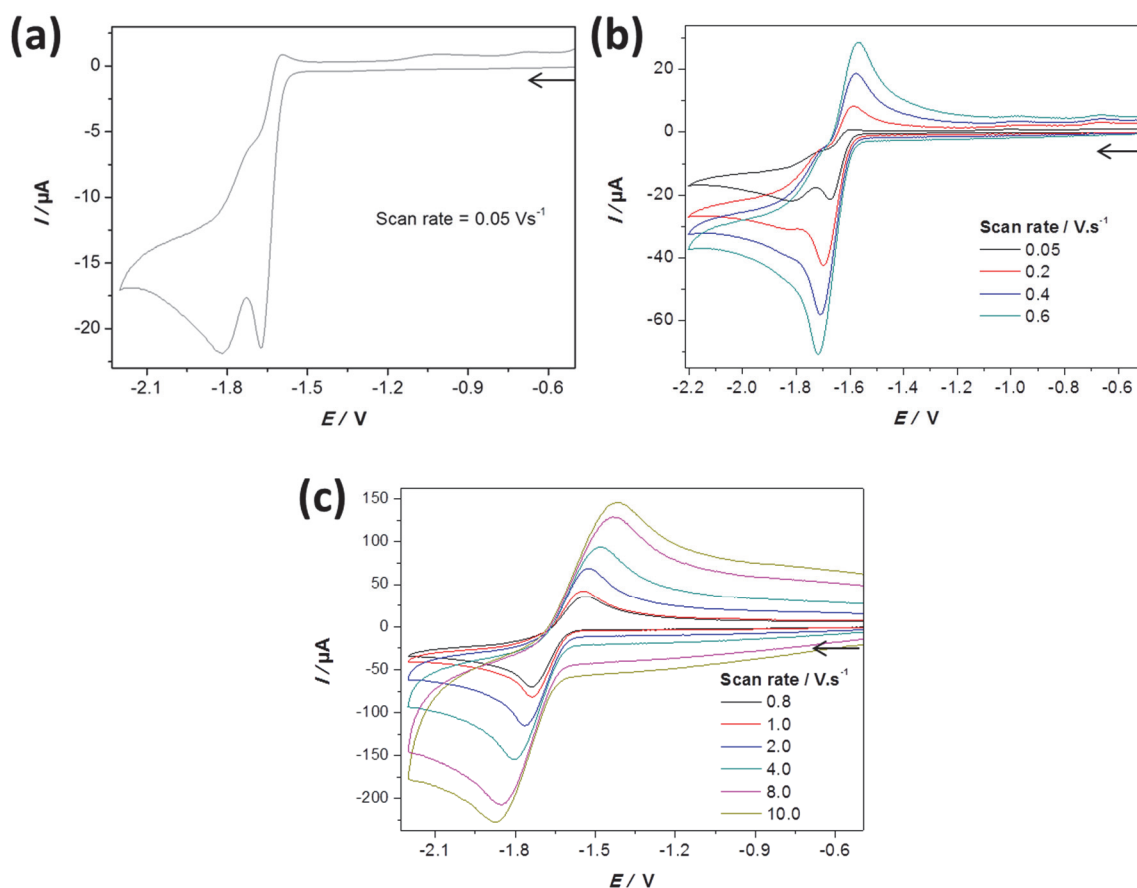
Figure 6-5. Cyclic voltammetry of 0.843 mM complex **150** in CH_2Cl_2/NBu_4PF_6 solution under N_2 at (a) $0.05\ V\cdot s^{-1}$, (b) $0.05\ V\cdot s^{-1} \leq v \leq 0.6\ V\cdot s^{-1}$ and (c) $0.8\ V\cdot s^{-1} \leq v \leq 10\ V\cdot s^{-1}$. Glassy carbon electrode (d = 3 mm). *E* is in V against the ferrocenium/ferrocene couple. The arrows indicate the scan direction.

At 0.05 V·s^{-1} two reduction events are detected at -1.67 V and -1.82 V and no reversibility is observed in the backward scan (Figure 6-5a). The second reduction event disappears at higher scan rates and the first reduction process becomes quasi-reversible (Figures 6-5b and 6-5c). Thus, the second reduction event detected at slow scan rates does not arise from a second reduction step of **150**, but it is related to a follow-up reaction. Indeed, the disappearance of the second reduction wave and the enhancement of the reversibility of the first reduction upon increasing the scan rate were observed. Consequently, the first wave should be due to two-electron reduction of complex **150** in a single step because of potential inversion of the individual one-electron reduction steps: i.e., $E_1° - E_2° < 0$. At 0.2 V·s^{-1}, the current function ($I_{pc}/c·v^{1/2}$, c = concentration) of complex **150** (110.4 µA·mM^{-1}·V^{-1}·s$^{1/2}$) is comparable to that of complex [Fe$_2$(CO)$_6$\{μ-(S$_2$CH$_2$)$_2$C(CH$_2$OH)$_2$\}] (**147**) (116.8 µA·mM^{-1}·V^{-1}·s$^{1/2}$) that was previously shown to undergo a single step two-electron reduction (Chapter 5). This confirms the two-electron assignment of the first reduction wave of complex **150**. Figure 6-6 shows that the current function of complex **150** decreases significantly as the scan rate increases suggesting the presence of an intervening chemical process during the electron transfer processes; i.e. ECE mechanism. This chemical process probably involves the cleavage of one of the Fe-S bonds and the rotation of one Fe(CO)$_3$ unit to locate one of its CO ligands in a semi-bridging position between the two iron atoms. The complexes [Fe$_2$(CO)$_6$\{μ-(S$_2$CH$_2$)$_2$ER$_2$\}] (ER$_2$ = CMe$_2$ (**12**, see Chapter 5) and SiMe$_2$ (**25**)[49]) also undergo two-electron reduction with potential inversion. Because no splitting of the two-electron reduction wave of complex **150** is observed by increasing the scan rate up to 40 V·s^{-1}, the heterogeneous rate constant of the first electron transfer should be smaller than that of the second reduction process.[43,45,47b]
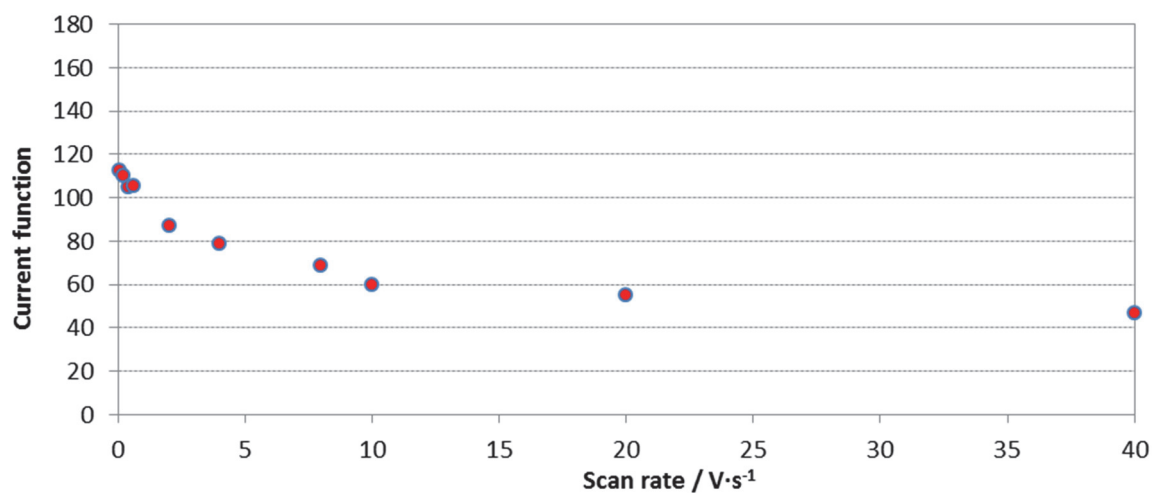
Figure 6-6. Scan rate dependence of the current function for the reduction of [Fe$_2$(CO)$_6${μ-(S$_2$CH$_2$)$_2$GeMe$_2$}] (**150**) (0.843 mM) in CH$_2$Cl$_2$/NBu$_4$PF$_6$ solution under N$_2$.

The follow-up reactions observed at low scan rates (Figure 6-5a) may involve loss of CO ligand from the reduced species of complex **150** as it was found for hexacarbonyl complexes.[34,156,215,236-240a,241] Thus, we have performed the experiments using CO-saturated solution and the results are depicted in Figure 6-7.
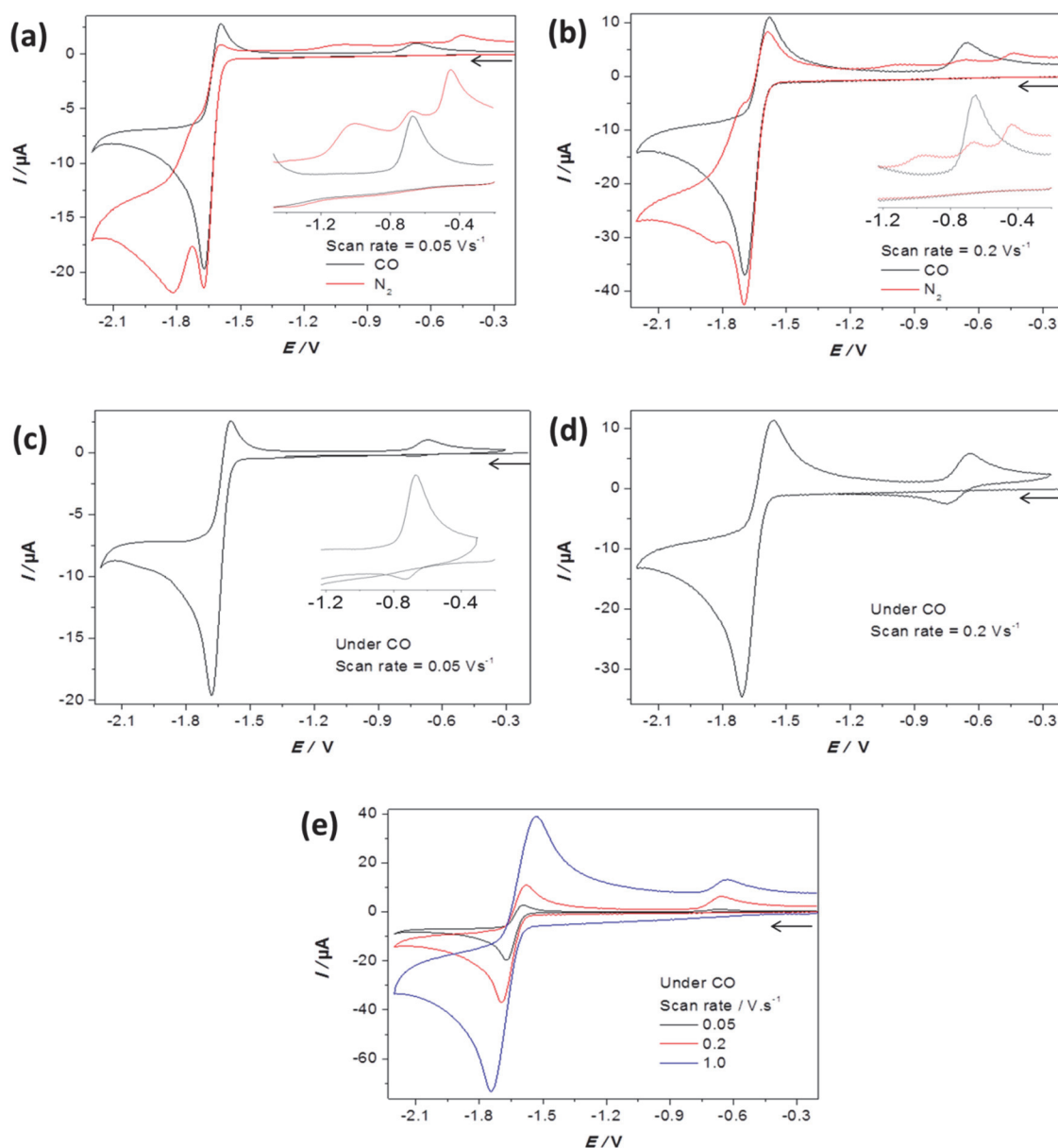
Figure 6-7. Cyclic voltammetry of 0.843 mM complex **150** in CH$_2$Cl$_2$/NBu$_4$PF$_6$ solution under conditions shown in the inset of each Figure. Part of the voltammograms a, b and c are enlarged and shown in the inset for clarification. Glassy carbon electrode (d = 3 mm). E is in V against the ferrocenium/ferrocene couple. The arrows indicate the scan direction.

The wave due to the reduction of the decomposition products is not observed when the solution of complex **150** is CO-saturated (Figure 6-7a and b) suggesting that the loss of CO ligands from the reduced species of **150** is prevented. Therefore, we would expect that the reduction of complex **150** should become reversible. However, we can notice in Figure 6-7a and Figure 6-7b that the reversibility is enhanced only very slightly. In addition, only one oxidation wave occurs at -0.67 V ($v = 0.05$ V·s^{-1}) or at -0.64 V ($v = 0.2$

V·s^{-1}) when the experiment is performed using CO-saturated solution of complex **150**. This oxidation event is also detected when the voltammetry is performed under N_2, but occurs with other oxidation processes (see the insets of Figures 6-7a and b). Thus, the presence of CO in the solution of complex **150** limits the possibilities of the follow-up reactions occurring under N_2 to probably one reaction between **150^{2-}** and CO leading to product **150CO^{2-}** responsible for the oxidation wave at -0.64 V (v = 0.2 V·s^{-1}). Figure 6-7d shows that this oxidation process is reversible; $E_{1/2}$ = -0.70 V (E_{pc} = -0.75 V and E_{pa} = -0.64 V). This behavior was also described for the complex [Fe$_2$(CO)$_5$P(OEt)$_3$$\{\mu$-$(S_2CH_2)_2(Ph)P=O\}$] (**139**). Scheme 6-3 summarizes the voltammetric reactions of complex **150** in the under N_2 as well as CO atmospheres.

Scheme 6-3. Electrochemistry of complex **150** under N_2 and CO (the red arrow) atmospheres.

In general, the DFT calculations of Chapter 3 on the the reaction of the dianion [Fe$_2$L$_6$$\{\mu$-$(S_2CH_2)_2E\}$]$^{2-}$ with CO shows that the product consists of an FeL$_4$ unit linked to a [FeL$_3$$\{(SCH_2)_2E\}$] fragment by a weak iron-iron contact. We therefore may propose similar structure for **150CO^{2-}**.

150CO^{2-}

Probably, the weak Fe-Fe contact in **150CO^{2-}** illustrates the slight chemical reversibility of oxidation event assigned for **150CO^{2-}** at slow scan rates (0.05 V·s^{-1}, Figure 6-7c).

6.1.5   Electrochemical Response of Complex 150 to Strong Acids

Electrochemical investigation on the behavior of complex **150** in the presence of CF$_3$SO$_3$H is shown in Figure 6-8.

Figure 6-8. Cyclic voltammetry of complex 1.01 mM complex **150** (CH$_2$Cl$_2$/NBu$_4$PF$_6$ solution) in the presence of 0.5-2 equiv. CF$_3$SO$_3$H at 0.2 V·s^{-1}. Glassy carbon electrode (d = 3 mm). *E* is in V against the ferrocenium/ferrocene couple. The arrow indicates the scan direction.

Because of the significant direct reduction of the acid, we show only the presence of 0.5-2 equiv. CF_3SO_3H. In the presence of 0.5 equiv. CF_3SO_3H, only a shoulder at the original reduction wave (E_{pc} = -1.71 V at 0.2 V·s^{-1}) of **150** is observed at -1.60 V. This shoulder is shifted by 110 mV from the two-electron wave in the absence of acid and it is attributed to the protonation of the reduced species of complex **150**. Further additions of CF_3SO_3H increases the current of the shoulder to be comparable to that of the reduction wave in the absence of acid, but without further increase suggesting that no catalysis occurs at this potential. The cyclic voltammograms exhibit two additional waves (at -1.74 V and -2.07 V) in the presence of 1 and 2 equiv. CF_3SO_3H, which show catalytic response to the addition of acid. As we mentioned before, the direct reduction of CF_3SO_3H could contribute to any catalytic reduction at higher acid concentration. For this reason, we present herein only a qualitative description. We attribute the wave at -2.07 V to the reduction of **150H$^-$** to give **150H^{2-}**. The catalytic response at this potential occurs after protonation of **150H^{2-}** that releases H_2. The wave at -1.74 V, which is observed for equiv. $CF_3SO_3H \geq 2$, arises from the reduction of the protonated form of **150H$^-$** (i.e. **150H$_2$**). Scheme 6-4 summarizes these processes.

Scheme 6-4. Proposed reactions for the reduction of CF_3SO_3H catalyzed by complex **150**.

The presence of 1-2 equiv. $HBF_4·Et_2O$ in the solution of complex **150** (Figure 6-9, v = 1 V·s^{-1}) affects the electrochemical behavior in a similar manner described for CF_3SO_3H. However, the response of the process near -1.8 V to the acid is greater in the case of $HBF_4·Et_2O$ compared to that of CF_3SO_3H.

Figure 6-9. Cyclic voltammetry of complex 0.843 mM complex **150** (CH$_2$Cl$_2$/NBu$_4$PF$_6$ solution) in the presence of 0-2 equiv. HBF$_4$·Et$_2$O at 1 V·s^{-1}. Glassy carbon electrode (d = 3 mm). E is in V against the ferrocenium/ferrocene couple. The arrow indicates the scan direction.

6.2 Conclusions

A bioinspired model complex **150** containing the original μ-(SCH$_2$)$_2$GeMe$_2$ dithiolato linker has been synthesized and characterized. While the spectroscopic properties of **150** are not very different from those of other hexacarbonyl species, only **150** features, in solid state, a FeC$_2$S$_2$Ge ring in a half-chair conformation. IR spectroscopic study of the reactivity of **150** in the presence of strong acids suggests, unlike compounds [Fe$_2$(CO)$_6$$\{\mu$-(S$_2CH_2$)$_2ER_2\}$] (ER$_2$ = CMe$_2$ (**12**) and SiMe$_2$ (**25**)) in CH$_2$Cl$_2$, that only **150** is protonated, but there is an equilibrium between the μ-S-protonated complex **150** and its unprotonated form. This straight protonation of **150** may be induced by a symmetrically allowed filled-filled interaction σ(Ge-C) $\leftrightarrow$ 3p(μ-S) due to the planarity of the μ-(SCH$_2$)$_2$GeMe$_2$ ligand. The cyclic voltammetry of **150** shows that it undergoes an overall two-electron reduction in a single step with inverted potentials as it was found for hexacarbonyl complexes with μ-(SCH$_2$)$_2$XMe$_2$ dithiolates (X = C (see Chapter 5), Si[49]). At low scan rates, the two-electron reduction of **150** is followed by decomposition responsible for the irreversibility of the reduction. The presence of free CO in the solution prevents this reaction, but it reacts with the reduced species of **150** forming

spectroscopically uncharacterized product **150CO^{2-}** that undergoes reversible oxidation at half-wave potential ($E_{1/2}$ = -0.70 V at 0.2 V·s^{-1}) less negative than that of **150** ($E_{1/2}$ = -1.65 V at 0.2 V·s^{-1}); Scheme 6-3. The behavior of **150** in the presence of protons was studied by cyclic voltammetry, which suggests the protonation of the reduced species of **150** in the presence of acids.

Chapter 7

Monomeric and Dimeric Complexes Featuring Fe$_2$S$_2$(CO)$_6$ Clusters and μ-(SCH$_2$)$_2$SnR$_2$ Linkers

(Manuscript 4)
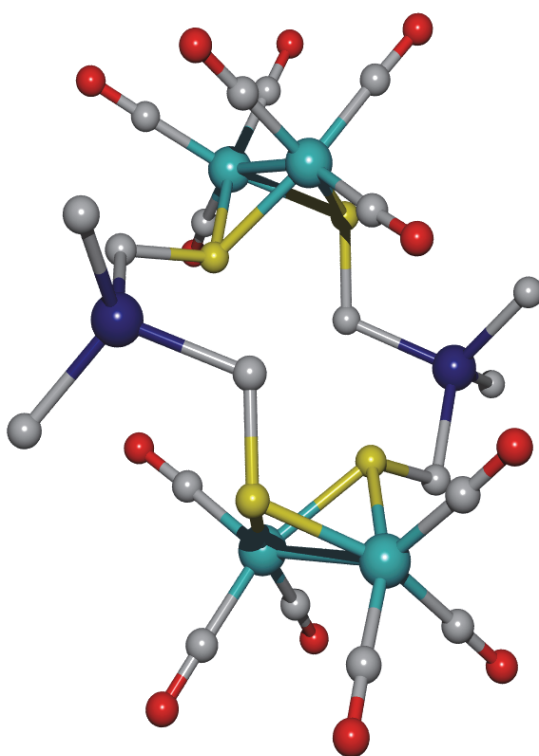
7   Monomeric and Dimeric Complexes Featuring Fe$_2$S$_2$(CO)$_6$ Clusters and μ-(SCH$_2$)$_2$SnR$_2$ Linkers

This chapter is a continuation of the chemistry discussed in Chapter 6 in which the novel planar complex [Fe$_2$(CO)$_6$\{μ-(S$_2$CH$_2$)$_2$GeMe$_2$\}] (**150**) is described. Indeed, the synthesis of an analogues Sn-containing complex has been already described by Glass et al. in 2005.[50] However, no X-ray structural determination for the complex [Fe$_2$(CO)$_6$\{μ-(S$_2$CH$_2$)$_2$SnMe$_2$\}] (**151**) is reported. Herein the synthesis, spectroscopic and crystallographic characterization of various Sn-containing complexes, including complex **151**, are described in order to have a full image of the effect of group IV elements (X = C, Si, Ge, Sn) on the structure of the diiron complex [Fe$_2$(CO)$_6$\{μ-(S$_2$CH$_2$)$_2$XR$_2$\}]. Furthermore, this chapter presents the isolation and characterization of dimeric metalloheterocycle containing two "butterfly" [Fe$_2$S$_2$] clusters, [Fe$_2$(CO)$_6$\{μ-(SCH$_2$)$_2$SnR$_2$\}]$_2$, obtained unexpectedly from the reaction of the in situ generated (μ-LiS)$_2$Fe$_2$(CO)$_6$ with R$_2$Sn(CH$_2$I)$_2$.

7.1   Results and Discussion

7.1.1   Synthesis and Characterization

The compounds R$_2$Sn(CH$_2$I)$_2$ (R = Ph and Me[244]) were synthesized according to Scheme 7-1. The reaction of R$_2$SnCl$_2$ with 2 equiv. of in situ generated IZnCH$_2$I afforded R$_2$Sn(CH$_2$I)$_2$ in ca. 60 % (R = Me) and 48 % (R = Ph) yield after purification by column chromatography as colorless liquids.

Scheme 7-1. Synthesis of R$_2$Sn(CH$_2$I)$_2$ compound, R = Me[244] or Ph.
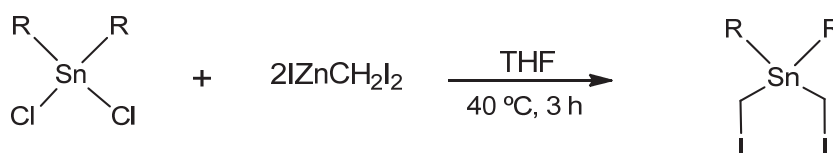
These compounds were used as ligands for the complexation reactions in Scheme 7-2. The reaction of in situ generated (μ-LiS)$_2$Fe$_2$(CO)$_6$[201] with 1 equiv. R$_2$Sn(CH$_2$I)$_2$ afforded [Fe$_2$(CO)$_6${μ-(SCH$_2$)$_2$SnR$_2$}] (R = Me (**151**) and Ph (**153**)) in 12-13 % yield as air-stable red solids as well as unexpectedly dimeric products [Fe$_2$(CO)$_6${μ-(SCH$_2$)$_2$SnR$_2$}]$_2$ (R = Me (**152**), 11 % yield, and R = Ph (**154**), traces) as air-stable orange solids.

Scheme 7-2. Syntheses of the monomeric (**151** and **153**) and the dimeric (**152** and **154**) complexes.

151 (R = Me)
153 (R = Ph)

152 (R = Me)
154 (R = Ph)
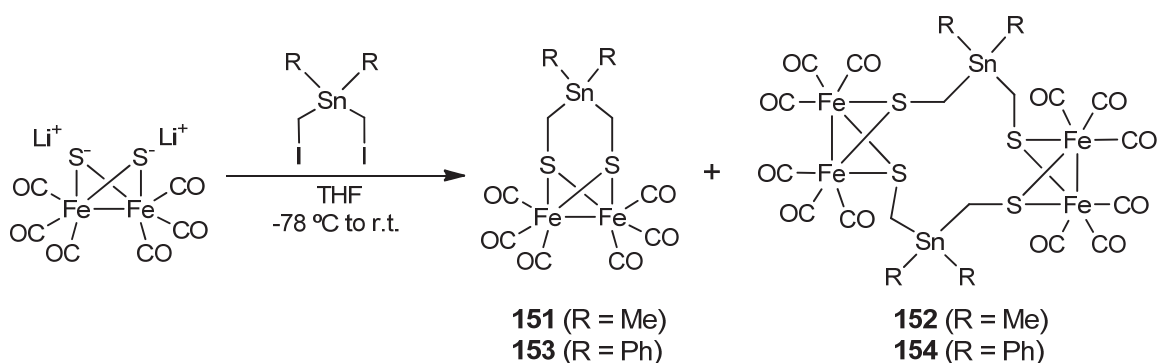
The new ligand Ph$_2$Sn(CH$_2$I)$_2$ was characterized by MS spectrometry as well as ^{1}H NMR and ^{13}C{^{1}H} NMR spectroscopic techniques.
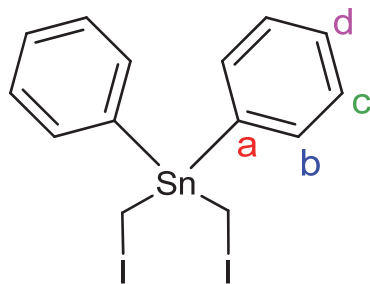
The DEI-MS spectrum of Ph$_2$Sn(CH$_2$I)$_2$ shows peaks at *m/z* 479 [PhSn(CH$_2$I)$_2$]$^+$, 415 [Ph$_2$SnCH$_2$I]$^+$, 351 [Ph$_2$Sn(CH$_2$I)(CH$_2$)]$^+$ and 273 [Ph$_2$Sn]$^+$. The ^{1}H NMR spectrum (CDCl$_3$, 400.08 MHz) exhibits a singlet at 2.41 ppm with Sn satellites (^2J{^{117}Sn,^{1}H} = 20.9 Hz and ^2J{^{119}Sn,^{1}H} = 41.8 Hz) for the C*H$_2$* hydrogen atoms. The hydrogen atoms at the positions c and d of the Ph groups show a multiplet in the region of 7.38-7.43 ppm and the hydrogen atoms located at position b resonate in the region of 7.55-7.60 ppm.

The $^{13}C\{^1H\}$ NMR spectrum shows a singlet at -10.53 ppm due to the CH_2 carbon atoms. The Ph groups appear as multiplets at 126.0-128.78 (c- and d-carbons), 136.85 (b-carbons) and 139.31 ppm (a-carbons) in the $^{13}C\{^1H\}$ NMR spectrum.

The diiron complexes **151-153** were characterized by ^1H, and $^{13}C\{^1H\}$ as well as IR spectroscopic techniques, MS spectrometry, elemental analysis and X-ray crystallography. The dimeric complex **154** was characterized only by X-ray crystallography because only traces could be obtained by the synthetic method in Scheme 7-2. The DEI-MS spectra of the monomeric complexes **151** and **153** show the parent ion peak at m/z 520 $[M]^+$ and 646 $[M]^+$, respectively, as well as the consecutive loss of the CO ligands. The IR spectrum (CH_2Cl_2 solution) of complex **151** shows four absorption bands at 2063, 2031, 1991 and 1974 cm^{-1} for terminal CO ligands. The $^{13}C\{^1H\}$ NMR spectrum of complex **151** shows a singlets at -7.1, 1.6 and 207.0 ppm for the CH_2, CH_3 and CO carbon atoms; respectively, while that of **153** exhibits a singlet at -10.50 ppm for the CH_2 groups as well as multiplets due to the Ph substituents in the region of 128.7-130.6 (c- and d-carbon atoms, see the labeling below) and 136.7-138.7 ppm (a- and b-carbon atoms).

153
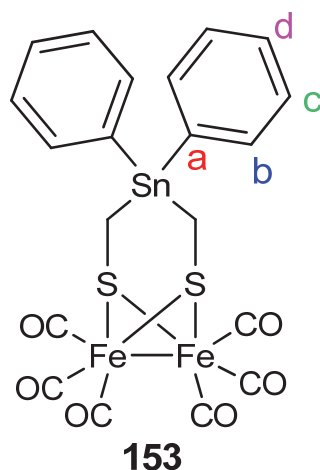
The CO ligands of **153** resonate at 208.6 and 209.1 ppm, which is in contrast to the $^{13}C\{^1H\}$ NMR spectrum of **151** that shows only one signal due to the CO ligands. The ^1H NMR spectra of complexes **151** and **153** exhibit a singlet at 1.79 ppm (**151**) and 2.27 ppm (**153**) for the CH_2 protons. Complex **151** shows a singlet at 0.25 ppm due to the CH_3 protons in the ^1H NMR spectrum, while the spectrum of complex **153** has a multiplet in the region of 7.35-7.70 ppm due to the Ph protons. The FAB-MS spectrum of complex

152 shows the parent ion peak at *m/z* 1041 [M]$^+$ and the consecutive loss of six CO ligands. The IR spectrum of **152** exhibits absorption bands at 2071, 2031 and 1991 cm^{-1} for terminal CO ligands. The ^{13}C{^{1}H} NMR of the dimeric complex **152** displays peaks at -8.1 (*C*H$_3$), 1.1 (*C*H$_2$) and 209 ppm (*C*O). A singlet at 2.00 ppm was observed in the ^{1}H NMR spectrum (**152**) for all of the C*H*$_2$ hydrogen atoms in the macrocycle and another singlet at 0.36 ppm due to the protons of the C*H*$_3$ groups.

Molecular Structures of the Monomeric Complexes. Crystals suitable for X-ray diffraction analysis were obtained by slow evaporation of pentane solution of complex **151** or **153** at 5 ºC. Figure 7-1 shows the molecular structures of the monomeric complexes **151** and **153**.

As can be seen from Figure 7-1, each iron atom of the monomeric complexes **151** and **153** is surrounded by three terminal CO ligands in a facial fashion as well as two S atoms that bridges both iron cores. Each iron core of complexes **151** and **153** has a structure of distorted octahedron. The bicyclic [Fe$_2$S$_2$] structure in these complexes reveals butterfly conformation as all other diiron models. The Sn atoms of complexes **151** and **153** are surrounded in a distorted tetrahedral fashion. The Sn-C-S bond angles (121.96º (**151**), 119.66º (**153**)) deviate significantly from the ideal tetrahedral angle as was observed for the [Fe$_2$(CO)$_6${μ-(SCH$_2$)$_2$XMe$_2$}] (X = Si (**25**)[49], Ge (**150**)) model complexes (Chapter 6). The Fe-Fe bond lengths in complexes **151** (2.5249(5) Å) and **153** (2.5158(7) Å) are comparable to those in complexes **25** and **150**. The average Fe-CO bond lengths are 1.802 Å and 1.798 Å in **151** and **153**, respectively. The average Fe-S bond lengths (2.2561 Å (**151**), 2.2582 Å (**153**)) are comparable to those in complexes **25** (2.2582 Å)[49] and **150** (2.2535 Å).
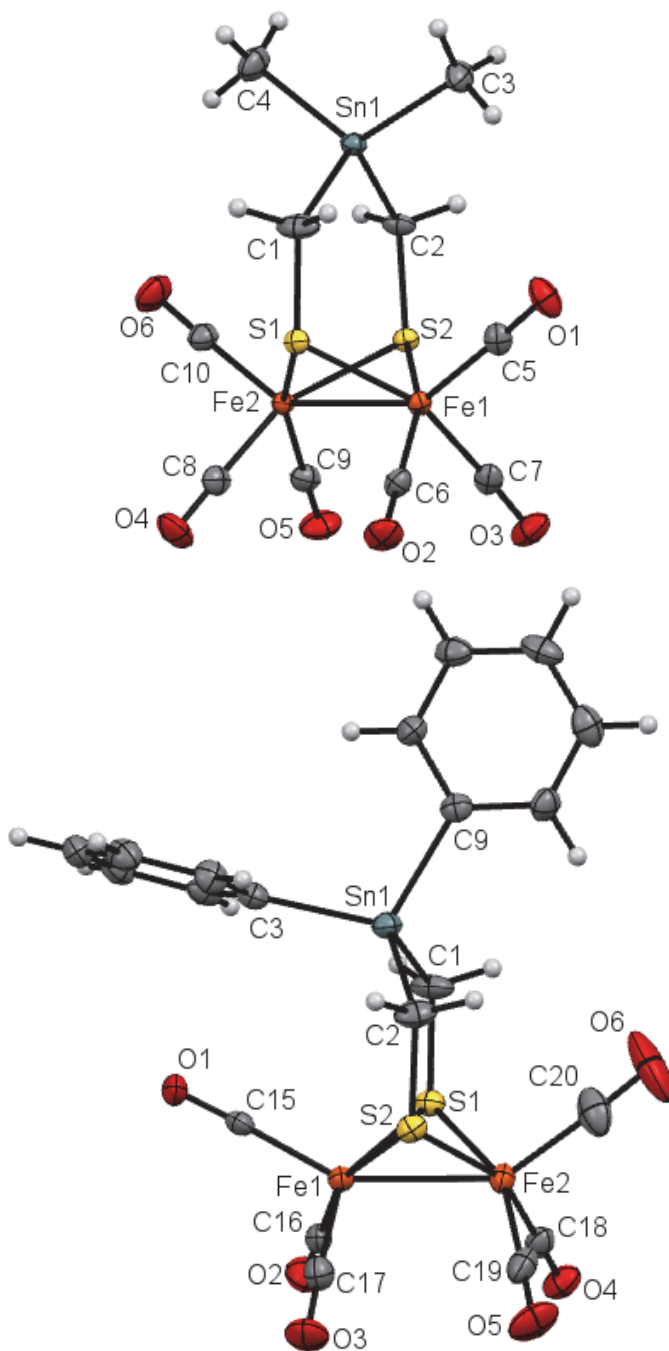
Figure 7-1. Molecular structures (50 % probability) of complexes **151** (top) and **153** (bottom).

7.1.2   Bridgehead Steric Effects on the Flap and Torsion Angles

Table 7-1 displays a comparison of some crystallographic distances and angles in complexes with bridgehead atoms of the group IV elements.

Table 7-1. Comparison of crystallographic parameters in $[Fe_2(CO)_6\{\mu\text{-}(SCH_2)_2XR_2\}]$ $(XR_2 = CR_2{}^{34,40}, SiMe_2{}^{49}, GeMe_2, SnR_2)$ complexes.

Complex	Fe-Fe (Å)	X-CH$_2$ (Å)[a]	α [°][b]	τ [°][c]	X$\cdots$Fe (Å)[d]
$[Fe_2(CO)_6\{\mu\text{-}(SCH_2)_2CH_2\}]$ (**3**)	2.5105(8)	1.460	137.09	0.0	3.50
$[Fe_2(CO)_6\{\mu\text{-}(SCH_2)_2CMe_2\}]$ (**12**)	2.4939(4)	1.531	135.74	5.7	3.74
$[Fe_2(CO)_6\{\mu\text{-}(SCH_2)_2CEt_2\}]$ (**13**)	2.501(4)	1.532	136.7	15.8	3.75
$[Fe_2(CO)_6\{\mu\text{-}(SCH_2)_2SiMe_2\}]$ (**25**)	2.5216(6)	1.871	150.02	0.0	3.95
$[Fe_2(CO)_6\{\mu\text{-}(SCH_2)_2GeMe_2\}]$ (**150**)	2.5128(4)	1.954	175.19	7.9	4.10
$[Fe_2(CO)_6\{\mu\text{-}(SCH_2)_2SnMe_2\}]$ (**151**)	2.5249(5)	2.146	173.61	5.2	4.23
$[Fe_2(CO)_6\{\mu\text{-}(SCH_2)_2SnPh_2\}]$ (**153**)	2.5158(7)	2.142	152.49	7.5	4.05

[a]Average value. [b]α = Flap angle. [c]τ = Torsion angle. [d]Distance between the bridgehead atom X and the nearest Fe site.

First of all, we may consider complex **3**, which has the least bulky dithiolato ligand among the complexes in Table 7-1, as a reference model featuring fully eclipsed Fe(CO)$_3$ units (τ = 0.0°) and a flap angle α = 137.09°. The replacement of its CH$_2$ bridgehead group by the bulkier CMe$_2$ results in a slightly distorted eclipsed conformation of the Fe(CO)$_3$ units in complex **12** (τ = 5.7°). The bulkier CEt$_2$ group in complex **13** compared to the CH$_2$ (in complex **3**) and CMe$_2$ (in complex **12**) moieties causes significant distortion indicated by the torsion angle τ = 15.8°. In this series the flap angles α are comparable, but a remarkable increase occurs upon replacing the C-bridgehead atoms by the heteroatoms Si, Ge or Sn (Table 7-1). Ongoing from complexes **3**, **12** and **13** to the Si-containing complex **25**, (*i*) the X-C bond distance increases by 0.37 Å due to larger size of X = Si compared to X = C, (*ii*) α increases by an average of 13.5° and the two Fe(CO)$_3$ units become again fully eclipsed (τ = 0.0) as in complex **3**. The larger size of the SiMe$_2$ moiety compared to the CMe$_2$ moiety favors the greater flap angle in complex **25** (α = 150.02°) compared to that in complex **12** (α = 135.74°), which alleviates the steric clash between the bridgehead and the apical CO making τ = 0.0° in **25** vs. τ = 5.7° in **12**. The shorter C-C bond (compared to the C-Si bond) and the smaller α of complex **12** (compared to α of **25**) makes the Me groups of complex **12** closer to the [Fe$_2$S$_2$] core than the Me groups of complex **25**, which is indicated by the shorter X$\cdots$Fe distance in complex **12** (3.74 Å, Table 7-1) compared to that in complex **25** (3.95 Å, Table 7-1). This closer proximity of CMe$_2$ to the [Fe$_2$S$_2$] core induces a partial rotation of the Fe(CO)$_3$ moiety (τ = 5.7°) that reduces steric hindrance, which explains the slightly longer

CH$_3$···OC$_{ap}$ (ap = apical) distance (2.651 Å) compared to that in complex **25** (2.579 Å) having $\tau = 0.0°$.
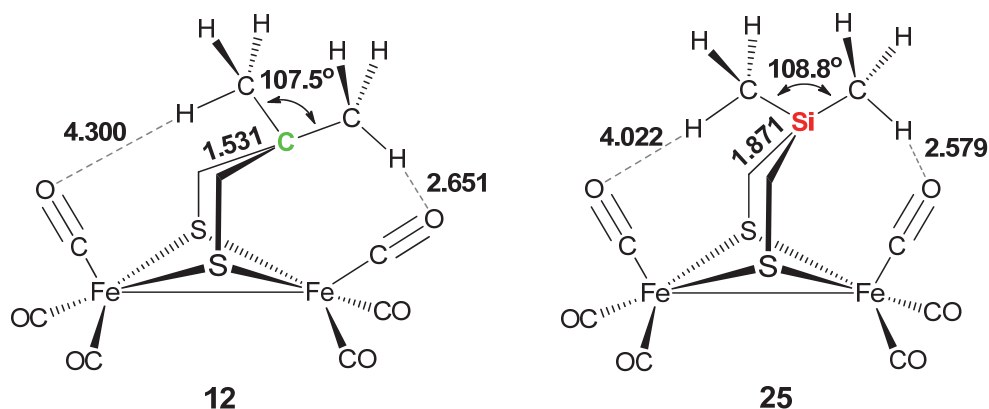
When the Si atom of complex **25** is exchanged by the larger Ge atom, the flap angle α increases to 175.19° and the Fe(CO)$_3$ positioned closer to the bridgehead rotates by 7.9° in the resulting complex **150**. This flap angle makes the complex **150** nearly planar with an almost C$_{2v}$ symmetry, if we do not consider the presence of the CO ligands. The torsion angle of 7.9° in complex **150** is an indicative of a steric clash between the GeMe$_2$ moiety and the Fe(CO)$_3$ unit located closer to the bridgehead. The dithiolato ligand in complex **150** adopts its planarity so as to relieve this steric interaction such that the two Me groups are almost equidistant from both Fe(CO)$_3$ units. Stannylation of [Fe$_2$(CO)$_6$\{μ-(SCH$_2$)$_2$XMe$_2$\}] shows that the resulting complex **151** also has an almost symmetric dithiolato ligand (α = 173.61°) with Me groups almost equidistant from the [Fe$_2$S$_2$] core.
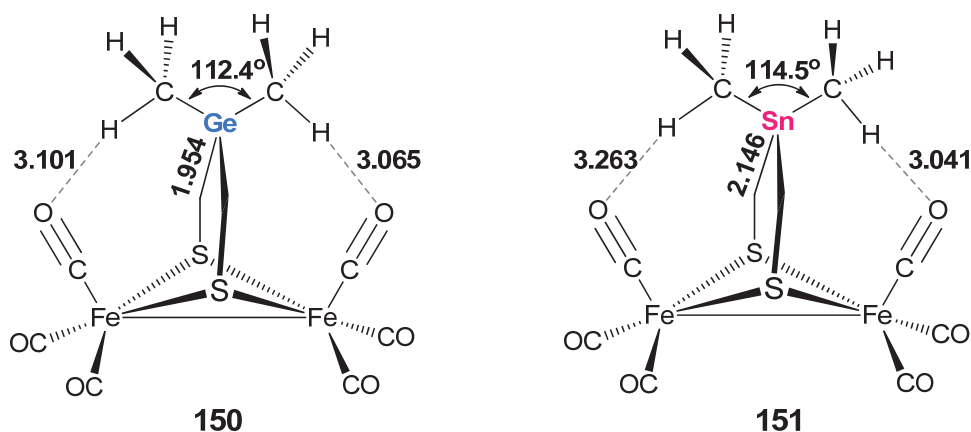
The two Fe(CO)$_3$ units in complex **151** are slightly less distorted from the symmetric eclipsed conformation (τ = 5.2º) compared to the case of complex **150** (τ = 7.9º). The smaller τ of **151** compared to that of **150** could be due to the longer Sn-CH$_2$ (2.146 Å) distances compared to the Ge-CH$_2$ (1.954 Å).

By changing the Me groups in complex **151** (α = 173.61º, τ = 5.2º) by Ph rings, a remarkable decrease of α occurs to become 152.49º in complex **153**, but τ increases slightly to 7.5º. Figure 7-1 clearly shows the planar structure of complex **151** versus the usual chair/boat structure of complex **153**. The flap angle of complex **153** (α = 152.49º) is very similar to that of complex **25** (α = 150.02º), but τ = 7.5º for complex **153** versus τ = 0.0º for complex **25** that is consistent with the greater steric effect of SnPh$_2$ compared to that of SiMe$_2$. DFT calculations are underway to disclose the origin of the different structural features observed in **153** versus **151** as well as all other complexes in Table 7-1. Nevertheless, the origin of the distortion of the μ-(SCH$_2$)$_2$SnPh$_2$ ligand in complex **153** might be understood if we *arbitrarily* assume the planarity of **153** with two possible structures (**153A** and **153B** shown below) that differ only in the orientation of the Ph groups.

153A   **153B**
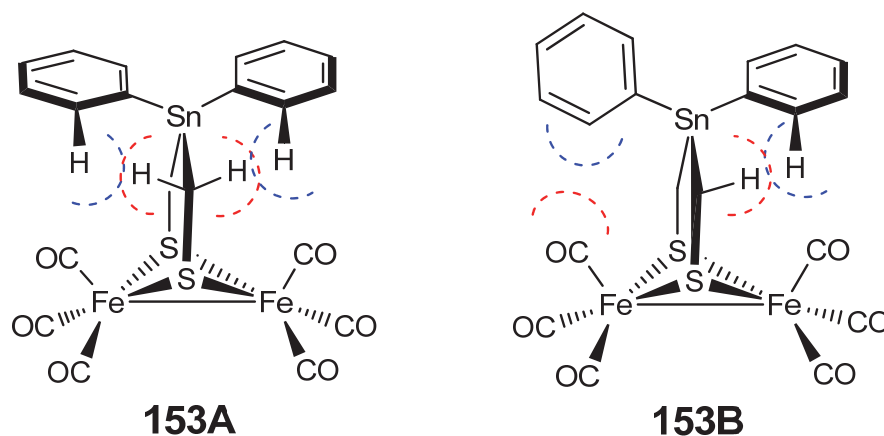
The best orientation of the Ph groups that minimizes the steric clash with the apical CO ligands is shown in **153A**, but a steric strain between the protons of the Ph groups with the CH$_2$ protons would be maximum. This strain in **153A** is lowered through rotation of one its Ph groups to yield **153B**. Nevertheless, **153B** would exhibit steric clash between one Ph ring and one apical CO as shown above. **153B** relaxes from the strain between the

Ph ring and the apical CO via flipping of the dithiolate and slight rotation of one $Fe(CO)_3$ unit leading to the distorted complex measured by X-ray crystallography.

<h3>7.1.3   The Dimeric Complexes</h3>

By slow evaporation of acetone solution of **152** or **154** at -20 °C, single crystals were obtained. The X-ray diffraction analyses confirmed the dimeric structures of **152** and **154** as a macrocycles in which each $Fe_2S_2(CO)_6$ unit has a nonequivalent axial (*a*) and equatorial (*e*) -CH_2- units (Figure 7-2). That is, the stereochemistry of the [Fe_2S_2] clusters in complex **152** or **154** is *e,a,e′,a′* (the stereochemical labels correspond with S(1), S(3), S(4) and S(2) sequentially-the unprimed labels correspond to one Fe_2S_2 cluster and the primed labels to the other Fe_2S_2 cluster).
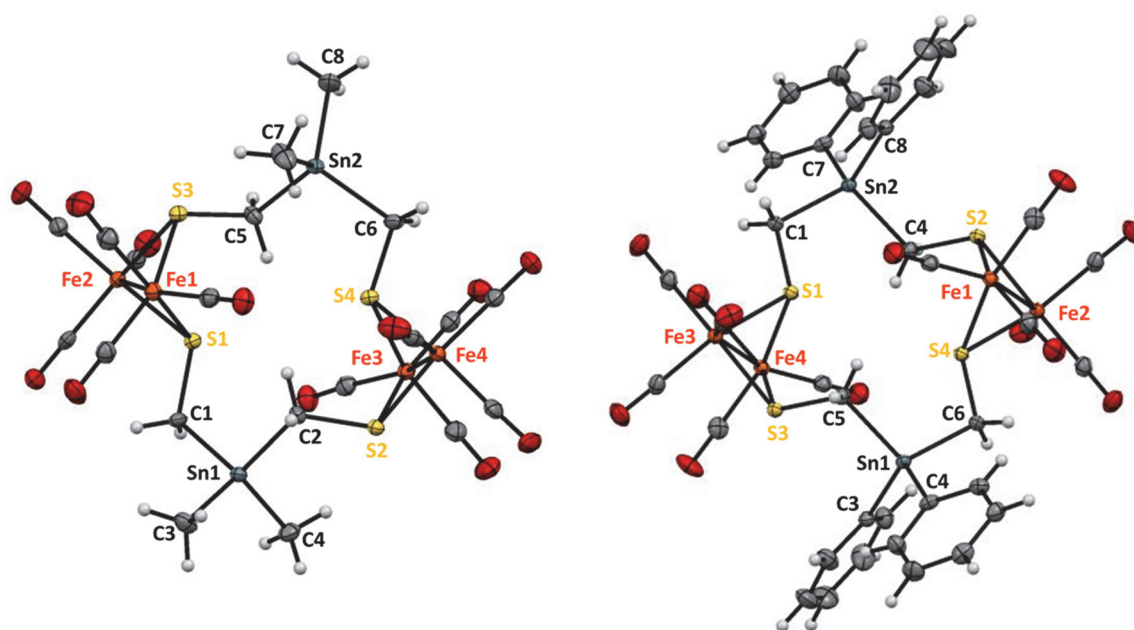
Figure 7-2. Molecular structures (50 % propability) of complexes **152** (to the left) and **154** (to the right).[†]

The average Fe-Fe, Fe-CO and Fe-S bond lengths in **152** (2.5224, 1.797 and 2.2638 Å, respectively) or **154** (2.517, 1.802 and 2.261 Å) are comparable to those in the monomeric complexes **151** and **153**. The angles Sn-C-S in **152** and **154** (107.2-114.08°)

[†] Crystallization of Complex **154** has been done by Hassan Abul-Futouh.

are smaller than those in the monomeric complexes **151** and **153**. Examples of dimeric complexes in which two butterfly [Fe$_2$S$_2$] clusters are part of a macrocycle are rare in the literature and are formed only when the dithiolato linker contains more than three atoms between the two sulfur atoms (-S-CH$_2$-(X)$_n$-CH$_2$-S- (n > 1)).[243,244] In our case, the formation of these macrocycles (**152** and **154**) is allowed by the longer dithiolato linker chain -S-CH$_2$-Sn-CH$_2$-S- due to the large size of the Sn atom and hence the relatively long Sn-CH$_2$ bond (2.174 Å for **152** and 2.171 Å for **154**, in average). Of particular relevance is the dimer [Fe$_2$(CO)$_6$$\{\mu$-(SCH$_2CH_2CH_2$)$_2O\}$]$_2$ (**D**, shown below)[245,246] in which two Fe$_2$S$_2$(CO)$_6$ moieties are connected by CH$_2$(CH$_2$OCH$_2$)$_2$CH$_2$ units forming a 24-membered ring with *e,a,e',a'*-stereochemistry similar to **152** and **154**.

X = CH$_2$CH$_2$OCH$_2$CH$_2$

D
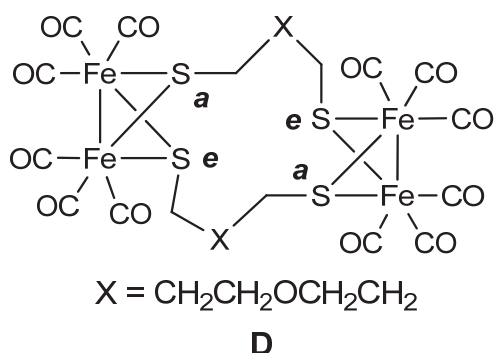
The structures of Fe$_2$S$_2$(CO)$_6$ units of complexes **152** or **154** and **D** are comparable. However, there is a 14-membered ring in complexes **152** or **154**, which results in the Fe$_2$S$_2$(CO)$_6$ units being much closer to each other than those in **D**. The intramolecular distances between Fe and S atoms in one unit and those in the other unit for **152** are listed in Table S7-1. As seen in Table S7-1, the shortest Fe···S distances are 4.841 and 4.874 Å. All of the Fe···S distances involving the Fe atom of one Fe$_2$S$_2$(CO)$_6$ and a S atom of the other cluster in **D** are greater than 7.39 Å.

The crystal structure of **152** or **154** shows that for each Fe$_2$S$_2$(CO)$_6$ unit there is an *a* and *e* CH$_2$ substituent. Typically such *a* and *e* substituents show different chemical shifts in their ^{1}H NMR spectrum. For example, the compound **M** shown below, in which one CH$_2$SnMe$_3$ substituent is *a* and the other is *e*, shows two singlets for the nonequivalent CH$_2$ groups at room temperature.[50] However, surprisingly the nonequivalent *a* and *e* CH$_2$ substituents of complex **152** appear as a singlet at room temperature at 2.00 ppm despite their nonequivalence.

a

CH$_2$SnMe$_3$

e

Me$_3$SnCH$_2$—S   S

(OC)$_3$Fe——Fe(CO)$_3$

M
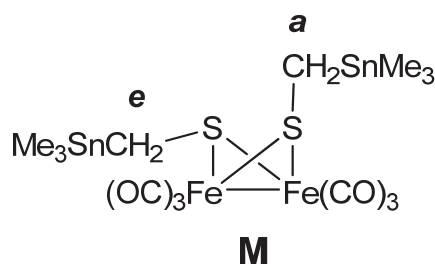
The basis for this unexpected result could be that the *a* and *e* CH$_2$ substituents in **152** undergo interconversion at room temperature or they coincidentally have the same chemical shift. Three mechanisms have been suggested for inversion at sulfur:[247] (*i*) dissociation-recombination, (*ii*) inversion through a trigonal planar state and (*iii*) inversion through a partially dissociated state with metal bonding to both unshared electron-pairs on tetrahedral sulfur. However, it is not apparent why inversion by these mechanisms would be more facile in dimer **152** relative to monomeric **M**. Furthermore, this assumption is validated computationally by DFT calculations on complex **152**.[*] An additional possibility is based on transannular interaction of the two Fe$_2$S$_2$(CO)$_6$ moieties facilitated by the constraints of the cyclic nature of the dimer **152**. This mechanism for a facilitated exchange process in complex **152** is delineated below.

It has been reported that Fe$_2$(SMe)$_2$(CO)$_6$ undergoes stepwise exchange with Et$_2$S$_2$ to provide Fe$_2$(SMe)(SEt)(CO)$_6$ (Scheme 7-3) and then Fe$_2$(SEt)$_2$(CO)$_6$.[248]

Scheme 7-3. Reaction between Fe$_2$(SMe)$_2$(CO)$_6$ and R$_2$S$_2$ (R = Et).[248]
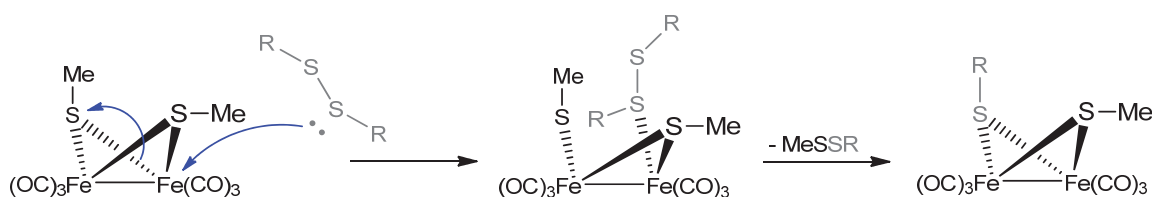
The first step in the mechanism proposed for this exchange (Scheme 7-3) involves nucleophilic attack by the sulfur of Et$_2$S$_2$ on an iron of Fe$_2$(SMe)$_2$(CO)$_6$ displacing MeS. Since EtSH does not participate in the exchange process when substituted for Et$_2$S$_2$ the supernucleophilicity (α-effect) of the disulfide was invoked. Similarly, intramolecular

---

[*] These calculations were done by Glass et al., but are not included in this thesis.

nucleophilic attack by one sulfur atom in complex **152**, perhaps rendered especially nucleophilic by the adjacent C-Sn bond[50,249,250] on the Fe six atoms away thereby displacing a bridging S is proposed. In particular, the electron-pair on the sulfur atoms with equatorial substitutents point towards the Fe atoms of the other Fe_2S_2 unit (and are aligned with the adjacent C-Sn bond). Note as well from Table S7-1 that the Fe(3)···S(1) (which bears an equatorial substituent) and Fe(2)···S(4) (which is equatorially substituted) are only 4.874 Å and 4.841 Å in the crystal. Nucleophilic attack on Fe(1) by S(4) followed by Fe-S cleavage of either Fe-S bond generates intermediate **I1** or intermediate **I2** (Scheme 7-4).

Alternatively, S(1) can attack the Fe across the ring forming **I3** or **I4** (Scheme 7-4). In each case, the divalent sulfur now has two unshared electron-pairs either of which can effect displacement of the tetracoordinated sulfur regenerating the starting material **152** or the isomer with inverted sulfur, i.e. **I1**, **I2**, **I3**, and **I4** can reclose to the *a,a,e',a'-*, *e,e,e',a'-*, *e,a,e',e'-*, and *e,a,a',a'-*isomers, respectively, or to the starting *e,a,e',a'-*stereoisomer. In effect, the sulfur with an equatorial substituent in one Fe_2S_2 unit can epimerize the sulfur atoms of the other Fe_2S_2 unit. These transannular interactions between the Fe_2S_2 clusters provide a route for equilibrating the *e,a,e',a'-*isomer to the *a,e,a,'e'-*isomer which renders the CH_2 and Me's equivalent on the NMR time scale. Some possible pathways are shown in Scheme 7-5. As noted in Scheme 7-5, isomers other than the *e,a,e',a'-*isomer are postulated. All of these possibilities have been evaluated computationally using DFT. Linear transit from **152** to **I1-I4** show substantial barriers of 20 kcal·mol⁻¹ or greater for the proposed intramolecular interactions and coupling these interactions provide even greater barriers. Thus, no low energy pathway for *a*, *e* interconversion has been found computationally.*

---

* As mentioned before, these calculations were done by Glass et al., but are not included in this thesis.

Scheme 7-4. Possible transannular interactions in complex **152** leading to four possible intermediates **I1** to **I4**. All CO and Me ligands are omitted for clarity.
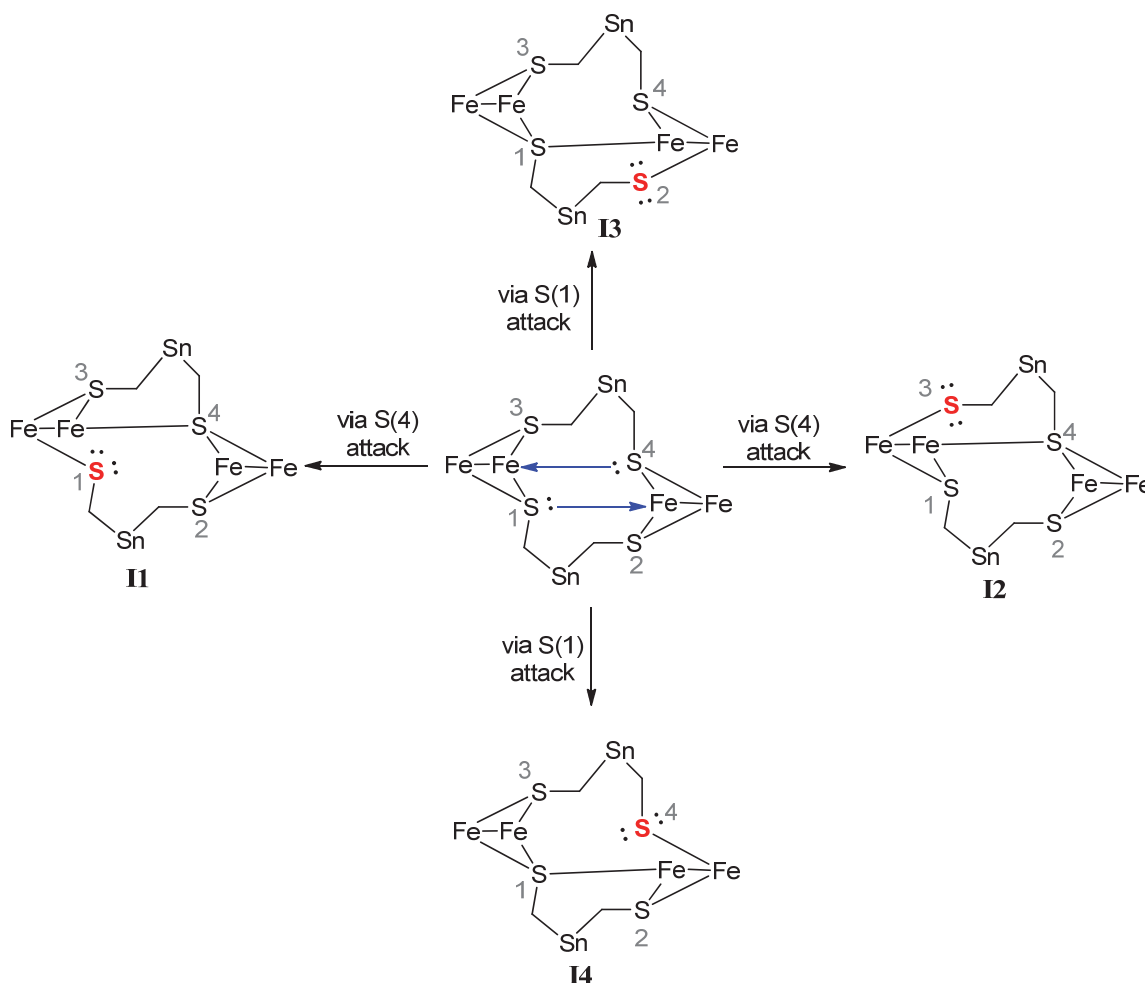
Scheme 7-5. Possible pathways for equilibrating *e,a,e',a'*- and *a,e,a,'e'*-**152**.
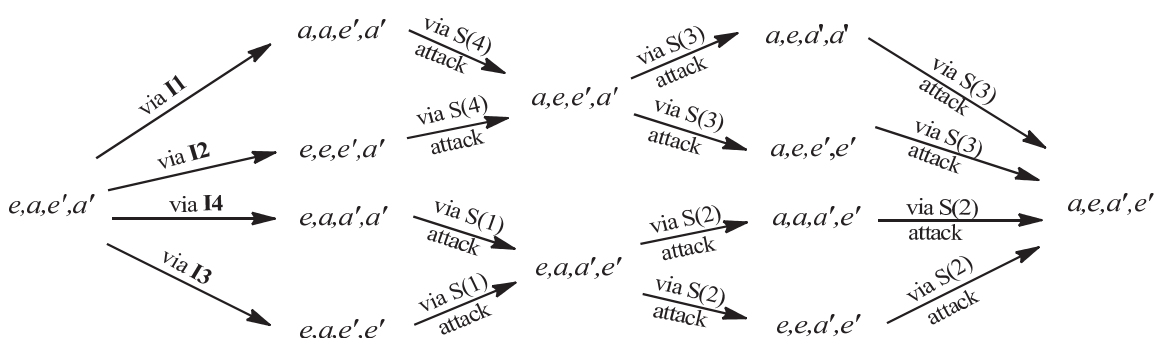
To provide experimental insights into the possible *a*, *e* interconversion in **152**, variable temperature ^{1}H NMR spectroscopic studies were undertaken. The results for the CH_2 absorptions in $CDCl_3$ at various temperatures are shown in Figure 7-3.
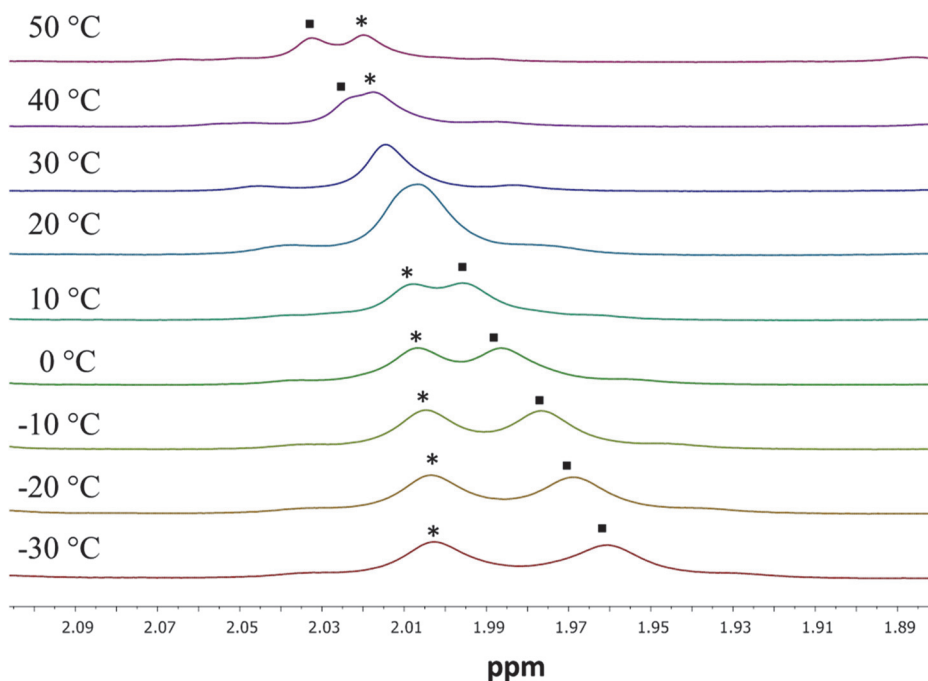
Figure 7-3. Variable temperature ^{1}H NMR spectra of compound **152** ($CDCl_3$ solution) in 1.9-2.1 ppm region.

Interestingly, as the temperature is lowered, two CH_2 absorptions are observed. It would appear that coalescence occurs at about room temperature. Typically if coalescence is due to going from the slow exchange regime to fast exchange there is peak broadening. This is not observed in Figure 7-3, but it should be noted that the chemical shifts of both CH_2 moieties are temperature dependent. Thus the upfield absorption at -30 ºC shows a greater downfield chemical shift change with temperature than the downfield peak resulting in their overlap at 22 ºC. At temperatures higher than 22 ºC, the singlet is splits into two peaks again, where the downfield peak in this case is the upfield absorption at -30 ºC. Therefore, based on the computational results and variable temperature NMR spectroscopic results we conclude that the singlet observed at room temperature for **152** is due to coincidental chemical shift overlap for the nonequivalent *a* and *e* CH_2 moieties and not conformational isomerization (fluxionality).

7.2   Conclusions

This chapter elucidates the influence of the size of the bridgehead heteroatoms on the structural parameters α (flap angle) and τ (torsion angle) of the diiron dithiolate complexes. The angle α is *a measure of distortion of the dithiolato ligand* from *planarity* whereas the angle τ is *a measure of distortion of the two Fe(CO)₃ units from being in a fully eclipsed conformation*. Scheme 7-6 summarizes how α and τ of $[Fe_2(CO)_6\{\mu\text{-}(SCH_2)_2XR_2\}]$ models is altered by changing X (X = C, Si, Ge, Sn) and R.

Scheme 7-6. Variation of α and τ of $[Fe_2(CO)_6\{\mu\text{-}(SCH_2)_2XR_2\}]$-hydrogenase models by changing X (X = C, Si, Ge, Sn) and R.

12
Flap angle = 135.74°
Torsion angle = 5.7°

25
Flap angle = 150.02°
Torsion angle = 0.0°

150
Flap angle = 175.19°
Torsion angle = 7.9°

Flap angle increases

3
Flap angle = 137.09°
Torsion angle = 0.0°

153
Flap angle = 152.49°
Torsion angle = 7.5°

151
Flap angle = 173.61°
Torsion angle = 5.2°
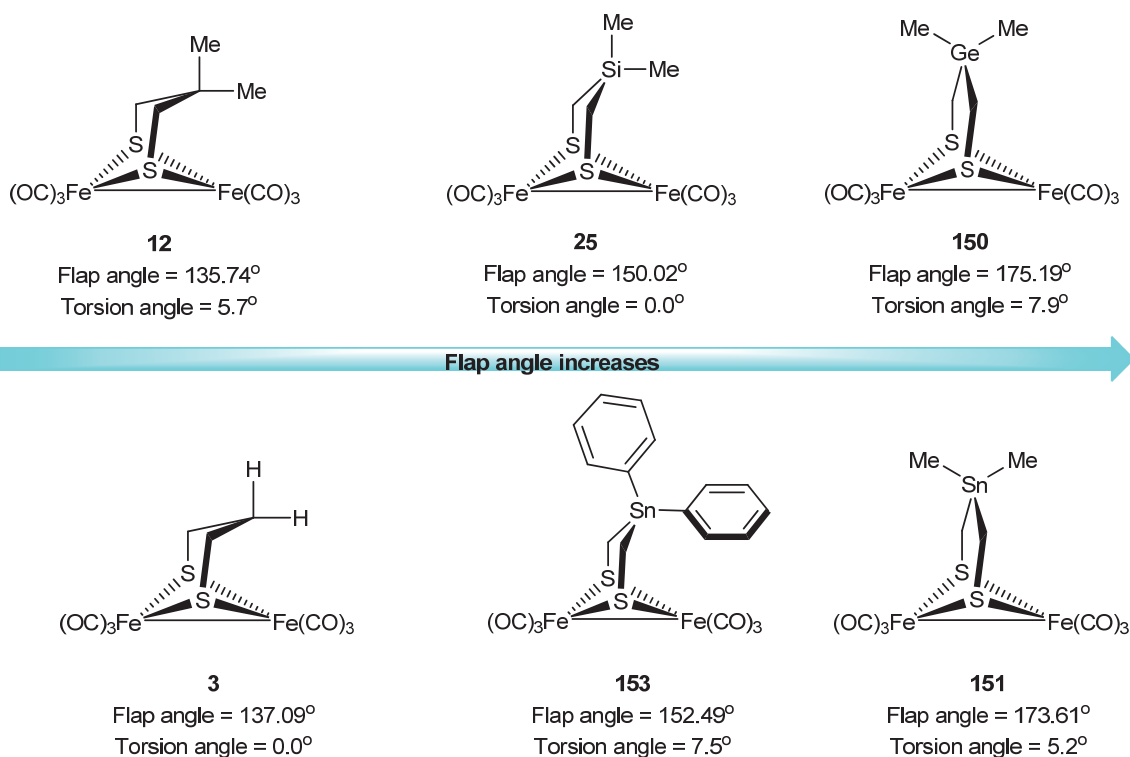
The typical structure of the μ-dithiolato ligands is the chair/boat conformation. As the size of the group IV bridgehead atom X of $[Fe_2(CO)_6\{\mu\text{-}(SCH_2)_2XMe_2\}]$ increases on going from C to Si, α increases by ~ 14° to relax the strain at the [Fe₂S₂] core (τ = 0.0° for **25**) whereas the increase reaches ~ 40° ongoing from C to Ge or Sn leading to a planar μ-$(SCH_2)_2XMe_2$. Complexes **150** and **151** reduce the strain at the diiron units not only though the planarization of the μ-dithiolate, but also a slight rotation of one Fe(CO)₃ unit

is necessary because of the bulkiness of the GeMe$_2$ and SnMe$_2$. The presence of Ph groups in complex **153** stabilizes the usual chair/boat conformation to minimize the steric strain between the CH$_2$S protons and the protons of the Ph rings.

Reaction of dithiolate Fe$_2$S$_2$(CO)$_6^{2-}$ with R$_2$Sn(CH$_2$I)$_2$ unexpectedly affords (in addition to monomers **151** and **153**) a dimeric products in which two -CH$_2$-SnR$_2$-CH$_2$- units bridge two Fe$_2$S$_2$(CO)$_6$ units. The long Sn-C bonding makes the formation of these dimers possible. The structures of the dimers **152** and **154** were unequivocally established by single crystal X-ray crystallographic methods. In the solid state each Fe$_2$S$_2$(CO)$_6$ unit has a nonequivalent axial and equatorial -CH$_2$- substituent, which is similar to all other reported dimers. Solution ^{1}H NMR spectroscopic studies show that these -CH$_2$- units coincidentally have the same chemical shift at room temperature, but split by increasing the temperature.

Chapter 8

Synthesis and Characterization of Ni^II, Pd^II and Pd^II Complexes Containing Carbamodithioato or Carbamoselenothioato Ligands

(Publication 4 and Manuscript 5)
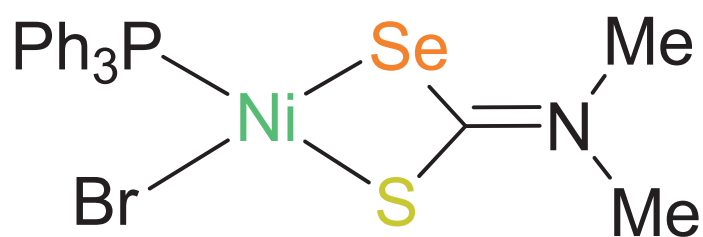
8 Synthesis and Characterization of Ni^{II}, Pd^{II} and Pt^{II} Complexes Containing Carbamodithioato or Carbamoselenothioato Ligands

The carbamodithioate ligands (R$_2$NCS$_2^-$) are versatile ligands capable of bonding to transition as well as main group metals.[251-254] These ligands have been widely investigated because of their importance in fields such as chemical industry, biology and biochemistry.[255-260] Coordination complexes of carbamodithioate ligands of Ni, Pd and Pt are known in the literature.[261-269] Complexes of Pt^{II} and Pd^{II} containing carbamodithioate groups together with mono- or diamine ligands are described by Faraglia and others.[267-270] These complexes include neutral complexes [M(S$_2$CNR$_2$)(amine)(Cl)] or cationic complexes such as [M(S$_2$CNR$_2$)(amine)$_2$]$^+$. Some of these complexes were tested in vitro against KB tumor cells; sub-line of the ubiquitous KER-ATIN-forming tumor cell line Hela. The derivatives [M(S$_2$CNEt$_2$)(bipy)]$^+$ and [M(S$_2$CNEt$_2$)(phen)]$^+$ showed antitumor activity against leukemic cells.[271] The analogous L-methioninol (= Mol) [M(S$_2$CNR$_2$)(Mol)]$^+$ (R = Me, CH$_2$CO$_2$Et) complexes have been prepared by the reaction of L-methioninol with [M(S$_2$CNR$_2$)Cl]$_n$ in a 1:1 molar ratio, while reaction of the same reactants in 1:2 molar ratio gave the binuclear species [M$_2$(S$_2$CNR$_2$)$_2$(Mol)Cl$_2$].[272]

Complexes of Pd and Pt with mixed tertiary phosphines and carbamodithioates have also been described by several groups.[273-278] The interaction of (Ph$_2$P(CH$_2$)$_n$PPh$_2$)PdCl$_2$ (n = 1-4) with R$_2$NCS$_2^-$ in MeCN gave the chelate complexes [(Ph$_2$P(CH$_2$)$_n$PPh$_2$)PdS$_2$CNR$_2$]$^+$.[273,276] The analogous Pt and Ni complexes [(Ph$_2$P(CH$_2$)$_2$PPh$_2$)M(S$_2$CNEt$_2$)]$^+$ were made in a similar way.[277] Complexes of Pt^{IV} and Pd^{II} of the type [Pt(S$_2$CNR$_2$)$_2$(PPh$_3$)Cl$_2$] and Pd(S$_2$CNR$_2$)$_2$PPh$_3$ were prepared from the corresponding dichlorides; [Pt(S$_2$CNR$_2$)$_2$Cl$_2$] or [M(S$_2$CNR$_2$)$_2$] suspended in CS$_2$, with phosphines dissolved in toluene.[278] In addition, the preparation of CpRu(PPh$_3$)(S$_2$CNC$_4$H$_8$) using ammonium pyrrolidinedithiocarbamate and the chloride CpRu(PPh$_3$)$_2$Cl is reported.[279] The dithiocarboxylates CpRu(PPh$_3$)S$_2$CR (R = 2-C$_4$H$_3$O, 2-C$_4$H$_3$S, C≡CR') have been obtained by a similar substitution reaction.[280]

This chapter describes the interaction of ammonium pyrrolidinedithiocarbamate with (PPh$_3$)$_2$MX$_2$ (for M = Ni, X = Br and for M = Pd or Pt, X = Cl) and (dppe)MCl$_2$ (M = Pd, Pt), which gave different products depending on the phosphine ligands and the molar

ratio of reactants, **155-160**. In general, coordination of chelating ligands with S-donor atoms to M^{II} metallic centers (M = Ni, Pd or Pt) forms stable complexes explaining the presence of numerous known complexes of this type in the literature.[261-269] In comparison, few coordination complexes of Ni^{II} attached to both S- and Se-donor atoms of a chelating ligand are known in the literature.[281] Among these complexes, only two complexes [Ni(L^{Se})(Mes^{Se})]$^-$ and [Ni(L^{Se})(Mes^{S})]$^-$ (L^{Se} = tridentate ligand with thiolate and selenolate donors, Mes^{Se} = mesityl selenolate) contain S- and Se-donor atoms of a chelating ligand. However, crystallographic disorder of the S and Se atoms in L^{Se} did not allow discussion of Ni-L^{Se} bonding.[281b] In this chapter, the synthesis and characterization of the first Ni^{II} complex (to the best of my knowledge) with $\kappa^2 S,Se$-bidentate ligand, namely (PPh$_3$)NiBr($\kappa^2 S,Se$-SSeCNMe$_2$) (**161**) is described. X-ray crystallographic determinations reveal the presence of six independent molecules in the crystal of **161**.

8.1 Results and Discussion

8.1.1 Synthesis and Characterization of the Carbamodithioate Complexes

Stirring a THF solution of equimolar amounts of (PPh$_3$)$_2$MCl$_2$ and the carbamodithioate ligand (NH$_4$S$_2$CNC$_4$H$_8$) in THF resulted in the formation of the (PPh$_3$)MCl($\kappa^2 S,S$-S$_2$CNC$_4$H$_8$) complexes (Scheme 8-1).

Scheme 8-1. Synthesis of complexes **155-158**.

155 (M = Ni, X = Br)
156 (M = Pd, X = Cl)
157 (M = Pt, X = Cl)

158
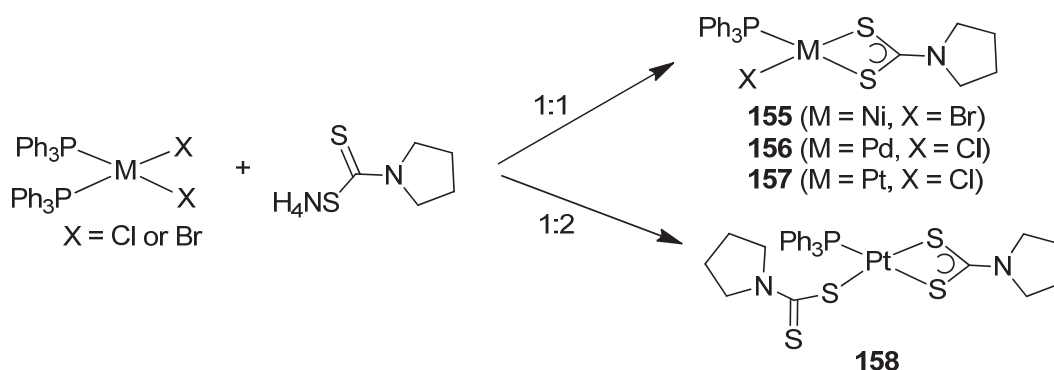
Another synthetic procedure is reported for complex **155** in 1996 by Pastorek et al.[282] and complex **157** has been recently prepared with a method[283] different from that in

Scheme 8-1. Complex **156**, which has a chloride, one PPh$_3$ and one chelated dithiocarbamato ligands, has been characterized by spectroscopic methods, elemental analysis and structural determination. The ^{1}H NMR spectrum of complex **156** contains the resonances of the pyrrolidine protons at 1.97 and 3.55 ppm. The multiplet at 7.31-7.64 ppm is due to the phenyl protons. The single P atom reveals its presence at 30.6 ppm in its ^{31}P{^{1}H} NMR spectrum. The ^{13}C{^{1}H} NMR spectrum of complex **156** shows six resonances corresponding to the six different carbon types in which the CS_2-carbon appears at 200.5 ppm.

Treating (PPh$_3$)$_2$PtCl$_2$ with 2 equiv. of the carbamodithiolato ligand (NH$_4$S$_2$CNC$_4$H$_8$) gave complex **158**, which has both terminal and chelating thiocarbamato ligands in addition to one PPh$_3$ ligand. The analogous reaction of the Pd-species produced only yellow insoluble materials regardless of the reaction solvent. Complex **158** is stable in the solid state and in solution. The ^{1}H NMR spectrum of complex **158** shows the presence of two sets of the two different methylene protons of the pyrrolidine rings. The first set appears as multiplets due to the CH$_2$ groups remote from the N atom at 1.95 and 2.04 ppm, while the other set is assigned to the CH$_2$ groups bonded to nitrogen, appearing as triplets at 3.60 and 3.91 ppm. In the ^{13}C{^{1}H} NMR spectrum of complex **158**, the methylene carbon atoms also show different signals, at 25.1 and 26.1 ppm for one set and at 50.8 and 55.1 for the set bonded to nitrogen. In addition, the spectrum contains three peaks for the carbon atoms of the phenyl groups of the PPh$_3$ ligand and a weak peak at 200.5 ppm for the carbon atom bonded to the two sulfur atoms. In the ^{31}P{^{1}H} NMR spectrum of complex **158**, one singlet at 17.43 ppm with platinum satellites ($J_{\text{P-Pt}}$ = 4603 Hz) is observed. The mass spectrum of complex **158** displays the molecular ion peak at m/z = 749 g/mol, in addition to peaks related to the fragmentation of this molecule.

The reaction of the bis(diphenylphosphino)ethane complexes (dppe)MCl$_2$ (M = Pt, Pd) with carbamodithioate ligand afforded the salts [(dppe)Pd(κ^2S,S-S$_2$CNC$_4$H$_8$)]Cl (**159**) and [(dppe)Pt(κ^2S,S-S$_2$CNC$_4$H$_8$)]Cl (**160**) as shown in Scheme 8-2.

Scheme 8-2. Synthesis of complexes **159** and **160**.

M = Pd (**159**), Pt (**160**)
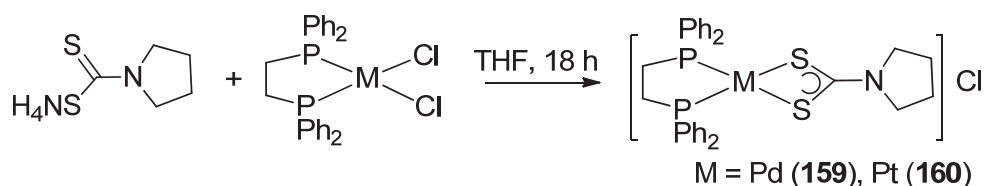
These complexes are stable both in solution and in the solid state and are soluble in polar organic solvents. The ^{1}H NMR spectra of complexes **159** and **160** show the two methylene groups of the pyrrolidine ring in the ranges of 1.95-2.05 and 3.71-3.74 ppm, which are comparable to those of complexes **156** and **158**. The ethylene group of the dppe ligand resonates at 2.81 and 2.89 ppm for **159** and **160**, respectively. The spectra of complexes **159** and **160** also show phenyl resonances in the range of 7.44-7.79 ppm. The ^{13}C{^{1}H} NMR spectra of **159** and **160** show the methylene groups of the pyrrolidene ring at 28.2 and 49.8 ppm for **160** and at 28.7 and 53.3 ppm for **159**, with that of the dppe ligand at 49.6 and 44.0 ppm for **160** and **159**, respectively. The spectra also show a singlet at 200.3 and 201.6 ppm for **160** and **159**, respectively, which is assigned to the CS_2-carbon. The ^{31}P{^{1}H} NMR spectrum of complex **160** shows a singlet at 46.6 ppm with a Pt-satellites (J_{P-Pt} = 3888 Hz) and that of complex **159** shows a singlet at 63.3 ppm. The mass spectra of complexes **159** and **160** show the molecular peak as [(dppe)M(S$_2$CNC$_4$H$_8$)]$^+$.

Crystal structures of Complexes 156, 158 and 159. Crystals suitable for X-ray diffraction analysis of **155**, **156** or **159** were obtained from CHCl$_3$/pentane solutions at 4 °C. In case of **158**, the crystals were obtained by diffusion of pentane into a CH$_2$Cl$_2$ solution at 4 °C. Molecular structures of the complexes (PPh$_3$)Ni(Br)(κ^2S,S-S$_2$CNC$_4$H$_8$) (**155**) (PPh$_3$)Pd(Cl)(κ^2S,S-S$_2$CNC$_4$H$_8$) (**156**), (PPh$_3$)Pt($\kappa S,S_2$CNC$_4$H$_8$N)(κ^2S,S-S$_2$CNC$_4$H$_8$) (**158**) and [(dppe)Pd(κ^2S,S-S$_2$CNC$_4$H$_8$)]Cl (**159**) with the atom numbering schemes are shown in Figures 8-1 to 8-4, respectively. The crystals of these complexes contain solvent molecules, which are omitted from the views of Figures 8-1 to 8-4. Selected bond distances and angles for the structures of complexes **156**, **158** and **159** are summarized in Table 8-1.
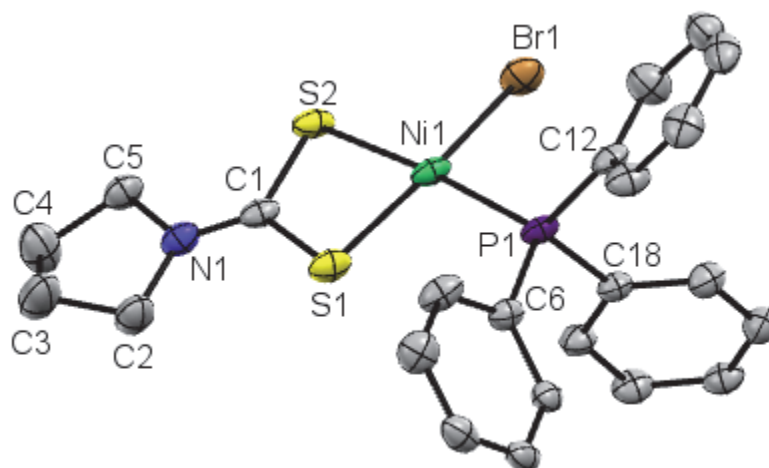
Figure 8-1. Molecular structure (50 % probability) of complex **155**.[††]
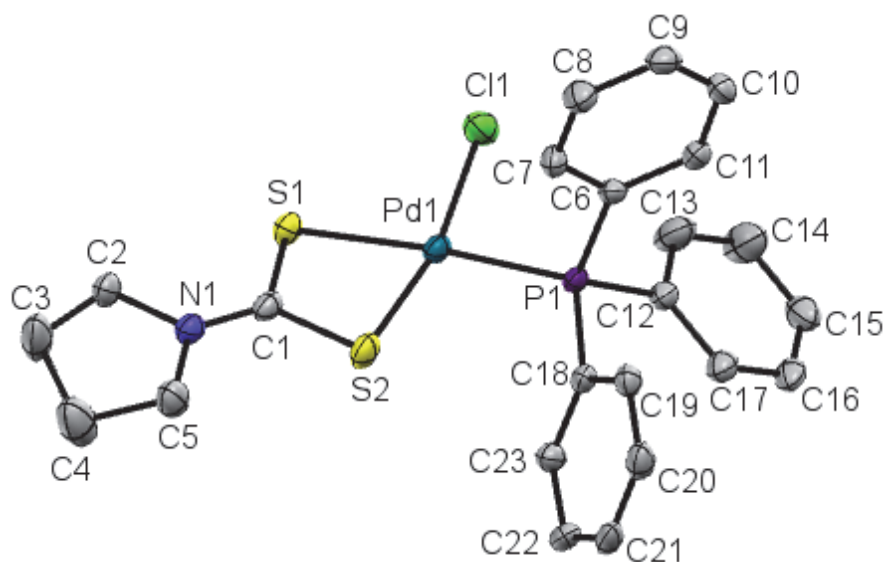
Figure 8-2. Molecular structure (50 % probability) of complex **156**.

[††] The crystal structure of complex **155** has been also determined by Pastorek et al..[282]
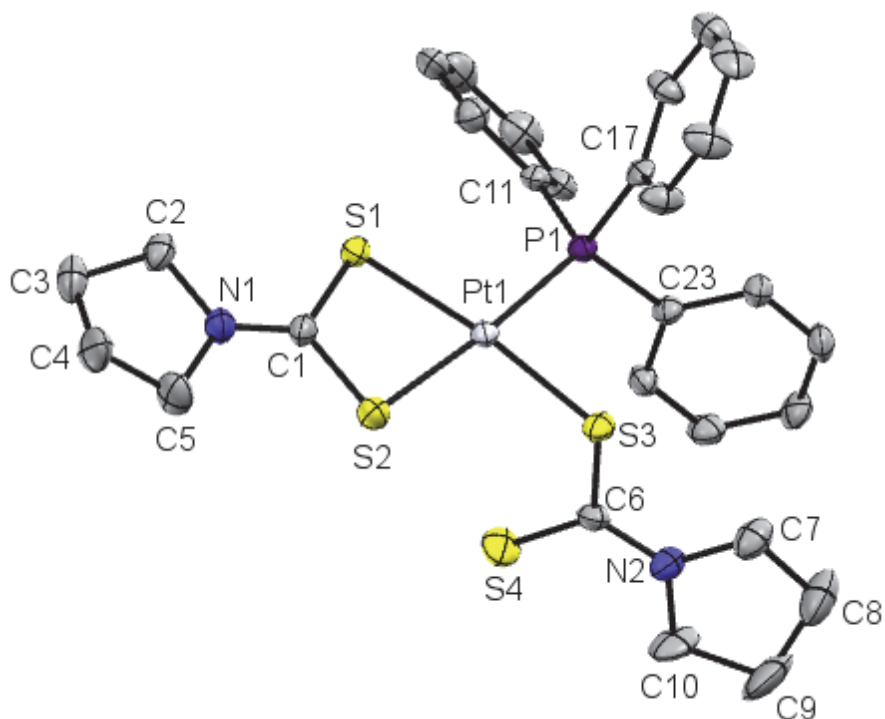
Figure 8-3. Molecular structure (50 % probability) of complex **158**.
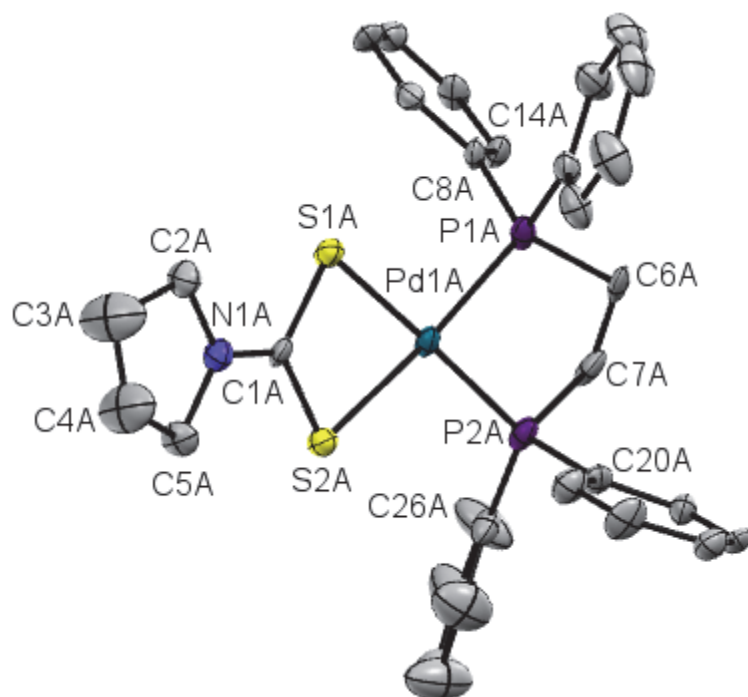
Figure 8-4. Molecular structure (50 % probability) of complex **159**.

Table 8-1. Selected bond lengths [Å] and bond angles [º] of (PPh₃)Pd(Cl)($\kappa^2 S,S$-S₂CNC₄H₈) (**156**), (PPh₃)Pt(κS,S₂CNC₄H₈)($\kappa^2 S,S$-S₂CNC₄H₈) (**158**) and [(dppe)Pd($\kappa^2 S,S$-S₂CNC₄H₈)]Cl (**159**).

156		158		159				
				Molecule	A	B	C	D
Pd-P1	2.2853(9)	Pt-P1	2.2537(17)	Pd-P1	2.2722(2)	2.271(2)	2.2750(2)	2.258(2)
Pd-S2	2.2886(11)	Pt-S3	2.3270(16)	Pd-P2	2.272(2)	2.2663(2)	2.289(2)	2.2827(2)
Pd-Cl1	2.3354(12)	Pt-S1	2.3360(15)	Pd-S1	2.340(2)	2.3514(2)	2.346(2)	2.3449(2)
Pd-S1	2.3503(9)	Pt-S2	2.3603(18)	Pd-S2	2.3603(2)	2.364(2)	2.3601(2)	2.361(2)
S1-C1	1.708(4)	S1-C1	1.725(7)	S1-C1	1.722(7)	1.711(9)	1.724(7)	1.717(9)
S2-C1	1.738(4)	S2-C1	1.716(7)	S2-C1	1.704(8)	1.734(7)	1.716(9)	1.740(7)
N1-C(1)	1.302(5)	S3-C6	1.740(7)	N1-C1	1.336(9)	1.316(10)	1.316(9)	1.306(10)
		S4-C6	1.692(7)					
P1-Pd-S2	96.57(4)	P1-Pt-S3	89.42(6)	P1-Pd-P2	85.47(8)	84.99(7)	84.73(8)	84.20(7)
P1-Pd-Cl1	94.58(4)	P1-Pt-S1	100.62(6)	P1-Pd-S1	97.21(7)	101.37(7)	96.99(8)	100.13(7)
S2-Pd-S1	75.61(4)	S3-Pt-S2	95.09(6)	P2-Pd1-S2	101.32(7)	98.27(7)	102.71(8)	100.45(7)
Cl1-Pd-S1	92.99(4)	S1-Pt-S2	74.77(6)	S1-Pd-S2	75.83(7)	75.63(7)	75.40(7)	75.89(7)
C1-S1-Pd	85.75(13)	C1-S1-Pt	86.9(2)	C1-S1-Pd	84.5(3)	85.5(2)	85.4(3)	85.7(2)
C1-S2-Pd	87.03(15)	C1-S2-Pt	86.3(2)	C1-S2-Pd	84.2(2)	84.7(3)	85.2(2)	84.7(3)

The Pd-S distance (2.2886(11) Å) and the Pd-P bond length (2.2853(9) Å) of **156** lie within the range found for the complexes (PPh$_3$)Pd(Cl)(κ^2S,S-S$_2$CNEt$_2$) and (PPh$_3$)Pd(κ^2S-S$_2$PPh$_2$)(κ^2S,S-S$_2$-PPh$_2$).[284,285] The chelate S-Pd-S angle of **156** is contracted to 75.61(4)° leaving more space for the other angles around Pd that are in the range of 92.99(4)-96.57(4)°. For compound **158**, the Pt-S distances of the chelating carbamodithioate ligand of 2.3360(15) and 2.3603(18) Å are longer than the Pt-S distances (terminal: 2.3270(16) Å) within the same molecules. The Pt-P bond length in **158** is 2.2537(17) Å. These values are also comparable to those found in the diethylcarbamato analog (PPh$_3$)Pt(κS,S$_2$CNEt$_2$)(κ^2S,S-S$_2$CNEt$_2$).[286] The S-Pt-S chelate angle of 74.61(14)° is smaller than the corresponding S-Pt-S and P-Pt-S bond angles within **158**.

The crystals of compound **159** contain four independent molecules, only one of which is shown in Figure 8-4. The Pd-S (2.340(2)-2.364(2) Å) and Pd-P (2.289(2)-2.258(2) Å) bond distances for **159** are similar to those found in **156** and other reported systems.[284,285] Compound **159** contains two chelate rings with S-Pd-S angles of 75.89(7)-75.40(7)° while the P-Pd-P angle is in the range 84.20(7)-85.47(8)°. The non-chelate P-Pd-S angles are in the range 96.99(8)-102.71(8)°, consistent with a pseudo-square planar structure for this complex.

8.1.2 Synthesis and Characterization of Carbamoselenothioate Ni^{II} Complexes (Unpublished)

Scheme 8-3 displays the synthetic pathway to the carbamoselenothioate Ni^{II} complex (PPh$_3$)Ni(Br)(κ^2S,Se-SSeCNMe$_2$) (**161**). Two possible products are shown in Scheme 8-3, **cis-161** and **trans-161** in which the PPh$_3$ ligand is in *cis* and *trans* fashions to the Se atom of the carbamoselenothioate.

Scheme 8-3. Synthesis of complex **161**.
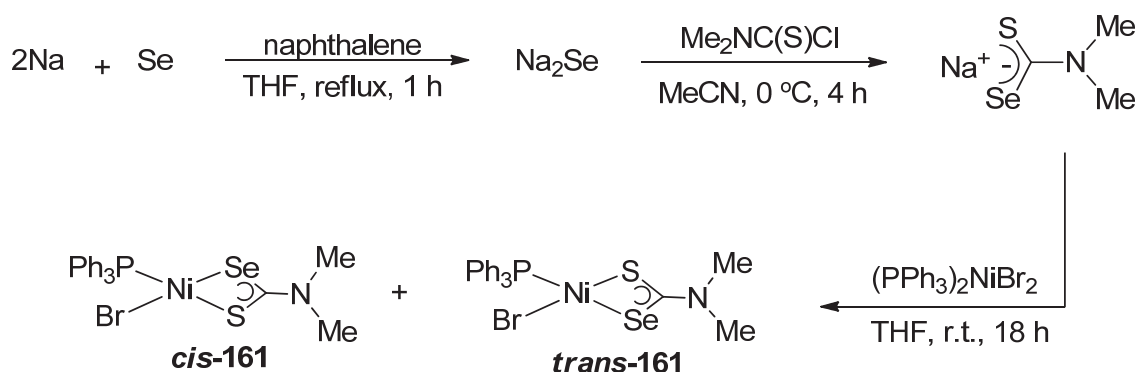
Refluxing a mixture of sodium and selenium powder in the presence of naphthalene (in 2:1:0.2 molar ratio, respectively) in THF gave a white suspension of the highly air sensitive Na$_2$Se. This redox reaction requires ~ 3 h reflux for completion of reduction.[287] Dropwise addition of a solution of N,N-dimethylcarbamoselenothioate, Me$_2$NC(S)Cl, in MeCN to the suspension of *excess* Na$_2$Se in MeCN at 0 °C over 1 h, which was followed by further 3 h stirring at the same temperature afforded a yellow powder of sodium N,N-dimethylcarbamoselenothioate, Me$_2$NCSSeNa, after filtration.[288] If the addition of the MeCN solution of Me$_2$NC(S)Cl was not slow, the resulting powder would be orange in colour due to the presence of sodium N,N-dimethylcarbamodiselenoate as well as sodium N,N-dimethylcarbamodithioate as side products. Stirring a mixture of Me$_2$NCSSeNa and (PPh$_3$)$_2$NiBr$_2$ in degassed solvents (MeCN or THF) under inert conditions at r.t. for ~ 18 h gave a violet solution of (PPh$_3$)Ni(Br)(κ^2S,Se-SSeCNMe$_2$) (**161**). The insoluble part was removed by filtration under N$_2$ atmosphere and the solvent was evaportaed using a vacuum transfer line to afford a violet powder of complex **161**. Complex **161** was characterized by ^{1}H, ^{13}C{^{1}H}, ^{31}P{^{1}H} and ^{77}Se NMR spectroscopy as well as mass spectrometry, elemental analysis and X-ray crystallography.

Spectroscopic Characterization of Complex 161. The DEI-MS spectrum of complex **161** shows the molecular ion peak at *m/z* 569 [M]$^+$. In the ^{1}H NMR spectrum, the protons of the nonequivalent methyl groups resonate as singlets at 3.01 and 3.07 ppm. The resonances of the protons of the PPh$_3$ ligand occur in the range 7.40-7.82 ppm as multiplet. The ^{13}C{^{1}H} NMR spectrum of complex **161** displays two signals at 39.09 and 40.41 ppm for the nonequivalent carbon atoms of the CH$_3$ groups. The carbon atoms of the PPh$_3$ ligand of complex **161** resonate in the range 126.1-138.3 ppm. In addition, the ^{13}C{^{1}H} NMR spectrum exhibits a signal due to the CSSe moiety at 198.03 ppm. The

^{31}P{^{1}H} NMR spectrum of complex **161** displays a singlet at 33.27 ppm for the PPh$_3$ ligand. The ^{77}Se NMR spectrum of complex **161** displays a signal at 317.3 ppm.

   Molecular Structures. Single crystal suitable for X-ray structure determination was obtained by diffusion of dry pentane into a dry CH$_2$Cl$_2$ solution of complex **161** under N$_2$ atmosphere at 4 °C. The crystal of complex **161** contains six symmetry independent molecules, only one is shown in Figure 8-5. All of the six structures of complex **161** reveal only the **cis-161** isomer. Table 8-2 summarizes selected bond lengths and angles for complex **161**.
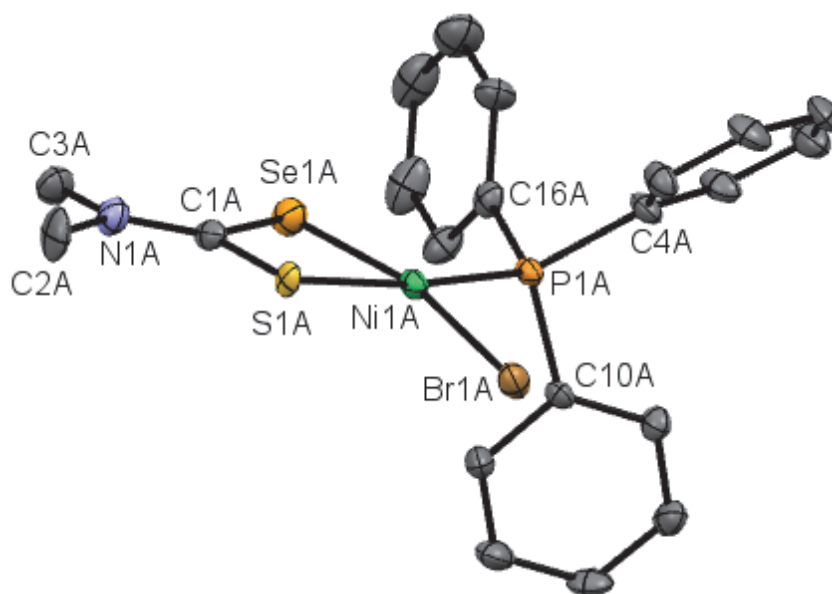
Figure 8-5. Molecular structure (50 % probability) of (PPh$_3$)Ni(Br)(κ^2S,Se-SSeCNMe$_2$) (**161**).

Table 8-2. Selected bond lengths [Å] and bond angles [º] of (PPh$_3$)Ni(Br)(κ^2S,Se-SSeCNMe$_2$) (**161**).

161

Molecule	A	B	C	D	E	F
Ni-P1	2.1987(18)	2.200(2)	2.2010(19)	2.1913(19)	2.2004(17)	2.1973(18)
Ni-S1	2.2460(16)	2.2455(17)	2.2542(16)	2.2502(17)	2.2500(16)	2.2474(16)
Ni-Se1	2.2969(11)	2.3030(12)	2.2966(12)	2.2961(12)	2.2932(11)	2.2967(11)
Ni-Br1	2.3403(10)	2.3267(11)	2.3202(11)	2.3145(11)	2.3384(10)	2.3389(10)
S1-C1	1.744(7)	1.725(8)	1.747(8)	1.724(8)	1.747(7)	1.753(7)
Se1-C1	1.882(6)	1.864(7)	1.868(7)	1.873(7)	1.875(7)	1.877(6)
N1-C1	1.321(9)	1.327(9)	1.303(9)	1.312(10)	1.319(9)	1.316(9)
S-Ni-Se	80.72(5)	80.17(5)	80.17(5)	80.33(5)	80.82(5)	80.65(5)
P-Ni-Br	95.17(6)	93.59(6)	92.33(6)	93.17(6)	95.79(6)	95.25(6)
P-Ni-Se	93.36(6)	96.30(6)	95.73(6)	95.64(6)	93.19(6)	93.48(6)
S-Ni-Br	91.36(5)	89.90(6)	91.79(5)	90.91(5)	91.00(5)	91.34(5)
S-C1-Se	108.4(3)	109.3(4)	108.3(4)	109.2(4)	108.8(4)	108.2(3)
C1-Se-Ni	83.0(2)	82.8(2)	83.7(2)	82.8(2)	83.0(2)	83.4(2)
C1-S-Ni	87.7(2)	87.7(2)	87.8(2)	87.5(3)	87.2(2)	87.7(2)

The average Ni-Se distance of 2.2971 Å in complex **161** is in consistent with that of [(dppe)Ni{κ^2Se,Se-(SeCH$_2$)$_2$C(CH$_2$OH)$_2$}] (2.3029 Å)[289] and [Ni{κ^2Se,Se-(SeCH$_2$)$_2$}$_2$]$^{2-}$ (2.306 Å)[290], but shorter than the Ni-Se distances in [Ni(terpy)(2,4,6-(Me)$_3$C$_6$H$_2$Se)$_2$] (terpy = 2,2′,2″-terpyridine) (2.440(3) Å)[291]. The average Ni-Se distance in complex **161** is shorter than that predicted for the *D. baculatus hydrogenase* (2.46 Å, EXAFS measurements)[292]. In complex **161**, the average Ni-Se bond distance is longer than the average Ni-S distance (2.2489 Å) by 0.0482 Å. The average Ni-S distance in complex **161** is longer than the Ni-S distances observed for various four-coordinate square planar Ni-thiolate complexes (2.14-2.20 Å)[293], but falls into the range of Ni-S$_{cys}$ bond lengths determined for the [NiFe]-hydrogenases (2.2-2.6 Å)[294]. The average S-C1 bond distance in complex **155** (1.723 Å) is very close to that in complex **166** (B and D, Table 8-2), but shorter than the average S-C1 distance (1.748 Å) determined for the other molecules (A, C, E and F) of compound **161**. The Se-C1 distances in complex **161** are longer than the S-C1 distances by at least 0.111 Å because of the larger size of the Se atom compared to the S atom. The E-C1 (E = S or Se) distances in complex **161** are significantly longer than the usual S=C in dithioesters (1.61-1.63 Å)[295] and the Se=C bonds in *S*-organyl selenothioester (1.785(4)-1.792(7) Å)[296]. The S-C1 (1.724(8)-1.753(7) Å) and Se-C1 (1.868(7)-1.882(6) Å) bond lengths in **161** are indeed comparable to the S-C(sp^2) single bonds in dithioesters (1.72-1.74 Å)[295] and the Se-C(sp^2) single bonds in *Se*-organyl selenoesters (1.868(5) Å)[297], respectively. The typical lengths of the N=C and N-C bonds are 1.29 Å[298] and 1.47 Å[299], respectively. Thus, the N-C1 distances determined for complex **161** (1.303(9)-1.327(9), Table 8-2) suggest a double bond character of the N-C1 bonds due to delocalization of the π-electron density over the SSeCN moiety. The above findings propose that the most favored resonance form of complex **161** among those shown in Scheme 8-4 is the one featuring C-S and C-Se single bond characters and C=N.

Scheme 8-4. Resonance forms of complex **161**.
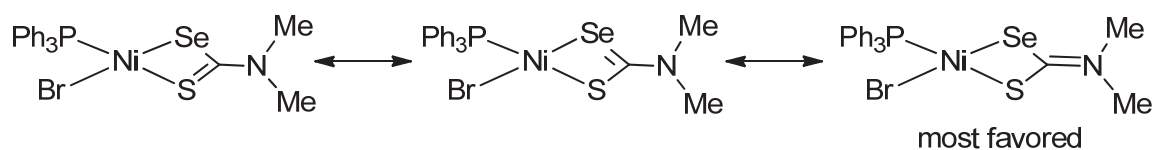
The average bite angle S-Ni-Se of the molecules of compound **161** (80.48º) is larger than the S-Ni-S bite angle in complex **155** (78.72(4)º) whereas the angle S-C1-S in the latter (108.6(2)º) is within the range observed for the S-C1-Se angles of the former (Table 8-2). The average C1-S-Ni bond angle in complex **155** (86.17º) is close to the C1-S-Ni angle in complex **161** while the C1-Se-Ni in the latter (83.1º) is smaller, which could be related to the less *s*-character of the Se atom compared to that of the S atom. The angles around the Ni metallic site in complexes **155** and **161** show deviation from that expected for an ideal square planar structure. Moreover, if we define the NiS$_2$ and the NiSSe as planes of planarity in complexes **155** and **161**, respectively, we find that the Br atoms (or both of the P and the Br atoms) point out of these planes resulting in distorted square planar structures of complexes **155** and **161**. The degree of distortion of the square planar structure can be measured by the dihedral angle Θ between the planes NiSE (E = S (for **155**) or Se (for **161**)) and NiPBr, *the twist angle*. We can notice from Figure 8-6 that molecule C of compound **161** shows the most perfectly planar arrangement of atoms in the [SSeNiPBr] core. In comparison, the P atom of complex **155** lies in the NiS$_2$ plane while the Br atom is displaced, resulting in Θ = 9.02º between the NiS$_2$ and NiPBr planes.
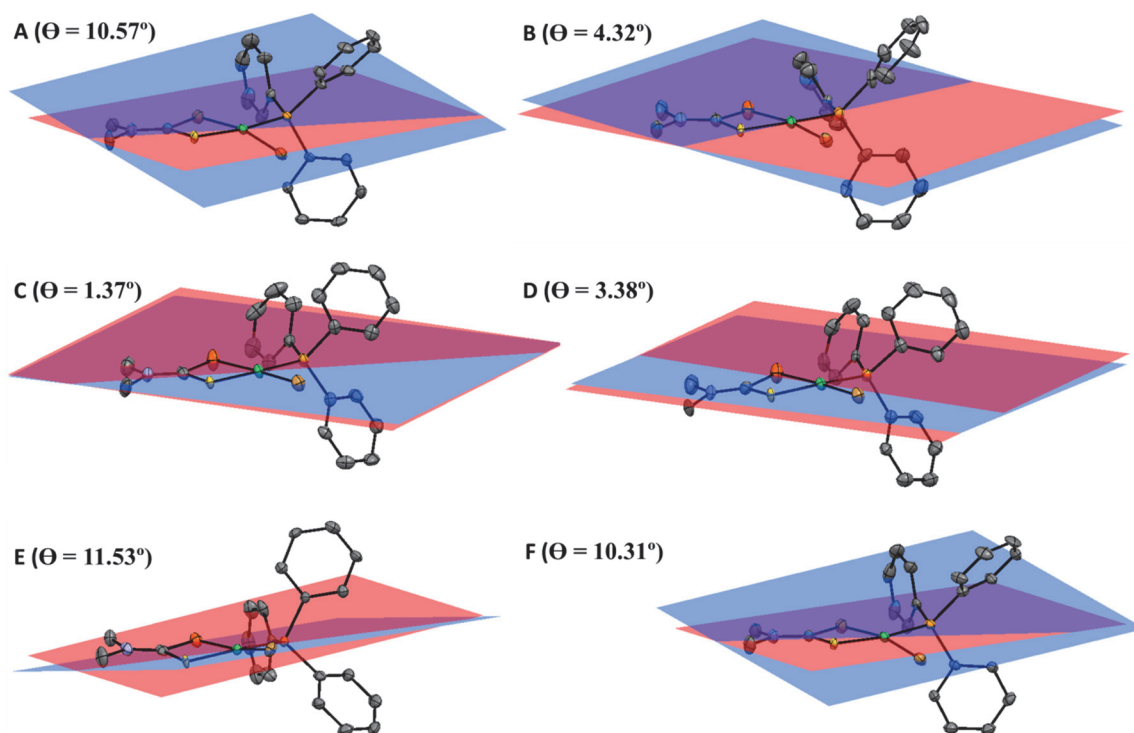
Figure 8-6. Twist angles (Θ in [°]) in the molecules A-F of compound **161**. The NiSSe and NiPBr planes are in red and blue, respectively.

Crystals of Me$_2$CNSSeK has been obtained by slow diffusion of hexane into its degassed dry MeOH solution at -17 °C.[288] When the same method is used to obtain crystals of the salt Me$_2$CNSSeNa, which is used for the synthesis of complex **161** (Scheme 8-3), in a non-degassed non-dry MeOH, X-ray crystallography revealed the formation of diselenide **162** (Figure 8-7) reflecting the higher reactivity of selenolates compared to thiolates toward oxidation. Unlike the yellow salt Me$_2$CNSSeNa, which is soluble in highly polar organic solvents (MeOH, MeCN), compound **162** (orange crystals) is soluble in less polar solvents such as CH$_2$Cl$_2$ and CHCl$_3$.
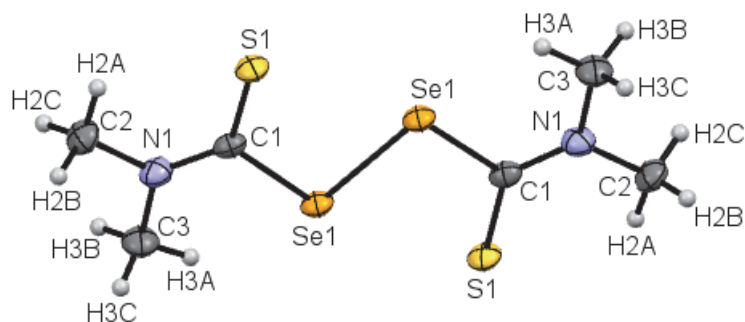
Figure 8-7. Molecular structure of compound **162**.

Compound **162** is almost planar with a C$_{2h}$ symmetry (Figure 8-8). The Se-Se distance in **162** (2.3576(11) Å) is close to the typical distance of the Se-Se single bond (2.32 Å).[299] The S-C1 distances in **162** (1.678(6) Å) are shorter than those in complex **161** (Table 8-2) in which these distances are closer to a single S-C(sp^2) bond. The N-C1 distances of 1.322(8) Å in **162** are comparable to those in complex **161**. The Se-C1 distance in **162** (1.956(6) Å) are longer than those in complex **161**. These findings show that the electronic delocalization occurs on the NCS moiety of **162** while it is on the NCSSe moiety of **161**.
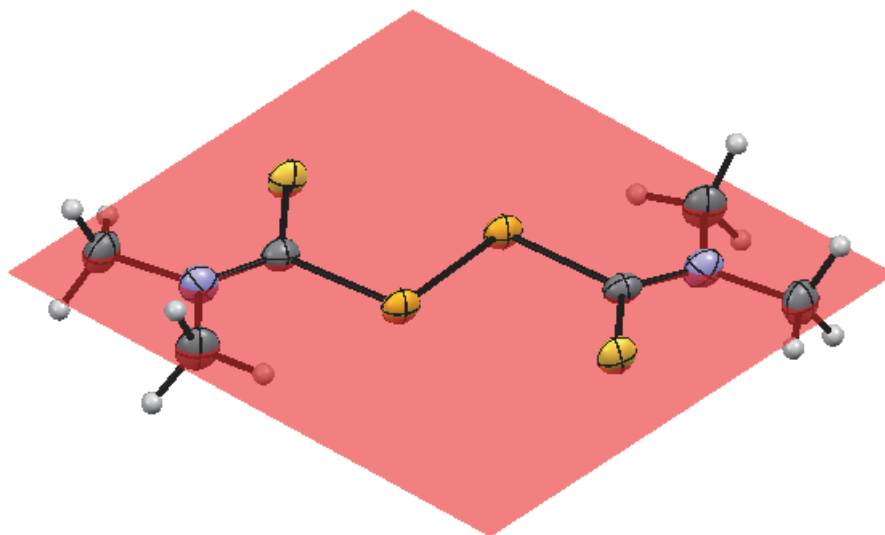
Figure 8-8. Mean plane of twelve atoms in the molecule of compound **162**.

Reaction of Complex 161 with PPh$_3$. It has been reported that the addition of KPF$_6$ in acetone to an acetone solution of PPh$_3$ and (PPh$_3$)Ni(Cl)($\kappa^2 S,S$-S$_2$CNR$_2$) (R = Me, Et, n-Bu), 1:1:1 molar ratio, gives a red product for [(PPh$_3$)$_2$Ni($\kappa^2 S,S$-S$_2$CNR$_2$)]PF$_6$.[300]

Following similar procedure to synthesize [(PPh$_3$)$_2$Ni(κ^2S,Se-SSeCNMe$_2$)]PF$_6$ (**163**) by addition of KPF$_6$ to acetone solution of complex **161** and PPh$_3$ did not show any color change of the violet solution even after stirring for 2 days, which is an indication of no reaction. However, using excess KPF$_6$ showed that the desired product **162** is formed, as indicated by the immediate color change from violet to red. The ^{13}C{^{1}H} NMR spectrum revealed two signals at 40.01 and 41.03 ppm for the nonequivalent CH_3 groups, signal in the range 129-135 ppm for the carbon atoms of the PPh$_3$ ligands and a signal at 194.14 ppm for the sp^2 carbon atom of the Me$_2$NC moiety. However, the ^{1}H NMR spectrum showed four singlets in the region expected for the protons of the CH_3 groups at 3.13, 3.16, 3.18 and 3.21 ppm as well as a multiplet in the region of 7.25-7.58 ppm for the protons of the PPh$_3$ ligands. It is expected that two singlets should be observed in the ^{1}H NMR spectrum of **163**. The presence of four singlets in the region 3.1-3.21 ppm suggests that not only the desired product **163** was formed, but also other products that are anticipated to be [(PPh$_3$)$_2$Ni(κ^2Se,Se-Se$_2$CNMe$_2$)]PF$_6$ and [(PPh$_3$)$_2$Ni(κ^2S,Se-S$_2$CNMe$_2$)]PF$_6$. The ^{31}P NMR spectrum of **163** is expected to display two doublets for the two non-equivalent PPh$_3$ ligands. However, the ^{31}P NMR spectrum is more complicated showing an overlap between the signals related to **163** with those for the possible side products [(PPh$_3$)$_2$Ni(κ^2Se,Se-Se$_2$CNMe$_2$)]PF$_6$ and [(PPh$_3$)$_2$Ni(κ^2S,S-S$_2$CNMe$_2$)]PF$_6$ in the range 30.58-33.48 ppm. All attempts to synthesize **163** following the established procedures failed due to the fast transformation of **163** into (probably) the analogues complexes with [NiP$_2$S$_2$] and [NiP$_2$Se$_2$] cores. By slow diffusion of pentane into the red CH$_2$Cl$_2$ or acetone solution under inert conditions revealed the molecular structure in Figure 8-9 containing [NiP$_2$S$_{0.50}$Se$_{1.50}$] core.
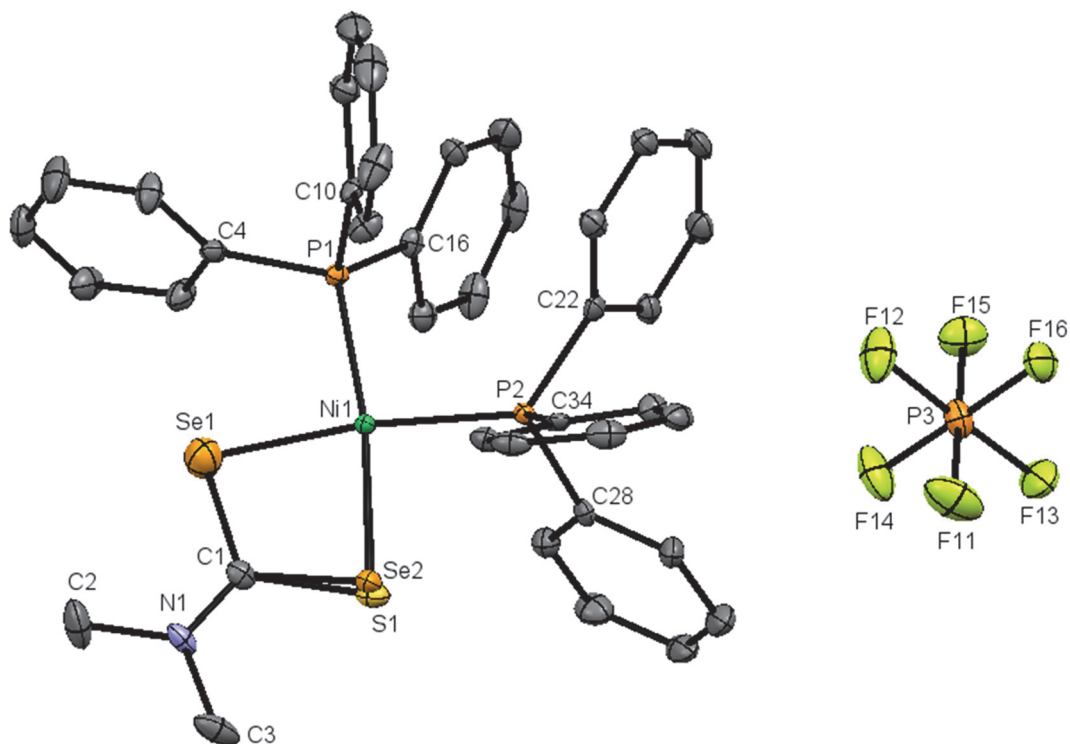
Figure 8-9. Molecular structure obtained from crystallization of the product of the reaction between KPF$_6$ (excess), PPh$_3$ and **161** in acetone under inert conditions.

8.2   Conclusions

The work presented in this chapter shows that either the halo- or the triphenylphosphine ligands of (PPh$_3$)$_2$MX$_2$ (M = Ni, Pd or Pt and X = Cl or Br) can be replaced by the carbamodithiolato or the carbamoselenothiolato ligands. However, only the chloro ligands are replaced by the carbamodithiolato ligand in the case of (dppe)MCl$_2$ complexes. The molecular structures of the synthesized complexes show that the bite angle of the carbamodithiolato ligand, which gives a four-membered chelate ring, is smaller than the angles within the five-membered dppe chelate ring or the other non-chelated angles.

In this chapter, the first molecular structure of a Ni^{II} complex featuring mixed bidentate ligand with S- and Se-donor atoms is reported, complex **161**. The X-ray structural determination shows the presence of six symmetry independent molecules, with distorted square planar structures, in the crystal of compound **161**. The PPh$_3$ ligands in all molecules of **161** are in *cis*-orientation with respect to the Se atoms. The S-C, Se-C

and C-N distances in **161** suggest that the most stable resonance form is the one featuring double bond character between the C(sp^2) and the N atoms.

Chapter 9

Summary / Zusammenfassung

9 Summary

This thesis provides the syntheses and detailed spectroscopic, crystallographic as well as electrochemical investigations of various novel models for the H cluster of the [FeFe]-hydrogenases. The topics of the thesis may be divided into the following parts:

1. Influence of bridgehead heteroatoms or groups of the dithiolato ligand toward the structural, electrochemical and protonation properties of the [FeFe]-hydrogenase models.

2. Influence of the substituents R attached to the bridgehead atoms of the [FeFe]-hydrogenases models toward the structural, electrochemical and protonation properties.

3. Influence of the μ-X atoms of the μ-$(XCH_2)_2C(CH_2OH)_2$ linker on the redox feature of the $[Fe_2X_2]$ cluster, where X = S or Se.

4. Influence of substituting one CO ligand in $[Fe_2(CO)_6\{\mu\text{-dithiolate}\}]$ by PR_3 toward the structural and the electrochemical properties.

5. Mechanistic investigations of the proton reduction catalyzed by $[Fe_2(CO)_6\{\mu\text{-}(SCH_2)_2RP=O\}]$ hydrogenases models.

6. A side project in this thesis describes the synthesis of various carbamodithiolate and carbamoselenothiolate complexes of Ni^{II}, Pd^{II} and Pt^{II} metals.

Part 1
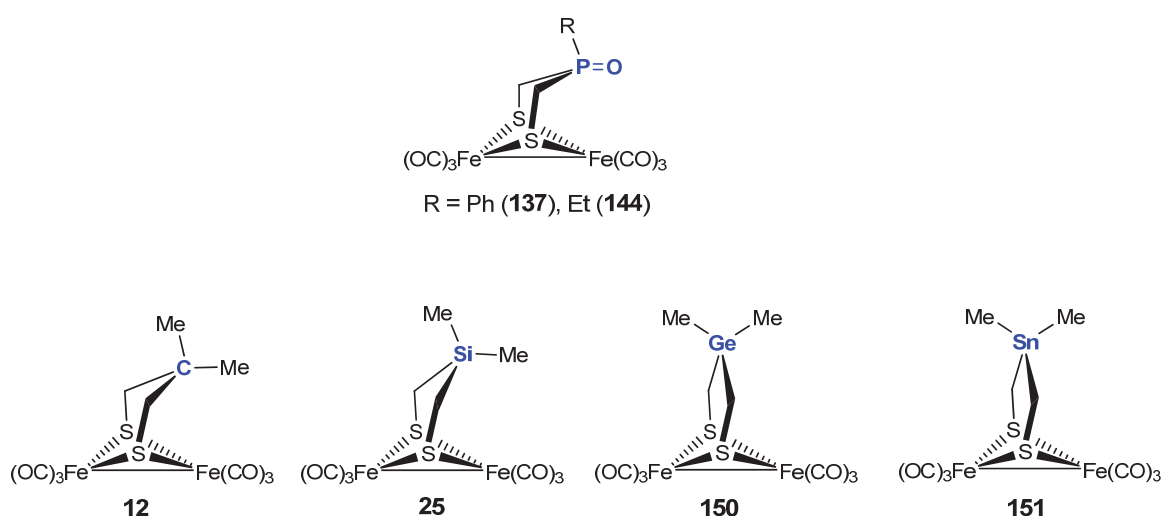
Figure 9-1. Representative [FeFe]-hydrogenase models for part 1.

[FeFe]-Hydrogenases Models with R-P=O moieties in the Bridgehead. X-ray determinations of the complexes **137** and **144** (Figure 9-1) reveal that the P=O functionality is oriented toward one iron center. Furthermore, due to the steric bulk of the R-P=O moiety, the two $Fe(CO)_3$ units are not in eclipsed conformation found for $[Fe_2(CO)_6\{\mu\text{-}(SCH_2)_2CH_2\}]$ (**3**). This steric effect lowers the rotational barrier of the $Fe(CO)_3$ resulting in a facile structural changes during the electron transfer and hence explaining the phenomenon of potential inversion observed for the reduction of these systems. In CH_2Cl_2 solutions, complexes **137** and **144** are protonable at the oxygen atom of the P=O group that was proved by IR and ^{31}P NMR spectroscopic methods as well as cyclic voltammetry in the oxidative region. The P=O-protonation by $HBF_4 \cdot Et_2O$ shifts the $\upsilon(CO)$ bands by 8-10 cm^{-1} to higher wavenumbers and a downfield shift of the resonance signal in the ^{31}P NMR spectrum (~ 35 ppm) is observed. The ion-pairing between the BF_4^- anion and the protonated complex is found to affect the shift of the carbonyl bands $\Delta\upsilon(CO)$ significantly. The DFT calculations on the P=O-protonated complexes show that $\Delta\upsilon(CO)$ is 20 cm^{-1} in the absence of BF_4^- while it is comparable to the experimental value when the $P=O\cdots F\text{-}BF_3$ hydrogen bonding is considered. The crystallization of the protonated P=O-complexes lead to the formation of $P=O\cdots BF_3$ adducts throughout loss of HF (Scheme 9-1):

Scheme 9-1. Formation of $P=O\cdots BF_3$ adducts.
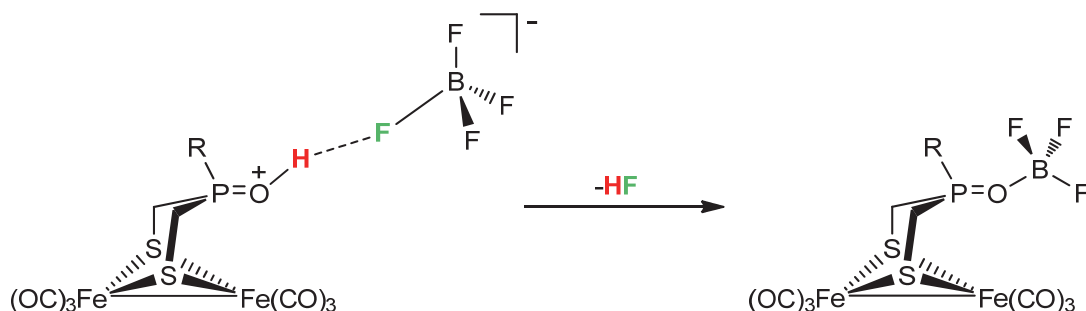
The formation of the $P=O\cdots BF_3$ adducts affects the $\upsilon(CO)$ bands in the IR spectrum and the chemical shift of the $^{31}P\{^1H\}$ NMR resonance less than the protonation, which is due to the weaker Lewis acidity of BF_3 compared to that of H^+. The protonability of the P=O group as well as its orientation toward one iron atom make the P=O-complexes as a

potential proton relay models. The electrochemical investigations show that the P=O-complexes are catalytically active toward the reduction of acids with various strengths.

[FeFe]-Hydrogenases Models with GeMe$_2$ and SnMe$_2$ Bridgehead Groups. The replacement of the bridgehead E group of the dithiolato ligand μ-(SCH$_2$)$_2$E (E = CR$_2$, NR, O, S, Se, R-P=O, SiR$_2$) by E = GeMe$_2$ or SnMe$_2$ results in a unique C$_{2v}$ symmetry of the complex [Fe$_2$(CO)$_6${μ-(SCH$_2$)$_2$E}] in which both FeS$_2$C$_2$E (E = GeMe$_2$ (**150**) or SnMe$_2$ (**151**), Figure 9-1) six-membered rings adopt a half-chair conformation. This conformation is indeed the transition state for the equilibration of the chair/boat conformers of all other complexes. The half-chair conformation may make the filled-filled interaction σ(Ge-C) $\leftrightarrow$ 3p(μ-S) or σ(Sn-C) $\leftrightarrow$ 3p(μ-S) symmetrically allowed. IR protonation studies on [Fe$_2$(CO)$_6${μ-(SCH$_2$)$_2$XMe$_2$}] (X = C (**12**), Si (**25**), Ge (**150**)) in CH$_2$Cl$_2$ solutions using strong acids suggest the presence of an equilibrium between the μ-S-protonated complex (X = Ge or Sn) and the unprotonated form (Scheme 9-2).

Scheme 9-2. Protonation of complex **150**.
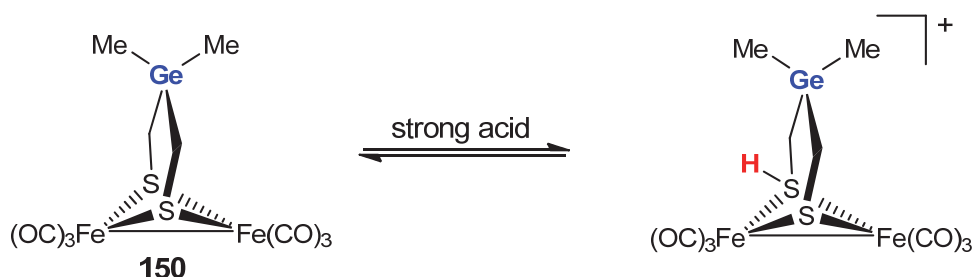
The planarity of the dithiolato linker in the Ge-containing complex **150** may play a role in the enhanced protonation properties of these complexes compared to the case of [Fe$_2$(CO)$_6${μ-(SCH$_2$)$_2$XMe$_2$}] (X = C (**12**), Si (**25**)) complexes. Cyclic voltammetry of [Fe$_2$(CO)$_6${μ-(SCH$_2$)$_2$GeMe$_2$}] (**150**) reveals that it undergoes two-electron reduction with potential inversion due to an ECE process. The reduction of complex **150** is chemically irreversible at low scan rates because of follow-up reactions involving loss of CO and decomposition. Performing the cyclic voltammetry using CO-saturated solutions does not enhance the reversibility because of the reaction between the reduced species of complex **150** and CO affording **150CO^{2-}** that undergoes reversible oxidation at more positive potential than the dianion **150^{2-}**. It is difficult to see the effect of protonation of the neutral complex **150** by cyclic voltammetry because of the requirement of excess

amount of strong acid to detect the protonated species and hence the direct reduction of the acid can be very significant. Thus, further structural modifications are required to increase the protophilicity of the μ-S atoms, such as substituting one or more CO ligands by phosphanes.

Formation of dimeric complexes (Figure 9-2). The reaction of the in situ generated $(\mu\text{-LiS})_2\text{Fe}_2(\text{CO})_6$ with 1 equiv. $\text{R}_2\text{Sn(CH}_2\text{I})_2$ affords the monomeric complexes $[\text{Fe}_2(\text{CO})_6\{\mu\text{-(SCH}_2)_2\text{SnR}_2\}]$ (R = Me (**151**) and Ph (**153**)) as well as the dimeric products $[\text{Fe}_2(\text{CO})_6\{\mu\text{-(SCH}_2)_2\text{SnR}_2\}]_2$ (R = Me (**152**) and Ph (**154**)). Examples of dimeric complexes in which two butterfly Fe_2S_2 clusters are part of a macrocycle are rare in the literature. The *large size of the Sn atom* may allow the formation of these dimeric complexes.

152   **154**
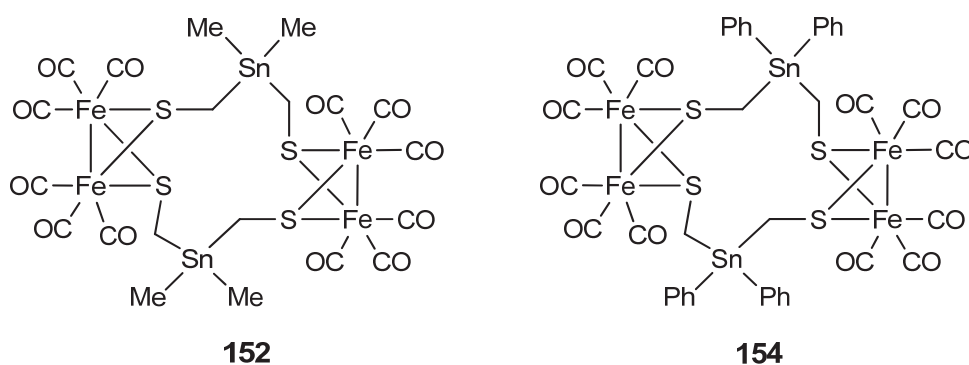
Figure 9-2. Dimeric complexes with two $\text{Fe}_2\text{S}_2(\text{CO})_6$ units connected by $\mu\text{-(SCH}_2)_2\text{SnR}_2$ linkers.

Part 2

[Fe₂(CO)₆{μ-(SCH₂)₂RP=O}]-Hydrogenase Models (Figure 9-3). The R substituents of the P=O-complexes affects the thermodynamic properties of the $[\text{Fe}_2\text{S}_2]$ core. Replacement of R = Ph (in **137**) by R = Et (in **144**) slightly shifts the υ(CO) bands to lower wavenumbers reflecting the increased electron density at the iron atoms. This effect is also revealed by cyclic voltammetry such that the reduction potential becomes more negative when R = Ph is replaced by R = Et. Furthermore, the oxidation potential of complex **144** is less positive than that of complex **137**. A significant effect of the R substituent is found toward the protonation properties of the P=O functionality. The R = Et group increases the basicity of the P=O group compared to R = Ph. It is possible

to protonate complex **144** using the moderately strong acid CF_3CO_2H (starting from 5 equiv.) in CH_2Cl_2 solution. In MeCN solution, complexes **137** and **144** are not protonable by CF_3CO_2H, which is attributed to the lower acidity of CF_3CO_2H in MeCN compared to CH_2Cl_2. This was shown by IR spectroscopy as well as cyclic voltammetry.
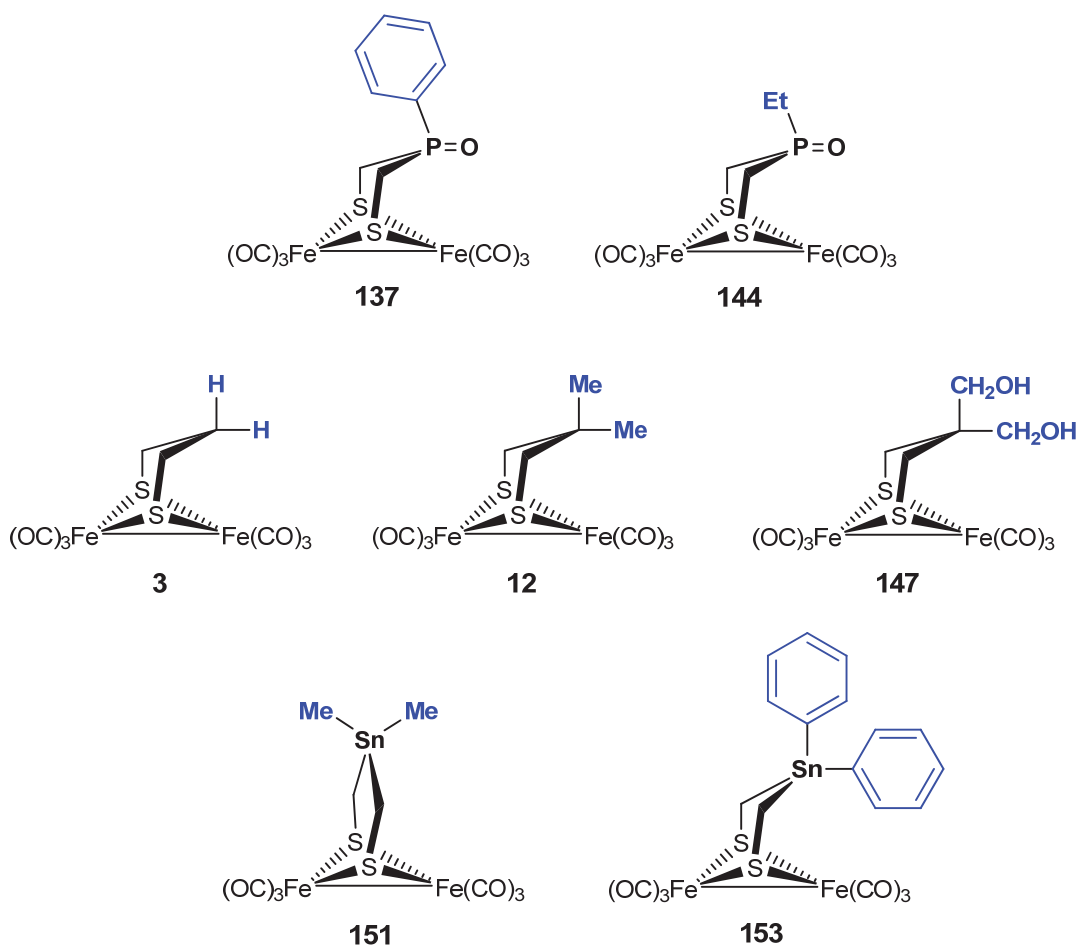
Figure 9-3. [FeFe]-hydrogenase models with various substituents at the bridgehead atom.

$[Fe_2(CO)_6\{\mu\text{-}(SCH_2)_2CR_2\}]$-Hydrogenases Models (Figure 9-3). Replacement of R = H (in **3**) by bulkier groups such as Me (in **12**) or CH_2OH (in **147**) results in a distortion of the eclipsed conformation of the two $Fe(CO)_3$ units measured by the torsion angle CO_{ap}-Fe-Fe-CO_{ap}. The barrier of $Fe(CO)_3$ rotation in the ground state (Fe^IFe^I) and the reduced states ($Fe^0Fe^{I/0}$) decreases when R = H (in **3**) is replaced by R = Me (in **12**) or CH_2OH (in **147**) due to the increased steric clash between R and the apical CO ligands. Therefore, the inversion of one $Fe(CO)_3$ unit to locate one of its CO ligands in a semi-bridging position during the electron transfer becomes kinetically favorable. Thus, the

steric effect of the R groups explains the ECE mechanism for the reduction of the complexes **12** and **147**. The replacement of R = Me in **12** by R = CH_2OH in **147** makes the reduction potential of the [Fe_2S_2] cluster less negative by ~ 100 mV, which is attributed to hydrogen bonding between the OH groups and the μ-S atoms or the reduced Fe atoms.

[$Fe_2(CO)_6\{\mu\text{-}(SCH_2)_2SnR_2\}$]-Hydrogenase Models (Figure 9-3). Replacement of R = Me (in **151**) by R = Ph (in **153**) affects the planarity of the dithiolato linker and leads to the usual chair/boat conformation of the FeS_2C_2Sn six-membered rings.

Part 3
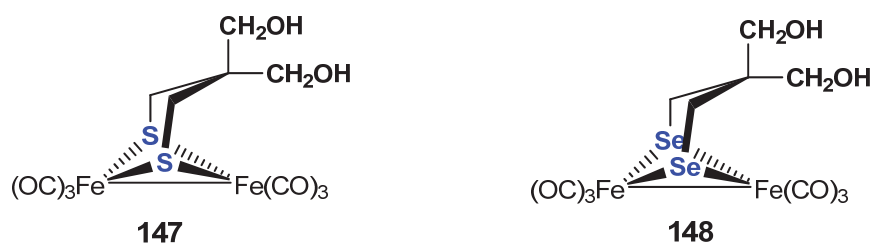
Figure 9-4. [FeFe]-hydrogenase models with μ-S and μ-Se atoms.

The replacement of the μ-S (in **147**) by μ-Se atoms (in **148**) results in: (*i*) elongation of the Fe-Fe bond due to the larger size of Se compared to S, (*ii*) shift of υ(CO) values to lower wavenumbers due to the increased electron density at the Fe sites and (*iii*) a shift of the reduction potential to a less negative value. The complex with μ-S atoms (**147**) catalyzes the reduction of CH_3CO_2H with less overpotential and higher activity than complex **148** with μ-Se atoms.

Part 4
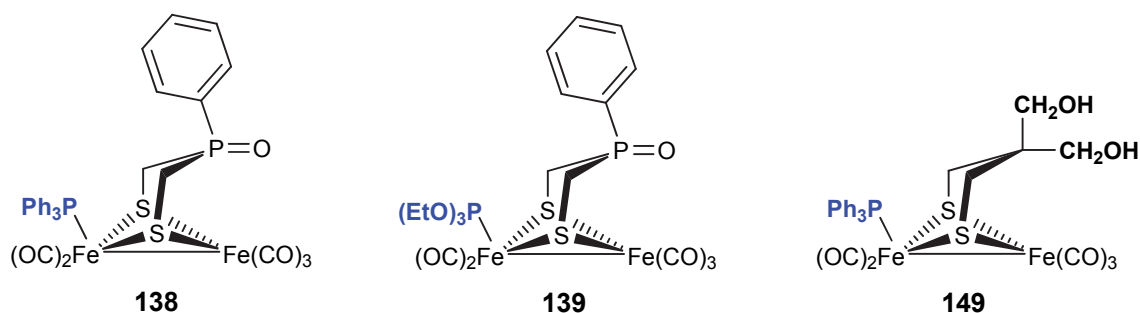
Figure 9-5. PR$_3$-substituted [FeFe]-hydrogenase complexes.

Substituting one CO ligand (in **137**) by PPh$_3$ (in **138**) makes the steric interaction between the Ph-P=O moiety and the [FeFe] core larger than in the case of P(OEt)$_3$ (in **139**) due to the larger cone angle of PPh$_3$ compared to P(OEt)$_3$. The steric clash between the CH$_2$OH groups and the PPh$_3$ in **149** is highly reflected by the large torsion angle P-Fe-Fe-CO$_{ap}$ (~ 33°). The reduction of the above PPh$_3$-substituted complexes **138** and **149** induces the dissociation of the Fe-PPh$_3$ bond and the subsequent formation of their parent hexacarbonyl complex. In comparison, the P(OEt)$_3$ ligand does not split after the reduction. Large steric clash between the PR$_3$ ligand and the dithiolato groups induces the dissociation. The stronger the π-acidity of the PR$_3$ the more stable Fe-PR$_3$ bonding against dissociation, P(OEt)$_3$ is stronger π-acid than PPh$_3$. Performing the electrochemistry of **149** in the presence of excess PPh$_3$, the free ligand, compensates any loss of PPh$_3$ from the reduced complexes. Performing the electrochemical experiments on **138** or **149** using CO-saturated solutions assists the formation of their parent hexacarbonyl complexes. Moreover, cyclic voltammetric experiments using CO-saturated solution showed that the reduced species of **149** (as well as its parent hexacarbonyl **147** produced after its reduction) react with CO to forming products **149CO^{2-}** and **147CO^{2-}** having remarkably more positive oxidation potential than **149^{2-}** and **147^{2-}**. Similarly, the reduction of the P(OEt)$_3$-substituted complex **139** under CO atmosphere leads to the formation of a product that is reversibly oxidized at a potential more positive than the reduced species of **139**.

Part 5

The proposed mechanism for reduction of protons catalyzed by complexes **137** and **144** is summarized in Scheme 9-3.

Scheme 9-3. Proposed mechanism for proton reduction catalyzed by **137** and **144**.
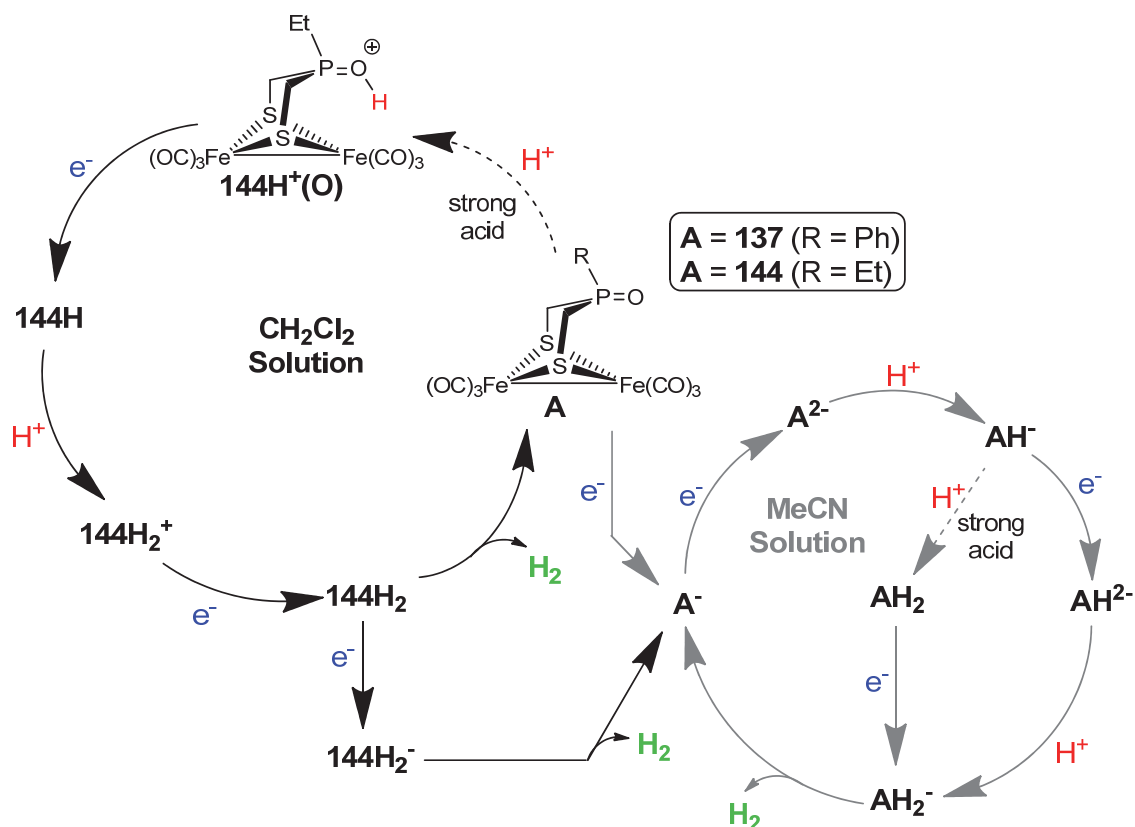
The mechanism is dependent on the solvent and the proton source. In MeCN solvent, the first protonation step occurs after the two-electron reduction of the neutral complex **137** or **147**. If the acid is weak in this case, further reduction of **AH⁻** is required for the second protonation and H_2 release to take place. In comparision, the moderately strong acids allow another pathway for H_2 release that starts with protonation of **AH⁻** (Scheme 9-3). The use of CH_2Cl_2 as a solvent leads to a different catalytic cycle that is initiated by P=O-protonation of the neutral complex **144** (not **137**). In the cycle, the first electron transfer process is the reduction of **144H⁺(O)** that is followed by a second protonation, reduction steps and H_2 release.

Part 6
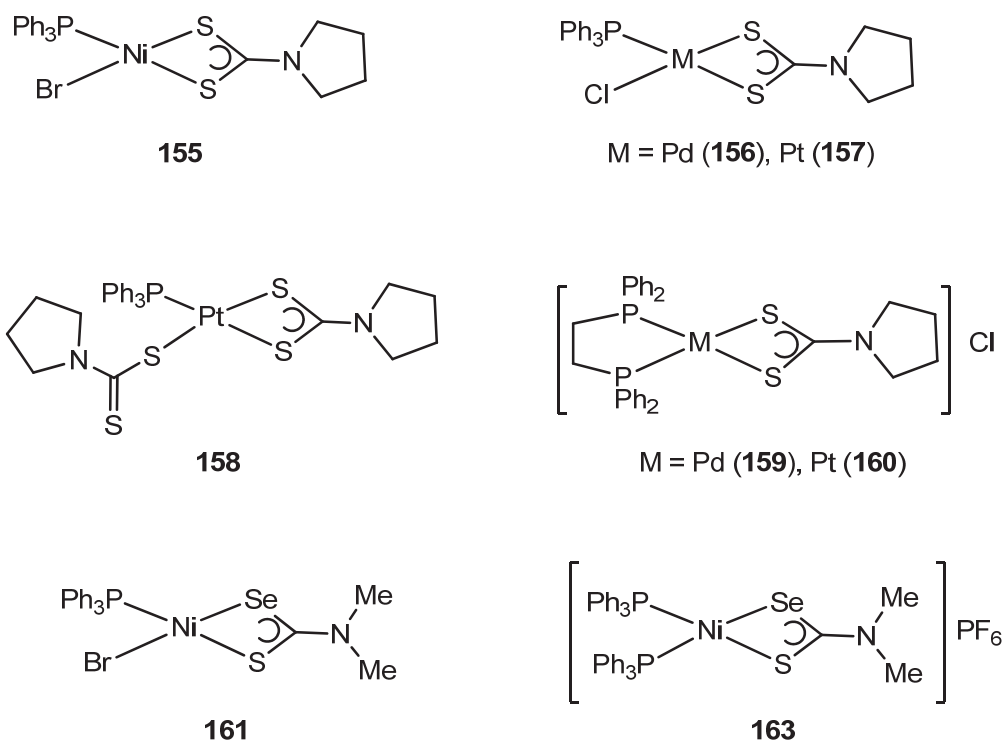
Figure 9-6. Carbamodithiolate and carbamoselenothiolate complexes of Ni^{II}, Pd^{II} and Pt^{II} metals.

The reaction of the carbamodithiolato ligands with $(PPh_3)_2MX_2$ (for X = Cl, M = Pt or Pd and for X = Br, M = Ni) in 1:1 ratio affords the neutral $(PPh_3)M(X)(\kappa^2 S,S\text{-}S_2CNC_4H_8)$ complexes (**155-157**) with distorted square planar structures (Figure 9-6). It might be that initially two Cl⁻ are substituted to give the cation $[(PPh_3)_2M(\kappa^2 S,S\text{-}S_2CNC_4H_8)]^+$ that undergoes sterically induced M-PPh$_3$ dissociation followed by coordination of the counteranion Cl⁻. In the presence of 2 equiv. carbamodithiolate, the reaction leads to the formation of $[(PPh_3)(\kappa S\text{-}S_2CNC_4H_8)Pt(\kappa^2 S,S\text{-}S_2CNC_4H_8)]$ (**158**). When dppeMCl$_2$ (M = Pt, Pd, Ni) is used, the carbamodithiolate substitutes two Cl⁻ ligands to afford **159** and **160** (Figure 9-6).

The synthesis of a Ni^{II} complex containing carbamoselenothiolate as a chelating ligand is described, complex **161** (Figure 9-6). The X-ray determination reveals the presence of six independent molecules in the unit cell of **161**. These six molecules feature distorted square planar structures in which the PPh$_3$ ligands and the Se atoms are in *cis*-orientation. The C(sp^2)-S and C(sp^2)-Se in **161** are longer than the typical distances for single bonds of C(sp^2)-S and C(sp^2)-Se. Moreover, the N-C(sp^2) distance suggests the

presence of π bonding. These findings propose that the most stable resonance form of **161** is the one with C-S and C-Se single bonds as well as N-C double bond:
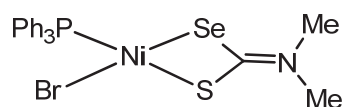
161

Complex **161** may be considered as a starting material for the synthesis of bimetallic complexes as models for the active site of [NiFeSe]-hydrogenases. The reaction of complex **161** with PPh$_3$ and KPF$_6$ led to the formation of complex **163** (Figure 9-6) as well as other side products, presumably the ionic complexes [(PPh$_3$)$_2$Ni($\kappa^2 Se,Se$-Se$_2$CNMe$_2$)]PF$_6$ and [(PPh$_3$)$_2$Ni($\kappa^2 S,S$-S$_2$CNMe$_2$)]PF$_6$.

9 Zusammenfassung

Diese Dissertationsschrift handelt von der Synthese verschiedener neuartiger Modelle des aktiven Zentrums der [FeFe]-Hydrogenasen („H-cluster") sowie deren spektroskopischen, kristallografischen und elektrochemischen Eigenschaften. Dabei werden folgende Schwerpunkte untersucht:

1. Einfluss des Brückenkopfheteroatoms oder der Brückenkopfgruppe des Dithiolato-Liganden auf die Struktur, die elektrochemischen und die Protonierungseigenschaften der [FeFe]-Hydrogenasemodelle.

2. Einfluss der Substituenten R am Brückenkopfatom des Dithiolato-Liganden von [FeFe]-Hydrogenasemodellen auf die Struktur, die elektrochemischen Eigenschaften und die Protonierungseigenschaften der Komplexe.

3. Einfluss des verbrückenden X-Atoms (X = S oder Se) des μ-(XCH$_2$)$_2$C(CH$_2$OH)$_2$-Linkers auf die Redoxeigenschaften des [Fe$_2$X$_2$]-Clusters.

4. Einfluss der Substitution eines Carbonylliganden in [Fe$_2$(CO)$_6$\{μ-dithiolato\}]-Komplexen durch PR$_3$ auf die strukturelle und elektrochemischen Eigenschaften der Komplexe.

5. Mechanistische Untersuchungen der durch $[Fe_2(CO)_6\{\mu\text{-}(SCH_2)_2RP=O\}]$-Hydrogenasesmodelle katalysierten Protonenreduktion.

6. Ein weiteres Kapitel dieser Dissertationsschrift handelt von der Synthese verschiedener Carbamodithiolato- und Carbamoselenothiolato-Komplexe des Platins, des Palladiums und des Nickels.

Teil 1

R = Ph (**137**), Et (**144**)
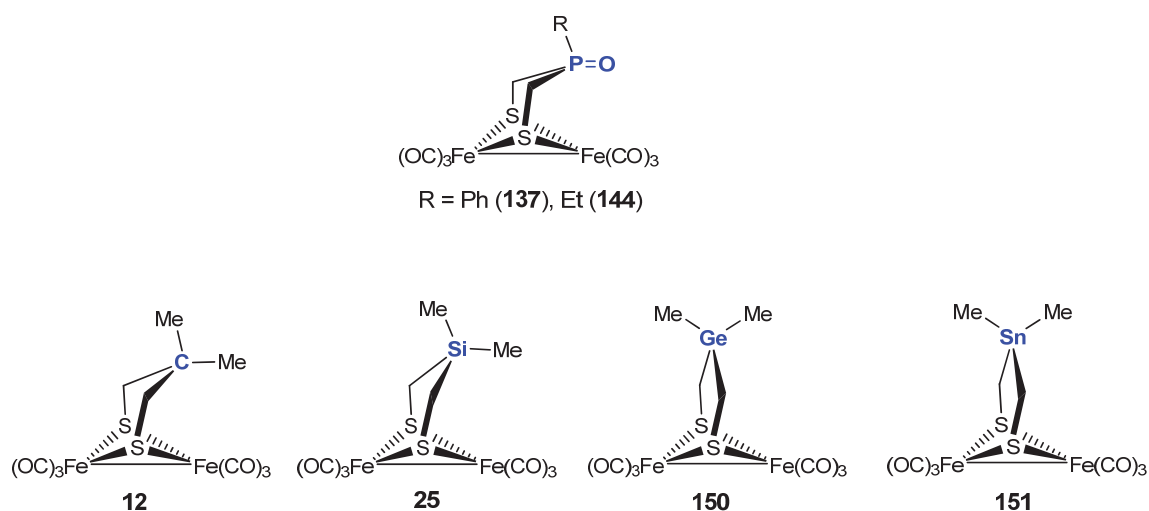
Abbildung 9-1. Repräsentative [FeFe]-Hydrogenasemodelle.

[FeFe]-Hydrogenasemodelle mit P=O-Brückenkopf. Aus röntgenkristallografischen Untersuchungen der P=O-Komplexe (**137** und **144**, Abbildung 9-1) geht hervor, dass die P=O-Einheit eine Ausrichtung weg vom Eisenzentrum einnimmt. Durch den hohen sterischen Anspruch der R-P=O-Einheit befinden sich die Fe(CO)$_3$-Einheiten nicht in ekliptischer Position, welche in $[Fe_2(CO)_6\{\mu\text{-}(SCH_2)_2CH_2\}]$ (**3**) beobachtet wird. Dieser sterische Effekt verringert die Rotationsbarriere der Fe(CO)$_3$-Einheiten und ermöglicht die strukturellen Änderungen während des Elektronentransfers. Dadurch wird die Potentialinversion ermöglicht, welche bei der Reduktion der P=O-Systeme anzutreffen ist. In Dichlormethan können diese Komplexe am Sauerstoffatom der P=O-Gruppe protoniert werden, was durch IR- und ^{31}P NMR-spektroskopische Untersuchungen und cyclovoltammetrischen Messungen im oxidativen Bereich belegt werden kann. Die P=O-Protonierung verschiebt die υ(CO)-Bande um 8-10 cm^{-1} hin zu höheren Wellenzahlen und im ^{31}P NMR-Spektrum verschiebt sich das Signal um etwa

35 ppm hin zu höheren Frequenzen. Durch die Ionenpaarung des BF_4^--Anions und dem protonierten Komplex wird eine deutliche Verschiebung der Carbonylbanden $\Delta\upsilon(CO)$ detektiert. DFT-Rechnungen in der Gasphase für die P=O-protonierten Spezies zeigen, dass die Verschiebung der Carbonylbanden $\Delta\upsilon(CO)$ in Abwesenheit des BF_4^--Anions 20 cm^{-1} beträgt, während diese unter Berücksichtigung von P=O···F-B Wasserstoffbrückenbindungen bezüglich der experimentellen Daten vergleichbare Werte annimmt. Die Kristallisation des protonierten P=O-Komplexes liefert das P=O···BF_3-Addukt, welches durch Verlust eines HF-Moleküls generiert wird.

Es wurde gezeigt, dass die Ausbildung des P=O···BF_3-Adduktes die Lage der Carbonylbanden $\upsilon(CO)$ im IR- und die chemische Verschiebung der Signale im ^{31}P NMR-Spektrum deutlich weniger beeinflusst als eine Protonierung, was durch die geringere Lewis-Acidität des BF_3 im Vergleich zu H^+ erklärt werden kann. Die Protonierbarkeit sowie die sterische Ausrichtung der P=O-Funktionalität machen die P=O-Komplexe zu potentiellen Protonenrelay-Modellen. In elektrochemischen Untersuchungen zeigen die P=O-Komplexe katalytische Eigenschaften hinsichtlich der Protonenreduktion unter Nutzung von Säuren unterschiedlicher Stärke (Schema 9-1).

Schema 9-1. Entstehung des P=O···BF_3-Adduktes.
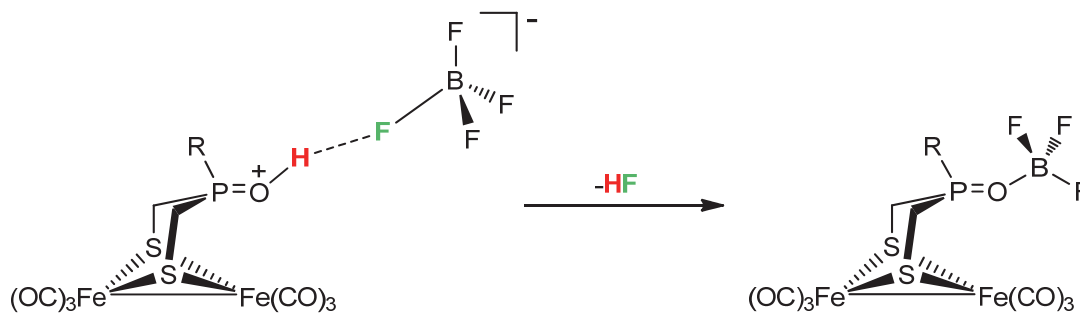
[FeFe]-Hydrogenasemodelle mit GeMe$_2$- und SnMe$_2$-Brückenkopfgruppen. Die Substitution der Brückenkopfgruppe E des Dithiolato-Liganden (E = CR_2, NR, O, S, Se, R-P=O, SiR_2) durch E = GeMe$_2$ oder SnMe$_2$ führt zu einer einzigartigen C_{2v} Symmetrie der Komplexe [Fe$_2$(CO)$_6${μ-(SCH$_2$)$_2$E}], in der beide FeS$_2$C$_2$E-Ringe (E = GeMe$_2$ oder SnMe$_2$, Komplexe **150** und **151** in Abbildung 9-1) eine Halbsessel-Konformation einnehmen. Diese beschreibt den Übergangszustand in dem Gleichgewicht zwischen Sessel- und Wannenkonformation aller anderen [FeFe]-Hydrogenasemodelle. Weiterhin

könnte die Halbsessel-Konformation die Ursache für die symmetrieerlaubte „filled-filled"-Wechselwirkung zwischen σ(Ge-C) $\leftrightarrow$ $3p(\mu$-S) oder σ(Sn-C) $\leftrightarrow$ $3p(\mu$-S) darstellen. IR-spektroskopische Protonierungsexperimente der Komplexe [Fe$_2$(CO)$_6${μ-(SCH$_2$)$_2$XMe$_2$}] mit X = C (**12**), Si (**25**), Ge (**150**) in Dichlormethan unter Nutzung starker Säuren zeigten, das es zwischen der μ-S-protonierten Komplexen (X = Ge, **150**) und den unprotonierten Spezies ein Gleichgewicht gibt:

Schema 9-2. Protonierung des Komplexes **150**.

Als mögliche Ursache für die günstigeren Protonierungseigenschaften des germaniumhaltigen Hydrogenasemodells **150** im Vergleich zu den Komplexen [Fe$_2$(CO)$_6${μ-(SCH$_2$)$_2$XMe$_2$}] mit X = C (**12**), Si (**25**) kann die Planarität des Dithiolato-Linkers angesehen werden, welche symmetriebedingt die „filled-filled"-Wechselwirkungen ermöglicht.

Cyclovoltammetrische Messungen des Komplexes [Fe$_2$(CO)$_6${μ-(SCH$_2$)$_2$GeMe$_2$}] (**150**) zeigen, das dieser eine Zwei-Elektronen-Reduktion eingeht. Dabei findet eine Potentialinversion statt, welche durch einen ECE-Prozess verursacht wird. Die Reduktion des Komplexes **150** ist bei kleinen Scanraten chemisch irreversibel, da es zu Folgereaktionen unter Abspaltung von CO und anschließender Zersetzung des Komplexes kommt. Entsprechende cyclovoltammetrische Messungen in einer CO-gesättigten Lösung führen jedoch nicht zur Erhöhung der Reversibilität, da eine Reaktion des zweifach reduzierten Komplexes mit CO unter Bildung von **150CO**$^{2-}$ stattfindet. Diese Spezies wird bei einem höheren Potential als für das Anion **150**$^{2-}$ notwendig ist reversibel oxidiert. Eine Effekt durch Protonierung der neutralen Spezies von Hydrogenasemodell **150** ist nur schwer zu erkennen, da dazu ein Überschuss einer starken Säure benötigt wird und diese unter den gegebenen Bedingungen ebenfalls reduziert wird. Aus diesem Grund ist eine weitere Modifikationen der Modellsysteme

wie zu Beispiel die Substitution ein oder zweier CO-Liganden durch Phosphane nötig, um die Protonenaffinität der μ-S-Atome zu erhöhen.

Bildung dimerer Hydrogenasemodelle (Abbildung 9-2). Bei der Reaktion des in situ generiertem (μ-LiS)$_2$Fe$_2$(CO)$_6$ mit einem Äquivalent R$_2$Sn(CH$_2$I)$_2$ bilden sich sowohl die monomeren Komplexe [Fe$_2$(CO)$_6${μ-(SCH$_2$)$_2$SnR$_2$}] (R = Me und Ph, Komplexe **151** und **153**) als auch die dimeren Produkte [Fe$_2$(CO)$_6${μ-(SCH$_2$)$_2$SnR$_2$}]$_2$. Ähnliche Beispiele, in denen zwei butterfly-artig angeordnete Fe$_2$S$_2$-Cluster Teil eines Makrocyclus sind, sind in der Literatur bisher nur selten beschrieben. Die Größe des Zinnatoms kann als mögliche Ursache für die Ausbildung derartiger Dimere angesehen werden.
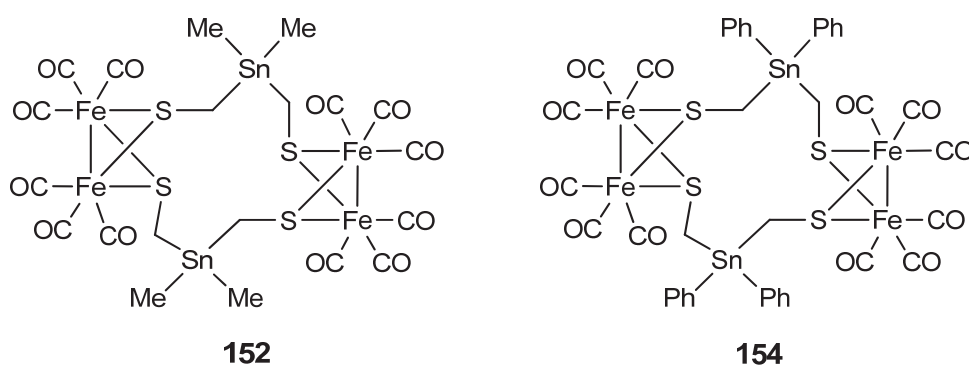
Abbildung 9-2. Dimere Komplexe mit zwei Fe$_2$S$_2$(CO)$_6$-Einheiten, welche über einen μ-(SCH$_2$)$_2$SnR$_2$-Linker verbunden sind.

Teil 2

[Fe$_2$(CO)$_6${μ-(SCH$_2$)$_2$RP=O}]-Hydrogenasemodelle (Abbildung 9-3). Der Substituent R in den P=O-Komplexen beeinflusst die thermodynamischen Eigenschaften des [Fe$_2$S$_2$]-Kernes. Eine Substitution von R = Ph (**137**) durch R = Et (**144**) verschiebt die υ(CO)-Banden leicht zu kleineren Wellenzahlen, wodurch die erhöhte Elektronendichte an den Eisenatomen zum Ausdruck kommt. Die erhöhte Elektronendichte wird auch bei den cyclovoltammetrischen Messungen beobachtet und zeigt sich in einer leichten Verschiebung des Reduktionspotentials in negative Richtung wenn R = Ph durch R = Et ersetzt wird. Weiterhin ist das Oxidationspotential des P=O-Komplexes mit R = Et (**144**) weniger positiv als das vom entsprechenden Komplex mit R = Ph (**137**). Einen deutlichen Einfluss zeigt der Substituent R bezüglich der Protonierungseigenschaften der P=O-

Funktionalität, indem im Fall von R = Et die Basizität der P=O-Gruppe im Vergleich zu R = Ph erhöht wird. Somit wird in Dichlormethan für R = Et (**144**) eine Protonierung der P=O-Einheit unter Nutzung der mittelstarken Säure CF_3CO_2H beobachtet (beginnend bei fünf Äquivalenten). In Acetonitril sind die P=O-Komplexe (R = Et und Ph, **137** und **144**) jedoch nicht durch CF_3CO_2H protonierbar, was in der geringeren Acidität der Trifluoressigsäure in Acetonitril im Vergleich zu der in Dichlormethans begründet ist. Dies wurde sowohl durch IR-Spektroskopie als auch durch Cyclovoltammotrie belegt.
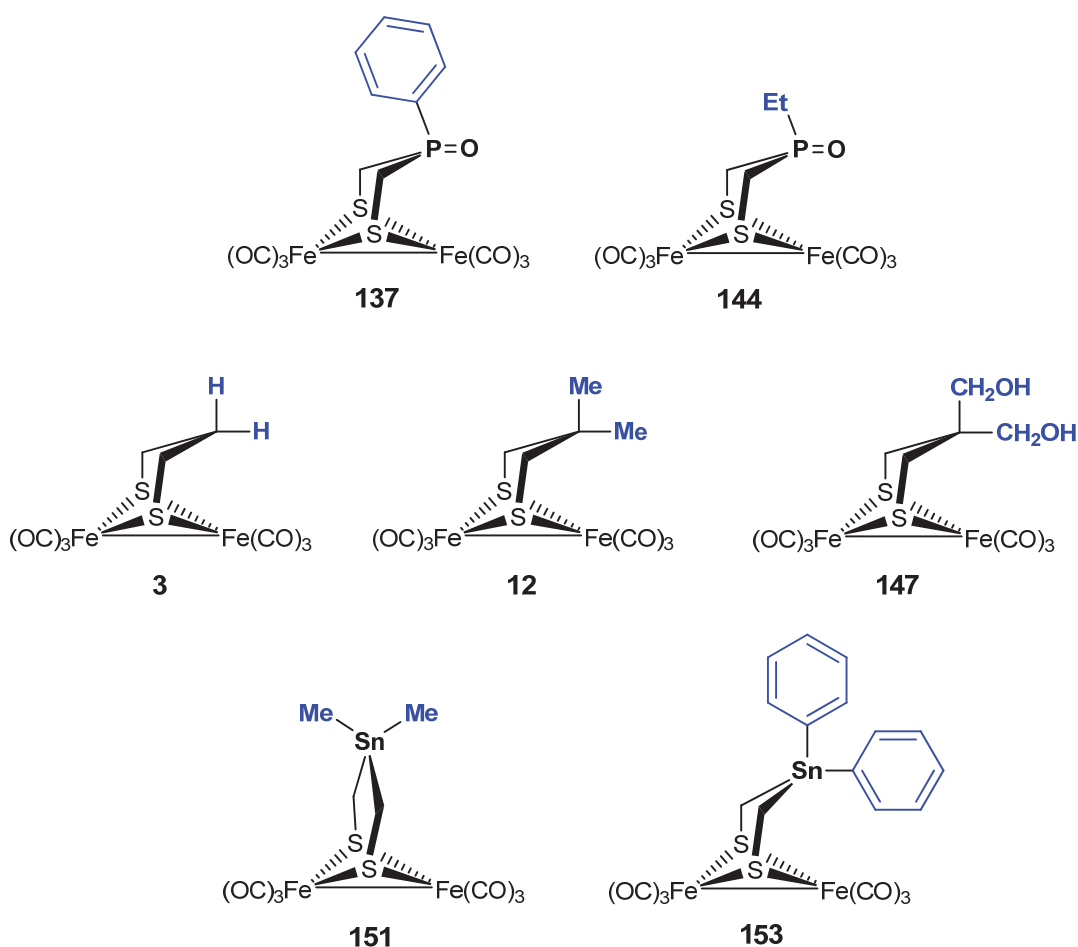
Figure 9-3. [FeFe]-Hydrogenasemodelle mit verschiedenen Substituenten am Brückenkopfatom.

[Fe$_2$(CO)$_6${μ-(SCH$_2$)$_2$CR$_2$}]-Hydrogenasemodelle (**Abbildung 9-3**). Eine Substitution von R = H (**3**) durch sterisch anspruchsvollere Gruppen wie Me (**12**) oder CH$_2$OH (**147**) resultiert in einer Störung der ekliptischen Konformation der beiden Fe(CO)$_3$-Einheiten, welche durch den Torsionswinkel CO$_{ap}$-Fe-Fe-CO$_{ap}$ beschrieben werden kann. Die Rotationsbarriere der Fe(CO)$_3$-Einheiten im Grundzustand (Fe^{I}Fe^I) und

den reduzierten Zuständen (Fe^{0}Fe$^{I/0}$) sinkt wenn R = H (**3**) durch R = Me (**12**) oder CH$_2$OH (**147**) ersetzt wird. Ursache davon ist die sterische Interaktion zwischen dem Substituenten R und dem apikalen Carbonylliganden. Dadurch wird die Inversion einer Fe(CO)$_3$-Einheiten, wodurch ein CO-Ligand während des Elektronentransfers eine semi-verbrückende Position einnimmt, kinetisch bevorzugt. Somit dient der sterische Effekt der R-Gruppen als Erklärung für den ECE-Mechanismus bei der Reduktion der Komplexe **12** und **147**. Die Substitution von R = Me (**12**) durch R = CH$_2$OH (**147**) verschiebt das Reduktionspotential um etwa 100 mV in positive Richtung, was durch die Wasserstoffbrückenbindungen den OH-Gruppen und den μ-S-Atomen oder den reduzierten Eisenatomen zustande kommt.

[Fe$_2$(CO)$_6${μ-(SCH$_2$)$_2$SnR$_2$}]-Hydrogenasemodelle (Abbildung 9-3). Eine Substitution von R = Me (**151**) durch R = Ph (**153**) hat Einfluss auf die Planarität des Dithiolato-Linkers und führt zu einer ungewöhnlichen Sessel/Wanne-Konformation des sechsgliedrigen FeS$_2$C$_2$Sn-Ringes.

Teil 3
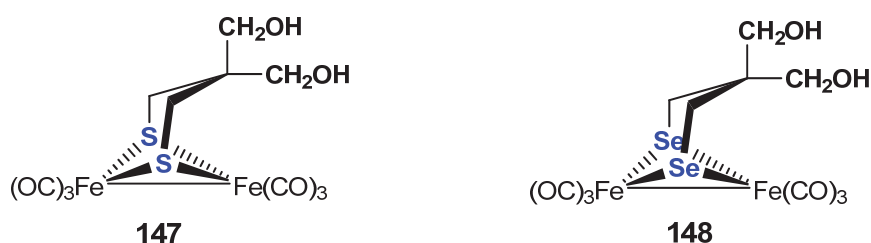
Abbildung 9-4. [FeFe]-Hydrogenasemodelle mit μ-S- and μ-Se-Atomen.

Die Substitution des μ-S-Atom des Komplexes **147** durch ein μ-Se-Atom (Komplex **148**) führt zu: (*i*) Verlängerung der FeFe-Bindung durch den höheren Radius des Selens im Vergleich zum Schwefels, (*ii*) Verschiebung der υ(CO)-Werte hin zu kleineren Wellenzahlen durch die erhöhte Elektronendichte an den Eisenatomen, (*iii*) Verschiebung des Reduktionspotentials in positive Richtung. Der μ-S-Komplex katalysiert die Reduktion von Protonen unter Nutzung von Essigsäure bei kleinerem Überpotential und höherer Aktivität als der μ-Se-Komplex.

Teil 4
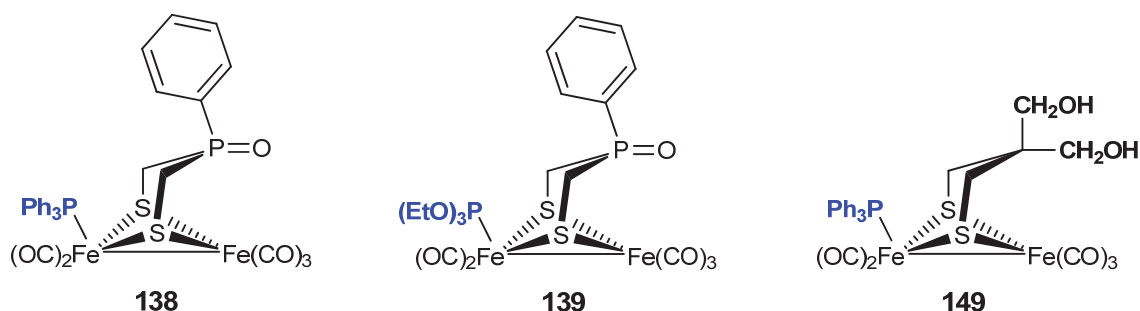
Abbildung 9-5. PR$_3$-substituierte [FeFe]-Hydrogenasemodelle.

Die Substitution eines CO-Liganden des Hexacarbonyl-P=O-Komplexes **147** durch PPh$_3$ (Komplex **138**) erhöht die sterische Abstoßung zwischen der P=O-Einheit und dem [FeFe]-Kern in größerem Ausmaß als durch Substitution durch P(OEt)$_3$ (Komplex **139**). Ursache dafür ist der größere Kegelwinkel des PPh$_3$ im Vergleich zum P(OEt)$_3$. Die starke sterische Abstoßung zwischen der CH$_2$OH-Gruppe und dem PPh$_3$-Liganden im Komplex [Fe$_2$(CO)$_5$(PPh$_3$){μ-(SCH$_2$)$_2$C(CH$_2$OH)$_2$}] (**149**) wird durch den Torsionswinkel P-Fe-Fe-CO$_{ap}$ (~ 33°) verdeutlicht. Während der Reduktion der oben erwähnten PPh$_3$-substituierten Komplexe **138** und **149** kommt es zur Dissoziation des PPh$_3$ und zur anschließenden Ausbildung des entsprechenden Hexacarbonyl-Komplexe. Vergleichend dazu wird der P(OEt)$_3$-Ligand während der Reduktion nicht vom Eisenzentrum abgespalten. Es lässt sich die Tendenz erkennen, dass die Spaltung der Fe-P-Bindung während des Elektronentransfers sowohl von sterischen als auch von elektronischen Faktoren abhängt. Eine hohe sterische Abstoßung zwischen dem PR$_3$-Liganden und der Dithiolato-Gruppen begünstigt die Dissoziation des Phosphans. Je stärker die π-Acidität des PR$_3$ ist desto stabiler ist die Fe-P-Bindung gegenüber einer Dissoziation, P(OEt)$_3$ ist eine stärkere π-Säure als PPh$_3$. Wenn die elektrochemischen Messungen des Komplexes **149** in Anwesenheit von überschüssigem PPh$_3$ ausgetragen werden kompensiert dieser freie Ligand jeglichen Verlust des PPh$_3$ in den reduzierten Komplexen. Im Gegensatz dazu wird bei den elektrochemischen Messungen der PPh$_3$-substituierten Hydrogenasemodelle **138** oder **149** in mit CO gesättigten Lösungsmitteln die verstärkte Ausbildung der entsprechenden Hexacarbonyl-Komplexe beobachtet. Weiterhin zeigen Messungen in einer CO-gesättigten Lösung, dass das Dianion des Komplexes [Fe$_2$(CO)$_5$(PPh$_3$){μ-(SCH$_2$)$_2$C(CH$_2$OH)$_2$}] (**149**) sowie das Dianion des

entsprechenden Hexacarbonylsystems (**147**) mit CO reagiert, wobei die Produkte **149CO²⁻** und **147CO²⁻** generiert werden, welche ein deutlich positiv verschobenes Oxidationspotential im Vergleich zu den nicht mit CO reagierten Dianionen aufweisen. In ähnlicher Weise führt die Reduktion des P(OEt)₃-substituierten Hydrogenasemodelles **139** unter einer CO-Atmosphäre zur Bildung eines Produktes, welches reversibel bei einem Potential positiver als jenes der reduzierten Spezies von **139** oxidiert wird.

Teil 5

Der vermutete Mechanismus der Protonenreduktion, welche durch die Komplexe **137** und **144** katalysiert wird, ist in Schema 9-2 zusammengefasst.

Schema 9-3. Vorgeschlagener Mechanismus der durch Hydrogenasemodelle **137** und **144** katalysierten Protonenreduktion.
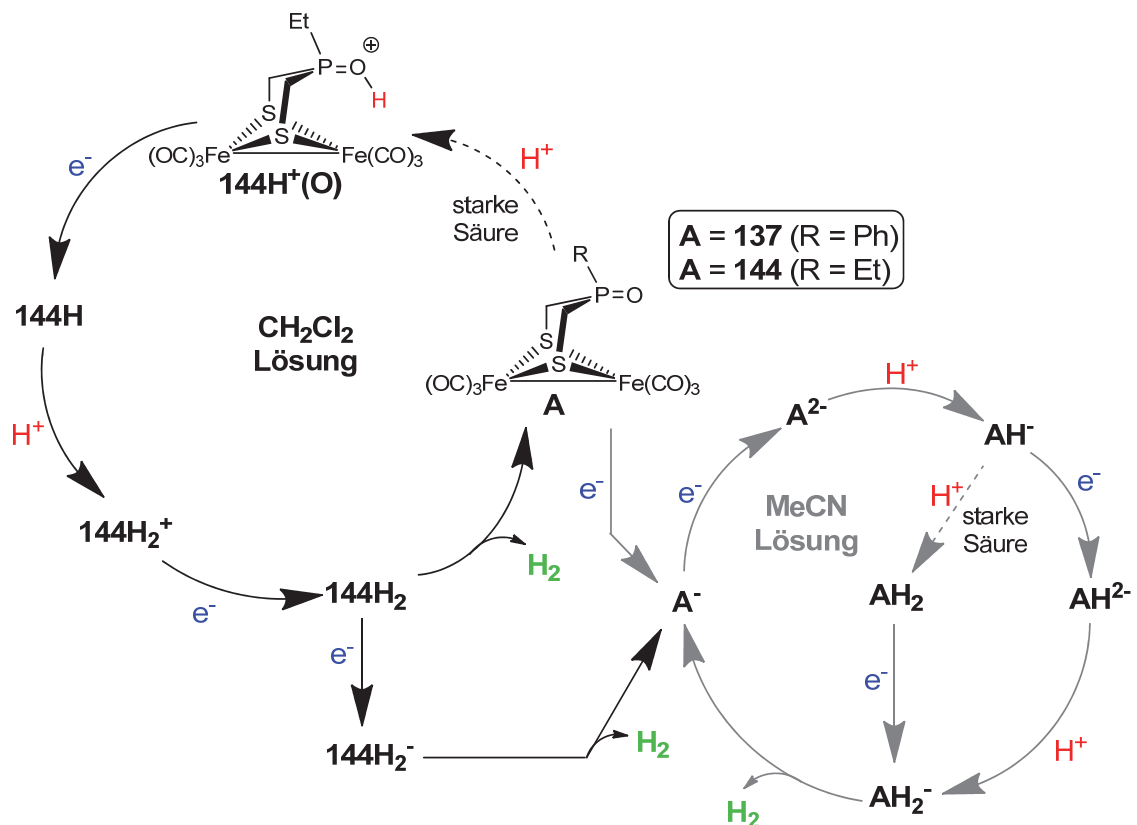
Der Mechanismus hängt sowohl von dem Lösungsmittel als auch von der Protonenquelle ab. In Acetonitril findet der erste Protonierungsschritt nach der Zwei-

Elektronen-Reduktion der neutralen Komplexe **137** oder **147** statt. Im Falle einer schwachen Säure wird eine weitere Reduktion der Spezies AH⁻ benötigt, um den zweiten Protonierungsschritt und die Abspaltung von H_2 zu ermöglichen. Im Vergleich dazu ist bei Nutzung einer mittelstarken Säure ein weiterer Weg der H_2-Freisetzung denkbar, welche die Protonierung der Spezies AH⁻ beinhaltet (Schema 9-3). Im Lösungsmittel Dichlormethan wird ein anderer Katalysemechanismus bevorzugt, welcher mit der Protonierung des neutralen Komplexes **144** (nicht **137**) eingeleitet wird. In diesem Katalysemechanismus beschreibt der erste Elektronentransfer die Reduktion von **144H⁺(O)** gefolgt von einer zweiten Protonierung, weiteren Reduktionsschritten und der H_2-Freisetzung.

Teil 6
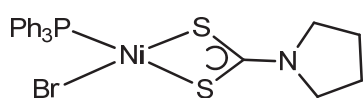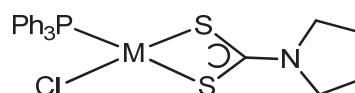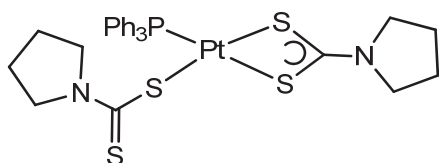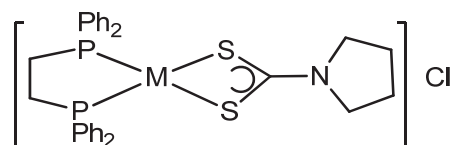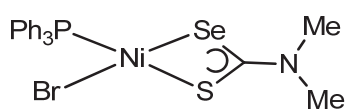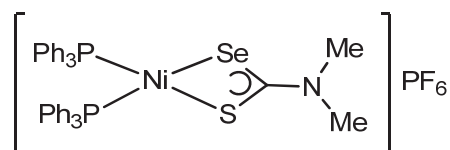
Abbildung 9-6. Carbamodithiolato- und Carbamoselenothiolato-Komplexes mit Ni^II-, Pd^II- und Pt^II-Zentren.

Bei der Reaktion der Carbamodithiolato-Liganden mit dem entsprechende Metallkomplex (PPh₃)₂MX₂ (X = Cl, M = Pt^II oder Pd^II; X = Br, M = Ni^II) im Verhältnis 1:1 werden in einer Substitutionsreaktion, bei der ein Cl⁻ und ein PPh₃ ausgetauscht

werden, die neutralen Komplexe (PPh$_3$)M(Cl)($\kappa^2 S,S$-S$_2$CNC$_4$H$_8$) (**155-157**) generiert. Diese weisen eine verzerrt quadratisch-planare Koordinationsumgebung auf (Abbildung 9-6). Ein möglicher Reaktionsmechanismus beginnt mit der Substitution zweier Chloridionen unter Bildung der kationischen Komplexe [(PPh$_3$)$_2$M($\kappa^2 S,S$-S$_2$CNC$_4$H$_8$)]$^+$. Im zweiten Reaktionsschritt wird aus sterischen Gründen die M-PPh$_3$-Bindung gespalten uns das als Gegenion vorliegende Cl$^-$ koordiniert erneut an das Metallzentrum. In Anwesenheit von zwei Äquivalenten des Carbamodithiolato-Liganden wird ein Metallkomplex der Zusammensetzung [(PPh$_3$)(κS-S$_2$CNC$_4$H$_8$)Pt($\kappa^2 S,S$-S$_2$CNC$_4$H$_8$)] (**158**) gebildet. Wenn dppeMCl$_2$ (M = Pt, Pd, Ni) als Ausgangsstoff eingesetzt wird, werden zwei Chlorid-Liganden durch den Carbamodithiolato-Liganden substituiert und die Verbindungen **159** und **160** generiert (Abbildung 9-6).

Weiterhin wird die Synthese eines Ni^{II}-Komplexes mit einer Carbamoselenothiolato-Gruppe als Chelatliganden (Komplex **161**) beschrieben (Abbildung 9-6). Eine röntgenkristallografische Untersuchung dieses Komplexes zeigt sechs unabhängige Moleküle in der Elementarzelle. Diese zeigen jeweils eine verzerrt quadratisch-planare Koordinationsumgebung, bei der der PPh$_3$-Ligand und das Selenatom in cis-Konfiguration zueinander stehen. Die C(sp^2)-S- und C(sp^2)-Se-Abstände in **161** sind als typische Bindungslängen einer C(sp^2)-S- und C(sp^2)-Se-Einfachbindung. Darüber hinaus deutet die N-C(sp^2)-Bindungslänge auf die Anwesenheit einer π-Bindung hin. Aus diesen Resultaten geht hervor, dass die stabilste Resonanzstruktur der Verbindung **161** eine C-S- und eine C-Se-Einfachbindung sowie eine N-C-Doppelbindung besitzt.
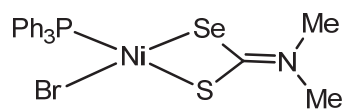
161

Die Verbindung **161** kann als Ausgangsstoff zur Synthese weiterer bimetallischer Komplexe, welche als Modelle des aktiven Zentrums der [NiFeSe]-Hydrogenasen angesehen werden können, dienen. Die Reaktion des Komplexes **161** mit PPh$_3$ und KPF$_6$ führt zur Bildung des Komplexes **163** (Abbildung 9-6) und andere Nebenprodukte, wahrscheinlich der ionischen Komplexe [(PPh$_3$)$_2$Ni($\kappa^2 Se,Se$-Se$_2$CNMe$_2$)]PF$_6$ und [(PPh$_3$)$_2$Ni($\kappa^2 S,S$-S$_2$CNMe$_2$)]PF$_6$.

Chapter 10

Experimental Part

10 Experimental Part

10.1 Materials and Techniques

All reactions were performed using standard Schlenk and vacuum-line techniques under an inert gas (argon or nitrogen). The ^1H, ^1H $\{^{31}P\}$, $^{13}C\{^1H\}$, $^{77}Se\{^1H\}$ and $^{31}P\{^1H\}$ spectra were recorded with a Bruker Avance 200 MHz, 400 MHz or 600 MHz spectrometer. Chemical shifts are given in parts per million with reference to internal $SiMe_4$ or $CHCl_3$. External standard 85 % H_3PO_4 was used as a reference for $^{31}P\{^1H\}$ spectral measurements. The ^{77}Se chemical shifts are reported relative to neat Me_2Se [$\delta(Me_2Se) = \delta(SeO_2) + 1,302.6$ ppm].[301] The mass spectrum was recorded with a Finnigan MAT SSQ 710 instrument. The IR spectra were measured with a Perkin-Elmer System 2000 FT-IR spectrometer. UV-vis spectrum was recorded with a Specord S600A. Büchi GKR-51 apparatus was used for the bulb-to-bulb distillations. Elemental analyses were performed with a Leco CHNS-932 apparatus. Silica gel 60 (0.015-0.040 mm) was used for column chromatography TLC was performed by using Merck TLC aluminum sheets (Silica gel 60 F254). Solvents from Fisher Scientific and other chemicals from Acros were used without further purification. All solvents were dried and distilled prior to use according to standard methods.[302]

10.2 Electrochemistry: Instrumentation and Procedures

Cyclic voltammetric experiments (except those of Figure 2-8, Figure S2-3, Figure 4-10, Figure 4-12, Figures 5-4 to 5-7, Figure 5-14 as well as Figures S5-1 to S5-6) were performed in a three electrodes cell using a Radiometer potentiostat (μ-Autolab Type-III or an Autolab PGSTAT 12) driven by the GPES software. The working electrode consisted of a vitreous carbon disk (d = 0.3 cm) that was polished on a felt tissue with alumina before each CV scan. The Ag/Ag$^+$ reference electrode was separated from the analyte by a CH_2Cl_2-[NBu$_4$][PF$_6$] bridge. All the potentials are quoted against the ferrocene/ferrocenium couple; ferrocene was added as an internal standard at the end of the experiments. These experiments do not involve corrections for the *iR* drop.

Cyclic voltammetric measurements (Figure 2-8 and Figure S2-3) were conducted in 3-electrode technique using a *Reference 600* potentiostat (GAMRY Instruments, Warminster, USA). The *DigiElch 7* software[212] was used for controlling the *Reference 600* potentiostat and for evaluating electrochemical experiments by digital simulation. The experiments were performed in acetonitrile containing 0.25 M tetra-n-butylammonium hexafluorophospate under a blanket of solvent-saturated argon. The ohmic resistance, which was compensated for during the experiment by means of positive feedback, was determined by measuring the impedance of the system at potentials where the faradaic current was negligibly small. Background correction was accomplished by subtracting the current curves of the blank electrolyte (containing the same concentration of supporting electrolyte) from the experimental CVs. The reference electrode was an Ag\AgCl electrode in acetonitrile containing 0.25 M tetra-n-butylammonium chloride. However, all potential values reported in this work are referenced to the potential of the ferrocenium/ferrocene couple. The reduction processes were measured on a hanging mercury drop (mHg-drop ≈ 2.85 mg) produced by the Controlled Growth Mercury Electrode (CGME, Bioanalytical Systems, Inc.,West Lafayette, USA) while a 3 mm glassy carbon disk electrode was used for measuring the half wave potential of the ferrocene/ferroceniumcouple and the oxidation of complex **137**.

Cyclic voltammetric measurements (Figure 4-10, Figure 4-12, Figures 5-4 to 5-7, Figure 5-14 as well as Figures S5-1 to S5-6) were conducted in three-electrode technique [glassy carbon disk (diameter = 1.6 mm), the working electrode; reference electrode, Ag/AgCl in MeCN; and a Pt wire, the counter electrode] using a Reference 600 Potentiostat (Gamry Instruments). All experiments were performed in MeCN solutions containing 0.1 M $^{n}Bu_4NBF_4$ at room temperature. The solutions were purged with N_2 for 5 minutes and a stream of N_2 was maintained over the solutions during the measurements. The working electrode was polished on a felt tissue with alumina before each voltammetric scan. All potential values reported in this paper are referenced to the potential of the ferrocenium/ferrocene couple.

10.3   Crystal Structure Determinations

The intensity data were collected on a Nonius KappaCCD diffractometer, using graphite-monochromated Mo-K_α radiation. Data were corrected for Lorentz and polarization effects; absorption was taken into account on a semi-empirical basis using multiple-scans.[303-305]

The structure was solved by direct methods (SHELXS[306]) and refined by full-matrix least squares techniques against Fo^2 (SHELXL-97[306]). All hydrogen atom positions were included at calculated positions with fixed thermal parameters. XP (SIEMENS Analytical X-ray Instruments, Inc.) was used for structure representations.

The crystal data of complex **149** were collected with an Oxford Diffraction X-Calibur-2 CCD diffractometer, equipped with a jet cooler device and graphite-monochromated Mo-K_α radiation ($\lambda = 0.71073$ Å). The X-ray of complex **149** was measured in the X-ray department of Université de Bretagne Occidentale (UBO) in Brest/France.

10.4   DFT Calculations

Full geometry optimizations (i.e., without symmetry constraints) were carried out with the GAUSSIAN09 program package using throughout the hybrid Hartree-Fock-DFT approach (B3LYP/6-311++G(d,p)) for complex **137** (Chapter 2).[307,308] For iron atoms, a relativistic ECP of the Stuttgart-Dresden group (SDD) was used replacing the 28 core electrons in transition-metal atoms by an effective core potential (ECP) and contracting valence basis set (8s7p6d) primitive sets to (6s5p3d).[309] Stationary points were rigorously characterized as minima according to the number of imaginary modes by applying a second-order derivative calculation (vibrational analysis). Zero-point energy (ZPE) corrections have been applied. Solvent effects were addressed by performing a polarizable continuum model calculation using the CPCM model.[310] All calculations on the complexes of Chapter 3 have been performed on the B3LYP/6-311++g(d,p) level of theory using the program package GAUSSIAN09.[307,308] In addition, frequency calculations have been performed to show that the structures are minima on the hyper surface. For iron atoms we used a relativistic ECP of the Stuttgart-Dresden group (SDD) replacing the 28 core electrons in transition-metal atoms by an effective core potential (ECP) and contracting valence basis sets (8s7p6d) primitive sets to (6s5p3d).[309]

DFT geometry optimizations (Chapter 4) have been carried out at the BP86/TZVP level and solvent effect has been treated according to the COSMO approach, considering a continuum dielectric with $\varepsilon = 8.93$ (CH_2Cl_2 solvent).

10.5   Synthetic Procedures and Characterization

10.5.1   Synthesis of O=PR(CH2Cl)2 (R = Ph, Et)
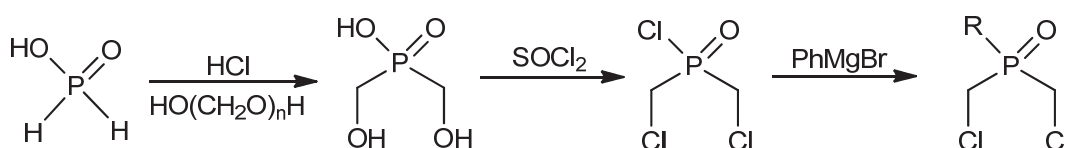
Step 1: Synthesis of O=P(OH)(CH2OH)2[203]

A mixture of H_3PO_2 (30.50 g, 0.32 mol, 50 % aqueous solution), 17.5 mL concentrated HCl and 14.5 g of paraformaldehyde, $HO(CH_2O)_nH$ (n = 8-100), was heated (40-45 ℃) with stirring for until it becomes clear. This requires ~ 4 h. The clear mixture was then refluxed for 30 h. The mixture was then evaporated to remove the water and further purified by Azeotropic distillation using toluene to afford highly viscous slightly yellow oil.
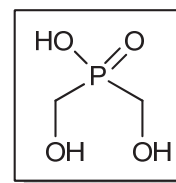
$^{31}P\{^1H\}$ NMR (200 MHz, D_2O): δ 48.66. $^{13}C\{^1H\}$ NMR (200 MHz, D_2O): δ 55.7 (d, $^1J_{CP}$ = 107.73 Hz, CH_2). ^1H NMR (200 MHz, D_2O): δ 3.75 (d, $^2J_{HP}$ = 5.31 Hz, CH_2).

Step 2: Synthesis of O=PCl(CH2Cl)2[203]

The viscous liquid O=P(OH)(CH2OH)2 (28 g) was added very slowly over 6 h to refluxing $SOCl_2$ (110 mL). The reaction mixture was then stirred overnight at room temperature. The crude product was purified by distillation (90 ℃ / 0.1 mmHg) to afford O=PCl(CH2Cl)2 (15.3 g) as a colorless liquid (50 % yield). Excess $SOCl_2$ was obtained first by distillation under atmospheric pressure.
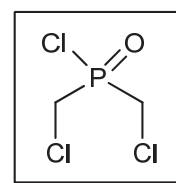
DEI-MS (*m/z*): 180 [M]$^+$, 146 [M - Cl]$^+$. ^{31}P NMR (200 MHz, CDCl$_3$): δ 54.88. ^{13}C{^{1}H} NMR (200 MHz, CDCl$_3$): δ 36.66 (d, $^1J_{CP}$ = 90.1 Hz, C*H$_2$*). ^{1}H NMR (200 MHz, CDCl$_3$): δ 3.9-4.2 (m, C*H$_2$*).

Step 3: Synthesis of O=PPh(CH$_2$Cl)$_2$[202]

To a solution of O=PCl(CH$_2$Cl)$_2$ (14 g, 0.078 mol) in ether (100 mL), PhMgBr (14 g, 0.078 mol) in ether (100 mL) was added dropwise at 15 ºC. An oily precipitate is formed. The mixture was refluxed for 1 h after complete addition of Grignard reagent. Then, solution of Na$_2$CO$_3$ (100 mL, 16.1 %) was added and the mixture was filtered. The organic phase was separated and the solvent was removed under reduced pressure. Soxhlet extraction of the yellow residue with Xylole (200 mL) afforded O=PPh(CH$_2$Cl)$_2$ (6.5 g) in 37 % yield as white crystals.
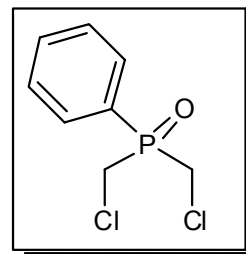
DEI-MS (*m/z*): 222 [M]$^+$. ^{31}P{^{1}H} NMR (200 MHz, CDCl$_3$): δ 35.23. ^{1}H NMR (200 MHz, CDCl$_3$): δ 3.95-4.00 (m, 4H, C*H$_2$*), 7.45-7.95 (m, 5H, Ph).

Step 4. Synthesis of O=PEt(CH$_2$Cl)$_2$[203]

Into a flask containing Mg powder (2.43 g) in ether (40 mL), a solution of ethyl bromide (10.9 g) in ether (15 mL) was added dropwise. Subsequently, the mixture was refluxed until Mg was completely consumed. To this solution, a solution of O=PCl(CH$_2$Cl)$_2$ (10.08 g) in ether (50 mL) was added dropwise at ~ 0 ºC and a green slime was observed. After 3 h reflux, an aqueous solution of Na$_2$CO$_3$ was added and a white solid was formed. The mixture was extracted three times with CHCl$_3$. The solvent was removed under reduced pressure and the crude product was purified by distillation (91-93 ºC / 0.5 mmHg) to give O=PEt(CH$_2$Cl)$_2$ (3.0 g) as colorless oil that form crystals upon cooling. This compound is hygroscopic and it must be stored under inert atmosphere.
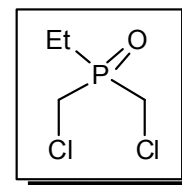
DEI-MS (*m/z*): 175 [M]$^+$, 146 [M - Et]$^+$. ^{31}P{^{1}H} NMR (200 MHz, CDCl$_3$): δ 49.88. ^{13}C{^{1}H} NMR (200 MHz, CDCl$_3$): δ 4.80 (d, $^2J_{CP}$ = 5.72 Hz, CH$_2$*C*H$_3$), 17.19 (d, $^1J_{CP}$ = 71.69Hz, *C*H$_2$CH$_3$), 33.33 (d, $^1J_{CP}$ = 68. 63 Hz, C*H$_2$*S) . ^{1}H NMR (200 MHz, CDCl$_3$): δ 1.15-1.35 (m, 3H, C*H$_3$*), 1.90-2.10 (m, 2H, C*H$_2$*CH$_3$), 3.61-3.83 (m, 4H, C*H$_2$*S).

10.5.2 Synthesis of (μ-S$_2$)Fe$_2$(CO)$_6$[201]

Fe(CO)$_5$ (50 mL, 0.378 mol), degassed MeOH (250 mL) and freshly prepared and degassed KOH solution (150 mL, ca. 50% aqueous) were added successively to a a three neck, 2 L round-bottomed flask connected to a bubbler. This mixture was stirred for 30 min, and after that it was cooled to 0 °C. To this cold solution, S$_8$ (65.33 g) was added over 5 min and the black mixture was stirred for 1 h. Degassed H$_2$O (500 mL), degassed hexane (1000 mL) and NH$_4$Cl (169 g, 3.16 mol) were added. At this stage, H$_2$S evolution starts. The reaction mixture was stirred at room temperature for 17 h. After this time, bubbling had slowed significantly and the resulting mixture appeared as a dark red layer of hexane and a black oily aqueous phase. The hexane layer was filtered over Celite, which was then rinsed with ~ 500 mL of hexane. The combined deep red hexane solution was washed with an approximately equal volume of water, dried over Na$_2$SO$_4$, and evaporated. Sublimation of the solid residue at room temperature gave red crystals of (μ-S$_2$)Fe$_2$(CO)$_6$ over several days, during which the red sublimate was periodically removed. Yield: 12 g Fe$_2$S$_2$(CO)$_6$. This compound was stored under non-inert conditions.
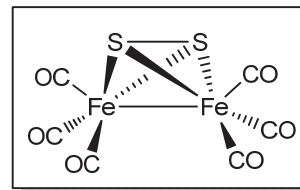
10.5.3 Pyridinium Tetrafluoroborate[311]

A solution of HBF$_4$·Et$_2$O (54 wt %, 2 mL, 14.5 mmol, 1.2 equiv) was added to an ether solution (5 mL) of pyridine (1 mL, 12.4 mmol) at 0 °C, affording immediately a white precipitate. Subsequently, the mixture was filtrated at room temperature and the white solid was washed twice with ether and dried under vacuum. Yield: 2.03 g (98 %).
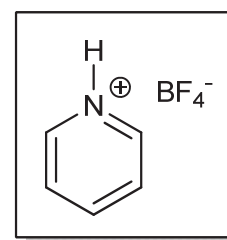
^{1}H NMR (200 MHz, DMSO): δ 8.97-8.78 (m, 2H, Ar*H*), 8.68-8.50 (m, 1H, Ar*H*), 8.20-7.92 (m, 2H, Ar*H*), 7.09 (s, 1H, N*H*).

10.5.4   Synthesis of [Fe₂(CO)₆{μ-(SCH₂)₂(Ph)P=O}] (137)

A red solution of (μ-S₂)Fe₂(CO)₆ (0.771g, 2.242 mmol) in THF (50 ml) was cooled to -78 ºC and treated dropwise with Et₃BHLi (1.0 M in THF, 4.5 mL, 4.5 mmol) to give a dark green solution. After stirring the solution for 30 min at -78 ºC, O=P(Ph)(CH₂Cl)₂ (0.500 g, 2.242 mmol) was added. The mixture was stirred for 18 h while slowly warming up to room temperature, giving rise to a dark orange solution. Solvent removal was performed under Ar using a vacuum transfer line. The residue was purified by column chromatography (SiO₂ / CH₂Cl₂). Yield: 0.23g (21 %) as orange powder**.**

137
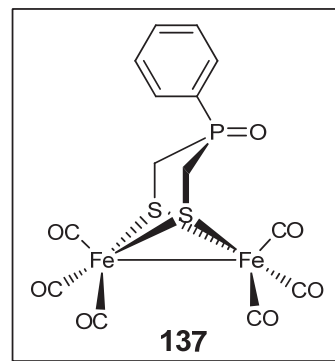
Anal. Calcd for C₁₄H₉Fe₂O₇PS₂: Calc. C, 33.90 %; H, 1.83 %; S, 12.93 %, Found: C, 33.68 %; H, 2.13 %; S, 12.57 %. DEI-MS (*m/z*): 440 [M - 2CO]⁺, 412 [M - 3CO]⁺, 384 [M - 4CO]⁺, 356 [M - 5CO]⁺, 328 [M - 6CO]⁺. IR (KBr): 1990 (CO), 2003 (CO), 2041 (CO), 2079 (CO) cm⁻¹. IR (CH₂Cl₂): 1989 (sh, CO), 2005 (CO), 2044 (CO), 2076 (sh, CO), 2081 (CO). ³¹P{¹H} NMR (81.0 MHz, CD₂Cl₂): δ 30.6. ¹³C{¹H} NMR (50.3 MHz, CDCl₃): δ 19.8 and 21.0 (d, $^2J_{CP}$ = 62.8 Hz, *CH₂PCH₂*), 128.9-132.9 (*C₆H₅*), 205.9 and 207.0 (*CO*). ¹H NMR (200.1 MHz, CDCl₃): δ 2.06 (d, $^2J_{HH}$ = 14.8 Hz, 2*H*, C*H*HPC*H*H), 2.75 (t, $^2J_{HH}$ = 14.9 Hz, $^2J_{HP}$ = 15.6, 2*H*, CH*H*PCH*H*), 7.2-7.6 (m, 5H, C₆*H₅*). ¹H{³¹P} NMR (200.1 MHz, CDCl₃): δ 2.1 (d, $^2J_{HH}$ = 14.8 Hz, 2*H*, C*H*HPC*H*H), 2.77 (d, $^2J_{HH}$ = 14.9 Hz, 2*H*, CH*H*PCH*H*), 7.2-7.6 (m, 5H, C₆*H₅*).

10.5.5   Synthesis of [Fe₂(CO)₆{μ-(SCH₂)₂(Et)P=O}] (144)

A red solution of (μ-S₂)Fe₂(CO)₆ (0.2 g, 0.582 mmol) in THF (10 mL) was cooled to -78 ºC and treated dropwise with Et₃BHLi (1.0 M in THF, 1.2 mL, 1.164 mmol) to give a dark green solution. After stirring the solution for 30 min at -78 ºC, a solution of O=P(Et)(CH₂Cl)₂ (0.102 g, 0.583 mmol) in 3 ml THF was added in one portion. The mixture was stirred for 18 h while slowly warming up to room temperature, giving rise to a dark orange solution. Solvent removal was performed under

144
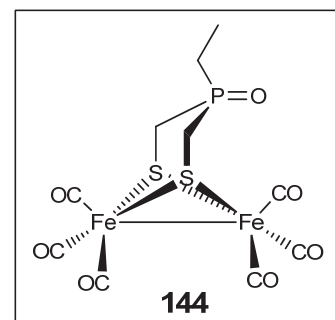
Ar using a vacuum transfer line. The residue was purified by column chromatography (SiO$_2$ / Acetone: CH$_2$Cl$_2$, 100:1). Yield: 0.024 g (10 %) as orange powder.

Anal. Calcd for C$_{10}$H$_9$Fe$_2$O$_7$PS$_2$: Calc. C, 26.81 %; H, 2.03 %; S, 14.32 %, Found: C, 26.65 %; H, 2.11 %; S, 14.01 %. Micro-DSI-MS (*m/z*): 470.7 [M + Na]$^+$. EI-MS (*m/z*): 278 [M - 6CO]$^+$. IR (KBr): 1951 (CO), 1970 (CO), 2034 (CO), 2076 (CO) cm^{-1}. IR (CH$_2$Cl$_2$): 1984 (CO), 2005 (CO), 2044 (CO), 2081 (CO) cm^{-1}. ^{31}P{^{1}H} NMR (81.0 MHz, CD$_2$Cl$_2$): δ 44.7. ^{13}C{^{1}H} NMR (50.3 MHz, CD$_2$Cl$_2$): δ 5.31 (d, $^2J_{CP}$ = 5.24 Hz, *C*H$_3$CH$_2$), 18.93 (d, $^1J_{CP}$ = 59.82 Hz, CH$_3$*C*H$_2$), 25.7 (d, $^1J_{CP}$ = 67.36 Hz, S*C*H$_2$), 206.81 and 207.63 (*C*O). ^{1}H NMR (400 MHz, CD$_2$Cl$_2$): δ 1.69 (d, $^2J_{HH}$ = 14.8 Hz, 2*H*, C*H*HPC*H*H), 2.71 (t, $^2J_{HH}$ = 14.8 Hz, $^2J_{HP}$ = 14.8, 2*H*, CH*H*PCH*H*), 1.053 (t, $^2J_{HH}$ = 14.8 Hz, 3H, C*H*$_3$CH$_2$), 2.53 (m, $^2J_{HH}$ = 14.8 Hz, 3H, CH$_3$C*H*$_2$). ^{1}H{^{31}P} NMR (200.1 MHz, CDCl$_3$): δ 2.1 (d, $^2J_{HH}$ = 14.8 Hz, 2*H*, C*H*HPC*H*H), 2.77 (d, $^2J_{HH}$ = 14.9 Hz, 2*H*, CH*H*PCH*H*), 7.2-7.6 (m, 5H, C$_6$H$_5$).

10.5.6   Synthesis of [Fe$_2$(CO)$_5$PPh$_3${μ-(SCH$_2$)$_2$(Ph)P=O}] (138)

To solution of complex **137** (46 mg, 0.093 mmol) in MeCN (20 mL), 1 equiv. Me$_3$NO·2H$_2$O (10 mg, 0.09 mmol) was added to give the respective nitrile complex within 30 min, visible by darkening of the red solution. Subsequently, 1 equiv. PPh$_3$ (24 mg, 0.092 mmol) was added, and the reaction mixture was stirred at room temperature for 18 h. The resulting red solution was then filtered and the solvent was evaporated using vacuum transfer line to give the complexes in 98 % yield.
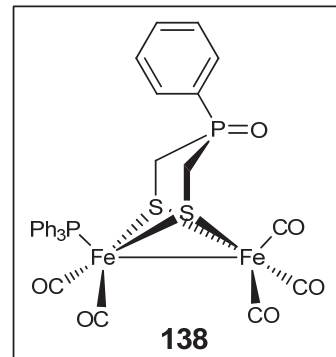
Anal. Calcd for C$_{31}$H$_{24}$Fe$_2$O$_6$P$_2$S$_2$·0.5CH$_2$Cl$_2$: C, 48.96 %; H, 3.26 %; S, 8.30 %. Found: C, 49.22 %; H, 3.27 %; S, 8.48 %. DEI-MS (*m/z*): 674 [M - 2CO]$^+$, 618 [M - 4CO]$^+$, 590 [M - 5CO]$^+$, 440 [M - CO - PPh$_3$]$^+$, 412 [M - 2CO - PPh$_3$]$^+$, 384 [M - 3CO - PPh$_3$]$^+$, 356 [M - 4CO - PPh$_3$]$^+$ and 328 [M - 5CO - PPh$_3$]$^+$. IR (CH$_2$Cl$_2$): 1941 (CO), 1983 (CO), 2002 (CO), 2056 (CO) cm^{-1}. ^{31}P{^{1}H} NMR (200 MHz, CD$_2$Cl$_2$): δ 30.7 (P=O), 65.8 (PPh$_3$). ^{13}C{^{1}H} NMR (50.3 MHz, CD$_2$Cl$_2$): δ 18.5 (d, $^1J_{CP}$ = 67.6 Hz, CH$_2$PCH$_2$), 128-136 (Ph), 208.7 and 213.5 (CO). ^{1}H NMR (200.1 MHz, CD$_2$Cl$_2$): δ 1.18 (d,

$^2J_{HH}$ = 15.2 Hz, 2H, CH*H*PCH*H*), 2.32 (t, $^2J_{HH}$ = $^2J_{HP}$ = 15.2 Hz, 2H, C*H*HPC*H*H), 6.8-7.8 (m, 20H, Ph).

10.5.7 Synthesis of [Fe₂(CO)₅P(OEt)₃{μ-(SCH₂)₂(Ph)P=O}] (139)

To solution of complex **137** (40 mg, 0.081 mmol) in MeCN (20 mL), 1 equiv. Me₃NO·2H₂O (9 mg, 0.081 mmol) was added to give the respective nitrile complex within 30 min, visible by darkening of the red solution. Subsequently, 1 equiv. P(OEt)₃ (14 μL, 0.082 mmol) was added, and the reaction mixture was stirred at room temperature for 18 h. The resulting red solution was then filtered and the solvent was evaporated using vacuum transfer line to give the complexes in 98 % yield.
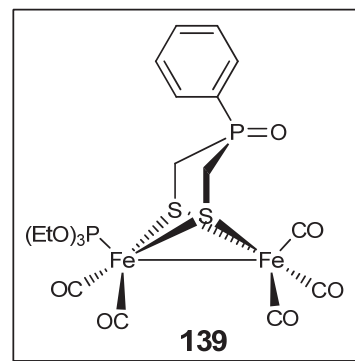
Anal. Calcd for $C_{19}H_{24}Fe_2O_9P_2S_2$: C, 35.70 %; H, 4.57 %; S, 10.03 %. Found: C, 35.30 %; H, 4.49 %; S 9.88 %. Micro-ESI-MS (*m/z*): 656.8 [M + Na]⁺. IR (CH₂Cl₂): 1946 (CO), 1983 (CO), 2003 (CO), 2058 (CO) cm⁻¹. $^{31}P\{^1H\}$ NMR (CD₂Cl₂, 161.95 MHz): δ 30.7 (P=O), 170 (broad at r.t., P(OEt)₃). $^{13}C\{^1H\}$ NMR (50.3 MHz, CD₂Cl₂): δ 16.4 (d, $^3J_{CP}$ = 6.41 Hz, P(OCH₂*C*H₃)₃), 19.6 (d, $^1J_{CP}$ = 62.09 Hz, CH₂PCH₂), 61.95 (d, $^2J_{CP}$ = 4.58 Hz, P(O*C*H₂CH₃)₃), 128-135 (Ph), 208, 212.35 (d, $^2J_{CP}$ = 16.1 Hz, CO). ^1H NMR (200 MHz, CD₂Cl₂): δ 1.38 (t, $^3J_{HH}$ = 7.03 Hz, 9H, P(OCH₂C*H₃*)₃), 2.20 (d, $^2J_{HH}$ = 14.7 Hz, 2H, CH*H*PCH*H*), 2.57 (t, $^2J_{HH}$ = 14.7, $^2J_{HP}$ = 15.5 Hz, 2H, C*H*HPC*H*H), 4.21 (q, $^3J_{HH}$ = $^3J_{HP}$ = 7.03 Hz, 6H, P(OC*H₂*CH₃)₃), 7.4-7.6 (m, 5H, Ph).

10.5.8 Protonation/Deprotonation of 137 by HBF₄·Et₂O/Et₃N

Protonation. To a dry CH₂Cl₂ solution (5 mL) of complex **137** (2.7 mg, 5.44×10^{-6} mol), HBF₄·Et₂O (74 μL, 100 equiv.) was added under N₂ atmosphere and the IR spectrum recorded. The same experiment was performed in CD₂Cl₂ to measure the $^{31}P\{^{1}H\}$ NMR spectrum. These spectroscopic experiments revealed the formation of **137H⁺(O)**. The protonated complex was stable over several hours at room temperature.
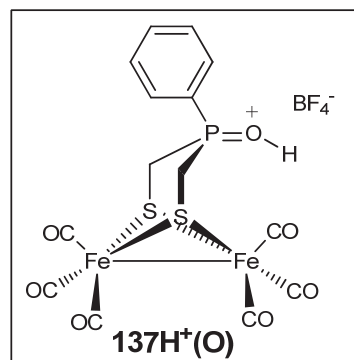
IR (CH₂Cl₂): 1999 (sh, CO), 2016 (CO), 2052 (CO), 2081 (sh, CO), 2089 (CO). $^{31}P\{^{1}H\}$ NMR (CD₂Cl₂, 200 MHz): δ 67.2 (broad).

Deprotonation. To the CH₂Cl₂ solution of **137** containing 100 equiv. HBF₄·Et₂O, Et₃N (76 μL) was added under N₂ atmosphere and the IR spectrum showed the υ(CO) bands of **137**. The same experiment was done for complex **144** and revealed the protonation/deprotonation processes in CH₂Cl₂, but not in MeCN in which only decomposition was observed over the time.

10.5.9 Protonation of 144 by CF₃CO₂H and HBF₄·Et₂O

To a dry CH₂Cl₂ solution (4 mL) of complex **144** (2.6 mg, 5.80×10^{-6} mol), CF₃CO₂H (5 μL, 10 equiv.) was added under N₂ atmosphere and the IR spectrum was recorded. An average shift of the υ(CO) bands by 5 cm^{-1} to higher wavenumbers was observed revealing the formation of **144H⁺(O)**. The same experiment was performed in MeCN and showed only decomposition

over time. The protonated complex showed stability over hours at room temperature.
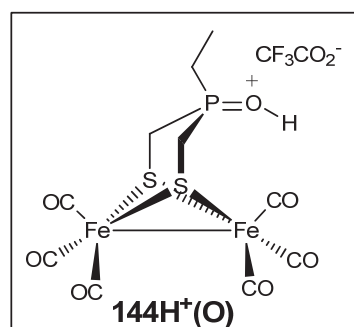
IR (CH₂Cl₂): 1990 (CO), 2011 (CO), 2048 (CO), 2085 (CO) cm^{-1}.

Protonation of complex **144** by HBF₄·Et₂O (1-100 equiv.) in CH₂Cl₂ has been also tested using procedure similar to that above. The presence of 1-3 equiv. HBF₄·Et₂O did

not affect the υ(CO) bands of complex **144**. In the presence of equiv. HBF$_4$·Et$_2$O $\geq$ 6, full protonation was observed.

IR (CH$_2$Cl$_2$): 2015 (CO), 2052 (CO), 2088 (CO) cm^{-1}.

Note: Transient species were observed in the presence of 6 equiv. HBF$_4$·Et$_2$O by IR spectroscopy having υ(CO) = 2099, 2117 and 2136 cm^{-1}. These bands disappeared in the presence of higher equivelents of HBF$_4$·Et$_2$O. Addition of Et$_3$N to the solution of **144H$^+$(O)** restored the IR spectrum (υ(CO) region) of **144**.

10.5.10 Reaction of 137 with BF$_3$·Et$_2$O

Into an NMR containing dry CD$_2$Cl$_2$ solution of complex **137** (5 mg, 1.00 × 10^{-5} mol), BF$_3$·Et$_2$O (2 equiv.) was added under N$_2$ atmosphere to afford complex **145**.

145

^{31}P{^{1}H} NMR (CD$_2$Cl$_2$, 121.49 MHz): δ 54.1. ^{19}F NMR (CD$_2$Cl$_2$, 282.40 MHz): δ -142.5 (P=O-B*F*$_3$), -153.7 (B*F*$_3$). ^{11}B NMR (CD$_2$Cl$_2$, 128.34 MHz): δ 0.04 (P=O-*B*F$_3$), 0.80 (*B*F$_3$) ppm. IR (CH$_2$Cl$_2$, 4 equiv. BF$_3$·Et$_2$O): 1989 (sh, CO), 2014 (CO), 2050 (CO), 2086 (CO) cm^{-1}.
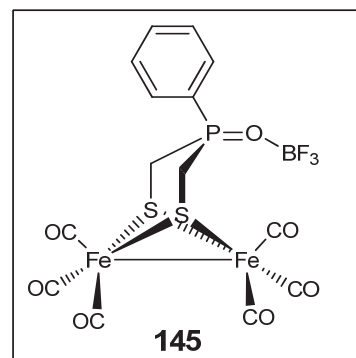
10.5.11 Reaction of 144 with BF$_3$·Et$_2$O

Into an NMR containing dry CD$_2$Cl$_2$ solution of complex **144** (7 mg, 1.56 × 10^{-5} mol), BF$_3$·Et$_2$O (2 equiv.) was added under N$_2$ atmosphere to afford complex **146**.

146

^{31}P{^{1}H} NMR (CD$_2$Cl$_2$, 121.49 MHz): δ 67.01. ^{19}F NMR (CD$_2$Cl$_2$, 282.40 MHz): δ -144.2 (P=O-B*F*$_3$), -153.8 (B*F*$_3$). ^{11}B NMR (CD$_2$Cl$_2$, 128.34 MHz): δ 0.1 (P=O-*B*F$_3$), 0.80 (*B*F$_3$).
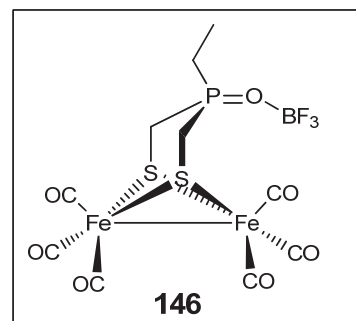
10.5.12   Synthesis of Me$_2$Ge(CH$_2$Cl)$_2$[242]
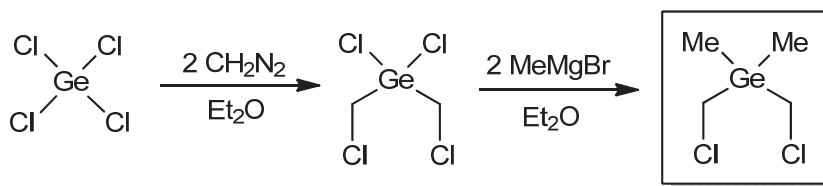
Step 1: Synthesis of 0.5 M CH$_2$N$_2$

Caution! *Diazomethane (CH$_2$N$_2$) is explosive, very toxic and cancerogenic. It is stable only in cold solution (T ≤ 0 °C) for few days, but it is better to use fresh solutions of diazomethane for the syntheses. The Erlenmayer flask containing the Diazomethane solution should not be tightly closed and plastic caps are used. When using the Diazomethane solution, all work must be done in a fume hood.*

To an 500 ml Erlenmayer flask contaning KOH (20 g), H$_2$O (30 mL) and ether (100 mL) at 0 °C, 1-methyl-1-nitrosourea (5 g, 0.05 mol) was added in portions (every 1-2 min) with stirring while the temperature is 0 °C. The color of the solution turns yellow due to formation of CH$_2$N$_2$. After complete addition, stirring was continued for 15 min. The yellow organic layer was then separated into an Erlenmayer flask containing KOH and kept at -20 °C for 3 h. The purpose of KOH is for drying the ether solution containing the in situ generated CH$_2$N$_2$.

Determination of the concentration of the diazomethane solution. The concentration of the diazomethane solution is determined by titration using 2,2,4,4-tetramethyl-3-sulfanylidenecyclobutan-1-one to prepare the titrant solution.

2,2,4,4-tetramethyl-3-thioxocyclobutanone
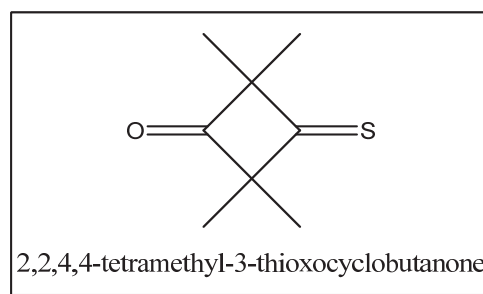
A red solution of 2,2,4,4-tetramethyl-3-sulfanylidenecyclobutan-1-one (0.156 g, 1 mmol) in ether (4.0 mL) is transferred to a titration buret to titrate the CH$_2$N$_2$ solution (1.0 mL). At the end point, the yellow CH$_2$N$_2$ solution becomes colorless. The concentration of CH$_2$N$_2$ ($M_{analyte}$) can be determined using the equation: $M_{titrant} \times V_{titrant} = M_{analyte} \times V_{analyte}$, where $M_{titrant}$ is the concentration of the titrant solution, $V_{titrant}$ volume of titrant required to reach the end point and $V_{analyte} = 1.0$ mL.

Step 2: Synthesis of Cl$_2$Ge(CH$_2$Cl)$_2$

GeCl$_4$ (2.8209 g, 13.16 mmol) was dissolved in a dry ether (20-30 mL) containing Cu (0.2564 g) under N$_2$ atmosphere and the resulting solution was cooled to -70 °C. Two equiv. volume of CH$_2$N$_2$ solution (61 mL, 0.4343 M) were added dropwise during 1 hour. *Note: Use small syringe (2 mL volume) for the addition. During this time the CH$_2$N$_2$ solution is kept at low temperature (T < 0 °C).* After complete addition, the solution was stirred for 12 h while the temperature was increasing slowly to r.t. The solution was then decanted from the Cu and the solvent is removed under reduced pressure. The crude product was purified by distillation (97 °C / 35 mmHg) to afford Cl$_2$Ge(CH$_2$Cl)$_2$ in 70 % yield as a colorless liquid. This compound was stored under N$_2$ at 5 °C.
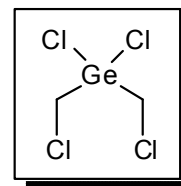
^{13}C{^{1}H} NMR (600 MHz, CD$_2$Cl$_2$): δ 31.6 (s, *C*H$_2$). ^{1}H NMR (600 MHz, CD$_2$Cl$_2$): δ 3.68 (s, C*H*$_2$).

Step 3: Reaction of Cl$_2$Ge(CH$_2$Cl)$_2$ with MeMgBr

Cl$_2$Ge(CH$_2$Cl)$_2$ (1.188 g, 4.9 mmol) was added to ether (80 mL) and the resulting solution was cooled to 0 °C. 2 equiv. volume of MeMgBr solution (3.3 mL, 0.3 M) in ether (10 mL) were added dropwise. After complete addition, the solution was stirred for 16 h at r.t. and was then refluxed for 4 h. The reaction mixture was filtered and the filtrate was extracted two times with an ice cold saturated solution of NH$_4$Cl in water. The combined etheryl solution was dried over Na$_2$SO$_4$. The solvent was the removed under reduced pressure and the crude product was distilled (78 °C / 20 mmHg) to afford Me$_2$Ge(CH$_2$Cl)$_2$ in 60 % yield as colorless liquid.
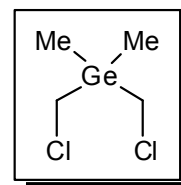
^{13}C{^{1}H} NMR (600 MHz, CD$_2$Cl$_2$): δ -5.61 (s, *C*H$_3$), 3.098 (s, *C*H$_2$) ppm. ^{1}H NMR (600 MHz, CD$_2$Cl$_2$): δ 0.429 (s, 6H, C*H*$_3$), 3.098 (s, 4H, C*H*$_2$) ppm.

10.5.13   Synthesis of Bis(iodomethyl)diphenylstannane, Ph₂Sn(CH₂I)₂

Into a 100 mL three-necked round-bottom flask, Cu(OAc)₂·H₂O (0.026 g, 0.13 mmol) and CH₃CO₂H (6.0 mL) were mixed and heated to 90-100 °C while stirring. To this hot solution, granular zinc (30-mesh, 1.700 g, 26.0 mmol) was added and the mixture was stirred for 2 min while heating. CH₃CO₂H was removed from the settled Cu-Zn couple using

syringe and fresh CH₃CO₂H (6.0 mL) was added. The mixture was stirred hot for 2 min. CH₃CO₂H was again removed and the couple was cooled, washed with Et₂O (3 × 7.0 mL) and dried by a stream of N₂. The deep grey / black colored couple was covered with THF (7.0 mL) and few drops of CH₂I₂ were added to initiate the reaction. When the color appears purple, THF (11.0 mL) was added followed by dropwise addition of CH₂I₂ (2.09 mL, 6.96 g, 26.0 mmol) in THF (6.0 mL) using an addition funnel. The addition should be with a rate that maintains the temperature at 40 °C. The addition took 1 h and mild heating was required during the last 15 min. This THF solution of IZnCH₂I was then cooled to ~ 0 °C and filtered under N₂ into a three necked round bottom flask. A solution of diphenyltin dichloride (Ph₂SnCl₂) (1.788 g, 5.2 mmol) in THF (6.0 mL) was added dropwise to the in situ generated IZnCH₂I during 1 h at 40 °C. For an additional 2 h, the reaction mixture was stirred at 40 °C. The cloudy, deep purple reaction mixture was diluted with equal volume of benzene (30 mL), extracted with 5 % HCl (4 × 60.0 mL). The organic phase was dried with Na₂SO₄, concentrated and purified by column chromatography (SiO₂ / hexane:CH₂Cl₂, 1:1) to afford Ph₂Sn(CH₂I)₂ (1.393 g, 48.3 % yield) as a colorless oil containing semi-crystalline particles of the same compound.
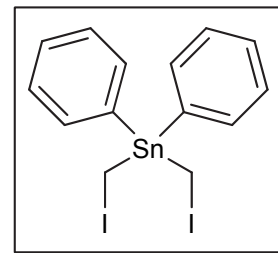
DEI-MS (m/z): 479 [PhSn(CH₂I)₂]$^+$, 415 [Ph₂SnCH₂I]$^+$, 351 [PhSn(CH₂I)(CH₂)]$^+$ and 273 [Ph₂Sn]$^+$. ^{13}C{^{1}H} NMR (400.08 MHz, CDCl₃): δ -10.53 (s, CH_2), 126.0-128.78 (m, CCHCHCH), 136.85 (m, CCHCHCH), 139.31 (m, CCHCHCH). ^{1}H NMR (400.08 MHz, CDCl₃): δ 2.41 (s with Sn satellites, ^2J{^{117}Sn,^{1}H} = 20.9 Hz, ^2J{^{119}Sn,^{1}H} = 41.8 Hz, 4H, CH_2), 7.38-7.43 (m, 4H, CCH$CHCH$), 7.55-7.60 (m, 2H, CCHCHCH).

10.5.14   Synthesis of Bis(iodomethyl)diphenylstannane, Me₂Sn(CH₂I)₂[244]

A mixture of Cu(OAc)$_2$·H$_2$O (0.040 g, 0.2 mmol) and CH$_3$CO$_2$H (8.0 mL) in a 100 mL three-necked round-bottom flask was heated to 90-100 °C while stirring. To this hot solution, granular zinc (30-mesh, 2.615 g, 40.0 mmol) was added and the mixture was stirred for 2 min while heating. CH$_3$CO$_2$H was then removed using syringe and fresh CH$_3$CO$_2$H (6.0 mL) was added. The mixture was stirred hot for ~ 2 min. CH$_3$CO$_2$H was again removed and the couple was cooled, washed with Et$_2$O (3 × 7.0 mL) and dried by a stream of N$_2$. The deep grey / black colored couple was covered with THF (7.0 mL) and few drops of CH$_2$I$_2$ were added to initiate the reaction giving very slight purple color. Subsequently, THF (11.0 mL) was added followed by dropwise addition of CH$_2$I$_2$ (3.22 mL, 10.714 g, 40.0 mmol) in THF (6.0 mL) using an addition funnel. The addition should be with a rate maintaining a temperature of ca. 40 °C. The addition took 1 h and mild heating was required during the last 15 min. This THF solution of IZnCH$_2$I was then cooled to ca. 0 °C and filtered under N$_2$ into a three necked round bottom flask. A solution of dimethyltin dichloride (Me$_2$SnCl$_2$) (1.758 g, 8 mmol) in THF (6.0 mL) was added dropwise to the in situ generated IZnCH$_2$I during 1 h at 40 °C. For an additional 2 h, the reaction mixture was stirred at 40 °C. The cloudy, deep purple reaction mixture was diluted with equal volume of benzene (35 mL), extracted using 5 % HCl (4 × 70.0 mL). The organic phase was dried with Na$_2$SO$_4$, concentrated and purified by column chromatography (SiO$_2$ / hexane) to afford Me$_2$Sn(CH$_2$I)$_2$ (70 %) as a colorless oil.
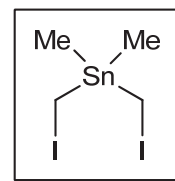
^{13}C{^{1}H} NMR: δ -8.1 (*C*H$_3$), -25.7 (*C*H$_2$). ^{1}H NMR: δ 0.35 (s, 6H, C*H*$_3$), 2.04 (s, 4H, C*H*$_2$).

10.5.15   Synthesis of [Fe₂(CO)₆{μ-(SCH₂)₂GeMe₂}] (150)

A red solution of (μ-S$_2$)Fe$_2$(CO)$_6$ (150 mg, 0.436 mmol) in THF (10 mL) was cooled to -78 ºC and treated dropwise with Et$_3$BHLi (0.9 mL, 0.872 mmol, 1.0 M in THF) to give a dark green solution. After stirring the solution for ~ 20 min at -78 ºC, Me$_2$Ge(CH$_2$Cl)$_2$ (88 mg, 0.436 mmol) in THF (3 mL) was added. The mixture was stirred for 18 h while slowly warming up to room temperature, giving rise to a dark red solution. Solvent removal was performed under N$_2$ using a vacuum transfer line. The residue was extracted several times with pentane and the extracts were collected and dried under N$_2$ using a vacuum transfer line. The red residue was then purified by column chromatography (SiO$_2$ / hexane) to give complex **150**.
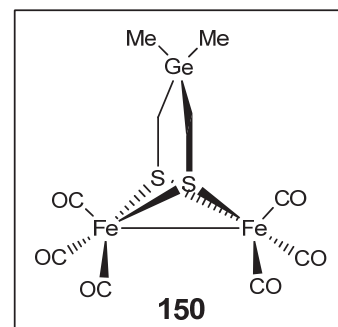
Anal. Calcd for C$_{20}$H$_{20}$Fe$_2$O$_6$S$_2$Ge: C, 36.90 %; H, 3.10 %; S, 9.85 %. Found: C, 36.88 %; H, 2.98 %; S 9.86 %. Micro-ESI-MS (*m/z*): 476 [M]$^+$, 448 [M - CO]$^+$, 420 [M - 2CO]$^+$, 392 [M - 3CO]$^+$, 364 [M - 4CO]$^+$, 334 [M - 5CO]$^+$, 308 [M - 6CO]$^+$. IR (CH$_2$Cl$_2$): 1989 (CO), 1996 (CO), 2031 (CO), 2070 (CO) cm^{-1}. ^{13}C{^{1}H} NMR (300 MHz, CD$_2$Cl$_2$): δ 0.13 (*CH$_3$*), 6.5 (*CH$_2$*), 207.95 (*CO*). ^{1}H NMR (300 MHz, CD$_2$Cl$_2$): δ 0.26 (s, 6H, C*H$_3$*), 1.66 (s, 4H, C*H$_2$*).

10.5.16   Synthesis of [Fe₂(CO)₆{μ-(SCH₂)₂SnMe₂}]ₙ (151 (n = 1), 152 (n = 2))

A different procedure for the synthesis of **151** is reported.[50] A red solution of (μ-S$_2$)Fe$_2$(CO)$_6$ (92.2 mg, 0.268 mmol) in THF (15 mL) was cooled to -78 ºC and treated dropwise with Et$_3$BHLi (0.6 mL, 0.536 mmol 1.0 M in THF) to give a dark green solution. After stirring the solution for ~ 20 min at -78 ºC, Me$_2$Sn(CH$_2$I)$_2$ (115 mg, 0.268 mmol) in THF (3 mL) was added. The mixture was stirred for 18 h while slowly warming up to room temperature, giving rise to a dark red solution. Solvent removal was performed under N$_2$ using a vacuum transfer line. The residue was extracted several times with pentane and the extracts were collected and dried under N$_2$ using a vacuum transfer line. The red residue was then purified by column chromatography (SiO$_2$ / hexane) and two red bands were identified being for **151** and **152**, respectively.

Complex 151: Micro-ESI-MS (*m/z*): 520 [M]$^+$. IR (CH$_2$Cl$_2$): 2063 (CO), 2031(CO), 1991 (CO), 1974 (CO) cm^{-1}. ^{13}C{^{1}H} NMR (200 MHz, CD$_2$Cl$_2$): δ -7.1 (*C*H$_3$), 1.6 (*C*H$_2$), 207.0 (*C*O). ^{1}H NMR (200 MHz, CD$_2$Cl$_2$): δ 0.25 (s, 6H, C*H*$_3$), 1.79 (s, 4H, C*H*$_2$).

Complex 152: mp 169-170 °C. Micro-ESI-MS (*m/z*): 520 [M]$^+$. FAB-MS (*m/z*): 1041, 1013, 957, 929, 901, 873. IR (CHCl$_3$): 2071 (CO), 2031 (CO), 1991 (CO) cm^{-1}. ^{13}C{^{1}H}NMR (200 MHz, CD$_2$Cl$_2$): δ -8.1 (*C*H$_3$), 1.1 (*C*H$_2$), 209 (*C*O). ^{1}H NMR (200 MHz, CD$_2$Cl$_2$): δ 0.36 (s, 12H, C*H*$_3$), 2.00 (s, 8H, C*H*$_2$).

151

152
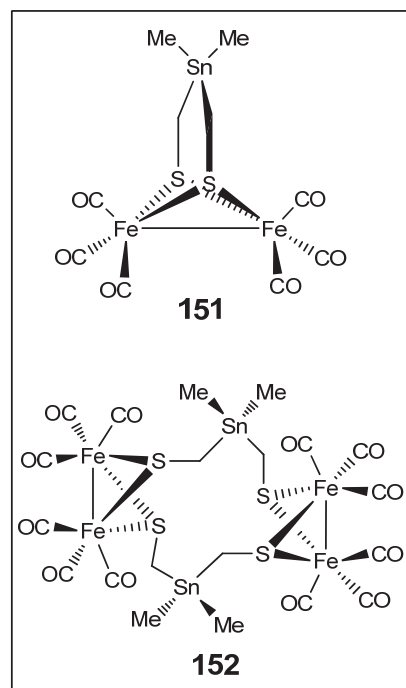
10.5.17 Synthesis of [Fe$_2$(CO)$_6${μ-(SCH$_2$)$_2$SnPh$_2$}]$_n$ (153 (n = 1), 154 (n = 2))

A red solution of (μ-S$_2$)Fe$_2$(CO)$_6$ (95.1 mg, 0.277 mmol) in THF (15 mL) was cooled to -78 ºC and treated dropwise with Et$_3$BHLi (0.6 ml, 0.553 mmol 1.0 M in THF) to give a dark green solution. After stirring the solution for ~ 20 min at -78 ºC, Ph$_2$Sn(CH$_2$I)$_2$ (154 mg, 0.277 mmol) in THF (3 mL) was added. The mixture was stirred for 18 h while slowly warming up to room temperature, giving rise to a dark red solution. Solvent removal was performed under N$_2$ using a vacuum transfer line. The residue was extracted several times with pentane and the extracts were collected and dried under N$_2$ using a vacuum transfer line. The red residue was then purified by column chromatography (SiO$_2$ / hexane) and two red bands

153

154
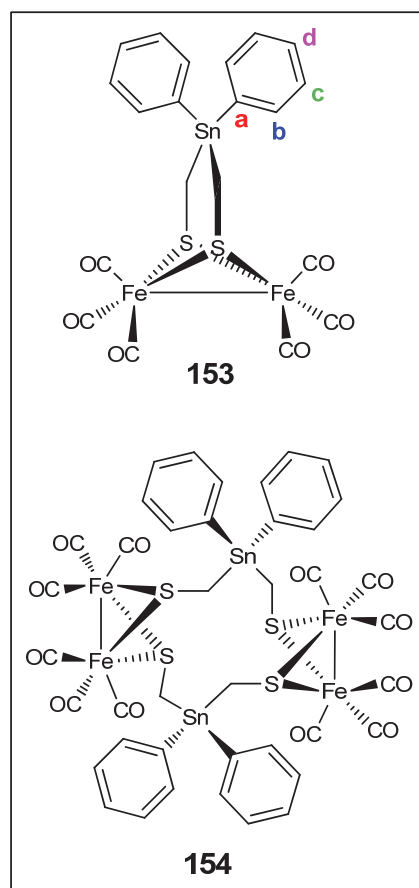
were identified being for **153** (a red oil) and **154** (traces), respectively.

Complex 153: Anal. Calcd for $C_{20}H_{14}Fe_2O_6S_2Sn$: C, 37.25 %; H, 2.19 %; S, 9.94 %. Found: C, 37.23 %; H, 2.20 %; S 9.96 %. Micro-ESI-MS (m/z): 646 $[M]^+$. $^{13}C\{^1H\}$ NMR (200 MHz, CD_2Cl_2): δ 1.70 (CH_2), 128.7-130.6 (c,d-C_{Ph}), 136.7-138.7 (a,b-C_{Ph}), 208.6 (CO), 209.1 (CO). ^1H NMR (200 MHz, CD_2Cl_2): δ 2.27 (s, 4H, CH_2), 7.35-7.70 (m, 10H, $2C_6H_5$).

Complex 154: traces.

10.5.18 Synthesis of (PPh₃)Ni(Br)(κ²S,S-S₂CNC₄H₈) (155)

This compound was synthesized before by different method.[282] A solution of $(PPh_3)_2NiBr_2$ (0.2 g, 0.365 mmol) and ammonium pyrrolidine dithiocarbamate (0.06 g, 0.366 mmol) in CH_2Cl_2 or MeCN (50 mL) was stirred for 18 hr. The color of the solution changes from dark green to violet

155

during the reaction. The solution was filtered and the solvent was removed under reduced pressure to afford violet oil. After washing several times with pentane, a violet powder of **155** was obtained in 80 % yield.
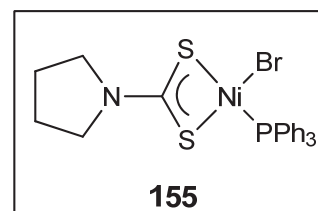
DEI-MS (m/z): 569 $[M]^+$. $^{31}P\{^1H\}$ NMR (200 MHz, $CDCl_3$): δ 27.19 ppm. $^{13}C\{^1H\}$ NMR (200 MHz, $CDCl_3$): δ 24.14 (CH_2), 48.65 (NCH_2), 128.1-134.6 (PPh_3), 199.68 (CS_2). ^1H NMR (200 MHz, $CDCl_3$): δ 1.91 (m, 4H, NCH_2CH_2), 3.47 (t, $^3J = 6.0$ Hz, 4H, NCH_2CH_2), 7.35-7.65 ppm (m, 15H, PPh_3).

10.5.19 Synthesis of (PPh₃)M(Cl)(κ²S,S-S₂CNC₄H₈) (M = Pd (156), M = Pt (157)[283])

The molecular structure of complex **157** has been recently published.[283] A general procedure for preparation of complexes **156** and **157** is shown here. A solution of $(PPh_3)_2MCl_2$ (0.14 mmol) and ammonium pyrrolidine dithiocarbamate (23 mg, 0.14 mmol) was stirred in THF (50 mL) for 18 h. After filtration, the THF

M = Pd (**156**), Pt (**157**)
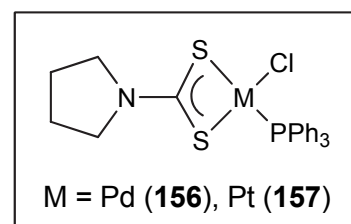
was removed under reduced pressure, and the residue was washed several times with hexane. The resulting solid was extracted with CH_2Cl_2. The solvent was removed and the resulting powder was dried under vacuum.

Complex 156: Yield: 75 %. Anal. Calcd for $C_{23}H_{23}ClN_2PPdS_4 \cdot 0.5CHCl_3$: C, 46.3 %; H, 3.9 %; N, 2.3 %; S, 10.5 %. Found: C, 46.9 %; H, 4.4 %; N, 2.2 %; S, 10.9 %. DEI-MS (m/z): 629 $[M]^+$. $^{31}P\{^1H\}$ NMR (CDCl$_3$): δ 30.6 ppm. $^{13}C\{^1H\}$ NMR (CDCl$_3$): δ 25.3 (CH_2), 48.9 (NCH_2), 128.2, 131.2 and 132.7 (PPh$_3$), 202.0 (CS$_2$). ^1H NMR (CDCl$_3$): δ 1.97 (m, 4H, NCH$_2$CH_2), 3.55 (t, 4H, 2NCH_2CH$_2$, ^3J = 6.8 Hz), 7.31-7.64 (m, 15H, PPh$_3$).

10.5.20   Synthesis of (PPh$_3$)M(κS,S$_2$C-NC$_4$H$_8$)($\kappa^2 S$,S-S$_2$CNC$_4$H$_8$) (158)

A solution of (PPh$_3$)$_2$PtCl$_2$ (0.11 g, 0.14 mmol) and ammonium pyrrolidinedithiocarbamate (46 mg, 0.28 mmol) in THF (50 mL) was stirred for 48 h. After filtration, the THF was removed under reduced pressure. The resulting solid was extracted with CH_2Cl_2 and extracts concentrated to dryness. Yield: 81 %.

158
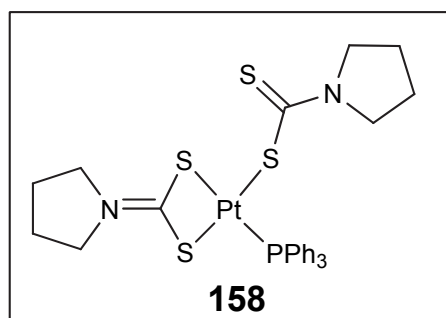
Anal. Calcd for $C_{28}H_{31}N_2PPtS_4 \cdot 0.25C_{10}H_{12} \cdot 2CH_2Cl_2$: C, 40.0 %; H, 4.1 %; N, 3.0 %; S, 13.7 %. Found: C, 40.4 %; H, 4.3 %; N, 2.8 %; S, 13.4 %. DEI-MS (m/z): 749 $[M]^+$. $^{31}P\{^1H\}$ NMR (CDCl$_3$): δ 17.43 (^{195}Pt satellites, $^2J_{PPt}$ = 4603 Hz). $^{13}C\{^1H\}$ NMR (CDCl$_3$): δ 25.1 and 26.1 (CH_2), 50.8 and 55.1 (NCH_2), 127.6, 129.5 and 133.1 (PPh$_3$), 200.5 (CS$_2$). ^1H NMR (CDCl$_3$): δ 1.95 (m, 4H, NCH$_2$CH_2), 2.04 (m, 4H, NCH$_2$CH_2), 3.60 (t, 4H, 2NCH_2CH$_2$, ^3J = 6.8 Hz), 3.91 (t, 4H, 2NCH_2CH$_2$, ^3J = 6.8 Hz), 7.35-7.55 (m, 15H, PPh$_3$).

10.5.21   Synthesis of [(dppe)M(κ^2S,S-S$_2$CNC$_4$H$_8$)]Cl (M = Pd (159), Pt (160))

A solution of (dppe)MCl$_2$ (0.19 mmol) and ammonium pyrrolidine dithiocarbamate (32 mg, 0.19 mmol) in THF (50 mL) was stirred at room temperature for 18 h. The resulting yellow mixture was filtrated and the solvent was evaporated under reduced pressure. The obtained solid was washed several times with hexane and extracted with CH$_2$Cl$_2$.

M = Pd (**159**), Pt (**160**)
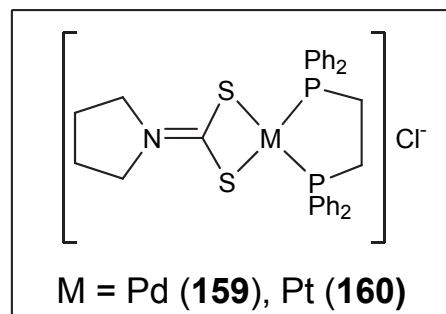
Complex 159: Yield: 75 %. Anal. Calcd for C$_{31}$H$_{32}$ClNP$_2$PdS$_2$·1.33H$_2$O·CHCl$_3$: C, 46.3 %; H, 4.3 %; N, 1.7 %; S, 7.7 %. Found: C, 46.9 %; H, 4.5 %; N, 1.7 %; S, 7.9 %. DEI-MS (*m/z*): 651 [M$^+$ - Cl]. ^{31}P{^{1}H} NMR (CDCl$_3$): δ 63.27. ^{13}C{^{1}H} NMR (CDCl$_3$): δ 28.7 (*C*H$_2$); 53.3 (N*C*H$_2$); 44.0 (P*C*H$_2$); 126.7, 127.5, 128.3 (P*Ph*$_2$); 201.6 (*C*S$_2$). ^{1}H NMR (CDCl$_3$): δ 1.95 (t, 4H, NCH$_2$C*H*$_2$, ^3J = 6.8 Hz), 2.81 (d, 4H, PC*H*$_2$, $^2J_{HP}$ = 22.2 Hz), 3.74 (t, 4H, NC*H*$_2$CH$_2$, ^3J = 6.5 Hz), 7.48-7.75 (m, 20H, P*Ph*$_2$).

Complex 160: Yield: 88 %. Anal. Calcd for C$_{31}$H$_{32}$ClNP$_2$PtS$_2$: C, 48.0 %; H, 4.2 %; N, 1.8 %; S, 8.3 %. Found: C, 48.3 %; H, 4.4 %; N, 1.6 %; S, 8.0 %. DEI-MS (*m/z*): 739 [M$^+$ - Cl]. ^{31}P{^{1}H} NMR (CDCl$_3$): δ 46.6 (^{195}Pt satellites, $^2J_{PPt}$ = 3888 Hz). ^{13}C{^{1}H} NMR (CDCl$_3$): δ 28.2 (*C*H$_2$); 49.8 (N*C*H$_2$), 49.6 (P*C*H$_2$), 127.3, 129.7 and 132.5 (P*Ph*$_2$), 200.3 ppm (*C*S$_2$). ^{1}H NMR (CDCl$_3$): δ 2.05 (m, 4H, NCH$_2$C*H*$_2$), 2.89 (d, 4H, PC*H*$_2$, $^2J_{HP}$ = 18.8 Hz), 3.71 (t, 4H, NC*H*$_2$CH$_2$, ^3J = 5.8 Hz), 7.44-7.79 (m, 20H, P*Ph*$_2$).

10.5.22   Synthesis of Sodium *N,N*-dimethylcarbamoselenothioate, Me$_2$NCSSeNa[288]

To reaction flask containing Na (1.468 g), Se (2.522 g) powder and naphthalene (0.818 g), degassed THF (50 mL) was added and the mixture was refluxed for 3 h. Solvent removal was performed under N$_2$ using a vacuum transfer line to afford
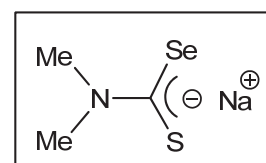
the sodium selenide as white solid.[287] *Na$_2$Se undergoes immediate decomposition upon contact with air*. After that, MeCN (10 mL) was added to the white solid and the

suspension was cooled to 0 °C. A solution of 0.987 g *N,N*-dimethylcarbamoyl chloride, (Me$_2$CSCl) in MeCN (10 mL) was added very slowly over 1 h to the suspension of Na$_2$Se. After complete addition, the reaction mixture was stirred at 0 °C for 3 h. After filtration under inert conditions to remove the insoluble NaCl and the excess Na$_2$Se, the orange filtrate was evaporated to afford 1.7 g of a yellow powder of sodium *N,N*-dimethylcarbamoselenothioate (85 % yield).

DEI-MS (*m/z*): 168 M$^+$. ^{77}Se NMR (600 MHz, CD$_3$OH): δ 503.2. ^{13}C{^{1}H} NMR (600 MHz, CD$_3$OH): δ (s, *C*H$_3$), (s, *C*H$_3$), 207.3 (s, *C*SSe). ^{1}H NMR (600 MHz, CD$_3$OH): δ 3.49 (s, 3H, *C*H$_3$), 3.64 (s, 3H, *C*H$_3$), 3.61-3.83 (m, 4H, *C*H$_2$S).

Attempts to crystallize jMe$_2$NCSSeNa led only to the formation of crystals of compound **162**.

DEI-MS (*m/z*): 336 [M]$^+$. ^{1}H NMR (600 MHz, CD$_2$Cl$_2$): δ 3.43 and 3.52 ppm (s, *C*H$_3$).

162
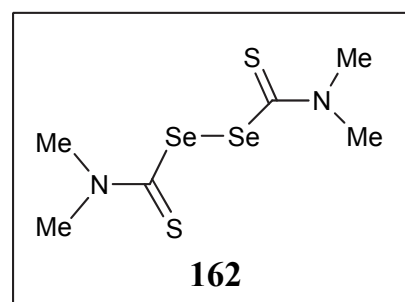
10.5.23 Synthesis of (PPh$_3$)Ni(Br)(κ^2*S,Se*-SSeCNMe$_2$) (161)

A solution of (PPh$_3$)$_2$NiBr$_2$ (0.5 mg) and sodium *N,N*-dimethylcarbamoselenothioate (0.128 g) in MeCN (50 mL) was stirred for 18 hr. The color of the solution changes from dark green to violet during the reaction. After filtration under N$_2$, solvent was removed using a vacuum transfer line to afford a violet powder of (PPh$_3$)Ni(Br)(κ^2*S,Se*-SSeCNMe$_2$) in 75 % yield.

161
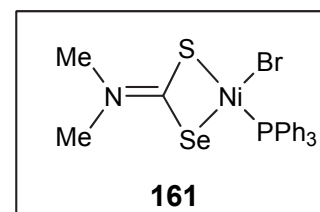
Anal. Calcd for C$_{21}$H$_{21}$BrNNiPSSeC, 44.41 %; H, 3.73 %; N, 2.47 %; S, 5.65 %, Found: C, 44.52 %; H, 3.76 %; N, 2.28 %; S, 5.14 %. DEI-MS (*m/z*): 569 [M]$^+$. ^{77}Se NMR (600 MHz, CD$_2$Cl$_2$): δ 317.3. ^{31}P{^{1}H} NMR (600 MHz, THF-d): δ 33.27. ^{13}C{^{1}H} NMR (600 MHz, THF-d): δ 39.09 (s, *C*H$_3$), 40.41 (s, *C*H$_3$), 126.1-138.3 (PPh$_3$), 198.03 (*C*SSe). ^{1}H NMR. (600 MHz, THF-d): δ 3.01 (s, 3H, *C*H$_3$), 3.07 (s, 3H, *C*H$_3$), 7.40-7.82 (m, 15H, PPh$_3$).

Supporting Information

S2 Chapter 2
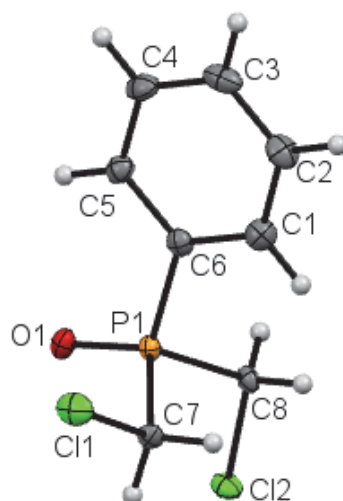
Figure S2-1. Molecular structure (50 % probability) of O=P(Ph)(CH$_2$Cl)$_2$. Selected Bond distances [Å] and angles [°]: P1-O1 1.495(4), P1-C6 1.802(6), P1-C7 1.819, P1-C8 1.818(5), C7-Cl1 1.772(6), C8-Cl2 1.789(5); O1-P1-C6 113.8(3), C6-P1-C8 105.2(3), C6-P1-C7 107.6(3), O1-P1-C8 114.2(2), O1-P1-C7 113.5(2), C7-P1-C8 101.5(3).

Table S2-1. Calculated energies and numbers of imaginary frequencies.

Compound	E_{corr} [a.u.]	NImag	E_{CPCM} [a.u.][a]
137	-2451.470784	0	-2451.651661
137H$^+$(O)	-2451.824499	0	-2452.064392
137H$^+$(S)	-2451.791518	0	-2452.037430
137HBF$_4$(O)	-2876.632191	0	-2876.853232
137HBF$_4$(S)	-2876.610110	0	-2876.817666
137HPy$^+$(O)	-2700.145509	0	-2700.460840
137HPy$^+$(S)	-2700.120349	0	-2700.450497

[a]Corresponding to CH$_2$Cl$_2$ as the solvent

Table S2-2. Calculated bond lengths compared to X-ray data of **137** (acid: HPy$^+$) [Å].

Bond[a]	137_{exp}	137_{calc}	$137H^+(O)$	$137H^+(S)$	$137HPy^+(O)$	$137HPy^+(S)$
Fe1-Fe2	2.515	2.512	2.520	2.561	2.513	2.514
Fe1-S1	2.259	2.327	2.321	2.299	2.329	2.351
Fe1-S2	2.256	2.327	2.321	2.336	2.320	2.319
Fe2-S1	2.258	2.319	2.310	2.277	2.315	2.327
Fe2-S2	2.260	2.319	2.310	2.329	2.313	2.324
S1-C1	1.824	1.843	1.848	1.839	1.843	1.845
S2-C2	1.831	1.843	1.848	1.854	1.841	1.845
C1-P1	1.796	1.832	1.812	1.864	1.824	1.839
C2-P1	1.799	1.832	1.812	1.838	1.826	1.834
P1-O1	1.484	1.497	1.596	1.493	1.518	1.497
H-O		-	0.968	-	1.530	-
H-O		-	2.114		-	2.472
H-S		-	-	1.354	-	2.238
H-F		-	-	-	-	-
H-N		-	-	-	1.065	1.043

[a]Atom numbering corresponds to Figure 2-4, atoms without numbering correspond to protonation of O or S, respectively.
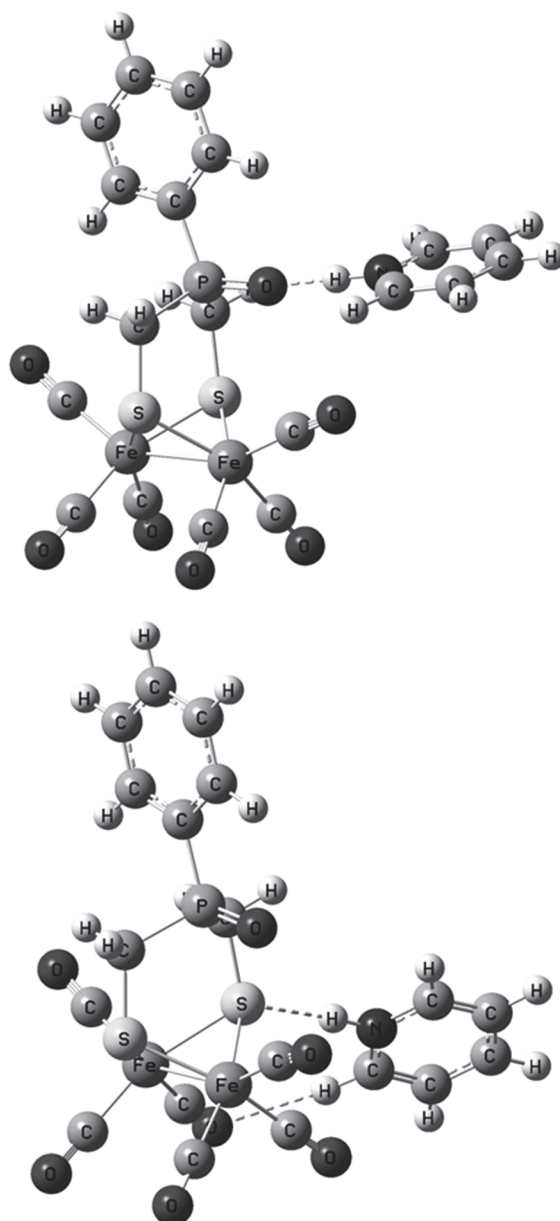
Figure S2-2. Calculated structures of **1HPy⁺(O)** (left) and **1HPy⁺(S)** (right).

Ion-pairing Effect. The shift of the calculated $\upsilon(CO)$ values (compared to the experimental values) to higher wavenumbers can be explained by the fact that the calculations were performed in the gas phase. According to Table S2-3, protonation of complex **137** at the oxygen atom of the P=O functionality shifts the $\upsilon(CO)$ in average of ~ 7 and 20 cm⁻¹ to higher wavenumbers in case of **137HBF₄(O)** and **137H⁺(O)**, respectively. The smaller shift in case of **137HBF₄(O)** can be attributed to the effect of ion-pairing between the protonated complex and BF₄⁻, which minimizes the hydrogen bonding toward the apical CO calculated for **137H⁺(O)** (Figure 2-7). Indeed, the

calculated shift due to the formation of **137HBF$_4$(O)** is in good agreement with the experimental value, indicating the role of BF$_4^-$ in the solution.[86]

Table S2-3. Calculated carbonyl stretching frequencies, υ(CO) [cm^{-1}].

137$_{calc}$	137H$^+$(O)	137H$^+$(S)	137HBF$_4$(O)	137HBF$_4$(S)	137HPy$^+$(O)	137HPy$^+$(S)
2157	2177	2200	2163	2163	2163	2171
2124	2137	2172	2130	2132	2118	2144
2095	2129	2142	2106	2101	2112	2114
2088	2102	2135	2097	2097	2089	2103
2067	2055		2071		2072	2074
						2039
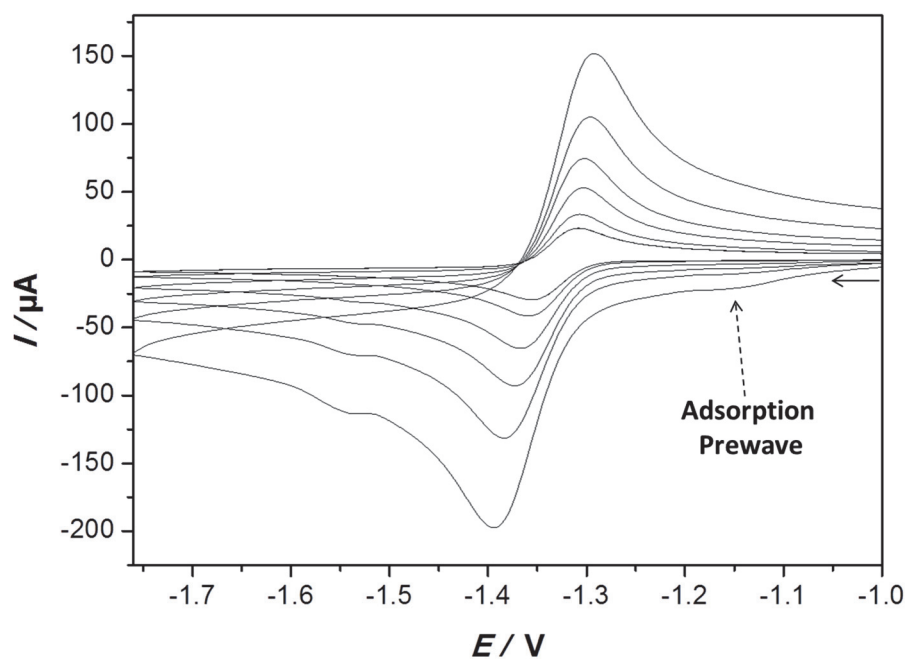
Figure S2-3. Cyclic voltammetric reduction of 0.9 mM complex **137** (MeCN/NBu$_4$PF$_6$ solution) on a mercury drop electrode using scan rates of 1, 2, 5, 10, 20 and 40 V·s^{-1}. Referenced against the ferrocenium/ferrocene couple. The direction of the scan is indicated by an arrow.
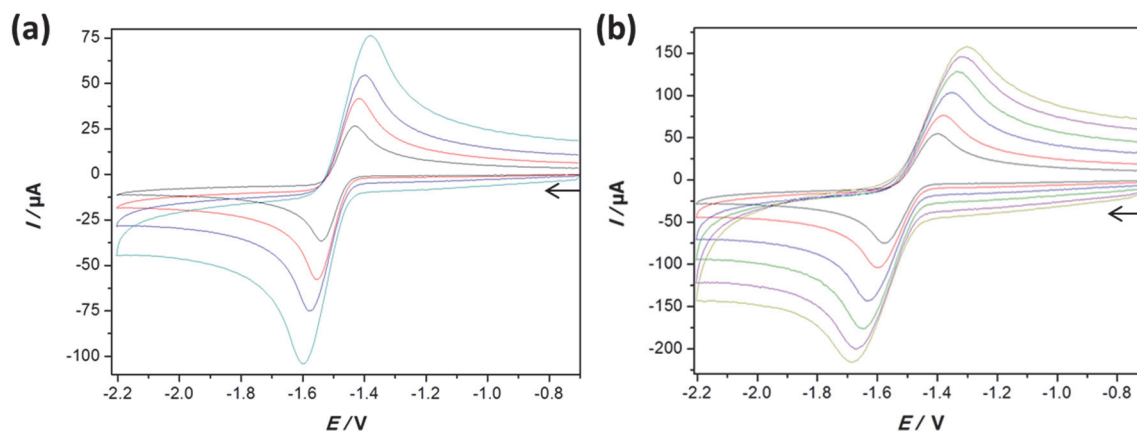
Figure S3-1. Cyclic voltammetry of 0.65 mM complex **137** (CH_2Cl_2/NBu_4PF_6 solution) at scan rates ($V \cdot s^{-1}$) = (a) 0.2 (black), 0.5 (red), 1 (blue), 2 (green), (b) 1 (black), 2 (red), 4 (blue), 6 (green), 8 (violet) and 10 (dark yellow). Glassy carbon disk (d = 3 mm). *E* is in V against the ferrocenium/ferrocene couple. The arrows indicate the scan direction.
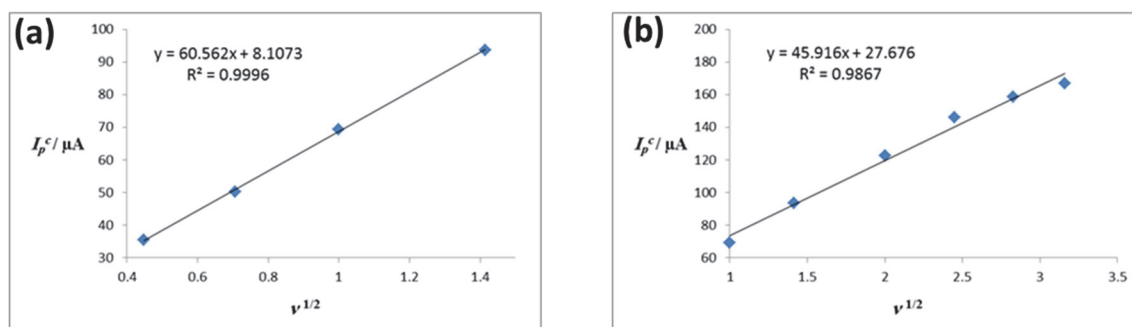
Figure S3-2. Plots of the cathodic current (I_p^c) versus square root of scan rate ($v^{1/2}$/ ($V \cdot s^{-1}$)$^{1/2}$) obtained from the cyclic voltammetry of complex **137** in (a) Figures S3-1a and (b) Figure S3-1b.
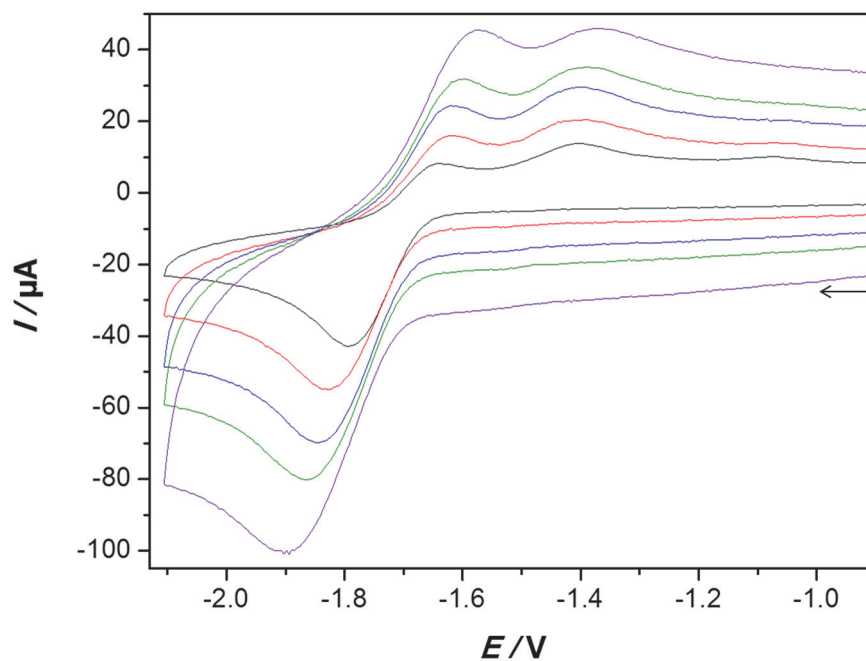
Figure S3-3. Cyclic voltammetry of 0.408 mM complex **138** (CH_2Cl_2/NBu_4PF_6 solution) at scan rates ($V·s^{-1}$) equal to 1 (black), 2 (red), 3 (blue), 4 (green) and 6 (purple). Glassy carbon electrode (d = 3 mm). *E* is in V against the ferrocenium/ferrocene couple. The arrow indicates the scan direction.

Table S3-1. Results of DFT calculations of **140** and **141** in the neutral, monoanionic and dianionic state as well as **P1**, **P2** and the reduced species derived from them.

	E_T [a.u.]	*NImag*	Stabilization [kJ·mol^{-1}]
140	-2799.196753	1^a	0
140$^-$	-2799.260484	1^a	-167.3
140^{2-}	-2799.206017	0	-24.3
140a^{2-}	-2799.225453	0	-75.4
140b^{2-}	-2799.212985	0	-42.6
141	-3024.944206	0	0
141$^-$	-3025.014420	0	-184.3
141^{2-}	-3024.951196	0	-18.4
141a^{2-}	-3024.963479	0	-50.6
141b^{2-}	-3024.956772	0	-33.0
P1	-3256.248118	0	
P2	-3256.238331	0	
P1$^-$	-3256.269607	0	
P1^0	-3256.190197	0	
P2^0	-3256.182587	0	

^{a}One imaginary frequency corresponds to the rotation of the PMe$_3$ ligand with respect to the [Fe$_2$S$_2$] cluster core and is of very low intensity.
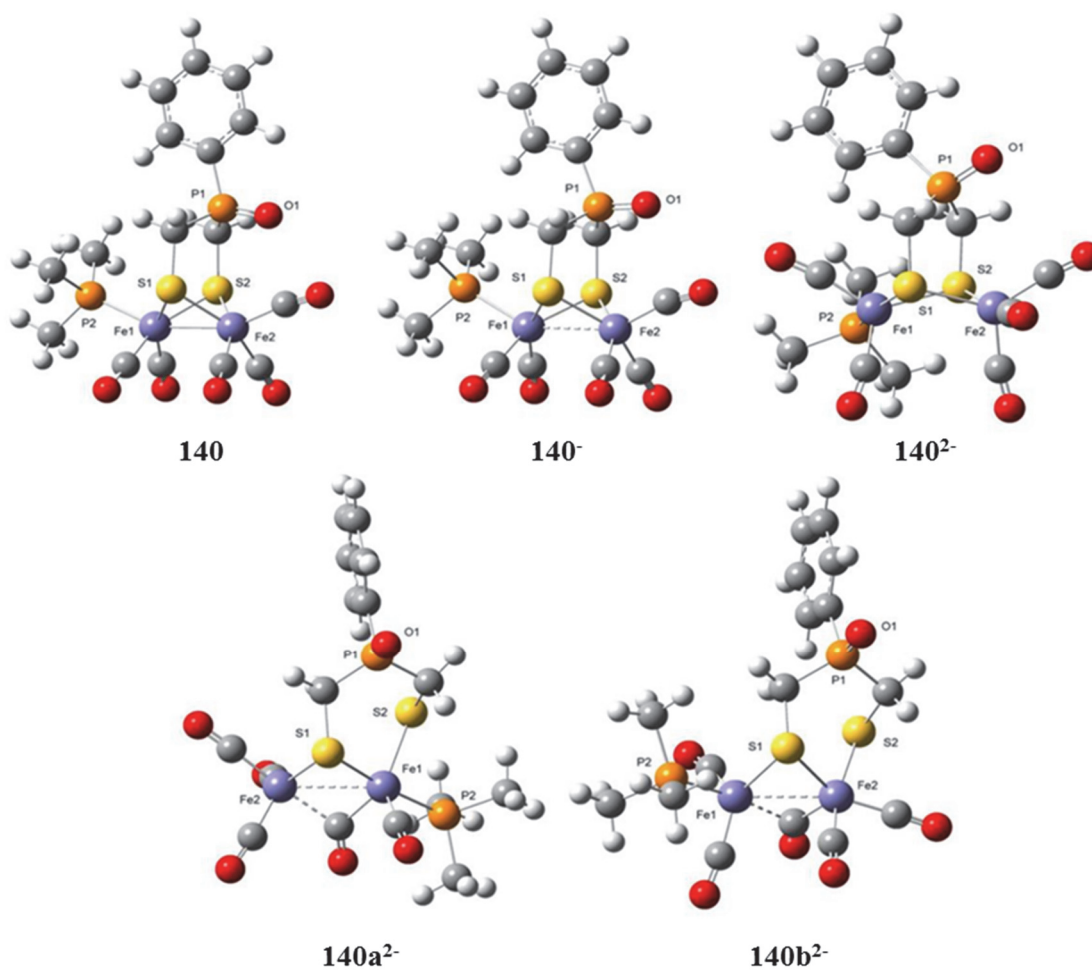
Figure S3-4. Calculated molecular structures and selected bond lengths [pm] of **140**: Fe1-Fe2 249.7, Fe1-S1 234.0, Fe1-S2 234.4, Fe2-S1 234.7, Fe2-S2 234.3, Fe1-P2 226.3, P1-O1 149.7; **140⁻**: Fe1-Fe2 274.0, Fe1-S1 237.8, Fe1-S2 237.9, Fe2-S1 240.0, Fe2-S2 239.7, Fe1-P2 234.1, P1-O1 150.0; **140²⁻**: Fe1-Fe2 350.7, Fe1-S1 236.9, Fe1-S2 244.7, Fe2-S1 242.2, Fe2-S2 239.9, Fe1-P2 220.0, P1-O1 151.2; **140a²⁻**: Fe1-Fe2 265.2, Fe1-S1 231.1, Fe1-S2 254.3, Fe2-S1 237.9, Fe1-P2 224.0, P1-O1 151.5; **140b²⁻**: Fe1-Fe2 271.8, Fe1-S1 244.0, Fe2-S1 234.7, Fe2-S2 245.1, Fe1-P2 220.2, P1-O1 151.6.
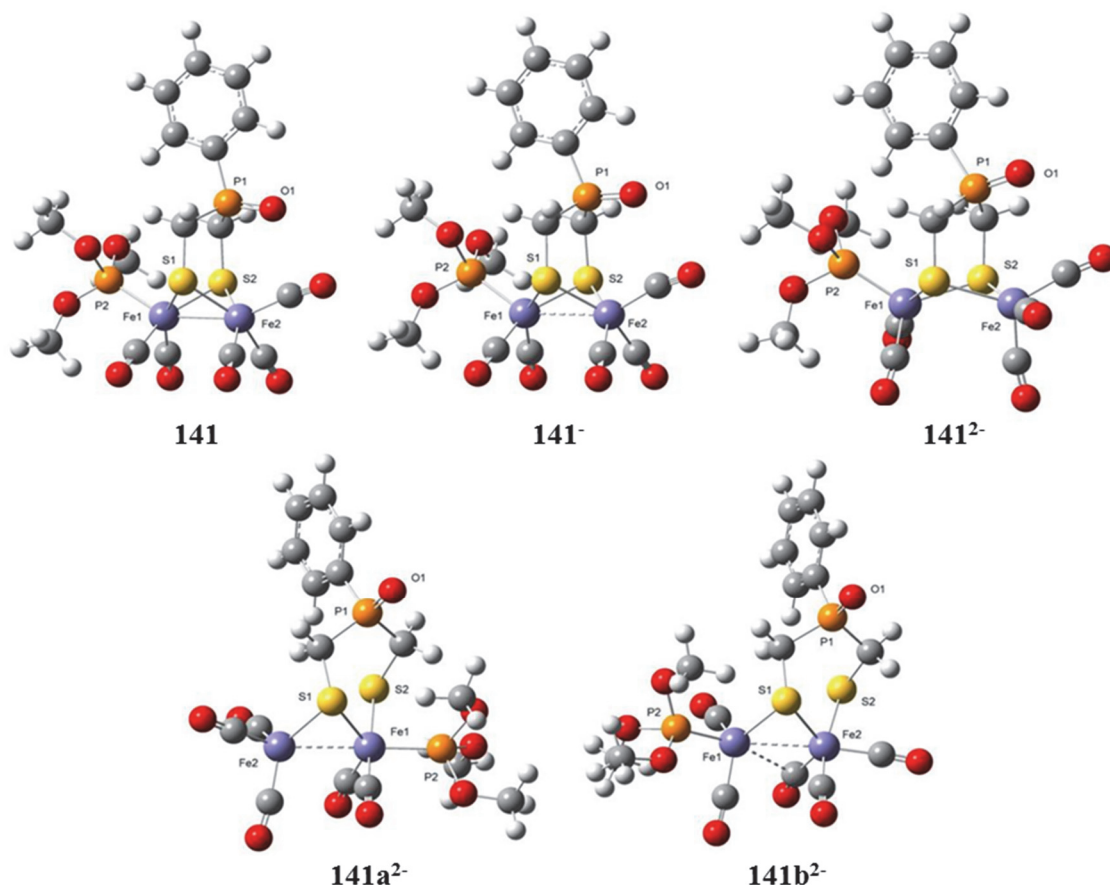
Figure S3-5. Calculated molecular structures and selected bond lengths [pm] of **141**: Fe1-Fe2 250.6, Fe1-S1 232.6, Fe1-S2 233.1, Fe2-S1 233.1, Fe2-S2 233.3, Fe1-P2 219.0, P1-O1 149.8; **141⁻**: Fe1-Fe2 276.3, Fe1-S1 236.9, Fe1-S2 237.8, Fe2-S1 237.7, Fe2-S2 238.4, Fe1-P2 219.8, P1-O1 150.2; **141²⁻**: Fe1-Fe2 344.7, Fe1-S1 240.7, Fe1-S2 240.4, Fe2-S1 244.0, Fe2-S2 239.7, Fe1-P2 210.0, P1-O1 150.8; **141a²⁻**: Fe1-Fe2 272.5, Fe1-S1 236.7, Fe1-S2 245.7, Fe2-S1 232.9, Fe1-P2 214.7, P1-O1 151.6; **141b²⁻**: Fe1-Fe2 273.9, Fe1-S1 234.7, Fe2-S1 235.9, Fe2-S2 244.6, Fe1-P2 211.1, P1-O1 151.6.

Structure of Species P. Another important question that arose during the electrochemical investigations was the molecular structure of compound **P**, which is formed by the reaction of the doubly reduced form of **139** with CO. We therefore calculated compounds with one additional CO ligand starting either from **139²⁻** or **139a²⁻**. In the case of **139a²⁻** as the substrate, we used a compound with two bridging CO ligands as the starting point for geometry optimization. Nevertheless, a convergence in the calculations was only reached after significant structural changes in the cluster core ending up with a situation in which a Lewis acid-Lewis base adduct, namely **P1**, consisting of a trigonal pyramidal [Fe(CO)₄] and a square planar {Fe(CO)₂(P(OEt)₃)[(SCH₂)₂(Ph)P=O]} fragment linked by an iron iron contact is observed (Figure S3-6). By forming this adduct, the coordination geometry of the first

iron is completed to a distorted trigonal bipyramidal coordination environment and the second iron then shows a distorted octahedral geometry. The iron-iron interaction is quite weak with a bond length of 312.5 pm. Perhaps this long distance shows how the compound might decompose. If on the other hand the thermodynamically less stable dianion **139**$^{2-}$ is used as the substrate for CO addition, one of the Fe-S bonds in the symmetrical [Fe$_2$S$_2$] core is broken upon geometry optimization. The resulting structure **P2** still shows one bridging sulfur that coordinates a [Fe(CO)$_4$] and a {Fe(CO)$_2$(P(OEt)$_3$)[(SCH$_2$)$_2$(Ph)P=O]} fragment (Figure S3-6). Both iron atoms exhibit trigonal bipyramidal coordination environments. The overall reactions for the formation of **P1** and **P2** from the respective starting compounds are slightly exothermic with an enthalpy of -33.9 kJ·mol^{-1} (**P1**) and -38.4 kJ·mol^{-1} (**P2**). Nevertheless, **P1** is 25.7 kJ·mol^{-1} more stable than **P2** if only those calculated compounds are compared. Table S3-1 above shows the DFT total energies E_T and the number of imaginary frequencies for all stationary points calculated for **P1** and **P2** as well as selected calculated bond lengths.

P1   **P2**
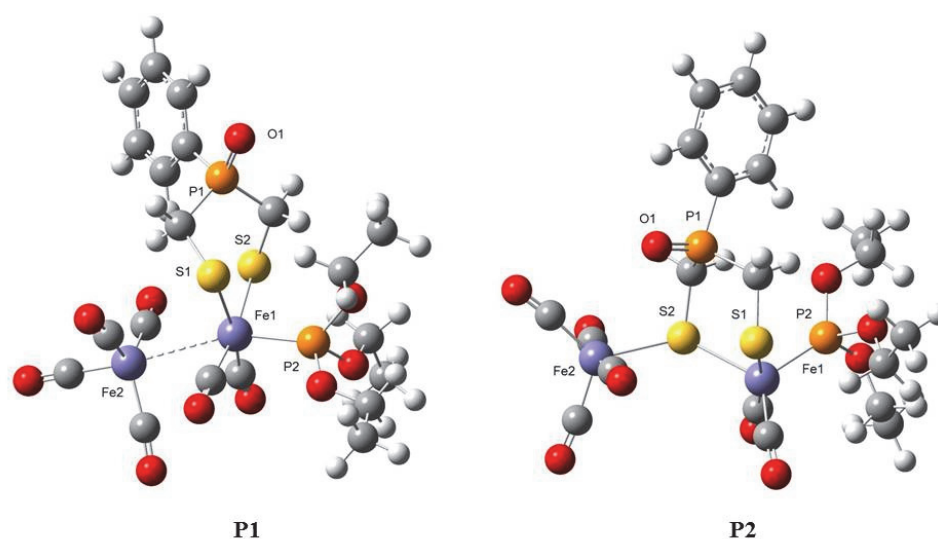
Figure S3-6. Calculated molecular structures and selected bond lengths [pm] of dianionic species **P1**: Fe1-Fe2 312.5, Fe1-S1 242.9, Fe1-S2 243.4, Fe1-P2 219.5, P1-O1 151.8; **P2**: Fe1-Fe2 451.3, Fe1-S1 241.2, Fe1-S2 248.5, Fe2-S2 243.9, Fe1-P2 212.1, P1-O1 150.7.

It has also been shown by cyclic voltammetry (Figure 3-7 and Scheme 3-3) that compound **P** undergoes a reversible oxidation process. We therefore calculated both monoanionic and neutral species with the calculated structures of **P1** and **P2** as the starting geometries. Whereas the geometry optimization of **P2** after one-electron

oxidation did not converge, the corresponding monoanionic species from **P1** could be calculated. In both cases neutral compounds that would be obtained from the loss of two electrons from **P1** or **P2**, respectively, could be calculated. The corresponding structures are depicted in Figure S3-7. The monoanion derived from **P1** shows the same connectivity pattern although it is obvious that upon loss of one electron the iron-iron bond length as well as the distances of Fe1 towards the coordinating sulfur atoms are shortened. If another electron is removed, electron demand in the cluster core is compensated by one of the sulfur atoms moving into a bridging position again. In addition, the iron-iron distance is further diminished. The same trend is observed if **P2** is oxidized. If two electrons are removed the iron atoms are again moved into close proximity to each other resulting in the same [Fe$_2$S$_2$] cluster core for **P2^0** as in **P1^0**. Both compounds are therefore isomers, which just differ in the dihedral angle of the Fe(CO)$_4$ group with respect to the rest of the molecule as well as in the conformation of the six-membered FeS$_2$C$_2$P ring. In summary, the addition of CO to the reduced species followed by oxidation of the resulting cluster compounds **P1** and **P2** results in the formation of compounds with the same connectivity as it has been observed for **139a^{2-}** and **139b^{2-}**. As it is expected from the Wade-Mingos rules, the composition of a transition metal cluster compound is determined by the number of electrons in the cluster irrespective whether electrons are provided by additional ligands (**P1^0**, **P2^0**) or by reduction (**139a^{2-}**, **139b^{2-}**).

P1$^-$ P1^0 P2^0
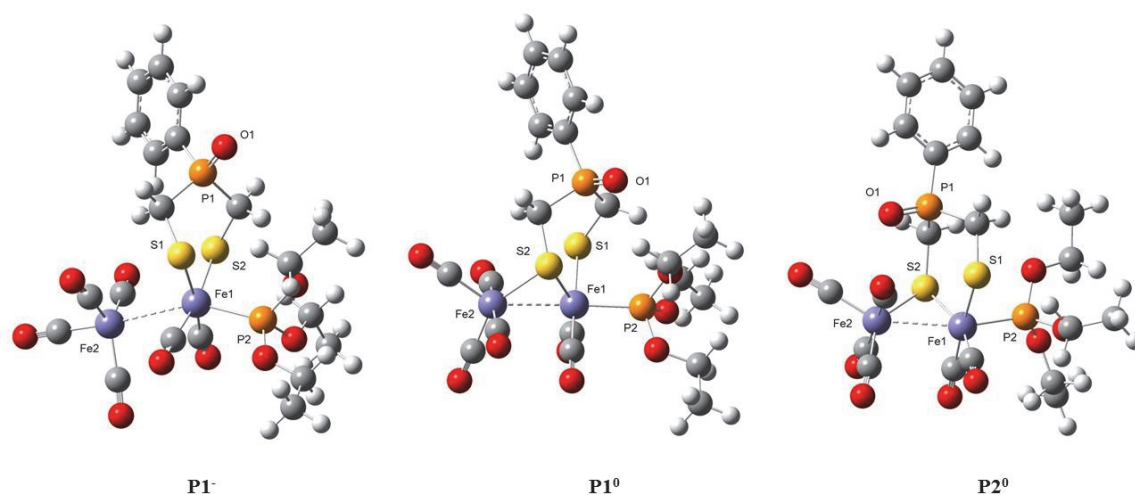
Figure S3-7. Calculated molecular structures and selected bond lengths of **P1$^-$**: Fe1-Fe2 303.1, Fe1-S1 235.9, Fe1-S2 236.1, Fe1-P2 228.4, P1-O1 151.0; **P1^0**: Fe1-Fe2 283.6, Fe1-S1 240.3, Fe1-S2 230.1, Fe2-S2 235.8, Fe1-P1 223.1, P1-O1 150.6; **P2^0**: Fe1-Fe2 282.4, Fe1-S1 240.0, Fe1-S2 227.3, Fe2-S2 235.7, Fe1-P1 221.2, P1-O1 150.2.

S5 Chapter 5
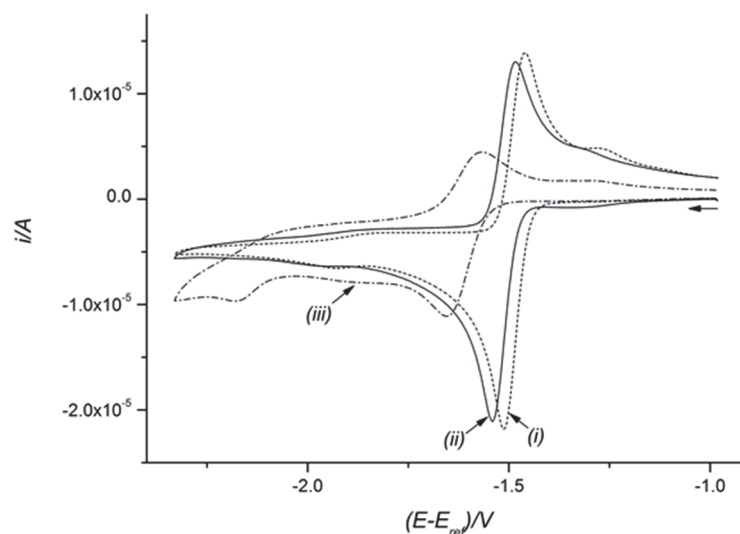
Figure S5-1. Cyclic voltammetry of equimolar complexes (1.0 mM) **147**, **148** and [Fe$_2$(CO)$_6${μ-(SCH$_2$)$_2$CH$_2$}] (**3**) in MeCN/[NBu$_4$][BF$_4$] measured at 0.2 V·s^{-1}, curves (*ii*), (*i*) and (*iii*), respectively. Glassy carbon disk (d = 1.6 mm).
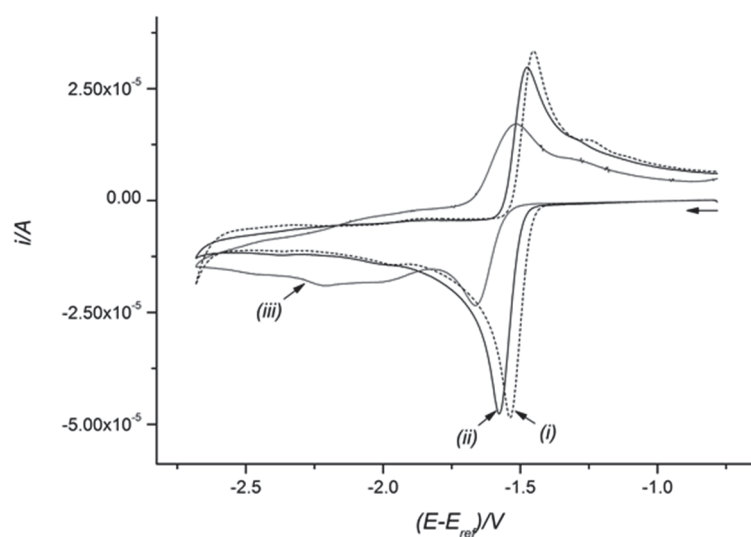
Figure S5-2. Cyclic voltammetry of equimolar complexes (1.0 mM) **147**, **148** and [Fe$_2$(CO)$_6${μ-(SCH$_2$)$_2$CH$_2$}] (**3**) in MeCN/[NBu$_4$][BF$_4$] measured at 1.0 V·s^{-1}, curves (*ii*), (*i*) and (*iii*), respectively. Glassy carbon disk (d = 1.6 mm).

Electrochemistry of $[Fe_2(CO)_6\{\mu\text{-}(SCH_2)_2CR_2\}]$ (R = H (3), R = Me (12)).[‡]

$[Fe_2(CO)_6\{\mu\text{-}(SCH_2)_2CH_2\}]$ **(3).** The cyclic voltammetry of complex **3** in $CH_2Cl_2/[NBu_4][BF_4]$ solution shows that the first reduction peak is irreversible at 0.05 $V·s^{-1}$ (Figure S5-3). This is because there is enough time for the reactions in Scheme 1-17 to occur, i.e. EC process. Increasing the scan rate (Figure S5-4) enhances the chemical reversibility since the mechanism is altered from EC (Scheme 1-17) to EE:

$$3 \overset{E^{\circ}_1}{\rightleftharpoons} 3^- \overset{E^{\circ}_2}{\rightleftharpoons} 3^{2-}$$

$$E^{\circ}_1 - E^{\circ}_2 > 0$$
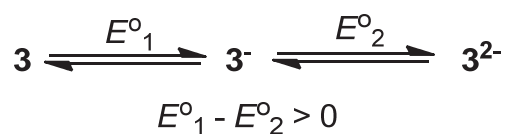
At $v \geq 5$ $V·s^{-1}$, the two separate one-electron transfer steps can be seen: peaks 1 and 2 are for the reduction of **3** and **3⁻**, respectively, and peaks 1′ and 2′ are for the oxidation of **3⁻** and **3²⁻**, respectively.

[‡] The electrochemical measurements of compounds **3** and **12** were repeated by Ralf Trautwein. Ralf Trautwein provided me with the data for the necessity to discuss them in this thesis as Supporting Information. See also reference 43 for the electrochemistry of complex **3**.
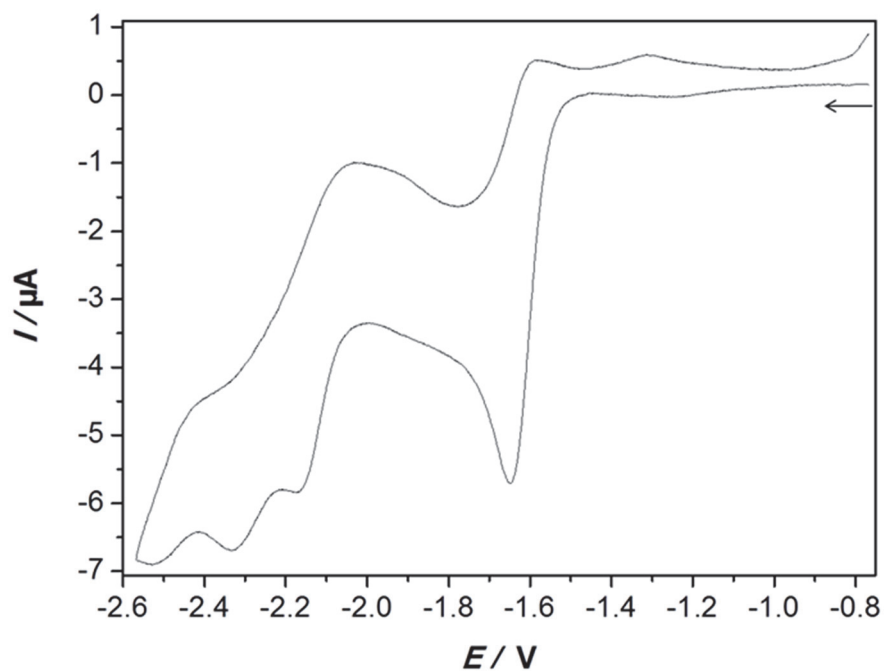
Figure S5-3. Cyclic voltammetry of 1.0 mM [Fe$_2$(CO)$_6${μ-(SCH$_2$)$_2$CH$_2$}] (**3**) in CH$_2$Cl$_2$/[NBu$_4$][BF$_4$] measured at 0.05 V·s^{-1}. *E* is in V against ferrocenium/ferrocene couple. Glassy carbon disk (d = 1.6 mm). The arrows indicate the scan direction of the reductive and the oxidative parts of the curves.
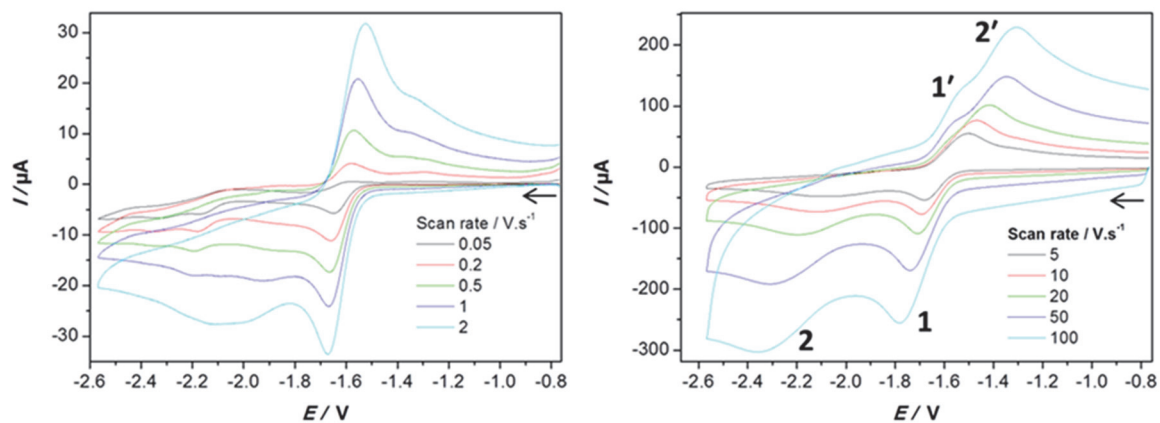
Figure S5-4. Cyclic voltammetry of 1.0 mM [Fe$_2$(CO)$_6${μ-(SCH$_2$)$_2$CH$_2$}] (**3**) in CH$_2$Cl$_2$/[NBu$_4$][BF$_4$] measured at various scan rates. *E* is in V against ferrocenium/ferrocene couple. Glassy carbon disk (d = 1.6 mm). The arrows indicate the scan direction of the reductive and the oxidative parts of the curves.

[Fe₂(CO)₆{μ-(SCH₂)₂CMe₂}] (12). As shown in Figure S5-5, complex **12** undergoes a quasi-reversible reduction at scan rates of 0.05-20 V·s⁻¹.
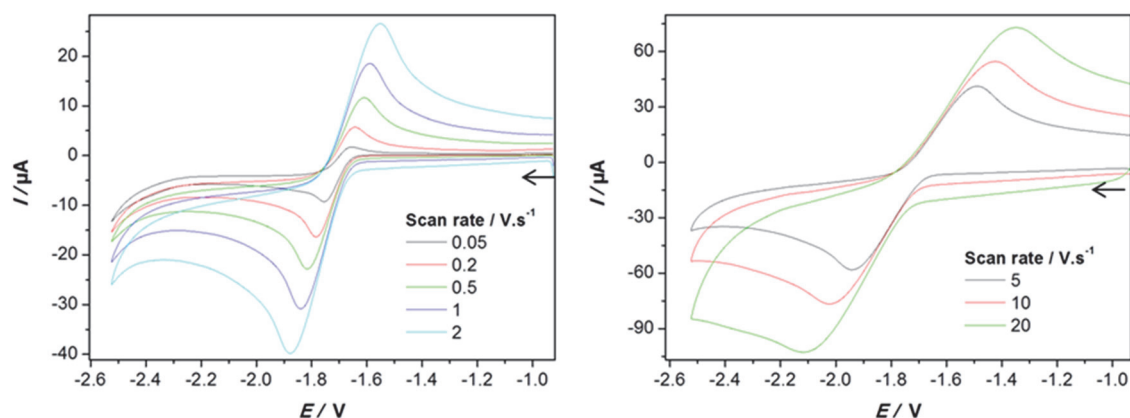
Figure S5-5. Cyclic voltammetry of 1.0 mM [Fe₂(CO)₆{μ-(SCH₂)₂CMe₂}] (**12**) in CH₂Cl₂/[NBu₄][BF₄] measured at various scan rates. *E* is in V against ferrocenium/ferrocene couple. Glassy carbon disk (d = 1.6 mm). The arrows indicate the scan direction.

Figure S5-6 shows a comparison between the cathodic peak heights of complexes **3** (1.0 mM) and **12** (1.0 mM) at scan rates 0.05-2 V·s⁻¹. At 0.05 V·s⁻¹, the peak height of the reduction peak of **12** is twice that of **3**. This suggests that the cathodic wave in the cyclic voltammogram of **12** arises from transfer of two electrons. Increasing the scan rate makes the cathodic peak heights of **3** and **12** comparable, for example at 2 V·s⁻¹. By comparing the effect of the scan rate on the current function ($I_{pc}/c \cdot v^{1/2}$) of **3** and **12** (Figure S5-7), we can see that the current function of **12** decreases significantly as the scan rate increases suggesting an ECE process.[153],[*]

---

[*] Indeed, the DFT calculations[43] showed that the most stable structure of **3⁻** is similar to that of **3**, but with elongated Fe-Fe distance, while **3²⁻** favours a rotated structure. The rotated state formation is responsible for potential inversion, which contrasts that **3** undergoes reduction in two separate steps with $E°_1 - E°_2 > 0$. Not only the thermodynamics of rotated state formation control the relative values of $E°_1$ and $E°_2$, but also the kinetics. **12** has bulkier bridgehead than **3** and hence the Fe(CO)₃ rotational barrier should lower for **12**. The lower Fe(CO)₃ rotational barrier in **12** allows the rotated state formation (the thermodynamic product) within the experimental time scale of the voltammetry explaining the observed potential inversion.
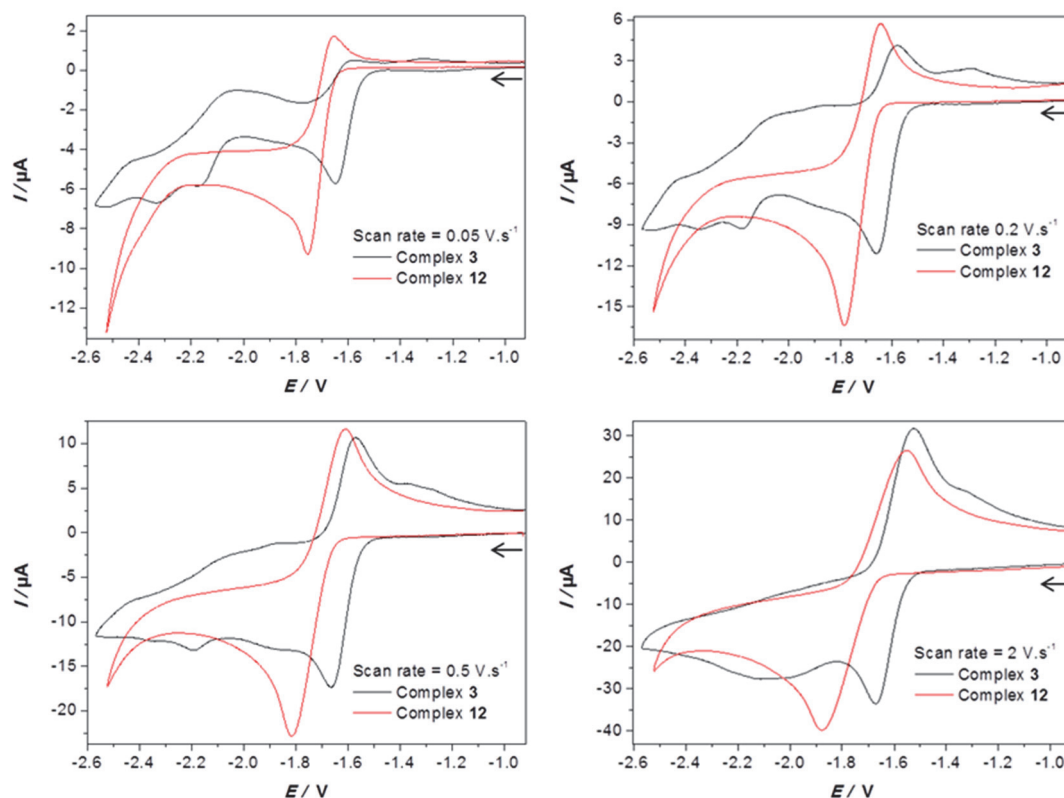
Figure S5-6. Cyclic voltammetry of 1.0 mM [Fe$_2$(CO)$_6${μ-(SCH$_2$)$_2$CMe$_2$}] (**12**) in CH$_2$Cl$_2$/[NBu$_4$][BF$_4$] measured at various scan rates. *E* is in V against ferrocenium/ferrocene couple. Glassy carbon disk (d = 1.6 mm). The arrows indicate the scan direction.
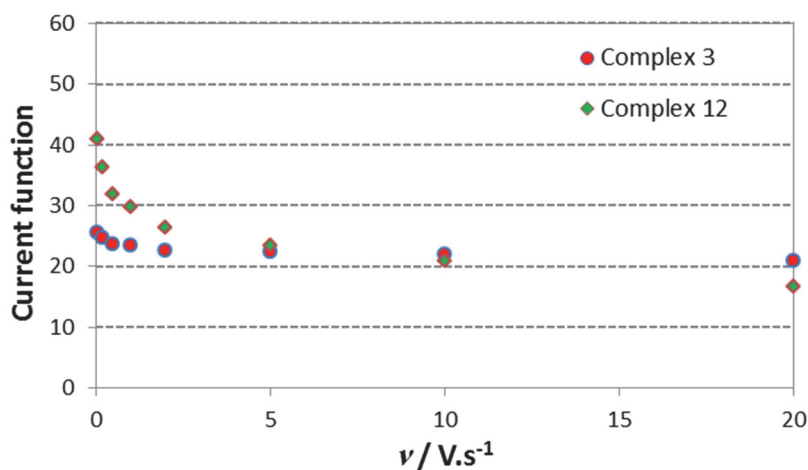
Figure S5-7. Scan rate dependence of the current function $I_{pc}/c \cdot v^{1/2}$ (μA·V$^{-1/2}$·s$^{1/2}$·mM^{-1}) of 1.0 mM [Fe$_2$(CO)$_6${μ-(SCH$_2$)$_2$CH$_2$}] (**3**) and 1.0 mM [Fe$_2$(CO)$_6${μ-(SCH$_2$)$_2$CMe$_2$}] (**12**) in CH$_2$Cl$_2$/[NBu$_4$][BF$_4$] solutions. Glassy carbon disk (d = 1.6 mm).

S7 **Chapter 7**

Table S7-1. Selected interamolecular distances [Å] for complex **152**.

Fe(1)···S(2)	6.923	Fe(3)···S(1)	4.874
Fe(1)···S(4)	6.028	Fe(3)···S(3)	5.860
Fe(2)···S(2)	6.237	Fe(4)···S(1)	6.013
Fe(2)···S(4)	4.841	Fe(4)···S(3)	7.122
S(2)···S(4)	4.317		

References

(1)   Wuebbles, D. J.; Jain, A. K. *Fuel Process. Technol.* **2001**, *71*, 99.

(2)   Koroneos, C.; Dompros, A.; Roumbas, G.; Moussiopoulos, N. *Int. J. Hydrogen Energy* **2004**, *29*, 1443.

(3)   Cammack, R.; Frey, M.; Robson, R. *Hydrogen as a Fuel. Learning from Nature*, London (**2001**).

(4)   Pilavachi, P. A.; Chatzipanagi, A. I.; Spyropoulou, A. I. *Int. J. Hydrogen Energy* **2009**, *34*, 5294.

(5)   (a) Pena, M. A.; Gomez, J. P.; Fierro, J. L. G. *Appl. Catal. A* **1996**, 144, 7. (b) Armor J. A. *Appl. Catal. A*, **1998**, *176*, 159. (c) Trimm, D. L.; Onsan, Z. I. *Catal. Rev. Sci. Eng.* **2001**, *43*, 31. (d) Navarro, R. M.; Pena, M. A.; Fierro, J. L. G. *Chem. Rev.* **2007**, *107*, 3952.

(6)   Ogden, J. M. *Annual Review of Energy and the Environment* **1999**, *24*, 227.

(7)   Müller-Langera, F.; Tzimas, E.; Kaltschmitt, M.; Peteves, S. *Int. J. Hydrogen. Energy* **2007**, *32*, 3797.

(8)   Winter, M.; Brodd, R. *J. Chem. Rev.* **2004**, *104*, 4245.

(9)   Borup, R.; Meyers, J.; Pivovar, B.; Kim, Y. S.; Mukundan, R.; Garland, N.; Myers, D.; Wilson, M.; Garzon, F.; Wood, D.; Zelenay, P.; More, K.; Stroh, K.; Zawodzinski, T.; Boncella, J.; McGrath, J. E.; Inaba, M.; Miyatake, K.; Hori, M.; Ota, K.; Ogumi, Z.; Miyata, S.; Nishikata, A.; Siroma, Z.; Uchimoto, Y.; Yasuda, K.; Kimijima, K. I.; Iwashita, N. *Chem. Rev.* **2007**, *107*, 3904.

(10)   Das, D.; Dutta, T.; Nath, K.; Meher Kotay, S.; Das, A. K.; Veziroglu, N. T. *Current Science* **2006**, *90*, 1627.

(11)   (a) Tard, C.; Pickett, C. *Chem. Rev.* **2009**, *109*, 2245. (b) Frey, M. *Chem Bio Chem* **2002**, *3*, 153. (c) Cammack, R. *Nature* **1999**, *397*, 214. (d) Vignais, P. M.; Billoud, B. *Chem. Rev.* **2007**, *107*, 4206. (e) Fontecilla-Camps, J. C.; Volbeda, A.; Cavazza, C.; Nicollet, Y. *Chem. Rev.* **2007**, *107*, 4273. (f) De Lacey, A. L.; Fernandez, V. M.; Rousset, M.; Cammack, R. *Chem. Rev.* **2007**, *107*, 4304. (g) Nicolet, Y.; Piras, C.; Legrand, P.; Hatchikian, C. E.; Fontecilla-Camps, J. C. *Structure* **1999**, *7*, 13. (h) Peters, J. W.; Lanzilotta, W. N.; Lemon, B. J.; Seefeldt, L. C. *Science* **1998**, *282*, 1853. (i) Roy, S.; Shinde, S.; Hamilton, G. A.; Hartnett, H. E.; Jones, A. K. Eur. *J. Inorg. Chem.* **2011**, 1050. (j) Gao, W.; Song, Li- C.;

Yin, B- S.; Zan, H- N.; Wang, D- F.; Song, H- B. *Organometallics* **2011**, *30*, 4097. (k) Durgaprasad, G.; Bolligarla, R.; Das, S. K. *J. Organomet. Chem*. **2012**, *706-707*, 37. (l) Topf, C.; Monkowius, U.; Knör, G. *Inorg. Chem. Commun*. **2012**, *21*, 147. (m) Adams, M. W.; *Biochim. Biophys. Acta* **1990**, *1020*, 115. (n) Holm, R. H.; Kennepohl, P.; Solomin, E. I.; *Chem. Rev.* **1996**, *96*, 2239. (o) Adams, M. W.; Mortenson, L. E.; *J. Bio. Chem.* **1984**, *259*, 704. (p) Lubitz, W.; Ogata, H.; Rüdiger, O.; Reijerse E. *Chem. Rev.*, **2014**, *114* (8), 4081.

(12)   Stryer, L. *Biochemistry*, 2nd Edition, New York (**1981**), 244.

(13)   Shepard, E. M.; McGlynn, S. E.; Bueling, A. L.; Grady-Smith, C. S.; George, S. J.; Winslow, M. A.; Cramer, S. P.; Peters, J. W.; Broderick J. B. *PNAS* **2010**, *107*, 10448.

(14)   Fan, H. -J.; Hall, M. B. *J. Am. Chem. Soc.* **2001**, *123*, 3828.

(15)   Cao, Z. X.; Hall, M. B. *J. Am. Chem. Soc* **2001**, *123*: 3734.

(16)   Liu, Z. P.; Hu, P. *J. Am. Chem. Soc.* **2002**, *124*: 5175.

(17)   Bruschi, M.; Fantucci, P.; De Gioia, L. *Inorg. Chem.* **2003**, *42*, 4773.

(18)   Nicolet, Y.; de Lacey, A. L.; Vernède, X.; Fernández, V. M.; Hatchikian, E. C.; Fontecilla-Camps, J. C. *J. Am. Chem. Soc.* **2001**, *123*, 1596.

(19)   Silakov, A.; Wenk, B.; Reijerse, E.; Lubitz, W. *Phys. Chem. Chem. Phys.* **2009**, *11*, 6592.

(20)   Ryde, U.; Greco, C.; De Gioia, L. *J. Am. Chem. Soc.* **2010**, *132*, 4512.

(21)   Esselborn, J.; Lambertz, C.; Adamska-Venkatesh, A.; Simmons, T.; Berggren, G.; Noth, J.; Siebel, J. F.; Hemschemeier, A.; Artero, V.; Reijerse, E. J.; Fontecave, M.; Lubitz, W.; Happe, T. Nat. Chem. Biol. **2013**, *9*, 607.

(22)   Berggren, G.; Adamska, A.; Lambertz, C.; Simmons, T.; Esselborn, J.; Atta, M.; Gambarelli, S.; Mouesca, J. M.; Reijerse, E. J.; Lubitz, W.; Happe, T.; Artero, V.; Fontecave, M. Nature **2013**, *499*, 66.

(23)   Greco, C.; Bruschi, M.; De Gioia, L.; Ryde, U. *Inorg. Chem.* **2007**, *46*, 5911-.

(24)   Z.-P. Liu, P. Hu, *J. Chem. Phys.* **2002**, *117*, 8177.

(25)   Silakov, A.; Reijerse, E. J.; Albracht, S. P. J.; Hatchikian, E. C.; Lubitz, W. *J. Am. Chem. Soc.* **2007**, *129,* 11447.

(26)   Reihlen, H.; Gruhl, A.; von Hessling, G. *Liebigs Ann. Chem.* **1929**, *472*, 268.

(27)   (a) Hieber, W.; Spacu, P. *Z. Anorg. Allg. Chem.* **1937**, *233*, 353. (b) Hieber, W.; Gruber, J. *Anorg. Allgem. Chem.* **1958**, *296*, 91. (c) Hieber, W.; Scharfenberg, C.

Ber. Dtsch. Chem. Ges. **1940**, *73*, 1012. (d) Hieber, W.; Beck, W. *Z. Anorg. Allg. Chem.* **1960**, *305*, 265.

(28) King, R. B. *J. Am. Chem. Soc.* **1962**, *34*, 2460.

(29) Dahl, L. F.; Wei, C. H. *Inorg. Chem.* **1963**, *2*, 328.

(30) (a) Winter, A.; Zsolnai, L.; Huttner, G. *Chem. Ber.* **1982**, *115*, 1286. (b) Winter, A.; Zsolnai, L.; Huttner, G. *Naturforsch.,* B **1982**, *37*, 1430.

(31) Peters, J. W.; Lanzilotta, W. N.; Lemon, B. J.; Seefeldt, L. C. *Science* **1998**, *282*, 1853.

(32) Nicolet, Y.; Piras, C.; Legrand, P.; Hatchikian, C. E.; Fontecilla-Camps, J. C. *Structure* **1999**, *7*, 13.

(33) Le Cloirec, A.; Best, S. P.; Borg, S.; Davies, S. C.; Evans, D. J.; Hughes, D. L.; Pickett, C. J. *Chem. Commun.* **1999**, 2285.

(34) Lyon, E. J.; Georgakaki, I. P.; Reibenspies, J. H.; Darensbourg, M. Y. *Angew. Chem., Int. Ed.* **1999**, *38*, 3178.

(35) Schmidt, M.; Contakes, S. M.; Rauchfuss, T. B. *J. Am. Chem. Soc.* **1999**, *121*, 9736.

(36) Lawrence, J. D.; Li, H. X.; Rauchfuss, T. B.; Benard, M.; Rohmer, M. M. *Angew. Chem., Int. Ed.* **2001**, *40*, 1768.

(37) (a) Li, H. X.; Rauchfuss, T. B. *J. Am. Chem. Soc.* **2002**, *124*, 726. (b) Song, L. -C.; Yang, Z. -Y.; Bian, H. -Z.; Liu, Y.; Wang, H. -T.; Liu, X. -F.; Hu, Q. -M.; *Organometallics* **2005**, *24*, 6126.

(38) Apfel, U. -P.; Halpin, Y.; Görls, H.; Vos, J. G.; Schweizer, B.; Linti, G.; Weigand W. *Chemistry & Biodiversity* **2007**, *4*, 2138.

(39) Xu, F.; Tard, C.; Wang, X.; Ibrahim, S. K.; Hughes, D. L.; Zhong, W.; Zeng, X.; Luo, Q.; Liu, X.; Pickett, C. J. *Chem. Commun.* **2008**, 606.

(40) Singleton, M. L.; Jenkins, R. M.; Klemashevich, C. L.; Darensbourg, M. Y. *C. R. Chimie* **2008**, *11*, 861.

(41) Apfel, U. -P.; Kowol, C. R.; Halpin, Y.; Kloss, F.; Kübel, J.; Görls, H.; Vos, J. G.; Keppler, B. K.; Morera, E.; Lucente, G.; Weigand W. *J. Inorg. Biochem.* **2009**, *103*, 1236.

(42) Thomas, C. M.; Rudiger, O.; Liu, T.; Carson, C. E.; Hall, M. B.; Darensbourg, M. Y. *Organometallics* **2007**, *26*, 3976.

(43)   Capon, J. -F.; Ezzaher, S.; Gloaguen, F.; Pétillon, F. Y.; Schollhammer, P.; Talarmin, J.; Davin, T. J.; McGrady, J. E.; Muir, K. W. *New J. Chem.* **2007**, *31*, 2052.

(44)   Wang, F.; Wang, M.; Liu, X.; Jin, K.; Dong, W.; Sun, L. *Dalton Trans*. **2007**, 3812.

(45)   Cui, H. -G.; Wang, M.; Dong, W. -B.; Duan, L. -L.; Li, P.; Sun L. -C. *Polyhedron* **2007**, *26*, 904.

(46)   Jiang, S.; Liu, J.; Sun, L. *Inorg. Chem. Commun.* **2006**, *9*, 290.

(47)   (a) Song, L. -C.; Yang, Z. -Y.; Hua, Y. -J.; Wang, H. -T.; Liu, Y.; Hu, Q. -M.; *Organometallics* **2007**, *26*, 2106. (b) Windhager, J.; Rudolph, M.; Brautigam, S.; Görls, H.; Weigand, W. *Eur. J. Inorg. Chem.* **2007**, 2748.

(48)   Harb, M. Ph.D. Dissertation, Friedrich-Schiller Universität Jena, Jena, Thüringen, **2009**.

(49)   Apfel, U. -P.; Troegel, D.; Halpin, Y.; Tschierlei, S.; Uhlemann, U.; Görls, H.; Schmitt, M.; Popp, J.; Dunne, P.; Venkatesan, M.; Coey, Rudolph, M.; Vos, G. J.; Tacke, R.; Weigand, W. *Inorg. Chem.* **2010**, *49*, 10117.

(50)   Glass, R. S.; Gruhn, N. E.; Lorance, E.; Singh, M. S.; Stessman, N. Y. T.; Zakai, U. I. *Inorg. Chem.* **2005**, *44*, 5728.

(51)   Gloaguen, F.; Morvan, D.; Capon, J. -F.; Schollhammer, P.; Talarmin, J. *J. Electroanal. Chem.* **2007**, *603*, 15.

(52)   Felton, G. A. N.; Vannucci, A. K.; Chen, J.; Lockett, L. T.; Okumura, N.; Petro, B. J.; Zakai, U. I.; Evans, D. H.; Glass, R. S.; Lichtenberger, D. L. *J. Am. Chem. Soc.* **2007**, *129*, 12521.

(53)   Schwartz, L.; Singh, P. S.; Eriksson, L.; Lomoth, R.; Ott, S. *C. R. Chimie* **2008**, *11*, 875.

(54)   Capon, J. -F.; Gloaguen, F.; Schollhammer, P.; Talarmin, J. *J. Electroanal. Chem.* **2004**, *566*, 241.

(55)   Chen, J.; Vannucci, A. K.; Mebi, C. A.; Okumura, N.; Borowski, S. C.; Swenson, M.; Lockett, L. T.; Evans, D. H.; Glass, R. S.; Lichtenberger D. L. *Organometallics* **2010**, *29*, 5330.

(56)   Adams, R. D.; Miao, S. *Inorg. Chem.* **2004**, *43*, 8414.

(57)   Z. Yu, M. Wang, P. Li, W. Dong, F. Wang, L. Sun. *Dalton Trans.*, **2008**, 2400.

(58) Harb, K.; Niksch, T.; Windhager, J.; Görls, H.; Holze, R.; Lockett, L. T.; Okumura, N.; Evans, D. H.; Glass, R. S.; Lichtenberger, D. L.; El-khateeb, M.; Weigand, W. *Organometallics* **2009**, *28*, 1039.

(59) Song, L. -C.; Gai, B.; Wang, H. -T.; Hu, Q. -M. *J. Inorg. Biochem.* **2009**, *103*, 805.

(60) Song, L. -C.; Li, Q. -L.; Feng, Z. -H.; Sun, X. -J.; Xie, Z. -J.; Song, H. -B. *Dalton Trans.* **2013**, *42*, 1612.

(61) Harb, M. K.; Windhager, J.; Niksch, T.; Görls, H.; Sakamoto, T.; Smith, E. R.; Glass, R. S.; Lichtenberger, D. L.; Evans, D. H.; El-khateeb, M.; Weigand, W. *Tetrahedron* **2012**, *68*, 10592.

(62) Gao, S.; Fan, J.; Sun, S.; Peng, X.; Zhao, X.; Hou, J. *Dalton Trans.* **2008**, 2128.

(63) Gao, W.; Song, L. -C.; Yin, B. -S.; Zan, H. -N.; Wang, D. -F.; Song, H. -B. *Organometallics* **2011**, *30*, 4097.

(64) Harb, M. K.; Apfel, U. -P.; Kübel, J.; Görls, H.; Felton, G. A. N.; Sakamoto, T.; Evans, D. H.; Glass, R. S.; Lichtenberger, D. L.; El-khateeb, M.; Weigand, W. *Organometallics* **2009**, *28*, 6666.

(65) (b) M. K. Harb, H. Görls, T. Sakamoto, G. A. N. Felton, D. H. Evans, R. S. Glass, D. L. Lichtenberger, M. El-khateeb, W. Weigand, *Eur. J. Inorg. Chem.* **2010**, *25*, 3976. (b) Harb, M. K.; Görls, H.; Sakamoto, T.; Felton, G. A. N.; Evans, D. H.; Glass, R. S.; Lichtenberger, D. L.; El-khateeb, M.; Weigand, W. *Eur. J. Inorg. Chem.* **2010**, *28*, 4561.

(66) Apfel, U. -P.; Görls, H.; Felton, G. A. N.; Evans, D. H.; Glass, R. S.; Lichtenberger, D. L.; Weigand. W. *Helv. Chim. Acta* **2012**, *95*, 2168.

(67) (a) Collman, J. P.; Rothrock, R. K.; Finke, R. G.; Moore, E. J.; Rose-Munch, F. *Inorg. Chem.* **1982**, *21*, 146. (b) Cheah, M. H.; Borg, S. J.; Bondin, M. I.; Best, S. P. *Inorg. Chem.* **2004**, *43*, 5635. (c) Dessy, R. E.; Kornmann, R. L.; Smith, C.; Haytor, R. *J. Am. Chem. Soc.* **1968**, *90*, 2001.

(68) Cheah, M. H.; Borg, S. J.; Best, S. P. *Inorg. Chem.* **2007**, *46*, 1741.

(69) Das, P.; Capon, J. -F.; Gloaguen, F.; Pétillon, F. Y.; Schollhammer, P.; Talarmin, J.; Muir, K. W. *Inorg. Chem.* **2004**, *43*, 8203.

(70) (a) Bennett, R. P.; *Inorg. Chem.* **1970**, *9*, 2184. (b) Doedens, R. J. *Inorg. Chem.* **1970**, *9*, 429. (c) Ellgen, P. C.; Gerlach, J. N. *Inorg. Chem.* **1973**, *13*, 1944. (d) Volkers, P. I.; Rauchfuss, T. B. *J. Inorg. Biochem.* **2007**, *101*, 1748. (e) Orain, P. -

Y.; Capon, J. -F.; Gloaguen, F.; Schollhammer, P.; Talarmin J. *Int. J. Hydrogen Energy* **2010**, *35*, 10797.

(71)   Li, P.; Wang, M.; He, C.; Li, G.; Liu, X.; Chen, C.; Åkermark, B.; Sun, L. *Eur. J. Inorg. Chem.* **2005**, 2506.

(72)   Wang, Z.; Jiang, W.; Liu, J.; Jiang, W.; Wang, Y.; Åkermark, B.; Sun, L. *J. Organomet. Chem.* **2008**, *693*, 2828.

(73)   Gloaguen, F.; Lawrence, J. D.; Schmidt, M.; Wilson, S. R.; Rauchfuss, T. B. *J. Am. Chem. Soc.* **2001**, *123*, 12518.

(74)   (a) Tye, J. W.; Lee, J.; Wang, H. -W.; Mejia-Rodriguez, R.; Reibenspies, J. H.; Hall, M. B.; Darensbourg, M. Y. *Inorg. Chem.* **2005**, *44*, 5550. (b) Thomas, C. M.; Liu, T.; Hall, M. B.; Darensbourg, M. Y. *Inorg. Chem.* **2008**, *47*, 7009.

(75)   Mejia-Rodriguez, R.; Chong, D.; Reibenspies, J. H.; Soriaga, M. P.; Darensbourg, M. Y. *J. Am. Chem. Soc*. **2004**, *126*, 12004.

(76)   Hou, J.; Peng, X.; Zhou, Z.; Sun, S.; Zhao, X.; Gao, S. *J. Organomet. Chem*. **2006**, *691*, 4633.

(77)   Schwartz, L.; Ekstrom, J.; Lomoth, R.; Ott, S. *Chem. Commun*. **2006**, 4206.

(78)   Wang, Z.; Liu, J. -H.; He, C. -J.; Jiang, S.; Åkermark, B.; Sun, L. -C. *J. Organomet. Chem.* **2007**, *692*, 5501.

(79)   Wang, W. -G.; Wang, H. -Y.; Si, G.; Tung, C. -H.; Wu, L. -Z. *Dalton Trans*. **2009**, 2712.

(80)   Na, Y.; Wang, M.; Pan, J.; Zhang, P.; Åkermark, B.; Sun, L. *Inorg. Chem*. **2008**, *47*, 2805.

(81)   Wang, Z.; Liu, J.; He, C.; Jiang, S.; Åkermark, B.; Sun, L. *Inorg. Chim. Acta* **2007**, *360*, 2411.

(82)   Apfel, U. -P.; Halpin, Y.; Görls, H.; Vos, G. J.; Weigand, W. *Eur. J. Inorg. Chem.* **2011**, 581.

(83)   Morvan, D.; Capon, J. -F.; Gloaguen, F.; Schollhammer, P.; Talarmin, J. *Eur. J. Inorg. Chem.* **2007**, 5062.

(84)   Li, P.; Wang, M.; He, C.; Liu, X.; Jin, K.; Sun, L. *Eur. J. Inorg. Chem*. **2007**, 3718.

(85)   Singleton, M. L.; Bhuvanesh, N.; Reibenspies, J. H.; Darensbourg, M. Y. *Angew. Chem., Int. Ed*. **2008**, *47*, 9492.

(86)   Gloaguen, F.; Lawrence, J. D.; Rauchfuss, T. B.; Benard, M.; Rohmer, M. -M. *Inorg. Chem*. **2002**, *41*, 6573.

(87) Capon, J. -F.; El Hassnaoui, S.; Gloaguen, F.; Schollhammer, P.; Talarmin, J. *Organometallics* **2005**, *24*, 2020.

(88) Li, T.; Darensbourg, M. Y. *J. Am. Chem. Soc.* **2007**, *129*, 7008.

(89) Justice, A. K.; De Gioia, L.; Nilges, M. J.; Rauchfuss, T. B.; Wilson, S. R.; Zampella, G. *Inorg. Chem*. **2008**, *47*, 7405.

(90) Ezzaher, S.; Capon, J. -F.; Gloaguen, F.; Pétillon, F. Y.; Schollhammer, P.; Talarmin, J. *Inorg. Chem*. **2007**, *46*, 9863.

(91) Ezzaher, S.; Capon, J. -F.; Gloaguen, F.; Pétillon, F. Y.; Schollhammer, P.; Talarmin, J. *Inorg. Chem*. **2009**, *48*, 2.

(92) Adam, F. I.; Hogarth, G.; Richards I. *J. Organomet. Chem*. **2007**, *692*, 3957.

(93) Morvan, D.; Capon, J. -F.; Gloaguen, F.; Le Goff, A.; Marchivie, M.; Michaud, F.; Schollhammer, P.; Talarmin, J.; Yaouanc, J. -J.; Pichon, R.; Kervarec, N. *Organometallics* **2007**, *26*, 2042.

(94) Gao, W.; Ekstrom, J.; Liu, J.; Chen, C.; Eriksson, L.; Weng, L.; Åkermark, B.; Sun, L. *Inorg. Chem*. **2007**, *46*, 1981.

(95) Jiang, W.; Li, Z.; Zeng, X.; Wei, G. *Asian J. Chem.* **2013**, *25* (*14*), 7655.

(96) Song, L. -C.; Li, C. -G.; Ge, J. -H.; Yang, Z. -Y.; Wang, H. -T.; Zhang, J.; Hu, Q. -M. *J. Inorg. Biochem*. **2008**, *102*, 1973.

(97) Si, Y.; Ma, C.; Hu, M.; Chen, H.; Chen, C.; Liu, Q. *New J. Chem*. **2007**, *31*, 1448.

(98) Schwartz, L.; Eilers, G.; Eriksson, L.; Gogoll, A.; Lomoth, R.; Ott, S. *Chem. Commun.* **2006**, 520.

(99) Eilers, G.; Schwartz, L.; Stein, M.; Zampella, G.; de Gioia, L.; Ott, S.; Lomoth, R. *Chem. Eur. J.* **2007**, *13*, 7075.

(100) Wang, Z.; Liu, J.; He, C.; Jiang, S.; Åkermark, B.; Sun, L. *Inorg. Chim. Acta* **2007**, *360*, 2411.

(101) Na, Y.; Wang, M.; Pan, J.; Zhang, P.; Åkermark, B.; Sun, L. *Inorg. Chem*. **2008**, *47*, 2805.

(102) Hou, J.; Peng, X.; Liu, J.; Gao, Y.; Zhao, X.; Gao, S.; Han, K. *Eur. J. Inorg. Chem*. **2006**, 4679.

(103) Ezzaher, S.; Orain, P. -Y.; Capon, J. -F.; Gloaguen, F.; Pétillon, F. Y.; Roisnel, T.; Schollhammer, P.; Talarmin, J. *Chem. Commun*. **2008**, 2547.

(104) Si, Y.; Ma, C.; Hu, M.; Chen, H.; Chen, C.; Liu, Q. *New J. Chem*. **2007**, *31*, 1448.

(105) Carroll, M. E.; Barton, B. E.; Rauchfuss, T. B.; Carroll, P. J. *J. Am. Chem. Soc*. **2012**, *134*, 18843.

(106) Barton, B. E.; Olsen, M. T.; Rauchfuss, T. B. *J. Am. Chem. Soc.* **2008**, *130*, 16834.

(107) Barton, B. E.; Rauchfuss, T. B. *Inorg. Chem.* **2008**, *47*, 2261.

(108) Zaffaroni, R.; Rauchfuss, T. B.; Gray, D. L.; De. Gioia, L.; Zampella, G. *J. Am. Chem. Soc.* **2012**, *134*, 19260.

(109) Lyon, E. J.; Georgakaki, I. P.; Reibenspies, J. H.; Darensbourg, M. Y. *J. Am. Chem. Soc.* **2001**, *123*, 3268.

(110) Crouthers, D. J.; Denny, J. A.; Bethel, R. D.; Munoz, D. G.; Darensbourg M. Y. *Organometallics* **2014**, *33*, 4747.

(111) 2e3c bond = two electron three center bond.

(112) R. H. Crabtree. *The Organometallic Chemistry of the Transition Metals*; Wiley, **2009**, Ed fifth.

(113) Izutzu, K., *Acid-Base Dissociation Constants in Dipolar Aprotic Solvents*, IUPAC Chemical Data Series No. 35, Blackwell Scientific Publications, Oxford, 1990.

(114) Matthews, S. L.; Heinekey, D. M. *Inorg. Chem.* **2010**, *49*, 9746.

(115) Windhager, J.; Seidel, R. A.; Apfel, U. -P.; Görls, H.; Linti, G.; Weigand, W. *Chem. Biodiversity* **2008**, *5*, 2023.

(116) Windhager, J.; Apfel, U. -P.; Yoshino, T.; Nakata, N.; Görls, H.; Rudolph, M.; Ishii, A.; Weigand, W. *Chem. Asian J.* **2010**, *5*, 1600.

(117) Liu, T.; Li, B.; Singleton, M. L.; Hall, M. B.; Darensbourg, M. Y. *J. Am. Chem. Soc.* **2009**, *131*, 8296.

(118) Li, B.; Liu, T.; Singleton, M. L.; Darensbourg, M. Y. *Inorg. Chem.* **2009**, *48*, 8393.

(119) X. Zhao; C.-Y. Chiang; M. L. Miller; M. V. Rampersad; M. Y. Darensbourg. *J. Am. Chem. Soc.* **2003**, *125*, 518.

(120) Tye, J. W.; Darensbourg, M. Y.; Hall, M. B. *J. Mol. Struct.*: THEOCHEM **2006**, *771*, 123.

(121) Stanley, J. L.; Heiden, Z. M.; Rauchfuss, T. B.; Wilson, S. R.; De Gioia, L.; Zampella, G. *Organometallics* **2008**, *27*, 119.

(122) Coetzee, J. F.; Padmanabhan, G. R. *J. Am. Chem. Soc.* **1965**, *87*, 5005.

(123) Moore, E. J.; Sullivan, J. M.; Norton, J. R. *J. Am. Chem. Soc.* **1986**, *108*, 2257.

(124) Ededin, R. T.; Sullivan, J. M.; Norton, J. R. *J. Am. Chem. Soc.* **1987**, *109*, 3945.

(125) Tschierlei, S.; Ott, S.; Lomoth, R. *Energy Environ. Sci.* **2011**, *4*, 2340.

(126) Löscher, S.; Schwartz, L.; Stein, M.; Ott S.; Haumann, M.; *Inorg. Chem*. **2007**, *46*, 11094.

(127) Ezzaher, S.; Gogoll, A.; Bruhn, C.; Ott, S. *Chem. Commun*. **2010**, *46*, 5775.

(128) Dong, W.; Wang, M.; Liu, X.; Jin, K.; Li, G.; Wanga, F.; Sun, L. *Chem. Commun*. **2006**, 305.

(129) Capon, J. -F.; Gloaguen, F.; Pétillon, F. Y.; Schollhammer, P.; Talarmin, J. *Coord. Chem. Rev*. **2009**, *253*, 1476.

(130) Bruschi, M.; Fantucci, P.; De Gioia, L. *Inorg. Chem*. **2004**, *43*, 3733.

(131) Tye, J. W.; Darensbourg, M. Y.; Hall, M. B. *Inorg. Chem*. **2006**, *45*, 1552.

(132) Justice, A. K.; Zampella, G.; De Gioia, L.; Rauchfuss, T. B.; van der Vlugt, J. I.; Wilson, S. R. *Inorg. Chem*. **2007**, *46*, 1655.

(133) Ezzaher, S.; Capon, J. -F.; Gloaguen, F.; Pétillon, F. Y.; Schollhammer, P.; Talarmin, J.; Pichon, R.; Kervarec, N. *Inorg. Chem*. **2007**, *46*, 3426.

(134) Ezzaher, S.; Capon, J. -F.; Gloaguen, F.; Kervarec, N.; Pétillon, F. Y.; Pichon, R.; Schollhammer, P.; Talarmin, J. *C. R. Chim*. **2008**, *11*, 906.

(135) Schwartz, L.; Eilers, G.; Eriksson, L.; Gogoll, A.; Lomoth, R.; Ott, S. *Chem. Commun*. **2006**, 520.

(136) Wright, J. A.; Pickett, C. J. *Chem. Commun*. **2009**, 5719.

(137) Jablonskytè, A.; Wright, J. A.; Pickett, C. J. *Dalton Trans*. **2010**, *39*, 3026.

(138) Liu, C.; Peck, J. N. T.; Wright, J. A.; Pickett, C. J.; Hall, M. B. Eur. *J. Inorg. Chem*. **2010**, *2011*, 1080.

(139) Olsen, M. T.; Gray, D. L.; Rauchfuss, T. B.; De Gioia, L.; Zampella, G. *Chem. Commun*. **2011**, *47*, 6554.

(140) Messelhäuser, J.; Gutensohn, K. U.; Lorenz I. -P.; Hiller, W. *J. Organomet. Chem*. **1987**, *321*, 377.

(141) Evans, D. H. *Chem. Rev*. **2008**, *108,* 2113.

(142) Evans, D. H. *Acta Chem. Scand*. **1998**, *52*, 194.

(143) Evans, D. H.; O'Connell, K. M., in: A. J. Bard (Ed.), *Electroanalytical Chemistry*, vol. 14, M. Dekker, New York, **1986**, pp 113-207.

(144) Geiger, W. E. *Prog. Inorg. Chem*. **1985**, *33*, 275.

(145) Geiger, W. E. *Organometallics* **2007**, *26*, 5738.

(146) Fernandes, J. B.; Zhang, L. Q.; Schultz, F. A. *J. Electroanal. Chem*. **1991**, *297*, 145.

(147) Uhrhammer, D.; Schultz, F. A. *J. Phys. Chem*. A **2002**, *106*, 11630.

(148)   (a) Capon, J. -F.; Gloaguen, F.; Pétillon, F. Y.; Schollhammer, P.; Talarmin, J., C. R. *Chimie* **2008**, *11*, 842. (b) Schwartz, L.; Eriksson, L.; Lomoth, R.; Teixidor, F.; Viñas, C.; Ott, S. *Dalton Trans.* **2008**, 2379.

(149)   Apfel, U. -P.; Pétillon, F. Y.; Schollhammer, P.; Talarmin, J.; Weigand, W. [FeFe] Hydrogenases Models: an Overview. In *Bioinspired Catalysis: Metal-Sulfur Complexes*, 1ˢᵗ ed.; Weigand, W., Schollhammer, P., Eds.; Wiley-VCH Verlag GmbH & Co. KGaA: U.K., **2015**; pp 79-103.

(150)   Gileadi, E. *J. Electroanal. Chem.* **2002**, *532*, 181.

(151)   Macías-Ruvalcaba, N. A.; Evans, D. H. *J. Phys. Chem. B* **2006**, *110*, 5155.

(152)   Hill, M. G.; Rosenhein, L. D.; Mann, K. R.; Mu, X. H.; Schultz, F. A. *Inorg. Chem.* **1992**, *31*, 4108.

(153)   Felton, G. A. N.; Petro, B. J.; Glass, R. S.; Lichtenberger, D. L.; Evans, D. H. *J. Am. Chem. Soc.* **2009**, *131*, 11290.

(154)   It has been reported that increasing the steric bulk of the dithiolato ligand lowers the barrier of Fe(CO)₃ rotation, see for example reference 110. To the best of my knowledge, this steric effect has been only related to the rotational barries of the Fe(CO)₃ unit in the neutral state of the model complexes, but not during the reduction processes. Nevertheless, the same effect should be at work in the ground state of the complex, i.e. the FeᴵFeᴵ state, or in the reduced states.

(155)   Borg, S. J.; Ibrahim, S. K.; Pickett, C. J.; Best, S. P. *C. R. Chim.* **2008**, *11*, 852.

(156)   Borg, S. J.; Behrsing, T.; Best, S. P.; Razavet, M.; Liu, X. M.; Pickett, C. J. *J. Am. Chem. Soc.* **2004**, *126*, 16988.

(157)   de Carcer, I. A.; DiPasquale, A.; Rheingold, A. L.; Heinekey, D. M. *Inorg. Chem.* **2006**, *45*, 8000.

(158)   Hu, M. -Q.; Ma, C. -B.; Si, Y. -T.; Chen, C. -N.; Liu, Q. -T. *J. Inorg. Biochem.* **2007**, *101*, 1370.

(159)   Razavet, M.; Davies, S. C.; Hughes, D. L.; Barclay, J. E.; Evans, D. J.; Fairhurst, S. A.; Liu, X.; Pickett, C. J. *Dalton Trans.* **2003**, 586.

(160)   Duan, L.; Wang, M.; Li, P.; Na, Y.; Wang, N.; Sun, L. *Dalton Trans.* **2007**, 1277.

(161)   Su, W. -L.; -P. H.; Huang, Chen, W. -T.; Hsu, W. -Y.; Chang, H. -Y.; Ho, S. -Y.; Wanga, S. -P.; Shyu, S. -G. *J. Chin. Chem. Soc.* **2011**, *58*, 163.

(162)   Crabtree, R. H.; Wiley, **2009**, Ed fifth, pp. 99-102.

(163)   Lever, A. B. P. *Inorg. Chem.* **1990**, *29*, 1271.

(164) Felton, G. A. N.; Mebi, C. A.; Petro, B. J.; Vannucci, A. K.; Evans, D. H.; Glass, R. S.; Lichtenberger, D. L. *J. Organomet. Chem*. **2009**, *694*, 2681.

(165) Pierce, D. T.; Geiger, W. E. *J. Am. Chem. Soc*. **1992**, *114*, 6063.

(166) Downard, A. J.; Bond, A. M.; Clayton, A. J.; Hanton L. R.; McMorran, D. A. *Inorg. Chem*. **1996**, *35*, 7684.

(167) Hush, N. S.; Blackledge, J. *J. Chem. Phys*. **1955**, *23*, 514.

(168) Surawatanawong, P.; Tye, J. W.; Darensbourg, M. Y.; Hall, M. B. *Dalton Trans*. **2010**, *39*, 3093.

(169) Borg, S. J.; Bondin, M. I.; Best, S. P.; Razavet, M.; Liu, X.; Pickett, C. J. *Biochem. Soc. Trans*. **2005**, *33*, 3.

(170) Greco, C.; Zampella, G.; Bertini, L.; Bruschi, M.; Fantucci, P.; De Gioia, L. *Inorg. Chem*. **2007**, *46*, 108.

(171) Capon, J. -F.; Ezzaher, S.; Gloaguen, F.; Pétillon, F. Y.; Schollhammer, P.; Talarmin, J. *Chem. Eur. J*. **2008**, *14*, 1954.

(172) Ott, S.; Kritikos, M.; Åkermark, B.; Sun, L.; Lomoth, R. *Angew. Chem. Int. Ed*. **2004**, *43*, 1006.

(173) The pK_a value of acetic acid in acetonitrile is 22.6 (reference 113) and that of pivalic acid should not be significantly different.

(174) Gloaguen, F.; Lawrence, J. D.; Rauchfuss, T. B. *J. Am. Chem. Soc*. **2001**, *123*, 9476.

(175) Zhao, X.; Georgakaki, I. P.; Miller, M. L.; Yarbrough, J. C.; Darensbourg, M. Y. *J. Am. Chem. Soc*. **2001**, *123*, 9710.

(176) Zhao, X.; Georgakaki, I. P.; Miller, M. L.; Mejia-Rodriguez, R.; Chiang, C. Y.; Darensbourg, M. Y. *Inorg. Chem*. **2002**, *41*, 3917.

(177) Li, T.; Lough, A. J.; Morris, R. H. *Chem.-Eur. J*. **2007**, *13*, 3796.

(178) Felton, G. A. N.; Glass, R. S.; Lichtenberger, D. L.; Evans, D. H. *Inorg. Chem*. **2006**, *45*, 9181.

(179) Justice, A. K.; Rauchfuss, T. B.; Wilson, S. R. *Angew. Chem., Int. Ed*. **2007**, *46*, 6152.

(180) Justice, A. K.; Nilges, M. J.; Rauchfuss, T. B.; Wilson, S. R.; De Gioia, L.; Zampella, G. *J. Am. Chem*. Soc. **2008**, *130*, 5293.

(181) Wang, W.; Rauchfuss, T. B.; Zhu, L. *J. Am. Chem. Soc*. **2014**, *136*, 5773.

(182) Huynh, M. T.; Wang, W.; Rauchfuss, T. B.; Hammes-Schiffer, S. *Inorg. Chem*. **2014**, *53*, 10301.

(183) Fourmond, V.; Jacques, P. -A.; Fontecave, M.; Artero, V. *Inorg. Chem.* **2010**, *49*, 10338.

(184) Razavet, M.; Davies, S. C.; Hughes, D. L.; Pickett, C. J. *Chem. Commun.* **2001**, 847.

(185) Jablonskytė, A.; Wright, J. A.; Fairhurst, S. A.; Webster, L. R.; Pickett, C. J. *Angew. Chem. Int. Ed.* **2014**, *53*, 10143.

(186) Lawrence, J. D.; Li, H.; Rauchfuss, T. B. *Chem. Commun.* **2001**, *16*, 1482-1483.

(187) Song, L. -C.; Yang, Z. -Y.; Bian, H. -Z.; Hu, Q. -M. *Organometallics* **2004**, *23*, 3082.

(188) Daraosheh, A. Q.; Harb, M. K.; Windhager, J.; Görls, H.; El-khateeb, M.; Weigand, W. *Organometallics* **2009**, *28*, 6275.

(189) Hu, M. -Q.; Ma, C. -B.; Si, Y. -T.; Chen, C. -N.; Liu, Q. -T. *J. Inorg. Biochem.* **2007**, *101*, 1370.

(190) Windhager, J.; Görls, H.; Petzold, H.; Mloston, G.; Linti, G.; Weigand, W. *Eur. J. Inorg. Chem.* **2007**, 4462.

(191) Goy, R.; Apfel, U. -P.; Elleouet, C.; Escudero, D.; Elstner, M.; Görls, H.; Talarmin, J.; Schollhammer, P.; González, L.; Weigand, W. *Eur. J. Inorg. Chem.* **2013**, 4466.

(192) Goy, R.; Bertini, L.; Elleouet, C.; Görls, H.; Zampella, G.; Talarmin, J.; De Gioia, L.; Schollhammer, P.; Apfel, U. -P.; Weigand, W. *Dalton Trans.* **2015**, *44*, 1690.

(193) Song, L. -C.; Zhao, P. -H.; Du, Z. -Q.; Tang, M. -Y.; Hu, Q. -M. *Organometallics* **2010**, *29* (22), 5751.

(194) Maresca, L.; Greggio, F.; Sbrignadello, G.; Bor, G. *Inorg. Chim. Acta* **1971**, *5*, 667.

(195) Ellegan, P. C.; Gerlach, J. N. *Inorg. Chem.* **1973**, *12*, 2526.

(196) Aime, S.; Gervasio, G.; Rossetti, R.; Stanghellini, P. L. *Inorg. Chim. Acta* **1980**, *40*, 131.

(197) Karaçar, A.; Klaukien, V.; Freytag, M.; Thönnessen, H.; Omelanczuk, J.; Jones, P. G.; Bartsch, R.; Schmutzler; R. *Z. Anorg. Allg. Chem.* **2001**, *627*, 2589.

(198) Matrosov, E. I.; Tsvetkov, E. N.; Mironova, Z. N.; Malevannaya; Kabachnik, R. A. Institute of Heteroorganie Compounds, Academy of Sciences of the USSR, Moscow. Translated from Izvestiya Akademii Nauk SSSR, Seriya Khimicheskaya, No. 6, pp. 1333-1337, June, **1975**.

(199) Seyferth, D.; Henderson, R. S.; Song, L. -C. *J. Organomet. Chem.* **1980**, 192, C1-C5.

(200) Song, L. -C.; Li, C. -G.; Gao, J.; Yin, B. -S.; Luo, X.; Zhang, X. -G.; Bao, H. -L.; Hu, Q. -M. *Inorg. Chem.* **2008**, *47*, 4545.

(201) Stanley, J. L.; Rauchfuss, T. B.; Wilson, S. R. *Organometallics* **2007**, *26*, 1907.

(202) Maier, L. *Helv. Chim. Acta* **1969**, *52*, 845.

(203) Maier, L. *J. Organomet. Chem.* **1979**, *178*, 157.

(204) Topf, C.; Monkowius, U.; Knör, G. *Inorg. Chem. Commun.* **2012**, *21,* 147.

(205) Nakamoto, K. *Infrared and Raman Spectra of Inorganic and Coordination Compounds, Part B*: *Applications in Coordination, Organometallic, and Bioinorganic Chemistry*, 5th ed.; Wiley: New York, **1997**; pp 126-148.

(206) Myers, E. L.; Butts, C. P.; Aggarwal, V. K. *Chem. Commun.* **2006**, 4434.

(207) Frisch, M.J.; Trucks, G.W.; Schlegel, H.B.; Scuseria, G.E.; Robb, M.A.; Cheeseman, J.R.; Scalmani, G.; Barone, V.; Mennucci, B.; Petersson, G.A.; Nakatsuji, H.; Caricato, M.; Li, X.; Hratchian, H.P.; Izmaylov, A.F.; Bloino, J.; Zheng, G.; Sonnenberg, J.L.; Hada, M.; Ehara, M.; Toyota, K.; Fukuda, R.; Hasegawa, J.; Ishida, M.; Nakajima, T.; Honda, Y.; Kitao, O.; Nakai, H.; Vreven, T.; Montgomery, Jr., J.A.; Peralta, J.E.; Ogliaro, F.; Bearpark, M.; Heyd, J.J.; Brothers, E.; Kudin, K.N.;. Staroverov, V.N.; Keith, T.; Kobayashi, R.; Normand, J.; Raghavachari, K.; Rendell, A.; Burant, J.C.; Iyengar, S.S.; Tomasi, J.; Cossi, M.; Rega, N.; Millam, J.M.; Klene, M.; Knox, J.E.; Cross, J.B.; Bakken, V.; Adamo, C.; Jaramillo, J.; Gomperts, R.; Stratmann, R.E.; Yazyev, O.; Austin, A.J.; Cammi, R.; Pomelli, C.; Ochterski, J.W.; Martin, R.L.; Morokuma, K.; Zakrzewski, V.G.; Voth, G.A.; Salvador, P.; Dannenberg, J.J.; Dapprich, S.; Daniels, A.D.; Farkas, O.; Foresman, J.B. Ortiz, J.V. Cioslowski, J.; Fox, D.J.; Gaussian, Inc., Wallingford CT, **2010**.

(208) (a) Becke, A. D.; *J. Chem. Phys.* **1993**, *98*, 5648. (b) Lee, C.; Yang, W. W.; Parr, R. G. *Phys. Rev.* **1988**, *B37*, 785.

(209) (a) Peng, B.; Li, Q. S.; Xie, Y.; King, R. B.; Schaefer III, H. F. *Dalton Trans.* **2008**, 6977. (b) Feng, X.; Gu, J.; Xie, Y.; King, R. B.; Schaefer III, H. F. *J. Chem. Theory Comput.* **2007**, *3*, 1580. (c) Imhof, W.; Anders, E.; Göbel, A.; Görls, H. *Chem. Eur. J.*, **2003**, *9*, 1166.

(210) (a) Dolg, M.; Stoll, H.; Preuss, H. *Theor. Chim. Acta*. **1993**, *85*, 441. (b) Bergner, A.; Dolg, M.; Küchle, W.; Stoll, H.; Preuss, H. *Mol. Phys*. **1993**, *80*, 1431.

(211)   (a) Barone, V.; Cossi, M. *J. Phys. Chem. A* **1998**, *102*, 1995. (b) Cossi, M.; Rega, N.; Scalmani, G.; Barone, V. *J. Comput. Chem.* **2003**, *24*, 669. (c) Surawatanawong, P.; Tye, J. W.; Darensbourg, M. Y.; Hall, M. B. *Dalton Trans.* **2010**, *39*, 3093.

(212)   DigiElch 7 simulation software developed by Manfred Rudolph available from GAMRY Instruments (Warminster, USA).

(213)   Gao, W.; Liu, J.; Ma, C.; Weng, L.; Jin, K.; Chen, C.; Åkermark, B.; Sun, L. *Inorg. Chim. Acta* **2006**, *359*, 1071.

(214)   A. Adamska, A. Silakov, C. Lambertz, O. Rüdiger, T. Happe, E. Reijerse, W. Lubitz, *Angew. Chem.* **2012**, *124*, 11624.

(215)   Tye, J. W.; Lee, J.; Wang, H. -W.; Mejia-Rodriguez, R.; Reibenspies, J. H.; Hall, M. B.; Darensbourg, M. Y. *Inorg. Chem.* **2005**, *44*, 5550.

(216)   Hsieh, C. -H.; Erdem, Ö- F.; Harman, S. D.; Singleton, M. L.; Reijerse, E.; Lubitz, W.; Popescu, C. V.; Reibenspies, J. H.; Brothers, S. M.; Hall, M. B.; Darensbourg. M. Y. *J. Am. Chem. Soc.* **2012**, *134*, 13089.

(217)   Olsen, M. T.; Bruschi, M.; De Gioia, L.; Rauchfuss, T. B.; Wilson, S. R. *J. Am. Chem. Soc.* **2008**, *130*, 12021.

(218)   Windhager, J.; Apfel, U. -P.; Yoshino, T.; Nakata, N.; Görls, H.; Rudolph, M.; Ishii, A.; Weigand, W. *Chem. Asian J.* **2010**, *5*, 1600.

(219)   (a) Durgaprasad, G.; Das, S. K. *J. Organomet. Chem.* **2012**, *717*, 29. (b) Durgaprasad, G.; Bolligarla, R.; Das, S. K. *J. Organomet. Chem.*, **2011**, *696*, 3097.

(220)   (a) Tolman, C. A.; *Chemical Reviews* **1977**, *77*, 313. (b) Bunten, K. A.; Chen, L. Z.; Fernandez, A. L.; Poe, A. J. *Coord. Chem. Rev.* **2002**, *233*, 41. (c) Tolman, C. A.; *J. Am. Chem. Soc.* **1970**, *92*, 2953.

(221)   Charreteur, K.; Kdider, M.; Capon, J. -F.; Gloaguen, F.; Pétillon, F. Y.; Schollhammer, P.; Talarmin, J. *Inorg. Chem.* **2010**, 49, 2496.

(222)   (a) Darensbourg, D. J.; Graves, A. H. *Inorg. Chem.* **1979**, *18*, 1257. (b) Wovkulich, M. J.; Atwood, J. D. *Organometallics* **1982**, *1*, 1316. (c) Atwood, J. D.; Wovkulich, M. J.; Sonnenberger, D. C. *Acc. Chem. Res.* **1983**, *16*, 350.

(223)   Liu, C.; Peck, J. N. T.; Wright, J. A.; Pickett, C. J.; Hall, M. B.; *Eur. J. Inorg. Chem.* **2011**, 1080.

(224)   Gao, S.; Fan, J.; Sun, S.; Song, F.; Peng, X.; Duan, Q.; Jianga, D.; Liang, Q. *Dalton Trans.* **2012**, *41*, 12064.

(225) Thomas, C. M.; Darensbourg, M. Y.; Hall, M. B. *J. Inorg. Biochem.* **2007**, *101*, 1752.

(226) Zampella, G.; Fantucci, P.; De Gioia, L. *Chem. Commun.* **2010**, *46*, 8824.

(227) Song, L. -C.; Xie, Z. -J.; Liu, X. -F.; Ming, J. -B.; Ge, J. -H.; Zhang, X. -G.; Yan, T. -Y.; Gao, P. *Dalton Trans.* **2011**, *40*, 837.

(228) Stiebritz, M. T.; Finkelmann, A. R.; Reiher, M. *Eur. J. Inorg. Chem.* **2011**, 1163.

(229) Chouffai, D.; Zampella, G.; Capon, J. -F.; De Gioia, L.; Gloaguen, F.; Petillon, F. Y.; Schollhammer, P.; Talarmin, J. *Inorg. Chem.* **2011**, *50*, 12575.

(230) Kania, R.; Frederix, P. W. J. M.; Wright, J. A.; Ulijn, R. V.; Pickett, C. J.; Hunt, N. T. *J. Chem. Phys.* **2012**, *136*, 044521/1-044521/9.

(231) Leidel, N.; Chernev, P.; Havelius, K. G. V.; Schwartz, L.; Ott, S.; Haumann, M. *J. Am. Chem. Soc.* **2012**, *134*, 14142.

(232) Weigand, W. W.; Nagel, U.; Beck, W. *J. Organomet.Chem.* **1988**, *352*, 191-198.

(233) Stephen Creager, S. "Solvents and Supporting Electrolytes" in Handbook of Electrochemistry, Ed. Zoski, C. G., Elsevier, Amsterdam, **2007**, Chapter 3, Section 3.2, pp 58-60.

(234) Trautwein, R.; Almazahreh, L. R.; Görls, H.; Weigand, W. *Z. Für Anorg. Allg. Chem.* **2013**, *639*, 1512.

(235) Discussion of the spectroscopic data of compound **149**, which was prepared by Ralf Trautwein. The $^{31}P\{^1H\}$ NMR spectrum of complex **149** in $CDCl_3$ shows a singlet at 64.76 ppm for the PPh_3. The $^{13}C\{^1H\}$ NMR spectrum of complex **149** shows singlets at 22.03 and 40.75 ppm due to the SCH$_2$ and CCH$_2$OH carbon atoms, respectively. The carbon atoms of the two CH$_2$OH groups appear nonequivalent and resonate at 66.26 and 69.14 ppm. The aromatic carbon atoms of the PPh_3 group resonate as doublets at 128.68 ($^3J_{PC}$ = 9.57 Hz; PCCHCH), 130.34 ($^4J_{PC}$ = 1.88 Hz; PCCHCHCH), 133.49 ($^2J_{P-C}$ = 10.96 Hz; PCCH) and 135.06 ppm ($^1J_{PC}$ = 39,51 Hz; PC). The singlet at 209.14 ppm is attributed to the Fe(CO)$_3$ carbonyl group while the doublet at 213.55 ppm arises from the Fe(CO)$_2$PPh$_3$ moiety and the coupling constant $^2J_{PC}$ equals 11.27 Hz. The ^1H NMR spectrum of complex **149** shows two doublets due to the SCH_2 moieties at 1.33 ppm ($^2J_{HH}$ = 13.72 Hz) and 1.97 ppm ($^2J_{HH}$ = 13.87 Hz). The CH_2OH groups appear nonequivalent since the protons of one group resonate as singlet at 2.80 ppm whereas the other one exhibits a singlet at 3.54 ppm. The protons of the PPh$_3$

group appear as multiplets in the region of 7.38-7.48 ppm for PCCHCHC*H* and PCCHC*H* and 7.63-7.72 ppm for PCC*H*.

(236) Lyon, E. J.; Georgakaki, I. P.; Reibenspies, J. H.; Darensbourg, M. Y. *J. Am. Chem. Soc.* **2001**, *123*, 3268.

(237) Chong, D.; Georgakaki, I. P.; Mejia-Rodriguez, R.; Sanabria-Chinchilla, J.; Soriaga, M. P.; Darensbourg, M. Y. *Dalton Trans.* **2003**, 4158.

(238) Zhao, X.; Georgakaki, I. P.; Miller, M. L.; Mejia-Rodriguez, R.; Chiang, C. -H.; Darensbourg, M. Y. *Inorg. Chem.* **2002**, *41*, 3917.

(239) Mejia-Rodriguez, R.; Chong, D.; Reibenspies, J. H.; Soriaga, M. P.; Darensbourg, M. Y. *J. Am. Chem. Soc.* **2004**, *126*, 12004.

(240) (a) Darchen, A.; Mousser, H.; Patin, H. *J. Chem. Soc., Chem. Commun.* **1988**, 968. (b) Mousser, H. *Ph.D. Thesis*, University of Rennes, France, **1987**.

(241) Robin, F.; Rumin, R.; Talarmin, J.; Pétillon, F. Y.; Muir, K. W. *Organometallics* **1993**, *12*, 365.

(242) (a) Tacke, Reinhold; Wagner, S. A.; Sperlich, J. *Chem. Ber*. **1994**, *127*, 639. (b) Barrau, J.; Rima, G.; Satgé, J. Synth. React. Inorg. Met.-Org. Chem. **1984**, *14 (1)*, 21.

(243) Bertini, L.; Greco, C.; De Gioia, L.; Fantucci, P. *J. Phys. Chem. A* **2009**, *113*, 5657.

(244) Seyferth, D.; Andrews, S. B. *J. Organomet. Chem*. **1971**, *30,* 151.

(245) Song, L. -C.; Gong, F. -H.; Meng, T.; Ge, J. -H.; Cui, L. -N.; Hu, Q. -M. *Organometallics* **2004**, *23*, 823.

(246) Song, L. -C.; Wang, J. -Y.; Gong, F. -H.; Cheng, J.; Hu, Q. -M. *J. Organomet. Chem*. **2004**, *689*, 930.

(247) (a) Turley, P. C.; Haake, P. *J. Am. Chem. Soc*. **1967**, *89*, 4617. (b) Natile, G.; Maresca, L.; Bor, G. *Inorg. Chim. Acta* **1977**, *23*, 37.

(248) Butler, A. R; Glidewell, C.; Hyde, A.R.; McGinnis, J.; Seymour, J. E. *Polyhedron*, **1983,** *2*, 1045.

(249) The lowest ionization energy of sulfides is lowered by an α-C-Sn moiety in a geometry dependent way due to C-Sn σ-MO and $3p$ lone pair orbital on S raising the HOMO energy.[50,248] It is hypothesized that this effect may render a sulfide appended with an appropriately oriented C-Sn bond more nucleophilic than sulfides devoid of such substituents.

(250) Glass, R. S.; Radspinner, A. M.; Singh, W. P. *J. Am. Chem. Soc*. **1992**, *114*, 4921.

(251)   Bond, A. M.; Martin, R. L. *Coord. Chem. Rev.* **1984**, *54*, 23.

(252)   Coucouvanis, D. *Prog. Inorg. Chem.* **1979**, *26*, 301.

(253)   Drake, J. E.; Yang, J. *Can. J. Chem*. **1998**, *76*, 319.

(254)   Bonamico, M.; Mazzone, G.; Vaciago, A.; Zambonelli, L. *Acta. Cryst*. **1965**, *19*, 898.

(255)   Cheon, J.; Kang, H. -K.; Zink, J. I. *Coord. Chem. Rev.* **2000**, *200-202*, 1009.

(256)   Li, J. W.; Su, Y. K.; Yokoyama, M. *Jpn. J. Appl. Phys.* **1993**, *32*, 1983.

(257)   Mclaughlin, M.; Sakeek, H. F.; Maguire, P.; Graham, W. G.; Molloy, J.; Morrow, T.; Laverty, S.; Anderson, J. *Appl. Phys. Lett*. **1993**, *63*, 1865.

(258)   Marzano, C.; Bettio, F.; Baccichetti, F.; Tevisan, A.; Giovagnini, L.; Fregona, D. *Chem. –Biol. Interactions* **2004**, *148*, 37.

(259)   Bodenner, D. L.; Dedon, P. C.; Keng, P. C.; Borch, R. F. *Cancer Res* **1986**, *46*, 2745.

(260)   Giovagnini, L.; Ronconi, L.; Aldinucci, D.; Lorenzon, D.; Sitran, S.; Fregona, D. *J. Med. Chem.* **2005**, *48*, 1588.

(261)   Pastorek, R.; Travnicek, Z.; Marek, J.; Dastrych, D.; Sindelar, Z. *Polyhedron* **2000**, *19*, 1713.

(262)   Atsuya, I.; Itoh, K.; Ariu, K. *Pure & Appl Chem* **1980**, *63*, 1221.

(263)   Faragalia, G.; Fregona, D.; Sitran, S.; Giovagnini, L.; Marzano, C.; Baccichetti, F.; Gasellato, U.; Graziani, R. *J. Inorg. Biochem.* **2001**, *83*, 31.

(264)   Scarcia, V.; Furlani, A.; Fregona, D.; Fargalia, G.; Sitran, S. *Polyhedron* **1999**, *18*, 2827.

(265)   Hilts, R. W.; Cowie, M. *Inorg. Chem*. **1990**, *29*, 3349.

(266)   Fackler, J. P. Jr.; Seidel, W. C. *Inorg. Chem*. **1969**, *8*, 1631.

(267)   Genre, C.; Levasseur-Thériault, G.; Reber, C. *Can. J. Chem.* **2009**, *87*, 1625.

(268)   Pasini, A.; D'Alfonso, G.; Manzotti, C.; Moret, M.; Spinelli, S.; Valsecchi, M. *Inorg. Chem.* **1994**, *33*, 4140.

(269)   Qu, Y.; Gama de Almeida, S.; Farrell, N. *Inorg. Chim. Acta.* **1992**, *201*, 123.

(270)   Galbraith, J. A.; Menzel, K. A.; Ratilla, E. M. A.; Kostic, N. M. *Inorg. Chem.* **1987**, *26*, 2073.

(271)   Mital, R.; Jain, N.; Srivastava, T. S. *Inorg. Chim. Acta*. 1989, *166*, 134.

(272)   Faraglia, G.; Fedrigo, M.; Sitran, S. *Transition Met. Chem.* **2002**, *27*, 200.

(273)   Exarchos, G.; Nyburg, S. C.; Robinson, S. D. *Polyhedron* 1998, *17*, 1257.

(274)   Lin, I. J. B.; Chen, H. W.; Fackler, J. P. Jr. *Inorg. Chem*. **1978**, *17*, 394.

(275)   Alison, J. M. C.; Stephenson, T. A. *J. Chem. Soc. Dalton. Trans.* **1973**, 254.

(276)   Exarchos, G.; Stephenson, S. D.; Steed, J. W. *Polyhedron* **2000**, *19*, 1511.

(277)   Exarchos, G.; Stephenson, S. D.; Steed, J. W. *Polyhedron* **2001**, *20*, 2951.

(278)   Manav, N.; Mishra, A. K.; Kaushik, N. K. *Spectrochim. Acta. Part A* **2004**, 60, 3087.

(279)   El-khateeb, M.; Harb, M.; Görls, H.; Weigand, W. *Jord. J. Chem.* **2008**, *3*, 147.

(280)   El-khateeb, M.; Görls, H.; Weigand, W. *J. Organomet. Chem.* **2006**, *691*, 2055.

(281)   (a) Chen, C. -H.; Lee, G. -H.; Liaw, W. -F. *Inorg. Chem.* **2006**, *45*, 2307. (b) Wombwell, C.; Reisner, E. *Dalton Trans.* **2014**, *43*, 4483. (c) Lee, C. -M.; Chen, C. -H.; Ke, S. -C.; Lee, G. -H.; Liaw, W. -F. *J. Am. Chem. Soc.* **2004**, *126*, 8406.

(282)   Pastorek, R.; Trávnček, Z.; Šindelář, Z.; Březina, F. Polyhedron **1996**, *15 (21)*, 3691.

(283)   Montagner, D.; Miguel, P. J. S. *J. Chem. Soc. Dalton. Trans*. **2011**, 40, 10809.

(284)   Cornock, M. C.; Stephenson, T. A. *J. Chem. Soc. Dalton Trans.* **1977**, 501.

(285)   Fackler, J. P. Jr.; Thompson, L. D.; Lin, I. J. B.; Stephenson, A.; Gould, R.; Alison, J. M.; Fraser, A. J. *Inorg. Chem.* **1982**, *21*, 2397.

(286)   Chan, L. T.; Chen, H. -W.; Fackler, J. P. Jr.; Masters, A. F.; Pan, W. -H. *Inorg. Chem.* **1982**, *21*, 4291.

(287)   (a) Silveira, C. C.; Rinaldi, F.; Guadagnin, R. C. *Eur. J. Org. Chem.* **2007**, 4935. (b) Thompson, D. P.; Boudjouk, P.; *J. Org. Chem.* **1988**, *53*, 2109.

(288)   Kawai, K.; Ibi, K.; Ebihara, M. *Z. Anorg. Allg. Chem.* **2007**, *633*, 625.

(289)   Niksch, T.; Görls, H.; Friedrich, M.; Oilunkaniemi, R.; Laitinen, R.; Weigand, W. *Eur. J. Inorg. Chem.* **2010**, 74.

(290)   Mareanian, C. A.; Baidva, N.; Olmstead, M. M.; Mascharak, P. K. *Inorg. Chem.* **1992**, *31,* 2992.

(291)   Marganian, C. A.; Vazir, H.; Baidya, N.; Olmstead, M. M.; Mascharak, P. K. *J. Am. Chem. Soc.* **1995**, *117*, 1584.

(292)   Eidsness, M. K.; Scott, R. A.; Prickril, B. C.; DerVartanian, D. V.; LeGall, J.; Moura, J. J. G.; Peck, H. D. Jr. *Proc. Natl. Acad. Sci. U.S.A.* **1989**, *86*, 147.

(293)   (a) Cha, M.; Gatlin, C. L.; Critchlow, S. C.; Kovacs, J. A. *Inorg. Chem.* **1993**, *32*, 5868. (b) Kruger, H. -J.; Holm, R. H. *J. Am. Chem. Soc.* **1990**, *112*, 2955. (c) Mills, D. K.; Reibenspies, J. H.; Darensbourg, M. Y. *Inorg. Chem.* **1990**, *29*, 4364. (d) Baidya, M.; Olmstead, M.; Mascharak, P. K. *Inorg. Chem.* **1991**, *30*, 929. (e) Kumar, M.; Colpas, G. J.; Day, R. O.; Maroney, M. *J. Am. Chem. Soc.*

1989, *111*, 8323. (f) Fox, S.; Wang, Y.; Silver, A.; Millar, M. *J. Am. Chem. Soc*. **1990**, *112*, 3218.

(294) Volbeda, A.; Garcin, E.; Piras, C.; de Lacey, A.; Fernandez, V. M.; Hatchikian, E. C.; Frey, M.; Fontecilla-Camps, J. C. *J. Am. Chem. Soc*. **1996**, *118*, 12989.

(295) (a) Laguno, E. C.; Mabuni, C. T.; Paul, C. *J. Chem. Soc., Perkin Trans. 2* **1976**, 239. (b) Mikołajczyk, M.; Kiełbasiňski, P.; Barlow, J. H.; Russel, D. R. *J. Org. Chem.* **1977**, *42*, 2345. (c) Adiwidjaja, G.; Voss, J. *J. Chem. Res.* (S) **1977**, 256.; (M) **1977**, 2923.

(296) Murai, T.; Kakami, K.; Hayashi, A.; Komuro, T.; Takaya, H.; Fujii, M.; Kanda, T.; Kato, S. *J. Am. Chem. Soc*. **1997**, *119*, 8592.

(297) Shefter, E.; Kennard, O. *Science* **1966**, *153*, 1389.

(298) Pauling, L. *The Nature of the Chemical Bond*, Cornell University Press., Ithaca, **1960**, pp. 224.

(299) Lide, D. R. (Editor), Handbook of Chemistry and Physics, 73rd Edition. CRC Press Inc., Boca Raton, Florida, **1992**.

(300) McCleverty, J. A.; Morrison, N. J. *J. C. S. Dalton* **1976**, 541.

(301) Burns, R. C.; Collins, M. J.; Gillespie, R. J.; Schrobilgen, G. J. *Inorg. Chem.* **1986**, *25(25)*, 4465.

(302) Schwetlick, K. *Organikum − Organisch-chemisches Grundpraktikum*, 21st ed., WILEY−VCH GmbH Weinheim New York Chichester Brisbane Singapore Toronto **2001**.

(303) COLLECT, Data Collection Software; Nonius B. V., The Netherlands **1998**.

(304) Otwinowski Z.; Minor, W. „Processing of X-Ray Diffraction Data Collected in Oscillation Mode", in Methods in Enzymology, Vol. 276, Macromolecular Crystallography, Part A, edited by C.W. Carter & R.M. Sweet, pp. 307-326, Academic Press, San Diego, USA, **1997**.

(305) SADABS 2.10, Bruker-AXS inc., **2002**, Madison, WI, U.S.A.

(306) Sheldrick, G. M. *Acta Cryst.* **2008**, *A46*, 112.

(307) Frisch, M. J.; Trucks, G. W.; Schlegel, H. B.; Scuseria, G. E.; Robb, M. A.; Cheeseman, J. R.; Scalmani, G.; Barone, V.; Mennucci, B.; Petersson, G. A.; Nakatsuji, H.; Caricato, M.; Li, X.; Hratchian, H. P.; Izmaylov, A. F.; Bloino, J.; Zheng, G.; Sonnenberg, J. L.; Hada, M.; Ehara, M.; Toyota, K.; Fukuda, R.; Hasegawa, J.; Ishida, M.; Nakajima, T.; Honda, Y.; Kitao, O.; Nakai, H.; Vreven, T.; Montgomery, Jr., J. A.; Peralta, J. E.; Ogliaro, F.; Bearpark, M.; Heyd, J. J.;

Brothers, E.; Kudin, K. N.; Staroverov, V. N.; Keith, T.; Kobayashi, R.; Normand, J.; Raghavachari, K.; Rendell, A.; Burant, J. C.; Iyengar, S. S.; Tomasi, J.; Cossi, M.; Rega, N.; Millam, J. M.; Klene, M.; Knox, J. E.; Cross, J. B.; Bakken, V.; Adamo, C.; Jaramillo, J.; Gomperts, R.; Stratmann, R. E.; Yazyev, O.; Austin, A. J.; Cammi, R.; Pomelli, C.; Ochterski, J. W.; Martin, R. L.; Morokuma, K.; Zakrzewski, V. G.; Voth, G. A.; Salvador, P.; Dannenberg, J. J.; Dapprich, S.; Daniels, A.D.; Farkas, O.; Foresman, J. B. Ortiz, J. V. Cioslowski, J.; Fox, D. J.; Gaussian, Inc., Wallingford CT, **2010**.

(308)   (a) Becke, A. D. *J. Chem. Phys*. **1993**, *98*, 5648. (b) Lee, C.; Yang, W. W.; Parr, R. G. *Phys. Rev.* 1988, *B37*, 785.

(309)   (a) Dolg, M.; Stoll, H.; Preuss, H. *Theor. Chim. Acta*. **1993**, *85*, 441. (b) Bergner, A.; Dolg, M.; Küchle, W.; Stoll, H.; Preuss, H. *Mol. Phys*. **1993**, *80,* 1431.

(310)   (a) Barone, V.; Cossi, M. *J. Phys. Chem. A* **1998**, *102*, 1995. (b) Cossi, M.; Rega, N.; Scalmani, G.; Barone, V. *J. Comput. Chem*. **2003**, *24*, 669.

(311)   Santoro, F.; Althaus, M.; Bonaccorsi, C.; Gischig, S.; Mezzetti, A. *Organometallics* **2008**, *27,* 3866.

Crystallographic Data

Compound	**137**	**138**	**139**
Empirical Formula	$C_{14}H_9Fe_2O_7PS_2$	$C_{31}H_{24}Fe_2O_6P_2S_2$ $\cdot CH_2Cl_2$	$C_{19}H_{24}Fe_2O_9P_2S_2$
Internal No.	fo4259	fo4516	fo4659
Formula Weight [g·mol^{-1}]	496.00	815.19	634.14
T [K]	133(2)	293(2)	133(2)
Crystal System	triclinic	monoclinic	triclinic
Space Group	$P\bar{1}$	$C2/c$	$P\bar{1}$
a [Å]	7.3196(4)	68.8713(17)	7.6319(5)
b [Å]	9.2393(4)	13.5987(4)	11.2407(7)
c [Å]	13.5606(4)	22.0300(6)	16.2017(11)
α [°]	101.279(3)	90	86.524(4)
β [°]	90.192(3)	100.563(1)	83.504(3)
γ [°]	93.730(2)	90	70.792(3)
V [Å^3]	897.34(7)	20282.8(10)	1303.70(15)
Z	2	24	2
ρ [g·cm^{-3}]	1.836	1.602	1.615
μ [mm^{-1}]	1.972	1.278	1.441
$F(000)$	496	9936	648
Crystal size [mm]	0.05×0.05×0.04	0.052×0.048×0.034	0.046×0.045×0.034
Θ range for data collection [°]	2.96-27.44	1.76-27.52	2.87-27.50
Limiting indices	$-8 \leq h \leq 9$ $-11 \leq k \leq 11$ $-17 \leq l \leq 13$	$-80 \leq h \leq 80$ $-14 \leq k \leq 15$ $-25 \leq l \leq 25$	$-9 \leq h \leq 9$ $-11 \leq k \leq 14$ $-20 \leq l \leq 18$
Reflections collected	5939	62336	6733
Independent reflections / R_{int}	4023 / 0.0282	17115 / 0.0540	5139 / 0.0289
Data / restraints / parameters	3607 / 0 / 235	13772 / 0 / 1246	5139 / 0 / 310
s^a	1.130	1.143	1.131
R_1 $(I > 2\sigma(I))^b$	0.0547	0.0990	0.0666
wR_2 (all Data, on F^2)^b	0.1395	0.2429	0.1703
Largest difference peak and hole [e·Å^{-3}]	1.039 / -0.560	2.910 / -1.703	0.911 / -1.486

[a] $s = \{\Sigma[w(F_o{}^2-F_c{}^2)^2]/(N_o-N_p)\}^{1/2}$. [b] Definition of the R indices: $R_1 = (\Sigma||F_o|-|F_c||)/\Sigma|F_o|$; $wR_2 = \{\Sigma[w(F_o{}^2-F_c{}^2)^2]/\Sigma[w(F_o{}^2)^2]\}^{1/2}$ with $w^{-1} = \sigma^2(F_o{}^2) + (aP)^2$.

Compound	**144**	**145**	**(ClCH$_2$)$_2$PhP=O**
Empirical Formula	C$_{10}$H$_9$Fe$_2$O$_7$PS$_2$	C$_{14}$H$_9$BF$_3$Fe$_2$O$_7$PS$_2$	C$_8$H$_9$Cl$_2$OP
Internal No.	fo4371	fo5038	fo4440
Formula Weight [g·mol^{-1}]	447.96	563.81	223.02
T [K]	133(2)	133(2)	133(2)
Crystal System	triclinic	monoclinic	monoclinic
Space Group	$P\bar{1}$	$P2_1/n$	$P2_1/c$
a [Å]	6.96040(10)	7.6033(3)	12.7410(4)
b [Å]	15.2584(2)	10.6223(4)	7.3835(2)
c [Å]	15.7650(3)	24.5954(9)	10.5054(3)
α [°]	89.156(1)	90	90
β [°]	80.380(1)	95.477(2)	102.665(2)
γ [°]	81.445(1)	90	90
V [Å^3]	1632.32(4)	1977.37(13)	964.23(5)
Z	4	4	4
ρ [g·cm^{-3}]	1.823	1.894	1.536
μ [mm^{-1}]	2.157	1.822	0.787
$F(000)$	896	1120	456
Crystal size [mm]	0.06×0.06×0.06	0.09×0.04×0.02	0.06×0.05×0.03
Θ range for data collection [°]	2.96-27.44	2.54-27.45	3.21-27.49
Limiting indices	$-9 \leq h \leq 7$ $-19 \leq k \leq 19$ $-19 \leq l \leq 19$	$-9 \leq h \leq 9$ $-13 \leq k \leq 13$ $-31 \leq l \leq 28$	$-16 \leq h \leq 15$ $-9 \leq k \leq 9$ $-13 \leq l \leq 13$
Reflections collected	11003	11398	6073
Independent reflections / R_{int}	7346 / 0.0234	4419 / 0.0341	2206 / 0.0244
Data / restraints / parameters	7346 / 0 / 399	4419 / 0 / 307	2206 / 0 / 109
s^a	1.042	1.207	1.221
R_1 $(I > 2\sigma(I))^b$	0.0380	0.0402	0.0645
wR_2 (all Data, on F^2)^b	0.0825	0.0812	0.2216
Largest difference peak and hole [e·Å^{-3}]	0.443 / -0.403	0.549 / -0.414	1.071 / -0.676

^{a} $s = \{\Sigma[w(F_o^2-F_c^2)^2]/(N_o-N_p)\}^{1/2}$. ^{b} Definition of the R indices: $R_1 = (\Sigma ||F_o|-|F_c||)/\Sigma|F_o|$; w$R_2 = \{\Sigma[w(F_o^2-F_c^2)^2]/\Sigma[w(F_o^2)^2]\}^{1/2}$ with $w^{-1} = \sigma^2(F_o^2) + (aP)^2$.

Compound	**149**	**150**	**151**
Empirical Formula	$C_8H_9Cl_2OP$	$C_{10}H_{10}Fe_2GeO_6S_2$	$C_{10}H_{10}Fe_2SnO_6S_2$
Internal No.	RT167	fo5092	fo4583
Formula Weight [g·mol^{-1}]	698.30	474.59	520.69
T [K]	170	133(2)	133(2)
Crystal System	triclinic	triclinic	triclinic
Space Group	$P\bar{1}$	$P\bar{1}$	$P\bar{1}$
a [Å]	10.1210(4)	9.0682(2)	9.1219(2)
b [Å]	10.1719(4)	9.7623(3)	9.8783(3)
c [Å]	16.8954(7)	10.3493(3)	10.3369(3)
α [°]	77.385(3)	62.871(1)	63.175
β [°]	73.793(4)	83.374(2)	83.661(2)
γ [°]	62.984(4)	88.509(1)	87.631(2)
V [Å^3]	1479.44(324)	809.58(4)	826.09(4)
Z	2	2	2
ρ [g·cm^{-3}]	1.568	1.947	2.093
μ [mm^{-1}]	1.224	3.889	3.503
$F(000)$		468	504
Crystal size [mm]	0.35×0.17×0.05	0.06×0.06×0.05	0.05×0.05×0.04
Θ range for data collection [°]	3.08-28.28	3.21-27.48	2.22-27.47
Limiting indices	$-13 \leq h \leq 13$ $-13 \leq k \leq 13$ $-21 \leq l \leq 22$	$-11 \leq h \leq 11$ $-12 \leq k \leq 11$ $-13 \leq l \leq 13$	$-11 \leq h \leq 11$ $-10 \leq k \leq 12$ $-11 \leq l \leq 13$
Reflections collected	7261	5247	5188
Independent reflections / R_{int}	4613	3625 / 0.0176	3741 / 0.0159
Data / restraints / parameters		3625 / 0 / 230	3741 / 0 / 192
s^a	0.939	1.068	1.117
R_1 $(I > 2\sigma(I))^b$	0.0751	0.0244	0.0260
wR_2 (all Data, on F^2)^b	0.1042	0.0556	0.0587
Largest difference peak and hole [e·Å^{-3}]	0.449 / -0.304	1.206 / -0.603	0.468 / -0.424

[a] $s = \{\Sigma[w(F_o^2-F_c^2)^2]/(N_o-N_p)\}^{1/2}$. [b] Definition of the R indices: $R_1 = (\Sigma||F_o|-|F_c||)/\Sigma|F_o|$; $wR_2 = \{\Sigma[w(F_o^2-F_c^2)^2]/\Sigma[w(F_o^2)^2]\}^{1/2}$ with $w^{-1} = \sigma^2(F_o^2) + (aP)^2$.

Compound	**152**	**153**	**154**
Empirical Formula	$C_{20}H_{20}Fe_4Sn_2O_{12}S_4$	$C_{20}H_{14}Fe_2SnO_6S_2$	$C_{40}H_{28}Fe_4Sn_2O_{12}S_4$
Internal No.	fo4544	fo4733	Fo5474
Formula Weight [g·mol^{-1}]	1041.38	644.82	1289.64
T [K]	133(2)	133(2)	133(2)
Crystal System	monoclinic	monoclinic	triclinic
Space Group	$P2_1/n$	$P2_1/n$	$P\bar{1}$
a [Å]	13.1549(2)	13.6259(3)	8.6642(2)
b [Å]	13.4408(2)	11.1499(2)	11.8378(3)
c [Å]	18.6019(4)	15.6755(4)	13.0867(3)
α [°]	90	90	116.501(1)
β [°]	90.483(1)	100.473(1)	104.012(1)
γ [°]	90	90	95.472(2)
V [Å^3]	3288.93(10)	2341.86(9)	1133.03(5)
Z	4	4	1
ρ [g·cm^{-3}]	2.103	1.829	1.890
μ [mm^{-1}]	3.520	2.492	2.575
$F(000)$	2016	1264	632
Crystal size [mm]	0.06×0.05×0.02	0.06×0.05×0.05	0.048×0.022×0.018
Θ range for data collection [°]	3.07-27.49	3.04-27.47	1.94-27.48
Limiting indices	$-13 \leq h \leq 17$ $-17 \leq k \leq 17$ $-24 \leq l \leq 24$	$-16 \leq h \leq 17$ $-14 \leq k \leq 14$ $-18 \leq l \leq 20$	$-10 \leq h \leq 11$ $-11 \leq k \leq 15$ $-16 \leq l \leq 16$
Reflections collected	19757	13574	7028
Independent reflections / R_{int}	7530 / 0.0295	5351 / 0.0422	5117 / 0.0175
Data / restraints / parameters	7530 / 0 / 383	5351 / 0 / 280	5117 / 0 / 336
s[a]	1.212	1.083	1.090
R_1 $(I > 2\sigma(I))$[b]	0.0271	0.0365	0.0262
wR_2 (all Data, on F^2)[b]	0.0561	0.0713	0.0601
Largest difference peak and hole [e·Å^{-3}]	0.737 / -0.599	0.531 / -0.483	0.601 / -0.594

[a] $s = \{\Sigma[w(F_o^2-F_c^2)^2]/(N_o-N_p)\}^{1/2}$. [b] Definition of the R indices: $R_1 = (\Sigma||F_o|-|F_c||)/\Sigma|F_o|$; w$R_2 = \{\Sigma[w(F_o^2-F_c^2)^2]/\Sigma[w(F_o^2)^2]\}^{1/2}$ with $w^{-1} = \sigma^2(F_o^2) + (aP)^2$.

Compound	**155**
Empirical Formula	$C_{23.50}H_{23.50}BrCl_{1.50}NNiPS_2$
Internal No.	fo4125
Formula Weight [g·mol^{-1}]	606.82
T [K]	133(2)
Crystal System	triclinic
Space Group	$P\bar{1}$
a [Å]	9.7584(3)
b [Å]	10.0211(3)
c [Å]	14.3727(8)
α [°]	90.649(3)
β [°]	90.640(3)
γ [°]	117.266(3)
V [Å^3]	1249.05(9)
Z	2
ρ [g·cm^{-3}]	1.613
μ [mm^{-1}]	2.781
$F(000)$	614
Crystal size [mm]	0.05×0.05×0.04
Θ range for data collection [°]	2.72-27.51
Limiting indices	$-12 \leq h \leq 12$ $-13 \leq k \leq 12$ $-18 \leq l \leq 14$
Reflections collected	7815
Independent reflections / R_{int}	5599 / 0.0198
Data / restraints / parameters	5599 / 0 / 298
s^a	1.042
$R_1\ (I > 2\sigma(I))^b$	0.0446
wR_2 (all Data, on F^2)^b	0.1060
Largest difference peak and hole [e·Å^{-3}]	1.217 / -1.261

[a] $s = \{\Sigma[w(F_o^2-F_c^2)^2]/(N_o-N_p)\}^{1/2}$. [b] Definition of the R indices: $R_1 = (\Sigma||F_o|-|F_c||)/\Sigma|F_o|$; w$R_2 = \{\Sigma[w(F_o^2-F_c^2)^2]/\Sigma[w(F_o^2)^2]\}^{1/2}$ with $w^{-1} = \sigma^2(F_o^2) + (aP)^2$.

Compound	**156**	**158**	**159**
Formula	$C_{23}H_{23}ClNPPdS\cdot$ $0.5CHCl_3$	$C_{28}H_{31}N_2PPtS\cdot$ $0.25C_5H_{10}\cdot2CH_2Cl_2$	$[C_{31}H_{32}NP_2PdS_2]^+$ Cl^- $\cdot CHCl_3\cdot1.33H_2O$
Formula Weight [g·mol^{-1}]	610.05	937.74	829.73
T [°C]	-140(2)	-90(2)	-140(2)
Crystal system	triclinic	triclinic	monoclinic
Space group	$P\bar{1}$	$P\bar{1}$	$P2_1/n$
a [Å]	9.5519(2)	9.3394(4)	32.5310(6)
b [Å]	10.0336(3)	14.9178(8)	12.7723(2)
c [Å]	14.5244(4)	15.6487(9)	34.4507(4)
α [°]	88.728(2)	116.102(3)	90
β [°]	87.543(2)	95.682(3)	97.888(1)
γ [°]	63.202(3)	98.091(3)	90
V [Å^3]	1241.37(6)	1906.36(17)	14178.7(4)
Z	2	2	16
ρ [g·cm^{-3}]	1.632	1.634	1.555
μ [cm^{-1}]	12.62	42.46	10.62
Measured data	10849	13492	56100
Data with $I > 2\sigma(I)$	5214	6637	15372
Unique data / R_{int}	5619 / 0.2190	8638 / 0.0501	25707 / 0.0973
wR_2 (all data, on F^2)[a]	0.1820	0.1247	0.2250
R_1 ($I > 2\sigma(I)$)[a]	0.0673	0.0514	0.0731
s[b]	1.012	1.039	1.053
Res. dens./e·Å^{-3}	1.651 / -2.336	1.138 / -2.358	1.919 / -1.427
Absorption method	NONE	NONE	NONE
CCDC No.	877671	806387	806388

[a] Definition of the R indices: $R_1 = (\Sigma||F_o|-|F_c||)/\Sigma|F_o|$; $wR_2 = \{\Sigma[w(F_o^2-F_c^2)^2]/\Sigma[w(F_o^2)^2]\}^{1/2}$ with $w^{-1} = \sigma^2(F_o^2) + (aP)^2$. [b] $s = \{\Sigma[w(F_o^2-F_c^2)^2]/(N_o-N_p)\}^{1/2}$.

.

Compound	161	162	163
Empirical Formula	$C_{21}H_{21}BrNPSSe$	$C_6H_{12}N_2S_2Se_2$	$C_{39}H_{36}F_6NNiP_3S_{0.5}Se_{1.50}$
Internal No.	fo4520	fo4518	fo5054
Formula Weight [g·mol^{-1}]	568.00	334.22	918.78
T [K]	133(2)	133(2)	133(2)
Crystal System	triclinic	monoclinic	orthrombic
Space Group	$P\bar{1}$	$C2/c$	Pbca
a [Å]	14.6863(3)	14.3130(13)	21.3735(2)
b [Å]	18.4671(3)	7.0659(11)	16.0891(2)
c [Å]	27.1139(5)	12.7870(16)	21.7752(3)
α [°]	80.780(1)	90	90
β [°]	86.577(1)	123.027(4)	90
γ [°]	66.882(1)	90	90
V [Å^3]	6675.7(2)	1084.2(2)	7488.06(16)
Z	12	4	8
ρ [g·cm^{-3}]	1.695	2.047	1.630
μ [mm^{-1}]	4.475	7.157	2.193
$F(000)$	3384	648	3704
Crystal size [mm]	0.06×0.05×0.05	0.05×0.05×0.04	0.08×0.06×0.06
Θ range for data collection [°]	1.80-27.49	3.80-27.56	2.29-26.37
Limiting indices	$-19 \leq h \leq 12$ $-23 \leq k \leq 23$ $-35 \leq l \leq 35$	$-18 \leq h \leq 18$ $-9 \leq k \leq 8$ $-15 \leq l \leq 16$	$-26 \leq h \leq 26$ $-20 \leq k \leq 19$ $-27 \leq l \leq 25$
Reflections collected	42098	3082	39991
Independent reflections / R_{int}	29579 / 0.0275	1226 / 0.0481	7643 / 0.0651
Data / restraints / parameters	29579 / 0 / 1471	1226 / 0 / 57	7643 / 0 / 481
s^a	1.094	1.134	1.074
R_1 $(I > 2\sigma(I))^b$	0.0779	0.0507	0.0680
wR_2 (all Data, on F^2)^b	0.2311	0.1444	0.2046
Largest difference peak and hole [e·Å^{-3}]	2.982 / -1.395	1.129 / -0.964	1.561 / -2.940

[a] $s = \{\Sigma[w(F_o^2-F_c^2)^2]/(N_o-N_p)\}^{1/2}$. [b] Definition of the R indices: $R_1 = (\Sigma ||F_o|-|F_c||)/\Sigma|F_o|$; $wR_2 = \{\Sigma[w(F_o^2-F_c^2)^2]/\Sigma[w(F_o^2)^2]\}^{1/2}$ with $w^{-1} = \sigma^2(F_o^2) + (aP)^2$.

Compound	**163**
Empirical Formula	$C_{39}H_{36}F_6NNiP_3S_{0.5}Se_{1.50}$
Internal No.	fo5054
Formula Weight [g·mol^{-1}]	918.78
T [K]	133(2)
Crystal System	orthrombic
Space Group	Pbca
a [Å]	21.3735(2)
b [Å]	16.0891(2)
c [Å]	21.7752(3)
α [°]	90
β [°]	90
γ [°]	90
V [Å^3]	7488.06(16)
Z	8
ρ [g·cm^{-3}]	1.630
μ [mm^{-1}]	2.193
$F(000)$	3704
Crystal size [mm]	0.08×0.06×0.06
Θ range for data collection [°]	2.29-26.37
Limiting indices	$-26 \leq h \leq 26$ $-20 \leq k \leq 19$ $-27 \leq l \leq 25$
Reflections collected	39991
Independent reflections / R_{int}	7643 / 0.0651
Data / restraints / parameters	7643 / 0 / 481
s[a]	1.074
$R_1 (I > 2\sigma(I))$[b]	0.0680
wR_2 (all Data, on F^2)[b]	0.2046
Largest difference peak and hole [e·Å^{-3}]	1.561 / -2.940

[a] $s = \{\Sigma[w(F_o^2-F_c^2)^2]/(N_o-N_p)\}^{1/2}$. [b] Definition of the R indices: $R_1 = (\Sigma||F_o|-|F_c||)/\Sigma|F_o|$; w$R_2 = \{\Sigma[w(F_o^2-F_c^2)^2]/\Sigma[w(F_o^2)^2]\}^{1/2}$ with $w^{-1} = \sigma^2(F_o^2) + (aP)^2$.

Acknowledgements

Thanks to individuals (technicians, co-workers, craftsmen and electricians) of the IAAC institute, especially everyone who measured NMR, IR and MS spectra and performed elemental analyses of my compounds.

During the time I spent at Friedrich-Schiller-Universität (FSU) Jena, I was fortunate to interact with many great individuals of the workgroup of Prof. Wolfgand Weigand (actual and former members, especially Karin Landrock) that provided a good working atmosphere. It was always very beautiful to celebrate together Christmas parties and to make some days of holiday in Singen and Bad Kösen. Special thanks to Ralf Trautwein for the German translation of the summary of this thesis.

Not to forget Heike Müller, who was a very nice and friendly person. She helped me always when I asked her. May her soul rest in peace.

I thank the Deutscher Akademischer Austausch Dienst (DAAD) for scholarship. Moreover, I thank the DAAD to give me an opportunity to study German language for six months at the interDaF e.V institute, Leipzig that helped me to intergrate in the German society. Special thanks to Ms. Birgit Klaes for advising and helping me every time I contacted her.

Last but not least, I would like to thank my whole family. Without their encouragement, guidance and emotional support, none of this would have been possible. Special thanks to my aunt Nabiha Amareen. May her soul rest in peace. Thomas Uwe Steinbrück, you are not forgotten. I also consider you and your parents as members of my family. Thanks to Thomas Uwe Steinbrück for being a great friend. I thank him for showing me many cultural and historical places (castles, museums, etc…) in Thuringia and other parts of Germany, which helped me to integrate in the German culture. I thank his parents for inviting me every Christmas and every Easter to their home in Sondershausen and for cooking delicious Thuringian food.

Curriculum Vitae

Name:	Laith Raja Almazahreh
Date of birth:	10. Dec. 1981
Place of Birth:	Amman / Jordan
Marital Status:	Single

Education

Since Oct.2009	Friedrich-Schiller-Universität Jena
	Ph.D. Thesis "Models for the H Cluster of the [FeFe]-Hydrogenase: Synthesis, Protonation and Electrochemical Investigations"
Sep. 2004-May. 2007	Jordan University of Science and Technology
	M.Sc. Thesis "Kinetics and Mechanism of Ligand-Substitution Reactions in (2,6-diaminopyridine)$[M(CO)_5]_2$ (M = W, Mo, Cr)"
Sep. 1999-Aug. 2003	Jordan University of Science and Technology
	B.Sc. in Applied Chemistry

Experiences

Sep. 2013-Apr. 2015	Scientific Employee at the Friedrich-Schiller-University Jena in the Institute of Inorganic and Analytical Chemistry in the Research Group of Prof. Weigand; Assistance of Lab Classes and Research Students
Nov. 2012 and Jun. 2013	Guest Researcher at the Université de Bretagne Occidentale-Brest / France
Sep.- Oct. 2012	Guest Researcher at the University of Lodz / Poland
Jan. 2008-Mar. 2009	Analyst at the Environmental Research Center of the Royal Scientific Society-Amman / Jordan
2004/2005-2005/2007	Lecturer at Jordan University of Science and Technology-Irbid / Jordan
Oct. 2003-May. 2004	Analyst of Bio-samples at the International Pharmaceutical Research Center-Amman / Jordan

Conferences

07. Mar. 2013	Presentation: "Novel [FeFe]-Hydrogenase Models with $(SCH_2)_2P=O$ Linker" in the conference "15th JCF-Frühjahrssymposium" at Humboldt-Universität-Berlin / Germany
10-14. Oct. 2012	Presentation: "Synthetic and Structural Investigations of Novel Monomeric and Macrocyclic [FeFe(Sn)]-Hydrogenase Models" in the conference "Lodz-Giessen Chemistry Workshop" at the University of Lodz-Lodz / Poland
20. Sep. 2012	Presentation: Synthetic and Structural Investigations of Novel Monomeric and Macrocyclic [FeFe(Sn)]-Hydrogenase Complexes" in the conference "10. Mitteldeutsches Anorganiker-Nachwuchs-Symposium" at Friedrich-Schiller-Universität Jena-Jena / Germany
May. 2007	Presentation: "Kinetics and Mechanism of Ligand-Substitution Reactions in (2,6-diaminopyridine)$[M(CO)_5]_2$ (M = W, Mo, Cr)" in the conference "Jordanian Day For Chemical Achievements" at Jordan University of Science and Technology-Irbid / Jordan

Awards

May. 2007	Best talk in the conference "Jordanian Day For Chemical Achievements" at Jordan University of Science and Technology-Irbid / Jordan
22. Jul. 2007	Honoring certificate for getting the 1st rank among the M.Sc. graduates of chemistry

Language Proficiency

Arabic (native language)

English

German

Jena,   …………………………

                                               Laith Almazahreh

List of Publications

1. **A Novel [FeFe] Hydrogenase Model with a (SCH₂)₂P=O Moiety:** <u>Almazahreh, L. R.</u>; Apfel, U. -P.; Imhof, W.; Rudolph, M.; Görls, H.; Talarmin, J.; Schollhammer, P.; El-khateeb, M.; Weigand, W. *Organometallics*, **2013**, *32*, 4523-4530.

2. **The Influence of OH Groups in [Fe(CO)₃]₂[(μ-ECH₂)₂C(CH₂OH)₂] (E = S, Se) Complexes toward the Cathodic Process:** Trautwein, R.; <u>Almazahreh, L. R.</u>; Görls, H.; Weigand. W. *Z. Anorg. Allg. Chem.*, **2013**, *639 (8-9)*, 1512-1519.

3. **Synthesis and Characterization of Platinum and Palladium Pyrrolidinedithiocarbamate Complexes:** <u>Almazahreh, L.</u>; El-khateeb, M.; Harb, M.; Görls, H.; Weigand, W. *Transition Met Chem*, **2013**, *38*, 377-383.

4. **Ligand Effects on the Electrochemical Behavior of [Fe₂(CO)₅(L){μ-(SCH₂)₂(Ph)P=O}] (L = PPh₃, P(OEt)₃) Hydrogenase Model Complexes:** <u>Almazahreh, L.</u>; Imhof, W.; Talarmin, J.; Schollhammer, P.; Görls, H.; El-khateeb, M. Y.; Weigand W. *Dalton Trans.*, **2015**, *44*, 7177-7189.

5. **Kinetics and Mechanism of Ligand Substitution Reactions of (2,6-diaminopyridine)[M(CO)₅]₂ (M = Cr, Mo, W):** Asali, K. J.; El-khateeb, M.; <u>Almazahreh, L</u>. *Transition Met Chem*, **2015**, DOI: 10.1007/s11243-015-9936-z.

Documentation of Authorship

Chapter 2: A Novel [FeFe]-Hydrogenase Model with (SCH₂)₂P=O Moiety (Published Work)

Laith R. Almazahreh, Ulf-Peter Apfel, Wolfgang Imhof, Manfred Rudolph, Helmar Görls, Jean Talarmin, Philippe Schollhammer, Mohammad El-khateeb, Wolfgand Weigand, *Organometallics*, **2013**, *32*, 4523-4530.

- **Almazahreh, L. R.** Syntheses of all compounds; Manuscript writing and preparation; Protonation studies and part of the electrochemical measurements.
- **Apfel, U. -P.:** Manuscript revision.
- **Imhof, W.:** DFT calculations.
- **Rudolph, M.:** Part of the electrochemical measurements.
- **Görls, H.:** Crystal structure Analyses.
- **Talarmin, J.:** Manuscript revision. Part of the electrochemical experiments was done by me under his supervision.
- **Schollhammer, P.:** Manuscript revision. The protonation experiments were done by me under his supervision.
- **El-khateeb, M.:** Manuscript revision. My co-advisor.
- **Weigand, W.:** Supervision.

Chapter 3: Ligand Effects on the Electrochemical Behavior of [Fe₂(CO)₅(L){µ-(SCH₂)₂(Ph)P=O}] (L = PPh₃, P(OEt)₃) Hydrogenase Model Complexes (Published work)

- Laith R. Almazahreh, Wolfgang Imhof, Jean Talarmin, Philippe Schollhammer, Helmar Görls, Mohammad El-khateeb, Wolfgang Weigand. *Dalton Trans*, **2015**, *Dalton Trans.*, **2015**, *44*, 7177-7189.

- **Almazahreh, L. R.:** Syntheses of all compounds; Manuscript writing and preparation; Electrochemical measurements.

- **Imhof, W.:** DFT calculations.

- **Görls, H.:** Crystal structure Analyses.

- **Talarmin, J.:** Manuscript revision and supervision.

- **Schollhammer, P.:** Manuscript revision and supervision.

- **El-khateeb, M.:** Manuscript revision. My co-advisor.

- **Weigand, W.:** Supervision.

Chapter 4: Mechanisms of Proton Reduction Catalyzed by [Fe$_2$(CO)$_6${μ-(SCH$_2$)$_2$(R)P=O}] (R = Ph, Et) Models

Laith R. Almazahreh, Jean Talarmin, Philippe Schollhammer, Catherine Elleouet, Helmar Görls, Federica Arrigoni, Luca Bertini, Luca De Gioia, Giuseppe Zampella, Mohammad El-khateeb, Wolfgang Weigand.

- **Almazahreh, L. R.** Syntheses of all compounds; Electrochemical measurements and evaluation; Manuscript writing and preparation.

- **Talarmin, J.:** Manuscript revision and supervision.

- **Schollhammer, P.:** Manuscript revision and supervision.

- **Elleouet, C.:** Part of the electrochemical measurements.

- **Görls, H.:** Crystal structure Analyses.

- **Arrigoni, F.; Bertini, L.; De Gioia, L.; Zampella, G.:** DFT calculations.

- **El-khateeb, M.:** Manuscript revision. My co-advisor.

- **Weigand, W.:** Supervision.

Chapter 5: Effect of the CH$_2$OH Bridgehead groups and the Bulky PPh$_3$ Ligand in [Fe$_2$(CO)$_5$L{μ-(ECH$_2$)$_2$C(CH$_2$OH)$_2$}] (E = S or Se and L = CO or PPh$_3$) Complexes toward the Cathodic Process

Part of this chapter is published **"The Influence of OH Groups in [Fe(CO)$_3$]$_2$[(μ-ECH$_2$)$_2$C(CH$_2$OH)$_2$] (E = S, Se) Complexes toward the Cathodic Process"**: Ralf

Trautwein, Laith R. Almazahreh, Helmar Görls, Wolfgang Weigand. *Z. Anorg. Allg. Chem.*, **2013**, *639 (8-9)*, 1512-1519.

- **Almazahreh, L. R.:** Electrochemical measurements and evaluation; Manuscript writing and preparation.
- **Trautwein, R.:** Syntheses of all compounds; Electrochemical measurements, Manuscript preparation.
- **Görls, H.:** Crystal structure Analyses.
- **Weigand, W.:** Supervision.

The authors of the unpublished part, which is related to the chemistry of complex **149**, are: Laith R. Almazahreh, Ralf Trautwein, Catherine Elleouet, Jean Talarmin, Philippe Schollhammer, Wolfgang Weigand.

- **Almazahreh, L. R.:** Crystallization of compound **149**; Crystal structure determination under the supervision of Dr. F. Michaud (X-ray department of UBO); Electrochemical measurements and evaluation; Manuscript writing and preparation.
- **Trautwein, R.:** Synthesis of compound **149**.
- **Elleouet, C.:** Part of the electrochemical measurements on compound **147**.
- **Talarmin, J.; Schollhammer, P. and Weigand, W.:** Supervision.

Chapter 6: A Novel [FeFe]-Hydrogenase Model with a μ-(SCH$_2$)$_2$GeMe$_2$ Moiety

Laith R. Almazahreh, Helmar Görls, Jean Talarmin, Philippe Schollhammer, Mohammad El-khateeb, G. Mloston, Wolfgang Weigand.

- **Almazahreh, L. R.** Syntheses of all compounds; Electrochemical measurements and evaluation; Manuscript writing and preparation.
- **Talarmin, J.; Schollhammer, P.; El-khateeb, M.; Mloston, G. and Weigand, W.:** supervision.

Chapter 7: **Monomeric and Dimeric Complexes Featuring Fe₂S₂(CO)₆ Clusters and *μ*-(SCH₂)₂SnR₂ Linkers**

Laith R. Almazahreh, Hassan Abul-Futouh, Helmar Görls, Richard S. Glass, Mohammad El-khateeb, Wolfgang Weigand.

- **Almazahreh, L. R.:** Syntheses of all compounds; Manuscript writing and preparation.
- **Abul-Futouh, H.:** Crystallization of compound **154**.
- **Görls, H.:** Crystal structure Analyses.
- **El-khateeb, M.; Glass R. S. and Weigand, W.:** Supervision.

Chapter 8: **Synthesis and Characterization of Ni^{II}, Pd^{II} and Pt^{II} Complexes Containing Carbamodithioato or Carbamoselenothioato Ligands**

Part of this chapter is published **"Synthesis and characterization of platinum and palladium pyrrolidinedithiocarbamate complexes":** Laith R. Almazahreh, Mohammad Harb, Helmar Görls, Mohammad El-khateeb, Wolfgang Weigand. *Transition Met. Chem.* **2013**, *38*, 377-383.

- **Almazahreh, L. R.:** Syntheses of all compounds; Manuscript preparation.
- **Harb, M.:** Manuscript preparation
- **Görls, H.:** Crystal structure Analyses.
- **El-khateeb, M. and Weigand, W.:** Supervision.

The authors of the unpublished part, which is related to the chemistry of complex **161**, are: Laith R. Almazahreh, Helmar Görls, Mohammad El-khateeb and Wolfgang Weigand.

- **Almazahreh, L. R.:** Syntheses of all compounds; Manuscript preparation.
- **Görls, H.:** Crystal structure Analyses.
- **El-khateeb, M.:** Co-advisor.
- **Weigand, W.:** Supervision.

Declaration of Authorship

I hereby declare that this thesis and the work presented herewith is my own and has been done by me as a result of my own original research.

I confirm that:

1. Where I have consulted the published work of others, this is always clearly attributed.
2. Where I have quoted from the work of others, the source is always given.
3. I have acknowledged all main sources of help.
4. Where the thesis is based on work done by myself jointly with others, I have made clear exactly what was done by others and what I have contributed myself.
5. Parts of this work have been published.

Selbstständigkeitserklärung

Ich erkläre, dass ich die vorliegende Arbeit selbständig und unter Verwendung der angegebenen Hilfsmittel, persönlichen Mitteilungen und Quellen angefertigt habe.

Jena,   …………………………………….

                                                          Laith Almazahreh